DOE/ER-0313/5

Fusion Reactor Materials

Semiannual Progress Report for Period Ending September 30, 1988

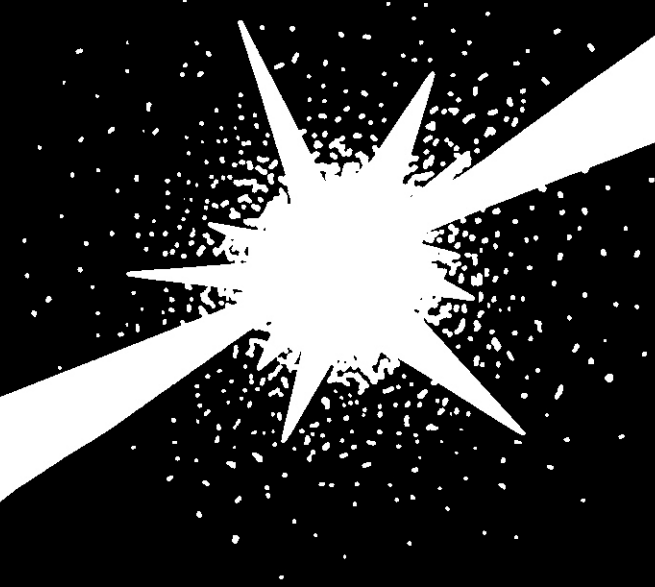

U. S. Department of Energy
Office of Fusion Energy

Printed in the United States of America Available from
National Technical Information Service
U S Department of Commerce
5285 Port Royal Road, Springfield. Virginia 22161
NTIS price codes—Printed Copy A-16Microfiche A01

DOE/ER-0313/5
Distribution
Categories
UC-423. -424

FUSION REACTOR MATERIALS SEMIANNUAL PROGRESS REPORT FOR THE PERIOD ENDING SEPTEMBER 30. 1988

Date Published: April 1989

Prepared for
DOE Office of Fusion Energy
(AT 15 02 00 0)

Prepared by
OAK RIDGE NATIONAL LABORATORY
Oak Ridge, Tennessee 37831-6285
operated by
MARTIN MARIETTA ENERGY SYSTEMS, INC.
for the
U.S. DEPARTMENT OF ENERGY
under Contract DE-AC05-840R21400

Reports previously listed in this series are as follows:

DOE/ER-0313/1	Period Ending September 30, 1986
DOE/ER-0313/2	Period Ending March 31, 1987
DOE/ER-0313/3	Period Ending September 30, 1987
DOE/ER-0313/4	Period Ending March 31, 1988

FOREWORD

This is the fifth in a series of semiannual technical progress reports on fusion reactor materials. This report combines research and development activities which were previously reported separately in the following technical progress reports:

- Alloy Development for Irradiation Performance
- Damage Analysis and Fundamental Studies
- Special Purpose Materials

These activities are concerned principally with the effects of the neutronic and chemical environment on the properties and performance of reactor materials; together they form one element of the overall materials program being conducted in support of the Magnetic Fusion Energy Program of the U.S. Department of Energy. The other major element of the program is concerned with the interactions between reactor materials and the plasma and is reported separately.

The Fusion Reactor Materials Program is a national effort involving several national laboratories, universities, and industries. The purpose of this series of reports is to provide a working technical record for the use of the program participants, and to provide a means of communicating the efforts of materials scientists to the rest of the fusion community, both nationally and worldwide.

This report has been compiled and edited under the guidance of A. F. Rowcliffe, Oak Ridge National Laboratory, and D. G. Doran, Battelle-Pacific Northwest Laboratory. Their efforts, the work of the publications staff in the Metals and Ceramics Division at ORNL, and the many persons who made technical contributions are gratefully acknowledged. T. C. Reuther, Reactor Technologies Branch, has responsibility within DOE for the programs reported on in this document.

R. Price, Chief
Reactor Technologies Branch
Office of Fusion Energy

TABLE OF CONTENTS

1. IRRADIATION FACILITIES, TEST MATRICES, AND EXPERIMENTAL METHODS

DESIGN AND FABRICATION OF HFIR-MFE RB* SPECTRALLY TAILORED IRRADIATION CAPSULES - A. W. Longest (Oak Ridge National Laboratory), J. E. Corum (Midwest Technical, Inc.), and O. W. Heatherly (Oak Ridge National Laboratory)

OBJECTIVE

The objective of this work is to design and fabricate irradiation capsules for testing magnetic fusion energy (MFE) first-wall materials in the High Flux Isotope Reactor (HFIR) removable heryllium (RB*) positions. Japanese and U.S. MFE specimens are being transferred to RB* positions following irradiation to 8 dpa at temperatures of 60, 200, 330, and 400°C in Oak Ridge Research Reactor (ORR) experiments ORR-MFE-6J and -7J.

SUMMARY

Design and fabrication of four HFIR-MFE RB* capsules (60, 200, 330, and 400°C) to accomnodate MFE specimens preirradiated in spectrally tailored experiments in the ORR are proceeding satisfactorily. These capsule designs incorporate provisions for removal. examination. and reencapsulation of the MFE specimens at intermediate exposure levels en route to a target exposure level of 30 displacements per atom (dpa). With the exception of the 60°C capsule, where the test specimens will be in direct contact with the reactor cooling water, the specimen temperatures (monitored by 21 thermocouples) will be controlled by varying the thermal conductance of a small gap region between the specimen holder and the containment tube. Hafnium sleeves will be used to tailor the neutron spectrum to closely match the helium production-to-atom displacement ratio (14 appm/dpa) expected in a fusion reactor first wall.

Assembly of the 60 and 330°C capsules is complete and irradiation of both will begin when the HFIR returns to full power operation. Preparation of fabrication drawings for the 200 and 400°C capsules is scheduled to be completed by the end of 1988. Fabrication of parts and assembly of the 200 and 400°C capsules are scheduled for completion by mid-FY 1990: operation of these two capsules will follow the first two (60 and 330°C).

PROGRESS AND STATUS

Introduction

A series of spectrally tailored irradiation capsules are being designed and fabricated as part of the U.S./Japan collaborative program for testing MFE first-wall materials in mixed-spectrum fission reactors. The test specimens will be irradiated in the new RB* facility[1] of the HFIR.

The first four HFIR-MFE RB* capsules are designed to accommodate Japanese and U.S. MFE specimens preirradiated to 8 dpa at temperatures of 60. 200, 330, and 400°C in the ORR spectrally tailored experiments ORR-MFE-6J and ORR-MFE-7J. Details of these ORR experiments, including descriptions of the test matrix, mechanical property specimens, and techniques of spectral tailoring, have been reported elsewhere.[2,3]

Spectral tailoring of the neutron flux to simulate in austenitic stainless steels the expected helium production-to-atom displacement ratio of 14 appmldpa in the fusion reactor first wall is accomplished by varying the amount of neutron moderator and thermal neutron ahsorber materials surrounding the capsule. This controls the two-step ^{58}Ni thermal neutron reaction producing helium, while fast neutrons are simultaneously producing atomic displacements. In general, the neutron energy spectrum must be hardened as the irradiation progresses: this requires ongoing neutronics analysis support as provided for the ORR experiments.[4]

The HFIR-MFE RB* capsules are designed for insertion into any of the eight large-diameter holes (46 mm) of the HFIR RR* facility. Damage rates will increase from about 4 dpalyear in the ORR experiments to B dpa/year in the HFIR RB* facility (based on 85-MW HFIR power).

Test specimen loadings for the first four capsules are given in Table 1. Beginning with return of the HFIR to full power in FY 1989, these capsules will be irradiated in pairs (first the 60 and 330°C capsules, then the 200 and 400°C capsules) to a damage level of 20 dpa. After these four irradiations, the test specimens will be removed, examined, and approximately one-half of them re-encapsulated for irradiation to 30 dpa.

Table 1. Test specimen loadings for the HFIR MFE RR* capsules

Specimen type	Number of specimens in capsule 60°C	200°C	330°C	400°C
Pressurized tube	38	26	45	39
Tube blank	9	9	9	9
Transmission electron microscope tuhe Length, mm				
16.5	2	2	0	0
19.1	0	0	4	4
25.4	5	7	6	6
SS-1 tensile	90	83	76	64
SS-3 tensile	54	54	15	15
Grodzinski fatigue	56	24	56	40
Crack growth	30	30	10	10
Rod tensile	0	0	4	0
Hourglass fatigue	0	0	0	5

60°C capsule. The 60°C capsule, designated HFIR-MFE-60J-1, will be uninstrumented with the test specimens in contact with the reactor coolant water. Predicted specimen temperatures are within ±10°C of 60°C.

Assemhly of the 60°C capsule and details of the specimen loading were described in the preceding progress report.[5] This capsule is in dry storage at the HFIR where it will remain until the reactor returns to power.

330°C capsule. The 330°C capsule design was described in detail previously.[6] A horizontal cross section through this capsule, designated HFIR-MFE-330-J-1, is shown in Fig. 1. This capsule will be cooled with 49°C reactor coolant water flowing downward over the containment tube surface. The specimen holder temperature (monitored by 21 type K thermocouples) will be controlled hy adjusting the composition of a flowing mixture of helium and neon in the control

ORNL-OWG-86-17330 (Rev. 1)

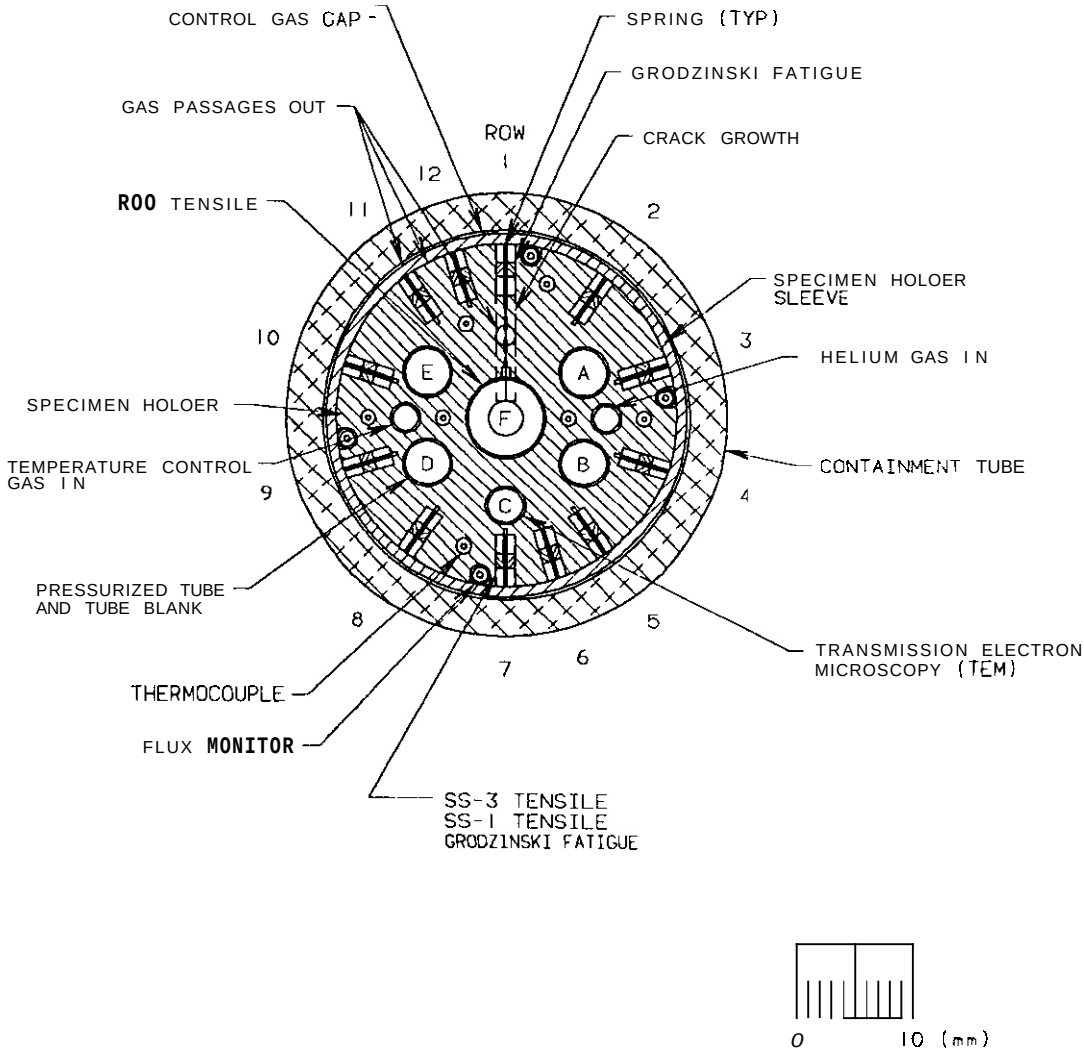

Fig. 1. Horizontal section through the HFIR-MFE-330-J1 capsule.

gas gap between the specimen holder sleeve and the containment tube. Calculated temperature distributions indicate that specimen temperatures will be within ±25°C of 330°C, which satisfies the temperature criterion for these experiments.

Assembly of the 330°C capsule has been completed, and the capsule has been placed in the HFIR pool where it will remain until the reactor returns to power. The radioactive test specimens were successfully loaded into the capsule in about two weeks. Special fixtures[6] developed for hot cell assembly and loading of the radioactive specimens were used as planned. Ttie specimen loading arrangement and the identification of the specimens in each position are given in Figs. 2 and 3, respectively.

200 and 400°C capsules. The 200 and 400°C capsule designs will be similar to the 330°C capsule. Thermal design analyses have been completed for both capsules. Preparation of fabrication drawings is scheduled to be completed by the end of 1988. Fabrication of parts and assembly of the capsules are scheduled for completion by mid-FY 1990. Operation of these two capsules will follow the first two (60 and 330°C).

As discussed in the preceding progress report,[5] the 200°C capsule presented a special design problem because it is difficult to remove the large amount of gama heat generated in the capsule while at the same time control operating temperature as low as 200°C. Of the several different design concepts under consideration at that time, the two leading ones were: (1) an aluminum alloy specimen holder with a conventional temperature control gas gap which would be only ~0.029 mm thick at operating temperature, and (2) use of a relatively large temperature control gas gap (~0.76 mm) filled with a binary (coarse/fine) mixture of metallic microspheres. In the latter concept, temperature would be controlled primarily by varying the inert gas pressure (and hence the mean free path of the gas molecules) in the particle bed to change its thermal conductance. The conventional temperature control gas gap design concept used for the 330 and 400°C capsules was also chosen for the 200°C capsule for the following two main reasons. First. this concept required little or no additional development. In view of the highly successful fabrication of the similar 330°C capsule specimen holder, we believe the tighter tolerances required for

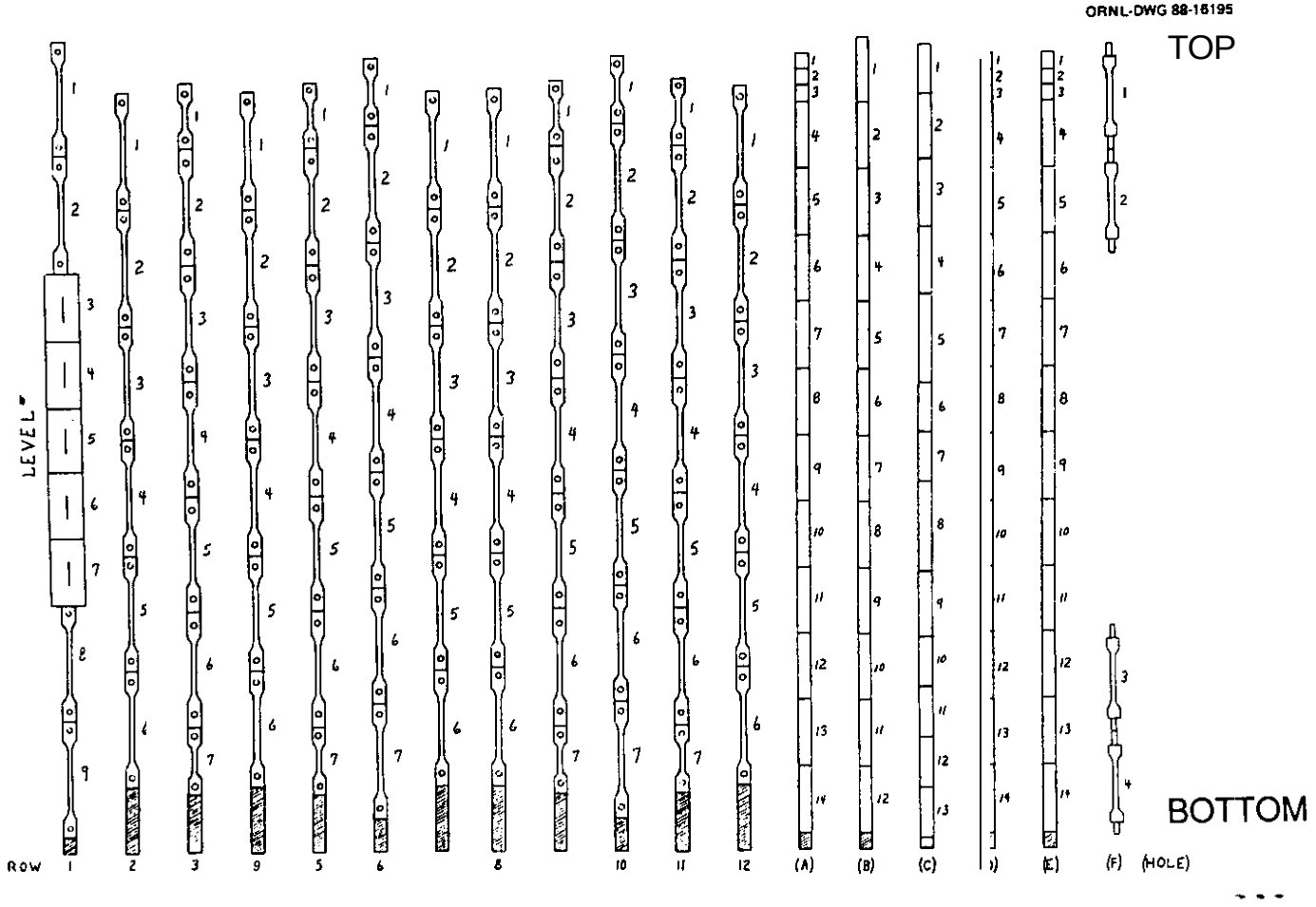

Fig. 2. Test specimen loading arrangement in HFIR-MFE-330-J1 capsule.

ORNL-DWG 88-16194

	Row 1	Row 2	Row 3	Row 4	Row 5	Row 6	Row 7	Row 8	Row 9	Row 10	Row 11	Row 12	Hole A	Hole B	Hole C	Hole D	Hole E	Hole F
Level 1	EL-13 CLW5	A01 A04	TN-12 TZ-14	FL-18 KL-2	TR-14 TT-13	DX-10 4X-08	FL-16 CL-13	F01 F02	TR-13 TU-14	TL-12 TF-13	TM-12 2L-08	EL-11 IL-1	SA1	C4B9	C	CA1	SXAX-1	TB-30
Level 2	GL-4 FL-23	S01 S03	GFB-11 GFA-10	CL-11 ML-2	GFD-13 GFC-5	HT-16 HW-17	DL-15 KL-1	T04 T05	GFB-5 GFA-6	FL-17 CL-18	GFD-6 GFC-11	FL-22 DLA-4	CC1	FA34	J-4	3S11-1	3S10-1	TB-31
Level 3	CGE-2 CGA-2	HX-02 HX-14	GFA-14 GFC-6	GL-3 ML-2	GFA-11 GFD-5	T07 F03	ML-1 CLW-6	B01 B04	GFB-6 GFD-11	CL-10 CL-16	GFB-9 GFC-12	DL-18 EL-9	CB1	SA09	J-6	PS11-1	FA-1	TE-29
Level 4	CGE-3 CGE-1	A03 A05	GFA-12 GFC-13	GL-1 ML-1	GFB-10 GFB-12	S02 A02	DLA-1 CL-12	C02 C03	GFB-14 GFD-10	DL-17 EL-4	GFA-8 GFD-8	DL-11 EL-8	3C03	C1C5	J-2	C4A6	C1A9	TE-32
Level 5	CG-A1 CG-F1	A06 A07	GFA-7 GFC-10	DL-10 EL-5	GFA-5 GFC-7	T02 T03	FL-19 DLA-3	S05 S06	GFA-9 GFA-13	GL-2 EL-6	GFD-14 GFC-9	DL-16 CL-15	C1C2	SA16	Spacer	S1A6	C5B3	
Level 6	CGB-2 CGB-1	T01 T06	GFC-8 GFC-14	B02 B03	GFB-7 GFD-9	C01 C04	DL-13 DL-14	S04 S07	GFB-8 GFD-7	DL-12 CL-14	GFB-13 GFD-12	CL-17 IL-2	3S06	C2C9	B	C4B5	SA38	
Level 7	CG-A3 CGF-2		TE-12 TZ-13		TP-12 TF-14	HU-11 HU-20			TU-13 TT-14	FL-20 FL-24	DL-13 4L-08		3S03	S1A2	JP-15	3C06	C581	
Level 8	EL-7 EL-12												FA19	FA08	Spacer	SA56	PS03	
Level 9	FL-21 DLA-2												FA33	FA28	J-5	C3C7	C3C3	
Level 10													C3B9	C4A1	JP-13	FA27	C3B3	
Level 11													S2A6	C4C9	JP-14	SA05	S1A7	
Level 12													C585	SA33	LF	C4A3	C3C8	
Level 13													S3A0		LE	SA01	S2A3	
Level 14													PS10			C1A0	C3A1	

Fig. 3. Test specimen identification in HFIR-MFE-33DJ-1 capsule

the 200°C capsule control gas gap can be met with only a small increase in fabrication cost. Second, an equipment (heater element) failure in an out-of-reactor test rig precluded further consideration of the binary microsphere gap concept for the 200°C capsule. At the time of the failure, sufficient data for evaluation of this concept had not been obtained and a spare test rig was not available. There are no current plans to resume development testing of this concept.

FUTURE WORK

Preparation of fabrication drawings for the 200 and 400°C HFIR-MFE RB* capsules is scheduled to be completed by the end of 1988. Preparation of fabrication drawings for reencapsulation of the MFE specimens after 20 dpa is scheduled to be completed in FY 1990. Fabrication of parts and assembly of the 200 and 400°C capsules will continue into FY 1990.

REFERENCES

1. K. R. Thoms et al., "HFIR Irradiation Facilities Improvements -- Completion of the HIFI Project," Proc. Third Intern. Conf. on Fusion Reactor Materials (Karlsruhe 1987): to he published in Journal of Nuclear Materials.

2. J. L. Scott et al., pp. 12–20 in ADIP Semiannual Progress Report for Period Ending March 31, 1985, DOE/ER-0045/14, U.S. DOE. Office of Fusion Energy.

3. J. L. Scott et al., Second Annual Progress Report on United States-Japan Collaborative Testing in the High Flux Isotope Reactor and the Oak Ridge Research Reactor for the Period Ending September 30, 1985, ORNL/TM-10102.

4. R. A. Lillie, pp. 36–38 in Fusion Reactor Materials Semiannual Progress Report for Period Ending September 30, 1986, DOE/ER-0313/1, U.S. DOE, Office of Fusion Energy.

5. A. W. Longest et al., "Design and Fabrication of HFIR-MFE RB* Spectrally Tailored Irradiation Capsules," Fusion Reactor Materials Semiannual Progress Report for Period Ending March 31, 1988, DOE/ER-0313/4, U.S. DOE, Office of Fusion Energy.

6. A. W. Longest et al., "Design and Fabrication of HFIR-MFE RR* Spectrally Tailored Irradiation Capsules," Fusion Reactor Materials Semiannual Progress Report, September 30, 1987, DOE/ER-0313/3, U.S. DOE, Office of Fusion Energy.

STATUS OF U.S./JAPAN COLLABORATIVE PROGRAM PHASE II HFIR TARGET CAPSULES — R. L. Senn (Oak Ridge National Laboratory)

OBJECTIVE

The objective of this program is to determine the response of various U.S. and Japanese austenitic and ferritic stainless steels with different pretreatments and alloy compositions to the combined effects of displacement damage and helium generation at temperatures in the range of 300 to 600°C and doses of 35, 55, and 100 dpa. Many advanced alloys and model alloys are being tested in the program including nickel-doped martensitic/ferritic steels (HT-9).

SUMMARY

The experiment matrix for the Phase II HFIR target capsules (JP-9 through -16) was refined by adding insulating spacers and adjusting the positions of certain specimens. Additional thermal analysis was required to account for these changes and to correct some discrepancies discovered in the earlier analyses. Selected parts required revision or remaking and are currently on order.

All specimen subassemblies were assembled during this period, although the SS-3 and Tensile Bar specimens were disassembled to incorporate the redesigned holders. These will be reassembled for installation into the various capsules as the parts become available.

As noted in previous reports, all eight capsules will be assembled and installed in the HFIR beginning with the first full power operating cycle.

PROGRESS AND STATUS

The program for U.S./Japan collaborative testing of the Phase II HFIR target capsules consists of eight capsules, JP-9 through -16. The mutually agreed upon revised matrix is shown in Fig. 1.

U.S./Japan Phase II HFIR Target Capsules

Introduction — All specimens were obtained and the specimen subassemblies were completed in preparation for final assembly into the various capsules. During loading of the capsules, it was noted that insulating spacers were not provided below the bottom specimens in JP-10, -11, and -14. This was corrected by adjusting the length of the spacer rings for the fatigue specimens in position 10 in JP-10 and -11 and adding a spacer at the bottom of each; and by moving the spacer previously shown between positions 7A and 7B in JP-14 and adding it to the bottom.

During recheck of the thermal calculations to examine the changes that might result from these small changes in elevation, it was discovered that some specimen materials used in the analyses were not correct, and further that an error was introduced regarding HT-9 material properties. These discoveries prompted a complete recalculation of the gas gaps required to achieve the design temperatures. New or revised parts have subsequently been ordered to accommodate these changes.

Experiment Matrix

The as-built Phase II experiment matrix is shown in Fig. 1. As previously reported, these experiments incorporate transmission-electron-microscopy (TEM), tensile bar (TB), hourglass fatigue (F), SS-3 sheet tensile [T(2) and T(4)], and welded sheet (SHEET) specimens. Specimen material, design specimen temperatures and the location of the various specimen holders are shown on the figure. The previously used position numbering system (from 1 at the top through 11 at the bottom) was modified by assigning positions 1A, 1B, etc. to the shorter specimens.

Thermal Analysis

As noted above, additional thermal analyses were completed. Detailed results from these calculations are shown in Tables 1 through 7 for capsules JP-9 through -16.

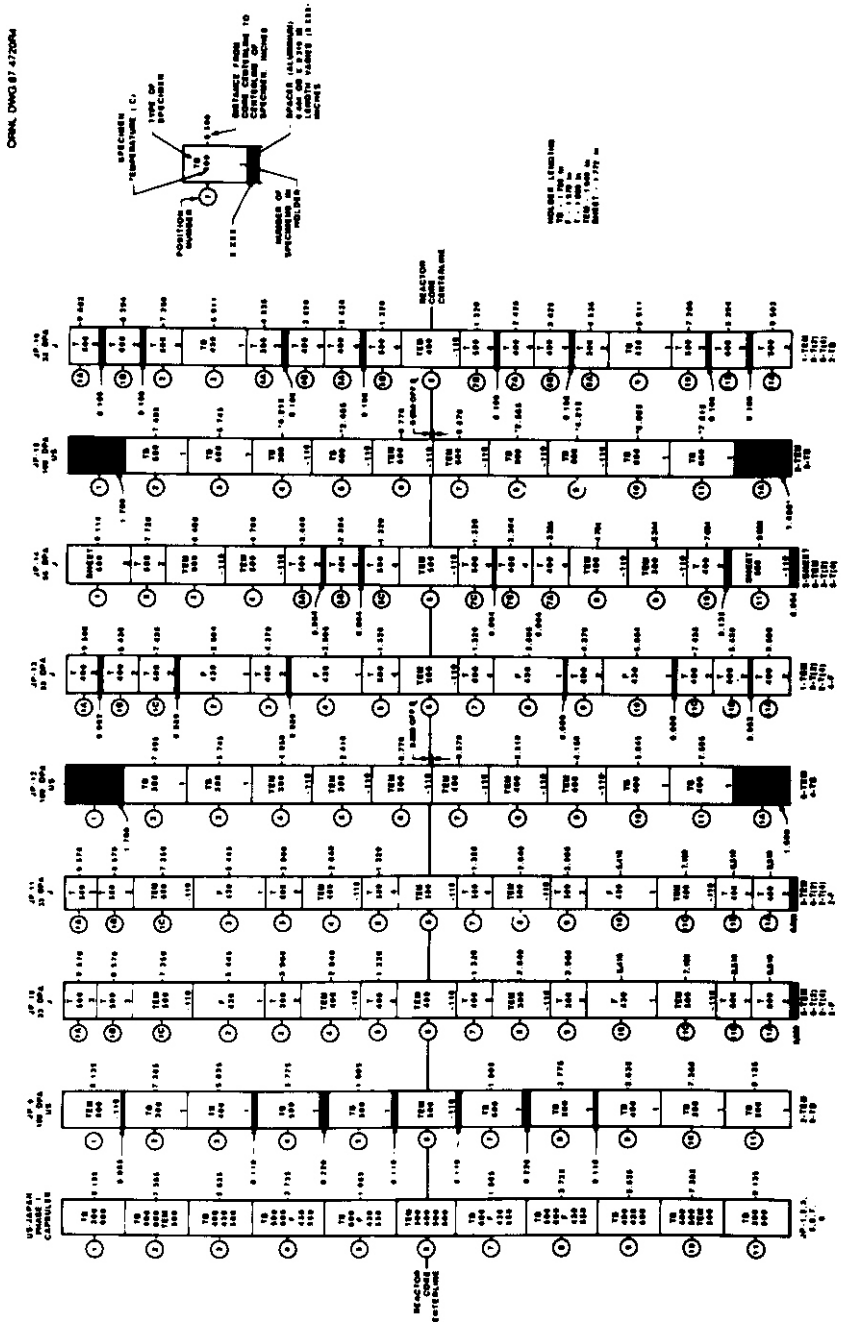

Fig. 1. U.S./Japan Phase II target capsules as-built matrix.

Table 1. HFIR TARGET CAPSULE JP-9 THERMAL ANALYSIS

POSITION NO.	ELEVATION FROM C/L INCHES	HEAT GEN. HGEN W/GM	SPEC. TYPE **	CAPSULE JP-9 SPECIMEN TEMP. C	COLD GAP IN.	HOLDER DIAM. "X" IN.	SPACER DIAM. "X" IN.
1	9.135	17.03	TEM	500	0.0420	0.2243	0.0100
	7.900	24.10	TOP		0.0098	0.1800	
2	7.385	26.76	TB	300	0.0227	0.1250	
	6.870	29.26	BOT.		0.0078	0.1760	
	6.150	32.46	TOP		0.0113	0.1830	
3	5.635	34.54	TB	400	0.0282	0.1360	
	5.120	36.46	BOT.		0.0099	0.1800	
	4.290	39.19	TOP		0.0132	0.1868	
4	3.775	40.67	TB	500	0.0357	0.1510	
	3.260	41.97	BOT.		0.0122	0.1848	
	2.320	43.92	TOP		0.0116	0.1836	
5	1.805	44.74	TB	500	0.0312	0.1420	
	1.290	45.40	BOT.		0.0111	0.1826	
---6---	0.000	46.30	TEM	-- 500	-0.0199	0.1638	0.0 80
	1.290	45.40	BOT.		0.0111	0.1826	
7	1.805	44.74	TB	500	0.0312	0.1420	
	2.320	43.92	TOP		0.0116	0.1836	
	3.260	41.97	BOT.		0.0122	0.1848	
8	3.775	40.67	TB	500	0.0357	0.1510	
	4.290	39.19	TOP		0.0132	0.1868	
	5.120	36.46	BOT.		0.0099	0.1800	
9	5.635	34.54	TB	400	0.0357	0.1360	
	6.150	32.46	TOP		0.0113	0.1830	
	6.870	29.26	BOT.		0.0078	0.1760	
10	7.385	26.76	TB	300	0.0227	0.1250	
	7.900	24.10	TOP		0.0098	0.1800	
	8.620	20.10	BOT.		0.0122	0.1848	
11	9.135	17.03	TB	300	0.0442	0.1680	
	9.650	13.79	TOP		0.0188	0.1980	

** TEM = TEM DISK SPECIMENS, TB= TENSILE BAR SPECIMENS
ASSUMES 85 MW REACTOR POWER.
ASSUMES 85% NEUTRONIC HEAT FOR SPECIMEN MATERIALS.
US CAPSULE, 100 dpa DWG. X2E41517-0025 R. L. Senn 9/30/88

Table 2. HFIR TARGET CAPSULES JP-10, -11 THERMAL ANALYSIS

POSITION NO.	ELEVATION FROM C/L INCHES	HEAT GEN. HGEN W/GM	SPECIMEN TYPE ***	CAPSULE JP-10 SPECIMEN TEMP. C	COLD GAP IN.	HOLDER DIAM. "X" IN.	SPACER DIAM. "X" IN.	CAPSULE JP-11 SPECIMEN TEMP. C	COLD GAP IN.	HOLDER DIAM. "X" IN.	SPACER DIAM. "X"
1A	9.570	14.31	T(2)	500	0.0160	0.3680		500	0.0160	0.3680	
1B	8.570	20.39	T(2)	500	0.0105	0.3790		500	0.0105	0.3790	
1C	7.250	27.43	TEM	500	0.0227	0.1857	0.0340	600	0.0315	0.2033	0.0 00
2T	5.945	33.31			0.0070	0.2630			0.0070	0.2630	
2	5.445	35.27	F	430	0.0155	0.1560		430	0.0155	0.1560	
2B	4.945	37.07			0.0070	0.2630			0.0070	0.2630	
3	3.960	40.16	T(2)	300	0.0011	0.3978		500	0.0043	0.3914	
4	2.640	43.32	TEM	400	0.0085	0.1573	0.0960	400	0.0085	0.1573	0.0960
5	1.320	45.37	T(4)	400	0.0022	0.0396		500	0.0038	0.3924	
--- 6 ---	0.000	46.30	TEM	400	0.0078	0.1559	0.0990	500	0.0119	0.1641	0 0 0
7	1.320	45.37	T(4)	400	0.0022	0.0396		500	0.0038	0.3924	
8	2.640	43.32	TEM	300	0.0048	0.1499	0.1110	500	0.0128	0.1659	0.0680
9	3.960	40.16	T(2)	300	0.0011	0.3978		500	0.0043	0.3914	
10T	4.915	37.18			0.0070	0.2630			0.0070	0.2630	
10	5.415	35.38	F	430	0.0155	0.1560		430	0.0155	0.1560	
10B	5.915	33.43			0.0070	0.2630			0.0070	0.2630	
11C	7.190	27.73	TEM	500	0.0227	0.1587	0.0340	400	0.0152	0.1707	0.0740
11B	8.510	20.73	T(2)	600	0.0145	0.3710		400	0.0065	0.3870	
11A	9.510	14.69	T(2)	600	0.0235	0.3530		400	0.0105	0.3790	

*** F = FATIGUE SPECIMENS, TEM = TEM DISK SPECIMENS, TB= TENSILE BAR SPECIMENS
T(2) = TWO SS-3 FLAT TENSILE SPECIMENS/HOLDER, T(4) = FOUR SS-3 FLAT TENSILE SPECIMENS/HOLDER
ASSUMES 85 MW REACTOR POWER AND 85% NEUTRONIC HEAT FOR CAPSULE MATERIALS.
NOTE: MOVED C/L SPEC. 10 UP 0.030", C/L SPEC 11-C, -B, -C UP 0.060". 8/29/88
J CAPSULES, 33 dpa each. DWG. X2E-41517-0026 (JP-10), -0027 (JP-11) R. L. Senn 9/30/88

Table 3. HFIR TARGET CAPSULE JP-12 THERMAL ANALYSIS

POSITION NO.	ELEVATION FROM C/L INCHES	HEAT GEN. HGEN W/GM	SPECIMEN TYPE **	CAPSULE JP-12 SPECIMEN TEMP. C	COLD GAP IN.	HOLDER DIAM. "X" IN.	SPACER DIAM. "X" IN.
1	9.099	17.25	SPACER				
	0.515						
2 T	8.010	23.51	TOP		0.0095	0.1794	
2	7.495	26.21	TB	300	0.0237	0.1270	
2 B	6.980	28.74	BOT.		0.0080	0.1764	
3 T	6.260	31.99	TOP		0.0070	0.1744	
3	5.745	34.11	TB	300	0.0162	0.1120	
3 B	5.230	36.06	BOT.		0.0060	0.1724	
4 T							0.1048
4	4.050	39.90	TEM	300	0.0055	0.1513	
4 B							0.1090
5 T							0.1090
5	2.410	43.75	TEM	300	0.0050	0.1503	
5 B							0.1117
6 T							0.1117
6	0.770	45.89	TEM	300	0.0045	0.1493	
6 B							0.1126
7 T							0.0991
7	0.870	45.81	TEM	400	0.0080	0.1563	
7 B							0.0974
8 T							0.0974
8	2.510	43.57	TEM	400	0.0085	0.1573	
8 B							0.0935
9 T							0.0935
9	4.150	39.61	TEM	400	0.0095	0.1593	
9 B							0.0865
10 B	5.330	35.70	BOT.		0.0105	0.1814	
10	5.845	33.71	TB	400	0.0292	0.1380	
10 T	6.360	31.56	TOP		0.0115	0.1834	
11 B	7.080	28.26	BOT.		0.0135	0.1874	
11	7.595	25.70	TB	400	0.0437	0.1670	
11 T	8.110	22.97	TOP		0.0165	0.1934	
12	9.127	17.08	SPACER				

** TEM = TEM DISK SPECIMENS, TB= TENSILE BAR SPECIMENS
TB DIMENSIONS RECALCULATED USING HT-9 AS SPECIMEN MATERIAL. 9/01/88
ASSUMES 85 MW REACTOR POWER AND 85% NEUTRONIC HEAT FOR CAPSULE MATERIALS.
US CAPSULE, 100 dpa Dwg. X2E41517-0044 R. L. Senn 9/30/88

Table 4 HIR TA BET CAPSULE JP-13 THERMAL ANALYSIS

POSITION NO.	ELEVATION FROM C/L INCHES	HEAT GEN. HGEN W/GM	SPECIMEN TYPE ***	CAPSULE JP-13 SPECIMEN TEMP. C	COLD GAP IN.	HOLDER DIAM. "X" IN.	SPACER DIAM. "X" IN.
1A	9.500	14.75	T(2)	400	0.0102	0.3796	
1B	8.438	21.14	T(2)	400	0.0065	0.3870	
1C	7.438	26.50	T(2)	400	0.0048	0.3904	
2T	6.364	31.54			0.0075	0.2640	
2	5.864	33.64	F	430	0.0170	0.1590	
2B	5.364	35.57			0.0075	0.2640	
3	4.379	38.92	T(2)	400	0.0028	0.3944	
4T	3.105	42.33			0.0055	0.2600	
4	2.805	42.98	F	430	0.0125	0.1500	
4B	2.305	43.94			0.0055	0.2600	
5	1.320	45.37	T(4)	500	0.0038	0.3924	
--- 6 ---	0.000	46.30	TEM	500	0.0119	0.1641	0.0740
7	1.320	45.37	T(4)	500	0.0038	0.3924	
8T	2.305	43.94			0.0055	0.2600	
8	2.805	42.98	F	430	0.0125	0.1500	
8B	3.105	42.33			0.0055	0.2600	
9	4.379	38.92	T(2)	400	0.0028	0.3944	
10T	5.364	35.57			0.0075	0.2640	
10	5.864	33.64	F	430	0.0170	0.1590	
10B	6.364	31.54			0.0075	0.2640	
11C	7.438	26.50	T(2)	400	0.0048	0.3904	
11B	8.438	21.14	T(2)	400	0.0065	0.3870	
11A	9.500	14.75	T(2)	400	0.0102	0.3796	

*** F = FATIGUE SPECIMENS, TEM = TEM DISK SPECIMENS, T(2) = 2 SS-3 FLAT TENSILE SPEC./HOLDER, T(4) = 4 SS-3 FLAT TENSILE SPEC./HOLDER
ASSUMES 85 MW REACTOR POWER AND 85% NEUTRONIC HEAT FOR CAPSULE MATERIALS.

J CAPSULE. 33 dpa DWG. X2E41517-0045 R. L. Senn 9/30/88

Table 5. HFIR TARGET CAPSULE JP-14 THERMAL ANALYSIS

POSITION NO.	ELEVATION FROM C/L INCHES	HEAT GEN. HGEN W/GM	SPECIMEN TYPE	CAPSULE JP-14 SPECIMEN TEMP. C	COLD GAP IN.	HOLDER DIAM. "X" IN.	SPACER DIAM. "X" IN.
1	9.114	17.16	SHEET	500	0.0128	0.3744	
2	7.728	25.01	T(2)	500	0.0080	0.3840	
3	6.408	31.35	TEM	600	0.0267	0.1937	0.0100
4	4.768	37.67	TEM	500	0.0153	0.1709	0.0550
5A	3.448	41.51	T(2)	500	0.0043	0.3914	
5B	2.384	43.80	T(4)	400	0.0024	0.3952	
5C	1.320	45.37	T(4)	500	0.0038	0.3924	
6	0.000	46.30	TEM	500	0.0119	0.1641	0.0740
7C	1.320	45.37	T(4)	500	0.0038	0.3924	
7B	2.384	43.80	T(4)	400	0.0024	0.3952	
7A	3.384	41.67	T(4)	400	0.0026	0.3949	
8	4.704	37.88	TEM	400	0.0103	0.1609	0.0860
9	6.344	31.63	TEM	300	0.0075	0.1553	0.1010
10	7.664	25.34	T(2)	400	0.0052	0.3892	
11	9.050	17.55	SHEET	500	0.0125	0.3750	

*** TEM = TEM DISK SPECIMENS, TB= TENSILE BAR SPEC., T(2) = TWO SS-3 FLAT TENSILE SPECIMENS/HOLDER, T(4) = FOUR SS-3 FLAT TENSILE SPECIMENS/HOLDER, SHEET = WELDED FLAT SHEET SPECIMEN.

ASSUMES 85 MW REACTOR POWER AND 85% NEUTRONIC HEAT FOR CAPSULE MATERIALS.
NOTE: MOVED C/L SPEC. 7A, 8, 9, 10 & 11 UP 0.064" TO ADD SPACER UNDER 11.
J CAPSULE, 55 dpa DWG. X2E41517-0046 R. L. Senn 9/30/88

Table 6. HFIR TARGET CAPSULE JP-15 THERMAL ANALYSIS

POSITION NO.	ELEVATION FROM C/L INCHES	HEAT GEN. HGEN W/GM	SPECIMEN TYPE **	CAPSULE JP-15 SPECIMEN TEMP. C	COLD GAP IN.	HOLDER DIAM. "X" IN.	SPACER DIAM. "X" IN.
1	9.330	15.82		ALUMINUM SPACER			
2 T					0.0235	0.2074	
2	7.715	25.08	TB	500	0.0757	0.2310	
2 B					0.0195	0.1994	
3 T					0.0165	0.1934	
3	5.965	33.23	TB	500	0.0477	0.1750	
3 B					0.0150	0.1904	
4 T	4.715	37.85			0.0059	0.1720	
4	4.215	39.42	TB	300	0.0134	0.1064	
4 B	3.715	40.83			0.0054	0.1710	
5 T	2.965	42.64			0.0084	0.1770	
5	2.465	43.65	TB	400	0.0202	0.1200	
5 B	1.965	44.50			0.0079	0.1760	
6 T							0.0709
6	0.770	45.89	TEM	500	0.0120	0.1643	
6 B							0.0735
7 T							0.0378
7	0.870	45.81	TEM	600	0.0175	0.1753	
7 B							0.0238
8 T	2.065	44.35			0.0156	0.1914	
8	2.565	43.46	TB	600	0.0502	0.1800	
8 B	3.065	42.42			0.0163	0.1928	
9 T	3.815	40.56			0.0173	0.1948	
9	4.315	39.12	TB	600	0.0607	0.2010	
9 B	4.815	37.52			0.0189	0.1980	
10 T					0.0210	0.2024	
10	6.065	32.81	TB	600	0.0802	0.2400	
10 B					0.0235	0.2074	
11 T					0.0280	0.2164	
11	7.815	24.55	TB	600	0.1462	0.3720	
11 B					0.0345	0.2294	
12	9.430	15.20		ALUMINUM SPACER			

** TEM = TEM DISK SPECIMENS, TB= TENSILE BAR SPECIMENS
ASSUMES 85 MW REACTOR POWER AND 85% NEUTRONIC HEAT FOR CAPSULE MATERIALS.
US CAPSULE, 100 dpa DWG. X2E-41517-0047 R. L. Senn 9/30/88

Table 7. HFIR TARGET CAPSULE JP-16 THERMAL ANALYSIS

POS. NO.	ELEV. FROM C/L INCHES	HEAT GEN. W/GM	SPEC. TYPE ***	SPECIMEN TEMP. E	CAPSULE COLD GAP IN.	JP-16 HOLDER DIAM. IN.	SPACER DIAM. IN.
1A	9.502	11.71	1121	SOD	0.0155	0.3690	
10	8.394	21.39	112)	600	0.0139	0.3722	
2	7.286	27.26	1121	500	0.0037	0.3854	
	6.426	31.27	TOP		0.0141	0.1884	
3	5.911	33.45	TB	130	0.0347	0.1190	
	5.3%	35.15	BOT.		0.0122	0.1846	
4A	4.536	38.13	1121	300	0.0012	0.3976	
10	3.128	11.56	T(4)	400	0.0026	0.3949	
5A	2.428	13.72	T(4)	400	0.0021	0.3952	
58	1.320	15.37	T(4)	500	0.0038	0.3924	
6	-0.000	46.30	TEM	400	0.0078	0.1559	0.0990
7B	1.320	45.37	T(4)	500	0.0038	0.3921	
7A	2.128	13.72	T(4)	LOO	0.0021	0.3952	
88	3.128	11.56	T(4)	400	0.0026	0.3949	
8A	4.536	38.43	T(2)	300	0.0012	0.3976	
	5.3%	35.4s	BOT.		0.0122	0.1846	
V	5.911	33.15	10	430	0.0347	0.1490	
	6.426	31.27	TOP		0.0111	0.1884	
10	7.268	27.35	112)	500	0.0037	0.3851	
110	8.394	21.39	T(2)	600	0.0139	0.3722	
111	V.502	11.74	T(2)	500	0.0155	0.3690	

*** TEM = TEM DISK SPECIMENS, TB= TENSILE BAR SPECIMENS
T(2) = TWO SS-3 FLAT TENSILE SPECIMENS/HOLDER
T(4) = FOUR SS-3 FLAT TENSILE SPECIMENS/HOLDER
ASSUMES 85 MW REACTOR POWER AND 85% NEUTRONIC HEAT.
J CAPSULE, 33 dpa. DWG. X2E-41517-0048 R. L. Senn 9/30/88

PRESENT STATUS

All specimen subassemblies were completed in preparation for loading the capsules. Revisions of the gas gaps for certain specimens required diassembly to accommodate new holders. These parts are presently on order.

Loading lists were developed showing the specimen type and identity for each position within each capsule. These lists are shown in Tables 8 through 15 for capsules JP-9 through JP-16, respectively.

FUTURE WORK

Assembly of the eight capsules is planned for completion as soon as the new parts become available, with installation in the HFIR at the earliest opportunity. Full power operation of the reactor is presently predicted to begin in early 1989.

Table 8. Loading list for capsule JP-9

Position	Specimen	
	Type	Identity
1	TEM	
2	Tensile bar	TM-28
3	Tensile bar	TL-28
4	Tensile bar	TL-26
5	Tensile bar	SU-14
6	TEM	
7	Tensile bar	SC-17
8	Tensile bar	SS-02
9	Tensile bar	SC08
10	Tensile bar	SC09
11	Tensile bar	SU-23

Table 9. Loading list for capsule JP-10

Position	Specimen	
	Type	Identity
1A	T(2)	AHAO, AAJ1
1B	T(2)	ANCB, AJJ8
1C	TEM	
2	Fatigue	AHT0
3	T(2)	AHA1, AAJ2
4	TEM	
5	T(4)	AHA2, AAJ3, AAJ4, AGAO
6	TEM	
7	T(4)	ANC9, AJJ9, AJKO, AMC8
8	TEM	
9	T(2)	AHA3. AGA1
10	Fatigue	AHT1.
11C	TEM	
11B	T(2)	AND0, AMC9
11A	T(2)	HJK1, HJK2

Table 10. Loading list for capsule JP-11

Position	Specimen	
	Type	Identity
1A	T(2)	VAJO. VGAO
18	T(2)	YAJ1, YGA1
1C	TEM	
2	Fatigue	AATO
3	T(2)	PJJO, PMCO
4	TEM	
5	T(4)	AHA8, AAJ8, AAJ9, AGA8
	TEM	
	T(4)	ANC5, AJJ4, AJJ5, AMC3
8	TEM	
9	T(2)	PJJ1, PMC1
10	Fatigue	AAT1
11C	TEM	
11B	T(2)	YAJ2, YGA2
11A	T(2)	YAJ3, VGA3

Table 11. Loading list for capsule JP-12

Position	Specimen	
	Type	Identity
1	Spacer	
2	Tensile bar	TD-20
3	Tensile bar	t1-02
4	TEM	
5	TEM	
6	TEM	
7	TEM	
8	TEM	
9	TEM	
10	Tensile bar	SS-10
11	Tensile bar	TM-30
12	Spacer	

Table 12. Loading list for capsule JP-13

Position	Specimen	
	Type	Identity
1A	T(2) flat tensile	AHA9, AGA9
1B	T(2) flat tensile	AAL3, AAL4
1C	T(2) flat tensile	EGAO. EGA1
2	Fatigue	AJV4
3	T(2) flat tensile	PJJ2, PMC2
4	Fatigue	ANV4
5	T(4) flat tensile	AHBO, AGBO, ANC3, AMC4
6	TEM	
	T(4) flat tensile	BHAO, BHA1, BGAO, BGA1
B	Fatigue	ANN5
9	T(2) flat tensile	PJJ3, PMC3
10	Fatigue	AJV8
11C	T(2) flat tensile	A05, C010
11B	T(2) flat tensile	AJL3, AJL4
11A	T(2) flat tensile	ANC4, AMC5

Table 13. Loading list for capsule JP-14

Position	Specimen	
	Type	Identitv
1	Sheet	1, 5
2	T(2) flat tensile	KJJO, KJJ1
3	TEM	
4	TEM	
5A	T(2) flat tensile	A01, B04
58	T(4) flat tensile	AHB2, AAK6, AAK7, AGB6
5c	T(4) flat tensile	AND3, AJK8, AJK9, AM07
6	TEM	
7c	T(4) flat tensile	A06, B06, C01, C02
7B	T(4) flat tensile	AND2, AJK6, AJK7, AMD6
7A	T(4) flat tensile	A07, B08, C09, C04
8	TEM	
9	TEM	
10	T(2) flat tensile	A010, C05
11	Sheet	2, 4

Table 14. Loading list for capsule JP-15

Position	Specimen	
	Type	Identity
1	Spacer	
2	Tensile bar	TD-28
3	Tensile bar	TM-21
4	Tensile bar	SS-28
5	Tensile bar	SV-30
6	TEM	
7	TEM	
8	Tensile bar	SU-12
9	Tensile bar	TL-09
10	Tensile bar	SS-30
11	Tensile bar	TM-09
12	Spacer	

Table 15. Loading list for capsule JP-16

Position	Specimen	
	Type	Identity
1A	T(2) SS-3 flat tensile	AGA7, AMD9
1B	T(2) SS-3 flat tensile	ANCO, AJJO
2	T(2) SS-3 flat tensile	AMJO, AMJ2
3	Tensile bar	AAR1
4A	T(2) SS-3 flat tensile	ANC1, AJJ1
4B	T(2) SS-3 flat tensile	BNAO, BNA1, BMAO, BMA1
5A	T(4) SS-3 flat tensile	AHB1, AGB1, ANC2, AMC6
5B	T(4) SS-3 flat tensile	BNA2, BNA3, BMA2, BMA3
6	TEM	
7B	T(4) SS-3 flat tensile	LJJO, LJJ1, HJJO, HJJ1
7A	T(4) SS-3 flat tensile	LJJ3, LJJ4, HJJ2, HJJ4
8B	T(4) SS-3 flat tensile	BHA2, BHA3 BGA2, BGA3
8A	T(2) SS-3 flat tensile	AJJ2, AMC1
9	Tensile bar	AHPO
10	T(2) SS-3 flat tensile	A04, C06
11B	T(2) SS-3 flat tensile	AJJ3, AMC2
11A	T(2) SS-3 flat tensile	AJLZ, AAL2

2. DOSIMETRY, DAMAGE PARAMETERS, AND ACTIVATION CALCULATIONS

HELIUM GENERATION IN FUSION REACTOR MATERIALS - D. W. Kneff and B. M. Oliver (Rockwell International)

OBJECTIVE

The objective of this work is to measure the total helium production cross sections of materials for fusion-energy neutrons.

SUMMARY

Helium analyses and neutron fluence characterization have been initiated for two Rotating Target Neutron Source-I1 (RTNS-II) irradiations, with the objective of determining several new total helium production cross sections. A constant temperature furnace has been rebuilt and tested for the measurement of helium concentrations in materials irradiated at significantly lower neutron fluences, and used for the measurement of helium generation in aluminum by 10-MeV neutrons.

PROGRESS AND STATUS

Four accelerator-based neutron irradiations have previously been performed to measure the total helium production cross sections of several materials in the 10- to 15-MeV neutron energy region.(1) These experiments include three irradiations at RTNS-II at the Lawrence Livermore National Laboratory (LLNL) using the T(d,n) source reaction, and one at the Los Alamos National Laboratory (LANL) using the $^{1}H(t,n)$ source reaction.

The RTNS-II irradiations, performed jointly with Argonne National Laboratory (ANL), included one primary-volume irradiation, one add-on irradiation at ~75° relative to the neutron source axis. and one add-on irradiation at 110°.(1) Helium analysis work has now been initiated for the primary-volume and 75° irradiations.

The RTNS-II primary volume irradiation was performed to measure total helium production cross sections at 14.6 MeV for selected materials, including, for example, N, Mg, S, Ge, W, and the separated isotopes of W, and to obtain additional data for other materials. This irradiation plus the 110° irradiation were also designed to provide energy-dependent information on the cross sections of selected low-2 elements over the energy range of 13.6 to 15 MeV.(1) Analyses have now been initiated for the primary-volume irradiation. York to date includes the analysis of the helium accumulation dosimetry rings, the initiation of the neutron fluence mapping for the irradiation volume, the post-irradiation preparation of a large number of platinum-encapsulated samples for helium analysis, and the helium analyses of several selected samples. The dosimetry rings, composed of pure-element copper wire, provide detailed information on the neutron fluence gradients within the irradiation volume. The analyzed samples include Be. TiN, ZrN, Al_2O_3, and Nb_2O_5, where the nitrides and oxides will be used to deduce the cross sections for nitrogen and oxygen, respectively.

The mass spectrometer system's constant temperature furnace was rebuilt for the analysis of the materials irradiated at LANL with 10-MeV neutrons. This furnace is designed for helium release from very large samples (up to about 1 g), with helium background levels much lower than our standard graphite crucibles. This provides the capability of performing Reasurements in neutron fields for which the neutron flux is orders of magnitude lower than that from RTNS-II. This furnace was subsequently tested successfully using aluminum samples irradiated to relatively low fluences (10^{15} to 10^{16} neutrons/cm^2) at 75° in RTNS-II, and beryllium samples from two different light-water reactor surveillance dosimetry experiments. The beryllium samples were selected for testing because of their previously characterized helium concentrations; and because of a requirement for low-fluence beryllium measurements in a potential joint experiment with ANL.

Analyses were initiated for materials irradiated in the 10-MeV $^{1}H(t,n)$ LANL experiment. This experiment was performed jointly with R. C. Haight of LANL. The first analyses performed were for aluminum, with measured helium concentrations in the 20 appt (atomic parts per trillion, 10^{-12} atom fraction) region. These measurements provide a first demonstration of our ability to measure helium generation rates for monoenergetic neutrons using accelerator neutron sources other than T(d,n). The total neutron fluence for this experiment was about 3 x 10^{14} neutrons/cm^2.

FUTURE WORK

Helium analyses and neutron fluence and spectrum characterization will continue for the RTNS-II T(d,n) and LANL $^{1}H(t,n)$ irradiations. The results will be combined to deduce total helium production cross sections at multiple neutron energies for several materials.

REFERENCES

1. D. W. Kneff, R. P. Skowronski. and B. M. Oliver, "Helium Production Cross Sections for Fusion-Energy Neutrons." pp. 40-41 in Fusion Reactor Materials, Semiannual Progress Report for Period Ending September 30. 1986, DOE/ER-0313/1, U.S. Department of Energy, June 1987.

NEUTRON FLUENCE MEASUREMENTS FOR HELIUM PRODUCTION EXPERIMENTS AT RTNS II - L. R. Greenwood, C. A. Seils, and A. Intasorn (Argonne National Laboratory)

OBJECTIVE

To provide dosimetry for fusion experiments at 14 MeV neutron sources and to determine helium production cross sections.

SUMMARY

Results are reported for two experiments at RTNS II designed to measure helium production Cross sections near 14 MeV. The first experiment in January, 1987, received fluences from 1 to 3×10^{15} n/cm^2 at an angle of 75° with an average neutron energy of 14.3 MeV. The second add-on experiment from February to May 1987 was irradiated at an angle of 1100 with a mean neutron energy of 13.8 MeV and neutron fluences of 1.5 to 2.0×10^{16} n/cm^2. Helium measurements are now in progress at Rockwell International.

PROGRESS AND STATUS

Numerous experiments have been perfonned at the Rotating Target Neutron Source II at Lawrence Livermore National Laboratory to measure helium production near 14 MeV neutron energies. Results for 25 elements, separated isotopes, and alloy steels have already been published1 in collaboration with D. Kneff (Rockwell International). Several add-on experiments were performed to look at additional materials.

The first experiment was a short irradiation (23.6 hours) on January 8-9, 1987. with the specimens located at ~75° to the beam and an average neutron energy of 14.3 MeV. Dosimetry and helium samples were irradiated in an aluminum capsule measuring 1.75 cm O.D.x2.41 cm thick. Dosimetry foils were located at 5 different positions interspersed with helium samples of Fe, Cu, Cr, Al, Ni, C, Mn, V, Ti, Si. and Be. The circular dosimetry foils measured 1 cm O.D. by 0.025-0.25 mm thick. All samples were gama counted in Order to detennine activation rates.

The activation measurements are listed in Table 1 in the order according to their placement in the assembly. Neutron fluences were then calculated by dividing the activation rate by the production cross section. Cross sections were taken from our previously published data;[2] however, it was necessary to extrapolate from our largest angle at 60° to 75° using the trend of the data as well as trends from ENDF/B-V.[3] The fluences have an uncertainty of ±4%, due to our normalization to the $^{93}Nb(n,2n)^{92}Nb$ reaction cross section of 463 mb, as well as counting uncertainties of 2-4%. The net absolute uncertainty is thus about 6%. The derived fluences are plotted in Fig. 1 as a function of distance into the assembly. As can be seen, fluences decline about a factor of three over a distance of 2.41 cm.

In order to determine the detailed fluence distribution over the surface of a foil, three niobium foils were segmented into 9 concentric pieces on diameters of 3 mm (1 piece), 6.5 and 10 mm (4 pieces each). Each segment was then gama counted and the results are listed in Table 2. As can be seen, the fluence gradients vary up to 17% over the 1 cm diameter discs.

The second experiment took place over the extended period between February 23, 1987 to May 23, 1987 (90 days). The purpose of the experiment was to measure helium production cmss sections near 14 MeV for various materials including Be, C, Nb, Al, Cu, and Fe.

The helium specimens and radiometric dosimeters were enclosed in a cylindrical package measuring 1.11 cm diameter by 0.64 cm thick. Dosimetry foils of Fe, Nb, and Co, each measuring 5 mils thick, were placed at seven different depths in the capsule in order to measure the neutron fluence gradients. Wires and helium accumulation fluence monitors were placed at four different locations in the assembly. The entire capsule was irradiated at 110° to the incident beam so that the average neutron energy was 13.8 MeV (±200 keV).

All of the dosimetry foils and helium sanples were gamma counted and saturated activation rates were calculated, as listed in Table 3. A detailed irradiation history was used to correct for decay during irradiation. The neutron fluences have an estimated absolute uncertainty of about 6-8% due to counting uncertainties (as listed) and cross section uncertainties (4-6%). The activity values and uncertainties are reported as the total number of active atoms per atom of target material. Neutron fluences were then derived by dividing by the appropriate neutron cross section. Cross section values were taken from ENDF/B-V[3] assuming a mean neutron energy of 13.8 MeV. In the case of the ^{59}Co reactions to ^{59}Fe and ^{58}Co, the cross sections were adjusted according to previous measurements at RTNS II.[2]

The neutron fluences range from $1.5\text{-}2.0 \times 10^{16}$ n/cm^2 and decline with increasing distance from the neutron source. The footnoted values represent wire and helium sanples which were much smaller than the 7/16' diameter dosimetry foils. Wire fluences thus show some scatter from the foil values since the neutron fluences are in fact changing across the dimensions of the foil.

Table 1. Activities and Neutron Fluences for RTNS II 75°)
(Jan. 8-9, 1987 at <E> = 14.3 MeV:
relative uncertainty 2-3%)

Distance (cm)	Sample-Position	Isotope	$\sigma\phi T$ ($\times 10^{-10}$ atom/atom)	Fluence ($\times 10^{15}$ n/cm^2)
0.0191	Fe-1	^{54}Mn	10.7	3.07
		^{51}Cr	2.89	**3.19**
0.0267	Ti-1	^{46}Sc	9.21	**3.01**
0.0406	Co-1	^{58}Co	23.8	**3.16**
0.0597	Nb-1	^{92m}Nb	14.3	3.09
0.0673	Ni-1	^{58}Co	10.8	**3.04**
0.0698	Au-1	^{196}Au	58.6	**2.76**
0.1219	Fe-He-3	^{54}Mn	10.2	**2.93**
		^{51}Cr	2.72	**3.00**
0.2235	Cu-He-4	^{60}Co	1.25	**2.84**
0.3759	Cr-He-2	^{51}Cr	10.7	-
0.5778	Ni-2	^{58}Co	8.47	2.39
0.5804	Au-2	^{196}Au	48.3	2.28
0.5842	Fe-2	^{54}Mn	8.40	2.41
		^{51}Cr	2.17	2.39
0.6515	Ni-He-1	^{58}Co	8.50	2.39
0.907	Mn-He-4	^{54}Mn	16.3	2.11
1.099	Ni-3	^{58}Co	6.82	1.92
1.101	Au-3	^{196}Au	39.1	1.84
1.109	Fe-3	^{54}Mn	6.55	1.88
		^{51}Cr	1.63	1.80
1.121	Nb-3	^{92m}Nb	9.11	1.97
1.243	Ti-He-2	^{46}Sc	5.95	1.94
1.910	Ni-He-4	^{58}Co	5.12	1.44
1.967	Ni-4	^{58}Co	5.05	1.42
1.970	Au-4	^{196}Au	28.1	1.33
1.974	Fe-4	^{54}Mn	4.74	1.36
	^{51}Cr	1.21	1.33	
2.181	Cu-He-2	^{60}Co	0.569	1.292.
2.239	Nb-5	^{92m}Nb	6.10	1.32
2.252	Ni-5	^{58}Co	4.29	1.21
2.264	Au-5	^{196}Au	25.5	1.20
2.283	CO-5	^{58}Co	9.51	1.26
		^{59}Fe	0.630	-
2.303	Ti-5	^{46}Sc	3.79	1.24
2.322	Zr-5	^{95}Zr	19.2	1.20
2.341	Fe-5	^{54}Mn	4.18	1.20
		^{51}Cr	1.12	1.23

FUTURE WORK

Helium measurements are now in progress by D. Kneff (Rockwell International). All of the data will be fit to a more detailed flux map in order to accurately predict fluences at the location of each helium sample.

REFERENCES

1. D. W. Kneff, B. H. Oliver, H. Farrar IV, and L. R. Greenwood, Nuclear Science and Engineering 92, 491-524 (1986).

2. L. R. Greenwood, Influence of Radiation on Materials Properties, ASTM-STP956, pp. 743-749 (1987).

3. Evaluated Nuclear Data File, Part B, Version V, Brookhaven National Laboratory, 1979.

Table 2. Neutron Fluence Gradients at RTNS II (75°)
(Results from $^{93}Nb(n,2n)^{92m}Nb$; counting uncertainty ±5%)

Foil Position	Segment	Fluence ($x10^{15}$ n/cm^2)
1	0	3.00
	1	3.11
	2	3.17
	3	3.00
	4	3.00
	5	2.92
	6	3.13
	7	2.90
	8	3.02
3	0	1.87
	1	1.75
	2	1.90
	3	1.97
	4	1.73
	5	1.94
	6	1.83
	7	1.95
	8	1.88
5	0	1.19
	1	1.26
	2	1.24
	3	1.14
	4	1.20
	5	1.33
	6	1.24
	7	1.31
	8	1.18

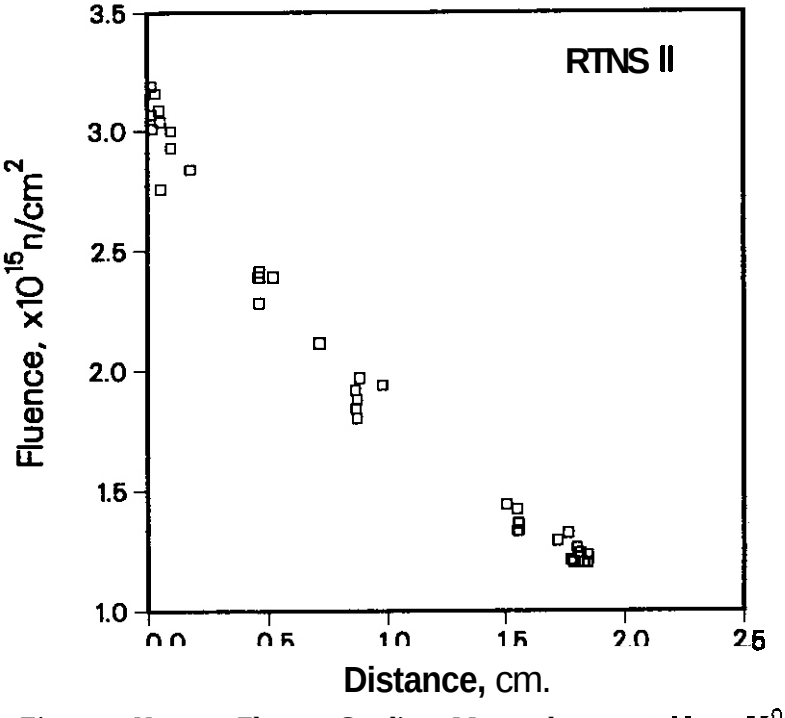

Fig. 1. Neutron Fluence Gradient Measured at RTNS II at 75° to the Beam. Distances Refer to the Front of the Helium Assembly.

Table 3. Activities and Neutron Fluences for RTNS II (110°)
(2/23/87 to 5/23/87; <E> = 13.8 MeV)

Sample-Position	Isotope	$\sigma\phi t$[d]	ϕt
		(10^{-9} atom/atom)	($\times 10^{16}$ n/cm^2)
Fe-F	^{54}Mn	7.35(0.7)	1.91
	^{51}Cr	1.70(2.6)	1.89
Co-F	^{58}Co	12.4(0.3)	1.80
	^{59}Fe	1.03(1.7	1.74
Nb-1	^{92m}Nb	9.07(0.9	1.95
Fe-1	^{54}Mn	7.31(1.1	1.90
	^{51}Cr	1.60(3.2)	1.78
Fe-S1[a]	^{54}Mn	7.35(1.8)	1.91
	^{51}Cr	1.49(6.0)	1.66
Nb-8D[b]	^{92m}Nb	9.30(1.2)	2.04
Fe-2	^{54}Mn	7.08(0.8)	1.84
	^{51}Cr	1.58(2.5)	1.76
Nb-S1[a]	^{92m}Nb	8.48(0.4	1.86
Nb-1E[b]	^{92m}Nb	8.73(1.3	1.92
Nb-7Yb	^{92m}Nb	7.87(0.9	1.73
Cu-S1[a]	^{60}Co	0.829(1.5)	1.88
Fe-3	^{54}Mn	6.78(0.8)	1.77
	^{51}Cr	1.51(3.1)	1.68
Fe-S3[c]	^{54}Mn	7.011(1.2)	1.83
	^{51}Cr	1.57(3.7	1.75
Nb-S3[c]	^{92m}Nb	8.62(1.1	1.89
Nb-9Y[b]	^{92m}Nb	8.39(1.3)	1.84
Cu-S2[a]	^{60}Co	0.772(1.2)	1.63
Cu-S4[c]	^{60}Co	0.763 (1.2)	1.73
Fe-4	^{54}Mn	6.70(1.3)	1.74
	^{51}Cr	1.50 (4.0)	1.67
Fe-S2[a]	^{54}Mn	6.52 (1.0)	1.70
	^{51}Cr	1.41(3.9	1.57
Nb-B2[b]	^{92m}Nb	8.61(1.5	1.89
Nb-S2[b]	^{92m}Nb	7.81 (1.1	1.72
Cu-S3[c]	^{60}Co	0.755(1.9)	1.71
Fe-5	^{54}Mn	6.44 0.9)	1.68
	^{51}Cr	1.41 4.3)	1.57
Nb-5	^{92m}Nb	7.89 0.7)	1.73
co-B	^{58}Co	10.8(0.4)	1.57
	^{59}Fe	0.901 (1.5)	1.52
Fe-B	^{54}Mn	6.38(0.9)	1.65
	^{51}Cr	1.37(4.2)	1.53

[a] Wire samples inside main assembly.

[b] Helium accumulation fluence monitors.

[c] Wire samples outside of main package.

[d] Relative counting uncertainties (%) are listed: absolute uncertainties also include 2% for detector efficiency and 4-6% for cross sections.

PRODUCTION OF ^{93}Mo and ^{93m}Nb FROM Mo AT 14.7 MeV - L. R. Greenwood, D. L. Bowers, and A. Intasorn (Argonne National Laboratory)

OBJECTIVE

To measure the production of long-lived isotopes in fusion reactor materials for activation and waste disposal applications.

SUMMARY

Ion-exchange chemical reactions have been performed to separate Mo and Nb in natural molybdenum samples irradiated with 14.7 MeV neutrons at RTNS II. X-ray counting has been performed to determine preliminary activation cross sections of about 580 mb for ^{94}Mo(n,2n)^{93}Mo(3500 y) and 0.73 mb for Mo(n,x)^{93m}Nb(16.1 y). Separations are now in progress for %-enriched sanples. These data are needed to calculate the production of long-lived isotopes in fusion reactor materials.

PROGRESS AND STATUS

We have been engaged in an ongoing program to measure neutron activation cmss sections near 14 MeV for long-lived isotopes. Such data areneeded to determine the activity of fusion reactor materials, especially for waste disposal applications. We have previously reported data for the production of ^{26}Al, ^{55}Fe, ^{63}Ni, ^{59}Ni, ^{91}Nb, and ^{94}Nb.[1,2,3] The present work summarizes our measurements of ^{93}Mo(3500 y) and ^{93m}Nb(16.1 y) from natural and ^{94}Mo-enriched sanples of molybdenum.

The Mo samples were metallic powders pressed into discs of 3 mm diameter by 1 mm thick. These discs were irradiated at the Rotating Target Neutron Source II at Lawrence Livermore National Laboratory to a neutron fluence of about 10^{18} neutron/cm^2. Details of the irradiation were published previously, where we reported cross sections for the 94110(n,p)^{94}Nb, ^{95}Mo(n,x)^{94}Nb, ^{92}Mo(n,x)^{91}Nb^m, ^{92}Mo(n,x)^{91}Nb^g, and ^{98}Mo(n,a)^{95}Zr reactions in the energy range from 14.5 to 14.8 MeV.[3] These same samples are now being analyzed for ^{93}Mo and ^{93m}Nb. ^{93}Mo and ^{93m}Nb both decay to the ground state of ^{93}Nb and emit Nb x-rays at 16.6 and 18.6 keV. Hence, it is necessary to chemically separate Mo and Nb in order to determine cross sections for each isotope. Furthermore, ^{93}Mo decays to ^{93m}Nb, thus complicating the analysis.

All of the sanples were dissolved in a mixture of concentrated HNO_3 and HCl. Ion-exchange chemical separations were then performed. Small aliquots of the dissolution and each fraction were then taken to dryness for x-ray analysis. Several checks were available to determine both the degree of separation as well as the absolute yields from the chemical procedures. Since ^{91}Nb^g (-680 y) is also present in the samples, we used the Zr x-rays at 15.7 and 17.6 keV as a Nb tracer. We were also able to obtain some ^{99}Mo, which was added to our samples as a Mo tracer. In both cases we were able to demonstrate that the chemical separation of Mo and Nb was good to at least 99%. Finally, we were able to demonstrate that the sum of the x-ray activities in the Nb and EIO fractions was equal to that of the original dissolution and that losses were less than 5X.

The natural Mo samples have now been analyzed and work on the ^{94}Mo-enriched samples is in progress. Preliminary results indicate a cross section of 580 mb for the ^{94}Mo(n,2n)^{93}Mo reaction and 0.73 mb for the Mo(n,x)^{93m}Nb reaction. Neither of these reactions have been measured previously. Data from the enriched targets will allow us to obtain separate cross sections for the production of ^{93m}Nb from both ^{94}Mo and ^{95}Mo. The results will then be used to predict the production of these isotopes in fusion reactor materials.

FUTURE WORK

We plan to measure cross sections for the long-lived isotopes ^{93}Zr(1.5x10^6 y), ^{14}C(5730 y), and ^{92}Nb(3.2x10^7 y) and to determine the half-lives more accurately for ^{59}Ni, ^{93}Mo, and ^{94}Nb.

REFERENCES

1. L. R. Greenwood, Influence of Radiation on Materials Properties," ASTM-STP956, pp. 743-749 (1988).

2. L. R. Greenwood and D. L. Bowers, Measurement of Long-Lived Radionuclides in Fusion Materials, ASTM-STP 1001, in press.

3. L. R. Greenwood, D. G. Doran, and H. L. Heinisch. Phys. Rev. 35C, 76-80 (1987).

RADIOACTIVE WASTE DISPOSAL FOR FISSION AND FUSION REACTORS. H. L. Heinisch and D. G. Ooran. Pacific Northwest Laboratory

OBJECTIVE

The objective of this work is to provide additional perspective on the desirability of developing reduced activation materials for fusion reactors by comparing the total radioactive inventories accrued during the lifetimes of a typical fission and fusion reactor.

SUMMARY

The calculated radioactive waste inventories of the Turkey Point pressurized water fission reactor (PWR) and the Starfire conceptual fusion tokamak are compared as a function of time from initial start-up to 10,000 years after decommissioning. Only material out of reactor at least one year is considered. The total activity in Ci/W(th) of the Starfire tokamak is slightly greater than that of the FWR during the active lifetimes of the two reactors and beyond 1000 years. However, using reduced activation materials in Starfire can result in about 1/2000 as much long-lived radioactivity as in the fission reactor. It is stressed that comparison of wastes on this basis is not straightforward. since the radioisotopes and methods required for their disposal are different for fusion and fission reactors.

PROGRESS AND STATUS

The development of reduced activation materials for fusion reactors is now a major objective of the fusion materials program. Since public perception of waste generation is a motivation for developing reduced activation materials, it is of interest to directly compare fusion reactor waste levels with those from competing power generating technologies, especially with fission reactors that are presently operating.

Significant amounts of radioactive materials are produced in both fission and fusion reactors, but the specific radioisotopes produced. their concentrations and volumes, their hazards to the biosphere and the methods required for their disposal are different. A comprehensive comparison was not attempted here; the difficulty of making simple comparisons should become evident in the following. We will compare the total radioactive inventory produced during the 30 year lifetime of an existing fission reactor [Turkey Point No. 3, a nominally 1200 M e (3600 MWth) pressurized water reactor (PWR)] and a specific conceptual fusion reactor [Starfire. nominally 1200 MWe (3600 MWth) tokamak].

In a fission reactor most of the radioactive materials requiring long-term waste disposal are in the spent fuel. which contains actinides and fission products. These high level wastes are the inescapable legacy of the fission process. During a 30 year lifetime a 1200 MWe PWR produces about 130 m^3 of spent fuel[1]. Reprocessing can reduce the volume of waste material significantly. Deep geological burial of this high level waste is required. Total activity of the fission reactor structural materials is insignificant by comparison. even though the volume of activated structural material is much larger than that of the fuel' (see Table 1).

The inventory of radioisotopes in a deuterium-tritium fusion reactor will result only from activation of reactor materials (excluding the tritium used as fuel). Over a 30 year lifetime a 1200 M e tokamak fusion reactor will produce on the order of 2000 m^3 of activated material. with about 300 m^3 of that being the highly activated first wall and blanket structural material[2]. Using conventional materials. some of this will not meet current requirements for shallow land burial.

Calculation of Radioactive Inventories

The inventory of radioactive isotopes for the fuel assemblies of the Turkey Point Reactor were calculated using the ORIGEN[3] computer code. Calculations were done for the fuel (UO_2), cladding (Zr-4) and other structural material (Inconel-718 and 304 stainless steel) of the fuel assemblies during three cycles each of 284 days up and 106 days down, for a total of 1064 days (2.9 years). The activities in curies of the fission products. actinides and activation products were determined separately at elapsed times after removal of the fuel from 0 to 10.000 years. The ORIGEN results were combined manually to construct the activity as a function of time for all spent fuel that has been out of reactor for at least one year, for the period from start-up to 10,000 years. It was assumed that all fuel assemblies in the reactor were changed every 3 years for 30 years. The activity in Ci/Wth as a function of time is shown in Figure 1.

The curve for Turkey Point in Fig. 1 begins at 4 years after start-up (one year after the first fuel elements are removed1 and continues through the life of the reactor, with new spent fuel assemblies added to the inventory every 3 years. Between 4 years and 31 years the curve should really have a saw-tooth shape with a period of 3 years. The maximum values lie on the curve. and the radioactivity decays by a factor of 2-3 less than the maximum during the 3 years before the next spent fuel is added to the waste inventory. After 31 years the curve simply displays the combined radioactive decay of all the spent fuel assemblies.

Table 1. Overview of Fusion and Fission Radioactive Wastes

Source	Lifetime Waste Volume (m3) High Level Waste	> Class C(a)	< Class C	< < Class C
FISSION (PWR)(b)				
Actinides/Fission Prod.				
No Reprocessing	~100			
With Reprocessing	~ 10			
Activated Haterials				
Conventional		~100	~ 1000	
Reduced Activation		(c)	(c)	
Contaminated Materials				~16,000
FUSION (STARFIRE)				
Activated Materials				
Conventional		~300	~ 1700	
Reduced Activation		~ 0	~ ***2000***	
Contaminated Materials				?

(a) Method of disposal not yet clear; in particular, not certain that geologic disposal required as for High Level Waste. Class C is most active waste permitted shallow land burial under 10CFR61.
(b) PWR waste burden generally ≥ BWR waste burden.
(c) The potential exists for decreasing the fraction of fission waste exceeding Class C through greater control of impurities in structural materials.

Within a few hundred years, the activity of the fission products decreases significantly. After about 500 years nearly all the activity is due to long-lived actinides. At 10,000 years the activity has dropped to 1/3 the value at 1000 years as the ^{240}Pu decays with a halflife of 6537 years. The activity is then dminated by ^{239}Pu with a halflife of 24,000 years.

The inventory of radioactivity for the Starfire fusion reactor was based on information in the Starfire documentation[2], where the material, volume and activity of each major component of the reactor is tabulated for 5 years of continuous reactor operation and 1-1000 years of decay. The radioactivity of Starfire is dminated (>95%) by radioisotopes formed in the PCA (a Ti- modified 316 stainless steel) used for the first wall and blanket structural material. The PCA canponents will not qualify for shallow land burial because of the long-lived activation products of the Mo, which makes up 2 wt% of PCA. According to recent calculations[4], the primary long-lived isotope of Ho is ^{99}Tc, which is not included in the activation calculations in the Starfire documentation. Thus. to evaluate the activity of Starfire. new values for the activity of PCA, calculated using the REAC*2 code[5], were substituted for the PCA contributions in Starfire Table 12-5. Activity due to the creation of tritium was not included. The calculations were extended to 10.000 years.

The Starfire design calls for replacement of 2 of the 24 blanket sectors every 6 months, a blanket sector being designed to last for 6 years. For calculating the reactor lifetime inventory. the values in our modified version of Starfire Table 12-5 were linearly extrapolated to values for 1-6 years of irradiation. and they were canbined to represent the changing of 1/6 of the blanket sectors each year of a 30 year reactor lifetime. As with the fission reactor, only material out of reactor for at least one year is considered part of the waste inventory. The Starfire curve for Ci/Wth as a function of time is shorn in Fig. 1.

The Starfire curve begins at 2 years, one year after the first blanket replacement. As in the fission case, the Curve for the first 31 years should be a sawtooth describing the decay between annual discharges

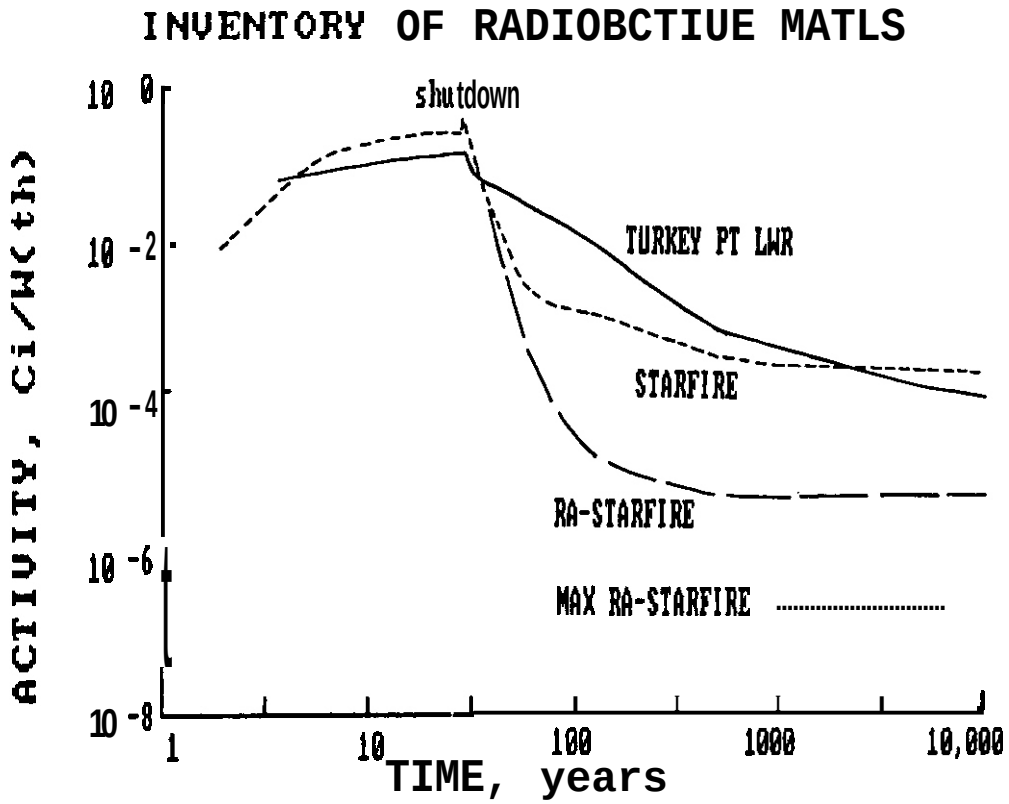

Figure 1. Inventory of Radioactive Materials for Fission and Fusion Reactors. The total inventory of radioactive materials out of reactor for at least one year in Ci/W(th) as a function of time for the Turkey Point pressurized water reactor (TURKEY PT LWR), the Starfire conceptual tokamak fusion reactor (STARFIRE). the Starfire reactor with reduced activation structural materials (RA-STARFIRE), and the Starfire reactor with maximum achievable reduced activation within the Starfire concept (MAX RA-STARFIRE).

of material to the inventory. The small spike at shutdown is caused by material from the entire reactor being added to the inventory at once. Activity is dominated through the first 20 years by ^{55}Fe, through the next 200 years by ^{63}Ni, and for several hundred thousand years by ^{99}Tc, which has a halflife of 2.13 x 10^5 years.

The effects of using reduced activation materials in the tokamak were also investigated in this fission-fusion comparison (Fig. 1). The Starfire waste inventory was recalculated, replacing the PCA with AMCR-33, a reduced activation austenitic stainless steel having no Mo and only 500 appm Ni. Although the activity of this "reduced activation tokamak" is the same as the original during its lifetime. at 1000 years it has two orders of magnitude less activity per watt than the FWR. Further reduction of long term activity can be achieved by replacing the ZrPb neutron multiplier and the $LiAlO_2$ tritium breeding material with less activating materials. Significant amounts of long-lived radioisotopes of Pb and Al are produced in these large volume components. The "maximum reduced activity tokamak" in Fig. 1, having no Pb or Al, has more than three orders of magnitude less activity than the FWR.

Comparison of Biological Hazard

Canparing fission and fusion wastes on the basis of total activity neglects the relative biological hazards of the various radioisotopes. The U. S. Nuclear Regulatory Commission (NRC) has addressed pathways by which radwaste could enter the biosphere in establishing radioisotope concentration limits for shallow land burial (10CFR61). The limits are given as the concentration of the isotope buried as waste that will produce the maximum permitted dose (0.5 rem/y) in an intruder who builds and occupies a house at the waste site at least 100 years after the waste is buried.

The shallow land burial methodology has been used to compare radioactive wastes fran different sources. Fetter[6] defined the "Intruder Dose" of a component disposed of by shallow land burial as the total dose to the intruder from all radioisotopes present, using pathway assumptions appropriate to each form of waste. To include waste volumes, he defined an Annualized Intruder Hazard Potential as the sum of the

TABLE 2

Radioactive Waste Indices for Reference Fusion Reactors

Type	Structure Material	Breeder Material	Coolant Material	Averaged Intruder Dose(a) (rem)	Annualized Hazard Potential (R-m3/y)
Tokamak	SiC	Li_2O	He	0.0053	0.53
Tokamak	RAF(b)	Li_2O	He	0.039	3.2
Tokamak	V alloy	Liquid Lithium		0.22	12
RFP(c)	RAF/Cu	Lithium-Lead		34	550
Large Scale Prototype Breeder Reactor				34,000	140,000

(a) Maximum permitted for shallow land burial is 0.5 rem.

(b) Reduced activation ferritic alloy.

(c) Reversed-Field Pinch
(high dose is due to the LiPb collant. not the RFP design per se)

products of the Intruder Dose and annual waste volume of each canponent. Table 2 contains values of these indices from the report of the DOE Senior Committee on Environmental. Safety and Economic Aspects of Magnetic Fusion Energy[7] for several fusion reactor concepts (generally involving reduced activation materials) and a prototype fission breeder reactor. All but one of the fusion reactors can be totally disposed of by shallow land burial (Intruder Dose less than 0.5 rem). The fission reactor wastes obviously fail the criteria by several orders of magnitude and require deep geologic disposal.

Discussion

As shown in Figure 1, the total activities of radioactive wastes produced during the lifetimes of a typical fission and (non-reduced activation) fusion reactor are canparable. Choosing reduced activation materials for fusion reactors can make a substantial reduction in long-lived radioisotopes. However. simply canparing total radioactive inventories is misleading. since the relative biological hazards of the isotopes and their pathways to the biosphere are not accounted for.

Quantitative comparison of fission and fusion wastes on the basis of Intruder Dose in shallow land burial scenarios is also highly questionable. It involves numerous assumptions about high level fission wastes in order for them to be considered as low level wastes for the sake of canparison with fusion wastes.

Perhaps the most meaningful comparison of fission and fusion wastes is simply qualitative: fission reactor wastes require deep geologic disposal. while fusion reactors can be made so that wastes can be safely disposed of by shallow land burial. Such a comparison. of course, still may not adequately address the public perception of the difference in "hazard" posed by fusion and fission wastes.

FUTURE WORK

No future work is anticipated at this time: however, further comparisons need to be done as part of the development of activation guidelines for fusion reactor materials.

ACKNOWLEDGEMENTS

The authors are grateful to F. A Schmittroth of Westinghouse Hanford Company for performing the ORIGEN canputer code run on spent fuel activation.

REFERENCES

1. Decommissioning U. S. Reactors: Current Status and Developing Issues, EPRI NP-5494. January, 1988.

2. Starfire - A Commercial Tokamak Fusion Power Plant Study, ANL/FFP-80-1, Vols. I and II, September, 1980.

3. A. G. Croff. ORIGEN2 -- evised and Undated Version of the Oak Ridge Isotope Generation and Depletion Code, ORNL-5621, July. 1980.

4. S. Fetter. E. T. Cheng and F. M. Mann. Fusion Eng. and Des. 6, 123 (1988).

5. F. M. Mann, Transmutation of Alloys in MFE Facilities as Calculated by REAC (A Computer Code for Activation and Transmutation), HEDL-TME 81-37. 1982.

6. S. A. Fetter, Radiological Hazards of Fusion Reactors: Models and Comparisons, PhD Dissertation, Univ. Of California. Berkeley (1985).

7. J. P. Holdren. et al., Summary of the Report of the Senior Committee on Environmental, Safety and Economic Aspects of Magnetic Fusion Energy, UCRL-53766-Summary (1987).

3. MATERIALS ENGINEERING AND DESIGN REQUIREMENTS

MATERIALS HANDBOOK FOR **FUSION ENERGY SYSTEMS - J.** W. Davis (McDonnell Douglas Astronautics Company - Missile and Defense Electronics Division)

OBJECTIVE

To provide a consistent and authoritative source of material property data for use by the fusion community in concept evaluation, design, and performance/verification studies of the various fusion energy systems. A second objective is the early identification of areas in the materials data base where insufficient information or voids exist.

SUWARY

The effort during this reporting period has focused on three areas:

Automation of the Handbook - Work is proceeding ahead of schedule in the development of an electronic materials handbook. with a prototype system now operational on the MFE computer network.

International Materials Handbook - In June agreement was reached on the creation of an International Fusion Materials Handbook, which would be under the auspices of the IEA and have a format similar to the **U.S.** Materials Handbook.

Support of ITER Materials Data Base - An International materials workshop was held in August at the ITER design site to review the status of the materials data base. Recommendations were made to create a design data book specifically tailored for use on **ITER.** that would not have the same level of authority as the U.S. and International Materials Handbook

PROGRESS AND STATUS

Automation of Handbook

Historically, the weakness of all handbooks is assuring that the user has an up-to-date version of a data page each time he/she uses the handbook. To accomplish this, **it** is incumbent upon the user to take the time to incorporate the latest revisions into their book. While many of the users make a conscientious effort to do this, many do not, and there are instances when handbook holders do not receive all of the data pages in their update. To make sure that all of the handbooks are up-to-date, a summary listing of the data pages contained in the handbook is usually distributed on an annual basis. This forces the user to check every page in their handbook to make sure that they have the latest revision. With an electronic handbook, many of these difficulties are avoided.

The first step in developing an electronic handbook was actually taken two years ago, when a computer code was developed to assist in the preparation and publication of the approved data pages. Since that time, as more data pages were developed using this program, the resident files essentially became a defacto electronic data bank. The next logical step was to modify this data bank into a form that the user could access, in essence an electronic version of the handbook. Most electronic data bases give the user a tabular list of properties because **it** is easier to program and access the electronic data files. However, in the Fusion Materials Handbook the properties of the various materials are sumnarized in a graphical format along with supporting text. Therefore. the decision was made not to go to a tabular format but to take the more difficult route and develop the capability to create an electronic data page in the same format that the user would see in the paper version of the handbook.

Once the decision was made regarding format, **it** was then possible to begin the actual development of the program architecture. The first step in creating the architecture was to determine how user friendly the program should be. The standard approach in making a program user friendly is to provide several menus and force the user to select several options before the actual selection of the data page is accomplished. The advantage in this approach is that the user does not have to have any knowledge of the computer or its operating system. The disadvantage is that, **if** too many menus are created, the program becomes cumbersome and takes too long to run, thus defeating the speed that the computer offers. In designing the electronic materials handbook, the decision was made to provide menus for use by the first time user who may not know what material or property he/she is seeking. along with short circuit paths to avoid the menus for those that know the specific data page that they are seeking. To improve operating speed, a search loop was created to reduce the search list until **it** only contains the entries which are to be outout.

When the program is initially started, the search list contains the entire table of contents for the handbook. During execution of the program, it is only changed through the search loop options. The basic search options are as follows:

1 Materials search - Selects a material chapter code, a material group code, or a full material code from a list of available items in the search list. Selection level is a function of what has been previously selected.

2 Property search - Same as materials search, except that it works on the components of the property code used in the paper version of the Materials Handbook.

3 Backup option - Expands the search list by undoing a material, property. or environmental effect search operation at the specified level. For each search mode, you will be asked to select one of the following levels:

1 Select a new chapter code
2 Select a new group code
3 Select a new item code
4 Leave item code unchanged

For the environmental effect codes, the options are:

1 Change
2 Do not change

Entering 1 for the material search option, 4 for the property option, and 2 for the environmental effects option will cause the new search list to contain all entries in the entire data base which give the selected property. The actual option list the user will see contains only those options relevant to selections which have already been made.

4 Output results - Copies items from the search list to the output list. Actual processing of the output list occurs when the program exits.

5 Exit option - User is given the choice of a normal termination or a quick abort. Upon normal termination, the output request is processed.

6 Environmental effects code search - Limits search list to only those items which have been previously identified with an environmental effects code and will select from the list of those codes available in the current search list.

7 Exoress material search option - Similar to option 1, except that at least one step is skipped. This allows the selection of a specific material or alloy without previously choosing a materials chapter or group. Since the list of available materials at this point is assumed to be large, the list of available codes is not presented. This option is recomnended only for users who are familiar with the contents of the handbook.

8 Express property search ootion - Equivalent to option 1, except that it works on the property codes rather than the material code.

9 Exoress page selection - Will prompt directly for an item code. without going through any menus. An item code without an environmental effect code appended to it is assumed to be equivalent to one ending in e-0 (i.e., no environmental effect).

Once a search mode has been selected, a menu is then displayed on the terminal listing all codes available on the current search list along with their definitions. If only one item is available, it is automatically selected. Otherwise, the user is asked to enter a code from the menu. After the material and property are selected, the user is asked if he/she would like either the data page, supporting documentation, or both and if the output is to be a hardcopy or for terminal viewing. In the case of a hardcopy, the files are directed to the printer at the user's site. In automated terminal viewing, the user is requested to identify the type of terminal in use and the baud rate. Currently the preferred terminals for displaying graphic files via the MFE network are the Northstar Advantage or the Tektronix. If a terminal emulator is used, the time required to create the display is significantly increased.

International Materials Handbook

The concept of an International Materials Data Base was initially proposed by the Amelinckx Panel, a Senior Advisory Panel chartered by the IEA's Fusion Power Coordinating Comnittee (FPCC). In the Advisory Panel's report to the FPCC. dated December 1986. the Panel recommended that "a mechanism be established to develop a common data base". Following their recomnendation, the IEA's Executive Comnittee in October 1987 at its Ispra meeting "agreed to the establishment of a Fusion Materials Data Base for Near-Term Design Applications. implicitly ITER (International Thermonuclear Experimental Reactor),' as a first step toward fulfilling the broader recomnendation of the Amelinckx Panel on a comnon data base.

Subsequent to this meeting, members of the Executive Comnittee held a planning meeting in Tokyo on February 12-13. 1988 to determine the most expeditious approach in developing a materials data base. At this meeting, it was agreed that, organizationally, the International Materials Data Base would be patterned after the U.S. Materials Handbook for Fusion Energy Systems, in that there would be a Steering

Committee to oversee the handbook activities and a coordinator responsible for the day-to-day management and operation. It was also agreed that the U.S. Handbook Coordinator would also serve as the International Coordinator. Members identified to serve on the Steering Comnittee were:

D. Smith (ANL, USA)
J. Davis (McDonnell Douglas, USA)
J. Nihoul (NET Team. EC)
S. Iwata (U. Tokyo. Japan)
H. Nakajima (JAERI. Japan)

Coordination of the handbook would be handled by J. Davis.

At a meeting of the Steering Comnittee during the same time frame, it was agreed to hold a workshop whose objectives would be to complete the definition and implementation procedures for the creation of the near-term data base and to recomnend an approach for the creation of a long-term data bank. This workshop was held in Petten (JRC) on June 8-10. 1988.

The primary objective of the workshop was to recomnend an approach for the creation of an International Materials Data Base. and determine its format and distribution. For the near-term. the data base will take the form of an engineering data base consisting of materials data and engineering curves, comparison of materials data, and recomnendations as to the application of these materials in a fusion environment. Distribution will be in both a paper and electronic form, using a central computer system. Authorized users will be identified by the IEA Executive Comnittee. Information sent to the handbook will be obtained from either existing data banks resident in the participating countries or developed by specific task groups. In either instance, task groups will be responsible for evaluating the data prior to submittal to the coordinator of the handbook. The coordinator will then submit the data pages to a separate view prior to publication. Participants of this review group will be identified by the Steering Committee.

Organizationally, the handbook is under the Steering Committee; however, the operation of the handbook resides with the coordinator, who is responsible for the day-to-day operation of the handbook, including its format, organization, review of the data pages, and publication and distribution of the approved data pages which is the same way that the U.S. Fusion Materials Handbook functions.

Support of ITER Materials Data Base

A specialists' meeting was held at Garching, FRG on August 22-26. 1988 for the purpose of reviewing the existing materials data base, reviewing the selection of materials for ITER, and to formulate recomnendations for the development of a common materials property data base for use on ITER. Roughly 45 people participated in this meeting, representing 12 countries. The U.S. Fusion Materials Handbook provided approximately 40 draft data pages on copper, vanadium, tantalum, and stainless steel along with recomnendations as to the impact of using molybdenum in a carbon environment.

It was generally concluded that the ITER study needs the assistance of a materials group on an interactive basis and that a ITER Design Databook. modeled along the lines of the U.S. Fusion Materials Handbook. should be developed. This book would provide a uniform set of materials property data for use on the ITER program but would not have the same formalized review that currently exists in the U.S. Handbook.

FUTURE WORK

During the next reporting period, work will continue on expanding the electronic version of the U.S. Materials Handbook and in developing a format for the International Haterials Handbook. Work on the ITER program will continue to be on an as-requested basis.

4. FUNDAMENTAL MECHANICAL BEHAVIOR

TENSILE PROPERTIES OF NEUTRON IRRADIATED A212B PRESSURE VESSEL STEEL - M. L. Hamilton and H. L. Heinisch (Pacific Northwest Laboratory)

OBJECTIVE

The objective of this work is to expand the tensile property data base for A2128 and to compare the behavior of two pressure vessel steels. A212B and A302B.

SUMMARY

A212B steel is the primary constituent of the pressure vessel of the High Flux Isotope Reactor (HFIR). Most of the existing data on mechanical properties of this and related steels are for higher temperatures and damage rates than those to which the HFIR pressure vessel is subjected. Data at lower temperatures and damage rates are, therefore, necessary to estimate the performance of A2126 steel at the conditions of service. provided that correlations can be developed which are applicable to data obtained at different temperatures, damage rates and neutron spectra.

To add to the data base for A2126 steel at laer temperatures and over a range of damage rates. miniature tensile specimens of A2126 were irradiated at 90% in the Omega West Reactor (OWR), receiving doses of from 9×10^{22} to 9×10^{23} total n m^{-2} (0.002 to 0.02 dpa) at a damage rate of 5×10^{-8} dpa s^{-1}. Roan temperature tensile tests showed more than a 50% increase in yield strength at the highest exposure. When dpa is used as the exposure parameter, the observed changes in yield strength of A212B are the same as those produced in A3026 pressure vessel steel irradiated both in OWR and with 14 MeV neutrons in RTNS-II. At 90°C, A3PTB shows little sensitivity to either neutron spectrum differences or to damage rates ranging from 3×10^{-9} to 5×10^{-8} dpa s^{-1}. Based on the similar behavior of A212B and A3026 in OWR, it appears that one can assume that A212B is similarly insensitive to displacement rate at low temperatures for levels above about 3×10^{-11} dpa s^{-1}.

PROGRESS AND STATUS

Introduction

The design of reactor pressure vessels requires conslderatton of radiation-induced changes in the strength and toughness of the vessel materials. It is essential to demonstrate that the vessel integrity will be maintained during normal operations as well as during postulated transients. The extrapolation of existing data bases is used extensively to predict the anticipated changes in behavior of the materials over the vessel lifetime. Changes in properties are monitored in surveillance programs that yield data on the irradiation environment and the resultant changes in uniaxial tensile properties and/or Charpy impact properties.

The body of reference data available at the time of the design of the High Flux Isotope Reactor (HFIR) in Oak Ridge, Tennessee predicted little or no embrittlement for the low fluences expected in the pressure vessel of HFIR. In 1986, however, routine testing of Charpy V-notch (C_v) surveillance specimens of the pressure vessel shell from HFIR revealed that a significant increase in the ductile-to-brittle transition temperature (DBTT) had occurred.[1,2]

One of the significant findings of the resulting reevaluation of the HFIR vessel integrity was that the degree of embrittlement observed in ferritic pressure vessel steels was dependent not only on the total neutron exposure, but on the exposure rate as well,[1,2] a phenanenon recently documented for the first time. but only in welded pressure vessel steels.[3] This observation is important because the data bases used to predict behavioral changes generally include only irradiations of test specimens at accelerated displacement rates to enable the determination in advance of the degree of embrittlement expected at a given total exposure.

To make reliable predictions of in-service behavior. it is necessary to develop a correlation between dlfferent neutron environments that takes into account the differences in the neutron spectrum and flux. The practice of quoting fluences of neutrons having energy greater than a threshold energy (e.g., E > 1 MeV) is an attempt to incorporate sane spectral sensitivity, and works reasonably well when canparing spectra that are not too dissimilar. Displacements per atom (dpa) has been shown to be a good correlation factor for the yield strength of alloys in a wider range of neutron environments, incorporating the effect of a neutron energy-dependent displacement cross section for the material of interest.[4]

The reevaluation of the Integrlty of the HFIR pressure vessel provided an opportunity not only to investigate the impact of displacement rate on embrittlement but also to investigate further the validity of dpa as a correlation parameter for pressure vessel steels by expanding the range of materials and irradiation conditions over which tensile data were available. The HFIR vessel integrity study[1,2] characterized the impact and tensile properties of the ferritic steel A212 grade B (hereafter referred

to as A212B) following irradiation at about 50°C in two reactors. HFIR and the Oak Ridge Research Reactor (ORR). Specimens were located in areas immediately adjacent to the HFIR pressure vessel or lust below the midplane at the edge of the core in ORR. The flux levels In the reactor positions where-the irradiations were conducted were roughly 10^{12} and 10^{17} n m^{-2} s^{-1} (E > 1 MeV), respectively.

For the present study. miniature tensile specimens of one of the same heats of material as the A212B in the HFIR pressure vessel were irradiated at 90°C in the Omega West Reactor (OWR) in Los Alamos, New Mexico at a flux of approximately 2.7 x 10^{17} n m^{-2} s^{-1} (E > 1 MeV), with a total neutron flux of 10^{18} n m^{-2} s^{-1}. Tensile data were collected and compared to the irradiation-induced changes in yield stress observed in A302B Irradiated in OWR and in RTNS-II with 14 MeV neutrons at much lower fluxes.

Experimental Procedure

Miniature tensile specimens were prepared from a full size, unirradiated. Charpy impact Specimen obtained from the archive stock of the HFIR A212B surveillance Specimens. The specimen was from heat PO818 and had the composition given in Table 1. [1] It was in the same final TMT as the HFIR pressure vessel. viz., having been given a final stress relief of 950°F (510°C) for 51 hours.

Table 1. Chemical Composition (wt. %) of A212B[13]

Element	A212B	A302B	Element	A212B	A3202B
Mn	0.85	1.34	Ti	0.01	0.015
Si	0.29	0.23	As	0.007	NA
C	0.26	0.24	P 0.006	0.011	
Ni	0.20*	0.18	N 0.0060	NA	
cu	0.15	0.20	V 0.005	0.001	
Cr	0.075	0.11	W <0.005	NA	
Al	0.07	0.04	0 0.0024	NA	
S	0.04	0.023	Zr	<0.001	NA
Mo	0.02	0.51	Nb	<0.001	NA
Sn	0.02	0.037	B <0.0005	NA	
co	0.015	NA	Fe	Bal	Bal

*Believed to be high; independent analysis at another laboratory showed 0.09.[2]

The fracture surface was ground off each half of the Charpy sample, which had been tested on the lower shelf at -20°F (-29°C). Slices with a nominal thickness of 0.010 In (0.25 mm) were electrical discharge machined from the Charpy sample halves. The miniature tensile specimens shown schematically in Figure 1 were punched from the slices according to established procedures.[5,6] The specimens were polished to remove burrs prior to subsequent use.

Three types of specimens were tested: irradiated specimens. thermally aged control specimens, and unirradiated and unaged control specimens. Specimens in the first category were irradiated at 90°C in the Omega West Reactor (OWR), operated by Los Alamos National Laboratory, using the In-Core Reactor Furnace. Eighteen specimens were Irradiated in three capsules to provide three dose accumulation levels at the same flux. yielding six Specimens for each combination of dose and irradiation temperature. Irradiation of a similar matrix at 290°C was recently completed, although tensile testing has not yet been started.

The thermally aged control specimens were aged in argon at the irradiation tmperature for times corresponding to the lengths of the irradiations: 13, 59 and 127.5 hours. The unlrradiated and unaged controls were tested to provide baseline data from which to measure the strength changes induced by irradiation. Due to the length of elapsed time between specimen fabrication and testing. these controls were repollshed prior to testing to remove the adherent oxide which had developed. The thermally aged controls were polished prior to encapsulation in argon and aging. The surfaces of the irradiated specimens were found to be free of oxidation after Irradiation and were therefore not polished prior to testing.

Specimen temperatures were maintained during irradiation by balancing gamma heating. coolant flow through the furnace. and resistance heating near the specimens. The specimens were contained in helium-filled aluminum capsules designed to minimize tmperature gradients caused by nuclear heating. Earlier calibrations of a prototypic capsule indicated all specimens to be within 10°C of the target temperature.[6] Reactor coolant water and helium gas were the coolants used to maintain the 90 and 290°C Irradiation temperatures. respectively. The resistance heater within the furnace allowed control of the temperatures to within one degree Centigrade. Accumulated total neutron exposures ranged fran 8.7 x 10^{22} n m^{-2} to 8.5 x 10^{23} n m^{-2}, ±10%. Corresponding dpa values, determined on the basis of total neutrons. were calculated using a spectral averaged displacement cross section of 222 b.[4]

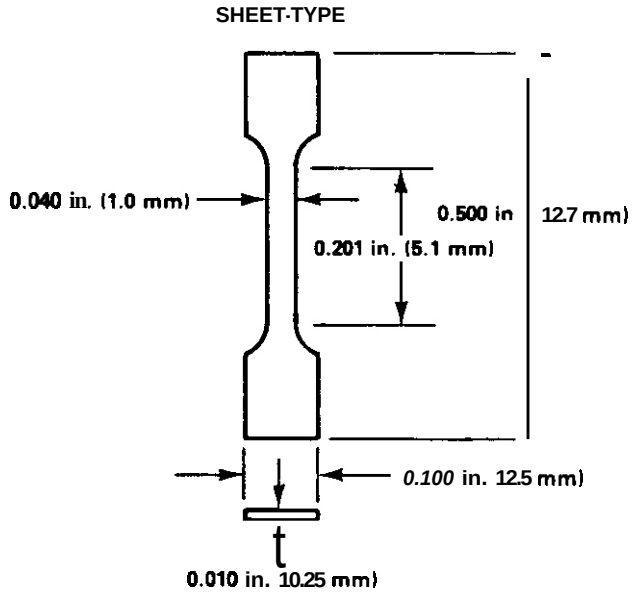

FIGURE 1. Miniature tensile specimen dimensions.

Tensile tests were conducted at roan temperature in a horizontal tensile frame designed specifically for miniature specimen testing.[5] All tests were performed with a free-running cross-head speed of 1.0 x 10^{-4} in s^{-1}, producing an initial strain rate of 4.0 x 10^{-4} s^{-1}. Two specimens of each of the six irradiated to a given dose level at 90°C have been tested. Diamond pyramid hardness measurements were also obtained on untested specimens using a 500 gram load.

Results

The tensile data are given in Table 2 and yield strength is shown as a function of damage level in Figure 2. Irradiation at 90°C to an exposure of ~0.02 dpa produced more than a 50% increase in yield strength and a 20% increase in the ultimate strength. The tensile data In Table 2 exhibit excellent reproducability throughout the range of aging and irradiation doses. Elongation data are included in Table 2 for completeness, but will be discussed only briefly. While the elongation data exhibit the reduction in ductility which is typically expected with increased strength, they should be viewed as trend indications only due to the tendency of elongation to be on the low side in miniature specimens. The relatively small amount of scatter present in the elongation data bespeaks good testing technique despite the difficulties discussed in the next section.

Discussion

Data Validity

The yield strength obtained in the current work fran the miniature punched specimens of unirradiated. unaged material is roughly 30% higher than the value obtained on larger specimens of the same material which had been fabricated by electrical discharge machining.[1,2] The values of ultimate strength obtained for the large and small specimens are canparable, however. Both machine calibration and size effects were eliminated as possible explanations for the observed differences, as was the use of slices cut from tested Charpy samples. Control tests on 304 stainless steel verified the operation of the test system. while the presence of at least ten grains across the thickness of the specimen is expected to be sufficient to produce bulk behavior for yield strength determinations.[5,7-9] The yield strength of larger specimens fabricated from the Charpy slices was consistent with the original vendor data on the steel, demonstrating that the gauge lengths in these specimens were far enough fran the Charpy fracture surface that there was no hardening fran the Charpy test.[1] The apparent source of the discrepancy in yield stress is the unexpected hardening introduced during punching of the miniature specimens.

Optical metallography revealed that the punching operation introduced more deformation into these specimens than is typically observed in the fabrication of this type of miniature specimen. Small cracks were present in the specimens immediately adjacent and parallel to the edges In both the gauge and tab sections. Transverse metallographic sections of unirradiated specimens revealed sheared zones at the specimen edges ranging in width from two to five percent of the gauge width. While hardness values in unpunched sheet and undeformed areas of punched miniature specimens ranged from 155 to 175 DPH, the hardness in the deformed areas of punched specimens was about 200 DPH.

Table 2. A212B Tensile Data on Specimens Irradiated at 90°C

Strain rate = 4.8 x 10^{-4} s^{-1}

Time at Temperature (hr)	Fluence (dpa)	Fluence ($n\ m^{-2}$)	Yield Strength (MPa)	Ultimate Strength (MPa)	Uniform Elongation (%)	Total Elongation (%)	Change* in Yield Strength (MPa)	Change* in Ultimate Strength (MPa)	Hardness (DPH)
UNIRRADIATED, UNAGED CONTROLS									
-	-	-	430	561	9.8	16.7	-	-	
-	-	-	437	571	8.8	14.4	-	-	
-	-	-	418	562	9.5	13.3	-	-	
		Average:	428	565	9.4	14.8	-	-	155-175
AGED CONTROLS									
13	-	-	420	579	4.6	8.2	-8	14	
13	-	-	411	542	6.3	9.2	-17	-23	
		Average:	416	561	5.5	8.7	-13	-5	
59	-	-	423	567	6.2	8.7	-5	2	
59	-	-	423	580	5.2	9.6	-5	15	
		Average:	423	574	5.7	9.2	-5	9	
127.5	-	-	410	563	6.8	9.6	-18	-2	
127.5	-	-	445	595	5.8	10.4	17	30	
		Average:	428	579	6.3	10.0	0	14	174
IRRADIATED									
13	0.0019	8.7E22	501	617	7.9	14.9	73	52	
13	0.0019	8.7E22	487	602	6.1	13.2	59	37	
		Average:	494	611	7.0	14.1	66	45	193
58	0.0086	3.9E23	615	663	4.1	8.5	187	98	
58	0.0086	3.9E23	611	645	2.6	7.7	183	80	
		Average:	613	654	3.4	8.1	185	89	214
127.5	0.0189	8.5E23	648	666	1.6	6.1	220	101	
127.5	0.0189	8.5E23	671	690	1.6	6.3	243	125	
		Average:	660	678	1.6	6.2	232	113	225

*Changes calculated relative to the unirradiated condition.

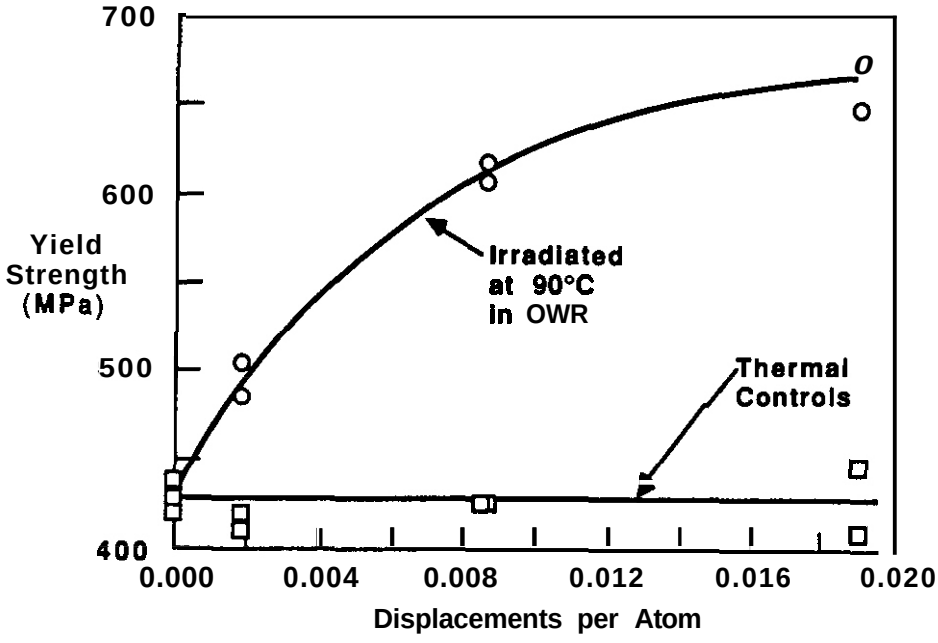

Figure 2. Roan Temperature tensile data on A212B irradiated at 90°C in WR. Controls were aged at 90°C for times corresponding to dpa levels.

It appears that the punching operation introduced sufficient hardening into the edges of the specimens that the aggregate yield strengths were canpranised on an absolute scale. The changes in yield strength which were observed with irradiation are considered valid, however, particularly since the values of ultimate strength obtained on the large and small unirradiated specimens are canparable (557 and 565 MPa, respectively) and are significantly higher than the corresponding yield strength values (35%). It is possible. however. that this argument would not hold if the yield strength continues to increase at the higher dose levels, since the increase in ultimate strength over yield strength drops from 35% in the unirradiated condition to 24, 7 and 3% with increasing damage levels.

The validity of the yield stress change data was investigated with Vickers microhardness tests on irradiated specimens in the interior regions of the specimen end tabs. which were not affected by the punching operation. Standard microhardness numbers can be related to the flow stress of a material at sane intermediate level of accumulated plastic strain. In the Vickers microhardness test. for example, DPH numbers are associated with flow stress at approximately 8% plastic strain.[10] This flow stress is related to the yield stress by the work hardening behavior of the material. It has been argued that if the work hardening response of a material does not change significantly then changes in the microhardness of the material will be proportional to changes in the yield stress.[11]

The results of the hardness tests are given in Table 2 and shown in Figure 3, which includes both hardness and yield strength as a function of damage level. The similarity in the curvature of the hardness and yield stress data suggests that the strength change data are valid; i.e., that the observed strength changes are not an artifact of a yield strength which has been increased through fabrication and irradiation to the point where the material has run out of work hardening capability.

The hardness data also provide evidence that the damage introduced into the specimens during the punching operation was not removed during irradiation. The hardness of the control specimen which was aged for the longest time was essentially identical to the hardness of the unirradiated, unaged material (Table 2), which indicates that thermal exposure at 90°C was not sufficient to relax the fabrication-induced dislocation structure. The black spot damage known to be introduced during irradiation at temperatures as low as 90°C is too small to affect the dislocation structure. The data obtained on the changes in yield strength induced in A212B during irradiation are therefore believed to be valid, despite the fact that the absolute values of the yield strength appear to have been canpranised.

Comparison to A302B Data

The changes in yield strength observed in A212B in this experiment are shown as a function of dpa in Figure 4. Also shown in this figure are the changes in the yield strength of A302B observed following irradiations in OWR and RTNS-II at 90°C.[4,6] Note the excellent agrement between changes observed in A212B and A302B after irradiation in WR. Irradiations in OWR were at a damage rate of about 5×10^{-8} dpa s^{-1}, while irradiations in RTNS-II involve a large spatial variation of neutron flux producing damage rates ranging fran 3×10^{-11} to 3×10^{-9} dpa s^{-1} (depending on the distance between specimen and source). up to three orders of magnitude less than in OWR.

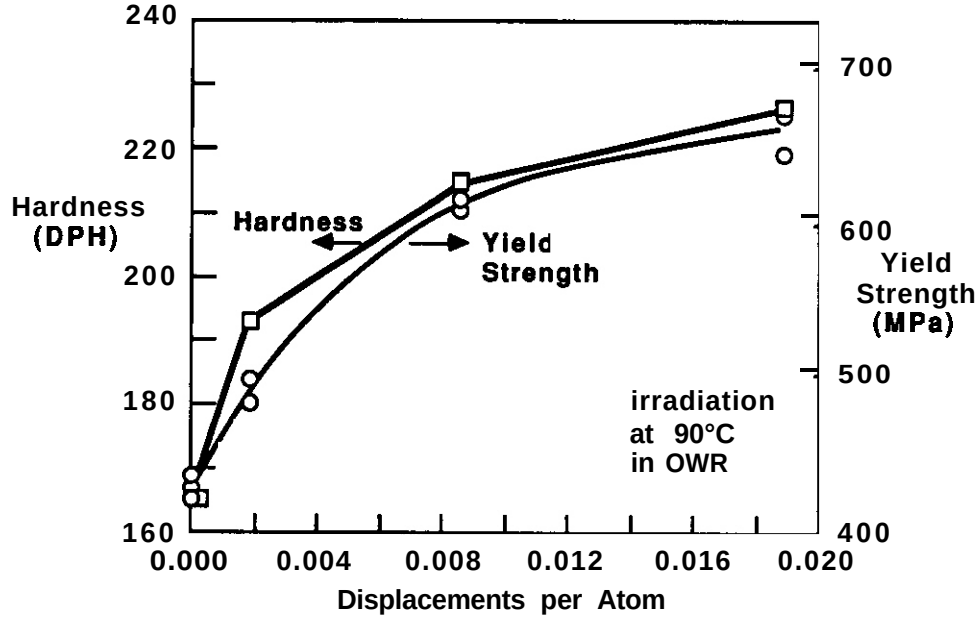

FIGURE 3. Hardness and yield strength of A2126 specimens irradiated at 90°C in OWR.

Two sets of A3028 data fran the RTNS-II experiment are shown in Figure 4, corresponding to two separate runs. R-1 and R-2. R-2 was irradiated further fran the neutron source for an order of magnitude longer than R-1; fluxes in R-1 ranged fran about 3 x 10^{14} to 1 x 10^{16} n m^{-2} s^{-1}, while fluxes in R-2 ranged fran about 1 x 10^{14} to 3 x 10^{15} n m^{-2} s^{-1}. Thus. within each run the range of fluences was achieved through a range of flux values. This is in contrast to the OWR, in which the flux was identical for all specimens but the length of irradiation was varied.

The A302B data fran OWR and fran RTNS-II experiment R-2 were used earlier[4] to infer that there is no effect of flux at 90°C in the range fran 10^{14} to 10^{18} n m^{-2} s^{-1}. The R-1 data have been added to support this conclusion and to extend slightly the flux range of the RTNS-II data. The correlation between OWR and RTNS-II data using dpa is very good, showing no apparent effect of differences in damage rate or neutron spectrum for A302B at 90°C.

While A302B was developed as the successor to A2128 in pressure vessel steel technology. the composition of A302B (see Table 1) is very similar to that of A2126 with respect to those elements now known to cause embrittlement in uniaxial tensile tests at temperatures at or above about 290°C. The elements most often considered responsible for the majority of the shift in impact behavior are nickel, copper and phosphorus. Nickel does not appear to have a significant effect in concentrations below about 0.5%.[11,12] At 290°C, the effect of copper saturates at about 0.2%[12] and it is expected that the trend towards lower saturation levels with decreasing irradiation temperature will continue to lower irradiation temperatures. Phosphorus appears to play only a minor role in tensile behavior at the levels in which it is present in these two steels. Thus the nickel. copper and phosphorus levels present in A2126 and A3028 are not expected to lead to significantly different degrees of uniaxial embrittlement in these two steels. Indeed. it has also been suggested that compositional variations between numerous older steels are not the daninant factor in the dose dependence of embrittlement.[2] Very little is known. however, about the effect of composition on embrittlement at temperatures below 290°C. Based on the similarity of the A2128 and the A3026 compositions and their yield strength change data, one could reasonably expect that the tensile behavior of A2126 will exhibit a similar insensitivity to damage rate and neutron spectrum under similar conditions.

The relative flux ranges of the various reactors used for tests on pressure vessel steels at low irradiation temperatures are shown in Figure 5. The regions marked for RTNS-II and OWR correspond to data generated on A212B and A3026 in the current study and the previous study of Heinisch, et al. for irradiation at 90°C.[4,6] The regions marked for ORR and the HFIR pressure vessel (PV) correspond to data on A212B which were generated following 50°C irradiation on HFIR surveillance specimens and on similar specimens irradiated in ORR.[1,2]

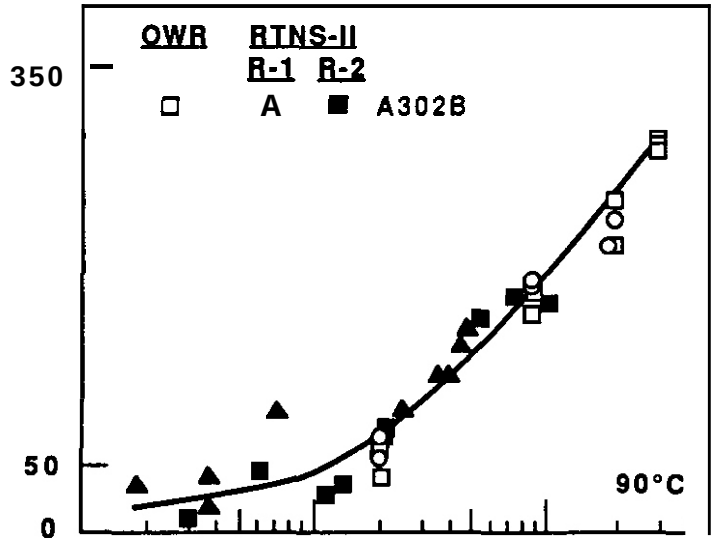

When correlated on the basis of dpa. A302B specimens irradlated at the hlghest flux (In OWR) exhibited changes in yield strength that were identical to those observed during irradlation in RTNS-II at fluxes two to four orders of magnitude laer. A212B, the HFIR pressure vessel steel. is expected to exhibit a similar flux independence on the basis of the considerations discussed above. However. in tests on A212B Irradiated in ORR and at the HFIR pressure vessel itself,[2] where fluxes are up to two orders of magnltude lower than the lowest flux In RTNS-II, a strong damage rate sensltivlty was found. Thus there appears to be a threshold displacement rate below which displacement rate influences Irradiation-Induced strength changes at low temperatures. At higher rates, irradiation-Induced changes can be correlated using dpa as an exposure parameter over a rather wide range of neutron energles and displacement rates.

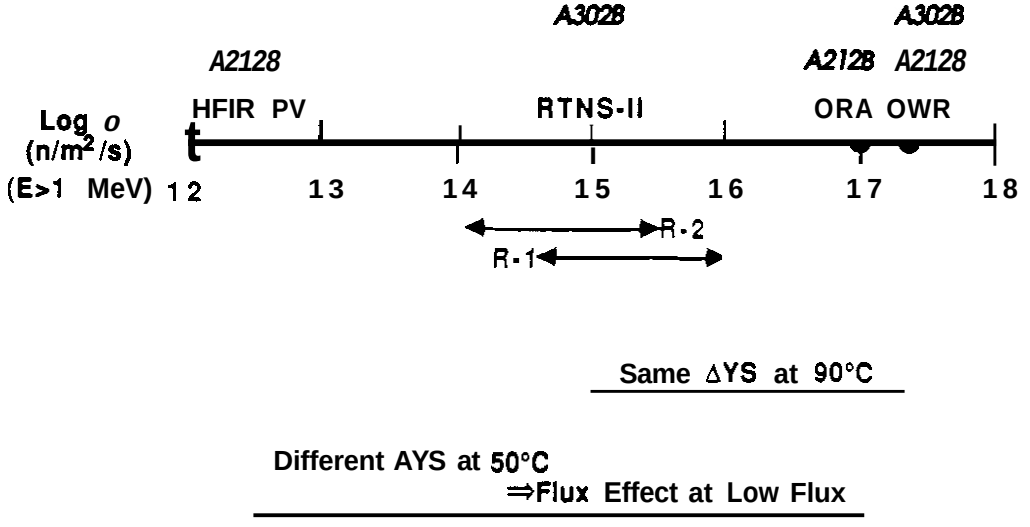

FIGURE 5. Schematic representation of the dependence of yield strength changes on flux (E > 1 MeV).

CONCLUSIONS

A2128 and A3028 pressure vessel steels exhibit essentially identical property changes during irradiation in WR at relatively high displacanent rates canpared to those at reactor pressure vessels. The response of A302B has been shown to be insensitive to displacement rate over the range 3 x 10^{-11} to 5 x 10^{-8} dpa s^{-1} at low temperature and it is argued here that A2128 will behave in a similar manner. Based on a canparison of these and other published results, there appears to be a lower threshold flux below which the displacement rate is important.

ACKNOWLEDGEMENTS

The Charpy specimen slices were provided by D. N. Braski of the Oak Ridge National Laboratory. Dosimetry was provided by L. R. Greenwood of the Argonne National Laboratory.

REFERENCES

1. R. O. Cheverton, J. G. Merkle. and R. K. Nansted. 'Evaluation of HFIR Pressure Vessel Integrity Considering Radiation Embrittlement." ORNL/TM-10444, to be published.

2. Nanstad. R. K., Farrell. K., Braski. D. N. and Cornin. W. R., "Accelerated Neutron Embrittlement of Ferritic Steels at Low Fluence: Flux and Spectrum Effects," to be published in the Journal of Nuclear Materials.

3. Priest. R. H., Charnock, W., and Neale, 8. K., "Fracture Toughness of Accelerated Irradiated Submerged-Arc Weld Metal." Effects of Radiation on Materials: Twelfth International Symposium. ASTM STP 870, F. A. Garner and J. S. Perrin. Eds., ASTM, Philadelphia. 1985, pp. 1150–1162.

4. Heinlsch. H. L., "Effects of the Neutron Spectrum on Mechanical Property Changes in Low Dose Irradiations." presented at the Third International Conference on Fusion Reactor Materials. Oct. 4-8, 1987, Karlsruhe. Germany. to be published in the Journal of Nuclear Materials in volumes 154–156.

5. Panayotou. N. F., Atkin, S. D., Puigh. R. J. and Chin. B. A., "Design and Use of Nonstandard Tensile Specimens for Irradiated Materials Testing." The Use of Small-Scale Specimens for Testing Irradiated Material, ASTM STP 888, W. R. Cornin and G. E. Lucas. Eds., ASTM. Philadelphia. 1986, pp. 201–219.

6. Heinisch. H. L., Atkin, S. D., and Martinez, C., "Spectral Effects in Low-Dose Fission and Fusion Neutron Irradiated Metals and Alloys," J. Nucl. Mat. 141-143 (1986) pp. 807-815.

7. Igata. N., Miyahara. K., Uda, T., and Asada, S., "Effects of Specimen Thickness and Grain Size on the Mechanical Properties of Types 304 and 316 Austenitic Stainless Steel," The Use of hall-Scale Specimens for Testing Irradiated Material. ASTM STP 888, W. R. Corwin and G. E. Lucas. Eds., ASTM. Philadelphia, 1986, pp. 161–170.

8. Igata. N., Miyahara. K., Tada. C., Blasl, D. and Lucas. G., "Phenomenological Studies of the Effects of Miniaturization and Irradiation on the Mechanical Properties of Stainless Steels," Radiation Effects 101 (1986) 131–146.

9. Kohyama, A., Asakura. K., and Igata. N., Wechanical Property Changes in Ferritic Steels by 14 MeV Neutron Bombardment," J. Nucl. Mater. 141-143 (1986) 921-925.

10. Tabor, P., The Hardness of Metals. Clarendon Press. London. 1951.

11. Lucas, G. E, Odette. G. R., Maiti, R and Sheckherd. J. W., Tensile Properties of Irradiated Pressure Vessel Steels." Influence of Radiation on Material Properties: 13th International Symposium (Part II), ASTM STP 956, F. A. Garner. C. H. Henager, Jr., and N. Igata. Eds., ASTM. Philadelphia, 1987. pp. 379–394.

12. Lucas. G. E. Odette, G. R., Lanbrozo. P. M., and Sheckherd. J. W., "Effects of Composition, Microstructure. and Temperature on Irradiation Hardening of Pressure Vessel Steels," Effects of Radiation on Materials: Twelfth International Symposium, ASTM STP 870, F. A. Garner and J. S. Perrin. Eds., ASTM, Philadelphia, 1985. pp. 900-930.

13. Hawthorne. J. R and Menke, 8. H. Light Water "Reactor Pressure Vessel Surveillance Dosimetry Improvement Program: Postirradiation Notch Ductility and Tensile Strength Determinations for PSF Simulated Surveillance and Through-Wall Specimen Capsules." NUREG/CR-3295 (MEA-2017). August 1983.

5. RADIATION EFFECTS: MECHANISTIC STUDIES, THEORY, AND MODELING

ON PRECIPITATE DISSOLUTION USING THE CASCADE SLOWING-DOWN THEORY –
S. P. Chou and N. M. Ghoniem (University of California, Los Angeles)

OBJECTIVE

The objective of this work is to extend our cascade slowing-down theory to the evaluation of the precipitate dissolution rate, and to illuminate the physical mechanism, which are responsible for the recent experimental observations of Muroga and coworkers.

SUMMARY

The dissolution parameter for precipitates under irradiation is evaluated using the cascade slowing-down theory. By using a diffusion length calculated for average recoils in a collision cascade and by including electronic stopping in the theory, the results from the cascade slowingdown theory are in reasonable agreement with the results by Muroga, Kitajima, and Ishino. Also, the results are consistent with the experimental observation by Sekimura, et al.

PROGRESS AND STATUS

1. Introduction

The effects of irradiation dissolution on the stability of precipitates are important for the performance of nuclear materials. Wilkes [1] investigated the atability of precipitates subjected to dissolution using the bubble resolution model developed by Hudson and others [2,3] for the treatment of fission gases in uranium fuels. Using the Monte Carlo method, Chou and Ghoniem [4] demonstrated that dissolution of precipitates by energetic collision cascade is possible. Chou and Ghoniem [5] then developed a cascade diffusion slowing-down theory which yields theoretical dissolution parametera. Sekimura, et al. [6] conducted experiments by irradiating precipitates with energetic ion beams. The results from those experiments indicate that the dissolution parameter in considerably smaller than that predicted by the Chou-Ghoniem model. Muroga, Kitajima, and Ishino (MKI)[7] incorporated the Monte Carlo ion transport calculation with the Gelles and Garner ion range distribution model [8] to obtain apparently smaller precipitate dissolution parameters than those inferred from the cascade slowing-down theory.

The purpose of this paper is to show that, by relaxing the assumptions used in the cascade slowing-down theory, good agreements between the results of the MKI model and the Chou-Ghoniem cascade slowing-down theory are obtained. Furthermore, the results are also consistent with recent experimental observations by Sekimura, et al. [6]. A brief outline of the Chou-Ghoniem cascade slowingdown theory and the MKI model are given in the next section. This is fallowed by an analysis of the average recoil dissolution rate in sect. 3. It will be shown that when the average recoil nuclear stopping is considered, the cascade slowing-down theory is consistent with the MKI model and with experimental observations.

2. Theoretical Background

2.1. Cascade slowing-down theory

The cascade diffusion slowing-down equation solved by Chou and Ghoniem taken the form [5]:

$$-D\nabla^2\Phi + \Sigma_t = \int_0^\infty dE'\Sigma_s(E' \to E)\Phi(\mathbf{r}, E') + Q + \frac{d[S(E)\Phi]}{dE} \quad , \tag{1}$$

where $\Phi(E)$ is the recoil flux at energy E, Q is the displacement rate, D is the diffusion coefficient, Σ_T is the totd interaction cross section, $\Sigma_s(E' \to E)$ is the differential scattering cross section from energies E' to E, and $S(E)$ is the electronic stopping.

To develop analytical solutions of Eq. (1), a number of physically reasonable assumptions were employed. It was assumed that scattering is represented by hard-sphere collisions, that the interaction cross section is independent of

energy, and that electronic stopping is negligible. Using these assumptions, Chou and Ghoniem utilized a Neumann's series expansion of the flux to produce analytical solutions for the dissolution rate. It was found that the dissolution parameter (dissolution rate to displacement damage-rate ratio) can asymptotically be expressed as:

$$b \simeq 1 , \qquad r_p \leq \frac{L}{\sqrt{3}} , \tag{2}$$

$$\simeq \frac{L}{\sqrt{3} r_p} , \qquad r_p \geq \frac{L}{\sqrt{3}} , \tag{3}$$

where r_p is the radius of the precipitate and L is a characteristic diffusion length. The diffusion length can be estimated form the projected range of cascade recoils. In this note, we will estimate the approximate value of L for average recoils such that Eqs. (2) and (3) can be directly compared to experiments and the MKI model. The projected range and the diffusion length are related by:

$$R^2 = \xi L^2 , \tag{4}$$

where ξ is the average number of collisions for a recoil with energy E to be slowed down to the displacement energy, E_d. For like atoms with hard-sphere collisions, the average energy loss for each collision is half of the incident atom energy. Accordingly,

$$\xi = \frac{\ell n(E/E_d)}{\ell n(2)} . \tag{5}$$

The relationship between the recoil projected range R and its energy E obtained by the TRIPOS calculations [4] can he approximated by

$$R(nm) = A[E(keV)]^n , \tag{6}$$

where A and n are fitting constants. For iron atom in iron, $A = 0.53$ and $n = 0.911$. Also from the cascade slowing-down theory, the flux spectrum of cascades in an infinite medium has the form:

$$\Phi(E) = \frac{2Q E_0}{\Sigma E_d} + \frac{Q}{\Sigma}\delta(E - E_0) , \tag{7}$$

where E_0 is the energy of the primary knock-on atoms or the cascades.

2.2. The MKI model

The MKI model [6] describes the dissolution parameter for a recoil in a collision cascade as

$$b = 1 , \qquad r_p \leq 0.5R , \tag{8}$$

$$= \frac{12X - X^3}{16} , \qquad r_p \geq 0.5R , \tag{9}$$

where r_p is the precipitate radius, R is the recoil range, and

$$X = \frac{R}{r_p} \tag{10}$$

In order to evaluate the average dissolution parameter for a complete cascade, MKI use the Monte Carlo ion transport method to evaluate the range distribution for a cascade. The average dissolution parameter can then be obtained by integrating the individual dissolution parameter and the recoil distribution over the whole recoil energy distribution range.

3. Analysis of Average Recoil Dissolution Rate

The dissolution of a precipitate by collision cascades results from the interaction with the recoils, particularly the higher order recoils generated in the precipitate. As such, those recoil atoms with enough energy to transport through the precipitate are dissoluted in the matrix. Furthermore, Lindhard's theory [9,10] indicates that none, or only a small fraction, of the PKA energy is consumed in electronic stopping for low-energy collision cascades. Also, the amount of nuclear stopping energy saturates at high PKA energies.

In this regard, the energy available for cascade generation is the nuclear stopping energy instead of the primary knock-on energy. The nuclear stopping energy for a PKA with an energy E_0 is given by

$$E = \frac{Ea}{1+0.13(3.4\epsilon^{0.167}+0.4\epsilon^{0.75}+\epsilon)} \quad , \tag{11}$$

where the reduced energy ϵ in given as

$$\epsilon = \frac{E_0}{2Z^2e^2/a} \quad , \tag{12}$$

and the Debye screening length, a, is

$$a = \frac{0.88a_B}{Z^{0.333}} \quad , \tag{13}$$

and a_B is the Bohr radius (0.053 nm), e is the electron charge, and Z is the atomic number of the recoils.

The average recoil range is obtained as

$$\bar{R} = \frac{\int R(E)\Phi(E)dE}{\int \Phi(E)dE} \tag{14}$$

$\Phi(E)$ is the recoil flux derived by Chou and Ghoniem [5] as given in Eq. (7). Likewise, the average number of collisions for precipitate recoils has the form:

$$\bar{\xi} = \frac{\int \xi(E)\Phi(E)dE}{\ell n(2)\int \Phi(E)dE} \quad , \tag{15}$$

$$= \frac{2E_0}{\ell n(2)(2E_0-E_d)}\{1-\frac{E_d}{E_0}[1+\ell n(\frac{E_0}{E_d}\} \tag{16}$$

The value for ξ is in a range of 1.30 to 1.45 for PKA energies of 1 keV to 10 MeV. Using the concept in the random walk theory, the diffusion length for an average recoil can be related to the average recoil range as: $\bar{L} = \bar{R}/\sqrt{\bar{\xi}}$.

The current application of the cascade diffusion theory to average recoils uses barred L and R instead of the originally defined L and R [5]. The average precipitate dis-solution parameter has the form:

$$b \simeq 1 \qquad r_p \le 0.48R \quad , \tag{17}$$

$$\simeq \frac{0.48R}{r_p} \quad , \qquad r_p \ge 0.48R \quad . \tag{18}$$

The coefficient 0.48 in the above equations is for high energy cascades. For low energy cascade, it is about 0.50. Generally speaking, the coefficient is not a sensitive function of the PKA energy. Asymptotically, the cascade slowing-down formula is very similar to the MKI formula for average cascade recoils. However, for very large precipitates, the MKI formula predicts a 50% higher cascade dissolution rate. Fig. 1 shows a comparison of the dissolution parameters between MKI and cascade slowing-down models. The cascade slowing-dawn results are smaller by less than a factor of 2.0. This is attributed to the differences in the coefficient of the dissolution parameter and the recoil spectrum. The average recoil dissolution parameter in the present work is consistent with the experimental results by Sekimura, et al. [6] where precipitate dissolution was found not to be significant under their experimental conditions.

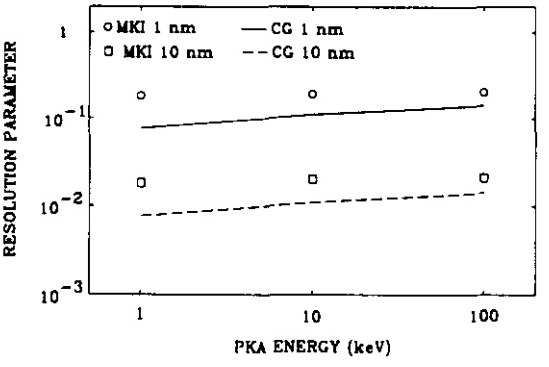

Fig. 1. A comparison of the dissolution parametera between MKI model and CG cascade slowing-dawn model for precipitates with sizes of 1 nm and 10 nm.

4. Conclusions

This work incorporates the concepts of the nuclear damage energy and the average recoil diffusion length in the cascade slowing-down theory. This relaxes the assumption of neglecting the electronic stopping in the original cascade slowingdown work. Also, adoption of an average recoil diffusion length decreases the characteristic diffusion length for a cascade. These allow the cascade slowing-down theory to yield precipitate dissolution parameters which are more consistent with experimental observations on high energy collision cascades. Also, the calculated precipitate dissolution parameter is found to be within 50% of the results of Muroga, Kitajima, and Ishino.

Acknowledgment

This work was supported by the U.S. Department of Energy, Office of Fusion Energy, Grant # DE-FG03-84ER52110, with UCLA.

References

[1] P. Wilkes, J. Nucl. Mater. 83 (1979) 66.

[2] J.A. Hudson, J. Br. Nucl. Energy Soc. 14 (1975) 127.

[3] R.S. Nelson, J.A. Hudson and D.J. Mazey, J. Nucl. Mater. 44 (1972) 318.

[4] P. Chou and N.M. Ghoniem, J. Nucl. Mater. 117 (1983) 55.

[5] P. Chou and N.M. Ghoniem, Nucl. Instr. Meth. BQ (1985) 209.

[6] N. Sekimura, T. Zama, H. Kawanishi and S. Ishino, J. Nucl. Mater. 141/143 (1986) 771.

[7] T. Muroga, K. Kitajima and S. Ishino (ASTM, Philadelphia, 1987) STP-955, p. 834.

[8] D.S. Gelles and F.A. Garner, J. Nucl. Mater. 86/86 (1979) 689.

[9] J. Lindhard, V. Nielsen, M. Scharff and P.V. Thompson, Mat. Fya. Medd. Dan. Vidensk. Selsk. 33 (1963) I

[10] M.T. Robinson, in: Radiation Induced Voids in Metals, eds., J.W. Corbett and L.C. Ianniello, USAEC Report CONF-710601 (NTIS, Springfield, 1972) pp. 397-429.

FUTURE WORK

This analytical approach has reached reasonable maturity, and we therefore are not planning to pursue further development along these lines. However, detailed molecular dynamics simulations may still be necessary to shed light on the energy and position distributions of disoluted atom from precipitates

EFFECTS OF PREINJECTED HELIUM IN HEAVY-ION IRRADIATED NICKEL AND NICKEL-COPPER ALLOYS - LM. Wang, R.A. Dodd, G.L. Kulcinski (University of Wisconsin) and S.J. Zinkle (Oak Ridge National Laboratory)

OBJECTIVE

The objective of this study is to determine if preinjected helium will promote void formation in Ni-Cu alloys during heavy ion irradiation.

SUMMARY

Pure nickel and two nickel-copper alloys (Ni-10 at.% Cu and Ni-50 at.% Cu) both containing *50* appm preinjected helium have been irradiated with 14 MeV nickel ions at a constant homologous temperature of 0.45 T_m. The radiation-induced crystal defects have been analyzed by TEM with samples prepared in cross-section. In the helium preinjected region of the pure nickel specimen, a substantial density of voids with an average diameter of 35 nm was observed. The nickel-copper alloys were found to contain a high density of small helium bubbles (under 5 nm in diameter) and dislocation loops. The density of both dislocation loops and helium bubbles increases with the increasing copper content, and the size decreases with increasing copper content. The observed resistance of the nickel-copper alloys to void formation regardless of the presence of helium bubbles, is considered to be the result of local clustering of like atoms.

PROGRESS AND STATUS

Introduction

Radiation induced void swelling is one of the serious material problems to be solved for proposed fusion reactors.' To better understand the mechanisms controlling the void formation process. pure metals and simple alloys are often chosen for radiation damage studies although they are unlikely to be used as fusion reactor materials. Ni-Cu alloys have been shown to be very resistant to void swelling under neutron,[2] ion[3-6] and electron' irradiations in the past decade. Such an observation is very significant because the alloy system form a complete solid solution over the entire composition range and voids can easily be produced in both pure nickel and copper in the presence of certain gas atoms. Helium is a transmutation product in fusion reactor materials due to (n,α) reactions and it is also known as a void nucleation agent. Zinkle et al.[8] injected 200 appm helium into nickel, copper and three Ni-Cu alloys at a homologous temperature of 0.65 T_m, and found nothing anomalous concerning helium bubble growth in the alloys which would explain the suppression of void swelling. Other than the above study, the effect of helium in Ni-Cu alloys has not been carefully investigated, even though some of the previously irradiated samples contain a certain amount of helium.[2-3] In this study, we have investigated the effects of preinjected helium in 14 MeV nickel-ion-irradiated Ni-10 at.% Cu and Ni-50 at.% Cu. A heavy ion irradiated pure nickel specimen with helium preinjection is included in the study for the purpose of comparison.

Experimental

The pure nickel specimen used in this study came from a degassed Marz grade (99.995 wt.% pure) sheet which contains 75 appn oxygen. Our previous results showed that at this residual oxygen level, the effect of preinjected helium on void formation is more pronounced than in the as-received foil which contains 180 appn oxygen.[9] This is because oxygen is also found to be a void stabilizer.[9-10] Two Ni-Cu alloys, Ni-10Cu (at.%) and Ni-50Cu were fabricated from Marz grade Ni and Cu (99.999 wt.% pure) by arc melting followed by a homogeneity treatment in flowing argon at 1000°C for 24 hours. Vacuum fusion analyses performed by Los Alamos National Laboratory indicated that the oxygen content in the alloys was about 100 appm. The ingots of the alloys were cold rolled with intermittent annealing in flowing argon at 800°C to 0.5 mm thick foils, which were then mechanically polished with 0.05 μm alumina abrasive.

Helium ions with energies between 200-400 keV were injected into the two Ni-Cu alloy samples at Oak Ridge National Laboratory and the pure nickel specimen was injected earlier with 200-700 keV helium using the University of Wisconsin 700 kV Accelerator Facility. The helium injections were all performed at ambient temperature and with the dose which gave an average concentration of *50* appm in the injected region.

The samples containing injected helium were then irradiated with 14 MeV Ni^{3+} ions at the University of Wisconsin Heavy Ion Irradiation Facility with a flux of ~ 3×10^{16} Ni^{3+}/m^2s at the constant homologous temperature, T/T_m = 0.45, i.e. 500°C, 485°C and 425°C for pure nickel, Ni-10Cu and Ni-50Cu respectively. The reason for choosing this homologous temperature for irradiation is that voids are known to form only in the temperature range of 0.3-0.6 T_m. At lower temperatures, vacancies are not mobile enough to move together to form voids and most of them will recombine with a mobile interstitial atom. When the temperature is higher than 0.6 T_m, the equilibrium vacancy concentration is very high, which makes the vacancy supersaturation insufficient for void nucleation and growth. The irradiation fluences were decided

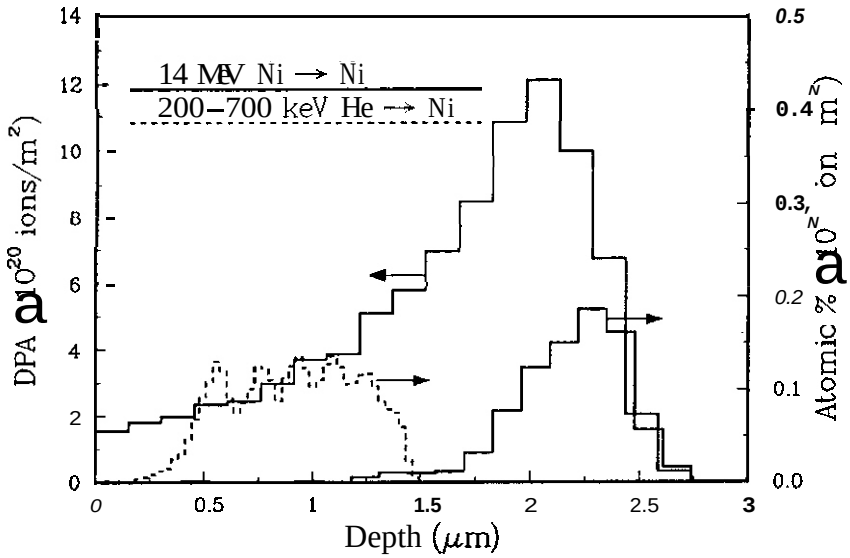

Fig. 1. Displacement damage (by 14 MeV Ni ions) and injected ion distributions (14 MeV Ni ions and 200-700 keV He ions) in pure Ni calculated by using the Monte Carlo code, TAMIX.[**]

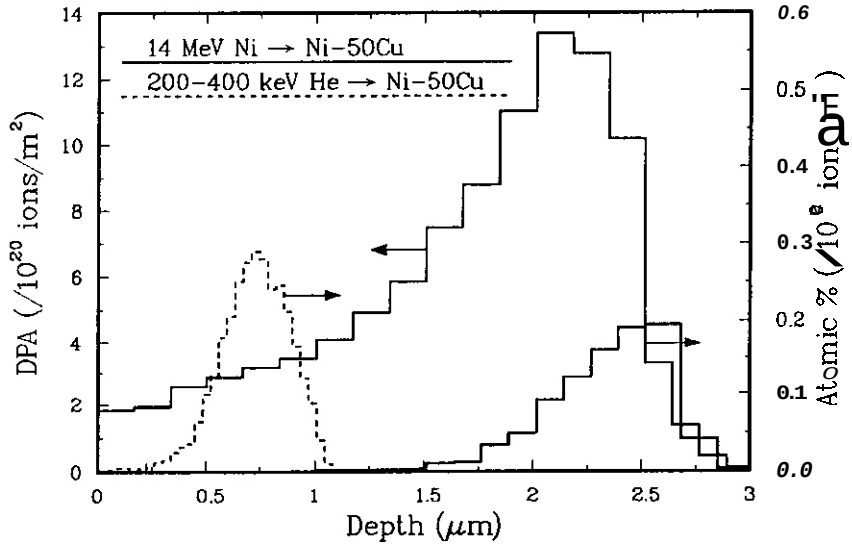

Fig. 2. Displacement damage (by 14 MeV Ni ions) and injected ion distributions (14 MeV Ni ions and 200-400 keV He ions) in Ni-50Cu calculated by using the Monte Carlo code, TAMIX.[**]

according to Monte Carlo calculations by the TAMIX code.[**] The pure nickel specimen received 3 dpa at the depth of 1 μm, while the Ni-Cu alloy samples received 5 dpa at the same depth. The calculated displacement damage (by 14 MeV nickel ions) and the injected ion distributions (14 MeV nickel ions and helium ions with the energy range used during preinjection) in pure nickel and Ni-50Cu are shown in Fig. 1 and Fig. 2, respectively.. It is fortunate that the preinjected helium range is separated from the injected nickel ion range so that their effects can be separated. The appm helium/dpa ratio in the helium injected region of this study is around 10 to 15, which is close to the ratio for potential fusion reactor materials.[1]

After irradiation, the samples were prepared into cross-section TEM specimens, so that the entire ion damage range could be studied. TEM observation was performed with a JEOL TEMSCAN-200CX electron microscope with attention mainly focused at the helium injected region.

Results

Figures 3 (A), (B) and (C) are the cross-sectional TEM micrographs showing the entire ion damaged range in the three irradiated samples. During preparation of the cross-section TEM specimens, the original surface of irradiation has been electroplated with nickel, so it becomes an interface in the micrograph. It should be mentioned that a surface layer of up to 0.3 μm thick was removed from the original surface before electroplating to insure good bonding at the interface. Therefore, the actual depth from the irradiated surface is about 0.3 μm more than the depth marked in the cross-sectional micrographs. The micrographs in Fig. 4 were taken at a higher magnification from each specimen at the actual depth of 0.6-1.0 μm, where the preinjected helium is present.

The defect structures in the three irradiated materials are distinctly different. In the irradiated pure nickel, the most obvious defect clusters are voids, although some prismatic dislocation loops are also present. Comparing the result reported earlier[3] on the nickel containing the same amount of residual oxygen but without helium preinjection, it appears that the relatively high density of voids in the first 1.5 μm of the nickel specimen shown in Fig. 3(A) is due to the presence of preinjected helium in that region.

In the two irradiated Ni-Cu alloy samples, dislocation loops constitute the major defect cluster. The loop density increased dramatically—with the copper content, while the loop size decreased concomitantly. Perfect loops on {111} planes with b = a/2<110> and Frank loops enclosing a stacking fault with b = a/3<111> are both identified in Ni-10Cu, but only perfect loops have been identified in Ni-50Cu. The density and size distribution of the loops are almost the same as the result of a previous study[6] on irradiated Ni-Cu alloys with 5 MeV oxygen ion preinjection. Since the 5 MeV oxygen was implanted deeper in the samples, the similarity in the loop distribution means that the preinjected helium did not have the power to alter the defect characteristics in the alloys under our experimental conditions. However, when dislocations are tilted out of contrast, e.g. the specimen is tilted away from the strong diffracting orientation, small bubbles with diameters less than 5 nm are observed at the helium injected depth in both Ni-10Cu and Ni-50Cu as shown in Fig. 5. The density of the helium bubbles in Ni-50Cu is an order of magnitude higher than that in Ni-10Cu, and the bubble size is larger in the latter. When comparing the size of the bubbles in the Ni-Cu alloys with the size of voids in pure nickel as shown in Fig. 5(A), please note that Figs. 5(B) and 5(C) have a much higher magnification.

Table 1 summarizes the defect characteristics in the helium injected region of the three materials irradiated in this study. The volume swelling in the helium preinjected region of the nickel specimen is about 3.5×10^{-3}, while the swelling due to the formation of small bubbles in the Ni-Cu alloys is estimated to be at least one order of magnitude lower, even though the Ni-Cu samples were irradiated to a higher displacement damage level.

Discussion

The formation of helium bubbles in the Ni-Cu alloys is expected, because there are theoretical and experimental indications that helium tends to undergo spontaneous precipitation when implanted in metals, including the void resistant Ni-Cu alloys.[8] The interesting point of our results is that the resistance to void swelling of the Ni-Cu alloys is maintained even in the presence of small helium bubbles during irradiation. A simple calculation based on the ideal gas law and the assumption of equilibrium bubble pressure indicated that some vacancies must be trapped in the helium bubbles to achieve the bubble volume observed in this study. Nevertheless, the majority of the excess vacancies which survived recombination apparently did not go to the bubbles to cause growth into larger voids. Instead, they form dislocation

Table 1. Defect characteristics* in 50 appm helium preinjected Ni and Ni-Cu alloys following 14 MeV Ni ion irradiation.

Material	dpa	Irradiation Temperature (°C)	Dislocation Loop density (m^{-})	Dislocation Loop average size (nm)	Helium Bubble (or Void) density (m^{-3})	Helium Bubble (or Void) average size (nm)
Ni	3	500	1×10^{20}	15.3	1.5×10^{20}	35 (void)
Ni-10Cu	5	405	1×10^{21}	21.5	3.0×10^{21}	3.5
Ni-50Cu	5	425	7×10^{21}	6.5	3.0×10^{22}	2.3

'Defect parameters in the table are measured from the region about 1 μm below the irradiated surface.

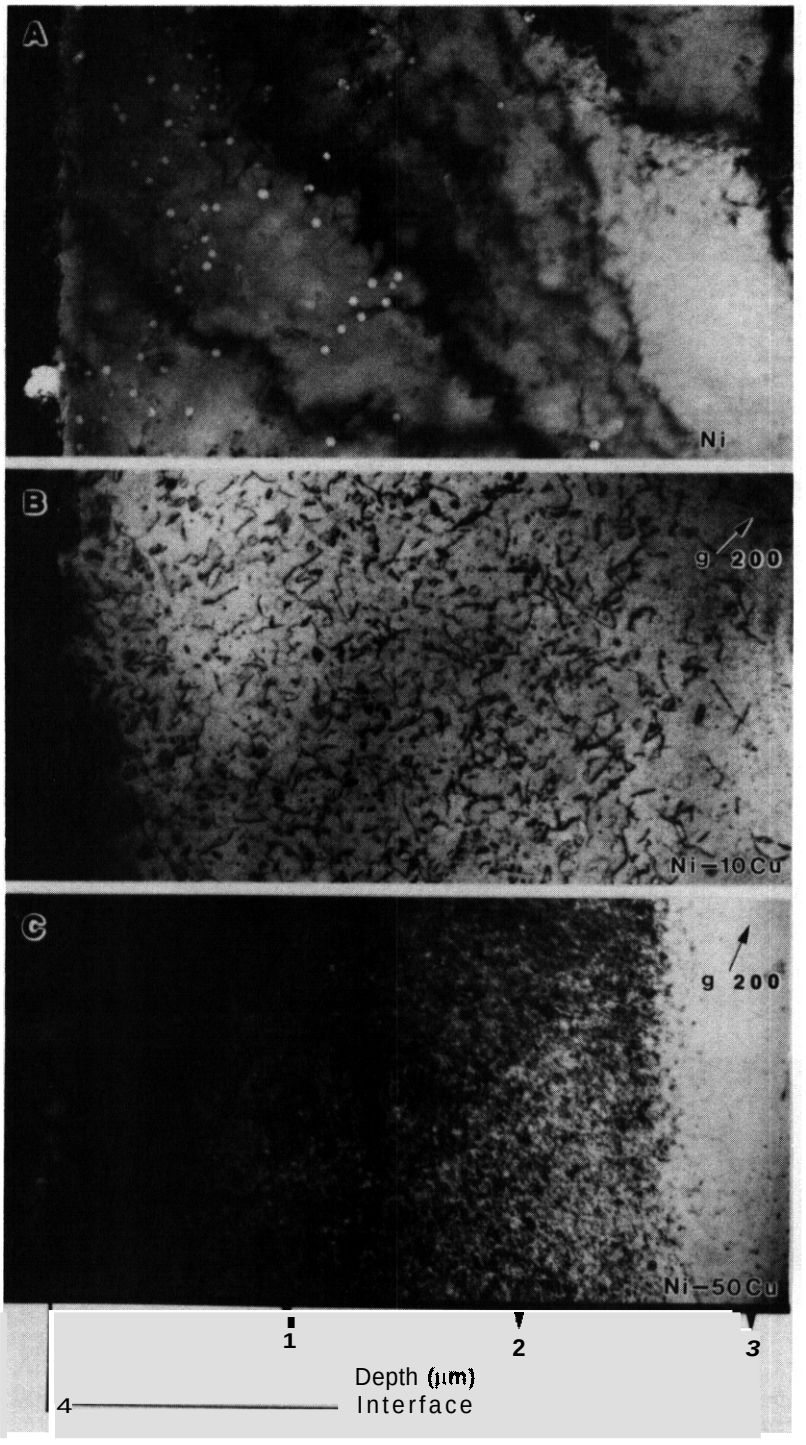

Fig. 3 Cross-sectional TEM micrographs showing the entire ion damaged region in 14 MeV Ni ion irradiated (A) pure Ni (3 dpa at 1 μm, 500°C), (B) Ni-10Cu (5 dpa at 1 μm, 485°C) and (C) Ni-50Cu (5 dpa at 1 μm, 425°C). 50 appm He (200-700 keV for pure Ni, 200-400 keV for the alloys) was preinjected at ambient temperature before Ni ion irradiation.

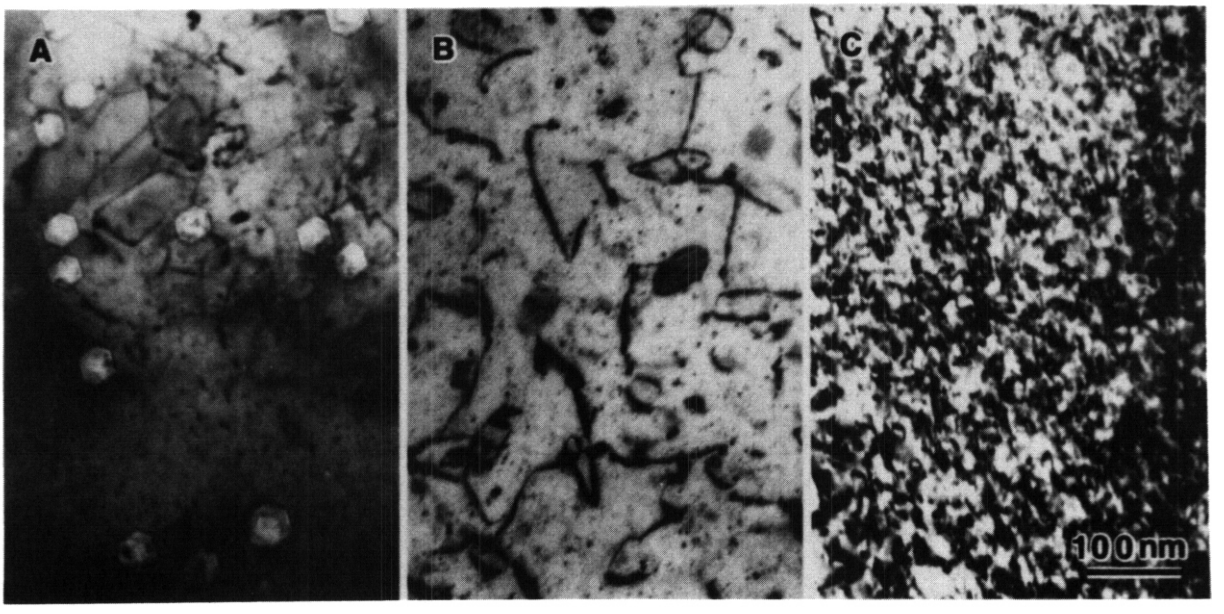

Fig. 4. TEM micrographs showing the comparison of major defect clusters in 14 MeV Ni ion irradiated (A) pure Ni, (B) Ni-10Cu and (C) Ni-50Cu, all with 50 appn He preinjection. The micrographs were taken from the region of 0.6-1 μm below the irradiated surface (g = [200]).

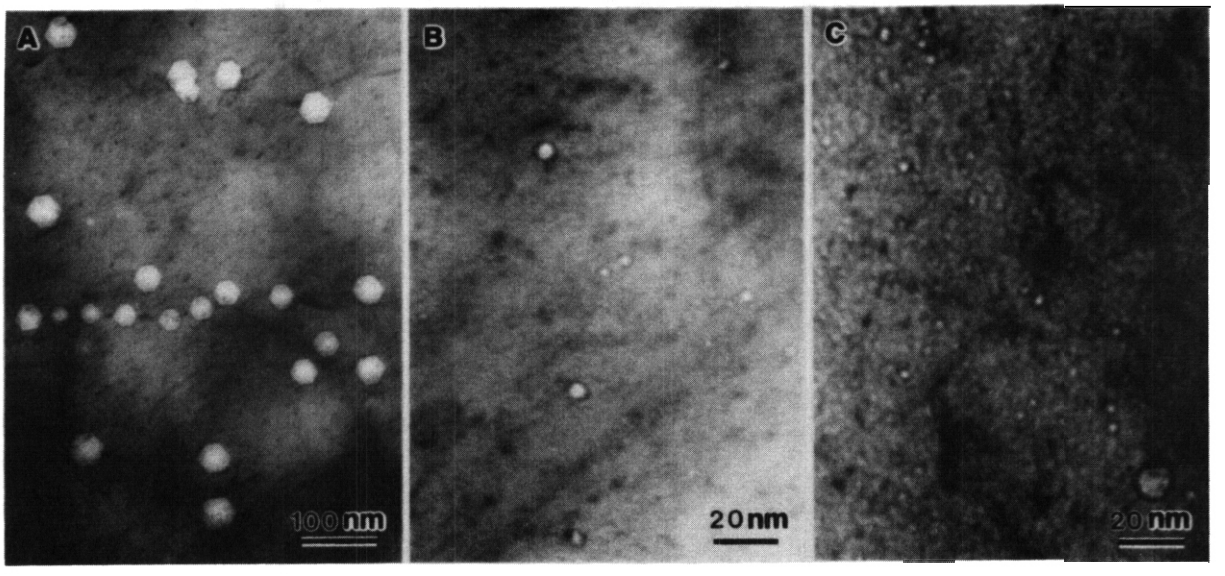

Fig. 5. Low contrast TEM micrographs showing the comparison of the effect of preinjected He in 14 MeV Ni ion irradiated (A) pure Ni, (B) Ni-10Cu and (C) Ni-50Cu. The micrographs were taken from the region of 0.6-1 μm below the irradiated surface.

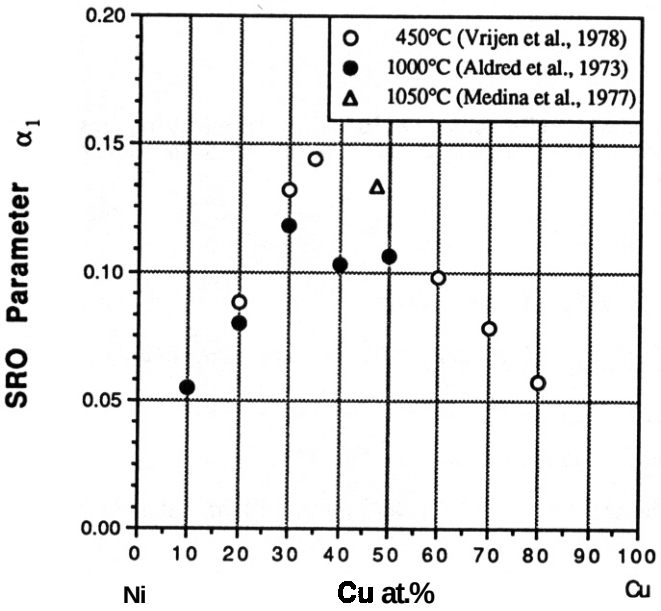

Fig. 6. Short range order parameter α_1 for Ni-Cu alloys measured by Vrijen et al.,[15] Aldred et al.[16] and Medina et al.[17] with diffuse neutron scattering after quenching from various temperatures.

loops just as if there is no heliun available to help void nucleation. It is thought that this phenomenon can be explained by the mechanism first proposed by Mazey and Menzinger[3] in 1973. namely that local clustering of like atoms might provide traps for vacancies and gas atoms in the Ni-Cu alloys. The mechanism has also been discussed in a recent publication[6] and it is extended here.

In a binary solid solution composed of elements A and B, local clustering is defined in terms of a reduced number of unlike nearest neighbors, or A-B pairs, than the number in a random solution.[12] The essential condition for that to happen is that similar atoms must attract each other more than dissimilar atoms in order to lower the free energy upon clustering, although the interaction is not strong enough for precipitation. In terms of interaction energies between pairs of atoms of the two atomic species, this condition can be expressed as $E_{AB} > 1/2\ (E_{AA}+E_{BB})$.[12,13] When the above condition is met, the short range order parameter α_1[14] should be greater than zero.[12,14] Vrijen and Radelaar,[15] in 1978, systematically studied the short range order parameters for the Ni-Cu system using diffuse neutron scattering. Their results from the alloys quenched at 450°C. along with some of the measurements made by Aldred et al. in 1973[16] and Medina et al. in 1977,[17] are plotted in Fig. 6. The data indicated not only that local clustering does occur in the Ni-Cu alloys but also that the tendency for clustering is higher in a more concentrated Ni-Cu solid solution than in a dilute solution.

The boundaries of fine clusters of like atoms in the alloy tend to trap vacancies and gas atoms to reduce the relatively high bonding energy and strain energy. When an abundance of this kind of trap is available, vacancy supersaturation can not be achieved fast enough at each site for vacancy clusters to grow beyond the critical size of the void embryo before collapsing into dislocation loops. For the same reason, helium bubbles cannot draw enough vacancies to grow into larger voids. Since Ni-50Cu contains more such fine scale clusters. gas atoms and vacancies are distributed among more traps than in the case of Ni-10Cu; therefore, a smaller size and higher density of bubbles and dislocation loops result. The tendency for clustering also increases with decreasing temperature[15] and during irradiation,[18] so that the higher density of bubbles observed in this study versus the relatively low density and alloy composition independent distribution of helium bubbles observed by Zinkle et al.,[8] after injecting helium at 0.65 T_m without further irradiation, can also be understood.

CONCLUSIONS

Preinjection of 50 appm helium into Ni-10Cu and Ni-50Cu has little effect on promoting void formation by irradiation with 14 MeV nickel ions to 5 dpa, while preinjection of 50 appn helium results in copious voids in pure nickel by irradiation to 3 dpa at the same homologous temperature of 0.45 T_m.

Most excess vacancies precipitate into dislocation loops in irradiated Ni-Cu alloys regardless of the presence of small helium bubbles. The density of both dislocation loops and heliun bubbles increases with increasing copper content, and the size decreases with increasing copper content.

The special swelling resistance of Ni-Cu alloys is considered to be the result of local clustering of like atoms.

ACKNOWLEDGEMENTS

The authors wish to thank S. Han for performing the Monte Carlo calculation using his TAMIX code to predict the ion range and the displacement damage distribution. This work has been supported by the U.S. Department of Energy, Office of Fusion Energy.

REFERENCES

1. G.L. Kulcinski: Contemp. Phys.. 1979, Vol. 20. pp. 417-447.

2. J.L. Brimhall and H.E. Kissinger: Radiat. Eff.. 1972, Vol. 15 , pp. 259-272.

3. D.J. Mazey and F. Menzinger: J. Nucl. Mater., 1973, Vol. 48, pp. 15-20.

4. K-H. Leister: Ph.D. Thesis, Kernforschungszentrum Karlsruhe. 1983.

5. P. Dauben and R.P. Wahi: Progress Report No. 2 (1981-1984). Reports of Hahn-Meitner-Institute. 1984.

6. L.M. Wang, R.A. Dodd and G.L. Kulcinski: J. Nucl. Mater., 1988. Vol. 155-157, pp. 1241-1248.

7. P. Barlow: Ph.D. Thesis, University of Sussex, 1977.

8. S.J. Zinkle, R.A. Oodd, G.L. Kulcinski and K. Farrell: J. Nucl. Mater., 1983. Vol. 117, pp. 213-217.

9. L.M. Wang, R.A. Dodd. G.L. Kulcinski, J. Nucl. Mater., 1986, Vol. 141-143, pp. 713-717.

10. L.E. Seitzman, L.M. Wang, G.L. Kulcinski and R.A. Oodd: J. Nucl. Mater., 1986. Vol. 141-143, pp. 738-742.

11. S. Han and G.L. Kulcinski: Fusion Reactor Materials, 1987, DOE/ER-0313/2, pp. 105-109.

12. W.R. Hibbard, Jr.: in Strengthening Mechanisms in Solid, American Society for Metals, Metals Park, OH, 1962, Ch. 1, p. 24.

13. T.B. Massal: in Physical Metallurgy. R.W. Cahn and P. Haasen, eds.. Elsevier Science Publishers B.V.,1983, Ch. 4, p. 213.

14. R.A. Swalin: Thermodynamics of Solids, John Wiley & Sons, New York, NY, 1972. p. 149.

15. J. Vrijen and S. Radelaar: Physical Review B, 1978, Vol. 17. pp. 409-421.

16. A.T. Aldred, B.D. Rainford. T.J. Hicks and J.S. Kouvel: Physical Review B, 1973, Vol. 7, pp. 218-229.

17. R.A. Medina and J.W. Cable, Physical Review B, 1977, Vol. 15, pp. 1539-1551.

18. R. Poerschke and H. Wollenberger: Radiat. Eff.. 1980, Vol. 49, pp. 225-232.

RADIATION DAMAGE AND COPPER DISTRIBUTION IN 14 MEV COPPER ION IMPLANTED NICKEL - TEM AND AEM ANALYSES IN CROSS SECTION - L. M. Wang, R. A. Dodd and G. L. Kulcinski (University of Wisconsin-Madison)

OBJECTIVE

To study the effect of a small concentration of implanted Cu on void formation in Ni.

SUMMARY

14 MeV Cu ions have been implanted into a pure Ni specimen at 500°C to a dose of 6 x 10^{20} ions/m^2. TEM and AEM analyses were performed in cross section to investigate the effect of implanted Cu on the formation of defect clusters. The TEM result has been compared with that obtained in another Ni specimen which was irradiated with 14 MeV Ni ions to the same damage level at the same temperature. While voids formed throughout the entire damage range in the Ni ion frradiated sample, they mainly appeared at the near surface region and at the peak damage depth in the Cu ion implanted specimen. A high density of dislocation loops formed in the region where implanted Cu ions were detected by AEM. The AEM result of the implanted Cu concentration profile has been compared with a Monte Carlo calculation.

PROGRESS AND STATUS

Introduction

Materials in future D-T fusion reactors will be subject to intense displacement damage from high energy fusion neutrons. The excess vacancy and interstitial concentrations produced by irradiation will result in the formation of voids and/or dislocation loops that will greatly alter the material performance. Heavy ion irradiation, which can give a displacement rate several orders higher than that presently available in neutron irradiations. has proven to be a very useful tool in the study of radiation induced defect cluster formation for fusion reactor material research [1].

Previous studies have revealed that Ni-Cu alloys are very resistant to void formation [2-7], although voids do form readily in both pure Ni and pure Cu. In the present study, the effect of a small concentration of implanted Cu on void formation has been studied by performing both transmission electron microscopy (TEM) and analytical electron microscopy (AEM) on a 14 MeV Cu ion implanted (irradiated) Ni cross section specimen. Since both the displacement damage and the Cu concentration resulting from the Cu ion implantation are depth dependent, TEM and AEM analyses in cross section permit a direct correlation of the microstructural and microchemical evolutions for the entire damage range within the same specimen.

Experimental Procedure

Marz grade (99.995 wt.% pure) Ni foil from the Material Research Corporation was used in this study. Two foils with 1 x 0.5 x 0.025 cm dimensions were mechanically polished with 0.05 μm alumina abrasive. They were first heated at 1000°C in flowing dry hydrogen for 4.3 x 10^4 s to reduce the oxygen content, and then annealed at 150°C in a vacuum of 6.6 x 10^{-7} Pa for 1.8 x 10^3 s to remove residual hydrogen since it has been shown that both oxygen and hydrogen greatly promote void formation in Ni [8-10]. Analyses performed by the Los Alamos National Laboratory indicated that the oxygen content in the Ni foil was reduced from the original 180 appm to 75 appm after such treatment. The samples were irradiated with either 14 MeV Cu^{3+} or 14 MeV Ni^{3+} ions at the University of Wisconsin Heavy-Ion Irradiation Facility at 500°C with a dose rate of 1.5 x 10^{16} ions/m^2 s. Since Cu and Ni ions have slightly different energy deposition characteristics, different ion fluences are required to reach the same dpa (displacement per atom) level. The sample irradiated with Cu ions received a total dose of 6 x 10^{20} ions/m^2 and that irradiated with Ni ions received a total dose of 6.5 x 10^{20} ions/m^2, so that the damage level at 1 μm depth equals 25 dpa (~ 75 dpa at peak damage depth) in both samples according to the Monte Carlo calculations performed using the TAMIX code [11]. The depth profiles of displacement damage and ion concentration, calculated for 14 MeV Cu ion irradiated Ni at the ion dose of 10^{20} ions/m^2, are shown in Figure 1.

After irradiation, the samples were electroplated with Ni on both sides and prepared in cross section for TEM and AEM analyses. The details of the sample preparation procedure have been reported earlier [12,13]. The cross sectioned samples were then examined in a JEM 200CX II TEMSCAN microscope operating at 200 keV. The radiation induced defect clusters in both samples were observed in TEM mode. The implanted Cu concentration in the Cu ion irradiated sample was studied by AEM in STEM mode with a beam spot size of < 20 nm using a TN-2000 energy dispersive X-ray spectroscopy (EDXS) system. During the AEM analysis, a series of points lying on a line normal to the interface between the plated and the irradiated Ni, i.e. parallel to the direction of incident ions and covering the entire damage range, was analyzed to provide the depth profile of the implanted Cu concentration. To prevent the interference of Cu signals from the brass sample holder, a graphite holder was used during the AEM study; this appeared to be very effective.

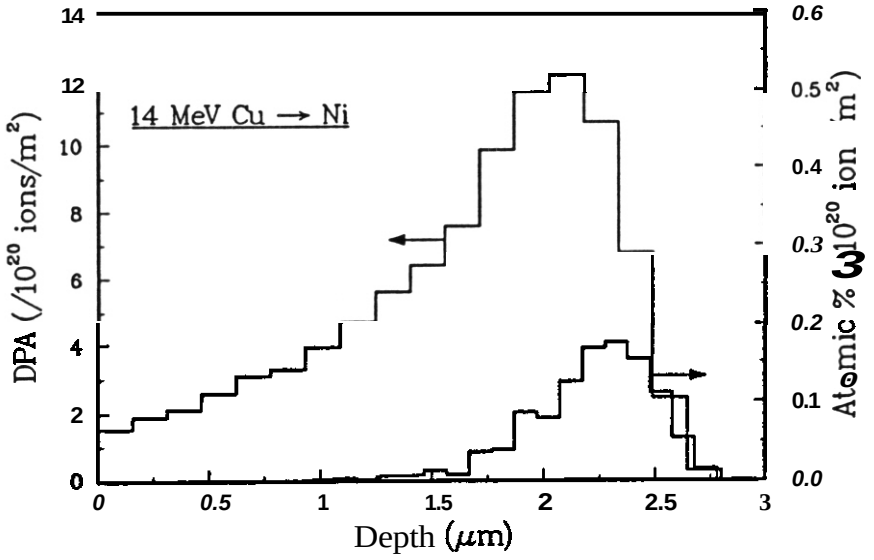

Fig. 1. Depth profiles of displacement damage and implanted ion concentration in the 14 MeV Cu ion irradiated Ni, calculated by a Monte Carlo code, the TAMIX (1000 histories).

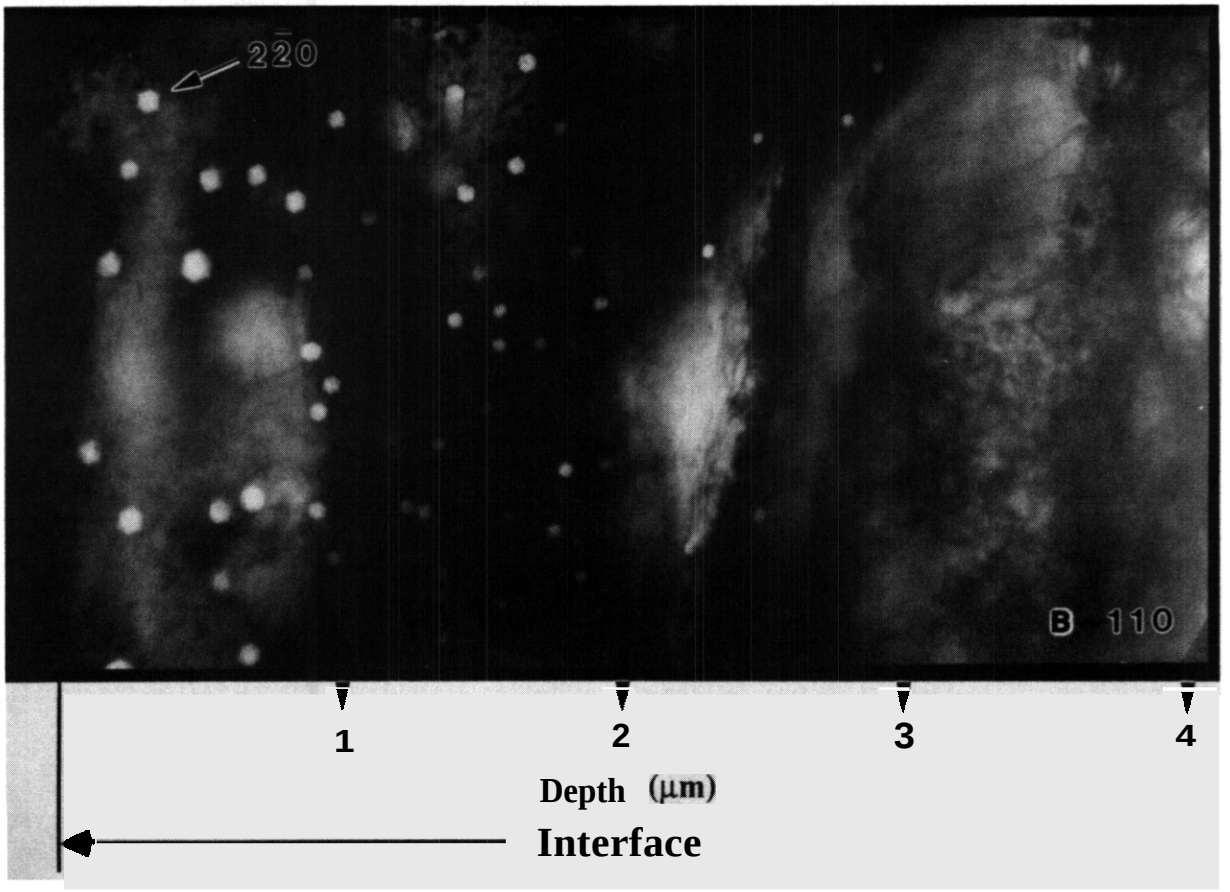

Fig. 2 TEM cross-section micrograph showing void distribution in 14 MeV Ni ion irradiated Ni. Since about 0.3 μm was removed from the original surface, the actual depth from the irradiated surface should be the depth from the interface plus 0.3 μm.

RESULTS AND OISCUSSION

TEM Observations

While voids were the only significant defect clusters observed in the Ni ion irradiated specimen, and they formed throughout the entire damage range, both voids and high densities of dislocation looos were seen in the Cu ion irradiated specimen. These voids were mainlv located in a region near the surface and in another region that was about 2.75 to 3 μm from the irradiated surface. The TEM cross section micrographs for the entire damage region of the two specimens are shown in Figure 2 and Figure 3, respectively. It should be noted that a surface layer ~ 0.3 μm thick was removed before Ni olatina in the orocess of cross section sample preparation to assure good bonding at the interface, so the'actuai depth from the original irradiated surface is ~ 0.3 μm deeper than the depth from the interface indicated in the two cross section micrographs.

The density and average diameter of the voids and swelling in both samples, as well as the dislocation loop density in the Cu ion irradiated specimen, have been plotted against the depth from the irradiated surface (the ~ 0.3 μm removed layer was added), and they are shown in Figure 4. To reduce the uncertainties in the swelling calculation, the morphology of voids was studied by viewing them with the electron beam close to several main zone axes. as shown in Figure 5. The voids in both samples were determined to be bounded by 100 and 111 faces (cubic truncated by octahedra), with truncation parameters [14] between 0.5 and 0.6. The void dimensions in the <110> direction and the appropriate volume factor [14] were used in the determination of void volume. The average diameter reported in Figure 4(b) is the diameter of the sphere which has the equivalent volume as the average void volume. The dislocation loops observed in the Cu ion irradiated specimen are mostly perfect loops with the Burgers vector of a/2 <110>. Figure 6 shows the typical dislocation loop images at various depths in the Cu ion irradiated sample. At both the surface and at the end of damage range. some large loops (~ 50 nm in diameter) were observed. In between, a high density of smaller loops (< 10 nm) was found. The analysis of the interstitial/vacancy nature of the dislocation loops has only been performed on some of the larger loops (> 50 nm) using the technique outline by Edington [15]. Both interstitial and vacancy loops have been identified.

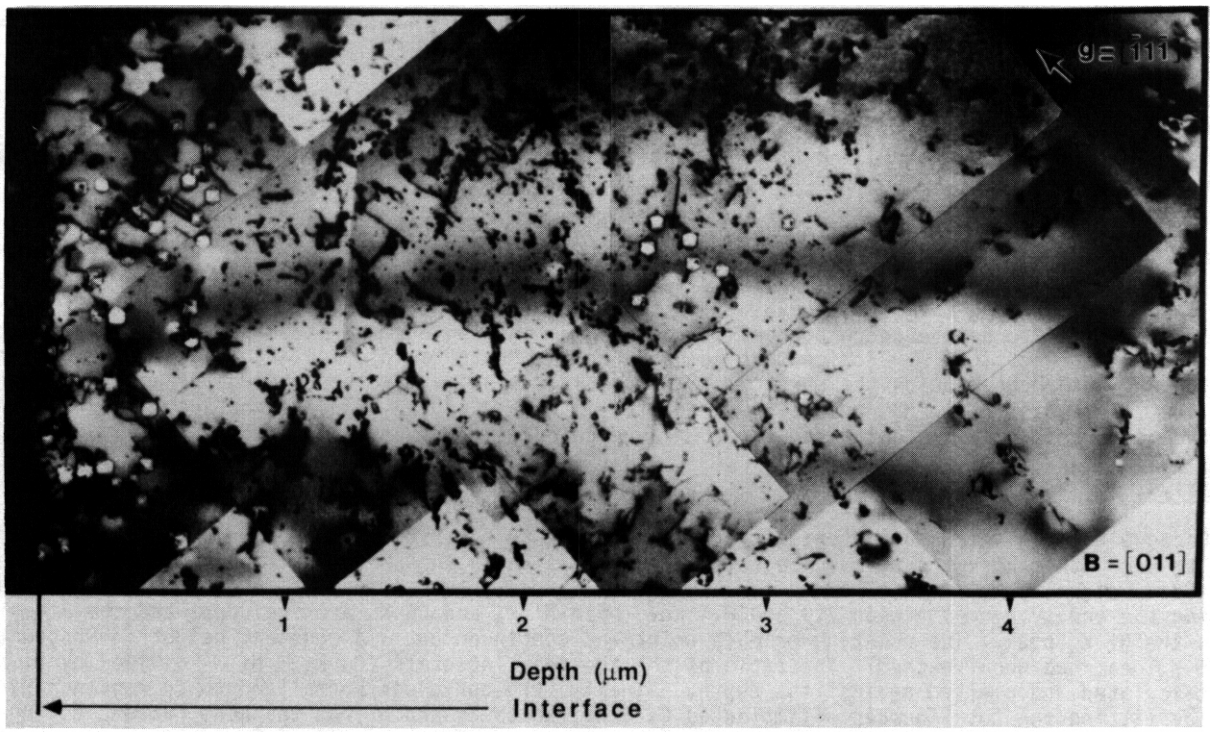

Fig. 3. TEM cross-section micrograph showing void and dislocation loop distribution in 14 MeV Cu ion irradiated Ni. Since about 0.3 u was removed from the original surface, the actual depth from the irradiated surface should be the depth from the interface plus 0.3 μm.

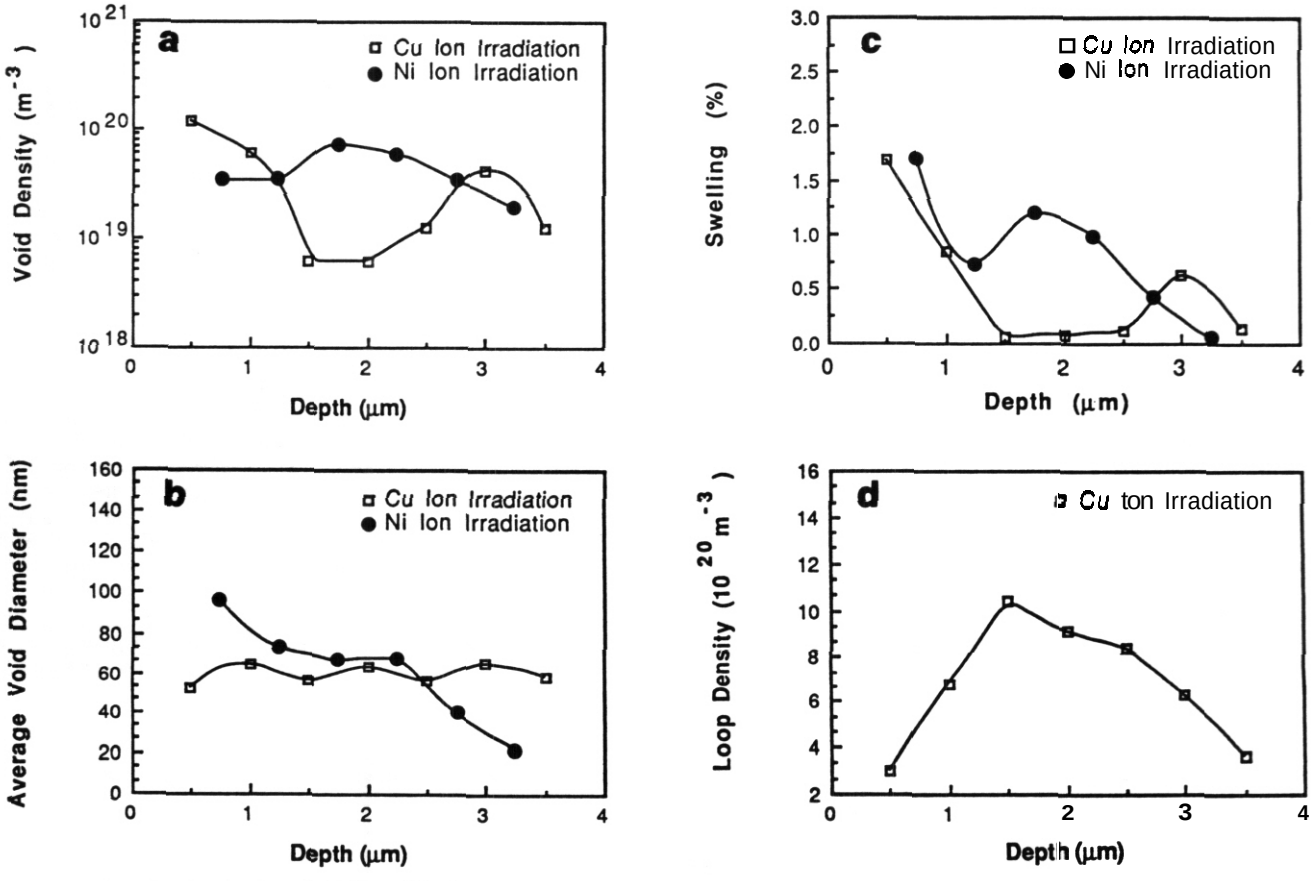

Fig. 4. Comparison of (a) void density, (b) average void diameter, (c) swelling versus depth from the irradiated surface curves for Cu and Ni ion irradiated Ni, and (d) dislocation loop density distribution in Cu ion irradiated Ni.

From Figure 4, it is very clear that there is a void suppression region, which extends from the depth of 1 μm to the depth of about 3 μm, in the Cu ion irradiated specimen. Also in that region, high densities of dislocation loops are formed. The void density and swelling peak at the depth of 3 μm for the same sample is believed to be the correspondent of the peak damage region, where the point defect production rate has a sharp increase. One may notice that compared to the Monte Carlo calculation, the observed damage peak location was much deeper below the surface. Similar discrepancies have been noted for a long time in the cross section studies of 14 MeV heavy ion irradiated materials [10,12,16]; the most common explanation is that the electronic stopping data used for the range calculation is usually too high c10.123.

AEM Analyses

Because the implanted Cu content is very low and the Cu K_α (8.04 keV) and the Ni K_β (8.26 keV) are close to each other, great care must be taken to distinguish Cu in AEM compositional studies. To detect the small Cu K_α signal which may be hidden beneath the Ni K_β peak, two regions of interest were selected, one covering the energy range between 7.9 and 8.4 keV (both Ni K_β and Cu K_α are included) and the other only covers the Ni K_α peak. The counting on each point was continued until a constant height (4096 counts) for the Ni K_α peak had been reached. The ratio of the two peak integrals (Cu K_α + Ni K_β divided by Ni K_α) was then calculated and plotted against the depth. Finally, the curve was normalized to Cu concentration versus depth by fitting the total number of implanted Cu ions, which is known from the beam current during irradiation, into the area underneath the peak integral ratio curve. That normalized Cu concentration versus depth curve is shown in Figure 7 along with the Cu distribution curve calculated by the Monte Carlo method for the irradiation dose. To determine the height of the error bar, the measurement at several depths was repeated three times. Although the scattering of the data is relatively large, the increase of the Cu signal in the region 1.5 to 2.75 μm below the implanted surface is distinct. Comparing Figure 7 with Figure 4 (a). (c) and (d), it is quite clear that the implanted Cu suppressed void formation and promoted dislocation loop formation.

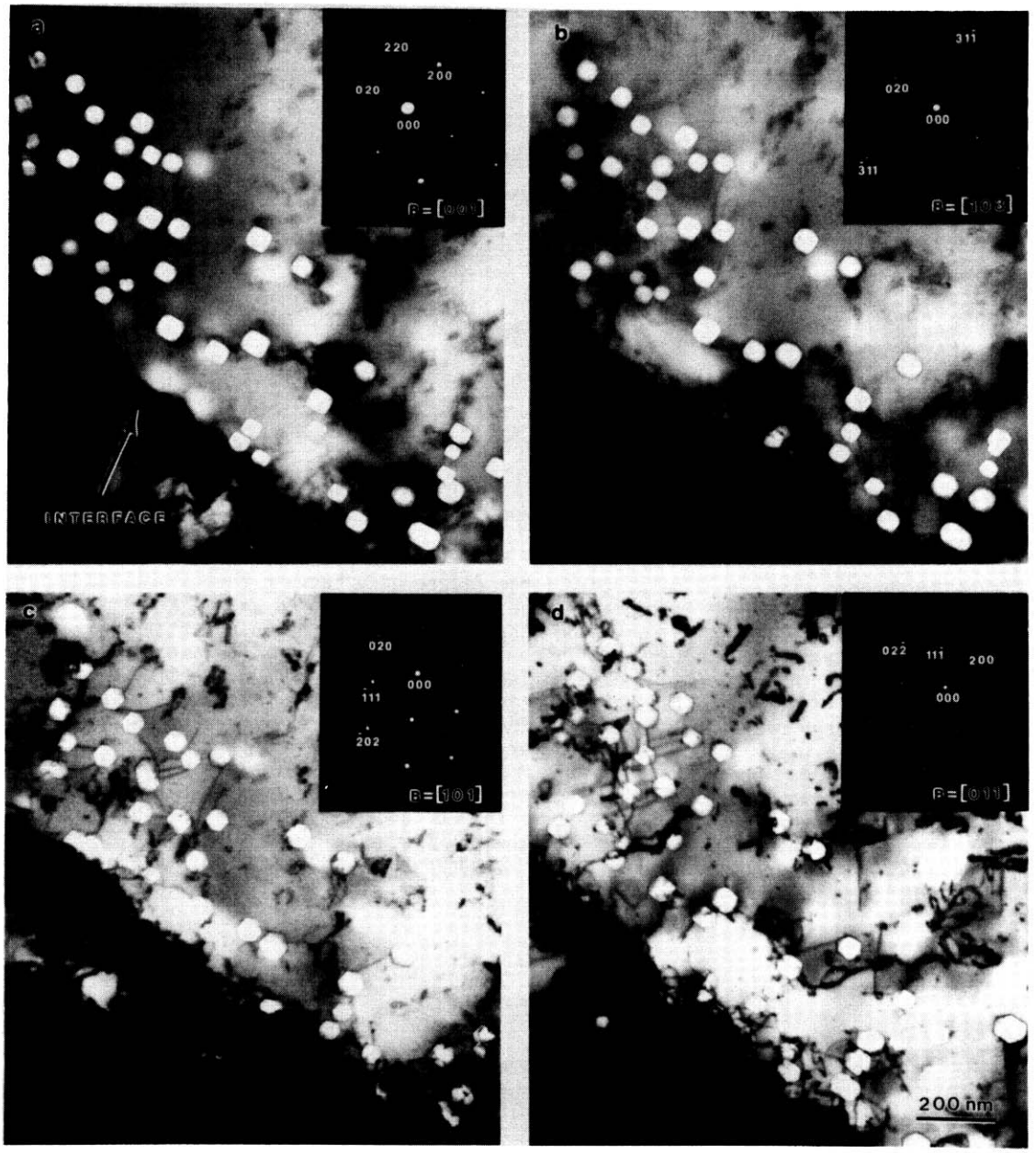

Fig. 5. The morphology of voids in 14 MeV Cu ion irradiated Ni. (a) B = [001], (b) B = [103], (c) B = [101] and (d) B = [011]. The voids shown in (a), (b), (c) and (d) are the same group located near the interface.

Several mechanisms have been proposed in the literature [2,3] to explain the void resistance in Ni-Cu alloys. The most plausible one seems to be the trapping of vacancies and interstitials at the boundaries of fine scaled clusters having compositions different from the matrix [7], because the clustering in the Ni-Cu alloys has been suggested both by experimental results and by thermodynamic considerations. The traps provided by clustering can operate as nucleation sites for vacancy clusters. When a relatively high density of this kind of trap is present, the arrival rate of irradiation produced vacancies at each site will be low, so the small vacancy clusters can not grow fast enough to reach the critical size of the void embryo before collapsing into dislocation loops. Although the Cu concentration in this study is quite low, it should still be able to provide enough Cu clusters as vacancy traps and the nucleation sites for the observed dislocation loops, because the observed loop density is only about five orders of magnitude lower than the atomic density of the Cu ions in the implanted region.

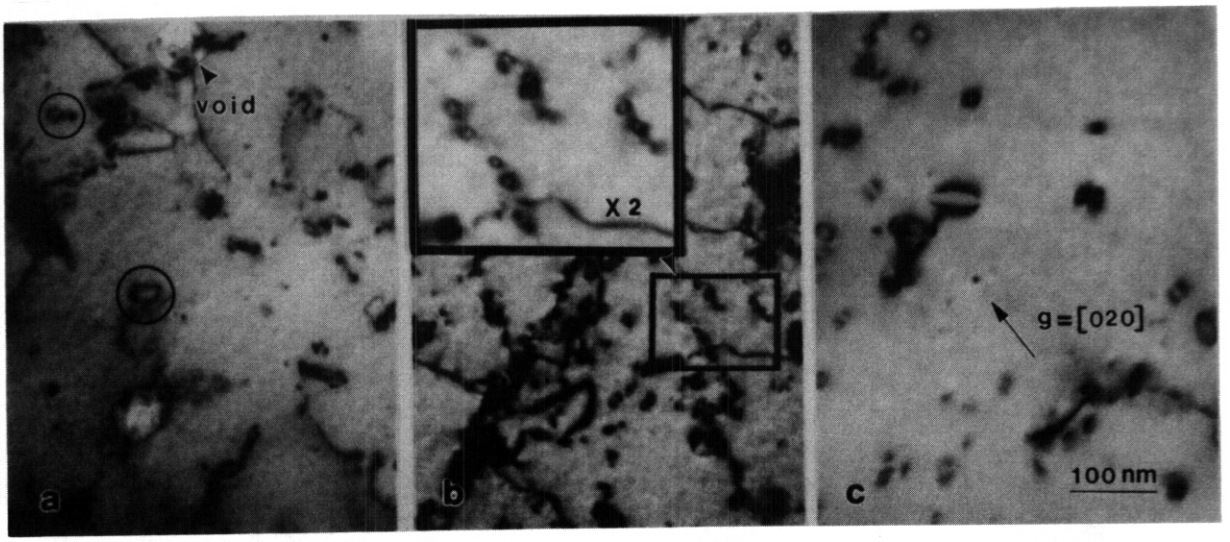

Fig. 6. The dislocation loop images taken from the various depths in the 14 MeV Cu ion irradiated Ni. (a) 0.5 μm deep, (b) 2 μm deep and (c) 3.5 μm deep.

From Figure 7, one can also see a relatively large discrepancy between the calculated and measured Cu range and concentration in the Cu ion implanted Ni specimen. The measured values are lower and cover a wider region. That is partly due to the radiation enhanced diffusion, because the diffusional spreading was not considered in the Monte Carlo calculation. There is some evidence showing that the irradiation enhanced diffusion coefficient of Cu in Ni-Cu alloy could be increased by two orders of magnitude by ion bombardment below ~ 550 °C [17]. In addition to the normal vacancy diffusion mechanism, one should note that the Cu ions are the injected interstitials in the sample. The diffusional spreading of migrating interstitials before they annihilate with the vacancies could be very significant. Another reason for the measured large Cu spreading is due to the beam broadening during AEM measurement. The area analyzed has a thickness of ~ 140 nm. Primary interaction volumes with a diameter < 200 nm could be created by the incident 200 keV electrons. It should also be recognized that part of the Cu range discrepancy in Figure 7 may arise because the AEM data is obtained at the detection limits of the EDS system. Nevertheless, the measured profile of dislocation loop density matched quite well with the measured Cu profile in this study.

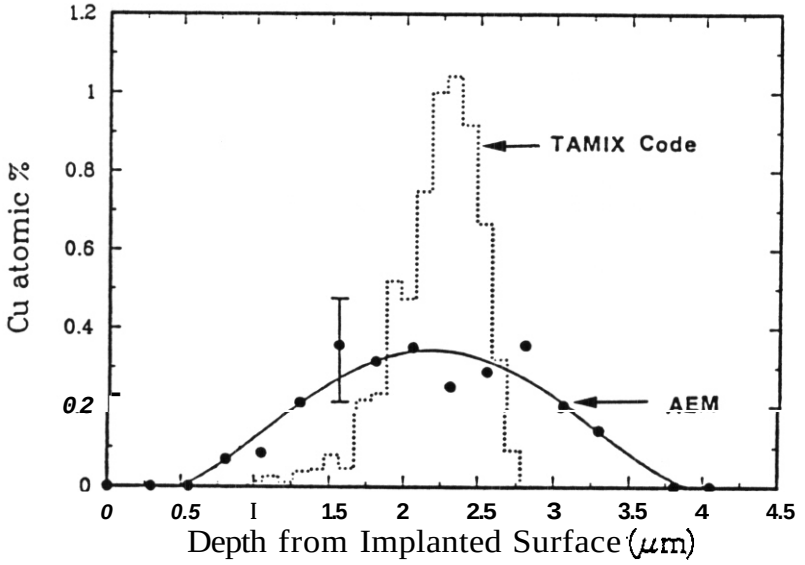

Fig. 7. The distribution of Implanted Cu in 14 MeV Cu *io!)* irradiated Ni measured by AEM in cross section (normalized by ion implantation dose = 6 x 10^{20} ions/m). The calculated Cu distribution, using the TAMIX code for the same dose, is dram in dotted line for comparison.

CONCLUSIONS

The TEM/AEM cross-section analysis method can be an effective tool for studying the effect of injected foreign interstitials in heavy ion irradiated materials, provided that the concentration of the implanted species is high enough to be detected.

A small amounts of implanted copper promote dislocation loop formation and suppresses void formation in ion irradiated nickel at 500°C.

ACKNOWLEDGEMENTS

The authors wish to thank S. Han for performing the Monte Carlo calculation and R.D. Griffin for her assistance during AEM analysis. Support for this work has been provided by the U.S. Department of Energy.

REFERENCES

[1] G.L. Kulcinski. A.B. Wittkower and G. Ryding, Nuclear Instruments and Methods **94 (1971) 365.**

[2] J.L. Brimhall and H.E. Kissinger. Radiat. Eff. **15 (1972) 259.**

[3] D.J. Hazey'and F. Menzinger, J. Nucl. Mater. **48 (1973) 15.**

C41 K-H. Leister, PhD Thesis, Kernforschungszentrum Karlsruhe (May **1983).**

[5] P. Dauben and R.P. Wahi, Progress Report No. **2 (1981-1984).** Report of Hahn-Meitner-Institute,

[6] P. Barlow, PhD Thesis, University of Sussex (April **1977).**

C71 L.M. Wang. R.A. Dodd and G.L. Kulcinski, J. Nucl. Mater. **155-157 (1988). 1241.**

[8] L.E. Seitzman, L.M. Wang, G.L. Kulcinski and R.A. Dodd, J. Nucl. Mater. **141-143 (1986) 738.**

[9] L.M. Wang, R.A. Dodd and G.L. Kulcinski. J. Nucl. Mater. **141-143 (1986) 713.**

[10] D.B. Bullen, PhD Thesis, University of Wisconsin-Madison (May **1984).**

[11] S. Han and G.L. Kulcinski, Fusion Reactor Materials. DOE/ER-0313/2 **(1987) 105.**

[12] J.B. Whitley, PhD Thesis, University of Wisconsin-Madison (August **1978).**

[13] L.E. Seitzman, L.M. Wang, R.O. Griffin, A.P. Komissarov, G.L. Kulcinski and R.A. Dodd, Ultramicroscopy, to be published.

[14] D.S. Gelles, R.M. Claudson and L.E. Thomas, to be published in Fusion Reactor Materials.

[15] J.W. Edington, Interpretation of Transmission Electron Micrographs, Monographs in Practical Electron Microscopy in Materials Science, Vol. 3 (N.V. Philips' Gloeilampenfabrieken, Eindhoven, 1975).

[16] R.L. Sindelar. PhD Thesis, University of Wisconsin-Madison **(1985).**

[17] N.Q. Lam, H.A. Hoff. H. Wiedersich and L.E. Rehn, Surface Science, **149 (1985) 517.**

MICROINDENTATION HARDNESS CHANGES IN ION-IRRADIATED NI-CU ALLOYS, D. H. Plantz, L. M. Wang, R. A. Dodd and G. L. Kulcinski (University of Wisconsin-Madison)

OBJECTIVE

To study the effect of heavy ion irradiation induced dislocation loops on the hardness of Ni-Cu Alloys.

SUMMARY

The effect of radiation-induced dislocation loops on hardness in ion-irradiated Ni-Cu alloys has been studied using a Mechanical Properties Microprobe (MPM). A well annealed Ni-10 at% Cu alloy and an alloy of Ni-50 at% Cu were irradiated with 14 MeV Ni ions to doses of 20 to 100 dpa peak damage (5 to 25 dpa at 1 μm) at 0.45 T_m (485°C and 425°C respectively). Ultra-low load microindentation hardness measurements and TEM analyseswere done using cross-section techniques. This method allows for direct hardness measurements of only the small irradiation zone (< 3 μm deep) which have been compared to the unirradiated materials. Irradiation induced a high density of dislocation loops with the size and density of the loops dependent on composition and independent of irradiation conditions. This high dislocation loop density caused a large increase in hardness. A reasonable correlation was found between measured hardness changes and calculated changes based on dislocation loop sizes and densities.

PROGRESS AND STATUS

Introduction

The Ni-Cu system has displayed a remarkable resistance to void formation under irradiation.[1-6] A recent study of two compositions of the Ni-Cu system has shown that dislocation loops are the dominant defect resulting from heavy ion irradiation.[6] The formation of only this type of defect in an essentially homogeneous alloy provides an excellent opportunity to study the effect of loops on radiation hardening. However, until recently the narrow damage region produced by heavy ion irradiation (~ 1 μm deep) has made mechanical property tests on these samples impractical. A new technique has recently been introduced with which direct measurements of the mechanical properties of such regions can be made.[7] An investigation has been made using this technique to study the effect of dislocation loops on the hardness and modulus of two Ni-Cu compositions following ion irradiation. These results were compared to the model of Ghoniem et al.[8]

Experimental Procedure

High purity Ni-10% Cu and Ni-50% Cu specimens were irradiated with 14 MeV Ni ions to doses of 5, 10, and 25 dpa at 1 μm (20, 40 and 100 dpa peak) at 0.45 T_m (485°C and 425°C respectively).[6] Irradiated samples were prepared for cross-sectional analysis using standard techniques.[9] Transmission electron microscopy was used to obtain data on dislocation loop sizes and densities.[6]

Ultra-low load microindentation hardness measurements were performed using a recently developed, fully automated mechanical properties microprobe (MPM).[10,11] A schematic of the MPM is shown in Fig. 1. A load is applied and removed, and is continuously monitored along with displacement with a resolution of 25 μN (250 μg) and 0.4 nm respectively. Figure 2 represents a typical load-displacement curve obtained from the MPM. Hardness under load (uncorrected for elastic effects) can be calculated from the loading curves as a function of depth using $H=AL/d^2$, where d is a depth on the loading curve, L is the load at that depth and A is a geometric factor relating depth to the projected area of the indent. A value for plastic hardness can be calculated from a load-displacement curve using the unloading part of the curve and is given by $H_p = AL_{max}/d_p^2$, where L_{max} is the maximum load applied and d_p is the maximum depth corrected for elastic effects.[12]

Cross-section specimens were mechanically polished to a 0.05 μm finish and then electropolished using 67% CH OH and 33% HNO_3 at 15 V and -30 to -50°C prior to indentation. A line of indents 5 μm apart were made a? an angle of ~ 5.7° relative to the interface between the Ni-Cu and the Ni plating (see Fig. 3), to a depth of 150 nm, at a constant displacement rate of less than 5 nmls. This resulted in indents about 1 μm across spaced at intervals of 0.25 μm from the interface. Ratios of hardness to the average hardness away from the irradiated zone were calculated as a function of distance from the interface.

Results

Figures 4a and 4b are examples of the microstructure of the two irradiated Ni-Cu compositions shown in cross-section. Both compositions display a high dislocation loop density in the irradiated region and are virtually defect free beyond that region. Figures 5a and 5b are enlargements of the irradiated region in Ni-10% Cu and Ni-50% Cu respectively. Table 1 shows the dislocation loop density and average diameter, and Fig. 6 shows the distribution of loop sizes. It can be seen that Ni-50% Cu has a very high density of small dislocation loops, while Ni-10% Cu has a lower density with a large range of loop sizes. A very few voids

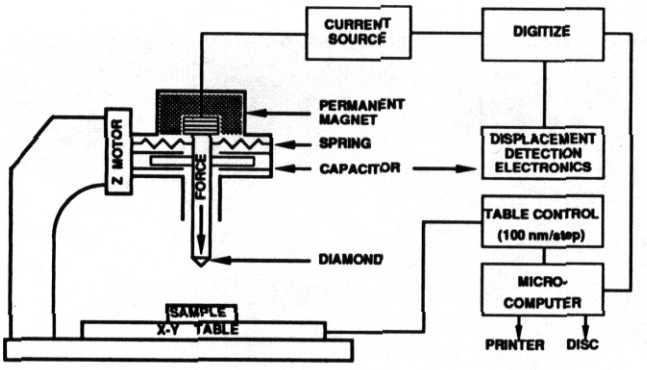

Fig. 1. Mechanical properties micropobe (MPM) schematic.

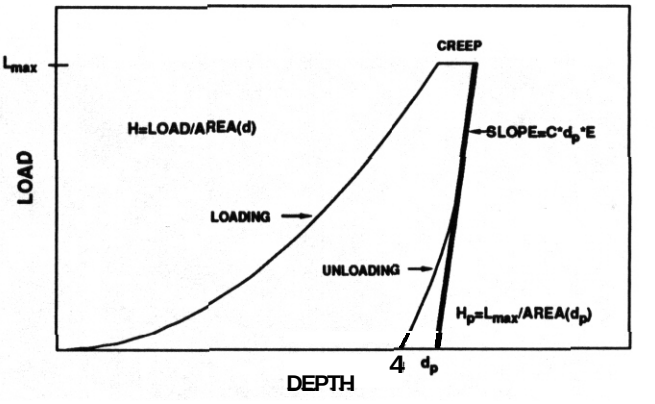

Fig. 2 Representative load-displacement from the mechanical properties microprobe.

were observed in Ni-10%Cu, but the volume fraction of voids was so small that they have been ignored for the purposes of this study.

Although the two compositions start out with approximately the same hardness, these alloys have very different radiation hardening characteristics (Figure 7). All the Ni-50% Cu samples display about a 55% increase in hardness in the irradiated region. The 5 and 10 dpa Ni-10% Cu samples have about a 25 to 30% increase in hardness while the 25 dpa sample has only about a 20% increase. All the hardness data has about a 10% standard deviation except near the end of range where the scatter is usually larger.

Discussion

Void suppression in Ni-Cu alloys has been attributed to clustering of like atoms, and this suppression leads to the nucleation of dislocation loops.[6] It is thought that clustering is on a finer scale in the Ni-50% Cu relative to Ni-10% Cu, thus resulting in a higher density of smaller loops in Ni-50% Cu.[6] The loop characteristics change very little in Ni-50% Cu with increasing dose and, correspondingly, there is little change in hardness. At the highest dose, more large loops ($d > 75$ nm) are observed than for the lower doses in the Ni-10% Cu and some of these larger loops are seen to extend beyond the end of ion range. This may account for the lower hardness in the 25 dpa sample relative to the 5 and 10 dpa samples.

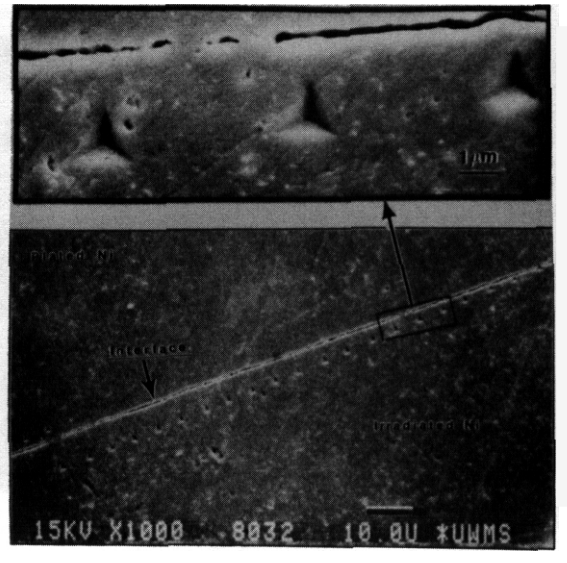

Fig. 3. SEM micrographs of indentations made in a cross-sectioned sample.

In all of the samples tested, the hardness is approximately the same across the irradiated zone despite the fact that dpa varies with depth. This trend has been seen in two other studies using this technique.[7,13] In Dart this can be accounted for by the fact that the actual size of the indents (~ 1 μm across) is smaller than the area which contributes to the hardness. Thus a single indent samples a wide range of dpa's.[14] It also appears from Fig. 4a and 4b that the dislocation loop sizes and densities are the same across the irradiated zone. This coupled with the hardness data indicates that radiation hardening probably saturates at lower dpa values than studied here.

Theoretical hardening due to dislocation loops can be represented by:[8]

$$\Delta\sigma_Y = \sqrt{3}\Delta\tau \approx Gb/2\sqrt{(Nd)} \text{ small loops}$$

or

$$\approx 1.2Gbd(N)^{2/3} \text{ large loops}$$

where σ_y is the yield strength. τ is the shear stress, G the shear modulus, b the Burgers vector, N the loop density and d the loop diameter. Small loops interact through short range forces while large loops interact through large range forces.[8] The cut off for small and large loops is relatively arbitrary but is often taken to be less than 10 nm.[8] Hardness can be related to yield strength by $H \approx C\sigma_y$, where H is the hardness and C is a

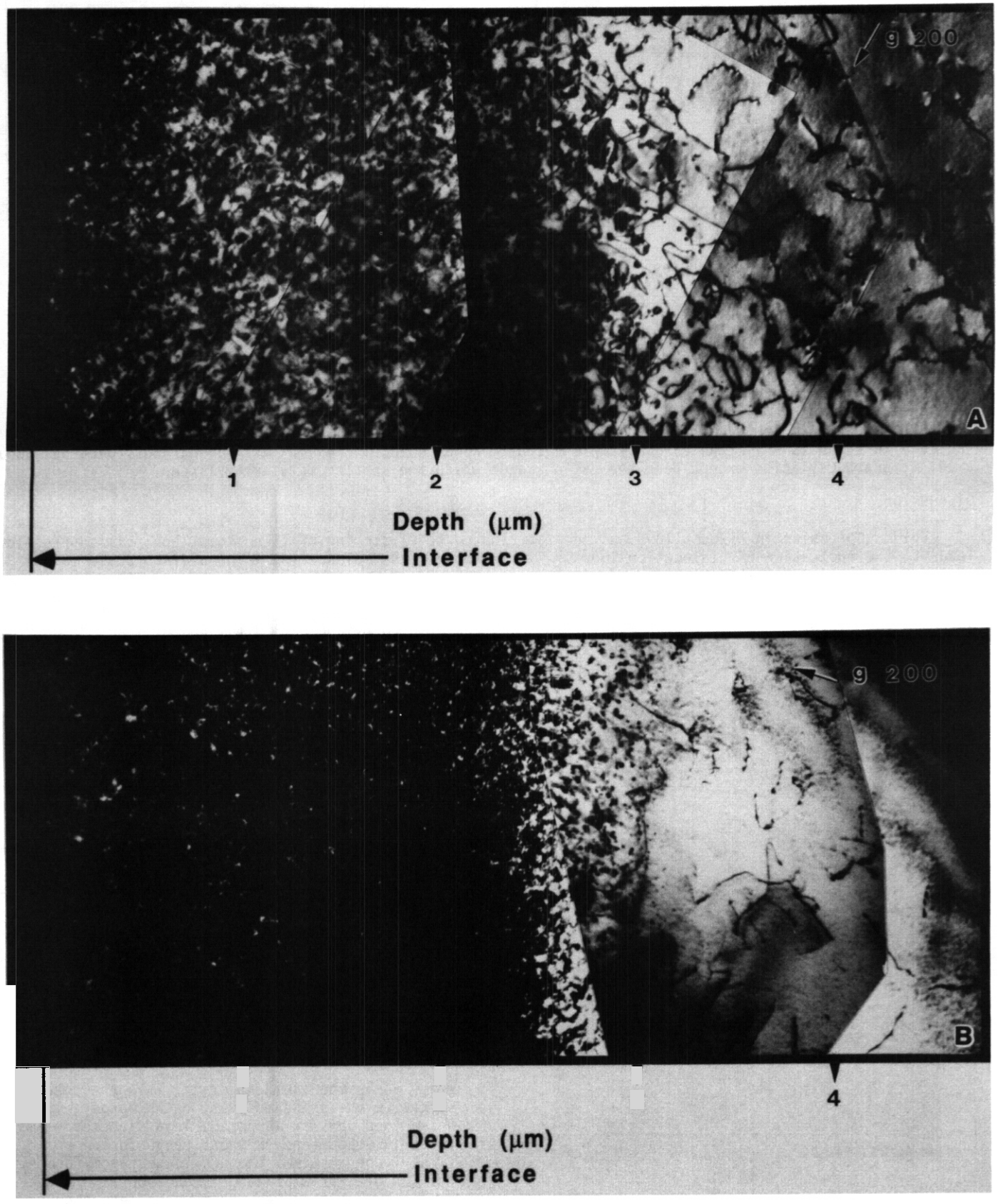

Fig. 4. TEM micrographs of Ni-10% Cu (a) and Ni-50% Cu (b) irradiated to 10 dpa at 1 μm at 0.45 Tm in cross-section showing the entire irradiated region.

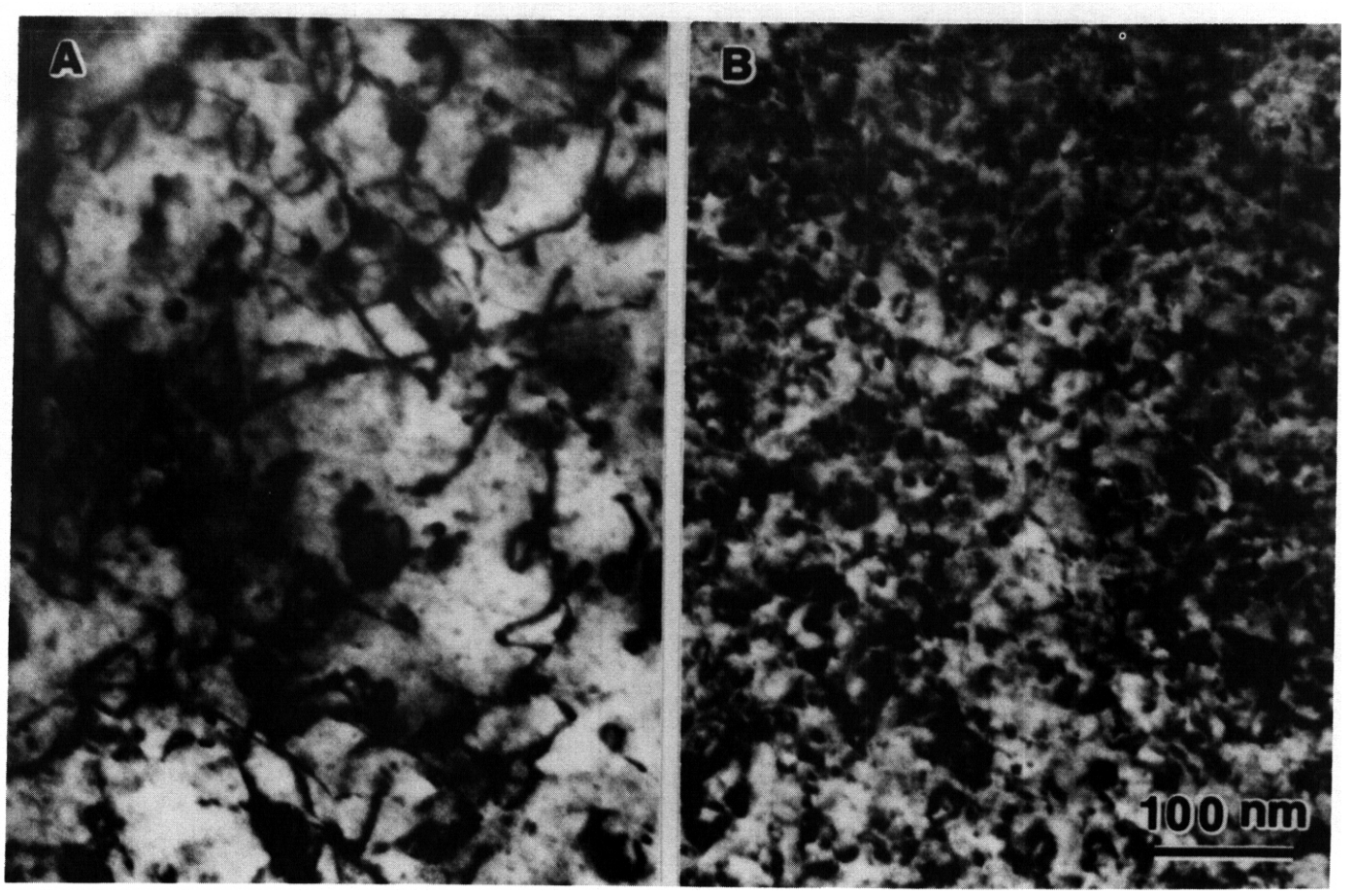

Fig. 5 Enlargements of the irradiated regions from Fig. 4 for Ni-10%Cu (a) and Ni-50%Cu (b).

constant (usually taken to be 3 for diamond pyramid hardness tests).[15-17] Thus, the change in yield strength can be determined from:

$$\Delta\sigma_Y/\sigma_Y \approx \Delta H/H$$

or

$$\approx H_i/H_u - 1$$

where H_i and H_u are the irradiated and unirradiated hardnesses respectively. This ratio is constant for varying depth or load, thus absolute hardness values are not needed and the actual value for C does not need to be known. Table 2 shows the comparison of the change in yield strength calculated from theory and from

Table 1 Initial Hardness and Oislocation Loop Characteristics for Irradiated Ni-Cu

Composition	Unirradiated Hardness (300 nm) (GPa)	Temperature (°C)	Dpa (1 μm)	Dpa (Peak)	Dislocation Loop Density (m^{-3})	Average Loop Diameter (nm)
Ni-10% Cu	2.1	485	5	20	$1x10^{21}$	29
			10	40	$1x10^{21}$	19
			25	100	$1x10^{21}$	25
Ni-50% Cu	2.0	425	5	20	$7x10^{21}$	6
			10	40	$5x10^{21}$	7
			25	100	$5x10^{21}$	10

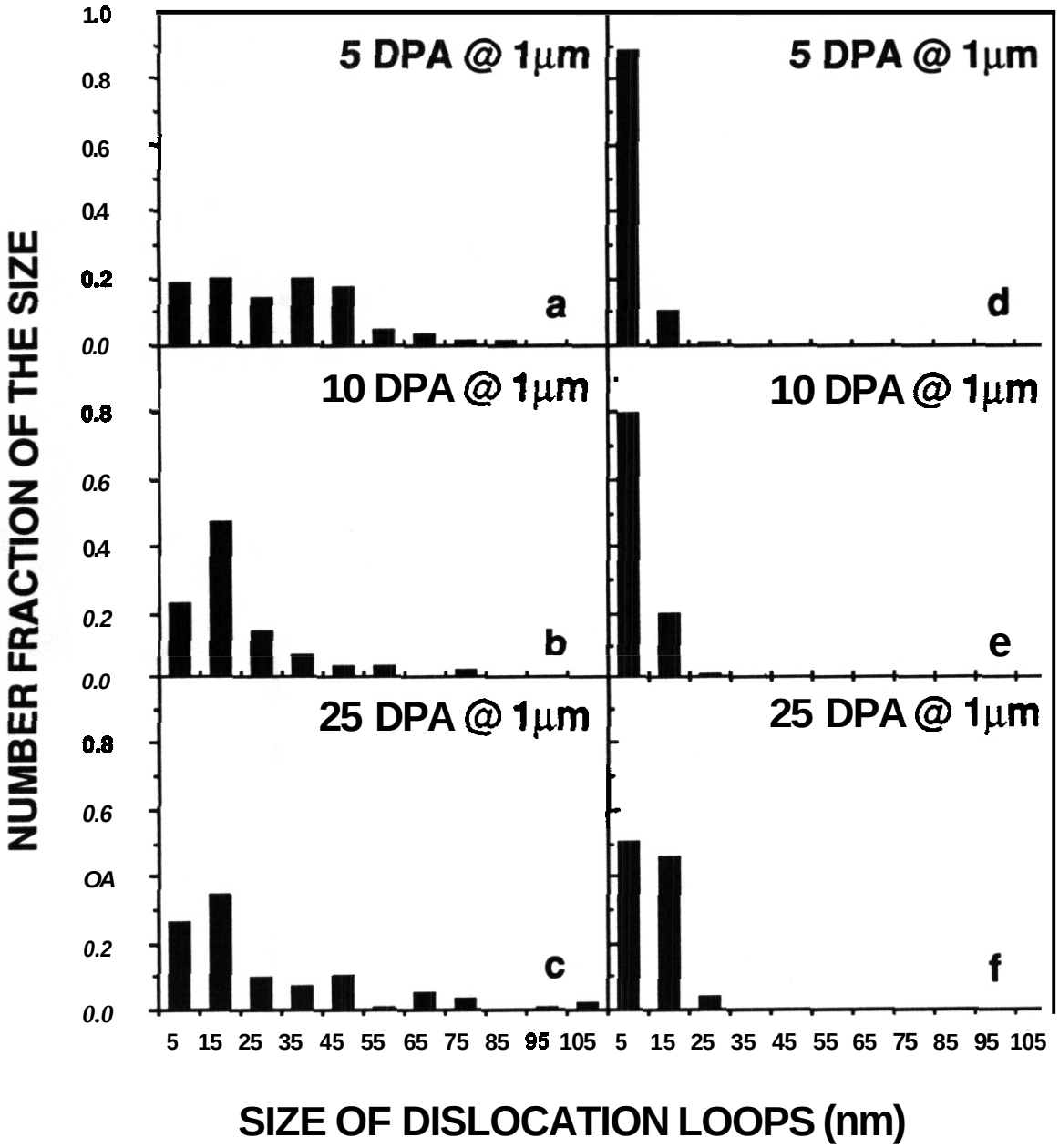

Fig. 6 Distribution of dislocation loops in irradiated Ni-10%Cu (a-c) and Ni-50% Cu (d-f) for different fluences.

hardness changes. The yield strength for the unirradiated samples was taken to be ≈ 150 MPa.[18] For Ni-10% Cu the results are remarkably close using either the small or large loop calculation; however, the large loop calculation is probably a more valid model for this composition. Fair agreement is achieved in Ni-50% Cu using the two models; however, even better agreement can be achieved if a combination of the two models is used ($\Delta\tau = \Delta\tau$ (small) + $\Delta\tau$ (large)) and it is assumed that about 85% of the loops are small (~ 5 nm) and the rest are large (~ 15 nm). With such a high density of small loops, it is possible that many loops under 5 nm were missed. Loop densities are probably known only to within a factor of 2 or 3.

CONCLUSIONS

The Ni-Cu system's resistance to void formation results in the nucleation of a high density of dislocatfon loops under irradiation. The higher density of smaller loops in Ni-50% Cu causes a hardness change twice that of Ni-10% Cu. Radiation hardening appears to saturate at or below 5 dpa for these compositions.

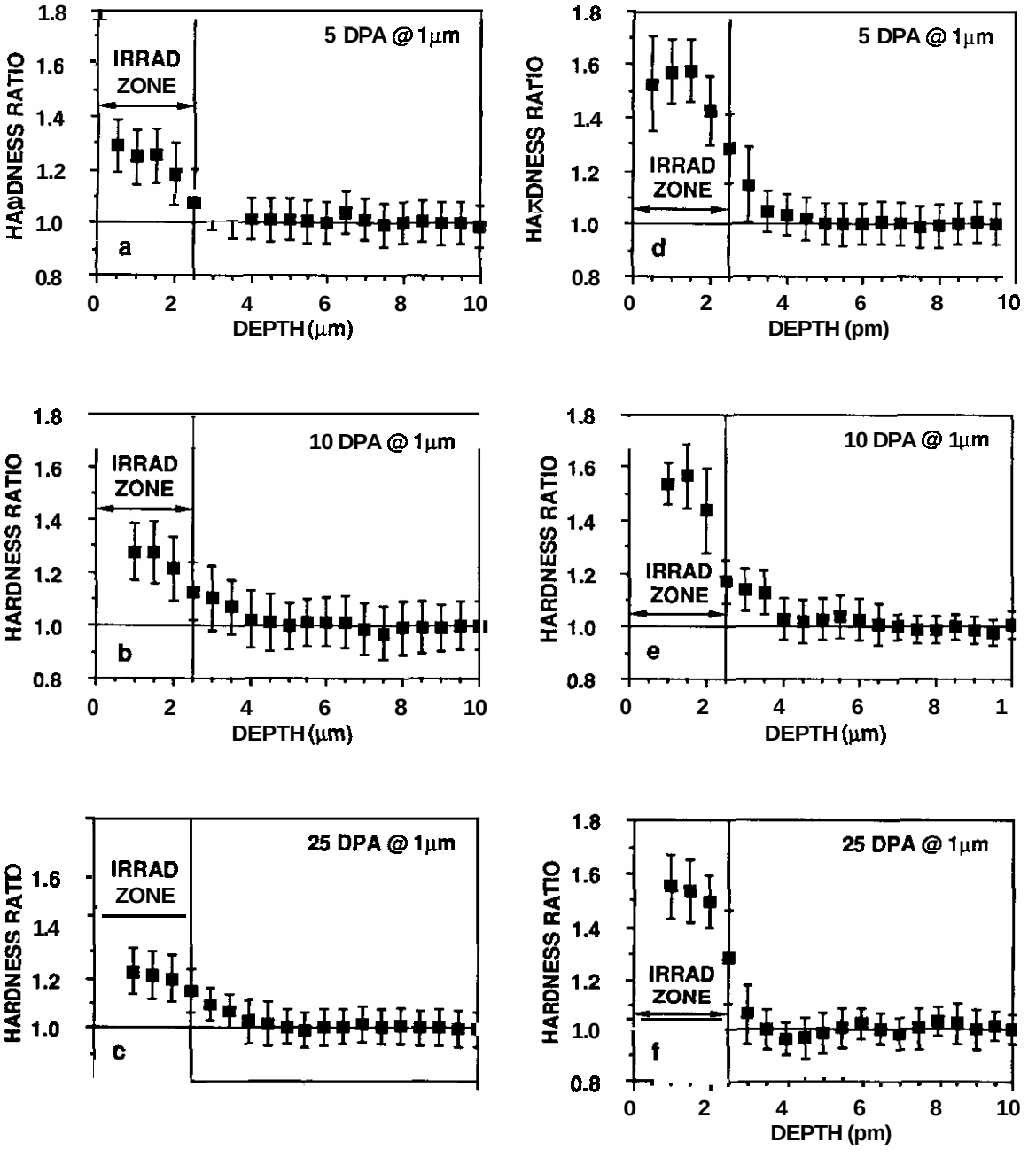

Fig. 7. Ratio of hardness to average unirradiated hardness versus depth in Ni-10% Cu (a-c) and Ni-50% Cu (d-f) irradiated at 0.45 Tm to various fluences.

Table 2. Comparison of Yield Strength Changes in Irradiated Ni-Cu from Hardness (MPM) Measurements and Theoretical Calculations in GPa.

Composition	MPM Measurement	Small Loop Model	Large Loop Model	Large + Small Loop Models
Ni-10% Cu	38±4	32	38	
Ni-50% Cu	83±8	52	51	73

The MPM appears capable of making direct hardness measurements in the narrow irradiated region. Measurement of the change in hardness after irradiation compares favorably with theoretical calculations made using TEM measurements of loop sizes and densities.

ACKNOWLEDGEMENT

This work is supported by the U.S. Department of Energy, Office of Fusion Energy.

REFERENCES

1. J. L. Brimhall and H. E. Kissinger: Rad. Eff., 1972, vol. 15, pp. 259-272.

2. D. J. Mazey and F. Menzinger: J. Nucl. Mater., 1973, vol. 48, pp. 15-20.

3. K.-H. Leister: Ph.D. Thesis, Kernforschungszentrum, Karlsruhe, May 1983.

4. P. Dauben and R. R. Wahi: Progress Report No. 2 (1981-1984) Hahn-Meitner Institute.

5. P. Barlow: Ph.D. Thesis, University of Sussex, April 1977.

6. L. M. Wang, R. A. Dodd and G. L. Kulcinski: J. Nucl. Mater., in press.

7. S. J. Zinkle and W. C. Oliver: J. Nucl. Mater., 1986, vols. 141-143, pp. 548-552.

8. N. M. Ghoniem, J. Alhajji and F. A. Garner: Effects of Radiation on Materials, ASTM STP 782, pp. 1059-1072, ASTM. Philadelphia, 1982.

9. L. E. Seitzman. et al.: Ultramicroscopy, in press.

10. J. B. Pethica, R. Hutchings and W. C. Oliver: Phil. Mag. A, 1983, vol. 48. no. 4, pp. 593-606.

11. W. C. Oliver, P. Hutchings and J. B. Pethica: Microindentation Techniques in Materials Science and Engineering, ASTM STP 889, pp. 90-108, ASTM, Philadelphia, 1985.

12. M. F. Ooerner and W. D. Nix: J. Mater. Res., 1986, vol. I, no. 4, pp. 601-609.

13. D. ti. Plantz. R. A. Dodd, G. L. Kulcinski: Metall. Trans. A, in press.

14. L. E. Samuels and T. O. Mulhearn: J. Mech. Phys. Solids, 1957, vol. 5, pp. 125-134.

15. D. Tabor: The Hardness of Metals, p. 95, Clarendon Press, Oxford, 1951.

16. J. R. Cahoon, W. H. Broughton and A. R. Kutzak: Metall. Trans., 1971, vol. 2, pp. 1979-1983.

17. J. J. Gilman: The Science of Hardness Testing and Its Research Applications, American Society for Metals, Metals Park, pp. 51-72, 1973.

18. Metals Handbook, 9th ed., vol. 3, p. 660, American Society for Metals, Metals Park, 1980.

HIGH TEMPERATURE PHASE SEPARATION IN Fe-Ni AND Fe-Ni-Cr INVAR-TYPE ALLOYS - K. C. Russell (Massachusets Institute of Technology) and F. A. Garner (Pacific Northwest Laboratory)

OBJECTIVE

The object of this effort is to determine the fundamental processes involved in the phase stability of irradiated alloys.

SUMMARY

We summarize and discuss critically the evidence concerning a high-temperature miscibility gap in Fe-Ni and Fe-Cr-Ni Invar-type alloys. Independent data regarding phase separation are obtained from studies on three different classes of material: magnetic, low-expansion Invar-type alloys; Fe-Ni meteorites; and model austenitic Fe-Ni and Fe-Cr-Ni alloys studied for potential nuclear applications. These alloys show anomalies in magnetization, thermal expansion coefficient, lattice parameter, single crystal elastic constants, electrical resistivity, thermoelectric potential, solution thermodynamics, and interdiffusion coefficient. The response of these alloys to long-term aging in meteorites and to a variety of irradiation treatments is found to be inconsistent with most accepted or proposed phase diagrams. All results support the suggestion that Fe-Ni and Fe-Ni-Cr Invar alloys are very metastable and exhibit a narrow coherent miscibility gap with a peak at about 35% Ni and 1100K.

The existence of the high temperature miscibility gap has not been generally recognized for several reasons. Firstly, the narrowness of the miscibility gap at high temperatures virtually precludes incoherent or coherent nucleation of a new phase and limits spinodal decomposition to very small amplitude fluctuations which are hard to observe. Furthermore, the essentially equal scattering power of Fe and Ni for x-rays, as well as for electrons and neutrons makes the usual diffraction techniques inapplicable, and the fine scale of thermally-induced spinodal decomposition is not observable by optical or electron microscopy. Only under the extremely slow aging conditions found in meteorites or in the enhanced diffusion conditions inherent in irradiation studies does phase decomposition become sufficiently advanced to observe using conventional microscopic observation techniques. A very recent SANS study of Fe-34Ni isotopically enriched in Ni has confirmed the tendency for this alloy to decompose during thermal annealing and to develop large wavelength fluctuations in composition during proton irradiation.

PROGRESS AND STATUS

Introduction

Invar alloys exhibit a near zero thermal expansion coefficient over a substantial temperature range (see Figs. 1 and 2); this makes them valuable in applications which demand a high degree of dimensional stability. Invar behavior is found in a narrow composition range of a variety of Fe-X alloys (Fig. 1), where primarily X=Ni, Mn, Pt, or Pd. The most common Invar alloy is based on Fe-36 w/o Ni. Recently, Fe-Ni and Fe-Ni-Cr alloys in this Ni composition range were found to exhibit a remarkable resistance to dimensional changes arising from void swelling under neutron or heavy ion irradiation. In addition, some metallic meteorites found on the earth's surface are of the approximate composition Fe-35 %Ni. There are thus three separate pools of data available for studying phase stability of this class of alloy.

Although Fe-Ni Invar alloys typically are thought to be thermodynamically stable, the physics literature is littered with evidence which suggests the presence of a high temperature miscibility gap in these alloys. References to possible phase separation and phase decomposition extend back at least to 1969. Yet these results generally have not penetrated into the metallurgical phase diagram literature, which shows Fe-35% Ni alloys to be single phase austenite from the $(\gamma/\alpha + \gamma)$ boundary at 725K to the $(\gamma/\gamma+\ell)$ boundary at 1725K.[1]

The metallurgists' reluctance to accept the scattered evidence for the miscibility gap may be the absence, until very recently, of microscopic or diffraction evidence of decomposition. Very recently, the studies of Garner and co-workers[2-9] have provided clear microscopic evidence for a spinodal-type phase separation in a number of neutron or heavy ion irradiated Fe-Ni and Fe-Ni-Cr alloys over a temperature range of at least 700-925K.

This paper examines the evidence relevant to existence of a high temperature miscibility gap in Invar-type alloys, including studies of:

- Magnetic properties
- Thermal expansion coefficient
- Lattice parameter

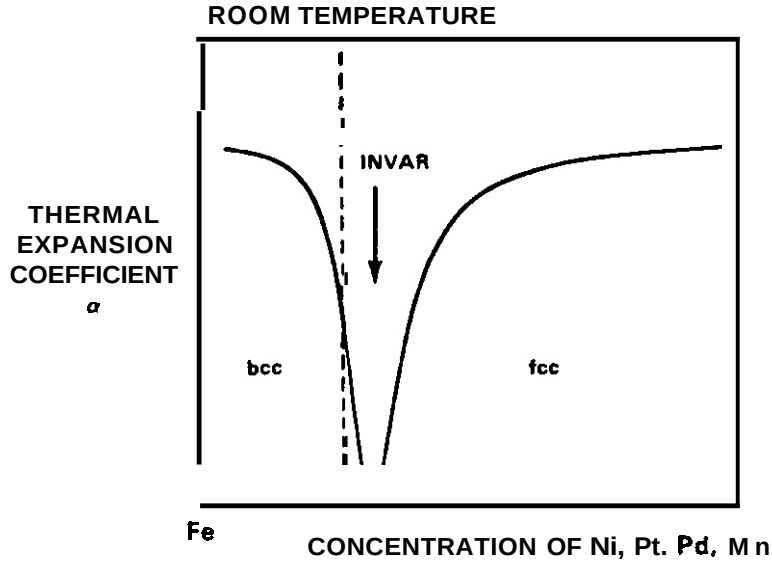

Fig. 1. Schematic illustration of compositional dependence of the thermal expansion coefficient of various iron-base binary alloys showing a minimum in the Invar range.

- Single crystal elastic constants
- Electrical resistivity
- Thermoelectric potential
- Solution thermodynamics
- Austenite decomposition kinetics
- Interdiffusion coefficient
- The microstructures and compositional distributions of meteorites
- Neutron, electron, and heavy ion induced microstructures and their associated compositional distributions.
- Neutron and electron induced changes in lattice parameter.

Review of the available literature was complicated somewhat because many of the studies were on samples which apparently had undergone a partial, uncontrolled and usually unrecognized phase separation. In addition, not all authors state whether their compositions are specified by weight percent or by atomic percent. Fortunately, for Fe-Ni alloys wt% and at.% are nearly the same.

Discussion of the Evidence

We will now consider the studies of Invar-type alloys which pertain to the high temperature structural stability of the solid solution.

Magnetic Properties

Invar alloys exhibit a low thermal expansion coefficient below the Curie temperature because of the gradual transition from ferromagnetic to paramagnetic behavior. This transition gives a volume contraction (magnetostriction) which approximately cancels out the normal volume increase due to thermal expansion, as shown in Fig. 2.

Numerous studies[10-15] have found that the magnetization of Invar alloys persists to higher temperatures than would be expected for a homogeneous alloy. Figure 3 compares the results of Asano[13] and Crangle and Hallam[14] to calculations of Curie temperature based on a uniform alloy. Asano[13] concluded that the gradual transition from ferromagnetic to paramagnetic behavior was partly due to development of microscopic compositional inhomogeneities in the FCC alloy. The Curie temperature of FCC Fe-Ni alloys increases with

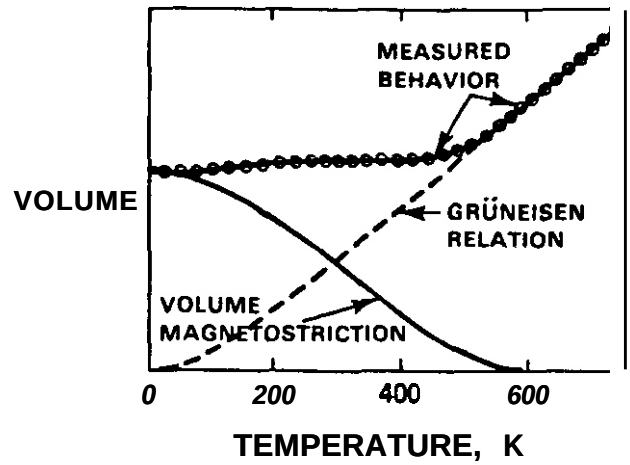

Fig. 2. Schematic representation of the origin of the Invar effect. The gradual transition from ferromagnetic to paramagnetic behavior contracts the lattice, thereby cancelling the expansion caused by thermal vibration.

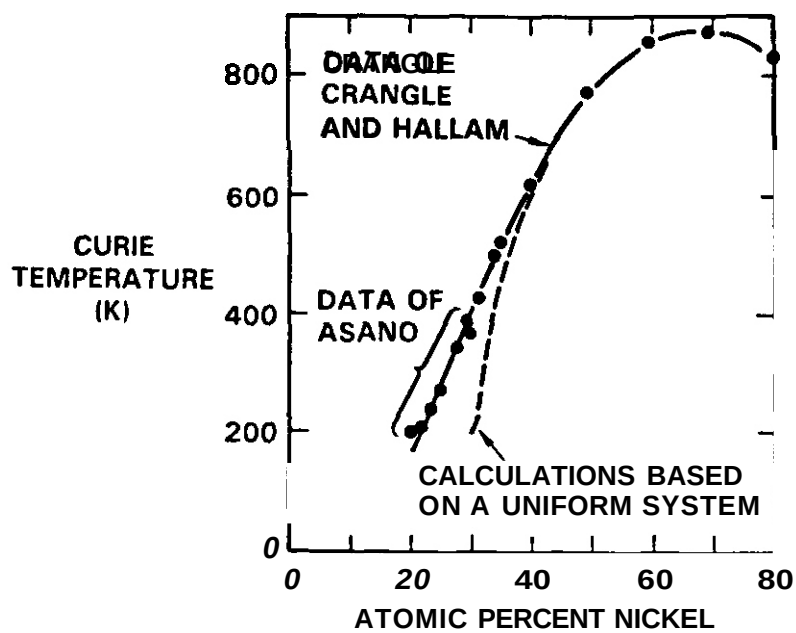

Fig. 3. Curie temperature vs. composition relationship observed for FCC Fe-Ni alloys. The behavior of a hypothetically uniform system is also shown with a dotted line. (After Asano[13]).

nickel content, so the lower nickel domains would transform at lower temperatures than would the higher nickel domains. Asano[13] found the observed magnetization behavior consistent with a domain size of about 60 atoms.

Such inhomogeneities are inconsistent with the published Fe-Ni phase diagrams (See, e.g. Fig. 4), which show only single phase austenite to exist from the $(\gamma/\gamma+\ell)$ boundary at 1725K to the $(\gamma/\alpha+\gamma)$ boundary at 725K. The evidence for inhomogeneity discussed thus far indicates partial decomposition which, due to sluggish diffusion in Fe-Ni alloys, must have taken place at an elevated temperature.

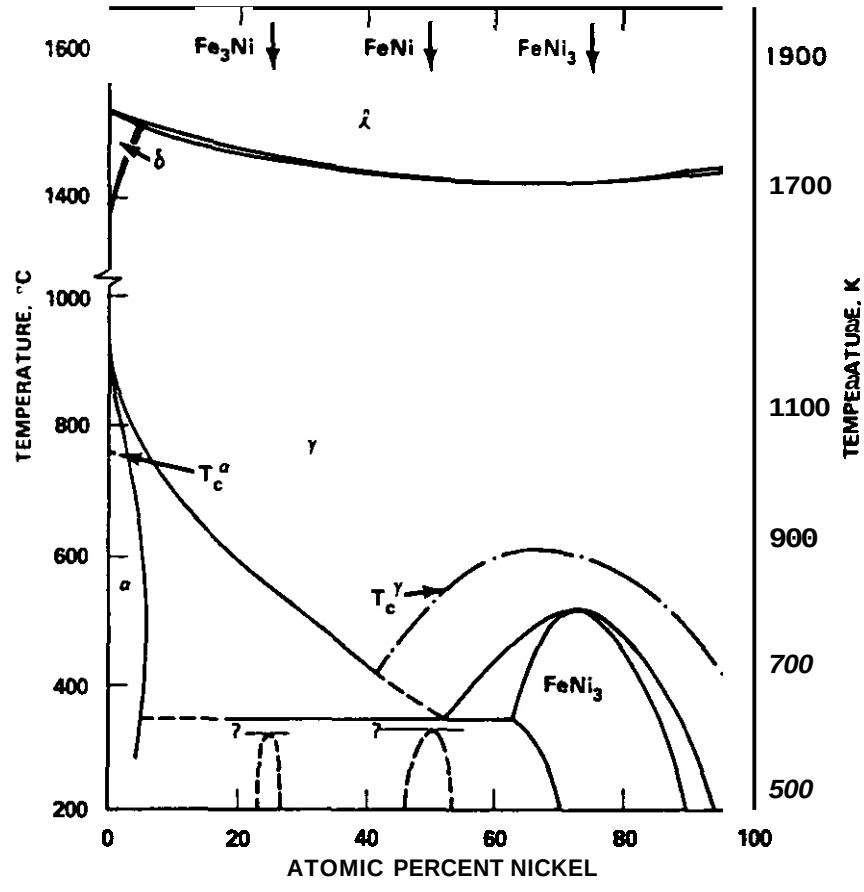

Fig. 4. Fe-Ni phase diagram as proposed by Kubaschewski." Other phase diagram collections present similar diagrams for Fe-Ni.

Thermal Expansion Coefficient

In commercial practice Fe-Ni Invar alloys are annealed at about 1100K and quenched to obtain the minimum thermal expansion coefficient.[16] There is enough diffusion at 1100K (Nakagawa, et al.[18] measured $D \approx 10^{-18}$ m2/s at 1120K) to obtain the fine scale decomposition suggested by Asano[13] if indeed there existed some driving force for separation. However, at 1120K Invar alloys are usually presumed to be in a single phase region far from any phase boundary, and thus there should be no thermodynamic driving force to give such decomposition. Should, however, the alloy composition at this heat treatment temperature lie within a miscibility gap, decomposition might occur, either by spinodal decomposition or by fine scale coherent nucleation and growth. Unfortunately, Fe and Ni have almost the same scattering power for electrons. A similar situation holds for x-rays and, in the absence of isotopic enrichment, for neutrons as well, so that the usual diffraction techniques cannot normally be used to study phase decomposition in Fe-Ni alloys. The postulated decomposed regions are of course far too small to be observed by optical metallography.

Splat quenching was used by Morita, et al.[10] to avoid the suspected decomposition during cooling of a Fe-34 at.% Ni alloy. The thermal dilatation of the homogeneous splatted alloy was slightly negative between 293K and 433K, compared to the slightly positive value of Invar alloys prepared in the usual manner. Annealing of the splat quenched alloy at 825K or higher caused its magnetization to persist to higher temperatures than were observed in the as-splatted material, consistent with decomposition into high and low nickel regions. Morita et al. noted that stress relief was complete at 725K, so additional magnetization changes arising from anneals at 825K and above were attributed to some other cause, presumably fine scale phase separation.

Lattice Parameter

The room temperature lattice parameter of Fe-Ni alloys shows a pronounced maximum between about 35 and 40 at % Ni [Fig. 5). Kachi and Asano" attributed this behavior to the sample being composed of higher density paramagnetic and lower density ferromagnetic regions of slightly different compositions, and they

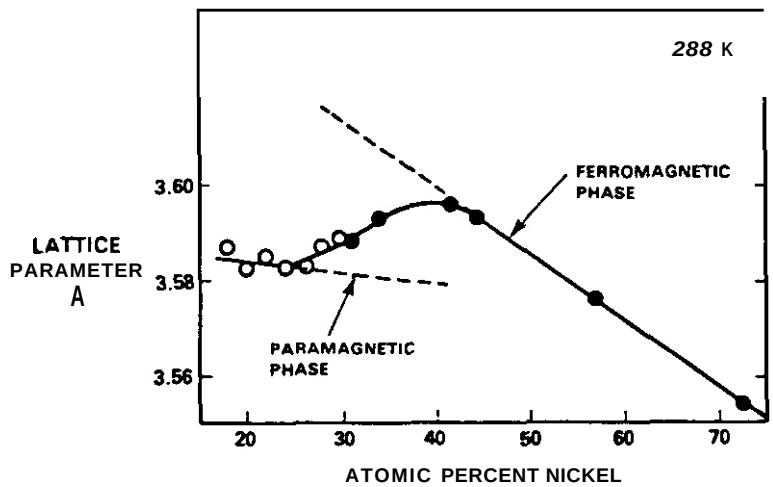

Fig. 5. Measured room temperature lattice parameters for Fe-Ni alloys. The lattice parameter for alloys between 25 and 50% Ni are taken to be the mass weighted averages of the paramagnetic and ferromagnetic values. (After Kachi and Asano").

presented line broadening measurements to support their assertion (Fig. 6). The Fe-20% Ni alloy exhibits the distinctive splitting of the (222) and (311) reflections expected from diffraction of Ka and $K\alpha_2$ x-rays from a uniform crystal. The Fe-30% Ni alloy, however, shows broad diffraction peaks, indicative of decomposition into regions of differing lattice parameter. The measured lattice parameter is then some weighted average of lower Ni, higher density, paramagnetic regions and higher Ni, lower density, ferromagnetic regions, as indicated in Fig. 5.

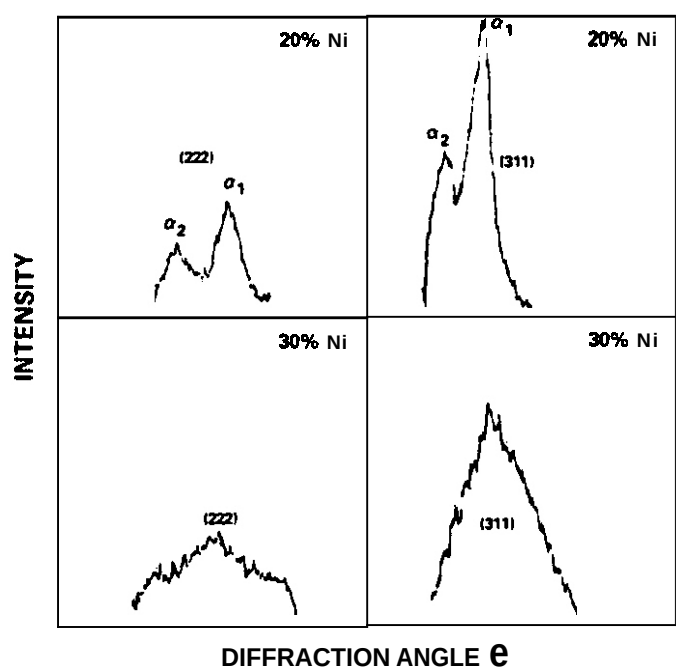

Fig. 6. X-ray broadening of diffraction peaks in Fe-Ni alloys. The 20% Ni alloy shows the expected splitting into two peaks due to reflections of the $K\alpha_1$ and $K\alpha_2$ X-rays from a uniform alloy. The 30% Ni alloy shows line broadening, a behavior characteristic of a non-uniform alloy. (After Kachi and Asano").

Single Crystal Elastic Constants

Hausch and Warlimont[19] measured the single crystal elastic constants of well-annealed, slowly cooled FCC Fe-Ni Invar alloys by an ultrasonic technique. Measurements were made on alloys containing from 30 to 50 w/o Ni at temperatures from 77-700K. Specifically, measurements were made of

$C_L = (C_{11} + C_{12} + c44)/2$

$C' = (C_{11} - C_{12})/2$

$C = c44$

where C_{11}, C_{12}, and C44 are the cubic elastic constants in the Voigt notation. Their results are shown in Figs. 7 and 8. The martensite start (M_s) and Curie (T_C) temperatures in these figures are indicated with arrows.

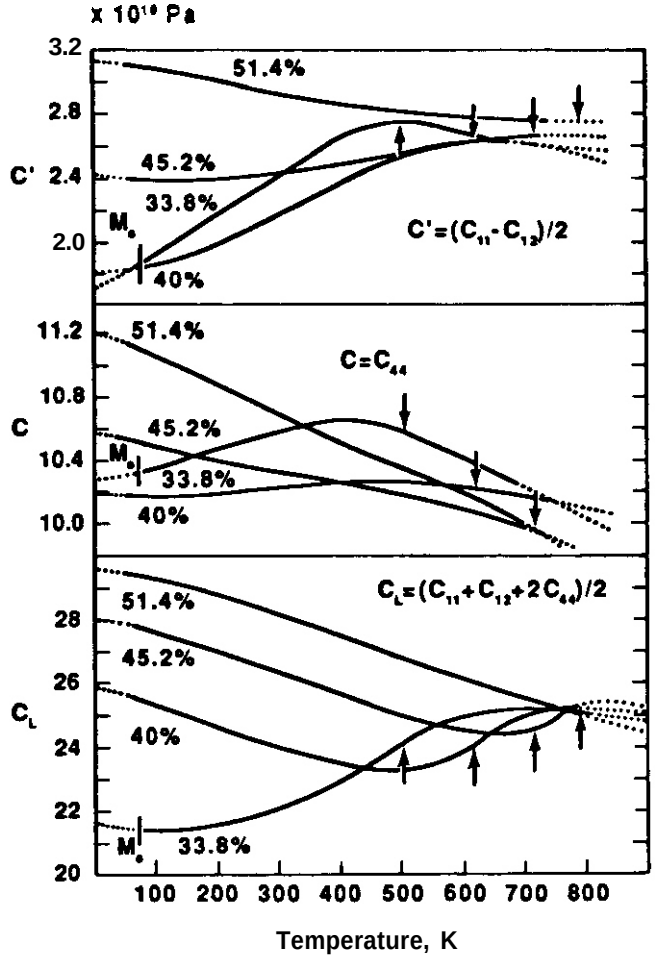

Fig. 7. Temperature dependence of single crystal elastic constants of Fe-Ni alloys. C and C' decrease linearly with temperature above T_C, as expected. C_L shows an anomalous increase with temperature well above T_C (After Hausch and Warlimont[19]).

Anomalous behavior of elastic constants is to be expected below the Curie temperature, T_C, where magnetic effects are important. However, C_L shows anomalous behavior for temperatures up to 200K above T_C. Specifically, C_L exhibits:

1) an anomalous increase with increasing temperature as high as 200K above T_C

2) a lower value when the alloy was magnetically saturated than when in the zero field condition. Both anomalies are strongest at ~33 w/o Ni and disappear at ~50 w/o Ni.

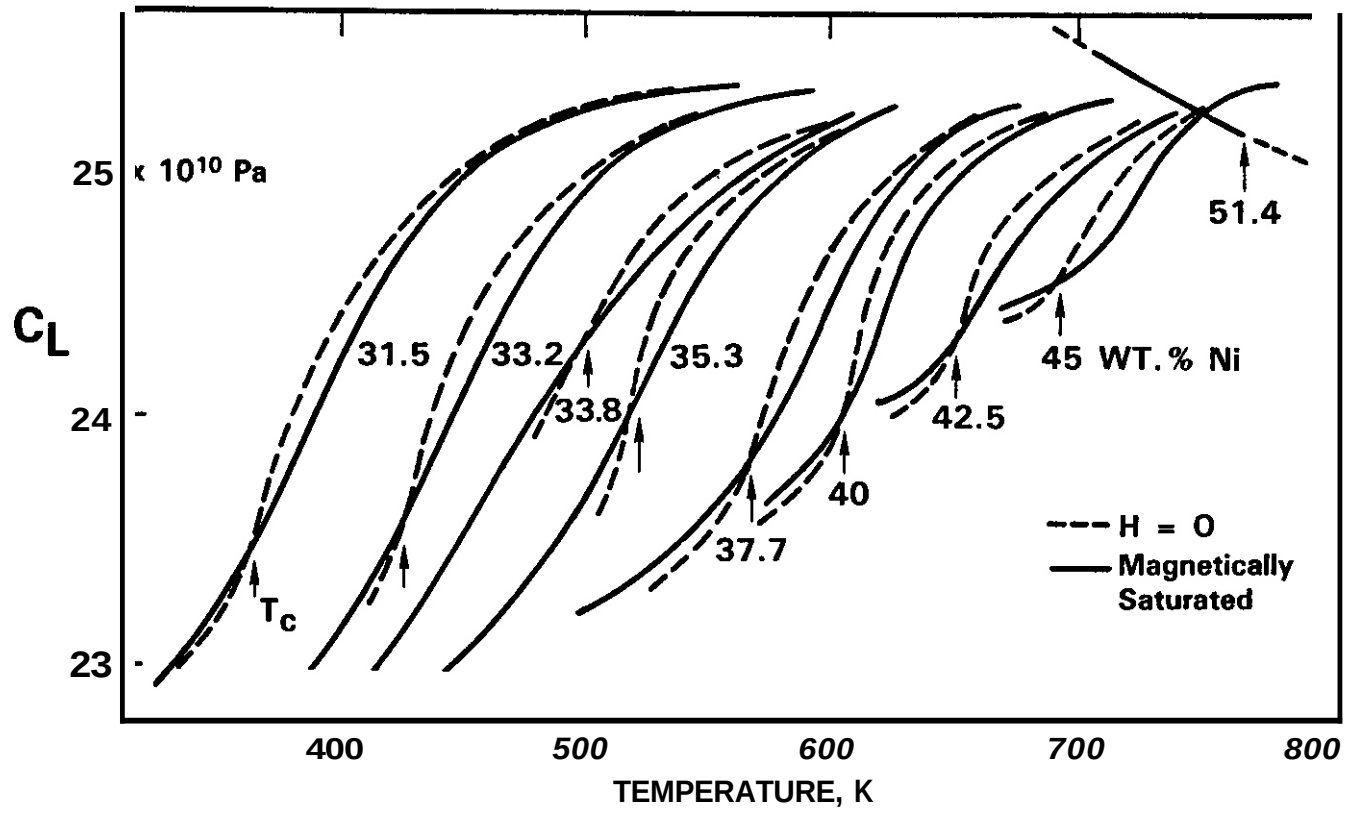

Fig. 8. Elastic constant C of Fe-Ni alloys in demagnetized and magnetically saturated states. Above T_C, C_L is less in the magneticalty saturated state for Ni contents below 50%. (After Ref. 19).

Hausch and Warlimont concluded that the observed behavior was inconsistent with structurally homogeneous alloys, and proposed that the alloy contained very small coherent precipitates of ordered Fe Ni (or possibly FeNi or $FeNi_3$). They proposed that cooling alloys in the Invar compositional regime to jus? below 1070K would result in decomposition into a Ni-rich FCC matrix with small, ordered precipitates which they assumed to be Fe_3Ni. Hausch and Warlimont presented an electron diffraction pattern of well annealed, slowly cooled Fe-31.5 wt% Ni showing <011> streaks around the main spots, which they attributed to elastic distortions around small, coherent Fe_3Ni particles. In a later paper[20] they showed that superlattice reflections developed from these streaks after heating of the thin foils for 15 minutes at 873K. They also observed images in dark field of small precipitates when using the superlattice reflection. The authors noted that while this is a relatively low temperature, beam heating and surface proximity may be influential in providing additional diffusion. Hausch and Warlimont[19] quoted the work of Khomenko, et al.[21] who found that quenching Fe-Ni Invar suppressed the anomalous dependence of C_L on magnetic field. Diffusion isslow enough in Fe-Ni alloys ($D = 10^{-18}$ m²/s at 1120K) that a rapid quench would suppress almost all volume diffusion-controlled decomposition. Jago and Rossiter[22] also observed extra diffraction spots in their foils of Fe-25 at % Ni annealed in vacuo. They concluded, however, that the superlattice reflections arose from formation of an epitaxial precipitate of nickel ferrite spinel ($NiFe_2O_4$), which forms in the microscope at very low oxygen partial pressures.

Electrical Resistivity

Fe-Ni alloys in the Invar range show an anomalously high residual resistivity at 4.2K,[23] (see Fig. 9) which is thought to be caused by some kind of fine scale heterogeneities." Kachi and Asano[11] determined from Mossbauer spectra measurements that at 4.2K this alloy is composed about equally of ferromagnetic and anti-ferromagnetic domains. The high residual resistivity was attributed to electron scattering at the interface between these domains. The existence of the domains was attributed to concentration fluctuations of the type and scale discussed earlier.

Shirakawa[24] made an exhaustive study of electrical resistivity in Fe-Ni alloys from 0-100% Ni at temperatures from 78K to 1120K. Tanji, et al.[25] noted that these resistivity data showed an anomaly between 40 and 50 a/o Ni which suggested to them the onset of a miscibility gap.

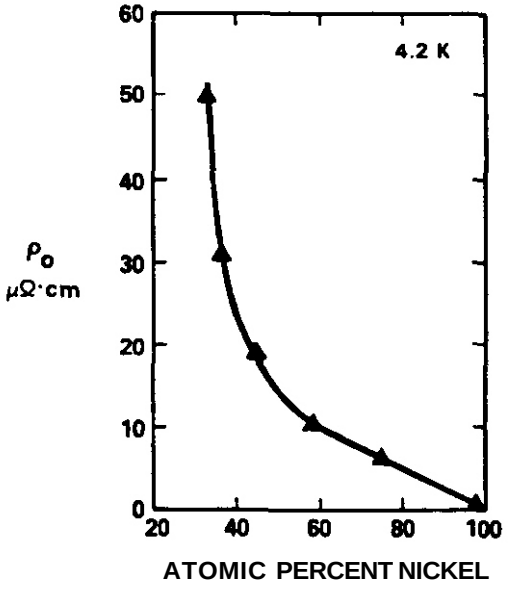

Fig. 9. Residual electrical resistivity in Fe-Ni alloys. Alloys in the 30-50% Ni range have an anomalously high residual resistivity. (After Kondorsky and Sedov,[23]).

Thermoelectric Potential

Measurements of the high-temperature thermoelectric potential of paramagnetic Fe-Ni alloys by Tanji, et al.[25] caused them to suggest that the alloys had separated into two FCC phases. Figure 10 shows the results of their study. The thermoelectric power shows a pronounced low temperature hump in the same composition region where other properties exhibit anomalies. Tanji, et al.[25,26] attributed this anomaly to concentration fluctuations involving large numbers of very small nickel-rich and iron-rich clusters. As shown in Fig. 10 the anomaly persists to at least 1073K and is clearly absent at 1273K.

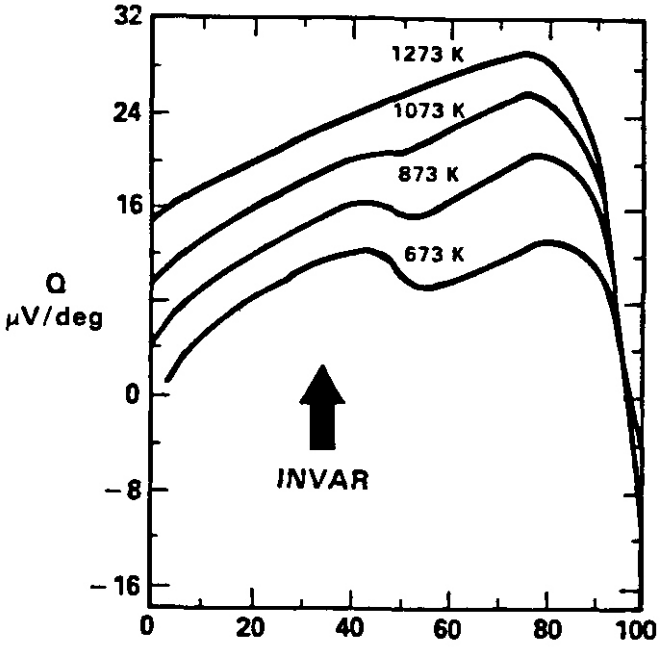

Fig. 10. Thermoelectric power of Fe-Ni alloys. The bump in the Invar composition region indicates partly decomposed alloys at temperatures of 1100K and below. (After Tanji, et al.[26]).

Solution Thermodynamics

Mixing enthalpies for solid Fe-Ni alloys are negative, which indicates a tendency toward ordering rather than phase separation.[27] Yet, thermodynamic measurements provide strong evidence for phase separation in these alloys. Figure 11 shows the comparison Kubaschewski, et al.[27] made of enthalpy of mixing measurements by themselves and other investigators. The data show a pronounced enthalpy hump at about 25 a/o Ni; Kubaschewski, et al. stated that the irregularity "... seems to be genuine." Such an irregularity would tend to give a corresponding hump in the free energy of mixing, leading, at sufficiently low temperatures, to a miscibility gap and phase separation.

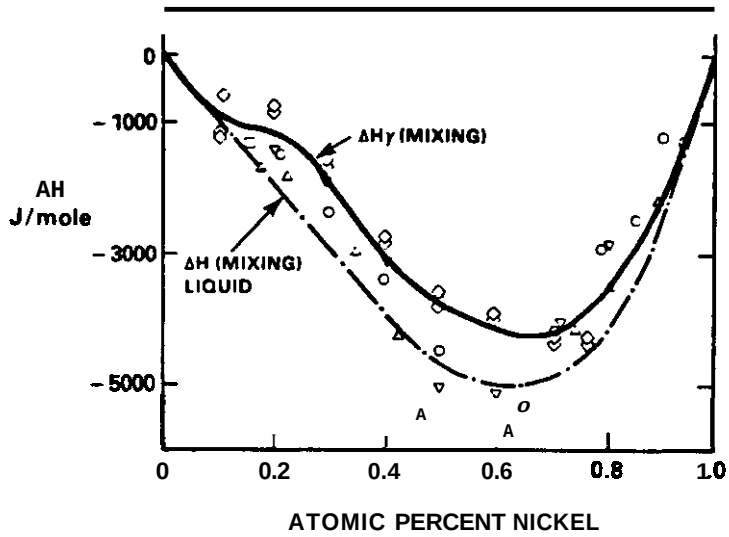

Fig. 11. Mixing enthalpies of solid and liquid Fe-Ni alloys as determined in a number of studies. The mixing enthalpy of the solid alloys shows a pronounced hump at about 25% Ni. (After Kubaschewski, et al.[27]).

Tanji, et al.[26] made isothermal EMF measurements of Fe-Ni alloys. The EMF of their cell was proportional to the partial molar free energy of Fe in their alloys. From this quantity they constructed the free energy of mixing vs. composition curves and the schematic phase diagram seen in (Fig. 12)

The ΔG vs. C curves clearly indicate a chemical miscibility gap with a maximum at about 1300K and about 30 a/o Ni. Tanji, et al.[26] included the closed circles along the high-Ni side of the gap to indicatethe thermoelectric power anomaly observed by their group[25] and the open circles to indicate the electrical resistivity anomaly seen in the data of Shirakawa.[24]

Decomposition Kinetics

Alloys inside a chemical miscibility gap of the type shown in Fig. 12 are metastable with respect to decomposition into two incoherent or semicoherent strain-free FCC phases. Nucleation of a phase either incoherent or semicoherent with the matrix, however, requires formation of a high energy(ca. 0.5 Jm^2) interface. A high thermodynamic driving force is needed to overcome such a high surface energy barrier and cause nucleation. The thermodynamic driving force ΔG_{chem} for nucleation from a matrix of composition C' is shown schematically in Fig. 13 as the distance from the extended tangent to G at the matrix composition to G at the composition of the nucleus.

The kinetics of decomposition are determined primarily by the rate of diffusion. Numerous measurements of the interdiffusion coefficient $\bar{D}$ have been made in Fe-Ni alloys but most were conducted at temperatures far above the range of interest of this study or under conditions where short circuit diffusion in grain boundaries may have affected the results at lower temperatures. In this paper we will use the data of Dean and Goldstein,[28] who devised a technique allowing low temperature (883-978 K) measurements in Fe-XNi alloys (X=15,20,25,30) without short circuit diffusion. If we use their measured values of $\bar{D}$ and assume D_o to be 1×10^{-4} m^2/sec we obtain an activation energy for diffusion of 298 kJ/mol. These diffusion parameters are used throughout this paper to estimate $\bar{D}$ at low temperatures.

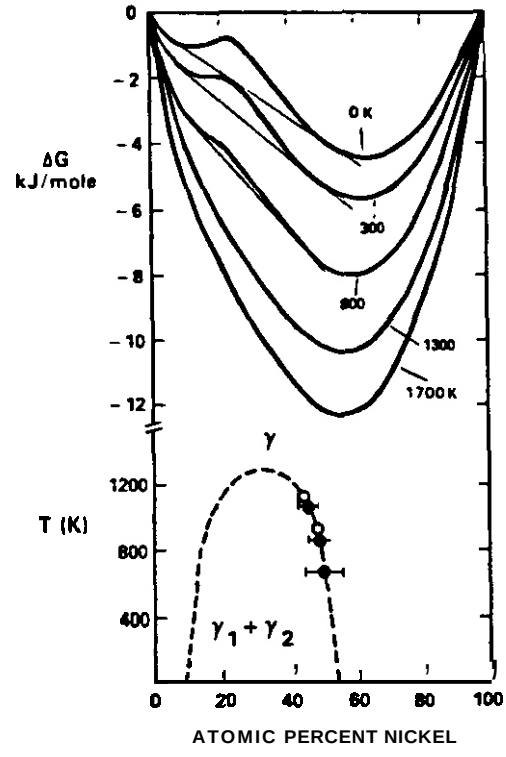

Fig. 12. Free energy of mixing and miscibility gap proposed by Tanji and coworkers[25] for solid Fe-Ni alloys. The open circles are derived from the anomaly observed in electrical resistivity and the closed circles from the anomaly observed in thermoelectric power.

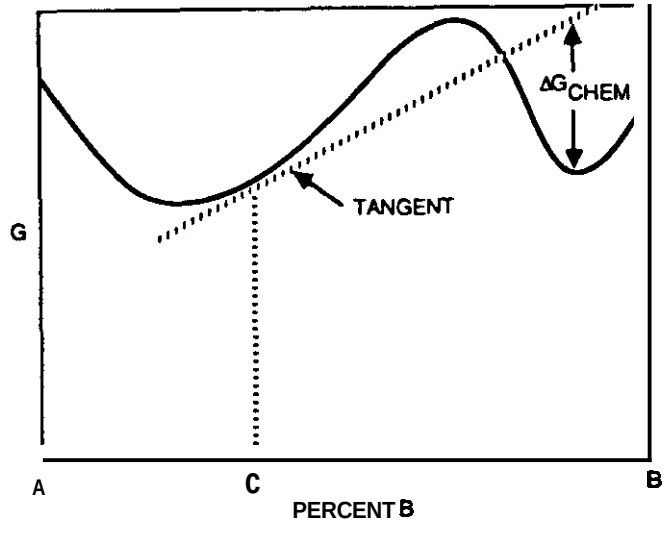

Fig. 13. Schematic plot of free energy vs. composition in a miscibility gap system. The construction to obtain ΔG_{chem} for nuclear from an alloy of composition C′ is shown.

Diffusion is very sluggish in FCC Fe-Ni alloys so that below about 800K where $D \approx 3 \times 10^{-24}$ m^2/s nucleation would be extremely slow. At higher temperatures, where diffusion is more rapid, Fig. 11 shows that ΔG has only a very slight hump near the Invar composition so that ΔG_{chem} is the order of (minus) a few hundred J/mol, at most. This is a very small driving force and would produce incoherent or semicoherent nucleation only in the presence of a very potent catalyst -- which we have no reason to believe exists.

The alloy may also decompose by coherent spinodal decomposition[29] or by coherent nucleation and growth.[30] In either case, part of the thermodynamic driving force for decomposition acts to overcome the

strain energy arising from lattice coherency strains. The coherent spinodal is defined by the locus of points for which:

$$\frac{\partial^2 G}{\partial C^2} - \frac{2\eta^2 E}{1-\nu} = 0 \qquad (1)$$

where:

$\eta = \frac{1}{a}\frac{da}{dC}$

a = lattice parameter,

E = Young's modulus,

ν = Poisson's ratio, and

C = composition, in atomic fraction

The first term in Eq. (1) is the chemical driving force for spinodal decomposition and the second is the strain energy acting to retard decomposition.

Cahn[29] estimated that a misfit of $\eta = 0.025$ would depress a spinodal by about 40K at the center of the miscibility gap where $\partial^2 G/\partial C^2$ is a maximum. Greater depressions would occur on either side of the center of the miscibility gap due to the fact that $\partial^2 G/\partial C^2$ is smaller.

The action of strain energy depresses the coherent miscibility gap below the incoherent miscibility gap by a similar amount. The lattice parameter in Fe-Ni alloys does vary with composition, causing significant strain energy to develop, so that both spinodal decomposition and coherent nucleation will be difficult, as noted by Tanji, et al.[31] Coherent nucleation is further hindered by the low thermodynamic driving forces which also make incoherent nucleation difficult.[29]

Guimaraes, et al.[32] calculated the strain energy associated with spinodal decomposition in the Fe-Ni system but made an error in units. Tanji, et al.[31] later corrected the strain energy calculations and twice differentiated the free energy of mixing to obtain $\partial^2 G/\partial C^2$.

The calculations showed that $\partial^2 G/\partial C^2$ is very small near either side of the miscibility gap so that the influence of strain energy is to give a very narrow composition range over which spinodal decomposition may occur. In addition the top of the coherent miscibility gap is depressed well below the top of the incoherent gap and narrowed significantly. These changes are shown schematically in Fig. 14, which is based roughly on the calculations of Tanji, et al.[31] and an estimated peak of the coherent miscibility gap at 1100K.

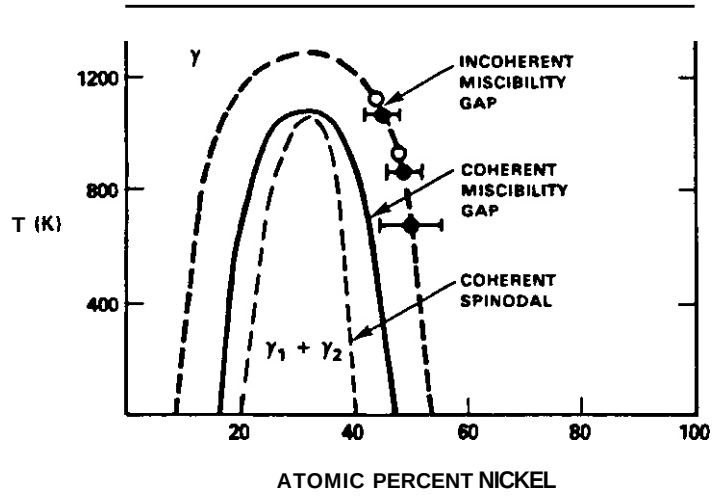

Fig. 14. Coherent miscibility gap and coherent spinodal proposed by the authors for Fe-Ni alloys. The strain energy depresses and compresses both the miscibility gap and the sponodal relative to the incoherent miscibility gap proposed by Tanji and coworkers.

There are significant uncertainties in the values calculated as input for both terms in Eq. (1). He believe that most measurements of lattice parameter and elastic modulus were made on partly decomposed alloys. Uniform alloys must be used for proper values. Even more important, the values of $\partial^2 G/\partial C^2$ come from twice differentiating the free energy of mixing, which itself contains substantial uncertainty which is then magnified by differentiation. Nonetheless it is clear that:

- Both the coherent miscibility gap and the coherent spinodal region span narrow composition ranges.
- The coherent miscibility gap and spinodal are depressed well below the chemical miscibility gap.

Therefore, at high temperatures the early stages of spinodal decomposition will give only small concentration fluctuations, and the decomposition will occur only at temperatures well below 1300K. Furthermore, the narrowness of the coherent miscibility gap leads to small driving forces which in turn make coherent nucleation very difficult. Thus, decomposition of metastable Invar-type alloys is very difficult at temperatures near the top of the miscibility gap where diffusion is reasonably fast. However, we will see shortly that either irradiation-enhanced diffusion or the extremely long aging times experienced in slowly cooling meteorites may give sufficient amounts of diffusion at lower temperatures where the thermodynamics of decomposition are favorable.

Interdiffusion Coefficient

The interdiffusion coefficient, $\tilde{D}$, is negative beneath a coherent spinodal, giving rise to uphill diffusion and thereby spinodal decomposition.[29] Interdiffusion measurements should therefore show anomalies when performed either beneath or just outside a coherent spinodal.

Nakagawa, et al.[18] measured interdiffusion coefficients for Fe-Ni alloys containing from 0-100% Ni at temperatures from 1123K to 1373K. Figure 15 shows some of their results; the arrows at the top of figure show the composition ranges of the diffusion couples employed. Figure 15 shows that at 1123K, certain of the experiments involving small compositional increments gave a deep minimum in $\tilde{D}$ in the Invar region. The 1123K temperature is near the top of the proposed coherent miscibility gap (see Fig. 14), where $\tilde{D}$ should be small or negative. The authors stated that small increment couples gave more reliable values for $\tilde{D}$. In fact Fig. 15 shows that at 1253K and 1373K $\tilde{D}$ values obtained from large increment couples do not approach D^* as $\%Ni \to 0$, as they should. It is therefore reasonable to rely more on the results from diffusion couples involving small increments of composition. It is these results which clearly indicate the existence of a miscibility gap.

Meteorite Microstructures

Meteorites are known to have reached very high average temperatures, becoming molten during their aggregation phase and then to cool at very slow rates, the order of 1K per million years.[33] The Santa Catharina Meteorite* fits this description and contains 35 wt% Ni and at most 2.5% of minor elements (C0, 0, S, P) in unweathered regions and as such is close to the Invar composition. Some portions of this meteorite have suffered extensive weathering and oxidation but Danon et al.[34] and Scorzelli and Danon[35] found unweathered portions of the meteorite to be decomposed into regions of 26-31% Ni and of 51.3-48.6 Ni on about a 10 μm scale as seen in Fig. 16. They also noted that the oxygen levels were much higher at cracks and veins where weathering had occurred in their specimens. The microstructure contained 35-42 vol% of the Ni-rich phase which is ordered with L10 structure and 63-56 vol% of the Fe-rich γ-phase. The remainder of the microstructure was made up of nonmetallic phases. Jago et al.[36] also noted that this meteorite was composed of iron-rich γ' and ordered FeNi. However, Clarke[57] was unable to observe the ordered FeNi phase in the portions of the meteorite that he studied.

The lattice parameter of the metallic portion of the meteorite was found to vary normally with temperature (Fig. 17) as is to be expected of a mixture of paramagnetic 25% Ni material and ferromagnetic 50% Ni material (see Fig. 5). Annealing a portion of the meteorite in the laboratory at 1073K for 24 hr restored the Invar qualities[35] (see Fig. 17). The anneal has clearly substantially homogenized the alloy. However, an 1103K anneal is used to produce fine compositional fluctuations in commercial Invar alloys. Therefore, at 35% Ni the coherent spinodal must be very near 1173K: Otherwise what is effectively the same anneal could not cause homogenization in a decomposed alloy and also give fine oscillations in a uniform alloy. We note that ageing a uniform alloy just above the top of the miscibility gap would produce critical point fluctuations which would give decomposition on the fine scale inferred from magnetic measurements.

The meteorite is thought to have cooled as part of the core of an approximately 1000 km diameter parent body.[33] Goldstein and Ogilvie[38] calculated the pressure at the center of the body to be the order of 1 Kbar, or 10^8 Pa. Buchwald[33] estimates a similar pressure. A 1% volume change** on transformation of

---

* Buchwald (33) gives the history of the meteorite and summarizes the results of studies thereon.

** As we shall show later, the phase separation appears to involve a net decrease in lattice parameter of −0.35% and a measured density increase of −1%.

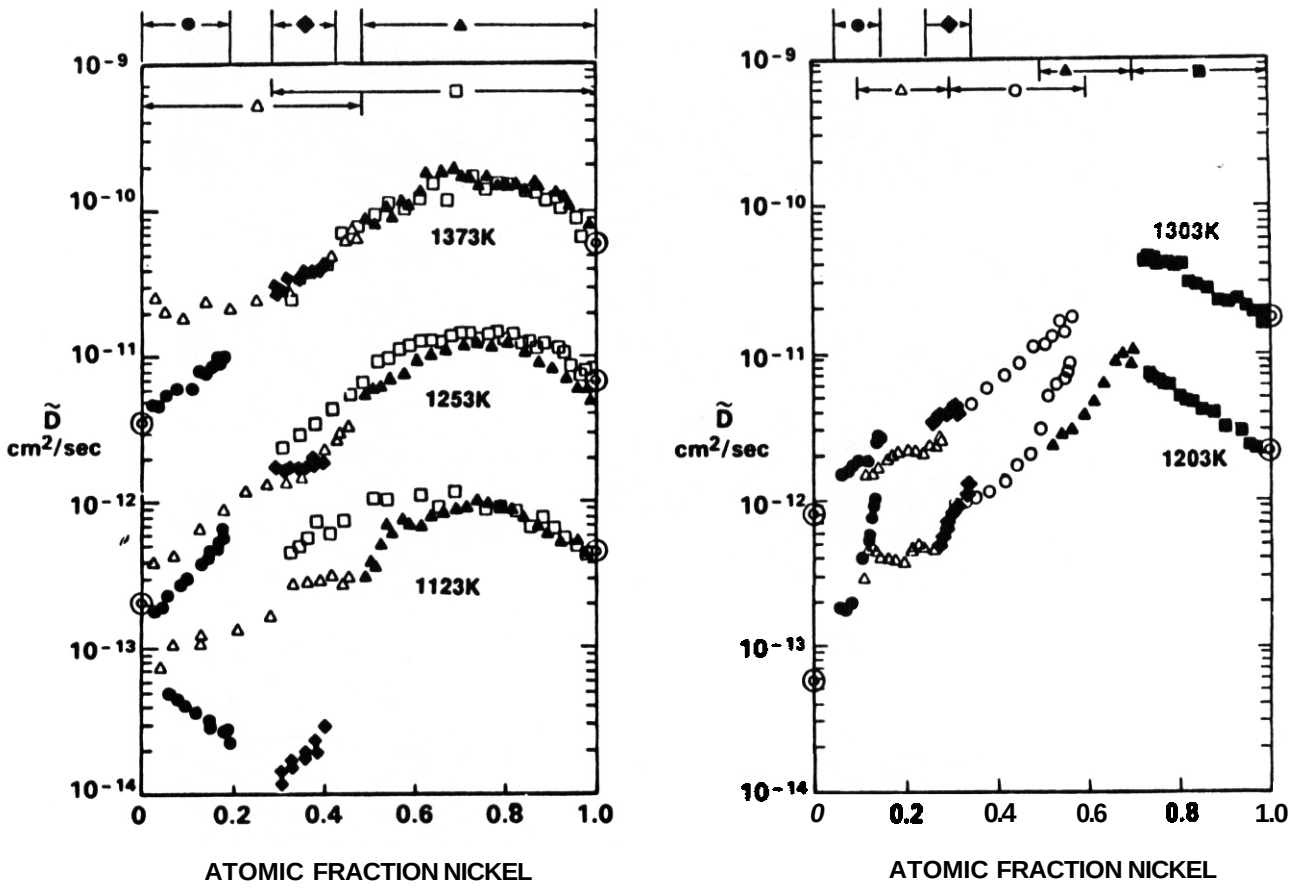

Fig. 15. Interdiffusion coefficients measured in the Fe-Ni system. At 1123K diffusion couples spanning small composition increments yields values of $\tilde{D}$ which go through a pronounced minimum at 30% Ni, indicating the proximity of a coherent spinodal. (After Nakagawa, et al. [18]).

Fe-35% Ni into 25% and 50% Ni regions would give a $P\Delta V$ contribution to the free energy of only about 10 J/mol. Phase equilibria would be shifted from those normally observed only in rare cases where the lower volume phase was very nearly stable at atmospheric pressure. The activation volume for diffusion is an order of maunitude or more laraer. Even so. the 100-1000 J/mol free energy change would have little effect on the diffusion coefficient. It is thus appropriate to use properties measured at 1 atm pressure in describing the behavior of the parent body.

The scale of the microstructure, the estimated cooling rate, and the interdiffusion coefficient may be used to help determine how the microstructure developed. The microstructure has a scale of about 10 μm; the coolina rate is estimated to have been a few dearees per million years. The microstructure might have formed-directly at the observed 10 μm scale or might have resulted from coarsening of a finer scale structure. We consider the former possibility first.

The minimum temperature which would have given diffusion over a 10 μm scale may be calculated from $10\ \mu m = \sqrt{\tilde{D}t}$, to yield 780K, based on $t=10^{14}$s (about 3 x 10⁶ yr) and $\tilde{D} = 10^{-24}$ m²/s. Wavelengths observed in typical terrestrial examples of spinodal decomposition are usually the order of nm. It is hardly conceivable that spinodal decomposition occurred with an initial wavelength of 10 μm.

It is also unlikely that nucleation occurred on a 10 μm scale. Homogeneous nucleation is most unlikely in this system (even in 10⁶ yr) due to the low chemical driving force. Homogeneous nucleation may of course occur readily just above the coherent spinodal, but under those conditions it is hardly distinguishable from spinodal decomposition. Although dislocation lines and grain boundaries are potential sites for heterogeneous nucleation, the incredibly slow cooling rate of the alloy produced grains of about 3 cm diameter[SS] and, of necessity, very low dislocation densities. Thus, during alloy decomposition both the grain diameter and the dislocation spacing were orders of magnitude greater than the 10 μm scale of the microstructure. It therefore appears that the alloy could not have decomposed by heterogeneous nucleation and growth on the 10 μm scale.

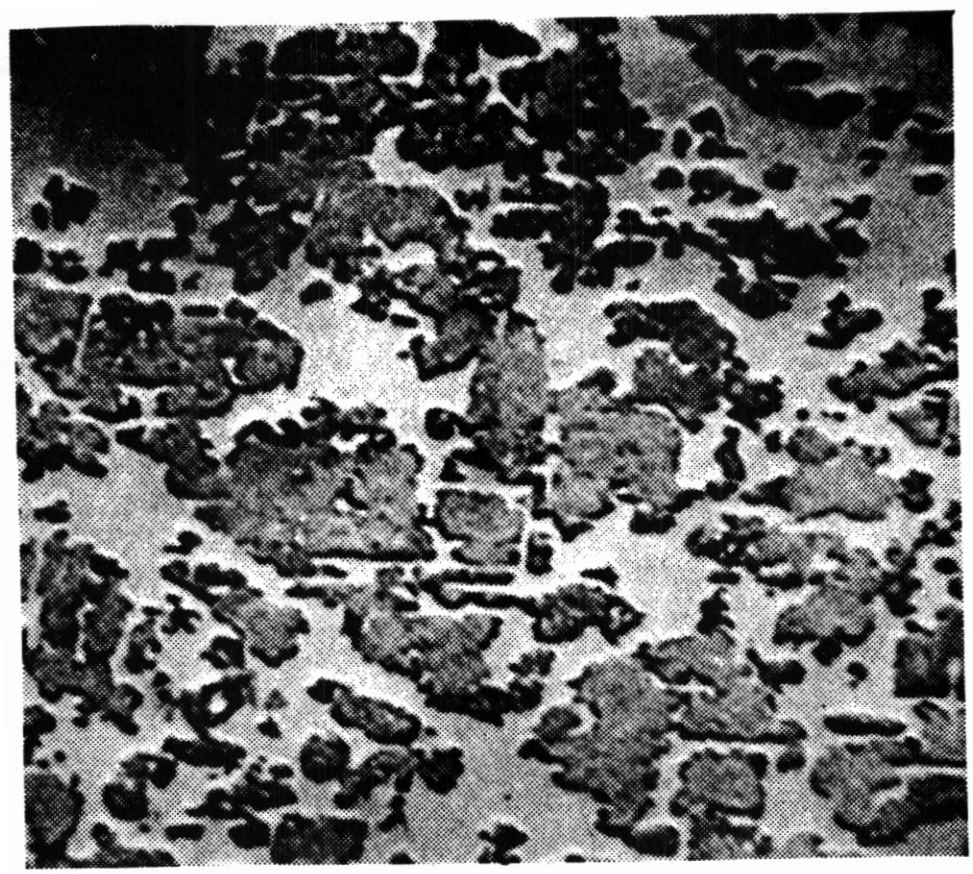

Fig. 16. Back-scatter electron image from electron microprobe analysis of a polished surface of the Santa Catharina meteorite. From point analysis determination it is found that the dark areas correspond to the FeNi ordered phase whereas the light areas correspond to the Fe-rich paramagnetic phase. (After Scorzelli and Danon et al.[35]).

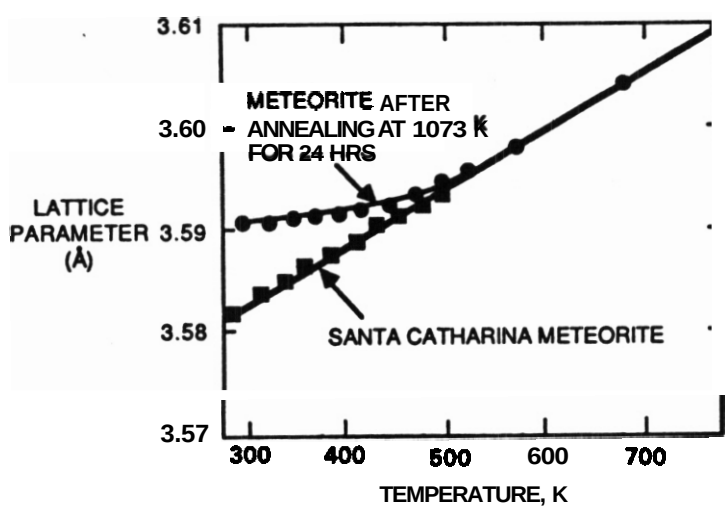

Fig. 17. Temperature-dependent lattice parameter of the Santa Catharina meteorite before and after annealing at 1073K for 24 hours. The appearance of Invar propoerties shows that annealing has substantially homogenized the alloy. (After Scorzelli and Danon[35]).

Furthermore, no accepted Fe-Ni phase diagram predicts that FCC Fe-35% Ni would decompose into ~25% and ~50% Ni regions at a temperature near 780K. The phase diagram of Kubaschewski, et al. (Fig. 4), for example, predicts that at 780K Fe-35% Ni is in the stable austenite region. Chamberod, et al.[39] propose the existence of Fe_3Ni and FeNi ordered phases, but the latter appears to be stable only below about 600K.

Chuang, et al.[40] predict that the composition dependence of the magnetic free energy would induce a FCC miscibility gap and an associated spinodal at much lower temperatures, as shown in Fig. 18. Spinodal decomposition of a 35 wt% alloy within this gap would occur only below about 600K and owing to low diffusion rates could not possibly produce the 10 μm scale microstructure observed in the meteorite.

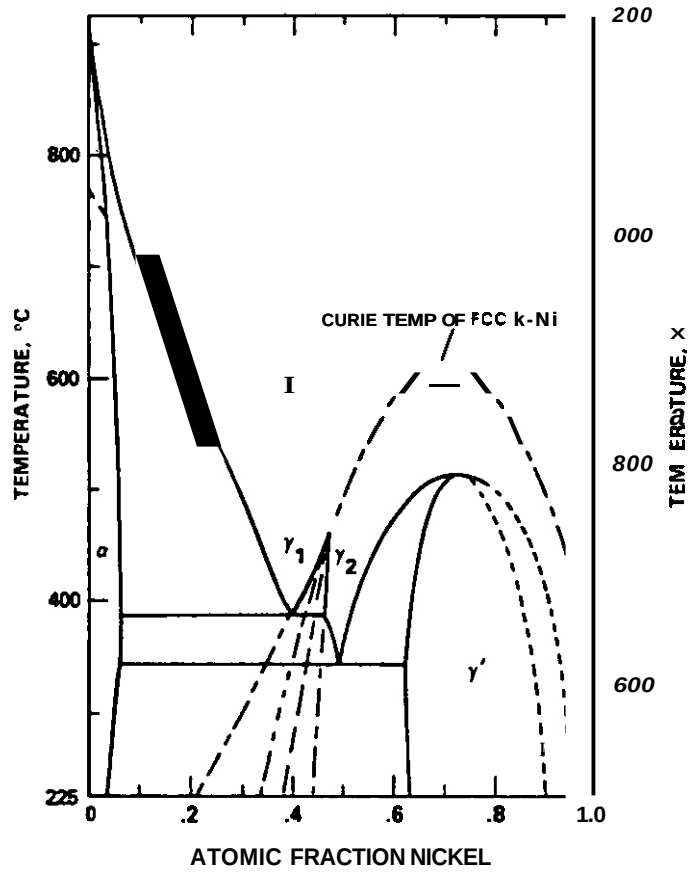

Fig. 18. Calculated Fe-Ni phase diagram showing a low temperature miscibility gap and spinodal induced by magnetic contributions to the free energy. (After Chuang, et al.[40]).

Suppose, instead, that the alloy initially underwent spinodal decomposition on a fine scale, then coarsened to the observed 10 μm scale. The Wagner-Lifshitz-Slyzov[41] theory of volume diffusion-controlled coarsening predicts that the mean particle size, $\bar{r}$, varies as:

$$\bar{r}^3 - \bar{r}_o^3 = \frac{8\gamma V_m^2 DCt}{9RT} \qquad (2)$$

where: D = diffusion coefficient

C = concentration

γ = interfacial energy

V_m = molar volume of material in the particle

RT = gas constant times absolute temperature

t = time

$\bar{r}_0$ = initial mean particle size

laking reasonable values for γ, V_m, C and T and choosing r = 10 μm, t=10^{14}s, and assuming $\bar{r}_0 \ll \bar{r}$, we obtain a diffusion coefficient corresponding to a coarsening temperature of about 1000K. The compositions of the high nickel and low nickel regions would adjust to the compositions defined by the miscibility gap until the temperature fell below ~780K. Below 780K diffusion on a 10 μm scale is no longer possible.

Thus, fine scale, high temperature spinodal decomposition followed by coarsening at about 1000K is entirely consistent with the observed meteorite microstructure and composition as well as the proposed high temperature miscibility gap. Coarsening at temperatures much below 1000K could not have given the 10 μm scale microstructure observed in the meteorite. Once this microstructure was established the meteorite would continue to cool and eventually fall below 575K (See Fig. 19a) where the Fe-50%Ni regions would begin to order. Such order was observed by Scorzelli and Danon[35] Danon et al.[34] and Jago et al.[36] The latter group noted that annealing of the Santa Catharina meteorite at temperatures of 473 to 673K was sufficient to cause some shift in the proportions of phases, indicating that at these low temperatures some additional small scale phase separation can occur.

Cooling a low-Ni meteorite below the (γ/α t γ) solvus produces low-Ni kamacite (ferrite) plates which grow by rejecting Ni into the taenite (austenite) matrix. The nickel concentration in taenite at the taenite:kamacite boundary follows the γ/α t 7 solvus, which increases in Ni content with decreasing temperature (Fig. 4). The result is a coarse Widmanstatten structure in which the nickel profile of the taenite plates has a characteristic "M" shape, ranging from ~50% at the edges to ~25% in the center of the plate. The high nickel region at the boundaries of the taenite plates is known as clear taenite; adjacent to these regions are slightly lower nickel regions designated as cloudy taenite. Cooling of low-Ni meteorites thus produces high-Ni regions which may also be studied for evidence of alloy decomposition.

Reuter et al.[42] used analytical electron microscope techniques in a study of several meteorites. The cloudy taenite region was found to be composed of a globular ordered FeNi phase containing 50.9 ± 1.4 wt% Ni and a honeycombed martenite phase containing 11.7 ± 0.5 wt% Ni. The ordered FeNi domain sizes ranged from 650 nm in the high nickel regions to 15 nm in the low nickel regions of the cloudy taenite plates.

Reuter et al.[42] concluded that the cloudy taenite region formed by spinodal decomposition of 28-46 wt% Ni FCC material at about 623K. The compositional amplitude increased as the temperature decreased but no further long range diffusion occurred below 623K. Ultimately the high nickel region ordered to FeNi and the low nickel region transformed to martensite.

In a later paper, Reuter et al.[43] concluded that at 473K the limits of the miscibility gap were at about 11.7 and 50.9 wt% Ni, the measured compositions of the ordered FeNi and martenite in the cloudy taenite. They thus concluded that at low temperatures the spinodal region is much narrower than the miscibility gap. Reuter et al.[42,43] interpreted their results in terms of the low temperature, magnetically induced miscibility gap and spinodal predicted by Chuang et al.[40] Their results are equally consistent, however, with the higher temperature miscibility gap and spinodal advanced in this paper.

Miller and Russell[33] made an atom probe study of the 27% Ni region in a taenite plate in the Cape York meteorite.[33] The atom probe investigation revealed that the 27% Ni region had phase separated to form an ultra-fine scale duplex microstructure. Composition modulations were found with a periodicity of less than 10 nm and amvlitude fluctuations from 50 at % Ni to aovroximately 10 at % Ni. Both the compositions and the scale of the' fluctuations are totally consistent with'the observations of Reuter et al.[42] on the decomposed structure in low nickel cloudy taenite.

It is also likely that the high and low Ni regions in the Santa Catharina meteorite show fine scale spinodal decomposition. Diffusion at temperatures below about 780K is too slow for the compositions of the high and low Ni regions to adjust to the changing limits set by the miscibility gap, so with decreasing temperature both the high and low Ni regions would tend to recross the spinodal and undergo fine scale decomposition.

We note that interiors of meteorites are not heated appreciably during passage through the earth's atmosphere.[33] Meteorite surfaces ablate so rapidly that only a thin layer is heated. The inside of the meteorite is at all times well below room temperature and thus the observed microstructures cannot be ascribed to abnormal heating or quenching experienced during descent to earth.[33]

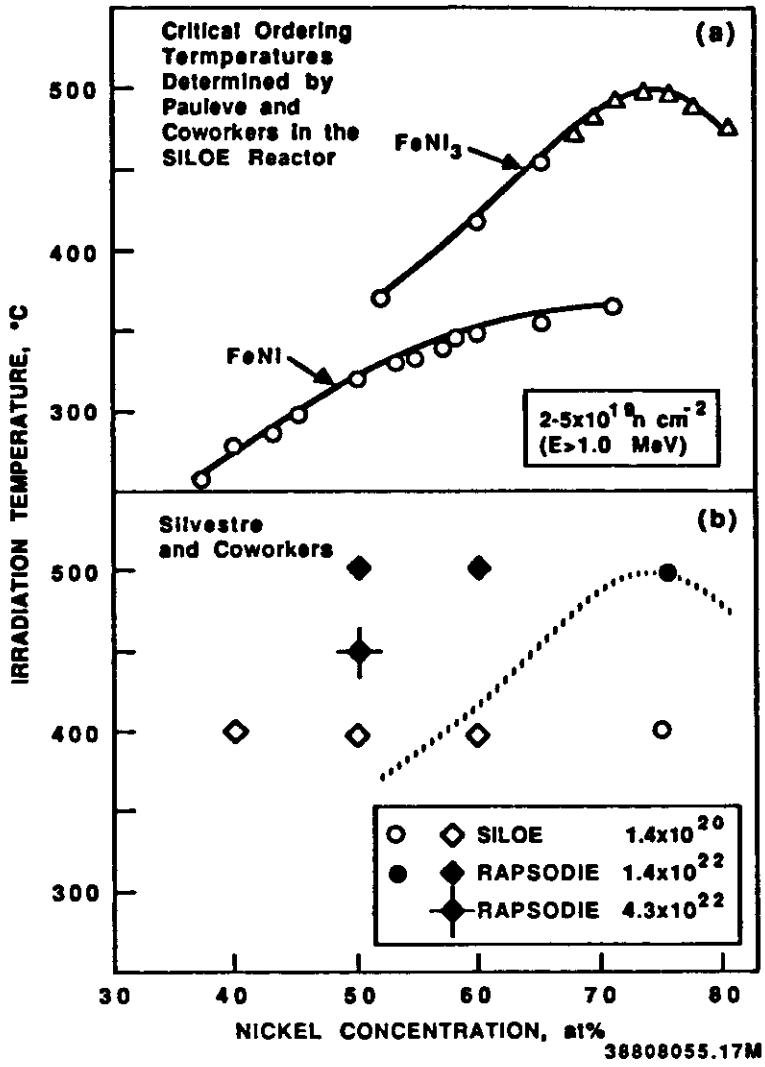

Fig. 19a. Order-disorder transition temperatures observed for FeNi and $FeNi_3$ in Fe-Ni alloys during low fluence neutron irradiations conducted in the SILOE Reactor at the temperatures shown (after Ref. 46).

Fig. 19b. Results of higher fluence irradiations of Fe-Ni alloys conducted in the SILOE and RAPSODIE reactors. Circles denote domains of Fe_3Ni and diamonds denote plate-like Fe_3Ni precipitates formed on Frank Loops (after Ref. 47).

Irradiation Experiments

Irradiation of alloys with energetic electrons, neutrons, or heavy ions produces displacement damage in the form of Frenkel pairs. The self interstitial is usually highly mobile and diffuses rapidly to defect sinks even at very low temperatures. The vacancy is somewhat less mobile, but may migrate at temperatures above about $T_m/4$, which is about 430K for Fe-Ni Invar alloys.

The production and annealing of Frenkel defects may induce a number of important microstructural effects in alloys, including compositional inhomogeneities, amorphization, disordering, and the production of thermally unstable phases.[45] However, to a zero order, the effect of irradiation may be taken as an increase in the diffusion coefficient over the thermal equilibrium value. In this approximation the effect of irradiation is simply to speed the approach to equilibrium while changing neither the approach path nor the final state. Irradiation effects in Invar-type alloys will first be analyzed in terms of enhanced diffusion, but with the realization that other second order effects such as solute segregation or irradiation-induced phase instabilities may be operative. We will address these later.

In the following sections we will be interpreting decomposition of irradiated alloys in terms of spinodal decomposition and coarsening, with irradiation affecting the diffusion coefficient. The dominant wavelength, λ_{max}, in the initial stages of spinodal decomposition is independent of diffusion coefficient[2]

and therefore also independent of atomic displacement rate.[45] The rate at which λ_{max} develops is of course very sensitive to the magnitude of the diffusion coefficient. The dominant wavelength is sharply dependent on $\partial^2 G/\partial C^2$ (Eq. 1) which in turn is a strong function of temperature. Thus the initial stages of spinodal decomposition should depend significantly on temperature but not displacement rate.

The observed wavelength in spinodally decomposed systems frequently-goes not correspond to λ_{max} but to that of a coarsened structure. Coarsening theory (Eq. 2) predicts that r varies with Dt. When the loss of point defects is primarily to fixed sinks rather than to mutual recombination, each defect produces a certain average amount of atomic mixing before being annihilated. The amount of mixing produced at a given displacement level is independent of the displacement rate, providing that all comparisons are made in the sink-dominated regime and that the sink density does not change.

In fact, however, radiation-produced sink densities tend to increase with increasing displacement rate and decreasing temperature, decreasing the mean free path for annihilation and the total amount of mixing. A tenfold change in either temperature or displacement rate will yield only a factor of about two change in the scale of the coarsened structure. Thus the scale of a coarsened microstructure should, at a given displacement level, depend only weakly on changes in temperature and displacement rate.

Published irradiation studies on Fe-Ni-Cr alloys provide valuable insight into both alloy decomposition kinetics and the construction of the equilibrium phase diagram. The irradiation studies separate into two distinct groups: low temperature ($T \leq 725K$), low fluence neutron and electron irradiations and high fluence, high temperature, neutron and heavy ion irradiations conducted at high irradiation fluxes.

High temperature irradiation results may be interpreted in terms of the proposed high temperature miscibility gap. Low temperature decomposition, however, may also be influenced by the low temperature magnetically-induced miscibility gap predicted by Chuang et al.[40] Both miscibility gaps and their associated spinodals represent metastable reactions at low temperatures where the equilibrium reaction is $\gamma \rightarrow a$ t γ' ($FeNi_3$).

Pauleve, et al.[46] used relatively low levels of neutron irradiation to accelerate the formation of the ordered FeNi and $FeNi_3$ phases in Fe-Ni alloys. Figure 19a shows that below 50% Ni only ordered FeNi forms, and only at irradiation temperatures below 600K. It is not clear whether decomposition is occurring according to the high temperature or low temperature miscibility gap. At higher neutron fluences, however, radiation-induced segregation of nickel on Frank interstitial loops (also produced by irradiation) has been observed to contribute to formation of plates of the $FeNi_3$ phase, as shown in Fig. 19b.[47] In this case, $FeNi_3$ forms outside of the miscibility gap defined in Fig. 19b. This occurs as a result of the local nickel concentration at the loop exceeding that necessary for formation of $FeNi_3$. In the absence of radiation, these plates are expected to eventually dissolve upon aging at the irradiation temperature.

Chamberod, et al.[39] and Morita, et al.[48] studied the effects of low fluence 2 MV electron irradiation on the lattice parameter and magnetic properties of Fe-Ni Invar alloys with 25-50 at % Ni. Irradiations were conducted at temperatures between 350K and 675K, to fluences between 4 x 1023 e-/m2 and 3.4 x 10^{24} e-/m^2, thus producing very low levels of displacement. The samples were then annealed for 1 hr. at 1000K. The stated purpose of this anneal was to remove the residual effects of irradiation, presumably point defects and small defect aggregates.

Figures 20 and 21 show the result of two separate studies on the effect of irradiation on the lattice parameter of the alloys. Electron irradiation relaxes the lattice parameter toward a value characteristic of an alloy which has decomposed into Ni-rich and Ni-poor phases. In some irradiations the decomposition is apparently still in progress, especially at the higher irradiation temperatures. The maximum change in lattice parameter is about 0.36% which corresponds to a densification or volume change of approximately 1%.

Figure 21 shows that the lattice parameter of irradiated Fe-35% Ni varies with temperature the same as that of the meteorite (Fig. 17), which was composed of regions of ~25% Ni and ~50% Ni. It thus appears that electron irradiation causes decomposition of the alloy into regions widely separated in composition.

It is remarkable that these low electron fluences produced any decomposition at all, as 10^{24} e-/m^2 will produce only the order of 10^{-2} displacements per atom (dpa).[42] Appreciable irradiation-induced composition changes usually only occur at displacement levels of 1 dpa and above.[45]

We may calculate the scale of any decomposition from the displacement level using simple diffusion theory, i.e. $x \approx \sqrt{Dt}$. Displacement to 10^{-2} dpa, followed by diffusion of the Frenkel defects to sinks the order of 10^{-7} m apart (for a typical dislocation density of 10^{14} m^{-2}) corresponds to $\sqrt{Dt} \approx 10^{-8}$ m, or about 10 nm. The irradiation-induced defects are thus clearly incapable of producing phase decomposition on a coarse scale comparable to that of the meteorite. The irradiation is, however, capable of producing fine scale spinodal decomposition, if it is thermodynamically possible. The lattice parameter changes indicate decomposition with Ni-enriched and Ni-depleted regions, showing that the alloys were irradiated inside the spinodal and that spinodal decomposition indeed occurred. The small change in lattice parameter in some of

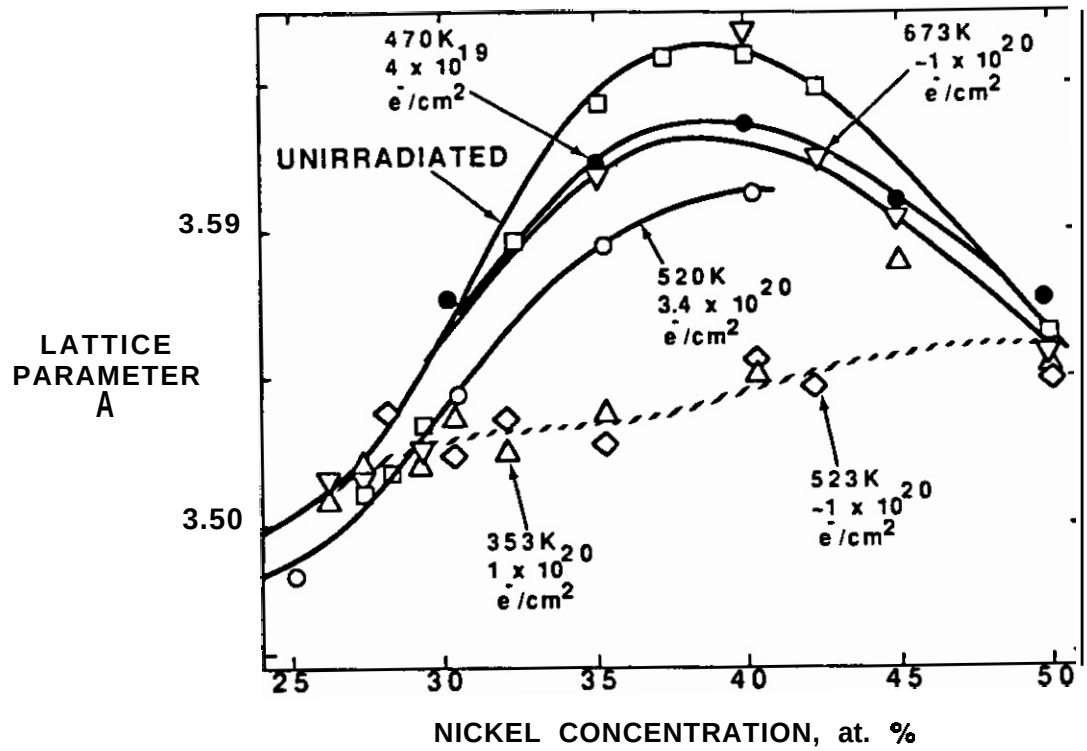

Fig. 20. Lattice parameter of Fe-Ni alloys after 2 MV electron irradiation to various levels. The decrease in lattice parameter indicates decompositon of the solid solution into Ni-rich and Ni-poor regions. (After Morita, et al.[48]).

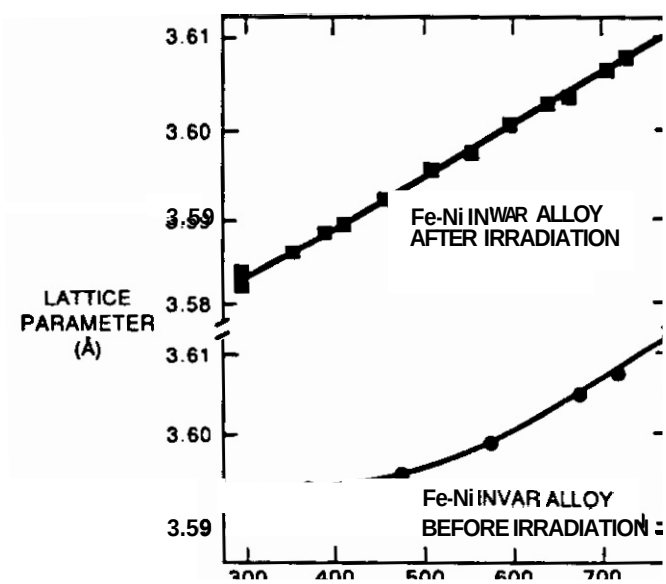

Fig. 21. Lattice parameter of Fe-Ni alloys before and after irradiation at 80°C with 4×10^{19} cm^{-2} 3 MeV electrons. Decomposition of the solid solution during irradiation leads to the loss of Invar properties. Irradiation has the same effect on the lattice parameter as does slow cooling in the meteorite (Fig. 17) (After Scorzelli and Danon[35]).

the higher temperature cases indicates that the alloys are still in the very early stages of spinodal decomposition. We suspect that there is more than one type of phase separation process acting here, including both our proposed miscibility gap and possibly the magnetically induced decomposition predicted by Chuang et al.[40]

The electron irradiation experiments are particularly enlightening because they establish the conditions needed for small to moderate levels of decomposition. While low fluence electron and neutron irradiations of Invar alloys below 673K may cause decomposition only on a very fine scale, recent studies by Garner and co-workers[2-9] have shown that decomposition can occur on a scale comparable to that observed in the Santa Catharina meteorite when the irradiation temperature is much higher and when the displacement level is relatively large (10-50 dpa).

The first hint of large scale decomposition arose from the observation during irradiation *in* liquid metal cooled fast reactors that Fe-Ni-Cr ternary alloys in the Invar regime often densified as much as 1%, as shown in Fig. 22. Note that relatively large displacement levels were required at these higher temperatures to cause densification. These neutron irradiations were conducted at 673-923K and ~10-6 dpa/sec to exposures of ≥10 dpa.[2,3] While the maximum densification was on the same scale as that induced by electron irradiation, the decomposition during high temperature neutron irradiation occurred on a

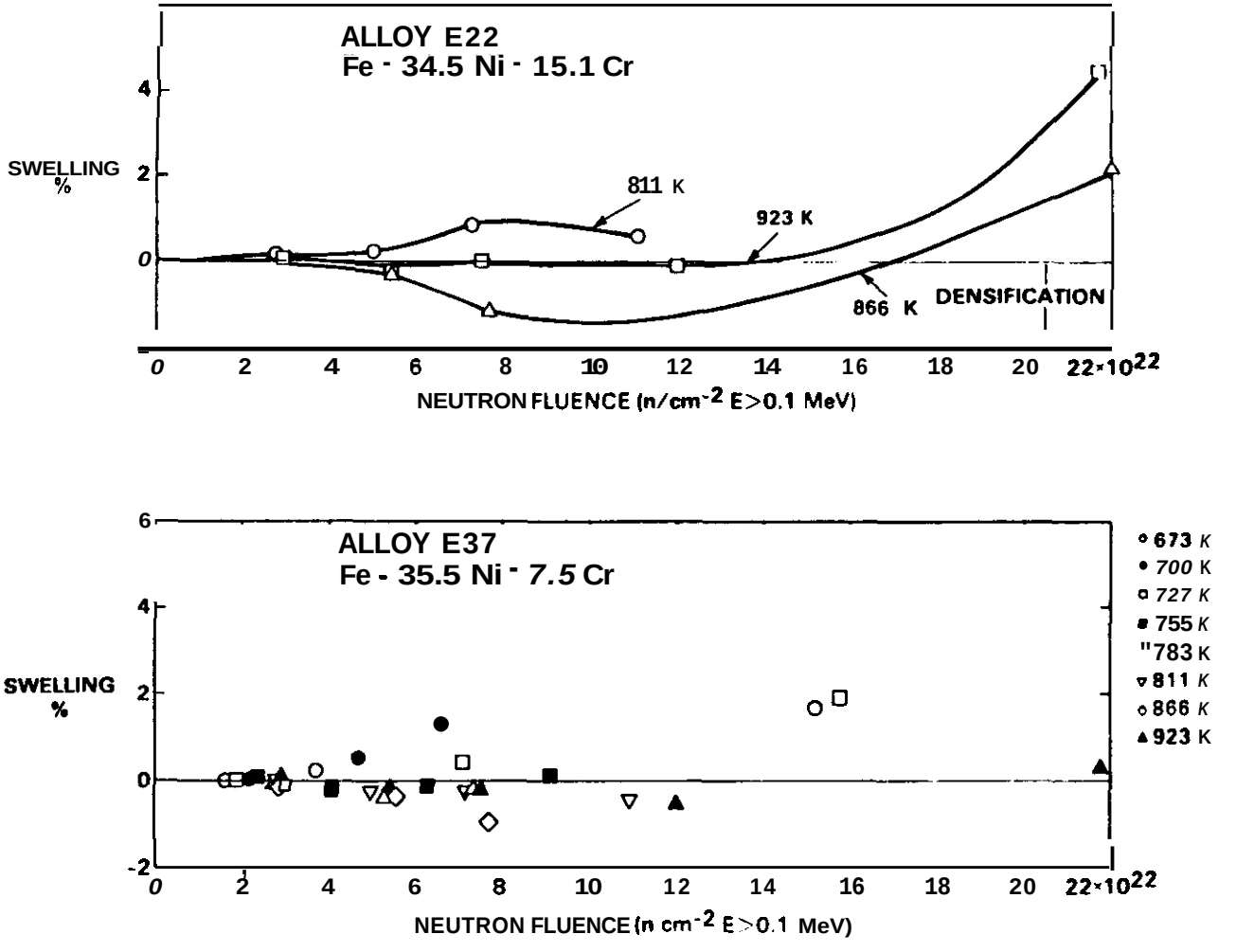

Fig. 22. Swelling and/or densification observed in two Fe-Ni-Cr alloys after irradiation in the EBR-II fast reactor at eight different temperatures. In EBR-II a neutron fluence of 1.0 x 10^{22} n/cm^2 (E > 0.1 MeV) produces approximately 5 dpa in these alloys. The swelling at higher dose levels arises from high densities of small cavities induced by radiation. (After Ref. 3.)

scale of large fractions of microns, with the period of compositional oscillation increasing from ~0.2 μm at 800K to ~1.0 μm at 900K. No phase boundaries or ordered phases were observed to develop but fluctuations in composition appeared to bounded by the stoichiometric limits of Fe_3Ni and FeNi, with chromium substituting for iron. The iron and chromium profiles were found to be mirror images of the nickel profile, with nickel fluctuatins between 25 and 50%, similar to the behavior observed in the meteorite. No correlation between the oscillations and currentlv existing microstructural components could be found at the higher irradiation temperatures. As shown in Fig. 23 and 24 the large scale of these oscillations at 600°C and the absence of phase boundaries requires tedious multiple measurements of composition in order to "image" the oscillations. These measurements are performed in an electron microscope using EDX (energy dispersive X-ray) analysis. It was found that the characteristic period of oscillation appeared to be along <100> directions, as would be expected for spinodal decomposition in Fe-Ni-Cr austenitic alloys.

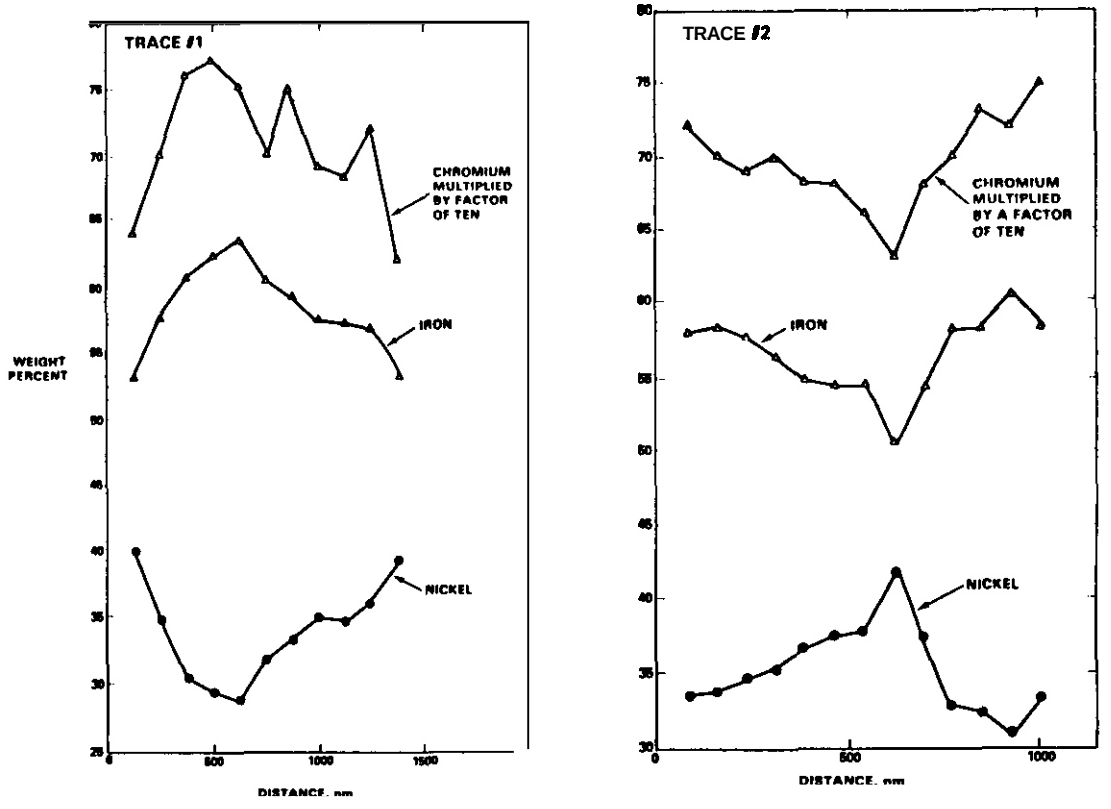

Fig. 23a. Compositional traces in a region ~15 nm thick along a <100> direction in Fe-35.5Ni-7.5 Cr, irradiated at 870K to 38 dpa in EBR-II. (After Ref. 3.)

Fig. 23b. Trace similar to that of Fig. 23a in a region ~100 nm thick. (After Ref. 3.)

At temperatures below 775K the period of oscillation is comparable to or smaller than the thickness of the thin foil and the effective diameter of the volume sampled by the electron beam. Thus, only the average composition of the alloy can be measured at ~725K. However, even at this temperature the oscillations can be sensed as a result of the spinodal-like hardening that occurs at smaller wavelengths.[4] Inpost-irradiation tensile tests it was possible to distinguish between irradiation-induced hardening contributions associated with discrete microstructural components (voids, Frank loops and dislocations) and that associated with the decomposition." As shown in Fig. 25 the spinodal-like component was essentially zero in Fe-15Cr-25Ni but grew progressively larger for the Fe-15Cr-35Ni and Fe-15Cr-45Ni. In the latter alloy the spinodal-like hardening component was larger than that associated with discrete microstructural features. At 35% Ni, the hardening was studied at 7.5 and 22% Cr as well as at the 15% level. The hardening was found to be independent of chromium level. In general, throughout the various studies described here, the level or even the absence of chromium was not found to affect any aspect of the decomposition process.

At intermediate temperatures (~800K) an alternate method of imaging the compositional oscillations was developed which involved adjustment of the polishing conditions so as to favor selective removal of the low nickel microvolumes.[3] On the surface of relatively thick foils this leads to an uneven and periodically undulating topography. Thinner foils develop small tunnel-like perforations designated as "worm-holes," a

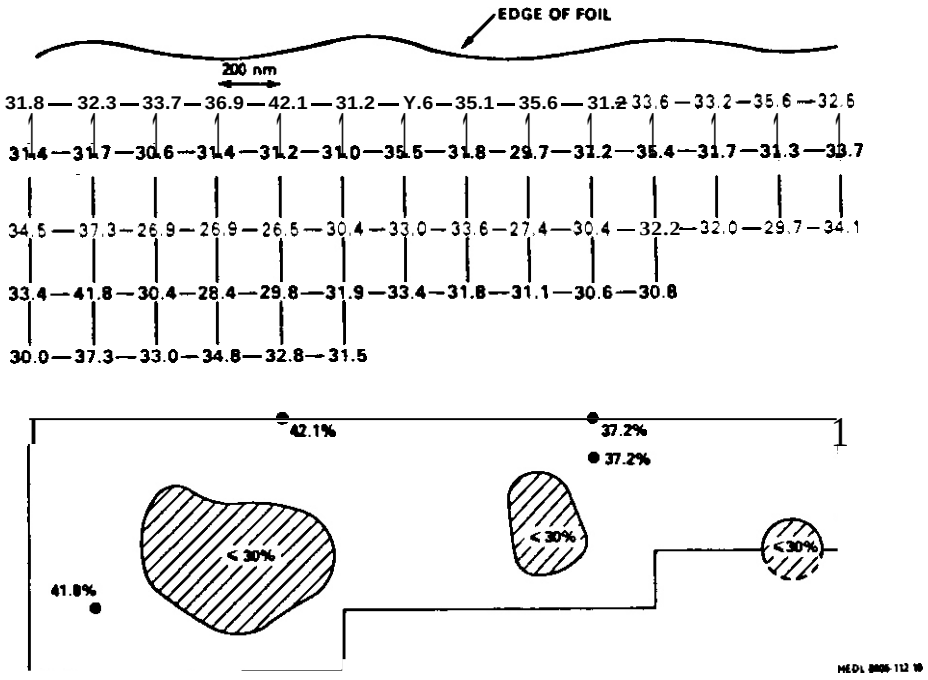

Fig. 24. Above: two-dimensional compositional map of Fe-35.5Ni-7.5Cr irradiated at 870K to 38 dpa in *EBR* II. Measurements are along <100> directions using a 200 nm sampling interval. Below: major features derived from the detailed map shown above. (After Ref. 3.)

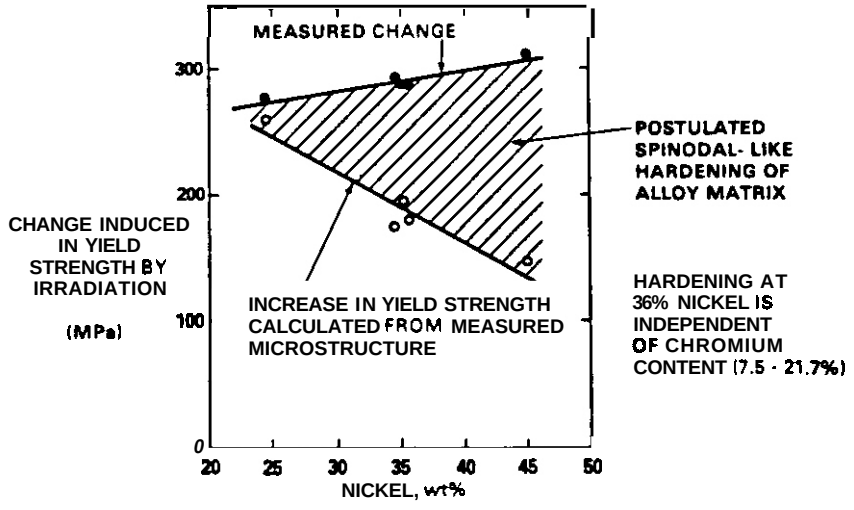

Fig. 25. Comparison of measured yield strength changes and microstructurally-based predictions in five Fe-Ni-Cr alloys after irradiation at 725K to 12.5 dpa in EBR-II. (After Ref. 4.)

phenomenon which is particularly pronounced in binary Fe-Ni alloys. The absence of chromium appears to accelerate electropolishing and thereby to accentuate the worm-holing process. Figure 26 shows a near-edge region of an Fe-35Ni foil irradiated in the Fast Flux Test Facility (FFTF) at ~3 x 10^{-6} dpa/sec to 14 dpa at BOOK. When viewed at lower magnification (Fig. 27) the crystallographic and periodic nature of the perforations is quite obvious, particularly when comparing three adjacent grains. The mean spacing of these perforations was on the order of 200-250 nm. The square array of perforations exists along <110> directions, a consequence of tunneling between low-nickel microvolumes when the major oscillation period lies along <100> directions. Reference (3) presents other polishing artifacts developed in the EBR-II reactor at comparable temperatures and slightly lower displacement rates (1 x 10^{-6} dpa/sec).

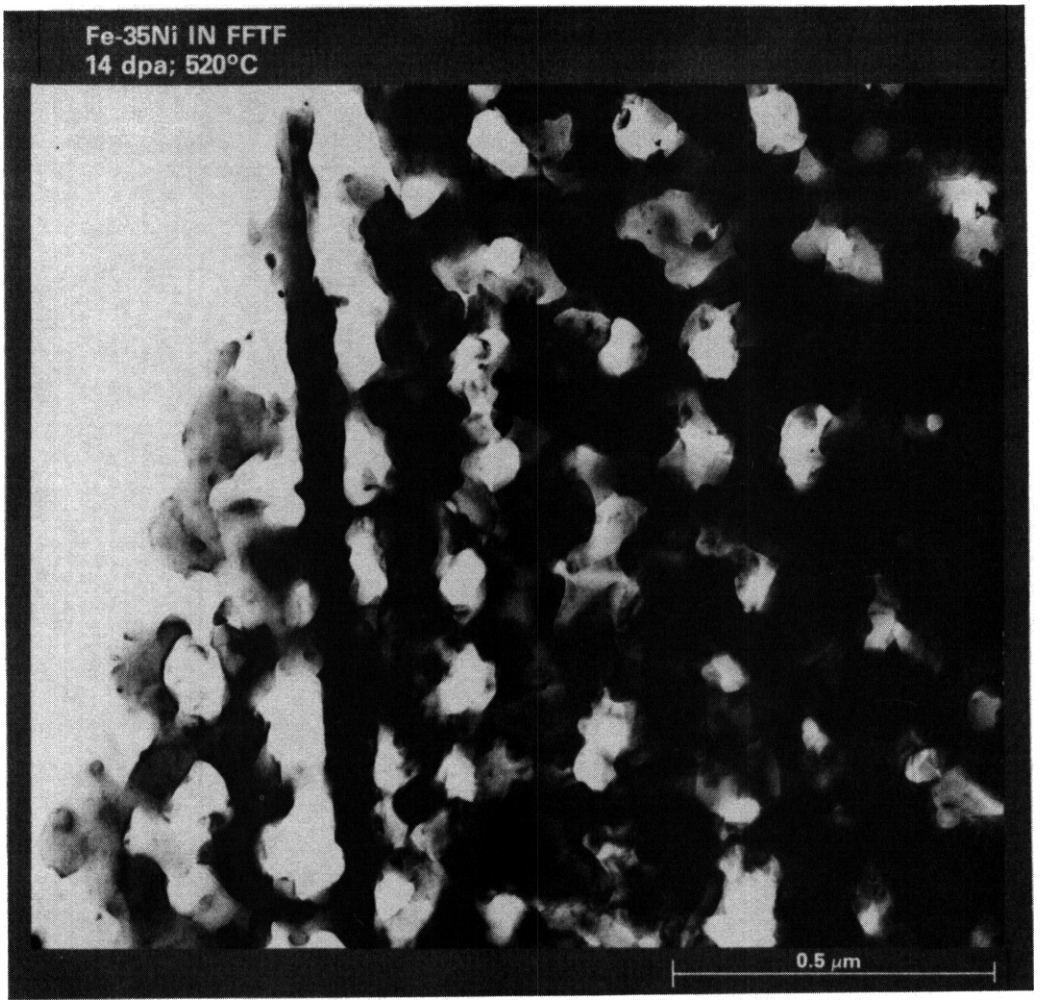

Fig. 26. Preferential attack of low nickel microvolumes in Fe-35 Ni (14 dpa at 800K in FFTF) after electropolishing at room temperature. The electrolyte has tunneled through the foil in many places, leaving features designated as "worm-holes." The linear feature on the left is a nickel-rich zone containing and generated by a grain boundary. (After Ref. 3.)

The neutron irradiation of these alloys was part of a test program designed to understand the compositional dependence of the often very large volume changes that arise due to radiation-induced void formation.[6,7] As a result of these studies it was postulated that the unusual dependence of swelling on nickel content arose from the competition of two processes, one of which is the tendency of Fe-Cr-Ni alloys in the Invar regime to decompose on a rather large scale at higher irradiation temperatures. In an effort to validate this hypothesis another series of EDX measurements were conducted on Fe-Ni and Fe-Ni-Cr alloys that had been lrradiated with 5 MeV Ni^+ ions at temperatures of 898, 948 and 998K at the very high displacement rate of 2 x 10^{-2} dpa/sec. These alloys exhibited the same dependence of void swelling on nickel content and were found to have developed compositional oscillations at all three irradiation temperatures.[8,9] Once again the period of oscillation increased with temperature and appeared to be unrelated to the level or presence of chromium. Figure 28 shows the results of Ni^+ ion irradiation of Fe-35% Ni to 117 dpa at 898K. When these results are compared with those of the neutron irradiations, it appears that the four order of magnitude increase in displacement rate associated with ion bombardment had very little influence on the magnitude of the oscillation period. The significance of this lack of influence will be discussed presently.

Figure 29 shows some examples of Ni^+ ion-irradiation induced oscillations. There appears to be irregular structure in the compositional profiles superimposed on the somewhat regular major oscillations. While this irregularity was observed in foils of other compositions, a fortuitous circumstance arose which in Fe-35Ni allowed a visualization of the reason for the irregularity. Figure 30 shows that relatively irregular martensite regions have formed in a cellular fashion upon cessation ofthe irradiation and cooling to room temperature. There is a large amount of internal strain in these regions, showing extensive

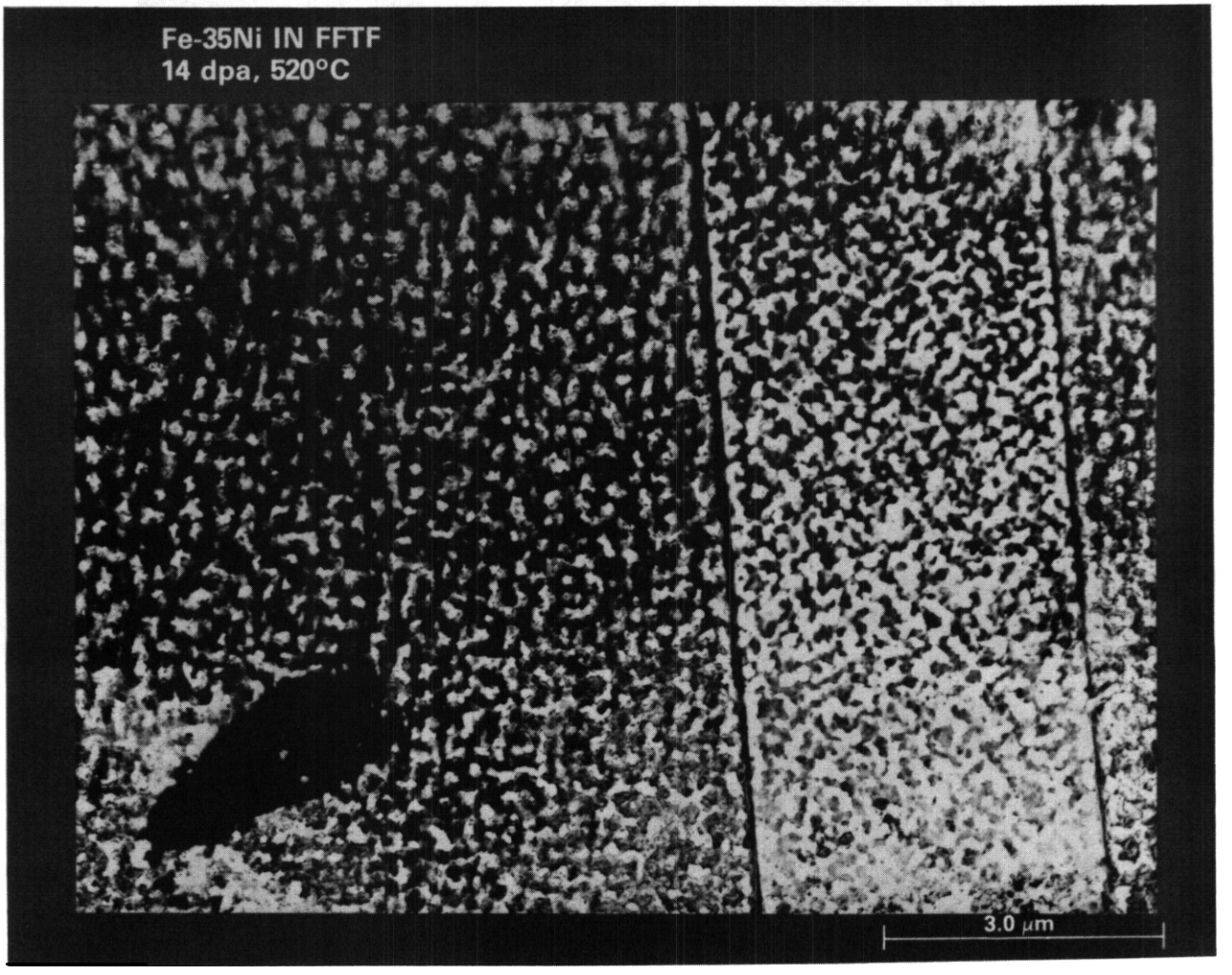

Fig. 21. Lower magnification micrograph of the specimen shown in Fig. 25. Three grains are visible, separated by grain boundaries which are enriched in nickel and thus resist electropolishing. Note the tendency toward a crystallograhic orientation of the etched out microvolumes, which lie along <110> directions. (After Ref. 3.)

twinning when the martensite is in the strongly diffracting condition and dislocation tangles when the martensite is not so strongly diffracting (lower left grain in Fig. 30).

Examination of a large number of martensitic regions showed that martensite formed in regions where the composition was in the range of 25-29% nickel. The sizes of these regions range from 100-250 nm and the foil thickness ranges from 100-150 nm. Figure 30 also demonstrates in another way the effect of composition on the martensitic transformation. The grain boundary that traverses this micrograph has been subjected to considerable radiation-induced segregation of nickel. This leads to a zone on each side of the boundary which is free of martensite. Figure 31 shows that decomposition of the Fe-35%Ni alloy produces low-Ni regions which are stable at the irradiation temperature but transform to martensite on cooling to room temperature.

Very recently Wiedenmann, Wagner and Wollenberger[49] used isotopic enrichment of Ni^{62} to produce Fe-34 a/o Ni samples in which decomposition could be studied by small angle neutron scattering. Samples which were proton irradiated to 0.5 dpa at 898K were found to have much greater scattering intensity than did non-irradiated samples quenched from 1273K. The excess intensity was due in equal parts to nuclear and magnetic contributions. The dependence of scattered intensity on scattering vector indicated concentration and magnetization fluctuations greater than 220 nm in extension. The fluctuation maxima reached over 36.5 ± 1.5 a/o Ni and the minima reached 28.5 ± 1.5 a/o Ni.

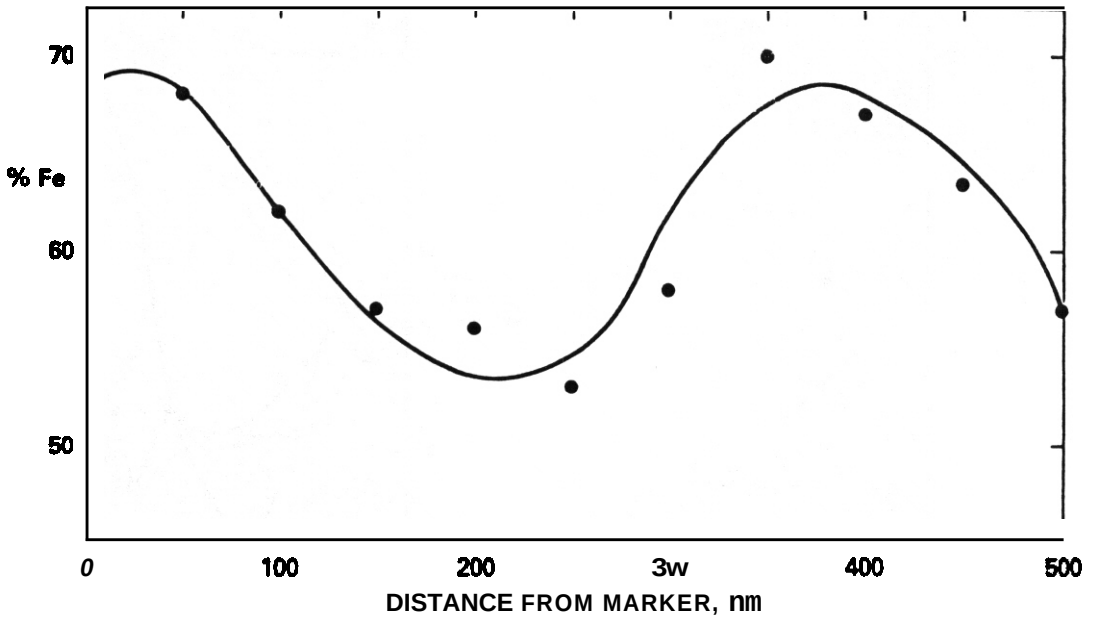

Fig. 28. Variation of composition with position in a foil of Fe-35% Ni irradiation to 117 dpa at 898K with 5 MeV Ni^+ ions (After Ref. 9).

These results clearly show decomposition of the alloy, apparently by spinodal decomposition. The transformation is in a fairly early stage as the composition extrema are much less pronounced then those observed in samples which were irradiated with neutrons or Ni^+ ions to much higher displacement levels.* Curiously, the wavelengths are comparable.

Decomposition was also observed in Fe-34Ni by Wiedenmann et al. after purely thermal anneals at 898K for 480 hr. The amount of decomposition was far less than in the irradiated alloys. The excess scattering intensity increased only slightly, which indicates that the thermally-induced decomposition reaction was in an even earlier stage. The fluctuation wavelength was about 50 nm, however, which is large for the initial stages of spinodal decomposition. We calculate that $\sqrt{Dt} \approx 40$ nm at 898K, which is very close to the decomposition wavelength. Thus, 480 hr was adequate only for the initial stages of decomposition to occur.

Williams et al.[50] studied the response at 673-918K to fast reactor irradiation of Fe-12Cr-15Ni (wt%) steel with silicon levels ranging from 0.14 to 1.42 wt%. At the higher silicon levels the alloy tended to decompose into α and γ phases, with the latter often exhibiting compositional oscillations where Ni and Si behaved as one species and Fe and Cr behaved as another. The wavelength of the oscillation increased from ~0.1 μm at 743K to 0.8 μm at 923K. At higher temperatures the oscillations could not be associated with currently existing microstructural sinks for point defects. No decomposition was observed in thermally aged specimens at any silicon level. Williams et al.[50] concluded that there was a radiation-induced process that tended to produce oscillations and that this process was considerably enhanced by the presence of silicon. The absence of such oscillations in comnercial austenitic steels was attributed possibly to the presence of molybdenum which was postulated to retard the segregation mechanism. Brager and Garner[51] had earlier investigated Fe-17Cr-12Ni-2.3Mo steels with 0.01 to 1.96 wt% silicon and had not found such oscillations.

It is not clear whether the oscillations observed in the Invar alloys and those of Williams et al. are produced by similar or different mechanisms. The nickel levels of the two groups of alloys are quite different and silicon obviously plays a strong role in Williams' alloys. Given the limited resolution of standard EDX techniques, we are not certain that Williams et al. can confidently state that decomposition did not occur thermally in his alloys, however.

---

* Protons and electrons are, however, known to produce a higher fraction of atomic displacements which survive recombination than do neutrons and self ions.[52-54]. In fact, 0.5 dpa by protons and 5 dpa by fast reactor neutrons would produce about the same number of the freely migrating defects which cause enhanced diffusion.

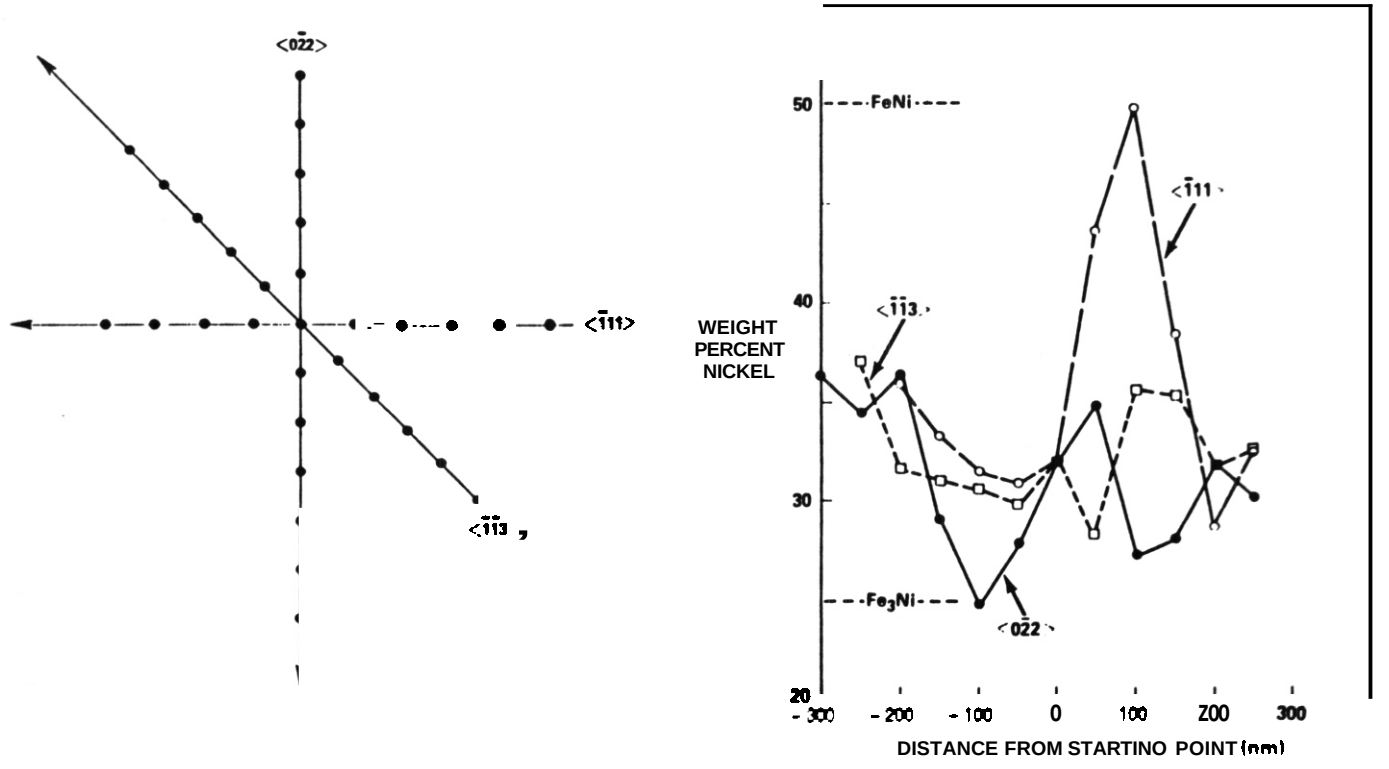

A

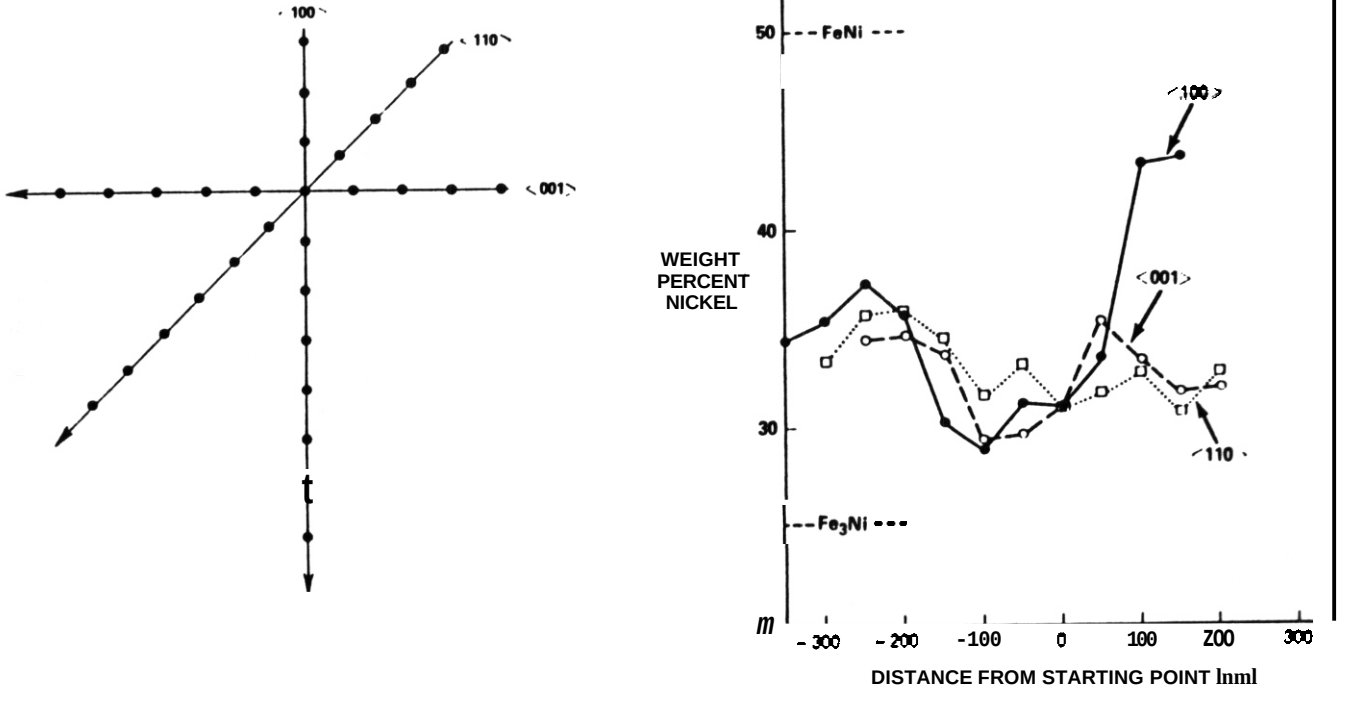

B

Fig. *29.* Compositional traces along defined crystallographic directions in two separate areas of Fe-35Ni irradiated to 117 dpa at 898K with 5 MeV Ni^+ lons. (After Ref. *9.)*

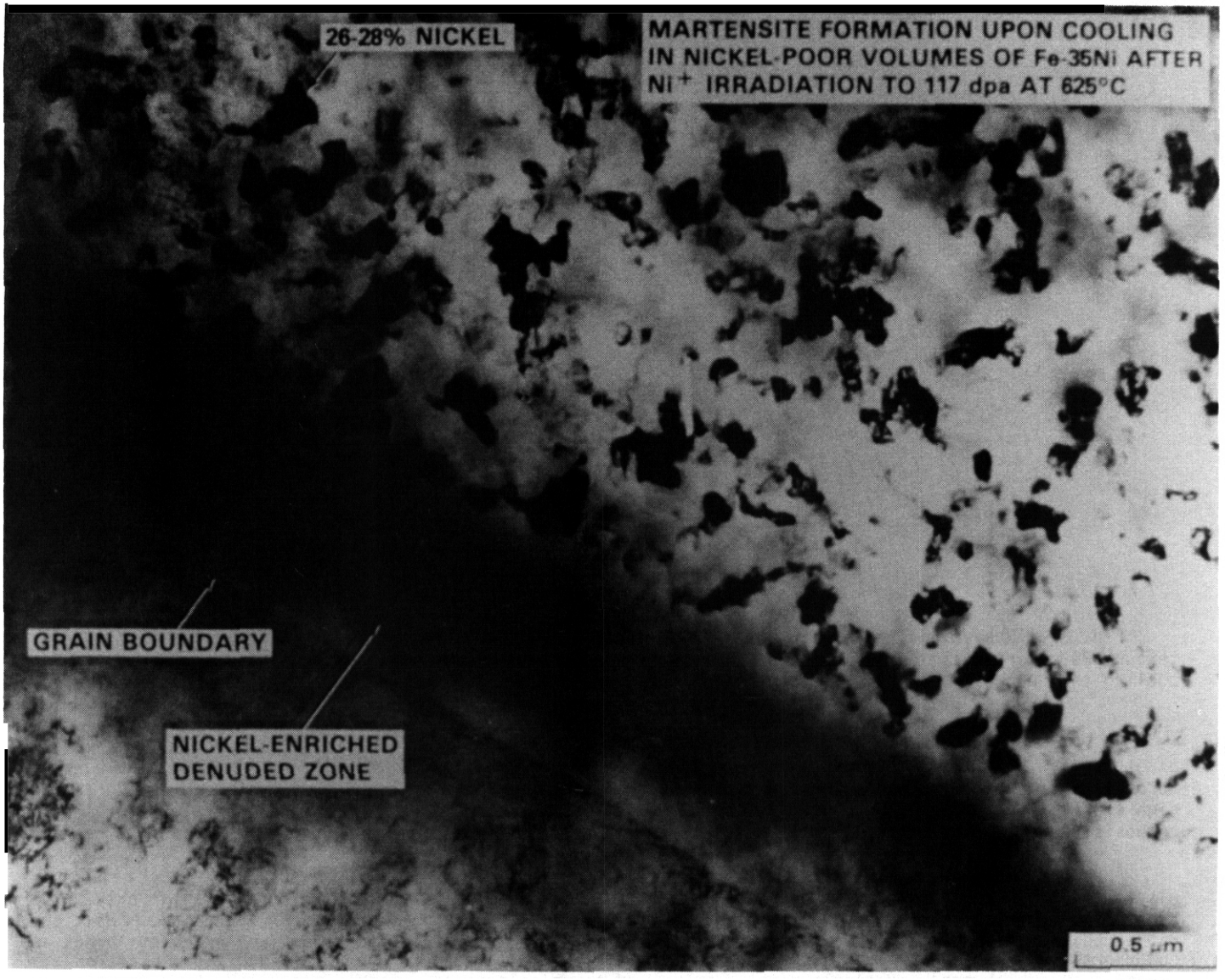

Fig. 30. Micrograph showing formation of cellular martensite in Fe-35 Ni after irradiation at 898K. Note denuding of martensite along a grain boundary where nickel segregates to levels >45%. The martensite is out of focus in the lower left grain. (After Ref. 9.)

Other Possible Irradiation Effects on Phase Transformations

We have thus far interpreted the effects of irradiation on alloy decomposition solely in terms of an enhanced diffusion coefficient. We now consider the possibility that irradiation may affect alloy decomposition in other nays. It is important to recall that we deduce alloy decomposition to occur primarily by spinodal decomposition or homogeneous nucleation and growth and that either process occurs so as to maintain lattice coherency. Volume changes, while significant, are not large - at most a few percent. Further, we are dealing with concentrated solid solutions.

Maydet and Russell[55] considered the effect of irradiation-induced defects on formation of incoherent precipitates having a large volumetric mismatch with the matrix. Their treatment is clearly irrelevant to the present case.

Martin,[56] Cauvin and Martin[57,58] found that a bias in point defect recombination at a coherent particle:matrix interface could induce homogeneous nucleation or spinodal decomposition during irradiation

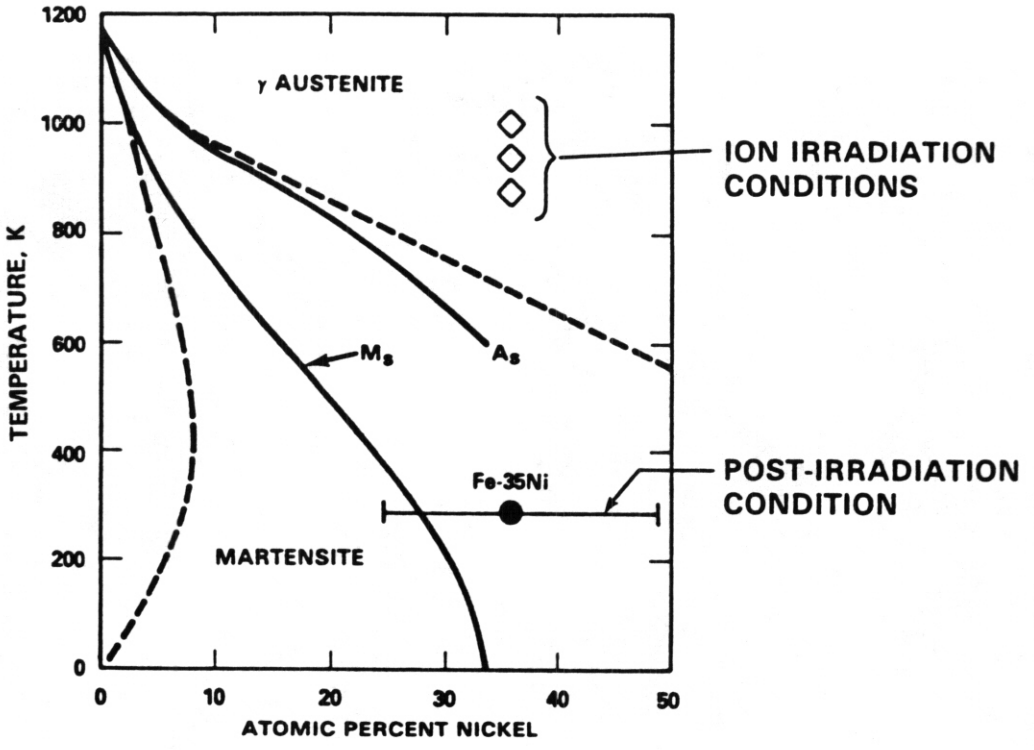

Fig. 31. Heavy ion irradiation conditions for Fe-35 Ni alloy under conditions described in Figs. 27 through 29. Martensite formed in Ni-poor regions generated at the irradiation temperature which during cooling fall below M_s.

of otherwise thermally stable alloys. This theory was formulated mostly for dilute solutions. However, Abromeit and Martin[59] predicted that a similar mechanism may operate in concentrated alloys. The predicted high sensitivity of the enhancement of decomposition to temperature, atomic displacement rate, and alloy composition are inconsistent with the results we have presented in this paper.

Abromeit, Naundorf and Wollenberger[60] considered the possibility that the disrupting effects of displacement cascades could cause precipitate particles to disappear. As in earlier analyses[45] extremely high displacement rates are needed to obtain an observable effect, which would be to hinder decomposition rather than to enhance it. However, heavy ion irradiation results at high displacement rates by Garner and coworkers[8] are consistent with the neutron results at lower displacement rates. In addition, electron irradiation, which produces single displacements and not displacement cascades also leads to decomposition. Thus, cascade effects appear not to be a major factor in decomposition of irradiated Invar-type alloys.

In any event, displacement cascades would tend to destroy small wavelength fluctuations in composition. The decomposition observed by Garner and coworkers thus occurs in spite of any cascade disruption, rather than as a result of it.

Krishan and Abromeit published a series of papers[61-63] on the effects of irradiation on alloy decomposition. These papers were largely concerned with the direct recombination regime, where very few point defects are lost to dislocations, grain boundaries and other fixed sinks. In the absence of sink-related recombination Krishan and Abromeit found significant effects of irradiation on alloy decomposition, especially at short wavelengths. Since all the irradiation experiments we have reported involve significant sink strengths, the Krishan and Abromeit calculations are not thought to be applicable.

Abromeit and Martin[64] recently extended the Krishan and Abromeit analysis to the fixed sink regime and found that compositional instabilities might form as a result of composition-dependent formation and migration energies. Comparison of these predictions with experimental results on irradiated alloys cannot at present be made because of a lack of knowledge of these dependencies on composition. However, the relative insensitivity of alloy decomposition to displacement rate (at constant displacement level) indicates that destabilization by this mechanism is probably not operative.

Murphy[65] considered the effect on decomposition kinetics of preferential interstitial exchange with one alloy component. Both her analytical results for the zero sink limit, and her numerical calculations for the more general case of defect migration to sinks showed that irradiation could in some cases produce alloy

decomposition in otherwise thermodynamically stable alloys. Significant effects in thermally stable alloys were predicted only for the case of conditions just outside the spinodal and when the interstitial was about ten times more likely to exchange with one alloy component than the other. It is possible that Murphy's postulated mechanism might be invoked to either initiate decomposition just outside the spinodal or assist decomposition just inside the spinodal.

During irradiation there is one mechanism which could easily lead to separation of nickel from chromium and iron and thus might play a role in producing phase decomposition. This is the inverse Kirkendall effect in which the slower diffusing elements segregate by default at the bottom of the often very steep vacancy gradients that develop in the vicinity of naturally occurring or radiation-produced sinks for point defects.[66,67] Free surfaces[68] and stationary grain boundaries[69] (see Figs. 26, 27 and 30) are particularly effective at segregating nickel at the expense of chromium and iron and to a lesser extent so are radiation-produced voids and Frank interstitial loops.[70,71] It has been proposed that interstitial binding with the slightly undersize nickel atoms would lead to segregation,[66,72] but Marwick and coworkers have shown that all facets of observed segregation in Fe-Cr-Ni ternary alloys can be explained in terms of the inverse-Kirkendall effect.[69] Reference (7) contains a compilation of data showing that the diffusivity of nickel is less than that of iron which in turn is less than that of chromium.

Irradiation induced Ni segregation to closely spaced defect sinks may well play a significant role in initiating the transformation. The lack of correlation of the compositional fluctuations with currently existing microstructural components in neutron-irradiated specimens,[2,3,8] however, shows clearly that radiation-produced sinks themselves are *not* necessary for the continued maintenance of high nickel microvolumes. While voids and Frank loops are both sessile, the latter are known to concentrate nickel until they unfault, transform into prismatic dislocations and glide away. Under these conditions the remaining high nickel volumes would quickly disperse. Obviously, the presence of such sinks mustclearly that radiation-produced sinks themselves are not necessary for the continued maintenance of high affect the kinetics at which the segregation proceeds. The contribution of irradiation-induced segregation to help initiate the decomposition will be strongest at lower temperatures (< 825K) where radiation-induced loop densities are the highest.

However, the obvious crystalline regularity of the neutron-induced sub-lattice does not mirror the relatively random distribution of voids and Frank loops produced by radiation. The large scale of the decomposition observed in the ion bombardment experiments in the range 900-1000K is also not reflected in the scale of the radiation-produced microstructure.

We are thus convinced that the primary effect of irradiation on the decomposition of solute-free Fe-Ni and Fe-Ni-Cr Invar-type alloys is through an enhanced diffusion coefficient. Other irradiation effects are of secondary importance, at most, with radiation-induced segregation of nickel at microstructural sinks playing the most plausible secondary role. However, results from a large number of studies cited previously in this overview demonstrate that decomposition occurs in Invar alloys even in the absence of radiation.

Silicon is known to bind strongly to self interstitials and to change the jump frequency of adjacent vacancies.[73,74] Accordingly, compositional oscillations found in the high silicon, low nickel alloys studied by Williams et al.[50] may well be the result of one of the processes proposed by Murphy.[65] Second order processes involving radiation-induced segregation *to* sinks may also be involved.

Proposed Fe-Ni Phase Diagram

Based on the foregoing we propose that the Fe-Ni equilibrium diagram should be reconstructed as shown in Fig. 32. The phase diagram is based on that of Kubaschewski (Fig. 4). We have accepted a 35% Ni, 1100K peak for the coherent miscibility gap and have taken composition limits of 25% Ni and 50% Ni at 825K. These limits are indicated by large amounts of thermal and irradiation data. The phase diagram then shows a ($\gamma_1 \rightarrow \alpha$ t γ_2) monotectoid reaction at about 825K and 25% Ni and a ($\gamma_2 \rightarrow \alpha$ t γ') eutectoid reaction at about 55% Ni and 700K, although there is a considerably uncertainty in the specification of these temperatures and compositions. The magnetically-induced phase separation proposed by Chuang et al.[39] then becomes only a metastable reaction. The proposed ordering reactions, $\gamma \rightarrow Fe_3Ni$ and $\gamma \rightarrow$ FeNi are buried deep in the α t γ' region.

While the authors have considered evidence for both higher and low temperature decomposition, they are considerably more confident concerning the former observations. The situation below ~700K is obviously much more complex and involve metastable phenomena not incorporated in our treatment. Low temperature phase boundaries in the Fe-Ni system are best determined from careful studies of meteorite microstructures, such as those of Reuter, et al.[42,43] and Miller and Russell.[44]

Summary and Conclusions

Many experimental results under a wide variety of conditions indicate that a high temperature coherent miscibility gap exists in the Fe-Ni system centered at about 35 a/o Ni and 1100K. We now summarize these results and consider alternative interpretations.

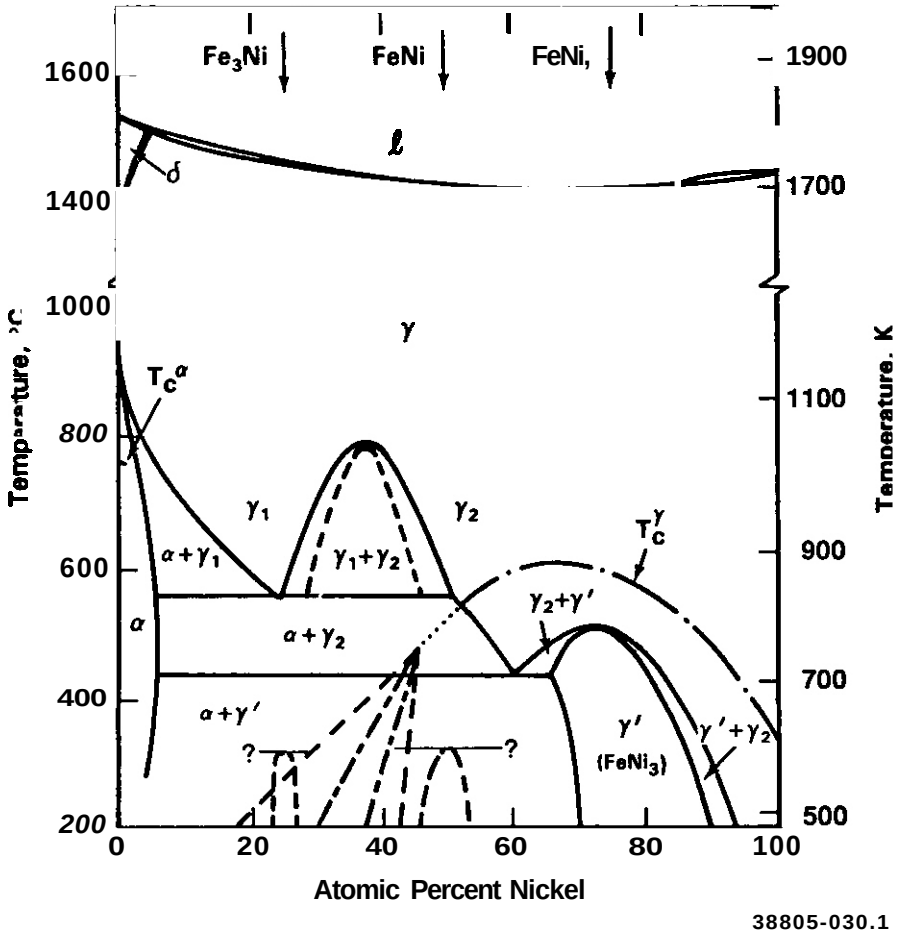

Fig. 32. Proposed Fe-Ni phase diagram produced by incorporating a high temperature $\gamma \rightarrow \gamma_1 + \gamma_2$ coherent miscibility gap into the phase diagram of Kubaschewski shown in Fig. 4.

The heat treatment of commercial Fe-35%Ni Invar alloy at 1100K to get a minimum thermal expansion coefficient is interpreted by us as giving fine scale spinodal decomposition. The Curie temperature in Invar alloys is stress dependent and the 1100K heat treatment would also have relieved internal stresses. However, slow cooling from 1100K removed the effect of the heat treatment, while certainly not inducing new stresses. The decomposition argument thus seems correct.

The anomalous dependence of magnetization of Invar on temperature was interpreted by others as being due to very fine scale decomposition of the alloy into regions of high and low nickel contents. However, magnetic measurements indicated heterogeneities in 20% Ni alloys. Most other experiments indicated that higher temperature phase separation occurred only at ≥25% Ni. The reason for this inconsistency is not known. The maximum in lattice parameter at room temperature found at about 35-40 a/o Ni and the broadening of X-ray peaks were also interpreted as due to decomposition into high and low nickel regions. The high residual resistivity of Fe-30% Ni at 4.2K was interpreted as being due to electron scattering at interfaces between domains of differing composition. It was noted by several authors that magnetic inhomogeneities could also have caused the high residual resistivity. Resistivity measurements at elevated temperatures also indicated the existence of a miscibility gap.

The single crystal elastic constant $C_L = (C_{11}+C_{12}+C_{44})/2$ exhibits anomalous behavior above T_C. It increases with increasing temperature, even above T_C and is smaller when the alloy is magnetically saturated than in the zero field condition. This behavior was attributed to the presence of small, coherent ordered precipitates.

An anomalous hump in the plot of thermoelectric power vs. composition in the Invar range at temperatures below 1273K was interpreted as being due to partial decomposition of the alloy.

Several measurements of the enthalpy and free energy of mixing of Fe-Ni alloys gave clear evidence of anomalies which would lead to a high temperature miscibility gap. Other measurements supported a miscibility gap less strongly. Kubaschewski et al.[27] considered the enthalpy anomaly to be genuine.

The more reliable of the measurements of the interdiffusion coefficient in Fe-Ni alloys are those involving small compositional increments; these show a pronounced minimum in $\tilde{D}$ at 1123K and about 30% Ni, which indicates that Fe-30Ni at this temperature is just above a coherent spinodal.

The compositional variations and scale of the microstructure observed in the Fe-35% Ni Santa Catharina meteorite are entirely consistent with fine scale spinodal decomposition followed by coarsening at about 1000K. It is conceivable that the 10 μm scale microstructure occurred directly by nucleation and growth or spinodal decomposition at some temperature between 780K and 1000K. However, the virtual absence of dislocations and grain boundaries in the slowly cooling parent body preclude heterogeneous nucleation on the observed scale, and low thermodynamic driving forces serve to eliminate homogeneous nucleation as a possibility. Spinodal decomposition would not occur with a 10 μm wavelength. Furthermore, the compositions of the several phases observed in the meteorite microstructure are not consistent with standard phase diagrams.

The fine-scale compositional oscillations observed in cloudy taenite in several meteorites are consistent with low temperature spinodal decomposition. Low fluence electron or neutron irradiation at 350-675K and high fluence, high flux neutron and heavy ion irradiation at 725-1000K all led to one form or another of decomposition of the Invar alloy, consistent with the high temperature miscibility gap proposed in this paper. At low temperatures magnetic contributions to the free energy proposed by Chuang et al. may also have played a role. It is also possible that the various kinds of decomposition observed were irradiation-induced and would not have occurred thermally, although the results of many thermal studies indicate otherwise. However, a careful examination of the various mechanisms proposed for irradiation-induced phase transformations leads us to the conclusion that irradiation affects decomposition of Fe-Ni and Fe-Ni-Cr Invar alloys mainly through an enhanced diffusion coefficient. Other effects of irradiation are considered to be secondary in importance and may only affect the rate of decomposition arising from the spinodal.

The totality of the evidence leads in a straightforward way to the following conclusions:

There is a coherent miscibility gap in the Fe-Ni system with the peak in the vicinity of 1100K and 35% Ni. The presence of the gap is indicated by anomalies in enthalpy and free energy of mixing and interdiffusion coefficient.

This gap is narrow at high temperatures, which prevents nucleation of a second phase and limits spinodal decomposition to low amplitude compositional fluctuations.

Spinodal decomposition to various degrees causes Fe-Ni Invar-type alloys to have anomalies in magnetization, lattice parameter, thermal-expansion coefficient, residual and high temperature resistivity, single crystal elastic constants and thermoelectric potential.

The microstructure of the Fe-35% Ni Santa Catharina meteorite is the result of high temperature spinodal decomposition followed by coarsening at about 1000K. Additional substructure imposed on that produced by the high temperature spinodal develops as the result of low temperature processes.

The fine-scale microstructure in the cloudy taenite plates in several meteorites is consistent with low temperature spinodal decomposition.

Irradiation with electrons, protons, heavy ions and neutrons over a wide range of temperatures, compositions, displacement rates, and displacement levels induces decomposition in Fe-Ni and Fe-Ni-Cr Invar alloys primarily through irradiation-enhanced diffusion. The large compositional wavelengths found in neutron and heavy-ion irradiated Invar alloys at temperatures above 675K are due to spinodal decomposition followed by substantial coarsening.

ACKNOWLEDGMENTS

K. C. Russell is pleased to acknowledge a Northwest College and Universities Association for Science (NORCUS) faculty appointment which supported his participation in this research. F. A. Garner's participation was sponsored by the Office of Fusion Energy, U.S. Department of Energy. We are grateful to Prof. R. Ogilvie for helpful discussions on the origins and physical metallurgy of metallic meteorites. We wish to thank Prof.-Dr. H. Wollenberger and coworkers, and Drs. Miller and Russell for permission to cite their results prior to publication.

REFERENCES

1. Hansen, M. (1958), "Constitution of Binary Alloys," McGraw Hill, New York.

2. H. R. Brager and F. A. Garner, in Effects of Radiation on Materials: Twelfth International Symposium, ASTM STP 870, F.A. Garner and J.S. Perrin, Eds., American Society for Testing and Materials, Philadelphia, p.139, 1985.

3. F. A. Garner, H. R. Brager and J. M. McCarthy, in Radiation-Induced Changes in Microstructure, 13th International Symposium (Part 1), ASTM STP 955, F. A. Garner, N. H. Packan and A. S. Kumar, Eds., American Society for Testing and Materials, Philadelphia, p.775, 1987.

4. H. R. Brager, F. A. Garner and M. L. Hamilton, J. Nucl. Mater., 133 & 134, p.594, 1985.

5. F. A. Garner, H. R. Brager, M. L. Hamilton, R. A. Dodd and D. L. Porter, Rad. Eff., 101, 37, 1987.

6. F. A. Garner and H. R. Brager, in ref.3, p. 187.

7. F. A. Garner and A. S. Kumar, in ref.2, p.289.

8. F. A. Garner, H. R. Brager, R.A. Dodd and T. Lauritzen (1986). Nucl. Instr. Meth. Phy. Res., B 16, p. 244.

9. R. A. Oodd, F. A. Garner, J-J. Kai, T. Lauritzen and W.G. Johnston, in ref.3, p.788.

10. Morita, H., H. Hiroyoshi, H. Fujimori, and Y. Nakagawa, J. Mag. & Mag. Mats., 15-18, 1197, 1980.

11. Kachi, S. and H. Asano, J. Phys. Soc. Japan, 27, 536, 1969.

12. Nakamura, Y., IEEE Trans. on Magnetics, 12, 278, 1976.

13. Asano, H., J. Phys. Soc. Japan, 27, 542, 1969.

14. Crangle, G. and G. C. Hallam, Proc. Roy. Soc., A272, 119, 1963.

15. Tino, Y. and T. Maeda, J. Phy. Soc. Japan, 24, 729, 1968.

16. fetals Handbook Vol. I, 8th ed., American Society for Metals, Metals Park, Ohio, p.817, 1961.

17. Kubaschewski, O., "Iron Binary Phase Diagrams, Springer Verlag, Berlin, Heidelberg, New York, p.73, 1982.

18. Nakagawa, Y., Y. Tanji, H. Morita, H. Hiroyoshi, and H. Fujimori, J. Mag. & Mag. Mats., 10, 145, 1979.

19. Hausch, G., and H. Warlimont, Acta Metall., 21, 401, 1973.

20. Hausch, G. and H. Warlimont, Physics Letters, 36A, 415. 1971.

21. Khomenko, O.A., A.M. Tseytlin, and G.A. Tarnavski, Fir. Metal-Metalloved, 30, 769, 1970.

22. Jago, R. A. and P.L. Rossiter, Phys. Stat. Sol. (a), 72, 497, 1982.

23. Kondorsky, E.I. and V.L. Sedov, J. Appl. Phys., 31, 331S. 1960.

24. Shirakawa, Y., Sci. Repts. Tohoku Imp. Univ. 27, 485, 1939.

25. Tanji, Y., Y. Nakagawa, Y. Saito, K. Nishimura, and K. Nakatsuka, Phys. Stat. Sol. A., 56, 513, 1979.

26. Tanji, Y., H. Moriya, and Y. Nakagawa, J. Phys. Soc. Japan, 45, 1244, 1978.

27. Kubaschewski, O., K.-H. Geiger, and K. Hack, Z. Metallk., 68, 337, 1977.

28. Dean, D. C., and J. J. Goldstein, Met. Trans., 17A, 1131, 1986.

29. Cahn, J. W., Acta Met., 9, 795, 1961.

30. Russell, K. C., "Nucleation in Solids: The Induction and Steady State Effects," Adv. Coll. and Int. Sci., 13, 205, 1980.

31. Tanji, Y., V. Nakagawa, and S. Steinemann, Physica, 119B, 109, 1983.

32. Guimaraes, J.R.C., J. Danon, R. B. Scorzelli, and I. S. Azevedo, J. Phys. F: Metal Phys., 10, L197, 1980.

33. Buchwald, V. G., Handbook of Iron Meteorites, 3 Vols., University of California Press, Berkeley., 1975.

34. Danon, J., R. Scorzelli, I. S. Azevedo, W. Curvello, J. F. Albertsen, and J. M. Knudsen, Nature, 277, 283. 1979

35. Scorzelli, R. B., and J. Danon, Physica Scripta, 32, 143, 1985.

36. Jago, R. A., P. E. Clark and P. L. Rossiter, Phys. Stat. Sol., (a), 74, 227, 1982.

37. Clarke, R. S., Jr., Meteorites, 19, 207, 1984.

38. Goldstein, J. I. and R. E. Ogilvie, Geochimica et Cosmochimica Acta, 29, 893, 1965.

39. Chamberod, A., J. Laugier, and J. M. Penisson, J. Mag. & Mag. Mats., 10, 139, 1979.

40. Chuang, Y.-Y., Y.A. Chang, R. Schmid, and J.-C. Lin, Met. Trans. 17A, 1361, 1986.

41. Kahlweit, M., Progress in Solid State Chemistry, 2, 134, 1965.

42. Reuter, K. B., D. B. Williams, and J. I. Goldstein, Geochimica et Cosmochimica Acta, 52, 617, 1988.

43. Reuter, K. B., D. B. Williams and J. I. Goldstein, "Determination of the Fe-Ni Phase Diagram Below 400°C." Met. Trans. A., 1988. (In press).

44. Miller, M. K. and K. F. Russell, Recent research supplied in advance of publication, 1988.

45. Russell, K. C., "Phase Stability Under Irradiation," frog. Mater. Sci., 28, 229-434, 1984.

46. Pauleve, J., A. Chamberod, K. Krebs and A. Marchand, IEEE Trans. Vol. MAG-2, No.3, 475, 1966.

47. Silverstre, G., A. Silvent, C. Regnard, and G. Sainfort, J. Nucl. Mater., 57, 125, 1975.

48. Morita, H., A. Chamberod, and S. Steinemann, J. Phys. F: Met. Phys., 14, 3053, 1984.

49. Wiedenmann, A., W. Wagner and H. Wollenberger, "Metastability of Fe-34 wt% Invar Alloys Above 600°C, E-MRS Strasbourg Meeting, Publ. J. Less Common Metals, (In press), 1988.

50. Williams, T. M., R. M. Boothby, and J. M. Titchmarsh,. "Composition Redistribution in Irradiated Austenitic Steels and Consequent Changes in Microstructure," AERE-R-12492, AERE, Harwell, England, 1986.

51. Brager, H. R., and F. A. Garner, in Phase Stability During Irradiation; J. R. Holland, L. K. Mansur, and D.I. Potter, Eds., The Metallurgical Society of AIME, Warrendale, PA, p. 219, 1981.

52. Garner, F. A., and J. J. Laidler, in "Proceedings of Workshop on Correlation of Neutron and Charged Particle Damage, CONF-760673," (Oak Ridge National Laboratory, Oak Ridge, TN), p.177, 1976.

53. Jung, P., J. Nucl. Mater., 117, 70, 1983.

54. Rehn, L. E., P. R. Okamoto and R. S. Averback, Phys. Rev., 830, 3073, 1984.

55. Maydet, S. I., and K. C. Russell, J. Nucl. Mater., 64, 101, 1977.

56. Martin, G., Phys. Rev. B21, 2122, 1980.

57. Cauvin, R. and G. Martin, Phys. Rev. B.23, p.3322, 1981.

58. Cauvin, R. and G. Martin, Phys, Rev, B.23, p.3333, 1981.

59. Abromeit, C., and G. Martin, in "Radiation Induced Changes in Microstructure," ASTM STP 955, F.A. Garner, N.H. Packan and A.S. Kumar. Eds., American Society for Testing and Materials, Philadelphia, PA, p.822, 1987.

60. Abromeit, C., V. Naundorf and H. Wollenberger, "Phase Stability Criteria for Ion and Neutron Irradiated Alloys," to be published in J. Nucl. Mater. as Proceedings of Third International Conference on Fusion Reactor Materials, Vols, 154-156 (In Press), 1987.

61. Krishan, K., and C. Abromeit, J. Phys. F. 14, 1103, 1984.

62. Abromeit, C. and K. Krishan, Acta Metall., 34, 1515, 1986.

63. Krishan, K. and C. Abromeit, in Irradiation-Induced Changes in Microstructure, 13th International Symposium, F. A. Garner, N. H. Packan, A. S. Kumar, Eds., American Society for Testing and Materials, Philadelphia, PA, p.809, 1987.

64. Abromeit, C., and G. Martin, "Adiabatic Approximation for Irradiation-Induced Instabilities in Concentrated Alloys," in Non-Linear Phenomena in Materials Science, G. Martin and L. P. Kieben, Eds., Trans. Tech. Pubs. (In press), 1988.

65. Murphy, S. M., "Instabilities in Concentrated Alloys Under Irradiation," Harwell Research Report TP1237, AERE-Harwell, England, (To be published in Phil. Mag. A), 1987.

66. Marwick, A. D., J. Phys., F 8, 1849, 1978.

67. Anthony, T. R., Acta. Met., 17, 603, 1969.

68. Sethi, V. K. and P. R. Okamoto in Phase Stability During Irradiation, J. R. Holland, L. K. Mansur. and D. I. Potter, Eds., TMS-AIME, p.165, 1981.

69. Marwick, A. D., R. C. Pillar and M. E. Horten, in Dimensional Stability and Mechanical Behaviour of Irradiated Metals and Alloys (vol 2), British Nuclear Energy Society, London, p.11, 1984.

70. Garner, F. A., in Ref. 51, P. 165.

71. Wolfer, W. G., F. A. Garner and L. E. Thomas, in Effects of Radiation on Materials: Eleventh Conference, ASTM STP 782, H. R. Brager and J. S. Perrin, eds., American Society for Testing and Materials, Philadelphia, PA, p.1023, 1982.

72. Wiedersich, H., P. R. Okamoto and N. Q. Lam, J. Nucl. Mater., 83, 98, 1979

73. Garner, F. A. and W. G. Wolfer, J. Nucl. Nater., 102, 143, 1981.

74. Garner, F. A. and A. S. Kumar, in ref. 3, p. 289.

COMPUTER SIMULATION OF HIGH ENERGY DISPLACEMENT CASCADES - H. L. Heinisch (Pacific Northwest Laboratory)

OBJECTIVE

This report is a review of a computer simulation methodology for addressing displacement cascade effects in fusion-fission correlations.

SUMMARY

A methodology developed for modeling many aspects of high energy displacement cascades with molecular level canputer simulations is reviewed. The initial damage state is modeled in the binary collision approximation (using the MARLOWE canputer code). and the subsequent disposition of the defects within a cascade is modeled with a Monte Carlo annealing simulation (the ALSOME code). There are few adjustable parameters. and none are set to physically unreasonable values. The basic configurations of the simulated high energy cascades in copper, i.e., the number. size and shape of damage regions. compare well with observations. as do the measured numbers of residual defects and the fractions of freely migrating defects. The success of these simulations is somewhat remarkable. given the relatively simple models of defects and their interactions that are employed. The reason for this success is that the behavior of the defects is very strongly influenced by their initial spatial distribution. which the binary collision approximation adequately models. The MARLOWE/ALSOME system, with input fran molecular dynamics and experiments. provides a framework for investigating the influence of high energy cascades on microstructure evolution.

PROGRESS AND STATUS

Introduction

One of the greatest challenges in developing materials to withstand the neutron radiation in deuterium-tritium fuslon reactors is having to proceed in the absence of a relevant fusion neutron environment. This has created a need for developing correlations so materials can be tested in other irradiation test facilities, primarily fission reactors. The basis of the correlation process lies in understanding the fundamental aspects of radiation effects. especially the energy dependence of radiation damage events. Because primary damage information is not easily accessible experimentally. quantitative results from primary damage modeling are valuable in developing the correlations, especially in the role of providing source terms for models of microstructure evolution.

Molecular level canputer simulations of radiation damage events can give quantitative information on the initial damage state. e.g., the energy dependence of the numbers of total defects. freely migrating defects, and clusters. More importantly. these simulations provide the most complete description of the initial spatial distribution of defects formed in cascades. which has a very strong impact on how the defects interact.

For about 25 years molecular dynamics has been used for modeling primary damage. but until recently, only very low energy events have been modeled. This method has suffered fran two major shortcomings preventing its usefulness in simulating displacement cascades: the lack of realistic interatomic potentials and the need for great canputer size and speed to model displacement cascades of sufficiently high energy to observe typical cascade effects. New approaches in which local electron densities are accounted for in a semi-empirical pair potential formulation[1] appear to be a major breakthrough in realistic treatment of atomic interactions at a level of realism and canputational complexity commensurate with molecular dynamics modeling of displacement cascades. The existence of large, fast vector computing machines should soon allow us to model displacement cascades that have sufficiently high energy to exhibit sane of the cascade effects relevant to fission-fusion correlations.

The operational definition of "high energy" in computer simulations of displacement cascades is that energy above which the problem saturates the largest available canputer. about 5 keV in the most recent molecular dynamics simulations[2]. With respect to damage correlation, "high energy" refers to the primary knock-on atan (PKA) energy above which most of the damage is produced in 14 MeV neutron irradiations. In typical structural alloys 90% of point defects fran 14 MeV neutrons are produced in cascades of 100 keV or greater. With respect to the physical processes being modeled. "high energy" might be defined as the PKA energy above which more than one distinct damage region is produced, about 20-50 keV. The break-up of high energy cascades into subcascades is well-established both theoretically[3] and experimentally[4]. The last definition of high energy will be used here.

The average energy of PKAs resulting fran 14 MeV neutrons is about 200 keV in structural metals. While modeling a 200 keV cascade with molecular dynamics is well beyond the capabilities of present or even planned supercomputers, it is very probable that at least individual subcascades of high energy cascades can eventually be modeled with molecular dynamics. However. there are aspects of high energy cascades that can never be studied with molecular dynamics. such as the spatial distribution of subcascades and the long-term development of the defect interactions in the cascade. Binary collision models. which ignore many of the low energy details of atanic interactions, are excellently suited for describing the gross

structural features of high energy cascades, and they will continue to be useful in the overall modeling scheme.

In this paper a methodology for modeling high energy cascades with the binary collision code MARLWE and the Monte Carlo annealing code ALSOME will be reviewed. Limitations of the models will be discussed, as well as the successes in simulating experimentally observed phenanena. Future directions for simulation of high energy cascades will be discussed.

Modeling High Energy Cascades

1. Stages of Cascade Oevelopment

Several stages of developnent can be identified during the production of a displacement cascade. First is the collisional stage of about 10^{-13} sec, ending approximately when no atom has enough energy to displace another atom fran its lattice site. The cascade quenching stage then occurs. During the next 10^{-11} sec, the region of the crystal that has been violently disturbed by the cascade approaches thermal equilibrium with Its surroundings while the defects athermally rearrange themselves. The effects of quenching are assumed to be independent of the crystal temperature. There is evidence from recent molecular dynamics simulations that a molten condition exists initially in the core of a cascade[2], and that it may lead to spontaneous formation of vacancy loops during quenching. Finally. during the short-term annealing stage. lasting another 10^{-8} sec or longer, the defects within the cascade interact among themselves through thermally activated processes determined by the local crystal temperature. The transitions fran one stage to the next are obviously not distinct; however, within the simulation scheme. criteria are arbitrarily chosen to define the end of each stage, since different models are used to describe each stage.

2. The MARLOWE Code

A comprehensive study of high energy cascades in copper was done utilizing the binary collision code MARLWE[5] and the Monte Carlo annealing simulation code ALSOME.[6] The methodology for modeling high energy cascades in copper was developed and laid out in a series of reports. First the link between molecular dynamics and the binary collision approach was established at low energies[7] and high energies[8]. Numbers of defects in MARLWE-generated cascades were compared with measured values at 4K[9]. The effects of including thermal displacements in MARLWE were studied[10]. Cascade configurations -- shape, size and subcascade structure -- were systematically studied[3,10]. The fast Monte Carlo annealing simulation code ALSOME was developed and used to model quenching and short-term annealing of the cascades[6,9]. More than a thousand cascades. ranging in energy fran 200 eV to 500 keV were simulated in copper[11] using MARLOWE with thermal displacements representative of 300 K and parameter settings as described in Table 1. Finally. functions describing production of total defects and freely migrating defects a, a functlon of pka energy were devised and used to generate neutron cross sections for defect production[12]. Throughout this work care was taken to match the model wherever possible to experimental measurements without introducing additional. artificial parameters.

TABLE 1

MARLWE PARAMETER SETTINGS
FOR CASCADES GENERATED IN COPPER AT 300 K

Code Version:	11
Interatanic Potential :	Moliere approximation to Thanas-Fermi, with screening length of 7.38 pm
Inelastic Losses:	Local (Firsov)
Lattice Parameter:	ALAT = 0.3615 nm
Maximum Impact Parameter:	RB = 0.62 lattice parameters
Debye Temperature:	TDEBYE = 314 K
Energy Criteria for Displaced Atoms:	EDISP = 5.0 eV EWIT = 4.8 eV EBND = 0.2 eV

In using the binary collision approximation the ability to deal exactly with the many-body aspects of low energy collisions is sacrificed for the facility of dealing with high energy cascades. The cascade is generated in a series of two-body collisions between atans that originally occupy lattice sites in the crystal. Target atans are added to the cascade if they receive a minimum kinetic energy in a collision. All displaced atans are required to surmount a binding energy. and they are followed until their energies fall below a cut-off energy. A lattice temperature is accounted for by imposing a randan thermal displacement on each target atan fran a Gaussian distribution of uncorrelated displacements in the Debye model. The results are sensitive to whether or not thermal displacements are included. but they are not very sensitive to the value of the temperature.[6] Electronic energy losses were accounted for in our modeling by subtracting the appropriate energy at each collision in the Firsov model. Quantitative measures of the damage energy referred to in this paper are the average damage energies determined in the MARLOWE code. The MARLOWE values of damage energy are within a fen percent of the damage energies calculated from Robinson's formula for the Lindhard theory[13].

Although the binary collision approximation is valid only for high energy collisions, the MARLOWE code contains parametric representation of sane kinematic phenomena that can be set to produce appropriate results at low energies. Robinson? investigated the low energy behavior of MARLOWE and determined parameter settings that gave a reasonable fit to the replacement sequence lengths in copper determined fran molecular dynamics. Robinson also concluded that it is necessary to include thermal displacements in MARLOWE to give correct low energy behavior. The values of the MARLOWE parameter settings for correct kinematic behavior in low energy events in copper are given in Table 1.

MARLOWE models only the collisional stage of the cascade and cannot model relaxation about defects or the dissipation of energy to the rest of the crystal. Thus. a "MARLOWE cascade" consists of a list of positions of vacant lattice sites (vacancies) and energetic displaced atoms (interstitials) "frozen" at the turning points of their last collisions. The approaches used to model the quenching and short-term annealing stages utilize the MSOME code. and will be discussed later.

3. Cascade Configurations

Our objective in modeling displacement cascades was to determine the numbers of defects produced and their spatial distribution as a function of cascade energy. along with the evolution and interaction of the defect distributions as a function of time and temperature. The evolution is strongly dependent on the defect configuration produced during the collisional phase[6].

The configurations of MARLOWE-generated cascades in copper were analyzed graphically[3,10]. Indispensable qualitative information was obtained from three-dimensional plots of the positions of vacancies and interstitials that were rotated in three dimensions in real time on a screen. Graphical analysis of hard-Copy plots and numerical analysis of defect distributions were also done to obtain quantitative results. Figure 1 shows 3-D plots of cascades with energies ranging fran 1 keV to 100 keV.

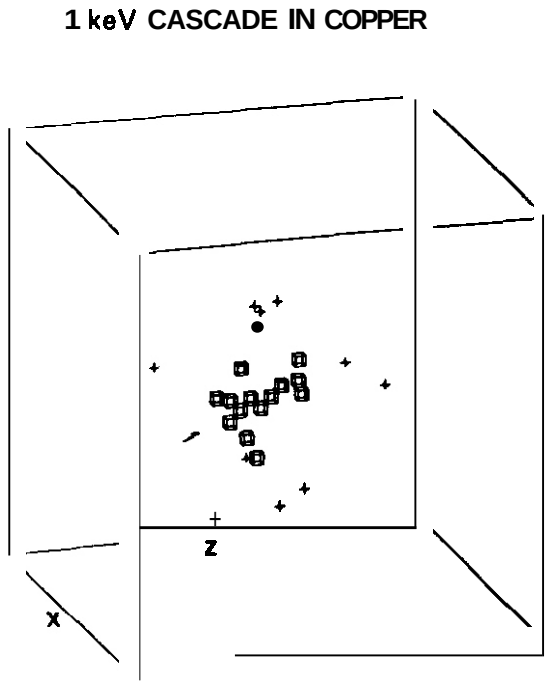

Figure 1a BOX = 7 nm PAIRS = 14

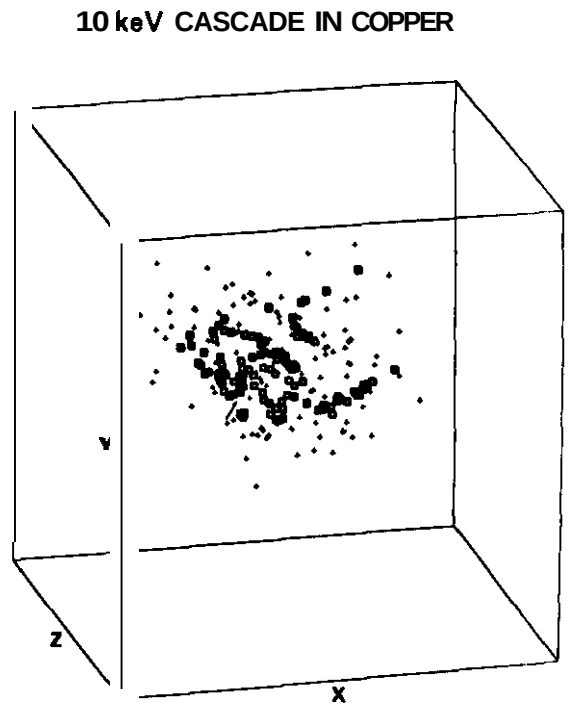

Figure 1b BOX = 14nm PAIRS = 113

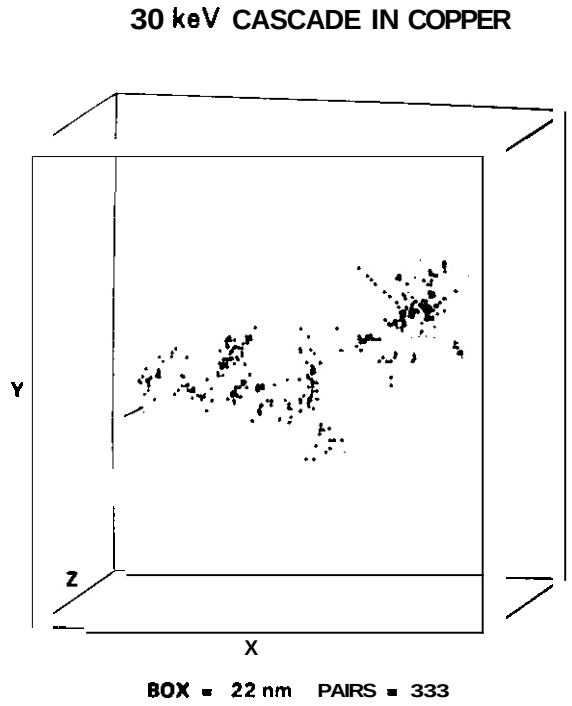

Figure 1c

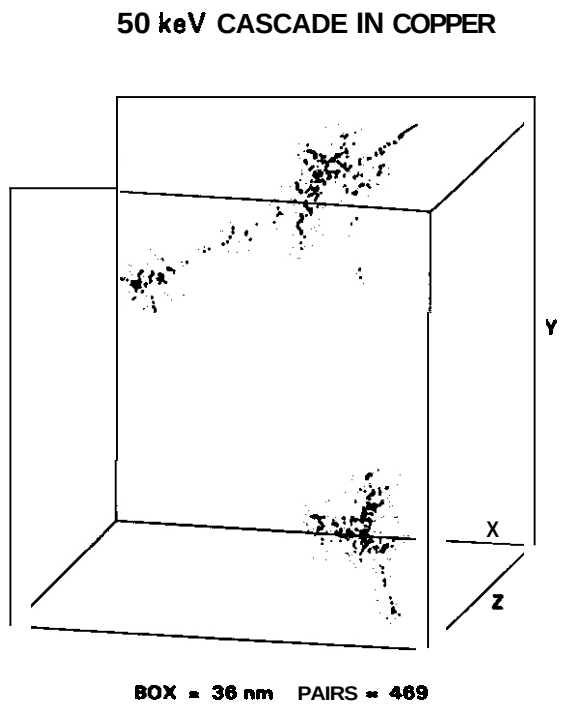

Figure 1d

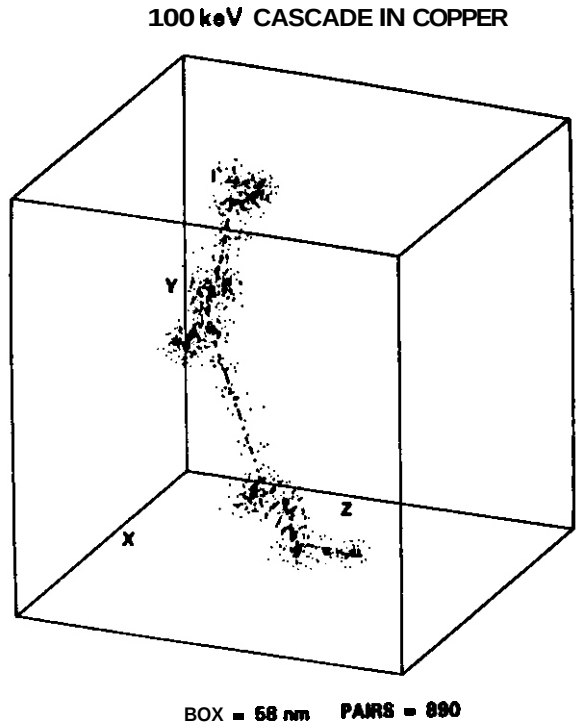

Figure 1e

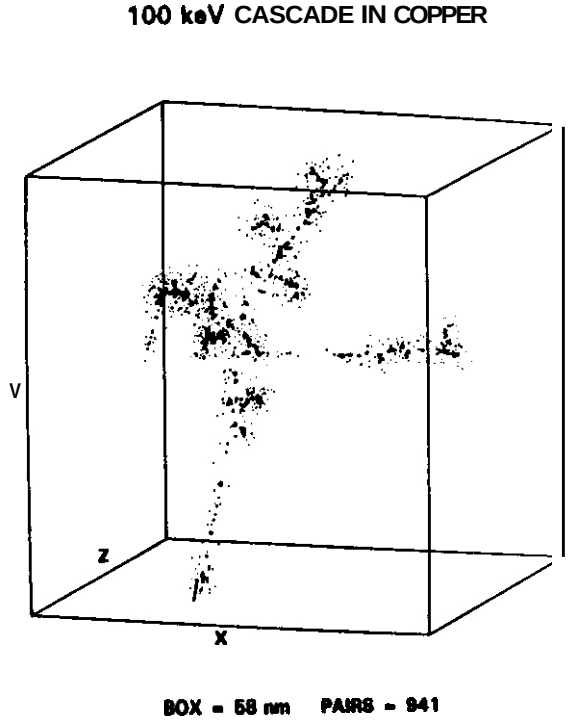

Figure 1f

Figure 1. Three-dimensional views of cascades in copper at 300 K generated with MARLWE. The small cubes represent vacancies and the pluses represent interstitials. A small arrow indicates the location and direction of the PKA. The cascades were subjected to a recombination radius of 2 lattice parameters. yielding numbers of defects equal to that calculated by the modified Kinchin and Pease expression.

Distinct subcascades (damage regions separated by relatively undamaged material) are produced regularly at 50 keV and above. At lower energies and within individual subcascades there are separate. distinct regions of high defect density. often in close proximity (Figure 1). Thus, a separate category of cascade sub-region. the "lobe," was defined as the basic unit of cascade configurations. (An "L" shaped distribution. for example. would be considered to have two lobes.) A special category of subcascade was also defined: widely-separated subcascdes, for which the edge-to-edge separation is at least as large as the subcascade dimensions.

The energy dependence of lobe production is illustrated in Figure 1. At PKA energies up to a few keV the cascades have no fully developed lobes, but consist of a few scattered defects with the vacancies generally in the center. As the energy increases (to about 10 keV in copper), single lobes become fully developed. with the characteristic vacancy-rich depleted zone surrounded by a cloud of interstitials. By about 20 keV the tendency to form more than one depleted zone or lobe is observed. And by 100 keV, widely-spaced subcascades. each having its own lobe structure, occur regularly.

Sizes of our simulated cascades and the numbers, size and spacing of lobes were determined as a function of PKA energy and damage energy[10,11]. For the purpose of quantitative analysis. the minimum sized lobe was defined such that all 20 keV cascades have at least one lobe. Based on the present sample of cascades. extremely separated damage regions (with subcascade separations exceeding 2 or 3 times the average maximum extent for cascades of that energy) occur In less than 20% of cascades of 200 keV or less. and Only rarely below 50 keV. Thus, for most of the PKAs produced in copper by 14 MeV neutrons, subcascades from the same PKA should be clearly associated with each other.

In brief. a high energy cascade in copper was found to be a series of mostly-connected 5 to 30 keV lobes separated by an average center-to-center spacing of 14 nm (including distances between widely-separated subcascades). On average there is approximately one lobe per 13 keV of damage energy. The numbers of lobes and distinct subcascades as a function of PKA damage energy are shown in Figure 2.

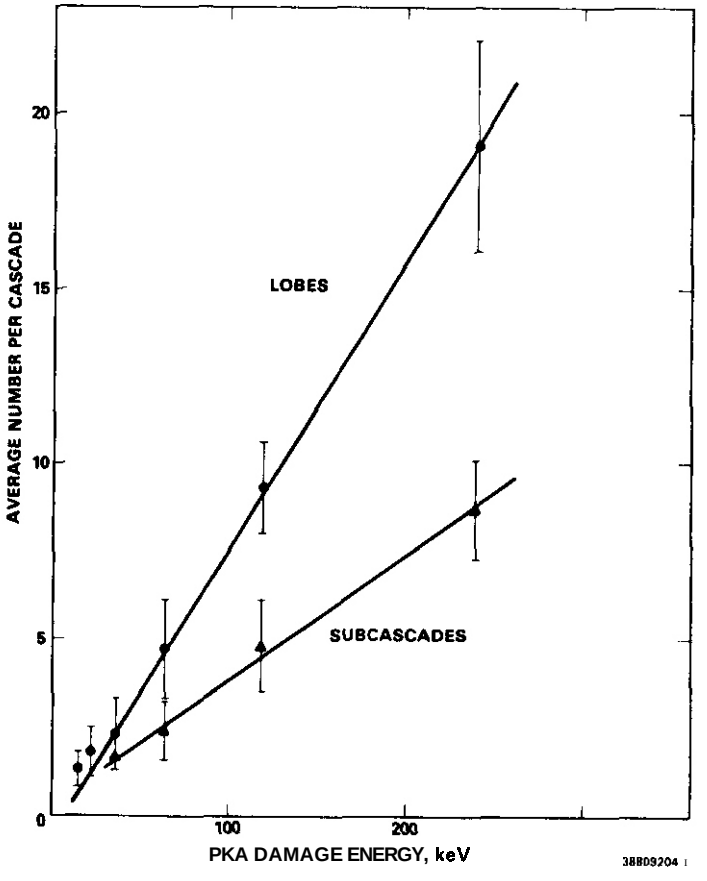

Figure 2. Average number of lobes and widely-spaced subcascades as a function of PKA damage energy, T_D, in keV.

In recent transmission electron microscopy (TEM) investigations of pure metals irradiated by 14 MeV neutrons. Kiritani[14] was able to resolve individual sub-regions of single cascades. The numbers of sub-regions and their spacings are consistent with the lobe structures of our simulated cascades. Kiritani reports an inter-lobe spacing of 12 nm for copper, in good agrement with our simulations.

The technique of imaging disordered regions caused by cascades in ordered alloys[15] can give quantitative information on cascade shapes and sizes even when the residual defects cannot be imaged. The transverse dimensions of disordered regions produced by 10-200 keV Cu^+ ions normally incident on ordered Cu_3Au were analyzed by Jenkins et al.[16] Closely spaced multiple damage regions were observed. Maximum zone size distributions were determined. and the average maximum transverse dimensions were determined as a function of energy.

A simulation of this experiment was performed using MARLOWE.[17] The sizes of the simulated point defect distributions were calfbrated to the measured size distributions of *disordered* zones at 10 keV and 30 keV. A comparison of the simulated and experimental cascade dimensions is in Figure 3. To account for the foil thickness used in the experiment, the simulated cascade damage residing in only the first 20 nm of the foil was analyzed. The agrement between the simulation for the thin foil and the experiment was quite good over the entire energy range.

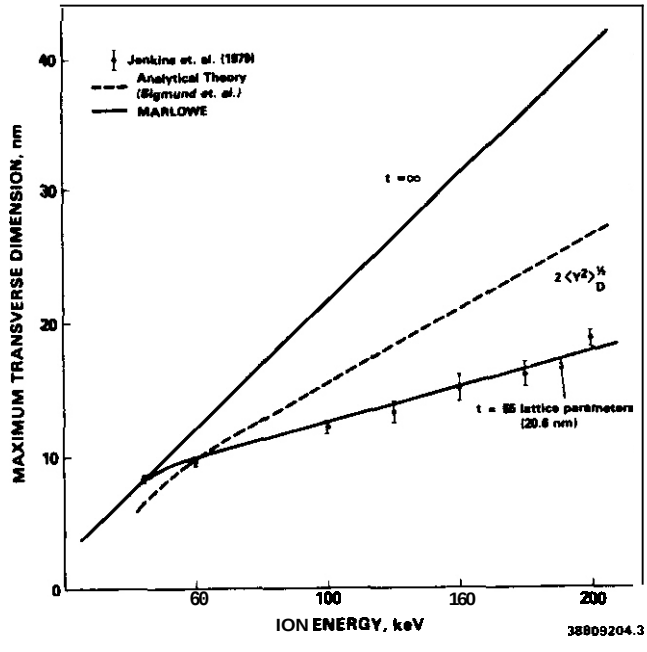

Figure 3. The measured maximum transverse dimension of disordered zones in ordered Cu_3Au irradiated with Cu^+ ions (points). The solid curves are results of MARLOWE simulations for thick ($t = \infty$) and thin (t = 20.6 nm) foils. The dashed line is the result of an analytical theory.

4. Defect Densities

Because high energy cascades are so irregular in shape. it is very difficult to make meaningful quantitative descriptions of their sizes or, especially. the density of defects. How one defines the density or volume depends 1 gely on the use to be made of the Information. In the narrowest definition of cascade volume. Robinson[11] multiplies the atomic volume by the *number* of *moving* atans in a MARLOWE cascade. The defect density remains constant with damage energy by that definition of volume. At the other extreme, we have measured the volume inside a rectangular parallelepiped just enclosing the cascade. Using that definition of volume, defect densities decrease with increasing energy by several orders of magnitude from 1-200 keV. Figure 4 is a plot of the average defect density within the parallelepiped as a function of PKA energy. The data display a different energy dependence above about 20 keV, indicating the transition to multiple lobe production.

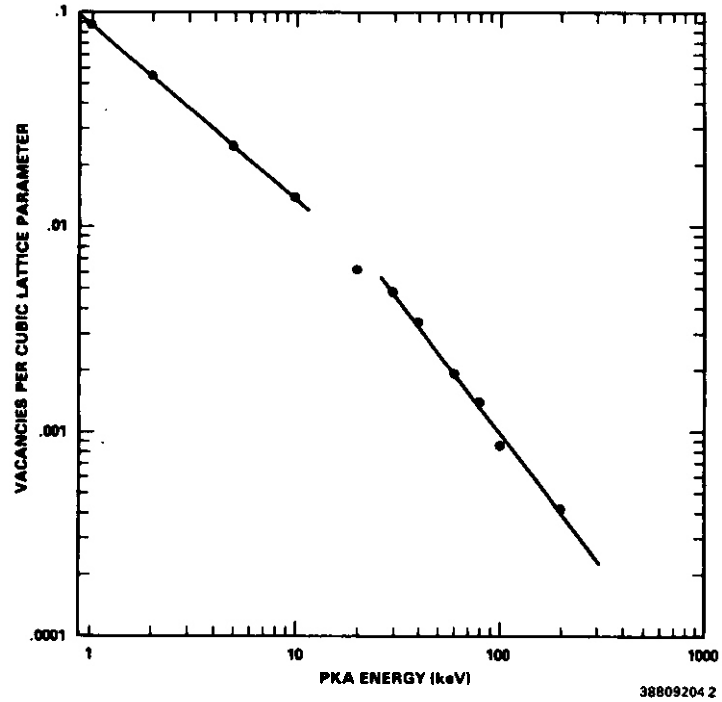

Figure 4. The average density of defects within the enclosing rectangular parallelepiped, oriented along the crystal axes, as a function of PKA energy.

Volume determinations deriving fran statistics of the defect distribution have been developed. They are best suited to single lobed cascades. The component analysis of ellipsoids was applied by Hou[19] to MARLOWE cascades up to 30 keV in tungsten. Dierckx[20] applied component analysis to individual subcascades in high energy cascades in alpha-iron. Benedek[21] analyzed cascades in copper using the radius of gyration of the defect distribution. The densities are proportional to the enclosing parallelepiped densities shown in Figure 4.

In Figure 5 the average defect density in a small region about each defect is plotted as a function of PKA energy for vacancies and interstitials. Above about 10 keV, the defects see the same average environment, independent of energy. The subsequent behavior of the defects will initially be most influenced by their immediate surroundings. thus, one can expect to learn much about high energy cascades by studying the evolution of individual lobes.

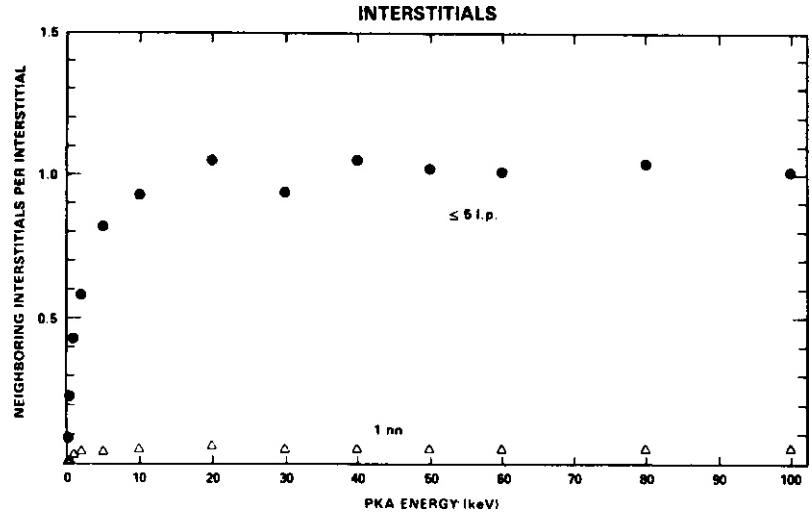

Figure 5a

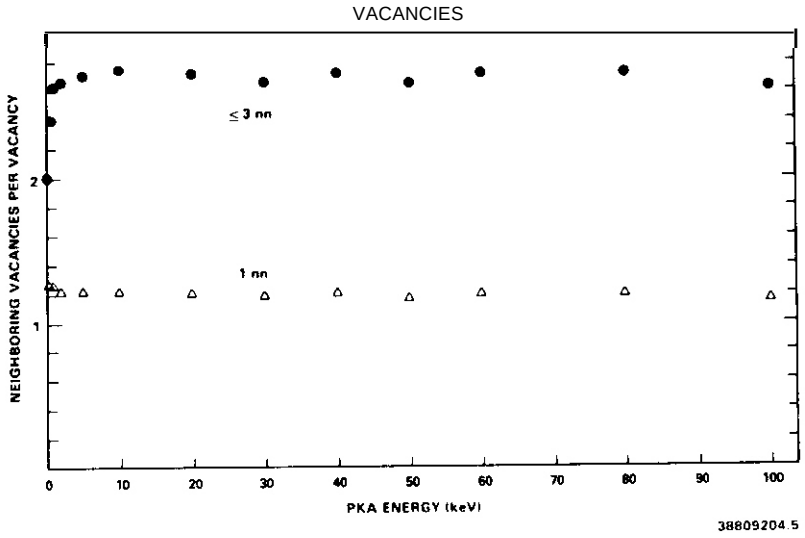

Figure 5b

Figure 5. Average local density of a.) interstitials and b.) vacancies as a function of FUA energy. defined as the average number of neighboring defects within 5 lattice parameters (≤5 l.p.) for interstitials or 3 nearest neighbors (≤3nn), 1.2 lattice parameters. for vacancies. The average number of nearest neighbor defects is also shan (1 nn) for each defect type.

5. Channeling

The production of subcascades is, In general, a manifestation of the increase in the mean free path between energetic collisions with increasing energy of the projectile atom. Another phenomenon that may have an influence on the configurations of cascades is inter-plane channeling. It occurs when an energetic primary or secondary knock-on atom is given a trajectory between two atanic planes such that relatively la energy collisions tend to confine the trajectory to that plane over a fairly large distance with Only a small loss of projectile energy. Upon de-channeling. the projectile can produce a damage region widely separated fran the rest of the cascade.

Computer simulations[11] indicate that channeling occurs in copper, though rarely, in cascades of 30 keV or less. In these laer energy cascades the appearance of channeling is quite dramatic. since in the absence of channeling. usually only a single, compact damage region is produced. In cascades with hundreds of keV of energy, subcascades are produced in locations that may or may not be the result of channeling. MARLOWE cascades of 200 and 500 keV in copper were analyzed graphically to determine the contribution of channeling to the cascade configuration. The trajectory directions for 14 events in 40 cascades were determined from debris along the trajectory (an occasional Frenkel pair) or inferred fran relative shapes and positions of damage regions. Figure 6a. Of the events measured, 68% have directions within 2 of a planar channeling direction. If directions were randomly chosen, about 41% of all directions would be in this category. Thus. It seems that channeling events occur frequently in high energy cascades in copper, but they are not the exclusive mechanism by which widely separated damage regions are produced.

The influence of channeling events on the configurations of high energy cascades was also investigated by comparing simulated cascades produced in crystalline and "amorphous" copper. MARLOWE models an amorphous material by performing a random rotation of the lattice after each collision. While this procedure does not rigorously represent the amorphous condition, nevertheless. the symmetry that permits channeling is destroyed. A Comparison of the vacancy distributions of 200 keV cascades in crystalline and amorphous copper showed that the cascades in crystalline material were only slightly larger in extent and aspect ratio. The amorphous cascades. Figure 6b, are generally indistinguishable fran the crystalline cascades, but on the average, they tend to have fewer widely-separated damage regions. In real situations if the opportunity for channeling is suppressed. the subsequent interactions of the defects may be affected. Additionally. conditions that suppress channeling would probably also suppress replacement collision sequences, which would have an even greater impact on subsequent defect interactions.

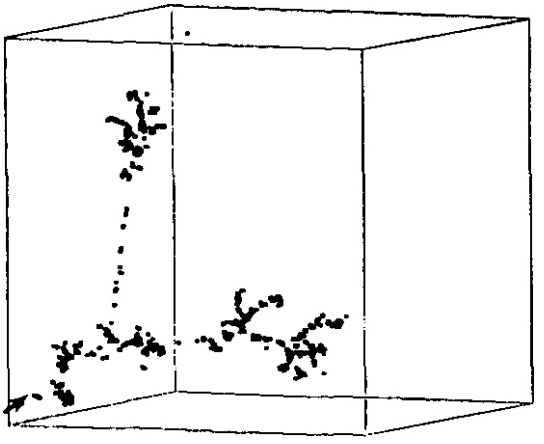

200 keV, BOX = *62* nm

Figure 6a

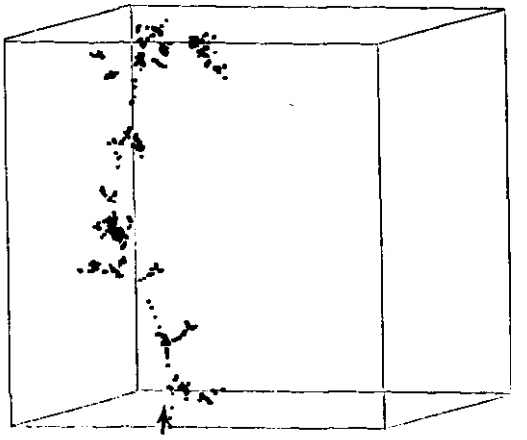

"AMORPHOUS COPPER"
200 keV, BOX = 69 nm

38809

Figure 6b

6. a.) Vacancy distribution for a 200 keV cascade in copper The cube edge is 170 lattice parameters (62 nm). The vertical trail of single vacancies indicates the trajectory of the energetic recoil that produced the upper subcascade. b.) Vacancy distribution for a 200 keV cascade in "amorphous" copper. The cube edge is 192 lattice parameters (70 nm).

6. Cascade Quenching and Short-term Annealing

The quenching stage of a high energy cascade can only be properly simulated by a fully dynamical model, a feat that has yet to be achieved above 5 keV in copper. The binary collision approach is inadequate for modeling the many body aspects of the quenching stage. Although it can model well the gross features developed during the collisional stage. it does not leave the defects or the surrounding crystal in the correct disposition. However, it may be possible that a simple parametric model of cascade quenching. applied to MARLOWE cascades. can bridge the gap in a physically reasonable way between the collisional stage and the beginning of the short-term annealing stage. The major physical effects of quenching are significant recanbination, clustering and. in sane cases, direct formation of vacancy loops. As quenching is independent of crystal temperature. the number of defects remaining immediately after quenching at any temperature is assumed equal to that measured in irradiations at liquid helium temperature (approx. 4 K) where defects are immobile. Analyses[22-24] of experimental information show the recoil energy dependence of defect production. It is generally accepted that the lower efficiency of defect production in cascades is a result of recanbination during quenching.

The simplest approach to representing the result of quenching in MARLOWE cascades is to ignore the kinetic and potential energy of the defects at the termination of the collisional stage and to statically recanbine the closest defect pairs, leaving the residual defects in the positions determined by MARLWE. In the earliest work[9], a single, energy-independent recanbination distance was found to give defect pair yields for cascades fran 10 keV to 500 keV in copper equal to the measured number of defect pairs extracted[22] fran resistivity measurements on copper irradiated with charged particles and neutrons at 4 K. The post-quenching number of defects was correct. but the spatial distribution of the residual defects was quite incorrect. About 25% of vacancies and 50% of interstitials became freely migrating defects during subsequent short-term annealing simulations of the recombined cascades. Experimental evidence (reviewed in Ref 25) indicates that only a few percent of the defects that exist in the post-quenching primary damage state escape their cascades and become freely migrating defects.

As a first step toward a more realistic quenching model, a semi-empirical kinetic quenching model was devised within the framework of the short-term annealing simulation code ALSOME[6]. When applied to MARLOWE cascades of 1-100 keV in copper, both the observed numbers of total defects and the fractions of freely migrating defects (those that escape interactions within their own cascade) were well-modeled throughout the energy range.

7. The ALSOME Code

The Monte Carlo annealing simulation code ALSOME[6] contains a number a simplifying assumptions about the physical processes that make it very fast even for the largest cascades. (ALSOME is not presently available for distribution.) Defect clusters are spherical and centered on lattice sites. Mobile defects are jumped in randan sequence, weighted by their relative jump probabilities. When two defects cane within a critical reaction distance. they are coalesced into a single defect. The only adjustable parameters in ALSOME are the relative jump probabilities of mobile defects and the critical reaction distances between various defect species. In practice. time is measured in terms of defect jumps and the concept of temperature enters when the sequence of events is interrupted. For example. if the

simulation is terminated when few mobile interstitials remain. but before vacancies have started moving. the result represents the short-term annealing at a temperature where interstitials are relatively mobile and vacancies are relatively immobile. The real time at temperature is reflected in the absolute jump frequencies: the simulated real elapsed time is the inverse of the sum of the jump frequencies of the jumping defects for the temperature being simulated. The results with ALSCME were found to be statistically indistinguishable[9] from simulations done with a more physically rigorous approach[26].

For isolated cascades in copper, the sequence of simulated annealing events is fairly insensitive to the relative jump frequencies. Indeed, in an extreme test, little difference was found when vacancies were allowed to move before interstitials. This is a further manifestation of the strong effect of the initial defect configuration on subsequent behavior.

The kinetic quenching model consists of annealing cascades with ALSCME for a very short time with exaggerated parameter values. The quenching lasts for 100 interstitial jumps, about 10^{-11} sec, which is consistent with arguments based on thermal conduction[27]. Cascades are taken from MARLOWE to *ALSOME* with no prior recanbination. They are quenched with quenching values of ALSOME parameters. then short-term annealed with the conventional parameter settings.

8. Freely Migrating Defects

The numbers of defects remaining immediately after the quench compare very well with the defect yields extracted fran resistivity measurements at 4 K, Figure 7. Then, after short-term annealing at approximately 300 K, the fractions of free defects compare well with measured values. 14% of the remaining interstitials[28] and 3.5% of remaining vacancies[29]. The defects that do not escape the cascade region remain simply as immobile clusters. The quenching model does not include provision for loop formation. However, during quenching, vacancy clusters were given radii representative of loops rather than spherical clusters, making large clusters more effective as sinks.

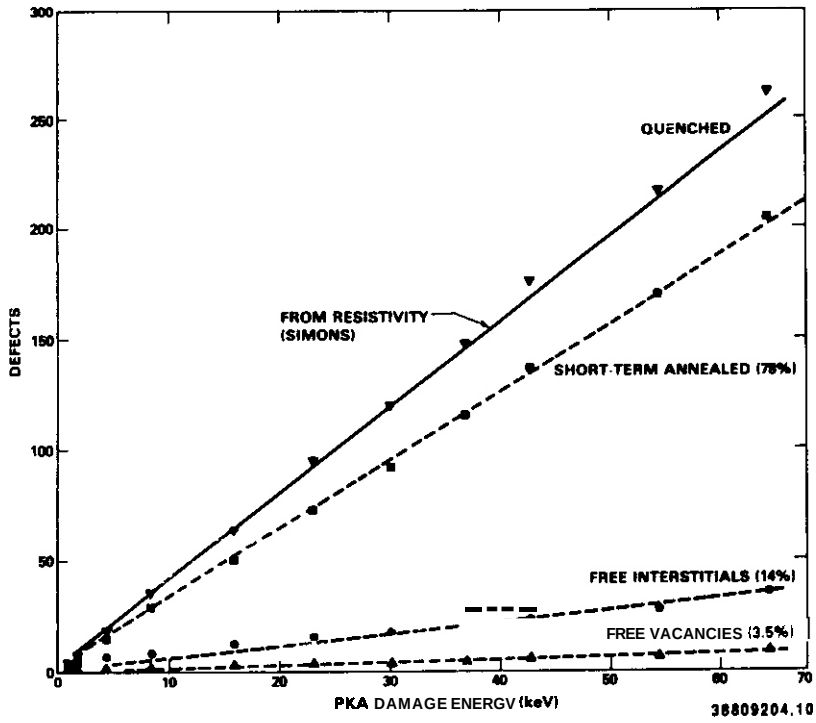

Figure 7. The number of defect pairs remaining after quenching and short-term annealing of isolated cascades in copper as a function of PKA damage energy. Free vacancies and interstitials are the defects that do not recombine or cluster within the cascade during annealing.

The fractions of free defects are sensitive to the critical reaction distances used, but their spatial distribution places bounds on their behavior. Regardless of the parameter settings. a minimum of 10% of the interstitials escape, because they are at the periphery of the cascade. A maximum of 10% of the vacancies can escape because of their concentration in the center of the cascade.

The energy dependence of free defect production at low energies is more specifically illustrated in Figure 8. The efficiency of total stable defect production measured at 4 K[22], relative to the displacements calculated fran the modified Kinchin and Pease expression[30] is plotted as a function of PKA energy in Fig 8a. The fractions of total stable defects that becane freely migrating defects after short-term annealing at 300 K are plotted in Figure 8b.

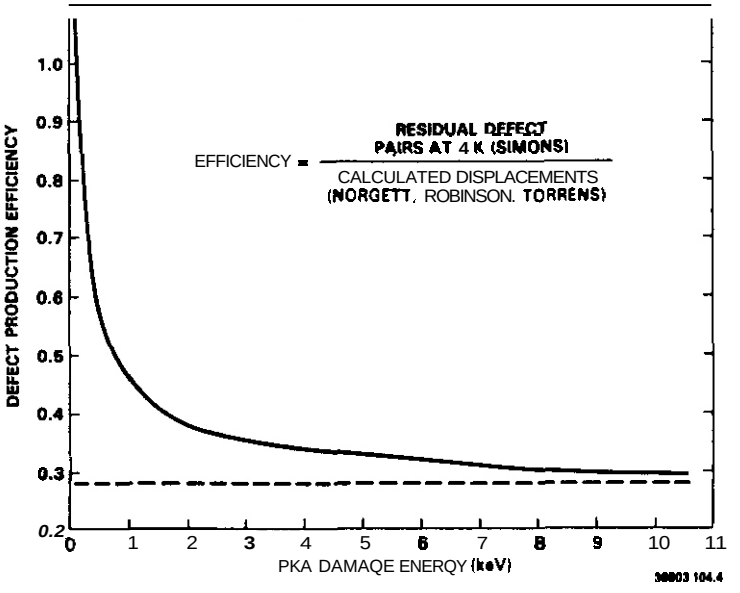

Figure 8a

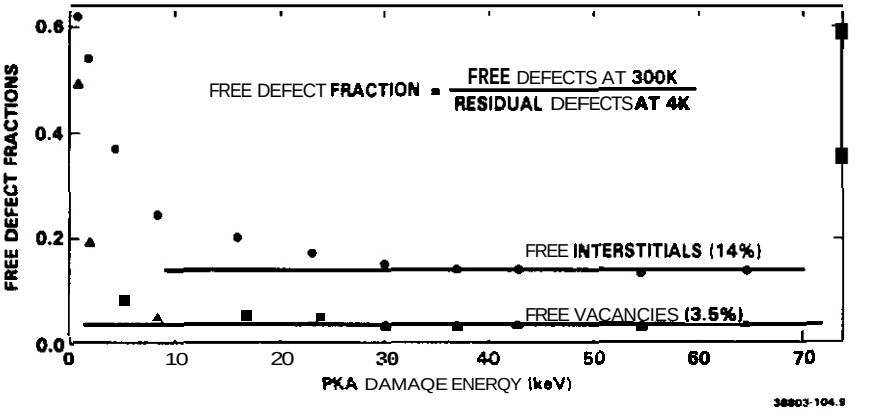

Figure 8b

Figure 8. a.) PKA pair production efficiency for copper. Efficiency is the ratio of the residual defect pairs at 4 K, extracted fran resistivity measurements (Simons). to the displacements calculated with the modified Kinchin and Pease expression (NRT). b.) The fractions of residual defects at 4 K that becane freely migrating vacancies and interstitials after short-term annealing at 300 K.

The higher efficiencies of total and free defect production at lower recoil energies are a manifestation of the energy dependence of lobe production, but in different ways. The energy dependence of the efficiency of total defect production is related to the density of defects in a cascade. Below about 1 keV there are few defect pairs created in close proximity. and the energy density of the cascade region is not great enough to cause recanbination by quenching. With increasing energy, the density of defects and energy in the cascade volume increases. and recanbination and clustering occur during quenching. The critical density for maximum quenching recombination (perhaps the critical energy density for formation of a molten phase[2]) is achieved by about 5 keV. As the energy increases further, the damage regions becane larger, but the defect densities rsnain constant, as illustrated in the behavior of the average local densities of defects in Figure 5. The production of lobes and subcascades guarantees constant efficiency with further increase in energy.

The fractions of freely migrating defects are influenced by the surface areas of the vacancy core and the interstitial cloud making up the cascade. As the cascades increase in size with energy. the free defect fractions. which depend on the surface-to-volume ratios, decrease until the maximum lobe size is achieved. after which they remain constant as the increasing energy simply results in more lobes. The effect is greatest for the interstitials. which lie at the outer edge of the cascade region.

Correlations of property changes that depend on total defect production by neutrons fran fission and fusion reactors should not be affected much by the recoil energy dependence of total defect production efficiency. In most fission reactors the vast majority of displacements result fran recoils above 1 keV. However. property changes that depend on freely migrating defects at roan temperature may show significant neutron spectral effects. Functions fitted to the simulation results for free defects[12] have been folded into PKA spectra for 14 MeV neutrons and the Fast Flux Test Facility (FFTF) at Hanford. Washington. The calculations predict that. compared to 14 MeV neutrons, FFTF produces twice as many free interstitials and three times as many free vacancies per DPA (displacements per atom), while producing the same number of total residual defects per OPA.

Recent experiments[25] measuring radiation induced segregation in ion banbarded Ni-Si and Cu-Au alloys at temperatures of 650-900 K, where clusters are unstable, show weighted recoil energy dependence of free defect production very similar to the modeling results in Figure 8b. This is evidence that even at high tmperatures the initial cascade configuration also strongly influences the behavior of defects in cascades. The basic cascade configuration just after the collisional phase, i.e. vacancies surrounded by a cloud of interstitials. is essentially independent of temperature. Evidently, this configuration results in subsequent intense recombination within each cascade at high crystal temperatures. As at lower temperatures. the fraction of freely migrating defects is controlled by the decreasing surface-to-volume ratio as cascade energy and size increase, leveling off as multiple lobe production begins at about 20-30 keV. This interpretation should be investigated by doing a short-term annealing simulation of cascades at high temperatures. The behavior implied by these experiments may lead to a considerable effect of the neutron spectrum on swelling and irradiation creep.

9. Cascade Interactions

The simulations discussed so far have been for single, isolated cascades. Phenanena of interest, and most experiments, take place with at least the possibility of cascade interactions. ALSOME simulations of cascade interactions have been done[6], and the results imply that the configuration of the initial damage state is a dominating influence. The free Interstitials interact almost exclusively with other interstitials, clustering either with the free interstitials from other cascades or with interstitial clusters at the periphery of another cascade. Figure 9 shows interstitial and vacancy cluster size distributions for isolated and interacting 30 keV MARLOWE cascades in copper after annealing at 50 K (Stage I recovery) with ALSOME. For cascades allowed to interact during annealing there are more and larger interstitial clusters, while the vacancy clustering is the same. Stage I recovery of 18% was experienced by both the interacting and isolated cascades, compared to 80% for electron irradiation[31] and 35% for d-Be neutron Irradiations[32]. The mall amount of recovery in the simulation must be due, at least in part. to using 30 keV cascades exclusively. Simulations of specific annealing experiments should be done using a distribution of cascade energies representative of the recoil spectrum being simulated.

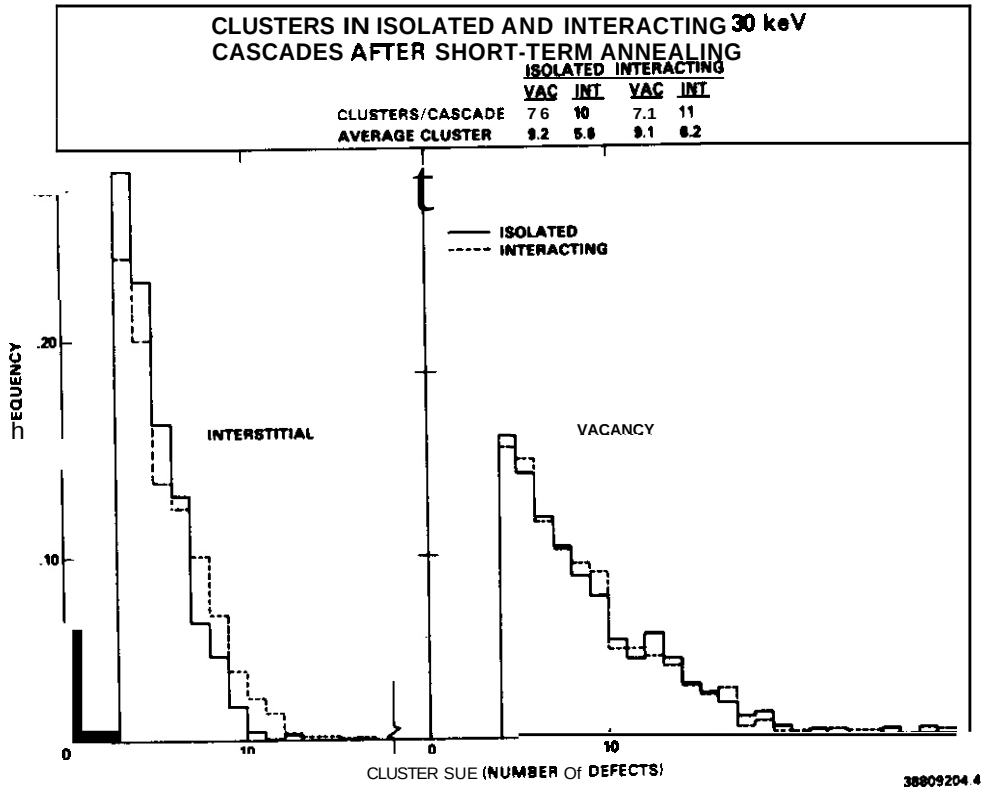

Figure 9.
Cluster size distributions of isolated and interacting 30 keV cascades in copper after short-term annealing at 300 K.

Discussion

Other High Energy Cascade Modeling

Earlier simulations of high energy cascades by Ooran and coworkers[26,33,34] included short-term annealing simulations and the determination of defect production functions. They used cascades generated in the pioneering simulation studies of Beeler[35]. Later cascades were generated in copper with an early version of MARLOWE. They annealed the cascades using a model sanewhat more physically realistic than in ALSOME. The cut-off energy EWIT used in MARLOWE was 25 eV, and no provision was made for recombination or clustering due to quenching. With the higher value of EWIT, long replacement sequences were not allowed, and the average pair separation was too mall; hence. more recombination would be expected during short-term annealing. However. since the effects of quenching were not taken into effect. the initial number of defects was too large in the annealing simulation. These factors apparently offset each other. because the residual defect production was very similar to that in Figure 7. While the total number of defects was fortuitously correct, the defects were not in the correct initial configuration: the post-annealing fractions of mobile defects were much too large.

Muroga and Ishino[36] have done binary collision simulations of high energy cascades in alpha-iron, along with short-term annealing simulations. With a high value of EQUIT (40 eV) and apparently no provision for quenching, their results are similar to those of Ooran et al. Total residual defect production is correct, but the free defect fractions are very large compared to measured values (in fcc metals). Muroga et al.[37] have determined the recoil energy dependence of free defect fractions in simulated cascades from 30 eV to 30 keV. While these fractions are still very high canpared to measured values. the overall energy dependence is similar to that obtained in our simulations for copper, Figure 8.

Dierckx[20] has generated cascades for PKAs fran 500 eV to 2 MeV in alpha-iron with MARLWE. using a fairly high value of EWIT (25 eV). The general configurations of the cascades should be independent of the value of EWIT used in various simulations. The cascade configurations were analyzed using a cluster identification algorithm. then each subcascade identified was treated by ellipsoid canponent analysis. The cluster algorithm cannot interpret the lobe structure of subcascades, so Dierckx's conclusions about the energy dependence of cascade configurations are sanewhat different from ours. The subcascades are reported to become larger and less dense with increasing damage energy throughout the energy range.

CONCLUSIONS

The major conclusion to be drawn from these simulations of high energy displacement cascades is that the initial defect configuration strongly influences the subsequent behavior of the defects. The entire simulation scheme from cascade production through short-term annealing is accomplished with very simple models. based on fundamental actions of interacting particles. There are few adjustable parameters, and no unphysical parameter values are needed to produce good agreement with experimental results. So strong is the influence of the spatial distribution of defects. that sane aspects of the annealing simulation are nearly insensitive to sane parameter values. However. it should be noted that the conclusions stated here for copper may not all apply in other systems. For example. in materials having more diffuse cascades, the influence of the initial configuration on the final disposition of the defects may not be as strong.

As with all modeling, one must keep the results in proper perspective. The detailed characteristics of individual defects and their interactions can never be modeled correctly with MARLOWE and ALSOME, but many effects governed by large-scale spatial relationships can be modeled with sufficient accuracy to provide important and unique insights.

Computer codes such as MARLWE and ALSOME should be used as a framework for investigating the influence of high energy cascades on microstructure evolution. The consequences of the detailed interactions can be determined with sufficient rigor elsewhere. most likely by molecular dynamics or direct experimental observation. and represented by simple models within a MARLOWE/ALSOME framework. Molecular dynamics simulations of critical sized lobes and loop formation in cascades are crucial to starting with the most realistic defect distributions. Careful, innovative experimental investigations of the primary damage state must continue to be done. Properly calibrated and parameterized for the problem under investigation, ALSOME can provide a realistic representation of many aspects of microstructure evolution because it incorporates the explicit spatial dependence necessary to study cascade effects.

FUTURE WORK

The models and methodology will continue to be developed. Immediate emphasis is on using MARLWE to model the subcascade configurations in many different metals and make comparisons with observed defect formations.

REFERENCES

1. M. S. Daw and M. I. Baskes, Phys. Rev. B **29**, 6443 (1984).

2. T. Dlaz de la Rubia, R. S. Averback and R. Eenedek, J. Mater. Res., in press. See also contribution to this conference.

3. H. L. Helnlsch. J. Nucl. Mater. 103 & **104**, 1325 (1981).

4. M. Kiritanl. J. Nucl. Mater. 133 6 **134**, **85** (1985).

5. M. T. Robinson and *I*. M. Torrens. Phys. Rev. B **9**, 5008 (1974).

6. H. L. Helnlsch. J. Nucl. Mater. **117**, 46 (1983).

7. M. T. Robinson. DAFS Quarterly Progress Report. January=March 1980, DOE/ET-0065/9, U.S. Department of Energy. 54 (1980).

8. H. L. Heinisch. J. O. Schlffgens and O. M. Schwartz, J. Nucl. Mater. **85** 6 **86**, 607 (1979).

9. H. L. Heinlsch. O. G. Doran and D. M. Schwartz, Effects of Radiation on Materials, ASTM Specfal Technical Publication 725 191 (1981).

10. H. L. Heinisch. J. Nucl. Mater. 108 6 **109**, 62 (1982).

11. H. L. Heinlsch. Computer Simulation of Displacement Cascades in Copper, HEOL-TME 83-17 (1983).

12. H. L. Heinlsch and F. M. Mann. J. Nucl. Mater., **122** 6 **123**, **1023** (1984).

13. M. T. Robinson, Nuclear Fusion Reactors, Proc. of the British Nuclear Energy Soc., UKAEA, Culham Laboratory. Sept. 1969.368 (1970).

14. M. Kiritani, "Recoil Energy Effects on Microstructures," Proc. Third International Conf. on Fusion Reactor Materials, Karlsruhe. Germany. Oct. 4-8, 1987 (1988).

15. M. L. Jenkins. K. H. Katerbau and M. Wllkens. Phil. Mag., **34**, 1141 (1976).

16. M. L. Jenkins. N. G. Norton and C. A. English. Phil. Mag. A, **40**, 131 (1979).

17. H. L. Heinlsch, Phil. Mag. A, **45**, 1085 (1982).

18. M. T. Robinson, Phys. Rev. B, **27**, 5347 (1983).

19. M. Hou, Phys. Rev. B, **31**, 4178 (1985).

21. R. Dierckx. J. Nucl. Mater., **144**, 214 (1987).

20. R. Eenedek. J. Appl. Phys., **52**, 5557 (1981).

22. R. L. Simons, J. Nucl. Mater., **141-143**, 665 (1986).

23. P. Jung et al., ASTM STP 782, eds. H. R. Erager and L. S. Perrin, 963 (1982).

24. J. H. Klnney. M. W. Gulnan and Z. A. Munir, J. Nucl. Mater., **122** 6 **123**, 1028 (1984).

25. L. E. Rehn and P. R. Okamoto. Mater. Sd. Forum. **15-18**, 985 (1987).

26. D. G. Doran and R. A. Burnett. in Interatomic Potentials and Simulation of Lattice Defects, eds P. C. Gehlen. J. R. Beeler. Jr. and R. I. Jaffee. Plenum Press. NY, 403 (1972).

27. J. E. Sanders, Rad. Eff., **51**, 43 (1980).

28. U. Theis and Wollenberger. J. Nucl. Mater., **88**, 121 (1980).

29. T. H. Blewitt, A. C. Klank. T. Scott and W. Weber. Proc. Int. Conf. on Radiation=Induced Voids in Metals, Albany, NY, 1971, eds J. W. Corbett and L. C. Iannlello. 757 (1972).

30. M. J. Norgett. M. T. Robinson and *I*. M. Torrens. Nucl. Eng. Design, **33**, 50 (1975).

31. W. Schilling. P. Ehrhart and K. Sonnenberg. Proc. Int. Conf. on Fundamental Aspects of Radiation Damage in Metals, Gatlinburg. TN, Oct, 1975. eds M. T. Robinson and F. W. Young. 470 (1976).

32. R. S. Averback. R. Benedek and K. L. Merkle, J. Nucl. Mater., 75, 162 (1978).

33. D. G. Doran, R. L. Simons and W. N. McElroy in Properties of Reactor Structural Alloys After Neutron or Particle Irradiation, ASTM STP 570, 290 (1975).

34. O. G. Doran and J. O. Schiffgens. Proc. of the Workshop on Correlation of Neutron and Charged , ——— Oak Ridge. TN, June, 1976. CONF-760673, (1976).

35. J. R. Beeler, Jr., Phys. Rev 150, 470 (1966).

36. T. Muroga and S. Ishino, J. Nucl. Mater., 117, 36 (1983).

37. T. Muroga. K. Kitajima and S. Ishino, J. Nucl. Mater., 133 6 134, 378 (1985)

6. DEVELOPMENT OF STRUCTURAL ALLOYS

6.1 Ferritic Stainless Steels

IRRADIATION CREEP BEHAVIOR OF THE FUSION HEATS OF HT9 AND MODIFIED 9Cr-1Mo

R. J. Puigh (Westinghouse Hanford Company) and F. A. Garner, (Pacific Northwest Laboratory)

OBJECTIVE

The object of this effort is to determine the creep behavior of ferritic steels that might be employed in the construction of fusion reactors.

SUMMARY

In-reactor creep data on the fusion heats of HT9 and a modified 9Cr-1Mo steel have been obtained from irradiation of pressurized tube specimens in the FFTF reactor. These irradiations were conducted on specimens which reached ~50 dpa at 400-540°C and which utilized hoop stresses ranging from 0 to 200 Mpa. The creep behavior of these two alloys was found to be similar and to be consistent with creep data on related alloys irradiated in either EBR-II or FFTF. A correlation describing the irradiation-induced creep component of deformation has been developed and compared to the available data.

These ferritic steels were also shown to exhibit a superior resistance to creep and swelling at temperatures <520°C when compared to that of the AISI 316 and PCA austenitic alloys also irradiated in the fusion materials program.

Introduction

The ferritic alloy class has been shown to exhibit a number of desirable properties when considered as a structural material for either fission or fusion energy devices. Foremost of these properties is that commercial ferritic alloys have shown an excellent resistance to neutron-induced swelling to very high displacement levels.[1-5] Moreover, the eventual swelling rate in simple ferritic alloys has been shown to be significantly less6 than that observed in the austenitic alloy class'. Microstructural examinations of these alloys, however, have shown that secondary phases are formed during neutron irradiation',' and these phases may affect the mechanical properties[3,9].

Recent results from in-reactor creep experiments have indicated that creep strains are also relatively small. Studies of selected ferritic alloys to a peak fluence of 37 dpa for irradiation temperatures of 400 to 500°C and hoop stresses of 205 and 290 MPa have shown small creep strains[10]. Data on HT9 to a peak fluence of 10 x 10^{22} n/cm^2 (E > 0.1 MeV) or approximately 50 dpa in EBR-II have shown a linear fluence dependence and a non-linear stress dependence[11]. Finally, in-reactor creep data on several comnercial ferritic alloys to a peak fluence of 5.7 x 10^{22} n/cm^2 [E > 0.1 MeV] or approximately 28 dpa in FFTF have shown similar dependencies on fluence and stress[12].

This report addresses the results of a ferritic creep experiment conducted in the Materials Open Test Assembly (MOTA) in FFTF. This experiment was undertaken to determine the in-reactor creep behavior of those heats of the ferritic alloys HT9 and 9Cr-1Mo currently employed in the U.S. Fusion Materials Program. These data are compared to data on similar ferritic steels as well as austenitic steels used in either the U.S. Liquid Metal Reactor or Fusion Materials programs.

Experimental procedure

Pressurized tubes were fabricated from the fusion heats of the ferritic alloys HT9 and 9Cr-1Mo using techniques described elsewhere". The composition and thennomechanical treatment for these and other alloys described in this report are given in Table 1. The HT9 alloy was received in the form of bar stock and was drilled to produce tubing with dimensions 4.78 mm OD x 4.17 mm ID. The 9Cr-1Mo alloy was received in the form of cladding measuring 4.55 mm OD x 4.22 mm ID. Endcaps for each alloy were fabricated from HT9 and were electron beam welded to tubing segments which were 19.81 mm in length. One endcap on each tube had a capillary hole for pressurization of the specimen. Specimens for irradiation at 420 and 520°C (and the HT9 specimen at 600°C) were filled with helium to the desired pressure. The 9Cr-1Mo specimens for irradiation at 600°C were filled with isotopically enriched Kr/Xe tag gas to provide in-reactor stress rupture data[14]. The closure weld for gas containment was made with a laser beam which passed through the glass port of the pressure vessel and sealed the hole in the endcap. All specimens were checked for helium leaks prior to irradiation. Definitions of the parameters describing the mechanical state of the pressurized tubes are given elsewhere[15].

The specimen diameters were measured using a non-contacting laser system which as an accuracy of ±2.5 x 10^{-4} mm. Measurements were performed at five equidistant positions (0.267 cm apart) which were symmetric about the axial midplane of the specimen. The middle three measurements were averaged to yield an average diameter for the tube. The hoop strain for a given specimen was determined from measurement of its diameter before and after irradiation. The repeatability in the hoop strain measurement is ± 0.05% for this size tube.

Table 1. Chemical Compositions (Weight Percent)**

Alloy (Heat No.) [TMT]*	C	Mn	P	S	Si	Ni	Cr	Mo	V	Nb	Ti	Co	Cu	Al	B	W
Fusion																
HT9 (9607R2) [1038°C/5m/AC+760°C/2.5h.AC]	0.20	0.57	0.016	0.003	0.17	0.51	12.1	1.04	0.28	--	0.01	5	0.07	0.007	<0.001	0.45
9C4-1Mo (30176) [1038°C/5m/AC+760°C/1h/AC]	0.081	0.37	0.010	0.003	0.11	0.09	8.61	0.89	0.209	0.072	0.01	10	0.04	0.007	<0.09	<0.01
PCA (K280) [20% CW]	0.048	1.83	0.014	0.02	0.52	16.13	14.31	1.95	0.04	0.02	0.01	4	0.02	0.05	0.001	--
LMR																
HT9/1 (84425) [1038°C/5m/AC+760°C/30m/AC]	0.20	0.51	0.002	0.005	0.28	0.54	11.86	1.02	0.30	--	0.01	1	0.01	0.002	<0.001	0.54
HT9/2 (91353) [1038°C/5m/AC+760°C/30m/AC]	*0.20*	*0.59*	--	--	*0.38*	*0.62*	*11.95*	*0.99*	*0.30*	--		--	--	--	--	0.52
HT9/3 (R74075) [1052°C/30m/AC+780°C/2.5h/AC]	0.20	0.64	--	--	0.3	0.64	12.3	0.86	0.29	--	-	25	--	--	0.008	0.44
9Cr-1Mo/1 (30394) [1038°C/30m/AC+760°C/30m/AC]	0.094	0.45	0.014	0.004	0.37	0.09	8.11	1.03	0.20	0.072	0.00	56	0.04	0.024	--	--
9Cr-1Mo/2 (91887) [1038°C/5m/AC+760°C/1h/AC]	0.045	0.38	--	--	0.09	0.08	8.99	0.94	0.19	0.18	0.00	--	--	--	--	<0.01
316 SS/1 (81600) [20% CW]	0.047	1.57	0.003	0.005	0.52	13.76	17.56	2.34	0.02	--		0.016	0.01	<0.005	<0.0005	--
316 SS/4 [20% CW]	0.047	1.65	0.002	0.006	0.58	13.30	17.29	2.61	0.01	--		0.03	0.01	<0.01	<0.0005	--

*TMT = Thermomechanical Treatment.
**Balance is iron (Fe).

The test matrix for this experiment contained six HT9 and five 9Cr-1Mo pressurized tube specimens for each irradiation temperature (420, 520 and 600°C). The hoop stresses for each alloy/irradiation temperature combination range from 0 to a maximum of 240 MPa at 420°C, 200 MPa at 520°C and 140 MPa at 600°C. This test matrix was placed in the (MOTA) irradiation vehicle for irradiation in the Fast Flux Test Facility (FFTF) located in Richland, Washington. Details of the MOTA configuration and its operation can be found in reference 14. Irradiation at 420°C was conducted in a weeper canister which operates at the reactor coolant temperature. The specimens for irradiation at 520 and 600°C were in gas-gapped canisters.

The irradiation began in January, 1984 with the beginning of FFTF cycle 4 operation. During the cycle 4 irradiation, one of the 9Cr-1Mo creep specimens ruptured in the 600°C canister. The canister apparently failed to vent in a timely fashion; therefore, the tubes were blanketed with gas and the temperature rose to a peak temperature of 820°C within several minutes. This elevated temperature led to additional specimen ruptures causing the loss of a majority of the creep specimens at this irradiation temperature. The canister temperature recovered after approximately five minutes of operation above its operating temperature range (595-605°C) but it was decided to discard the remaining specimens in the 600°C canister.

During FFTF cycle 4, the specimens at 420 and 520°C accumulated a peak fluence of 3×10^{22} n/cm^2 (E > 0.1 MeV) or approximately 15 dpa. The specimens were discharged from the MOTA, diameter measurements performed on the specimens irradiated at 420 and 520°C, and these specimens were reconstituted into new MOTA hardware for continued irradiation. These specimens were irradiated in FFTF cycles 5 and 6 before the second interim examination was conducted. The peak total fluence of cycles 4-6 was 10.6×10^{22} n/cm^2 (E > 0.1 MeV) or approximately 53 dpa.

Results

The stress dependence of in-reactor creep for the fusion heat of HT9 and the modified 9Cr-1Mo is shown in Fig. 1 for a fluence of approximately 10×10^{22} n/cm^2 (E > 0.1 MeV) and for irradiation temperatures of 420 and 520°C, respectively. The total diametral strains for the specimens with zero stress are negligible and do not indicate any evidence of irradiation-induced dimensional change. The in-reactor creep strains at 420°C are slightly less than the in-reactor strains observed at 520°C. Finally, at both temperatures the data suggest a non-linear dependence on stress similar to that observed in other ferritic alloys[11,12].

Shown in Fig. 2 and 3 are the effective creep strain data as a function of neutron fluence for the fusion heats of HT9 and 9Cr-1Mo, respectively. The effective creep strain for this size specimen is given by

$$\bar{\epsilon} = 1.27 \left[\left(\frac{\Delta D}{D_o}\right)_{\text{total}} - \left(\frac{\Delta D}{D_o}\right)_{PO} \right] \qquad [1]$$

where $\bar{\epsilon}$ is the effective creep strain, $\left(\frac{\Delta D}{D_o}\right)_{\text{total}}$ is the measured diametral strain and $\left(\frac{\Delta D}{D_o}\right)_{PO}$ is the specimen with zero stress at the same irradiation temperature and fluence. Also shown in Figures 2 and 3 are data on several Liquid Metal Reactor (LMR) heats of HT9 and 9CR-1Mo which were also irradiated in the same MOTA canisters. The compositions and final thermomechanical treatments for these heats are given in Table 1.

The creep data for both fusion alloys at approximately 420°C are consistent with a previously observed linear dependence on fluence in several ferritic alloys [10,12]. For HT9, the fusion heat exhibits less creep strain at 100 MPa when compared to the LMR heats at approximately 410°C. For 9Cr-1Mo, the heats irradiated in the fusion and LMR programs exhibit comparable strains at approximately 415°C. Comparing the LMR data at 490°C with the fusion data at 520°C, the data for both alloys are consistent with a linear fluence dependence. Also, the LMR and fusion heats of both alloys exhibit comparable strains.

Figure 4 shows the creep behavior of the fusion ferritic heats compared to that of the fusion PCA and the LMR 316 austenitic alloys, whose compositions and thermomechanical treatments are also given in Table 1. At approximately 420°C, both austenitic alloys exhibit larger creep strains than are observed in the fusion ferritic heats. Comparing the LMR austenitic data at 490°C with the ferritic alloy data at 520°C, the creep strains of the fusion ferritic heats and the PCA alloy are similar while the 316 SS alloy exhibits significantly larger strains.

Discussion

To investigate the temperature dependence of creep in the ferritic alloys the following model was assumed:

$$\bar{\epsilon} = B \, \Phi t \, \bar{\sigma}^{n}$$

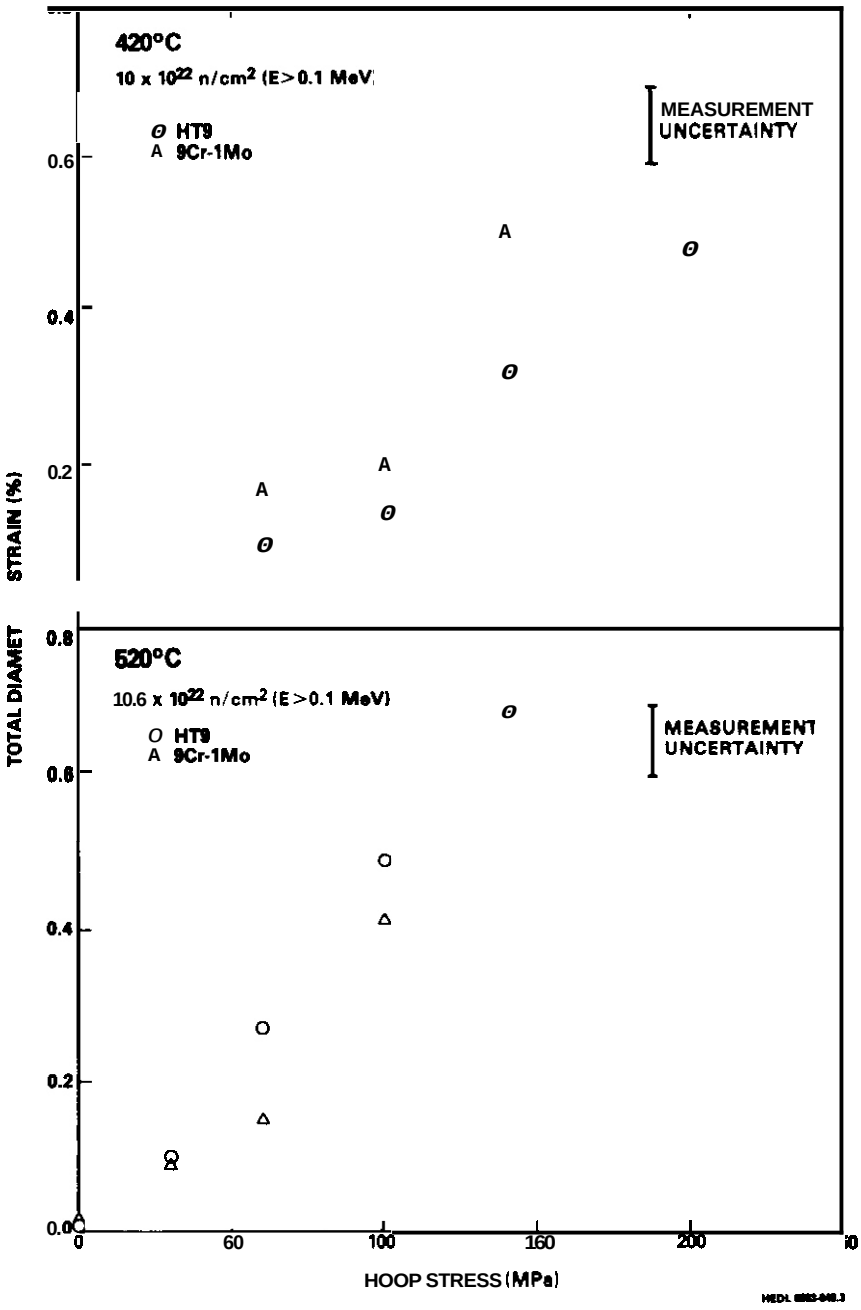

Fig. 1. Total diametral strains versus hoop stress, showing comparisons of the HT9 and 9Cr-1Mo fusion heats for the average irradiation temperatures of 420°C (top) and 520°C (bottom).

where $\bar{\epsilon}$ is the effective creep strain (%), Φt is the E>0.1 Mev fluence in units of (10^{22} n/cm^2), $\bar{\sigma}$ is the effective stress (MPa), and n is a stress exponent. The average creep coefficient, $\bar{B}$, contains the temperature dependence.

The data from this experiment and that of reference 12 are consistent with a stress exponent of $1 \leq n < 2$, with $n \approx 1.3$ providing the best fit to the data. These two sets of data were used to calculate the average creep coefficient for a given combination of fluence and irradiation temperature for each alloy. A plot of $\bar{B}$ as a function of irradiation temperature is shown in Fig. 5 for HT9 and 9Cr-1Mo. The standard deviation in these average values is indicated by error bars whenever they are larger than the symbol size. For irradiation temperatures less than 520°C, the values for $\bar{B}$ for each ferritic alloy increase only slightly. One interpretation of these results is that the average in-reactor creep coefficient for ferritic alloys is relatively insensitive to temperatures in the range 380-520°C. For HT9, the LMR heats exhibit the largest values of $\bar{B}$. For temperatures of approximately 420°C, the fusion heat shows a smaller average

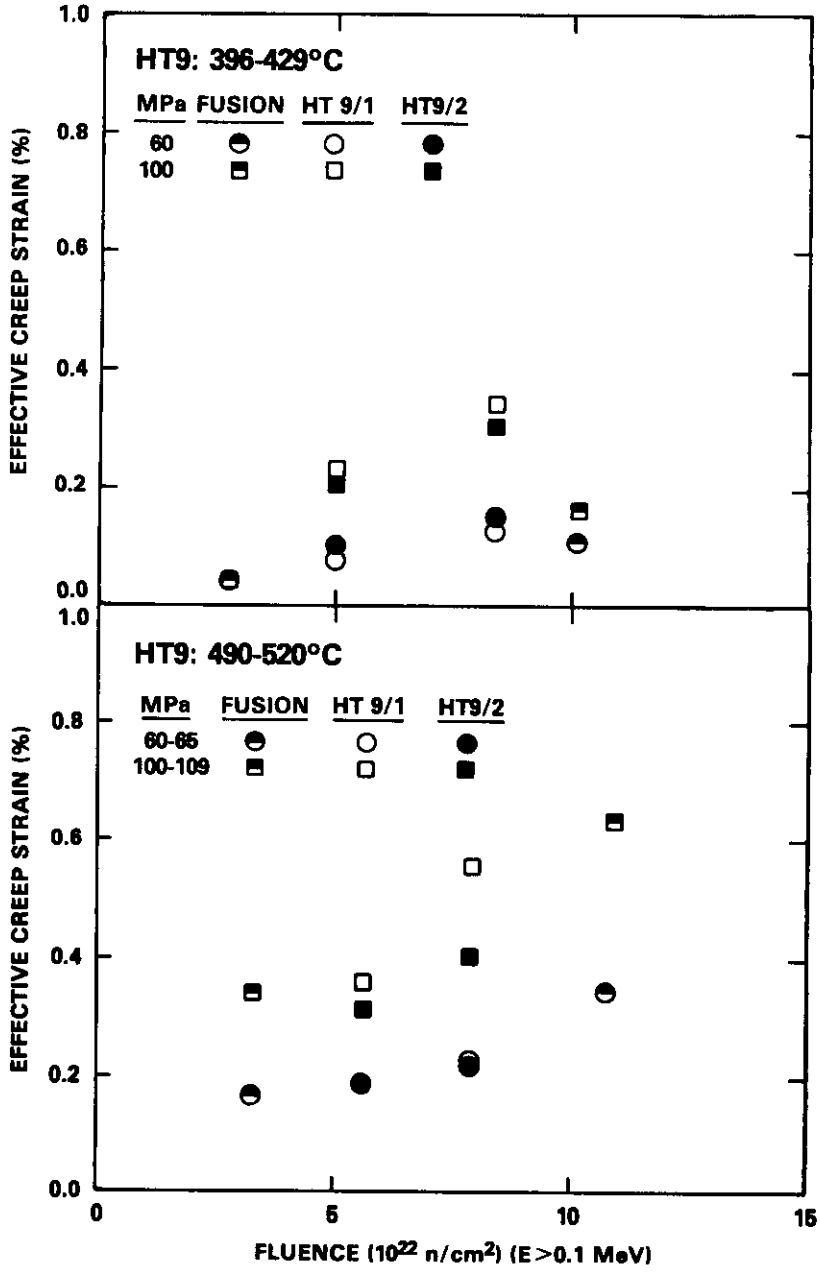

Fig. 2. In-reactor creep of various heats of HT9 at hoop stresses of approximately 60 and 100 MPa for irradiation temperaturs of 396-249°C (top) and 490-529°C (bottom).

creep rate when compared to the other heats investigated in this work. At 520°C, the fusion heat shows comparable behavior when compared to the other heats of HT9. Also, thee data from EBR-II exhibit slightly larger values for $\bar{B}$ when compared to the same heat irradiated in FFTF. For 9Cr-1Mo, all the heats exhibit comparable creep behavior over the temperature range of 400-520°C. At 570°C, the B values for all the LMR ferritic alloys investigated[12] are larger with $\bar{B}$ values in the range of 2.5 to 5 x 10^{-28} $MPa^{-1.3}$ $(n/cm^2)^{-1}$. Based upon limited thermal creep data discussed in reference 12, these larger values for $\bar{B}$ are attributed to the onset of thermal creep. Finally, as also reported in reference 12, the $\bar{B}$ values for HT9 at 653°C are significantly larger than their values at 570°C.

The following phenomenological creep model has been assumed previously to describe the in-reactor creep behavior of the ferritic alloys:

$$\bar{\epsilon} = B\sigma^n \phi t + DS_0 \sigma + \bar{\epsilon}_T \qquad (3)$$

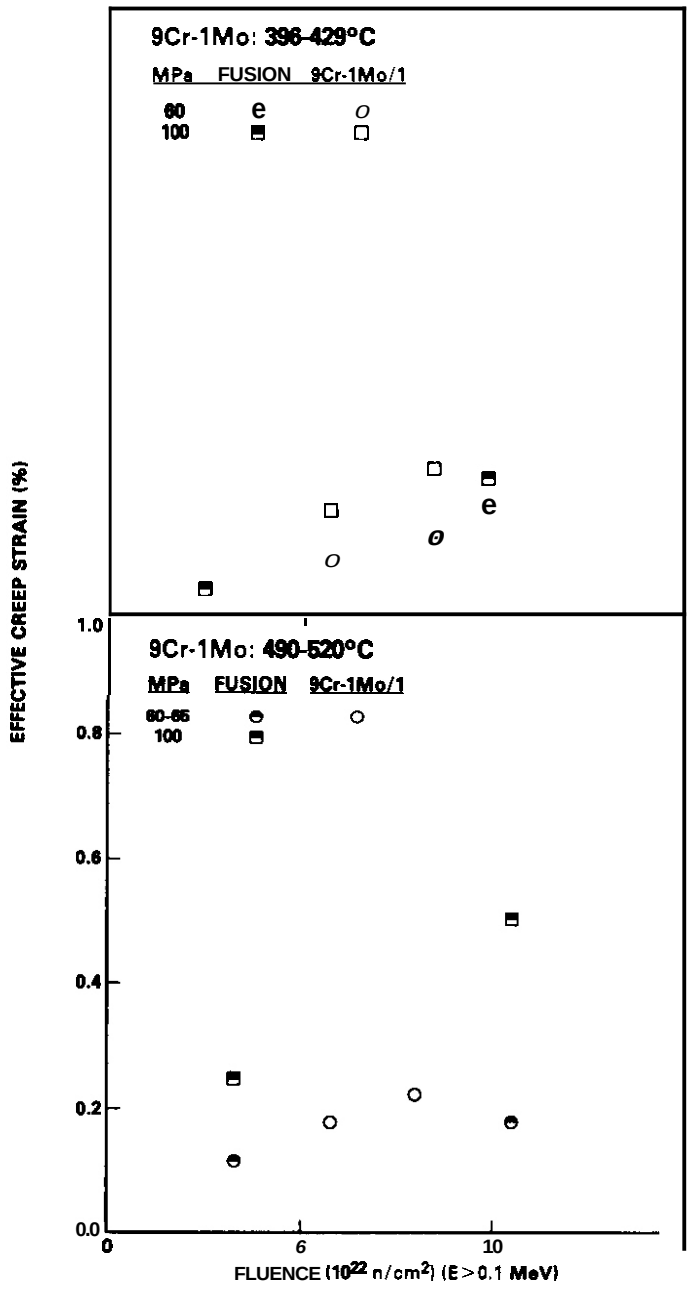

Fig. 3. In-reactor creep of various heats of 9Cr-1Mo at hoop stresses of approximately 60 and 100 MPa for average irradiation temperatures of 306-429°C (top) and 490-520°C (bottom).

where B is the irradiation-induced creep coefficient (possibly dependent on temperature), D is the swelling-enhanced creep coefficient (MPa^{-1}), S_o is the lineal swelling (%), and ϵ_T is the thermal component of the effective creep strain (%). This model was developed for austenitic steels[16] and has been applied to irradiation creep of ferritic alloy 2¼Cr-1Mo[17]. The value for n was assumed to be 1.3 for both HT9 and 9Cr-1Mo. The value for D (6.1×10^{-6} MPa^{-1}) is taken from the best fit to the 2¼Cr-1Mo data[17]. For fluences less than 10×10^{22} n/cm^2 (E > 0.1 MeV), however, the maximum contribution from the second term would be less than a fractional strain of 6×10^{-8} (at 420°C and 10×10^{22} n/cm^2) based upon the present data. Therefore, the second term in Eq. (3) was not included in the fitting process. The irradiation-induced creep coefficient B was modeled as a polynomial in temperature and a linear regression analysis was used to determine the best fits to the HT9 and 9Cr-1Mo data. Only the data from the MOTA irradiations were used to determine the coefficients of B. The contributions thermal creep were assumed to be small for irradiation temperatures <520°C.

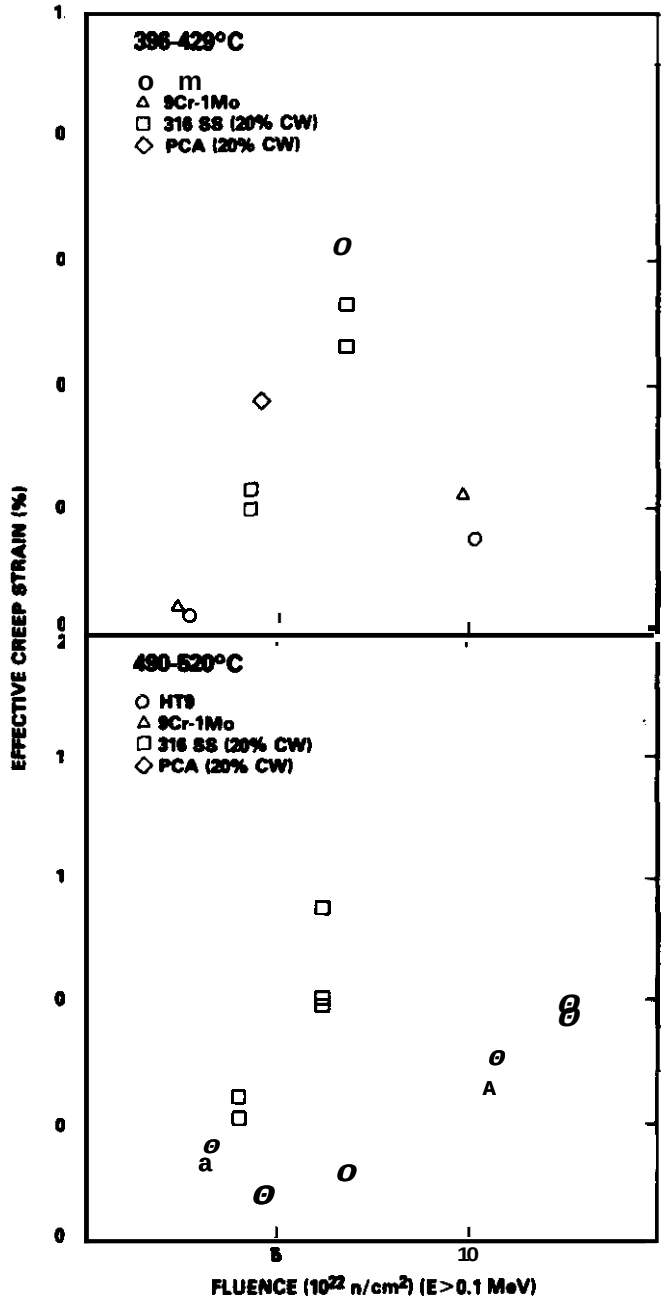

Fig. 4. Comparison of creep of the fusion heats of HT9 and 9Cr-1Mo and the 316 and PCA austenitic alloys at average irradiation temperatures of 396-429°C (top) and 490-520°C (bottom).

Therefore, B an B are equivalent over this temperature range. The coefficients developed for both HT9 and 9Cr-1Mo are summarized in Table 2. Predictions based on these coefficients are indicated by the solid curves in Fig. 5. The values of B for 9Cr-1Mo are slightly smaller than those for HT9.

This model is valid only over the temperature range of 400-540°C and should not be extrapolated to lower temperatures. For temperatures greater than 540°C, earlier studies have shown the thermal component of creep becomes important for reactor-relevant stresses (σ<150 MPa) and should be included. A phenomenological model for thermal creep of HT9 has been developed for the limited temperature range of 500 to 600°C[18] and could be utilized to describe the total in-reactor creep behavior of HT9 over the temperature range of 400-600°C. Similarly, an empirical model for the minimum thermal creep rates of 9Cr-1Mo[19] has been developed and could be utilized to predict the thermal component of the in-reactor creep strain.

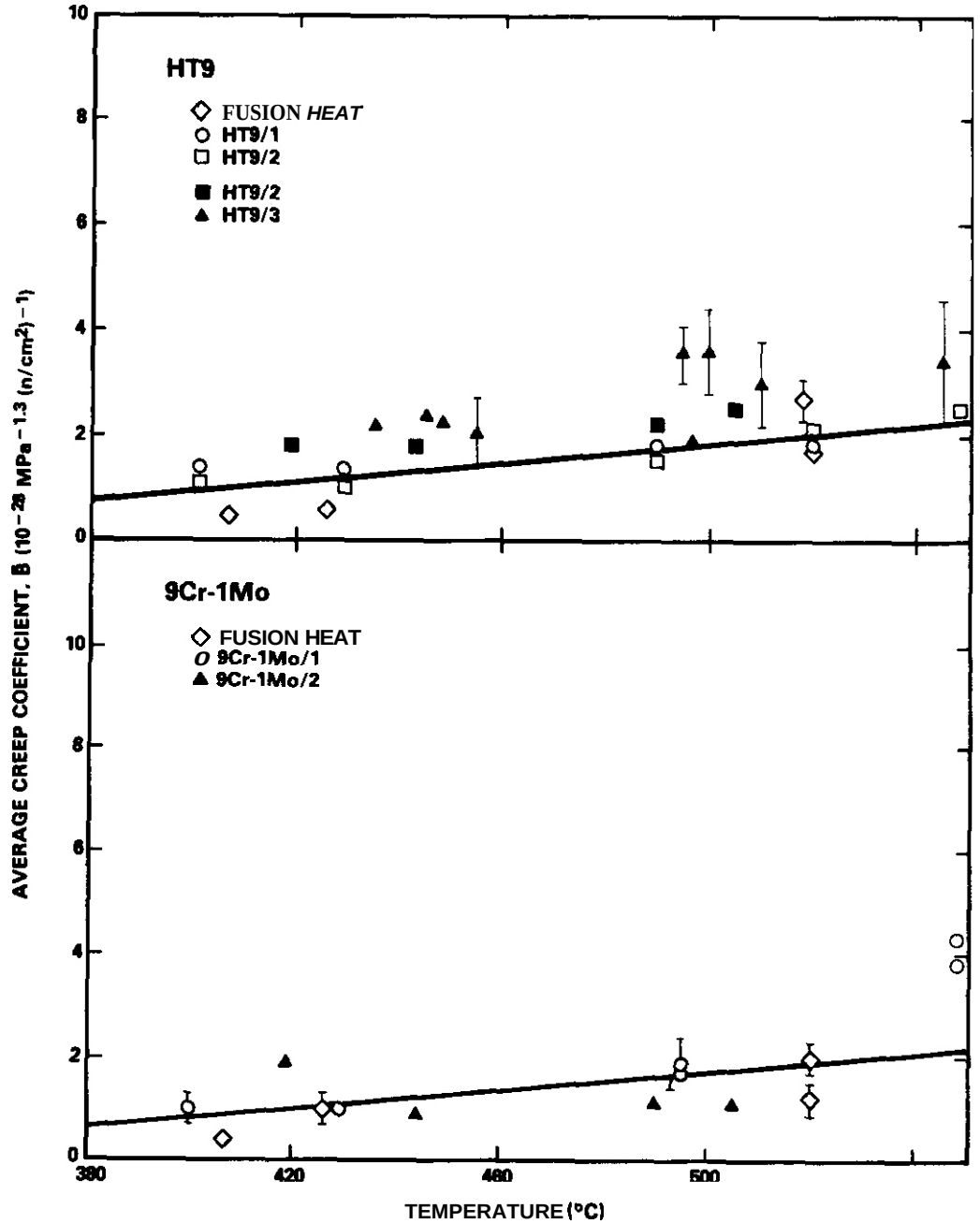

Fig. 5. Temperature dependence for the average creep coefficient B for different heats of HT9 (top) and 9C4-1Mo (bottom). The open symbols represent data from irradiations in FFTF, and the solid symbols represent data from irradiations in ERR-11.

Conclusions

Irradiation creep data for the fusion heats of HT9 and 9Cr-1Mo have been obtained to a peak fluence of 10 x 10^{22} n/cm^2 (E > 0.1 MeV) approximately 50 dpa. No evidence of swelling was observed. The in-reactor creep strains for both alloys were similar and consistent with in-reactor creep data on similar alloys irradiated in either ERR-I1 or FFTF. For irradiation temperatures less than 520°C the ferritic heats continue to exhibit superior creep resistance when compared *to* 316 stainless steel and the fusion PCA alloy.

Table 2. Model Coefficients for Irradiation Induced Creep of Ferritic Steels

Coefficient (units)	HT9	9Cr-1Mo
$B[10^{-26}\ \%\ MPa^{-1.3}\ (n/cm^2)^{-1}]$	$-2.9\ t\ 9.5 \times 10^{-3}T$	$-2.9\ t\ 9.0 \times 10^{-3}T$
$D[10^{-6}\ MPa^{-1}]$	6.1	6.1
n	1.3	1.3

T = temperature (°C).

FUTURE WORK

Data are now available to much higher fluence levels. These will be analyzed in the next reporting period.

References

1. Powell, R. W., Peterson, D. T., Zimmerschied, M. K., and Bates, J. F., *Journal* of Nuclear Naterials, Vols. 103 and 104, 1981, pp. 969-974.

2. Gelles, D. S., Journal of Nuclear Naterials, Vols. 103 and 104, 1981, pp. 975-980.

3. Gelles, D. S., Thomas, L. E., Topical Conference on ferritic Alloys for Use in Nuclear Energy Technologies, Snowbird, UT, 1983, pp. 559-568.

4. Gelles, D. S., Journal of Nuclear Materials, Vols. 122 and 123, 1984, pp. 207-213.

5. Garner, F. A. and Gelles, D. S., in this semiannual report.

6. Gelles, D. S. and Meinecke, R. L. in Alloy Development for Irradiation Performance Semiannual Progress Report, DOE/ER-0045/11, 1983, pp. 103-107.

7. Garner, f. A., Journal of Nuclear Naterials, Vol. 122, 1984, pp. 459-471

8. Gelles, D. S., Journal of Nuclear Naterials, Vol. 148, 1987, pp. 136-144.

9. Gelles, D. S., Journal of Nuclear Naterials, Vol. 149, 1987, pp. 192-199.

10. deBremaecker, A., and Huet, J. J., in Dimensional Stability and Wechanical Behaviour of Irradiated Metals and Alloys, Brighton, England, April 11-13, 1983, pp. 117-120.

11. Chin, B. A., in ref. 3, pp. 593-599.

12. Puigh, R. J., in Effects of Radiation on Materials: Twelfth Conference, ASTM STP 870, F. A. Garner and J. S. Perrin, Eds., 1984, pp. 7-18.

13. Puigh, R. J. and Wire, G. L., in ref. 3, pp. 601-606.

14. Puigh, R. J. and Schenter, R. E., in ref. 12, pp. 795-802.

15. Gilbert, E. R. and Blackburn, L. D., Journal Engineering Materials and Technology, Vol. 99, 1977, p. 168.

16. Weiner, R. A., Foster, J. P. and Boltax, A., in Radiation Effects in Breeder Reactor Structural Materials, M. L. Bleiberg and J. W. Bennett, Eds., TMS-AIME, New York, 1977, pp. 865-878.

17. Gelles, D. S. and Puigh, R. J., in ref. 12, pp. 19-37.

18. Amodes, R. J. and Ghonien, N. M., Journal of Nuclear Materials, Vol. 122, 1984, pp. 91-95.

19. Sikka, V. K., Cowgill, M. G. and Roberts, 8. W., in ref. 3, pp. 413-423.

THE EFFECT OF TEMPERING AND AGING ON A LOW ACTIVATION MARTENSITIC STEEL - R.D. Griffin, R.A. Oodd, G.L. Kulcinski (University of Wisconsin) and D.S. Gelles (Battelle Pacific Northwest Laboratory)

OBJECTIVE

The objective of this work is to characterize tempering and aging effects on a low activation 12 Cr martensitic steel.

SUMMARY

An aging and tempering study was done on a low activation martensitic steel. The steel was tempered at 400 C, 500 C, 600 C, 700 C, 800 C, and 900 C for two hours, and at 500 C and 700 C for twenty-four hours. Also, samples which had been tempered at 700 C for 2 hours were subsequently aged for 1000 and 5000 hours at 365 C, 420 C, 520 C, and 600 C. Optical metallography, microhardness tests, and transmission electron microscopy were used to characterize the samples. The results indicated that the Ac_1 for this steel lies between 700 and 800 C. Precipitate identification showed that $M_{23}C_6$ was the primary precipitate which formed. A manganese rich chi phase was also seen in the samples aged at 420 and 520 C.

PROGRESS AND STATUS

Introduction

Ferritic and martensitic steels are being considered as candidate materials for the first wall of fusion reactors because of their swelling resistance and their potential mechanical properties. A more recent requirement for these steels is that they decay to relatively low levels of radioactivity within one hundred to five hundred years. To reach this goal, alloying changes in the current steels must be made. The steel of this study, L9, was provided by Battelle Pacific Northwest Laboratories, and was patterned after HT-9 with the exception of a lower carbon content. The compositions of HT-9 and L9 are shown in Table 1. To achieve the desired decay in activation the nickel and molybdenum were eliminated. The tungsten content of L9 was increased to replace the molybdenum, which is needed for high temperature strength. The tungsten level was held at 1% to avoid formation of intermetallics. Nickel and carbon are austenite stabilizers, and their loss was compensated for by increasing the manganese content. Although neutron irradiation results on L9 have been published,[1-5] there has not been a study to show the response of this steel to heat treatment. In this work, this omission is addressed.

Table 1. The Composition of HT-9 and L9 in Weight Percent

	Cr	C	V	W	Mn	Ni	Mo	S	Si	N	P
HT-9	12	0.20	0.3	0.5	0.6	0.5	1.0	$\leq$ 0.02	0.4	---	$\leq$ 0.03
L9	11.81	0.097	0.28	0.89	6.41	---	---	0.005	0.11	0.003	0.005

Experimental Procedure

The alloy was received in the rolled condition and was first austenitized at 1000 C for twenty hours followed by an air cool to room temperature, and then reheated to 1100 C for ten minutes and allowed again to air cool to room temperature. To determine the tempering response of the steel it was held for two hours at 400, 500, 600, 700, 800, and 900 C, and for twenty-four hours at 500 and 700 C. Steels whfch were aged first received a two hour temper at 700 C, and then were aged for one thousand and five thousand hours at 365, 420, 520, and 600 C. Optical metallography, microhardness and transmission electron microscopy (TEM) were used to characterize the heat treated steel.

Results

The steel formed a fully martensitic structure when air cooled as shown in the optical images of the rolled, austenitized only, and tempered steel (Fig. 1). In many of the images prior austenite grain boundaries are visible. The average size of these grains was 120 μm.

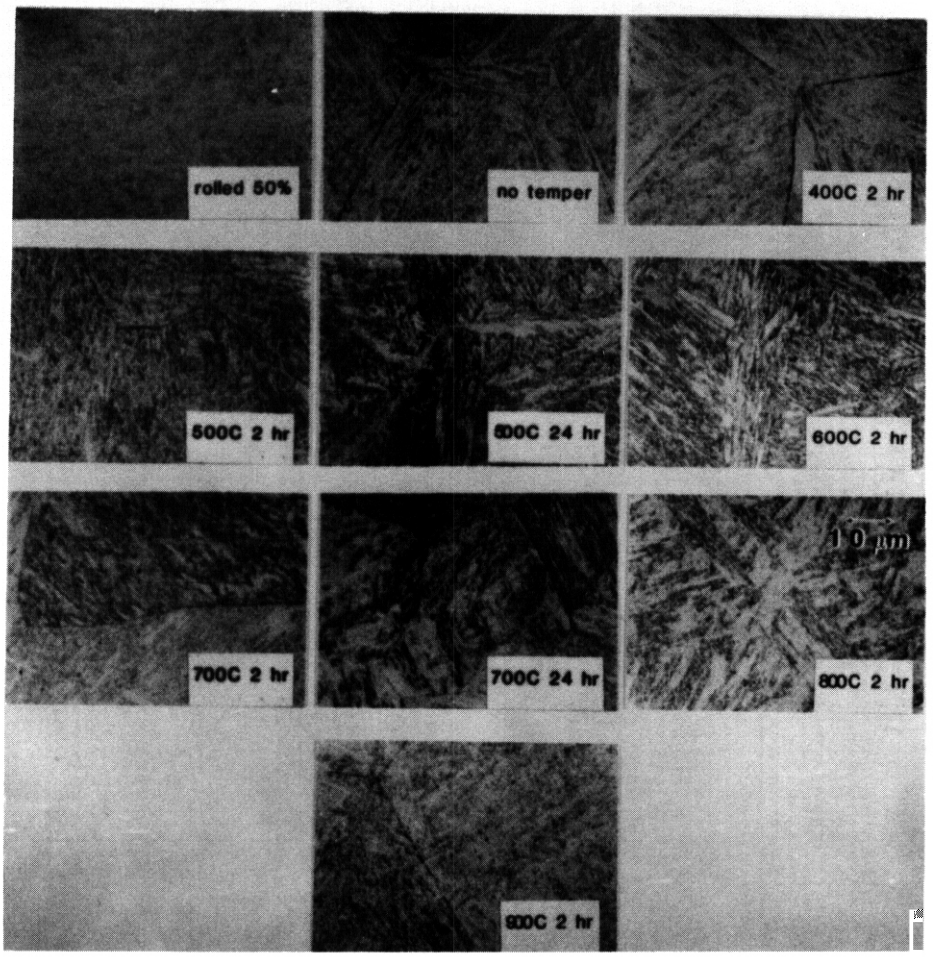

Figure 1. Optical images of the rolled, austenitized only, and tempered L9.

Figure 2 shows the Vickers microhardness results for the austenitized and tempered steel. The hardness dropped sharply when the steel was tempered between 500 and 700 C and then increased for tempering temperatures greater than 700 C. This increase indicated austenite formation with subsequent transformation to martensite on cooling to room temperature.

In Fig. 3, TEM images of the precipitates extracted from the tempered steel are shown. The precipitates which formed at 400 and 500 C for two hours within the martensite laths were elongated multigrains and were tentatively identified as M_3C. Figure 4 shows an EDS spectrum from one of these precipitates. The metal composition of this phase in weight percent was approximately 65% Fe, 30% Cr and 5% Mn. The precipitates in the sample tempered for twenty-four hours at 500 C were a mixture of M C and $M_{23}C_6$. The $M_{23}C_6$ tended to be somewhat rounder and single grain, although their shape varied. A? 600 C and higher, $M_{23}C_6$ was the only precipitate which was seen. At these higher temperatures it tended to form at the boundaries between the martensite laths. Most of the images in Fig. 3 contain prior austenfte grain boundaries which were dotted with precipitates. At all the tempering temperatures the grain boundary precipitates were identified as $M_{23}C_6$. Ffgure 5a shows an image from $M_{23}C_6$ and Fig. 5b is an EOS spectrm from $M_{23}C_6$. The metal composition of $M_{23}C_6$ was approximately 58% Cr, 27% Fe, 10% W, 3% Mn and 2% V. Figure 5c shows two micro-diffraction patterns used to identify the phase.

In the course of examination, two fnclusions were found scattered throughout the samples. Figures 6 and 7 are results from these inclusions. Figure 6a and 6b are TEM images of MnS. Figure 6c is a MnS EDS spectrum and Figs. 6d and 6e are its electron micro-diffraction patterns. The MnS particles were large round particles which were generally seen in groups. Figure 7a is an image of spinel, an oxide seen in the steel when it was tempered at greater than 500 C. The image shows the typical rectangular shape of the phase. Figure 7b shows its typical EDS spectrum, rich in manganese and chromium. The small amounts of titanium and alumfnum in the oxide must have originated during the steel's fabrication. Figure 7c and 7d are two characteristic convergent beam electron diffraction patterns from spinel.

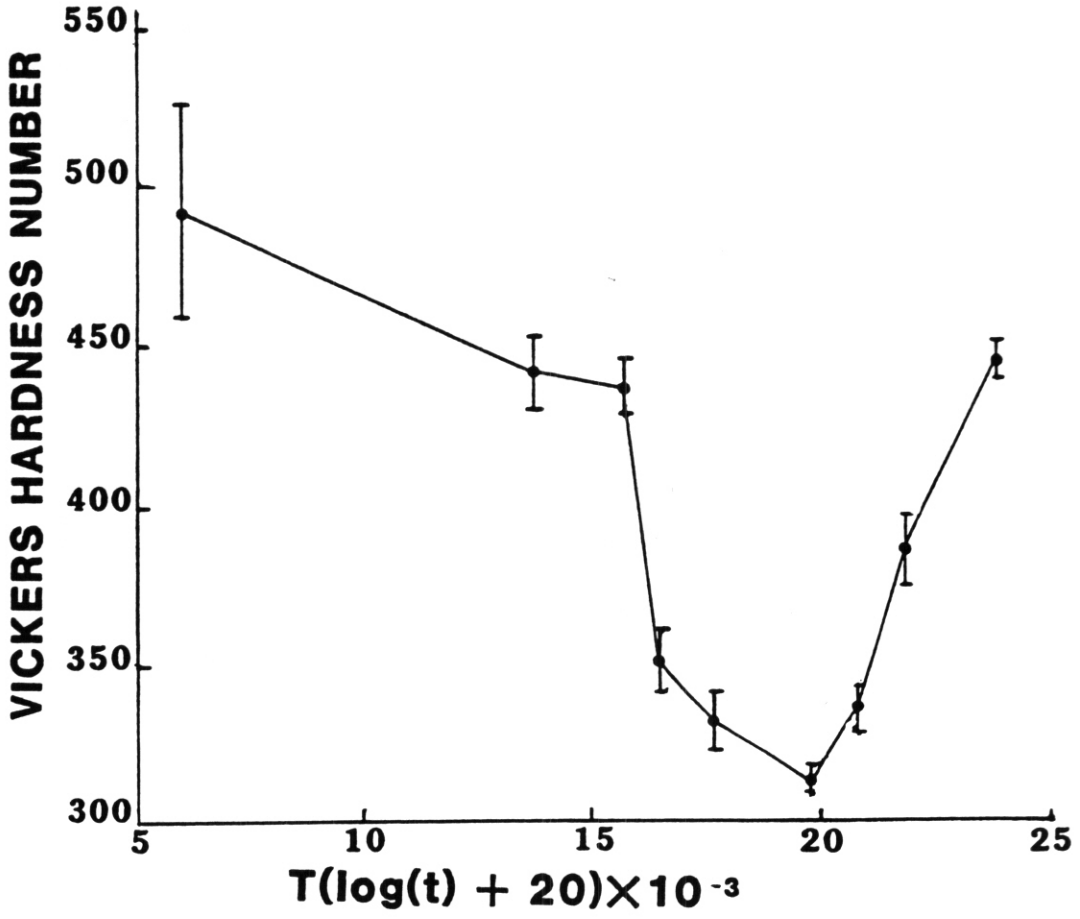

Figure 2. Vickers microhardness results from the austenitized only and tempered L9.

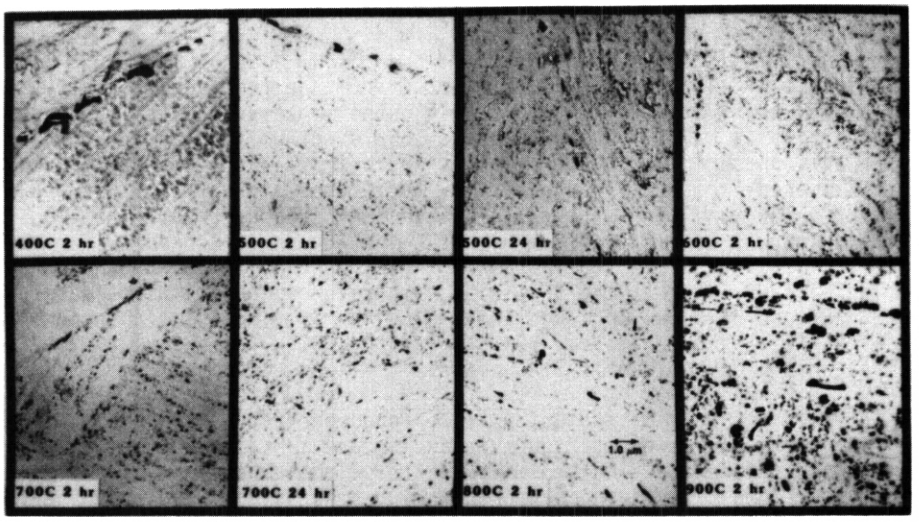

Figure 3. TEM images of extracted precipitates from tempered L9.

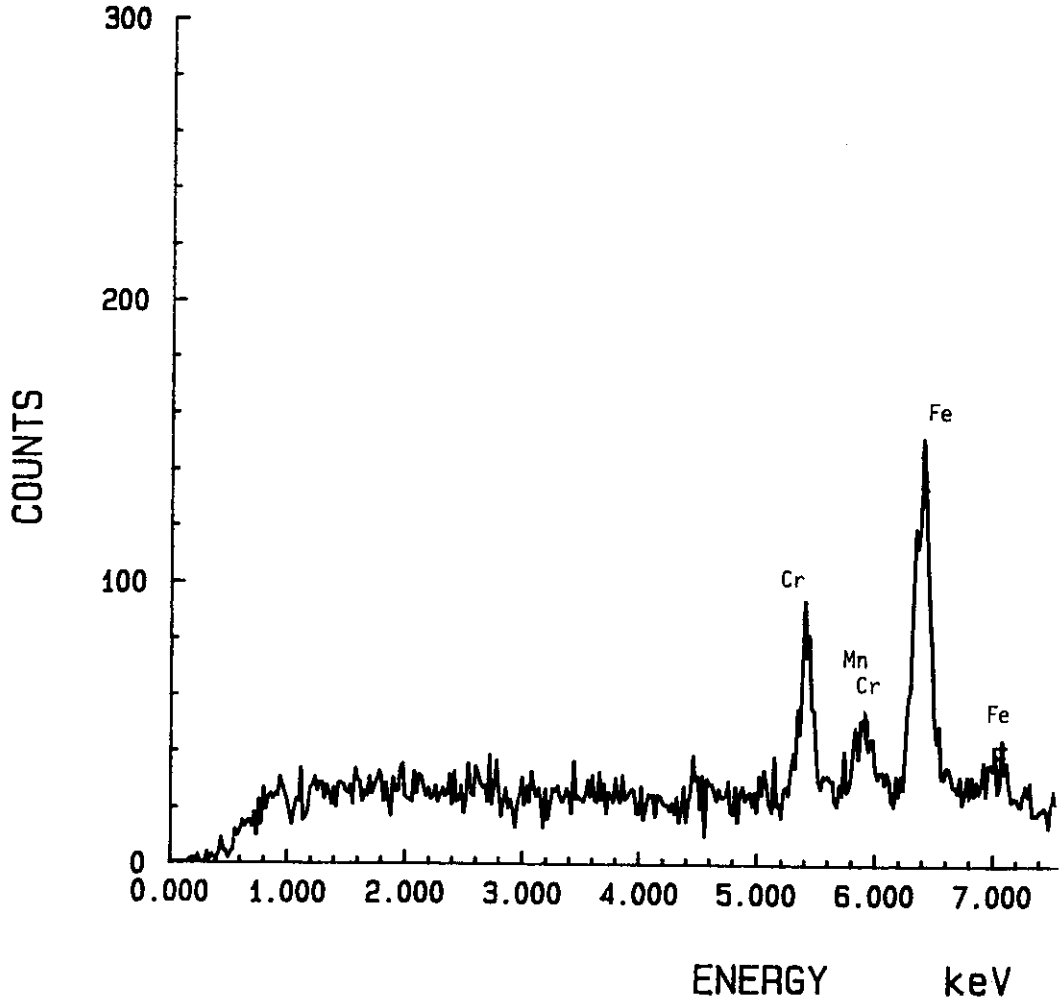

Figure 4. EDS spectrum from the phase which has been tentatively identified as M_3C.

The untempered steel consisted of lath martensite with a very high dislocation density. With tempering, the precipitate population developed and up to 800 C, the dislocation structure began to recover with the remaining dislocations tending to form subgrains. The body centered tetragonal martensite also transformed to body centered cubic ferrite. At 800 and 900 C, the precipitates have coarsened and some areas appear to be new untempered martensite. In Fig. 8, the TEM thin foil images of the tempered and untempered steel are shown.

In Fig. 9, a set of optical micrographs of the tempered steel aged for 1000 and 5000 hours is shown. The samples aged at the lower temperatures looked similar to the tempered steel while at the higher temperatures the structure was altered. Figures 10a and 10b present the Vickers microhardness results for the 1000 and 5000 hour aging treatments respectively. Again, at the two lower temperatures the results were similar to the steel tempered at 700 C, but at the higher temperatures the hardness has dropped off. Figure 11 shows a set of TEM images from the sample aged for 1000 hours. Figure 12 is a similar set from the 5000 hour aged L9. The aged samples appeared similar to the tempered material. However, at the higher temperatures there were some differences. At 520 and 600 C, more of the grains had a lower dislocation density, and the boundaries between the grains often showed regular dislocation structures. The precipitate structure was also much coarser. Another interesting feature seen in the samples aged at higher temperatures was the occasional appearance of round grains which were free of dislocations and had few, if any precipitates in them. Figure 13 is an image of one of these grains in the steel aged to 5000 hours at 520 C. These grains were shown to be ferrite grains which probably recrystallized during the aging.

Precipitate identification was also performed on the aged L9 conditions. In the steels aged for 1000 hours, $M_{23}C_6$ was the only phase which formed except in the case of the sample aged at 520 C. In this sample, two isolated examples of chi phase were seen. Figure 14a is a TEM image of the phase. Figure 14b shows the EDS spectrum and 14c is the selected area tilt sequence from chi in a ferrite matrix. The

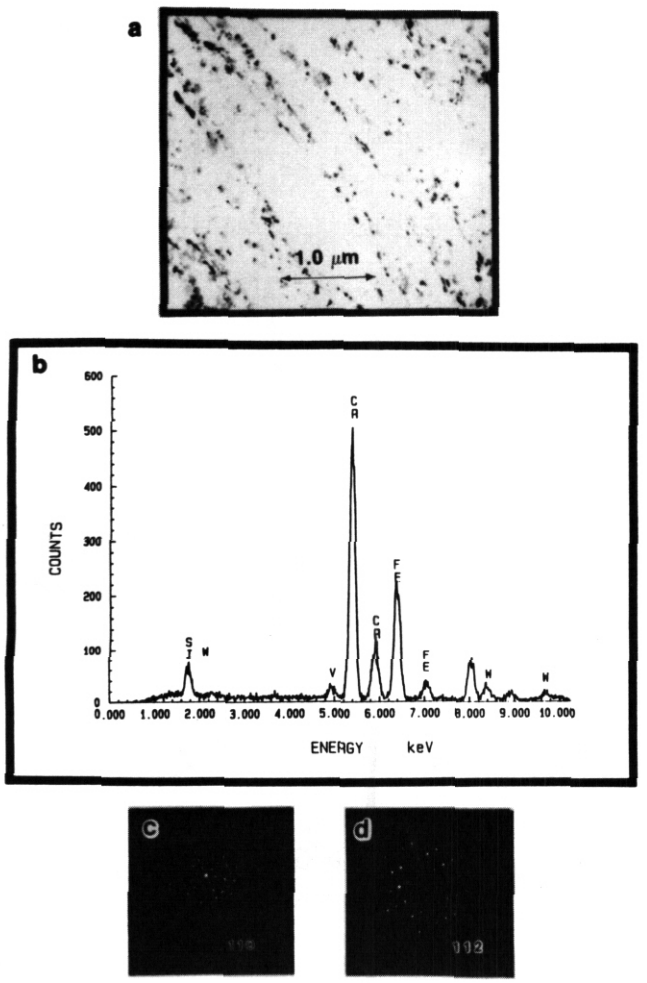

Figure 5. (a) A TEM Image of extracted $M_{23}C_6$.
(b) A typical EOS spectrun from $M_{23}C_6$.
(c) and (d) Micro-diffraction pattern from $M_{23}C_6$.

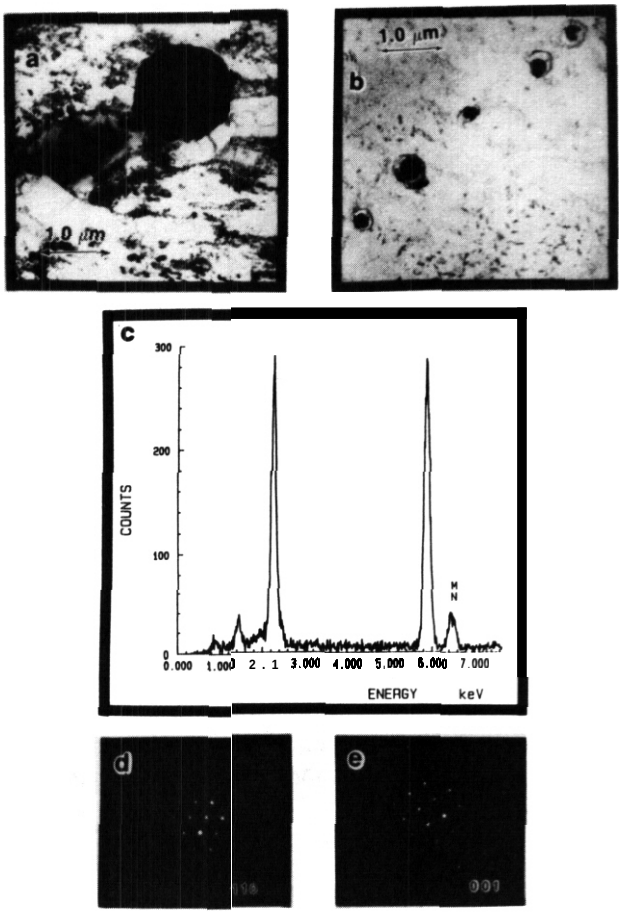

Figure 6. (a) and (b) TEM images of MnS.
(c) EDS spectrm from MnS.
(d) and (e) micro-diffraction patterns from MnS.

diffraction patterns show a cube-on-cube orientation relationship between chi and the ferrite. In the 5000 hour aged samples, the precipitate identification showed an increase in the amount of chi and in the temperatures at which it formed. At 420 C, no chi was seen in the extracted precipitates, but in the steel itself, chi was present in limited amounts. In the 5000 hour, 520 C steel, chi was seen in both the steel and in the extracted precipitates. The percentage of chi in the precipitates tested was 15% of the total. The chi which was seen in the aged samples was not associated with prior austenite grain boundaries. Chi was not seen at all in the samples aged at 600 or 365 C for either 1000 or 5000 hours.

Discussion

The tempering study indicated that the Ac_1 temperature for this steel lies between 700 and 800 C. The hardness increase occurred because the austenite transformed to new untempered martensite. There was no indication that the tempered samples formed new austenite at 700 C. The microstructure was that of a well annealed martensitic steel, where some of the tetragonal martensite had transformed to ferrite and the precipitate population had coarsened.

Samples which were aged for 1000 and 5000 hours at 365 and 420 C maintained a hardness close to that of the samples tempered at 700 C. However, as the aging temperature increased, the hardness began to drop off. This was due to a combination of recovery of the dislocation population, and coarsening of the precipitate structure. Also contributing to this hardness decrease was the .occasional recrystallization of the steel aged at high temperatures.

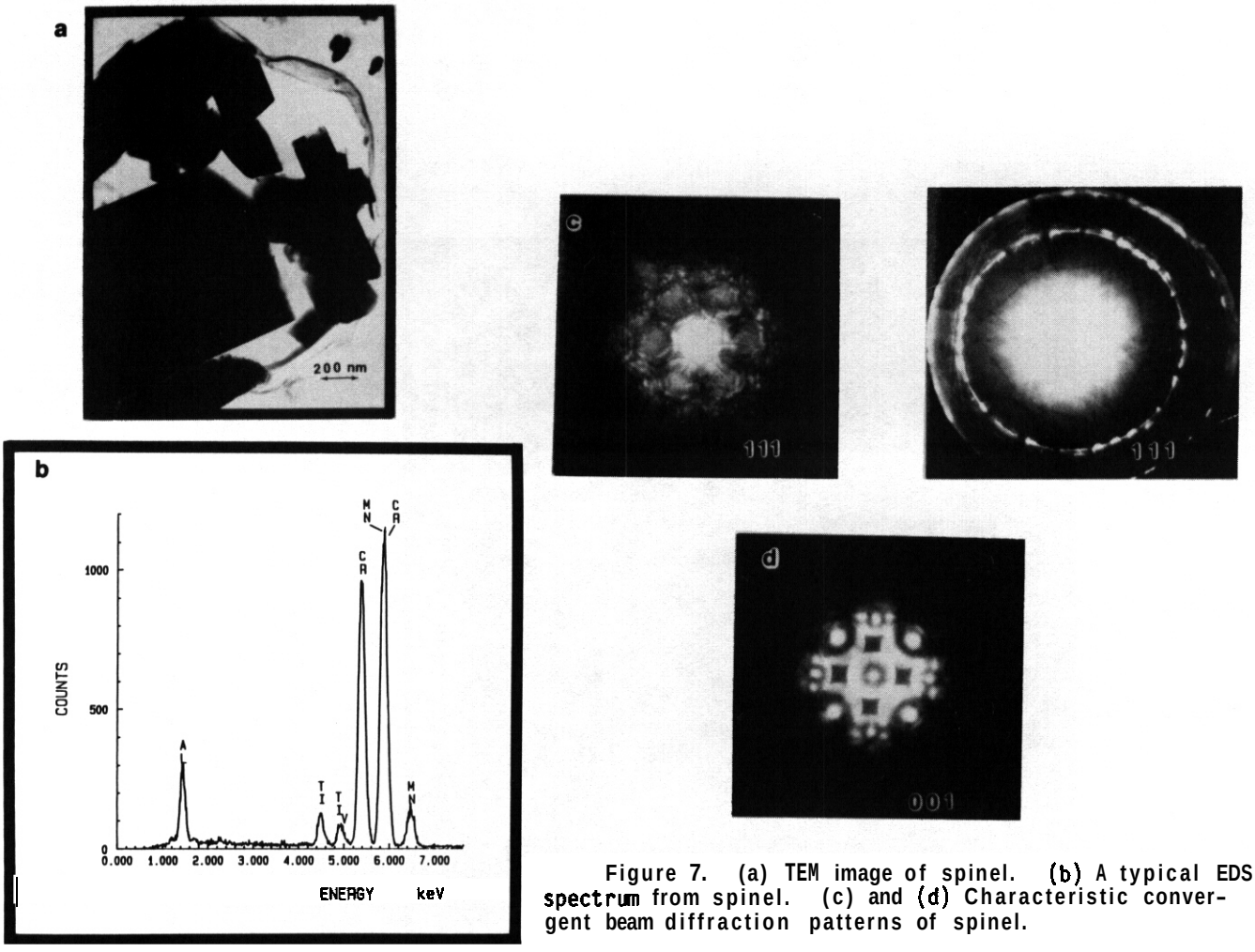

Figure 7. (a) TEM image of spinel. (b) A typical EDS spectrum from spinel. (c) and (d) Characteristic convergent beam diffraction patterns of spinel.

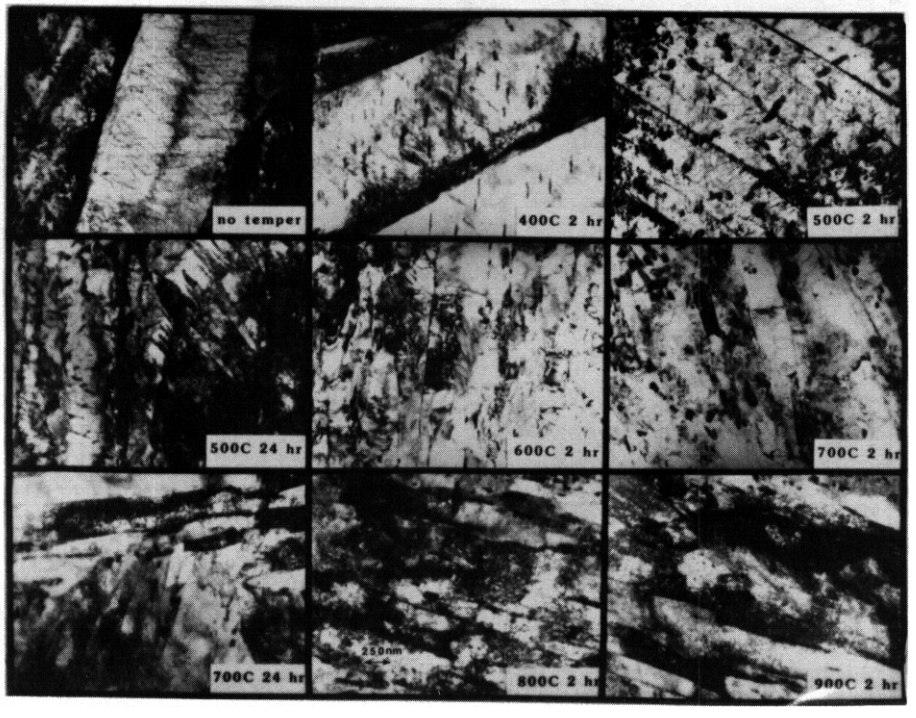

Figure 8. TEM images of the untempered and tempered L9.

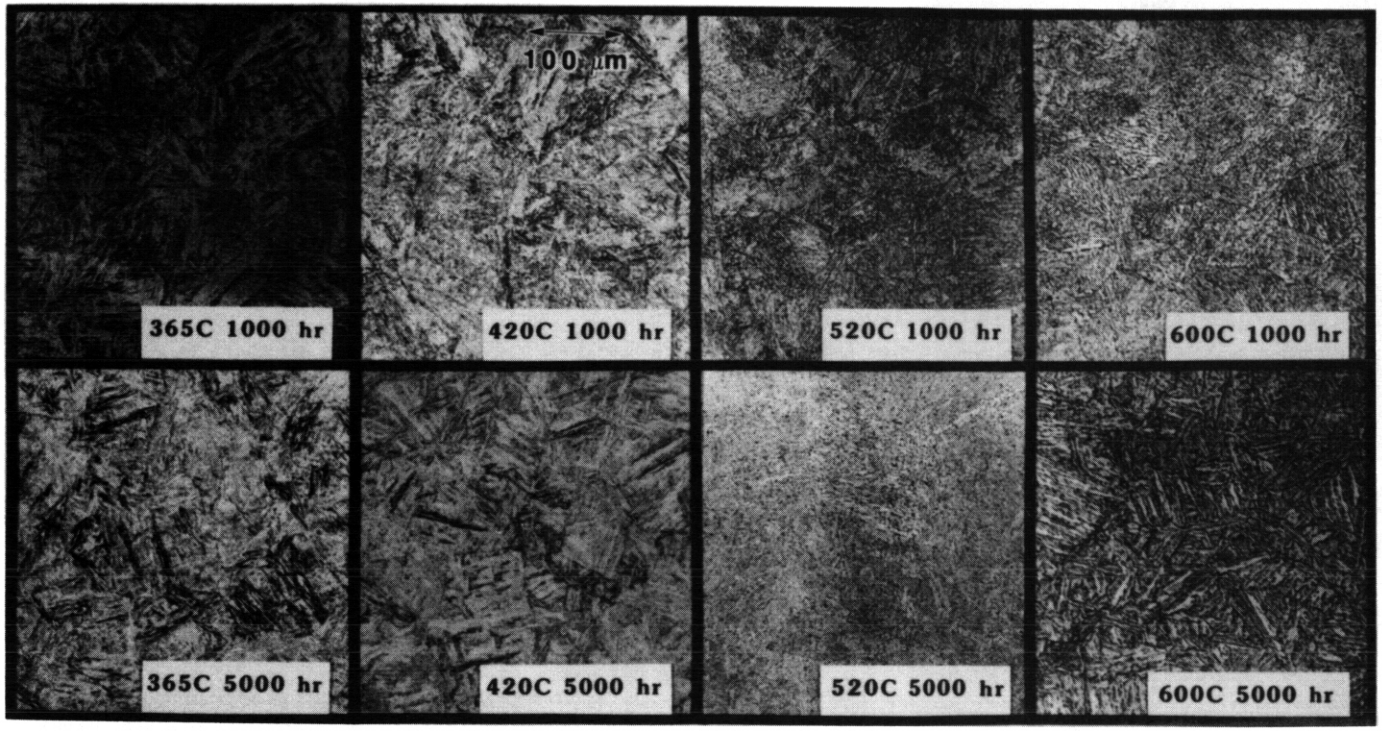

9. from L9 aged for 1000 and 5000 hours.

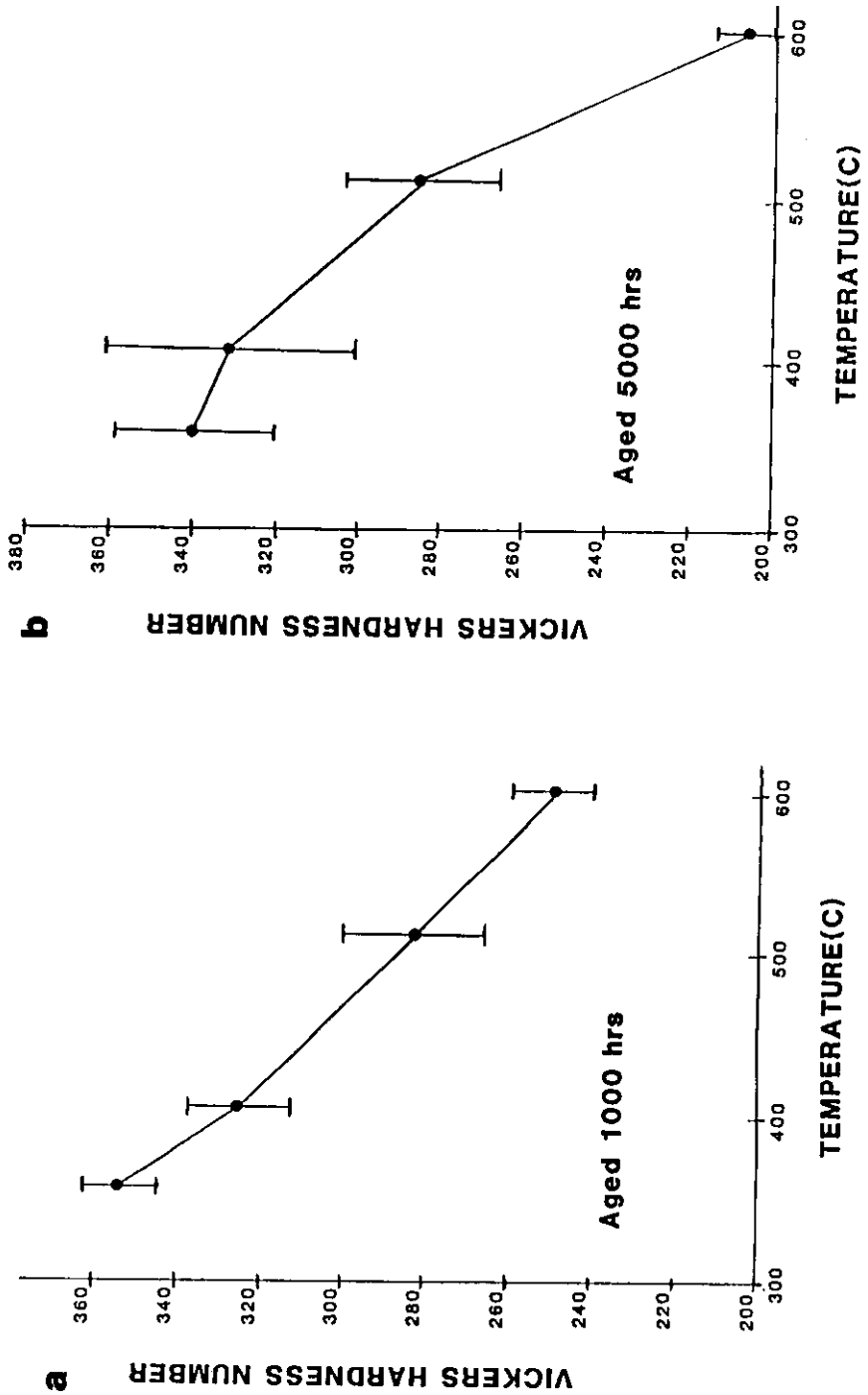

Figure 10. Microhardness results from (a) 1000 hour aged L9 and (b) 5000 hour aged L9.

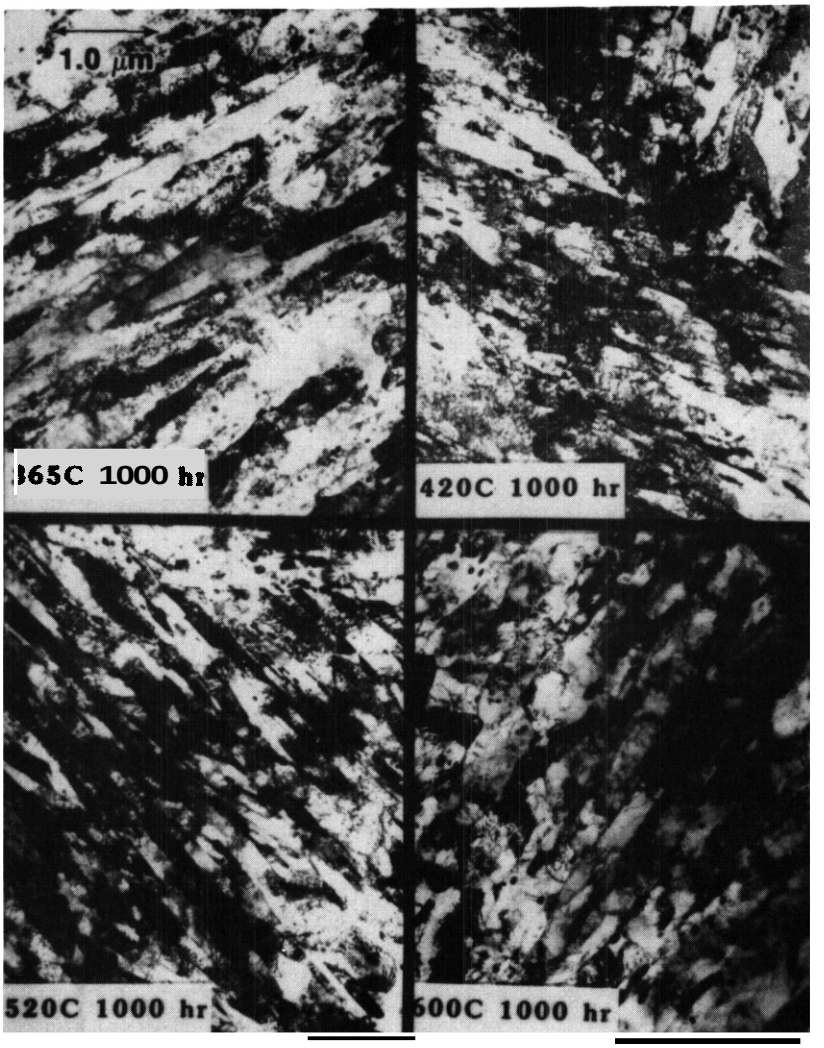

Figure 11. TEM images from L9 aged for 1000 hours.

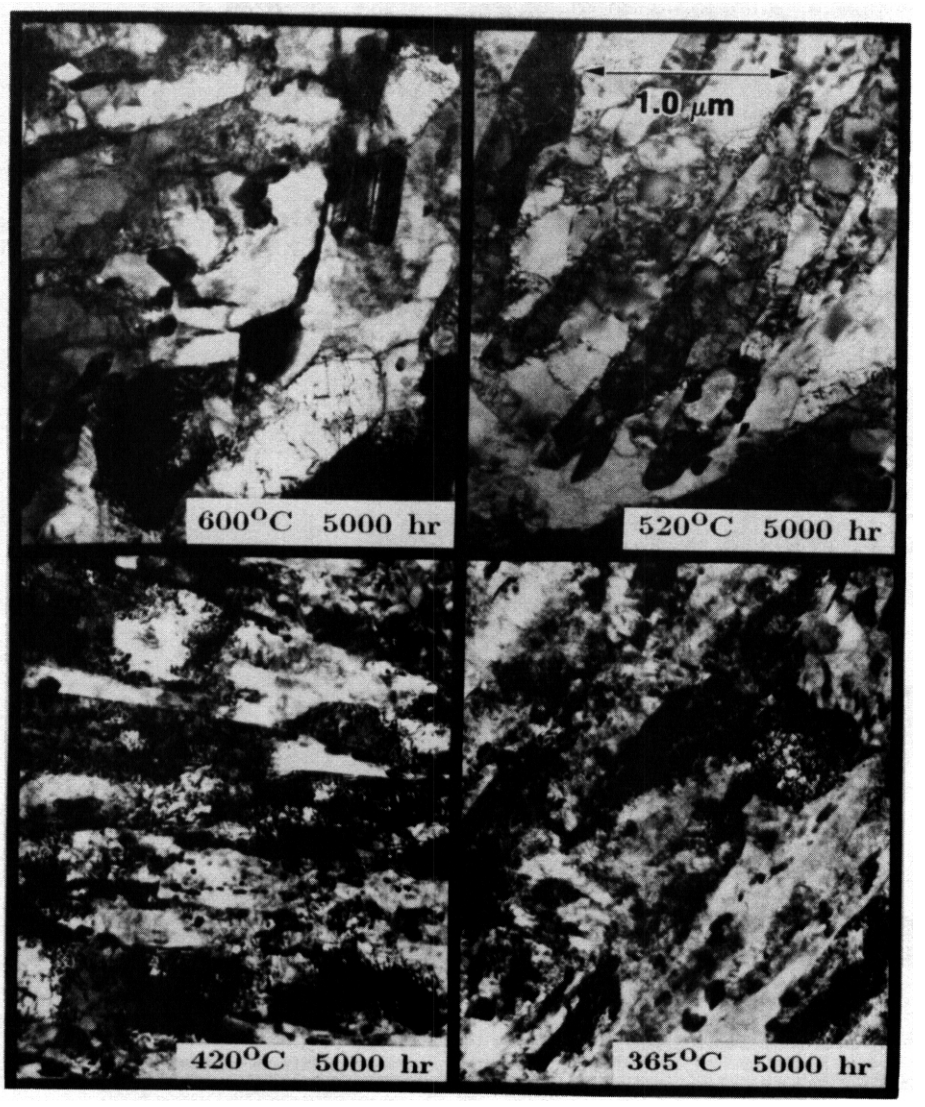

Figure 12. TEM images of L9 aged for 5000 hours.

Figure 13. Recrystallized ferrite in L9 aged for 5000 hours at 520 C.

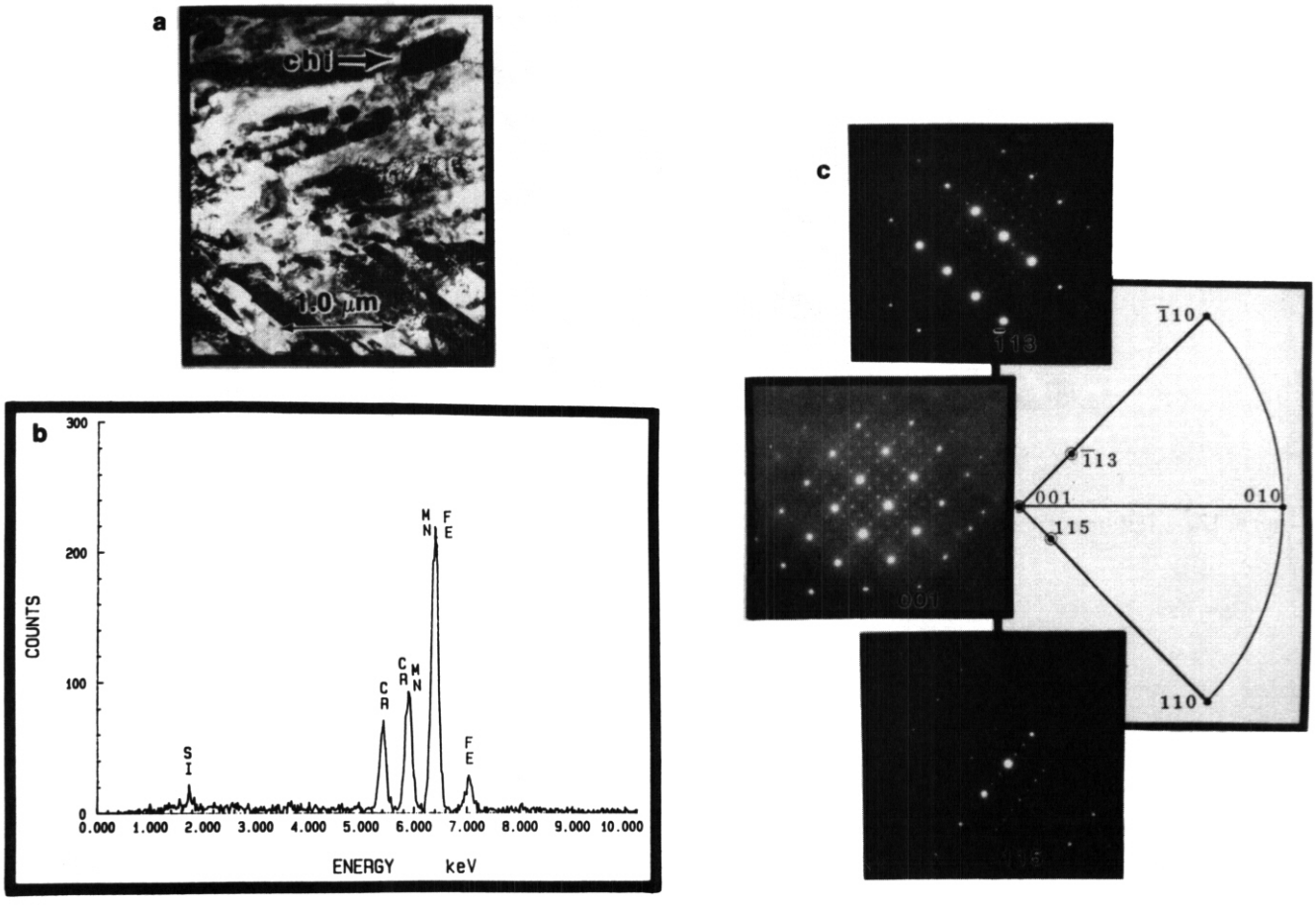

Figure 14. TEM results for chi phase. (a) Chi embedded in a ferrite matrix. (b) EDS spectrun from chi. (c) Tilt sequence from chi showing the cube-on-cube orientation relationship between chi and ferrite.

$M_{23}C_6$ was the major precipitate which formed in L9 during heat treatments. Tempering at 400 and 500 C led to another precipitate, tentatively identified as M_3C, to form within the martensite laths; but this phase is probably metastable because tempering at 500 C for twenty-four hours caused a mixture of M_3C and $M_{23}C_6$ to develop, and at the higher temperatures only $M_{23}C_6$ formed. At all the tempering temperatures, $M_{23}C_6$ was the precipitate which formed at prior austenite grain boundaries. Chi formed in the steel when it was aged for 1000 hours at 520 C and for 5000 hours at 420 and 520 C. This phase was shown to cause embrittlement when it formed in similar manganese stabilized steels at prior austenite grain boundaries that were irradiated at 365 C to 54 dpa.[6] This study has also shown that chi can form in high manganese steels in the absence of irradiation effects although its formation was sluggish. The phase may be metastable as it was not shown to form at 600 C.

CONCLUSIONS

Tempering and aging of L9 has shown results similar to those for other 12% Cr martensitic steels.? The precipitate and matrix structure which developed was not unexpected. The exception was the formation of a manganese rich chi phase in the samples aged at 420 and 520 C. This phase may be detrimental to the mechanical properties of the steel.

FUTURE WORK

Samples aged for 10,000 hours will be characterized again using TEM, optical metallography, and microhardness tests to complete the aging study.

REFERENCES

1. H.R. Brager, F.A. Garner, D.S. Gelles, and M.L. Hamilton: Journal of Nuclear Materials, 1985, Vols. 133 & 134, pp. 907–911.

2. R.L. Klueh, D.S. Gelles, and T.A. Lechtenberg, Journal of Nuclear Materials, 1986, Vol. 141-143, 1081–1087.

3. O.S. Gelles and M.L. Hamilton, Journal of Nuclear Materials, 1987, Vol. 148, 272–278.

4. D.S. Gelles and M.L. Hamilton, in Alloy Development for Irradiation Performance Semiannual Progress Report for the Period Ending March 31, 1986, DOE/ER-0045/16, 131–139.

5. N.S. Cannon, W.L. Hu and D.S. Gelles, in Fusion Reactor Materials Semiannual Progress Report for the Period Ending March 31, 1987, DOE/ER-0313/2, 119–130.

6. D.S. Gelles and W.L. Hu, in Fusion Reactor Materials Semiannual Progress Report for the Period Ending March 31, 1987, DOE/ER-0313/2, 251–261.

7. E.A. Little, D.R. Harris, F.B. Pickering, and S.R. Keown, Metals Technology, April 1977, 205–217.

CONTRIBUTIONS FROM RESEARM ON IRRADIATED FERRITIC/MARTENSITIC STEELS to materials science and engineering - D. S. Gelles (Pacific Northwest Laboratory)

OBJECTIVE

The objective of this work is to determine the applicability of ferriticlmartensitic alloys as fusion reactor structural materials. This report is intended to disseminate that work to a broader audience.

SUMMARY

A historical description of the development of ferritic/martensitic steels for use in irradiation environments is presented with the intention of showing how this development has benefitted materials science and engineering. Fast breeder reactor and fusion reactor alloy development program contributions are emphasized and it is demonstrated that HT-9 is now the leading candidate material for high radiation damage environments. The scientific basis for that selection is described by showing the underlying cause of the improved swelling resistance in martensitic steels. Examples are given demonstrating improvements in basic understanding, small specimen test procedure development and alloy development.

PROGRESS AND STATUS

Introduction

Over the last fifteen years. there has evolved a major change in the specification of steels for irradiation environments. Prior to 1974, the undisputed materials choice for liquid-metal-cooled reactor (LMR) structural components was AISI 316, an austenitic Stainless steel in the 17%Cr range with 13%Ni and 2% Mo (all canpositions given as weight percent). The choice was based on good high temperature properties. excellent corrosion resistance and ease of fabrication and welding. That choice was first challenged following the observation that AISI 316 developed cavities during neutron irradiation indicating a volumetric expansion of the material now called swelling[1]. Swelling, and its associated phenomenon irradiation creep. proved to be the life limiting factors in the application of AISI 316 for LMR fuel cladding. The discovery that cold working to the level of about 20% delayed the development of swelling[2] allowed interim use of AISI 316. In about 1974 a concerted effort was begun to find a replacement alloy, in order to permit optimization of fast breeder reactor systems[3]. That program. initially called the Alloy Development Program and later changed to the National Cladding/Duct Materials Development Program, was similar to British, French, Japanese and Russian efforts. The program was initially funded by the AEC (Atomic Energy Commission), later by ERDA (Energy Research and Development Administration) and DOE (Department of Energy).

The Alloy Development Program took as its mission the testing of alternate alloys for fast breeder reactor structural applications. The major goal was to reduce the tendency for irradiation induced swelling. but, at the same time. other materials properties such as creep. rupture strength, and postirradiation tensile strength were measured. A wide range of alloys was investigated including austenitic, ferritic and martensitic steels, nickel-based superalloys, and molybdenum- and niobium-based alloys. The primary candidates were titanium stabilized austenitic steels and precipitation-strengthened superalloys. Martensitic steels were included initially as a low priority option based on observations of swelling inhibition in the ferrite phase of a ferritic/austenitic dual phase steel[4]. However, as it became apparent that titanium stabilization only delayed the onset of swelling[5-7] and precipitation strengthening led to severe postirradiation embrittlement[8-9], the suitability of ferritic/martensitic alloys became more apparent.

Current Status of ferritic/martensitic alloys in nuclear systems

Ferritic/martensitic alloys are now finding expanded application in nuclear reactor systems as substitutes for austenitic steels. Two martensitic alloys are of greatest interest. Sandvik HT-9 is a 12%Cr, 1%Mo, 0.2% C alloy containing intentional additions of W and V. ASTM designation T91 is a modified 9%Cr alloy with 1%Mo, 0.1% C, 0.25% V, 0.1% Nb, 0.05% N. More complete compositional information is given in Table 1. Both alloys were developed for high temperature applications where the corrosion resistance inherent in austenitic stainless steels was not required. The high temperature mechanical properties of these alloys are similar, with the higher carbon and chromium additions of HT-9 balanced by careful control of vanadium, niobium and carbon additions in T91. However. T91 has inherently better resistance to low temperature embrittlement, whereas HT-9 has better corrosion and swelling resistance.

The most significant consequence of the Alloy Development Program has been the application of HT-9 to most of the internal components in the DOE experimental liquid metal-cooled test reactor FFTF (Fast Flux Test Facility) located in Richland, Wa[12]. Both fuel cladding and duct work which contains the cladded fuel have been manufactured fran HT-9 by cold tube drawing operations. As the duct geometry requires a hexagonal cross section, manufacture required development of hexagonal drawing operations for a martensitic

Table 1. Chemical analysis of martensitic steels used for nuclear systems.

Element	Content, wt % HT-9[10]	T91[11]
Carbon	0.20	0.08-0.12
Chromium	11.5	8.00-9.50
Molybdenum	1.0	0.85-1.05
Manganese	0.6	0.30-0.60
Silicon	0.4	0.20-0.50
Nickel	0.5	0.40 max
Tungsten	0.5	not spec.
Vanadium	0.3	0.18-0.25
Niobium	not spec.	0.06-0.10
Phosphorus	0.030 max	0.020 max
Sulfur	0.020 max	0.010 max
Aluminum	not spec.	0.04 max
Nitrogen	not spec.	0.030-0.070

steel with a OBTT (ductile brittle transition temperature) at about roan temperature. The transition from austenitic to martensitic stainless steel has dictated reduced operating temperatures in FFTF and consequential downgrading of the reactor from 400 to 300 MW in return for more efficient fuel cycle performance.

More recently, independent design efforts for the PRISM (Power Reactor Inherently Safe Module) and SAFR (Sodium Advanced Fast Reactor) systems have also recommended the use of HT-9 for in-core structural components[13-14]. In both cases, HT-9 was chosen for in-core structural applications to improve fuel cycle econany. Fuel recycling is anticipated only every 4 years to doses as high as 3.4 x 10^{23} n/cm^2 or 160 dpa for PRISM and 3.5 x 10^{23} n/cm^2 or 175 dpa for SAFR. Austenitic steels are not expected to remain serviceable to such high doses.

Concurrent with the Alloy Development Program for Fast Breeder Reactors, an effort has evolved to develop materials for fusion reactor applications. Of major concern in that effort is the development of materials for the first wall, the structural component nearest the plasma, hence experiencing the highest neutron fluxes. There are similarities between the Irradiation environments of a fusion first wall and fast reactor in-core components. As a result. development of fusion first wall materials has closely parallelled the Alloy Development Program effort. The Fusion Reactor Materials program was initiated in 1978 under the sponsorship of DOE, with similar efforts in Europe and Japan. As originally defined. materials development concentrated on four classes of materials: austenitic alloys, higher strength Fe-Ni-Cr alloys. refractory/reactive alloys and innovative concepts[15]. However. In part based on the encouraging re ults being obtained by the fast reactor effort. a fifth class of ferritic steels was added by late 1979[18].

Over the last ten years. the attractiveness of ferritic steels for first wall applications has steadily increased. A major concern. the effect of extremely high electranagnetic fields on a ferranagnetic structure. was alleviated when it was realized that a ferromagnetic material would behave paramagnetically in an extremely strong electranagnetic field[17-18]. A measure of the status of martensitic steels for fusion applications can best be judged based on the recommendations of fusion design studies. The five most recent design studies all seriously consider HT-9[19-23], ranking it second in comparison either with an austenitic steel or with a vanadium alloy for water-cooled Tokamak design. and. in the case of Tandem Mirror designs. ranking HT-9 first[21] or on an equal par with a vanadium alloy[22]. These design studies are particularly notable because, for the water cooled designs (a very inefficient concept). martensitic steels must be operated at temperatures where very little data is available and where the material is not expected to behave well. whereas. higher temperature designs will be more efficient and operate in a regime where martensitic steels can be expected to out-perform austenitic steels.

Therefore. martensitic steels have becane or are becoming the materials of choice for high neutron damage irradiation environments. In order to reach this status. it has been necessary to compile materials property data bases. including irradiation responses. This has been done both for LMR's[24] and for fusion systems[25] applications.

The remainder of this paper will describe sane of the contributions obtained fran these research programs to materials science and engineering.

2. Basic Science of ferritic/martensitic development

Ferritic/martensitic steels exhibit much higher resistance than austenitic steels. Figure 1 provides a comparison of swelling response for binary ferritic alloys, ternary austenitic alloys, austenitic canmercial alloys, and commercial ferritic alloys[26]. Figure la shows swelling measurements for simple Fe-Cr binary ferritic alloys as a function of temperature and dose, demonstrating that ferritic alloys do swell but at a low rate. After 100 dpa, maximum swelling was 5%. Fran Figure lb. it can be

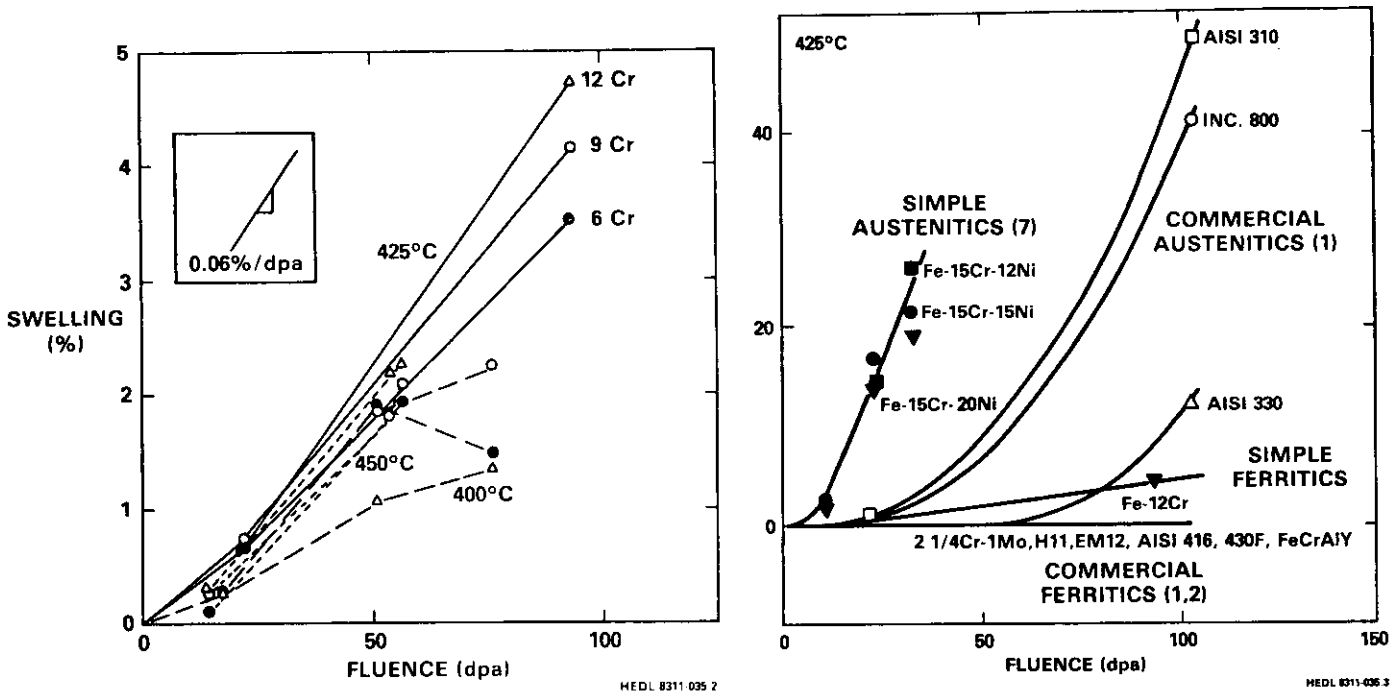

Figure 1. Comparison of swelling behavior for a) simple ferritic alloys and b) both austenitic and ferritic alloys following irradiation in a fast reactor at 425 C.

seen that for several simple austenitic alloys, swelling on the order of 20% will develop after irradiation to 25 dpa (displacements per atom). In comparison, commercial austenitic alloys such as AISI 310 and Incoloy 800 swell less, but by 100 dpa swelling values can reach 40%. Some austenitic alloys such as AISI 330 have even more swelling resistance, the swelling resistance has been attributed to high levels of silicon, but by about 100 dpa the swelling rate escalates. The rate of swelling for commercial alloys is expected to approach that found in simple alloys, as has been demonstrated recently with specimens irradiated to still higher fluences[27]. The swelling rate for simple binary ferritic alloys compared with simple austenitic alloys is 1/20 as large. Therefore, at very high damage levels, simple ferritic alloys can be expected to swell less than commercial austenitic alloys. But, as was found with austenitic alloys, commercial ferritic/martensitic alloys swell even less than simple alloys. Commercial alloys covering a range of compositions from 2 to 20% Cr are found to contain negligible cavities to fluences as high as 100 dpa. Commercial ferritic/martensitic alloys are expected to swell at higher fluences (indeed, swelling levels on the order of 0.5% have been measured) but the rate of swelling is expected to correspond to that in simple alloys.

The improved swelling resistance of ferritic/martensitic alloys is now fairly well understood. There have been several explanations given for this improved swelling resistance, as recently reviewed by Odette[28]. The arguments which relate to differences in behavior between simple austenitic and ferritic alloys will be summarized here:

Sneigowski and Wolfer[29] have noted that inherent with the differences in crystal structure between face centered cubic (FCC) and body centered cubic (BCC), is a difference in atom nearest-neighbor spacing such that the relaxation volumes of vacancies and interstitials are different. For FCC structures, the relaxation volume for an interstitial is large and that of a vacancy small, whereas for BCC structures, the relaxation volumes for interstitials are smaller and for vacancies, larger. As a consequence, the difference between relaxation volumes of interstitials and vacancies is larger in FCC structures than in BCC structures. This difference in relaxation volumes leads to a larger net attraction of interstitials to dislocations in comparison with voids (called bias) and promotes preferential absorption of vacancies at voids. Both void nucleation and steady state void growth are similarly affected. Calculations indicate that a factor of 5 to 10 difference in steady state swelling rate can be explained by this mechanism.

2. Bullough et al[30] and Gelles[31] provide possible explanations based on the fact that two dislocation Burgers vectors are found in irradiated ferritic alloys: the commonly observed a/2 <111> and the irradiation induced a<100>. Bullough et al apply the argument that dislocations act as biased sinks for interstitials resulting in a potential net excess vacancy flux to any more neutral sink. If a neutral sink is not available, void nucleation and subsequent growth can result. A second Burgers vector present provides a more neutral sink, preventing a vacancy concentration build-up and nucleation of voids. Alternatively, Gelles noted that ferritic alloys represent an unusual class of materials where the irradiation induced dislocation network contains a sessile Burgers vector component, a<100>, making the dislocation network

that forms during irradiation sessile, so that dislocation glide is not allowed. A sessile dislocation network would have reduced dislocation mobility and therefore preferential absorption of interstitials would be reduced. The argument of Bullough et al would only explain the results shown in Fig. 1 for the non-swelling commercial ferritic alloys. but not the results for simple ferritic alloys. The argument by Gelles is very difficult to quantify and therefore the magnitude of its contribution is not yet determined.

3. Horton and Mansur[32] and Coghlan and Gelles[33] have considered the swelling response in ferritic alloys fran the perspective of the critical cavity radius for void swelling nucleation. Horton and Mansur based their analysis on ion irradiation experimental results and Coghlan and Gelles on fast neutron irradiation response. Both studies assumed a bias of 0.2 or less. in agrement with Sniegowski and Wolfer[29]. Horton and Hansur were able to obtain a reasonable fit to swelling data, giving critical radius estimates in the range of 3 to 4 nm, whereas the Coghlan and Gelles calculations arrived at a sanawhat lower critical radius of 0.2 to 2nm, depending on temperature. Also. Horton and Mansur noted that their calculations provided reasonable estimates also for void growth. Therefore. the values of bias deduced by Sniegowski and Wolfer appear to be confirmed by critical radius calculations.

It has been shown conclusively that irradiation damage can result in solute segregation as a result of point defect/solute interactions[34]. Both interstitials and vacancies can play a role. either by point defect drag to sinks or by a reverse-Kirkendall mechanism. Solute segregation behavior has been extensively demonstrated in experiments using austenitic specimens. but relatively few definitive experiments have been performed to demonstrate the behavior in ferritic/martensitic experiments. However. those few experiments (see for example the work of Japanese experimenters[35-37]) do clearly demonstrate solute segregation in BCC as well as FCC crystal structures. The number of such experiments is small in part because segregation plays a less important role in controlling properties than is the case in austenitic alloys. Most ferritic/martensitic alloys have canpositions based on Fe-Cr binary alloys and it has been found that Cr tends to move away from point defect sinks such as dislocations, voids and grain boundaries. Therefore, major consequences of irradiation induced solute segregation arise only due to minor element additions to ferritic/martensitic alloys.

An example of solute segregation worth noting is the effect of solute additions on void shape in ferritic alloys. It has been found that the common void shape in pure iron and Fe-Cr binary alloys is octahedral with {111} faces. However. in a series of alloys based on Fe-10% Cr in which solute had been added to levels of 1%, both dislocation evolution and void shape were altered[38]. Solute additions caused the voids to become either cuboidal with {100} faces. or dodecahedral (twelve sided) with {110} faces. Examples are shown in Fig. 2 which compares void shape in a series of Fe-Cr-M alloys where M was either Si, V, Mn, W, Ta or Zr. It is believed that void shape has been altered as a result of solute segregation to void surfaces, changing either the relative surface energies of the different planes or altering the void growth behavior. Void shape in austenitic alloys shows less variation: only octahedral and cuboidal void shapes have been reported.

Precipitation Reactions Martensitic stainless steels derive high temperature strength fran precipitation strengthening which is relatively insensitive to coarsening at high temperatures. Strengthening in HT-9 is predominantly due to Cr rich $M_{23}C_6$, but T91 employs both $M_{23}C_6$ and MC (V_4C_3) strengthening with evidence for Cr_2N as well. Laves phase has been reported following tempering and following long term aging in HT-9[39-40], and evidence for chi phase formation (Fe-Cr-Mo intermetallic) has also recently been found[41]. Irradiation Is found to significantly alter precipitate development in these steels. and. furthermore. the irradiation environment can alter the distribution of phases that form. Following irradiation in fast reactors. '(Cr rich BCC), G phase (a nickel silicide), chi and M_6C have been identified[42-43]. Furthermore, Maziasz has reported that. following irradiation at 500 C in a mixed spectrum reactor. as tempered $M_{23}C_6$ particles are replaced by irradiation-produced M_6C[44]. Therefore, irradiation does alter precipitation sequences significantly. leading to considerable change in properties.

Engineering Applications

It was quickly recognized that limited irradiation test volumes behooved the development of mall specimen testing procedures in order to maximize data accumulation in irradiation test programs. As a consequence, miniaturization has been accomplished for several specimen geometries[45].

me development of small specimen techniques for Charpy impact energy and fracture toughness measurements is especially relevent to ferritic/martensitic alloys. Specimen geometries for measurments are shown in Fig. 3. Impact energy measurement procedures have been evaluated for both half-sized and third-sized Charpy specimens. It has been demonstrated that reduction of specimen size affects upper shelf energy (USE) and ductile-brittle transition temperature (DBTT), but the shift in transition temperature due to irradiation is independent of specimen size. Recently, a successful correlation of USE and DBTT for HT-9 as a function of specimen size has been demonstrated[46].

Fracture toughness miniature specimen development has considered several geometries. both circular and rectangular. but in all cases compact tension geometries were used. Examples of the circular gemtry are shown in Fig. 3b. Specimen thickness is often dictated by function, so that optimum thickness is

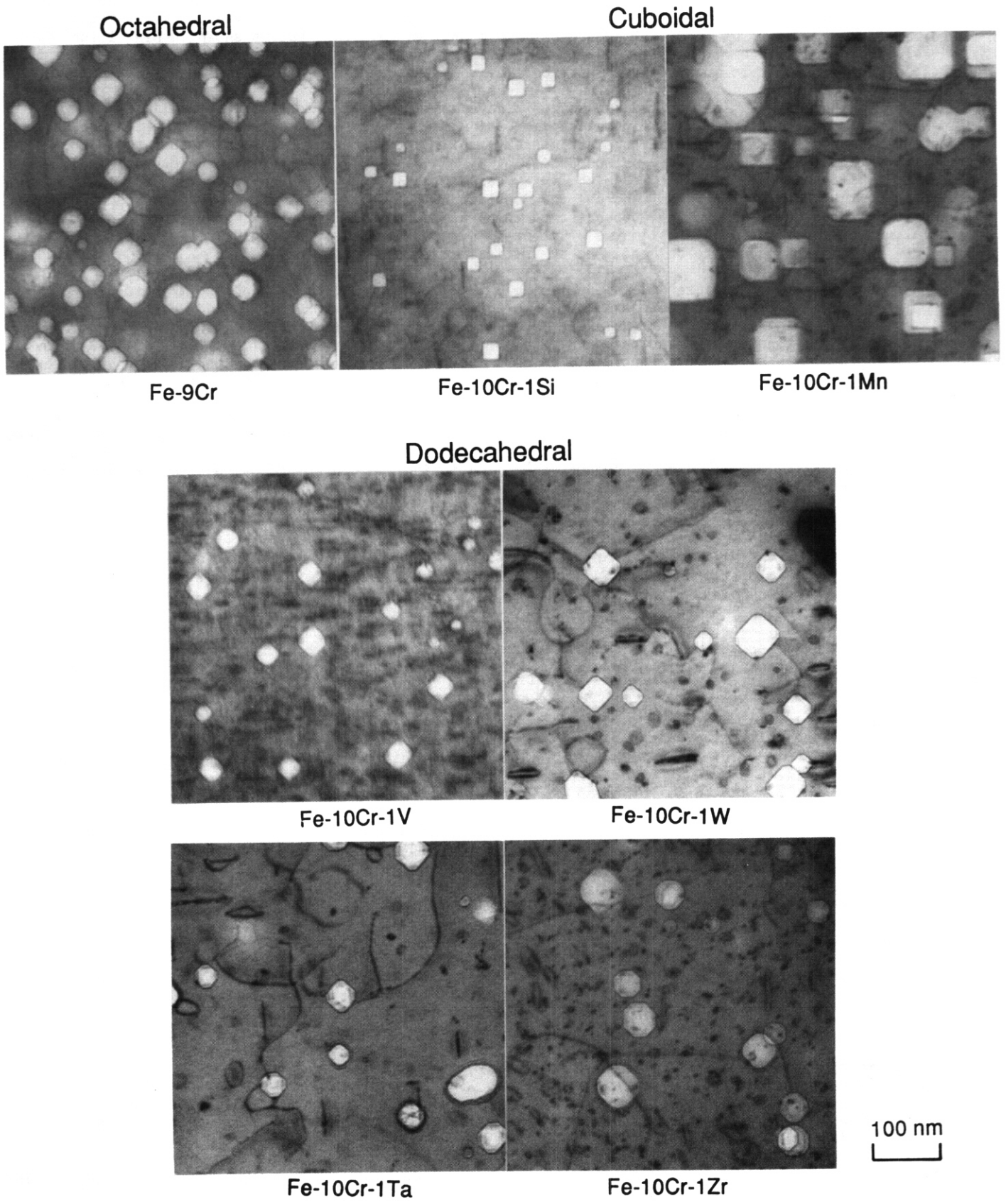

Figure 2. Examples of void shapes in simple ferritic alloys. All micrographs are taken with foil orientation near (001) and cube directions horizontal and vertical.

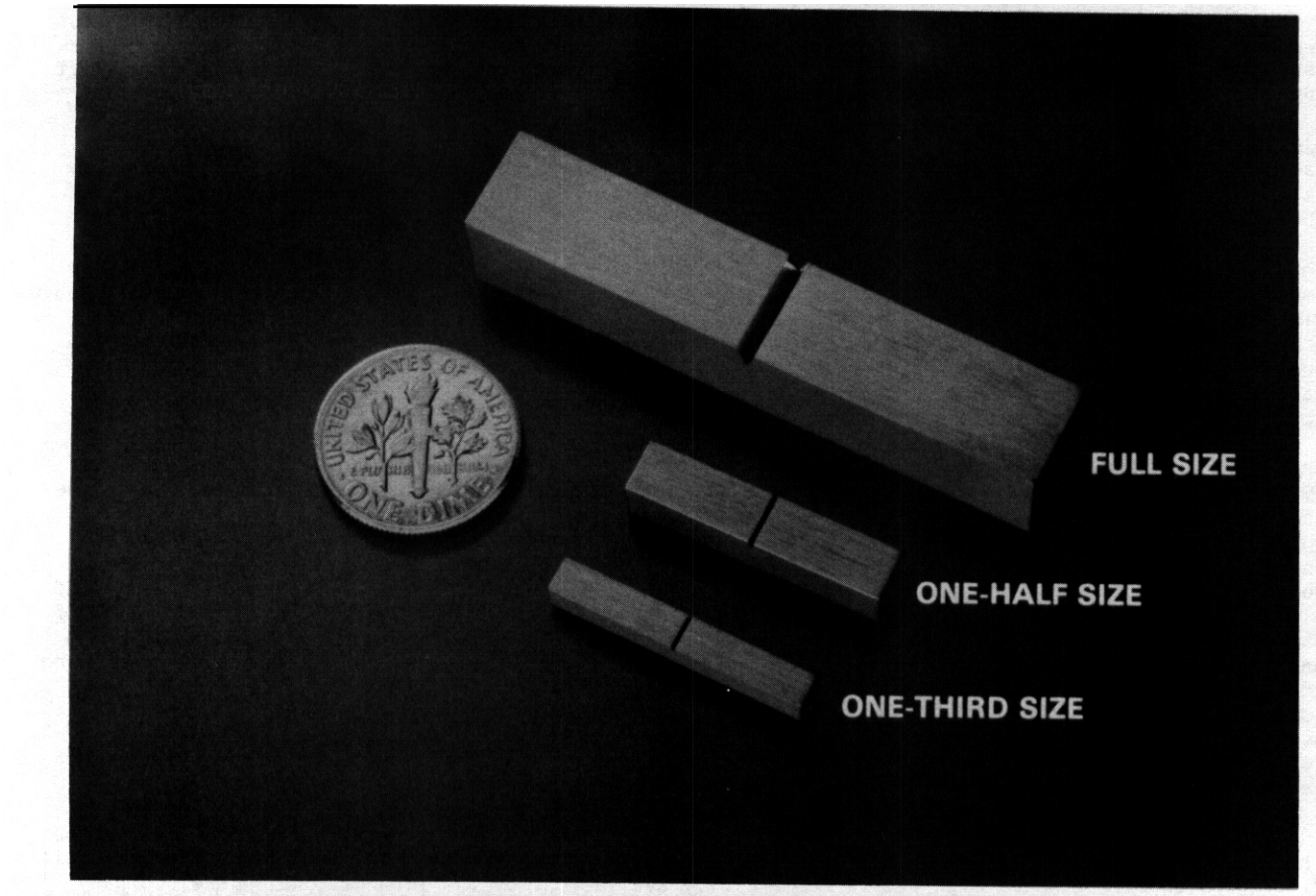

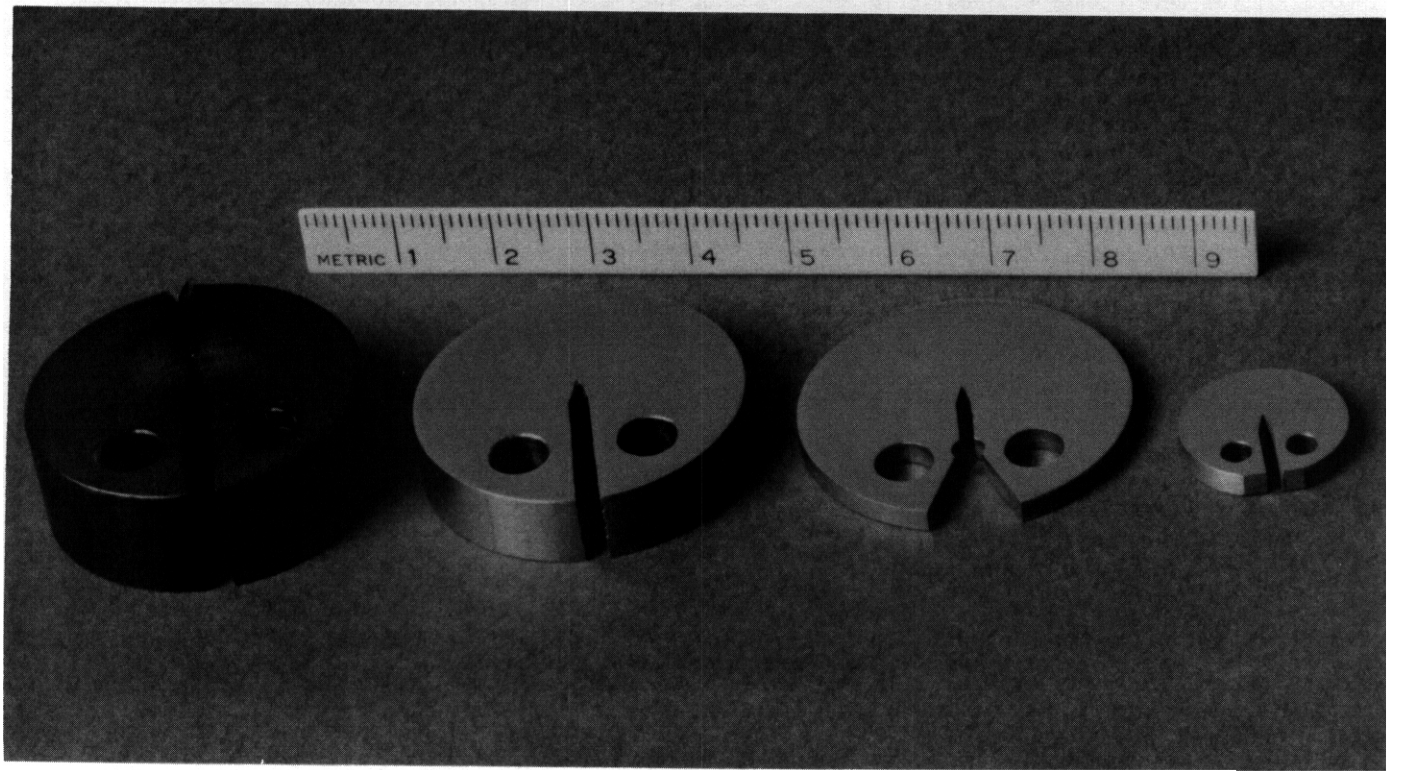

Figure 3. Examples of small specimen geanetries for Charpy impact testing and fracture toughness measurement.

equal to canponent thickness[47]. Initially, multiple specimens were required to generate a J/R curve. but more recently, single specimen techniques were developed using resistance measurements to determine crack extension[48]. Although miniature specimen development was originated for testing irradiated specimens. it is also applicable to testing of non-standard geanetries such as thin-walled pipe.

Alloy development Opportunities for modern alloy research and development are rare due to the high expense of doing such work. However, three examples will be described of successful efforts to develop ferriticlmartensitic steels for nuclear reactor applications. The alloys created are available for use in other service environments.

The major alloy development success story concerns the alloy T91 mantioned earlier (see Table 1). T91 is a modified 9Cr-1Mo alloy containing carefully controlled ratios of additions of carbon. vanadium, niobium and nitrogen. The alloy development work was initiated by Combustion Engineering. Inc. of Chattanooga. TN[49], but was assimilated into a DOE program for the development of an advanced alloy for Out-Of-Core fast reactor structural applications. Programmatic responsibility resided at Oak Ridge National Laboratory[11]. The program not only provided a properties data base for T91, but also arranged for fabrication of several big heats of the alloy. at both U.S. and Japanese steel production facilities. The end product of that effort is a code qualified steel which provides high temperature properties comparable to HT-9 and only slightly below those of austenitic stainless steel. but which is much less costly to produce than are austenitic steels. A similar steel has been developed in Japan using the same ratios of carbon, vanadium, niobium and nitrogen[50].

A second example of ferritic/martensitic alloy research and development is in support of fusion. 'It has been noted that an inherent advantage of fusion over fission is that the nuclear reaction involves no long-lived radioactive isotopes,[51]. Therefore, within a few years after a machine has reached the end of its useful lifetime. the only radioactivity remaining canes from the structural materials from which the fusion reactor is made. Five years ago, the fusion materials program began an effort to minimize the long term radioactivity of the structural components. The most direct approach is to exclude niobium. molybdenum, nickel, nitrogen, aluminum and copper fran the steel. The investigation of a number of possible compositions[52] has shown that the option of such a "low activation" alloy is viable[53]. Therefore. this line of research and development is expected to provide new alloys, with properties as good as presently available high temperature martensitic stainless steels, for other nuclear applications.

Finally. an example is provided where private industry. in supporting research on materials development for irradiation environments, has developed a novel alloy. Alloy MA957 is a mechanically-alloyed ferritic alloy. dispersion strengthened with yttria commercially available from the International Nickel Company (INCO). It was developed specifically for fast reactor fuel cladding applications at a time when INCO was assisting the Alloy Development Program[54]. An alloy with good high temperature strength and high radiation resistance was needed. The mechanical alloying process applies high energy ball milling tc produce powders with dissimilar ingredients dispersed on a very fine scale[55]. The powders are then consolidated using powder metallurgy procedures. For MA957, the result is an alloy of base composition, Fe-14Cr-1Ti-0.25Mo, to which has been add $0.25Y_2O_3$ as 5nm particles uniformly dispersed through the material. The cost of MA957 is significantly higher than material processed by more standard techniques and component fabrication procedures are much more complicated and expensive. However. a component made from MA957 can be expected to have unsurpassed capability; fast breeder reactor fuel cladding made from MA957 is expected to provide at least a five year fuel lifetime with improved high tmperature performance in comparison with HT-9[56]. Application of MA957 (for fast to LMR's) follows the trend of using metal-matrix canposites to solve extremely difficult metallurgical problems.

CONCLUSIONS

Research and development efforts on ferritic/martensitic alloys for use in irradiation environments have been described with regard to liquid metal reactor and fusion reactor applications, and some contributions of those efforts to materials science and engineering have been enumerated. It can nor be claimed that martensitic steels have become the materials of choice for high neutron dose environments. To a large extent, this is due to the high swelling resistance compared to austenitic steels. imparted by the difference in crystal structure. Studies of irradiated ferritic/martensitic steels have demonstrated solute segregation and precipitation phenomena similar to that found in austenitic steels. but playing a lesser role in determining post-irradiation performance. Contributions to materials engineering include the development of small specimen test procedures and new alloys.

FUTURE WORK

This report is intended for inclusion in the proceedings of the Symposium on Irradiation-Enhanced Materials Science and Engineering to be published in Metallurgical Transactions.

REFERENCES

1. C. Cawthorne and E. J. Fulton. Nature, 216 (1967) 515.

2. J. L. Straalsund, H.R. Brager and J. J. Holmes, in Radiation-Induced Voids in Metals, CONF-710601, April 1972, pp. 142-155.

3. J. J. Laidler, J. J. Holmes and J. W. Bennett. in Radiation Effects in Breeder Reactor Structural Materials, M. L. Eleiberg and J. W. Bennett, eds., pp. 41-52. The Metallurgical Society of AIME, N.Y., NY, 1977.

4. S. D. Harkness, E. J. Kestel and P. Okamoto, ibid Ref. 2, pp. 334-337.

5. F. A. Garner. H. R. Erager and R. J. Puigh, J. Nucl Mater. 133 & 134 (1985) pp. 535-539.

6. J. L. Seran et al, in Effects of Radiation on Materials: Twelfth International Symposium. F. A. Garner and J. S. Perrin. Eds., pp.233-247, ASTM STP 870, ASTM, Philadelphia, PA. 1985.

7. R. J. Puigh and F. A. Garner, in Radiation-Induced Changes in Microstructure: 13th International Symposium (Part 1) F. A Garner. N. H. Packan and A. S. Kumar. Eds. pp. 154-160, ASTM STP 955. ASTM. Philadelphia, PA. 1987.

8. R. Bajaj et al. in Effects of Radiation on Materials: Tenth Conference, ASTM STP 725, D. Kramer, H. R. Brager and J. S. Perrin. Eds., pp. 326-351, ASTM. Philadelphia, PA. 1981.

9. W. J. S. Yang. D. S. Gelles, J. L. Straalsund and R. Bajaj, J. Nucl. Mater. 132 (1985) 249-265.

10. Sandvik HT-9 data sheet S-1,720-ENG, May 1981.

11. V. K. Sikka. in Proceedings of Topical Conference on Ferritic Alloys for use in Nuclear Energy Technologies, pp. 317-327, The Metallurgical Society of AIME, Warrendale, PA, 1984.

12. A. J. Lovell. A. L. Fox, W. H Sutherland and S. L. Hecht. in International Conference on Reliable Fuels for Liquid Metal pp.3-25 to 3-36, ANS, 1987.

13. F. E Pippets et al, Proc. Amer. Power Council, 49 (1987) 874-883 or S. Vaidyanathan and R. E. Murata, ibid Ref. 12, pp. 1-43 to 1-50.

14. D. S. Bost and L. D. Felten, ibid Ref. 12, pp. 1-61 to 1-68.

15. The Fusion Reactor Materials Program Plan Section 1, Alloy Development for Irradiation Performance, DOE/ET-0032/1, July 1978.

16. Alloy Development for Irradiation Performance Quarterly Progress Reports beginning with the period ending December 31, 1979, DOE/ER-0045/1-16.

17. S. N. Rosenwasser. P. Miller, J. A. Dalessandro. J. M. Rawls, W. E. Toffolo and W. Chen. J. Nucl. Mater. 85 & 86 (1979) 177-182.

18. H. Attaya. G. L. Kulcinski and W. G. Wolfer. J. Nucl. Mater. 122 & 123 (1984) 96-100.

19. Starfire. A Commercial Tokamak Fusion Power Plant Study, ANL/FPP-80-1, V1, Sept. 1980, p. 10-232.

20. A Demonstration Tokamak Power Plant Study, ANL/Fpp/82-1, Sept. 1982, p. 2-3.

21. MARS Mirror Advanced Reactor Study Final Report, Volume 1-B, UCRL-53480, July 1984, pp. 12-9 to 12-24.

22. Blanket Comparison and Selection Study, Final Report, ANL/FPP-84-1, Sept. 1984, pp. 7.3-4.

23. Modelina. Analysis & Experiments for Fusion Nuclear Technology, FNT Progress Report: Modeling and FINESSE, Jan. 1987, p. 1021.

24. J. L. Straalsund and D. S. Gelles, oral presentation, ibid Ref. 11, HEOL-SA-2771. May 1983.

25. D. S. Gelles, J. Nucl. Mater. 149 (1987) 192-199.

26. D. S. Gelles and R. L. Meinecke Ermi. ibid Ref. 11, DOE/ER-0045/11 (1983) pp. 103-107.

27. F. A. Garner and D. S. Gelles, to be published in Fusion Reactor Materials DOE/ER/0313/5, Sept. 1988, PNL-SA-15471.

28. G. R. Odette. ibid Ref. 27, DOE/ER-0313/4, Sept. 1987. pp. 106-114.

29. J. J. Sniegowski and W. G. Wolfer, ibid Ref. 11, pp. 579-591.

30. R. Bullough, M. H. Wood and E. A. Little. ibid Ref., pp. 593-609.

31. D. S. Gelles. J. Nucl. Mater., 108 & 109 (1982) 515-526.

32. L. L. Horton and L. K. Mansur, ibid Ref. 6.. pp. 344-362.

33. W. A. Coghlan and D. S. Gelles, ibid Ref. 27, DOE/ER-0313/2, March 1987, pp. 88-98.

34. See for example, Workshop on Solute Segregation and Phase Stability During Irradiation, in J. Nucl. Mater. 83 (1979).

35. S. Ohnuki. H. Takahashi and T. Takeyama. J. Nucl. Mater. 103 6 104 (1981) pp. 1121-1126.

36. S. Ohnuki. H. Takahashi and T. Takeyama, J. Nucl. Mater. 122 6 123 (1984) pp. 317-321.

37. T. Muroga, A. Yamaguchi and N Yoshida, "Characteristics of Radiation-Induced Solute Segregation in Candidate and Model Ferritic Alloys." accepted for publication in the proceedings of the 14th ASTM International Symposium on Effects of Radiation on Materials, held June 1988 in Andover. MA.

38. D. S. Gelles, "Neutron Irradiation Damage in Ferritic Fe-Cr Alloys," ibid Ref. 37, PNL-SA-15258.

39. T. A. Lechtenberg. reference still to be determined.

40. P. Chen and R.C. Wilcox. "Effects of Thermal Aging on Precipitation Development of Alloy HT-9," ibid Ref. 37.

41. R. D. Griffin et al, "Tempering and Aging Effects on a Low Activation Martensitic Stainless Steel," this proceedings.

42. D. S. Gelles and L. E. Thomas. ibid Ref. 11, pp. 559-568.

43. P. J. Maziasz in Materials for Nuclear Reactor Core Applications, BNES, London, 1987. pp. 61-71.

44. P. J. Maziasz. R. L. Klueh and J. M. Vitek. J. Nucl Mater. 141-143 (1986) pp. 929-937.

45. The Use of Small-Scale Specimens for Testina Irradiated Material, W. R. Corwin and G. E. Lucas. Eds., ASTM STP 888, ASTM. Philadelphia, PA. 1986.

46. B. S. Louden. A. S. Kumar. F. A. Garner. M. L. Hamilton and W. L. Hu, in Ref. 37.

41. F. H. Huang in Ref. 45, pp. 290-304.

48. F. H. Huang, J. Test. & Eval., V. 13 (1985) pp. 257-264.

49. G. C. Bodine and R. E. McDonald. in Ferritic Steels for High-Temperature Applications, A. K. Khare, Ed.. American Society for Metals, Metals Park. OH. 1983, pp. 9-20.

50. K. Hashimoto. et al, ibid Ref. 11, pp. 307-315.

51. Report of the DOE Panel on Low Activation Materials for Fusion Applications. R.W. Conn, Panel Chairman. UCLA/PPG-728, June 1983.

52. R. L. Klueh. D. S. Gelles and T. A. Lechtenberg. J. Nucl Mater. 141-143 (1986) pp. 1081-1087.

53. D. S. Gelles, "Effects of Irradiation on Low Activation Ferritic Alloys, A Review," PNL-SA-15681FP, accepted for publication in the proceedings of the 14th ASTM International Symposium on Effects of Radiation on Materials, held June 1988 in Andover, MA.

54. J. J. Fischer. U.S. Patent 4,075,010, Feb. 21, 1978.

55. Frontiers of High Temperature Materials II, J. S. Benjamin and R. C. Benn, Eds., International Nickel Company, 1985.

56. R. W. Powell, G. D. Johnson M L. Hamilton and F. A. Garner, ibid Ref., pp. 4-17 to 4-29.

FLUENCE AND HELIUM EFFECTS ON THE TENSILE PROPERTIES OF FERRITIC STEELS AT LOW TEMPERATURES — R. L. Klueh (Oak Ridge National Laboratory)

OBJECTIVE

The goal of this study is to evaluate the properties of irradiated ferritic steels. Irradiation in the High Flux Isotope Reactor (HFIR) is used to produce both displacement damage and transmutation helium at levels relevant to fusion reactor service.

SUMMARY

Tensile specimens of 9Cr-1MoVNb and 12Cr-1MoVW steels with up to 2% Ni and 2¼Cr-1Mo steel were tested at room temperature after irradiation at ~50°C to displacement-damage levels of 25 dpa in the HFIR. Nickel was added to the ferritic steels to produce helium by a two-step (n,α) reaction with thermal neutrons during irradiation in the mixed neutron spectrum of HFIR. Up to 327 appm He was produced in the steels with 2% Ni. Irradiation caused an increase in the strength of all the steels. With an increase in fluence, there was a decrease in the rate of strength increase, but the strength was still increasing after 20 to 25 dpa. Strength increases were accompanied by a loss of ductility, although the ductility appeared to go through a minimum and was greater at the highest fluences than at intermediate fluences. The results were interpreted to mean that the transmutation helium that was generated during irradiation caused part of the strength increase.

PROGRESS AND STATUS

Introduction

Ferritic (martensitic) steels are being considered for use as first-wall and blanket-structure materials for fusion-reactor applications. The ferritic steels of primary interest are 9Cr-1MoVNb, 12Cr-1MoVW, and 2¼Cr-1Mo. To simulate the effect of fusion-reactor irradiation on the mechanical properties of the steels, specimens are irradiated in fission reactors, after which tensile,[1-3] impact,[4-5] and fatigue[6] data are obtained.

Irradiation by neutrons results in displacement damage that is caused by collisions of high-energy neutrons with atoms of the alloy. Atoms are displaced from their normal lattice position into interstitial positions, leaving behind a vacancy. It is the disposition of the interstitials and vacancies that determines the effect of the irradiation on properties. Another irradiation effect that will be important in a fusion reactor is the high helium concentrations that will be generated in the structural materials by transmutation reactions.

One way to study both displacement-damage and helium effects in the ferritic steels is to irradiate nickel-doped versions of the steels in a mixed-spectrum reactor. such as the HFIR. Displacement damage is produced by the fast neutrons in the spectrum, and helium is produced by a two-step (n,α) reaction of ^{58}Ni with the thermal neutrons in the spectrum.

When the steels are irradiated at the HFIR coolant temperature (~50°C), displacement damage causes an increase in strength.[1-3] Previous studies have examined the effect of irradiation after displacement-damage levels of <10 dpa (refs. 1-3). Under the test conditions used for the previous studies, no helium effect was detected.[1-2] This report extends the previous tensile results on undoped and nickel-doped 9Cr-1MoVNb and 12Cr-1MoVW steels irradiated at the HFIR coolant temperature up to ~25 dpa. Data are also presented on 2¼Cr-1Mo steel irradiated up to 18 dpa.

Experimental procedure

Electroslag-remelted heats of standard 9Cr-1MoVNb (0.1% Ni) and 12Cr-1MoVW (0.5% Ni) steels were prepared by Combustion Engineering, Inc., Chattanooga, Tennessee. These compositions with 1 and 2% Ni. designated 9Cr-1MoVNb-2Ni, 12Cr-1MoVW-1Ni, and 12Cr-1MoVW-2Ni, were also prepared. In addition to the experimental heats, a limited number of specimens obtained from comnercial-size heats of 9Cr-1MoVNb (heat 30176) and 12Cr-1MoVW (heat 91354) steels were also irradiated and tested, along with specimens from a commercial tubing heat of 2¼Cr-1Mo steel (heat 72768). and a 2¼Cr-1Mo steel specimen from heat 56447, a large vacuum-arc remelted heat. Chemical compositions of all the steels are given in Table 1.

Two types of tensile specimens were obtained from these heats. Cylindrical specimens were machined from 6.35-mn-diam rods; the specimens had a reduced section of 2-mn diam by 18.3-mn long. Sheet tensile

Table 1. Composition of Ferritic Steels

Element	Concentration,[a] wt %								
	9Cr-1MoVNb Heat Nos.			12Cr-1MoVW Heat Nos.				2¼Cr-1Mo Heat Nos.	
	30176	XA3590	XA3591 2% Ni	91354	XAA3587	XAA3588 1% Ni	XAA3589 2% Ni	72768	56447
C	0.092	0.09	0.064	0.21	0.21	0.20	0.20	0.12	0.10
Mn	0.48	0.36	0.36	0.47	0.50	0.47	0.49	0.12	0.49
P	0.012	0.008	0.008	0.004	0.011	0.010	0.011		0.01
S	0.004	0.004	0.003	0.004	0.004	0.004	0.004		0.007
Si	0.15	0.08	0.08	0.21	0.18	0.13	0.13	0.31	0.23
Ni	0.09	0.11	21.7	0.54	0.43	1.14	2.27	0.07	0.14
Cr	8.32	8.62	8.57	11.2	11.97	11.71	11.71	2.2	2.15
Mo	0.86	0.98	0.98	0.96	0.93	1.04	1.02	0.8	1.03
V	0.20	0.209	0.222	0.31	0.27	0.31	0.31		0.007
Nb	0.06	0.063	0.066		0.018	0.015	0.015		
Ti	0.001	0.002	0.002		0.003	0.003	0.003	0.01	0.01
Co	0.017	0.013	0.015	0.02	0.017	0.015	0.021	0.003	0.01
Cu	0.03	0.03	0.04	0.04	0.05	0.05	0.05	0.1	0.06
Al	0.011	0.013	0.015	0.03	0.030	0.017	0.028	0.1	0.06
B	0.006	<0.001	<0.001	<0.0001	<0.001	<0.001	<0.001		
W	<0.01	0.01	0.01	0.50	0.54	0.53	0.54		
As	0.001	<0.001	<0.001	0.01	<0.001	0.002	<0.002		
Sn	0.002	0.003	0.003	0.01	0.002	0.001	0.002		
Zr	<0.001	<0.001	<0.001		<0.001	<0.001	<0.001		
N	0.055	0.050	0.053		0.020	0.016	0.017	0.016	
O	0.010	0.007	0.006		0.005	0.007	0.007	0.007	

[a]Balance Fe.

specimens were machined from 0.76-mn-thick cold-rolled sheet. These specimens had gage lengths parallel to the rolling direction with a reduced section 20.3-mn long by 1.52-mm wide by 0.76-mn thick.

The specimens were irradiated in the normalized-and-tempered condition. For the rod specimens, heat treatment was carried out on the rods prior to machining; the sheet tensile specimens were heat treated after machining. Heat treatments were carried out in a helium atmosphere. The normalizing treatment for all of the 9Cr steels was 0.5 h at 1040°C and for the 12Cr steels 0.5 h at 1050°C. After normalizing, the steels were pulled into the cold zone of the tube furnace and cooled in flowing helium. All of the 9Cr-1MoVNb steels were tempered 1 h at 760°C. All of the 12Cr-1MoVW and 12Cr-1MoVW-1Ni steels were tempered 2.5 h at 780°C. The 9Cr-1MoVNb-2Ni and 12Cr-1MoVW-2Ni steels were tempered 5 h at 700°C. Tempered martensite microstructures were obtained for the 9Cr and 12Cr steels by such heat treatments. The 2¼Cr-1Mo steel specimens were normalized by annealing 0.5 h at 900°C and cooling in flowing helium; they were tempered 1 h at 700°C. The microstructure after this heat treatment was 100% tempered bainite. Details on heat treatment and microstructure have been published.[1-3,7]

Specimens were encapsulated in thin-wall aluminum tubes that were hydrostatically collapsed onto the specimens prior to irradiation in HFIR at the reactor coolant temperature of ~50°C. For irradiation, the specimens capsules containing rod-tensile specimens were irradiated in the peripheral target positions of the reactor and were designated as HFIR-CTR-TI and HFIR-CTR-T2. Sheet specimens were also irradiated in the beryllium-reflector region of the reactor in capsules designated HFIR-CTR-RB1 and HFIR-CTR-RB2. Individual cylindrical specimens were aligned along the length of the capsule, while sheet specimens were stacked in sets of five along the length before encapsulation. These sealed tubes were irradiated in direct contact with the coolant.

Irradiation fluence and displacement-damage level for each specimen depended on the position of the specimen in the capsule. Fluence was a maximum at the reactor centerline and decreased as the distance from the centerline increased. The cylindrical specimens were irradiated as follows: HFIR-CTR-T1 was irradiated to a fast fluence of 2.0 to 3.2 $\times 10^{26}$ neutrons/m^2 ($E > 0.1$ MeV), corresponding to displacement-damage levels of 15 to 24 dpa. Irradiation of HFIR-CTR-T2 was to a fluence of 4.4 to 6.9 $\times 10^{25}$ neutrons/m^2 ($E > 0.1$ MeV), corresponding to 3.2 to 5.1 dpa. The sheet specimens were irradiated as follows: HFIR-CTR-RB1 received a fluence of 8.6 to 9.0 $\times 10^{25}$ neutrons/m^2 with damage levels of 5.2 to 5.5 dpa; HFIR-CTR-RB2 received a fluence of 0.8 to 1.7 $\times 10^{26}$ neutrons/m^2 with damage levels of 5.0 and 10.3 dpa. Helium concentration also depended on the position of the specimen in the capsule and the amount of nickel in the material. Calculated displacement-damage level and helium concentrations for each specimen are given in Table 2

Table 2. Room-Temperature Tensile Properties for Irradiated and Unirradiated 9Cr-1MoVNb and 12Cr-1MoVW Steels With and Without Nickel

Experiment	Displacement Damage (dpa)	Helium (appm)	Strength (MPA) YS	Strength (MPA) UTS	Elongation (%) Uniform	Elongation (%) Total
9Cr-1MoVNb Steel, Heat XA-3590						
RB,33 control	0	0	541	656	5.1	9.6
T1,T2 control	0	0	528	659	5.2	12.9
T2	4.3	3	907	921	0.6	4.0
T2	4.7	4	932	935	0.3	2.8
RB2	7.1	7	990	990	0.3	2.4
33	9.3	11	878	878	0.2	3.2
T1	20.2	20	1009	1022	0.4	5.4
T1	22.3	22	1010	1014	0.4	5.5
9Cr-1MoVNb Steel, Heat 30176						
RB1	5.3	5	879	881	0.3	2.0
9Cr-1MoVNb-2Ni Steel, Heat XA-3591						
RB,33 control	0	0	734	851	3.7	7.5
T1,T2 control	0	0	750	856	2.7	8.4
T2	4.5	37	1230	1264	0.6	2.8
RB2	5.0	80	1255	1258	0.3	1.5
33	9.3	80	1289	1297	0.4	1.6
T1	21.1	289	1357	1383	0.4	6.3
12Cr-1MoVW Steel, Heat XAA-3587						
RB,33 control	0	0	553	759	8.1	11.2
T1,T2 control	0	0	569	759	5.1	13.0
T2	3.2	8	950	978	0.8	4.9
T2	4.7	11	976	1004	0.8	5.1
33	9.3	22	980	992	0.4	2.9
RB2	10.3	44	1027	1047	0.6	6.5
T1	15.1	56	1041	1060	0.6	6.4
T1	22.4	83	1049	1082	0.6	6.5
12Cr-1MoVW Steel, Heat 91354						
R8.33 control	0	0	549	716	6.6	9.9
RB1	5.5	19	986	998	0.4	2.0
33	9.3	26	983	987	0.3	2.1
12Cr-1MoVW-1Ni Steel, Heat XAA-3588						
RB,33 control	0	0	576	800	7.1	10.6
T1,T2 control	0	0	583	791	7.8	10.5
T2	4.2	17	1064	1098	0.9	3.5
T2	5.1	36	1033	1087	1.0	2.8
RBZ	9.0	73	978	1001	0.6	2.6
33	9.3	45	1115	1134	0.6	3.0
T1	18.4	129	1152	1194	0.6	5.0
T1	23.7	167	1147	1180	0.6	5.1
12Cr-1MoVW-2Ni Steel, Heat XAA-3589						
RB,33 control	0	0	719	899	4.6	7.8
T1,T2 control	0	0	754	920	3.9	9.0
T2	5.1	42	1220	1277	0.9	2.9
33	9.1	74	1227	1249	0.5	2.2
RB2	9.3	145	1264	1298	0.8	2.5
T1	24.1	327	1338	1400	1.0	6.1
2¼Cr-1Mo Steel, Heat 72768						
RB,33 control	0	0	581	663	8.4	12.8
T1,T2 control	0	0	535	632	5.8	12.7
T2	4.0	3	948	953	0.4	2.9
33	6.4	8	1027	1027	0.1	1.7
T1	18.4	18	1016	1016	0.3	5.6
2¼Cr-1Mo Steel, Heat 56447						
RB control	0	0	645	a34	6.3	9.6
RB1	5.2	5	973	995	0.5	3.1

In addition to the specimens irradiated in the T1, T2, RB1, and RB2 experiments, specimens irradiated in HFIR-CTR-33 will also be discussed. This was an irradiation capsule[1-3] that contained sheet specimens and was irradiated at the HFIR coolant temperature to a maximum fast fluence of 1.3×10^{26} neutrons/m^2 (E > 0.1 MeV), which gave ~9 dpa. The control specimens for that experiment are the same as those for RB1 and RB2.

Room-temperature tensile tests were conducted in a vacuum chamber on a 44-kN capacity Instron universal testing machine using a crosshead speed of 0.0085 mm/s, which gives a nominal strain rate of 4.6×10^{-4}/s for the sheet specimens and 4.2×10^{-4}/s for the rod specimens. Unirradiated controls were tested for comparison with the irradiated specimens.

Results

Table 2 lists the tensile properties for the control specimens and the specimens irradiated in the HFIR-CTR-T1, -T2, -RB1, -RB2, and -33 capsules. Irradiation conditions for each irradiated specimen are also given.

Results for the control specimens indicated that there was good agreement between the yield stress (YS) and ultimate tensile strength (UTS) for the rod (T1 and T2 experiments) and sheet specimens (RB1, RB2, and 33 experiments). Even the uniform and total elongation values were similar. This agreement occurred despite the fact that the materials were heat treated separately and in different geometrical product forms.

The YS and UTS data for the unirradiated and irradiated 9Cr-1MoVNb and the 9Cr-1MoVNb-2Ni steel are shown in Fig. 1 as a function of displacement-damage level (fluence). Although there was scatter in the data, the trends for both the YS and UTS were quite clear. The character of the curves for both the 9Cr-1MoVNb and 9Cr-1MoVNb-2Ni steel were similar: both showed an increase in strength with increasing displacement-damage level. However, with increasing fluence, the rate of increase in strength leveled off.

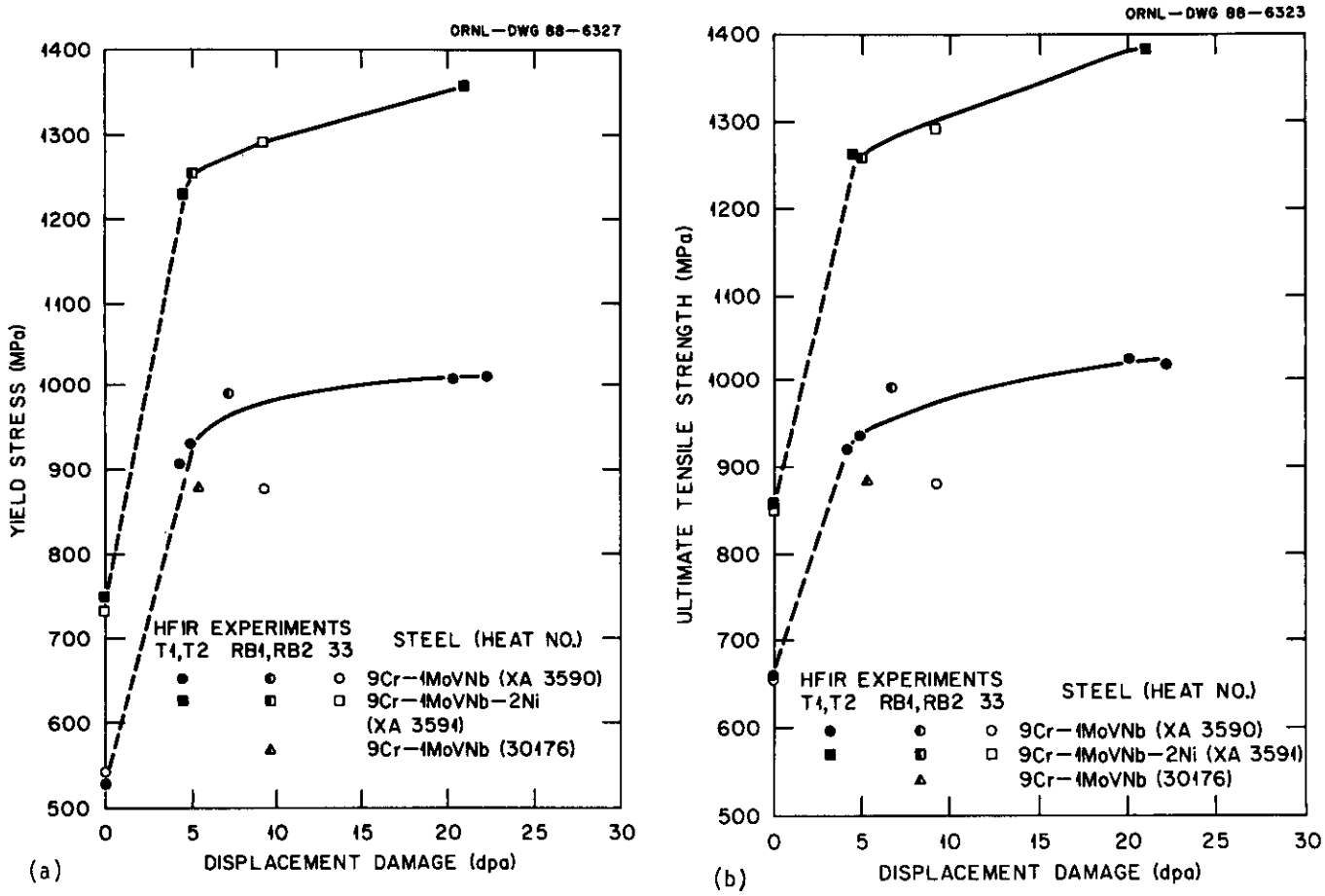

Fig. 1. The (a) yield stress and (b) ultimate tensile strength of the 9Cr-1MoVNb and 9Cr-1MoVNb-2Ni steels as a function of fluence.

Because of the different tempering temperatures used for the 9Cr-1MoVNb and the 9Cr-1MoVNb-2Ni, the unirradiated YS of the 9Cr-1MoVNb-2Ni was greater than that of the 9Cr-1MoVNb. As the displacement damage increased, however, the difference in strength for the two steels increased, indicating that the 9Cr-1MoVNb-2Ni had hardened more than the 9Cr-1MoVNb. There was about a 200 MPa difference in YS in the unirradiated condition that increased to about a 350 MPa difference after 20 dpa. The UTS showed a similar behavior.

The uniform and total elongation are shown in Fig. 2. In Fig. 2(a), the total elongation is shown as a function of displacement damage for the 9Cr steels. Considerable scatter is evident in the data. Irradiation to damage levels of 4 to 10 dpa caused a considerable loss of ductility for both the 9Cr-1MoVNb and the 9Cr-1MoVNb-2Ni steels. After irradiation to 4 to 10 dpa, there was little difference in total elongation for the 9Cr-1MoVNb and 9Cr-1MoVNb-2Ni steels. Although only one specimen of 9Cr-1MoVNb-2Ni steel and two specimens of 9Cr-1MoVNb steel were irradiated to ~20 dpa, both steels showed an increase in total elongation over that after irradiation to 4 to 10 dpa. There was also good agreement among all three values. It appears from these results that the total elongation went through a minimum with fluence.

The change in uniform elongation with displacement damage showed a similar decrease with increasing damage level, but an eventual increase in elongation at higher fluences was not found [Fig. 2(b)]. The uniform elongation for both the 9Cr-1MoVNb and the 9Cr-1MoVNb-2Ni steels dropped to quite low values after irradiation. After ~4.5 dpa, a value of 0.6% was observed; this dropped to 0.2 to 0.4% after 5 to 10 dpa. Finally, after ~20 dpa, a value of 0.4% is observed for both steels.

Results for the 12Cr-1MoVW, 12Cr-1MoVW-1Ni, and 12Cr-1MoVW-2Ni steels (heats 91354, XAA-3587, -3588, and -3589) were similar to those for the 9Cr steels (Figs. 3 and 4). With increasing displacement damage, the YS and UTS increased. The rate of increase decreased as the damage level increased, especially above about 5 dpa (Fig. 3). The effect of nickel content on strength noted for the 9Cr steels was also observed for the 12Cr steels. This effect was most easily seen by comparing the YS and UTS behavior of the 12Cr-1MoVW and 12Cr-1MoVW-1Ni steels, which had similar strengths in the unirradiated condition. After irradiation to ~20 dpa, the YS of the 12Cr-1MoVW-1Ni steel increased about 100 MPa more than that for 12Cr-1MoVW steel. Likewise, although the YS of the 12Cr-1MoVW-2Ni steel was about 135 MPa above that for the 12Cr-1MoVW-1Ni steel in the unirradiated condition, the difference was about 175 MPa at 20 dpa [Fig. 3(a)]. The UTS difference [Fig. 3(b)] went from ~115 to 185 MPa.

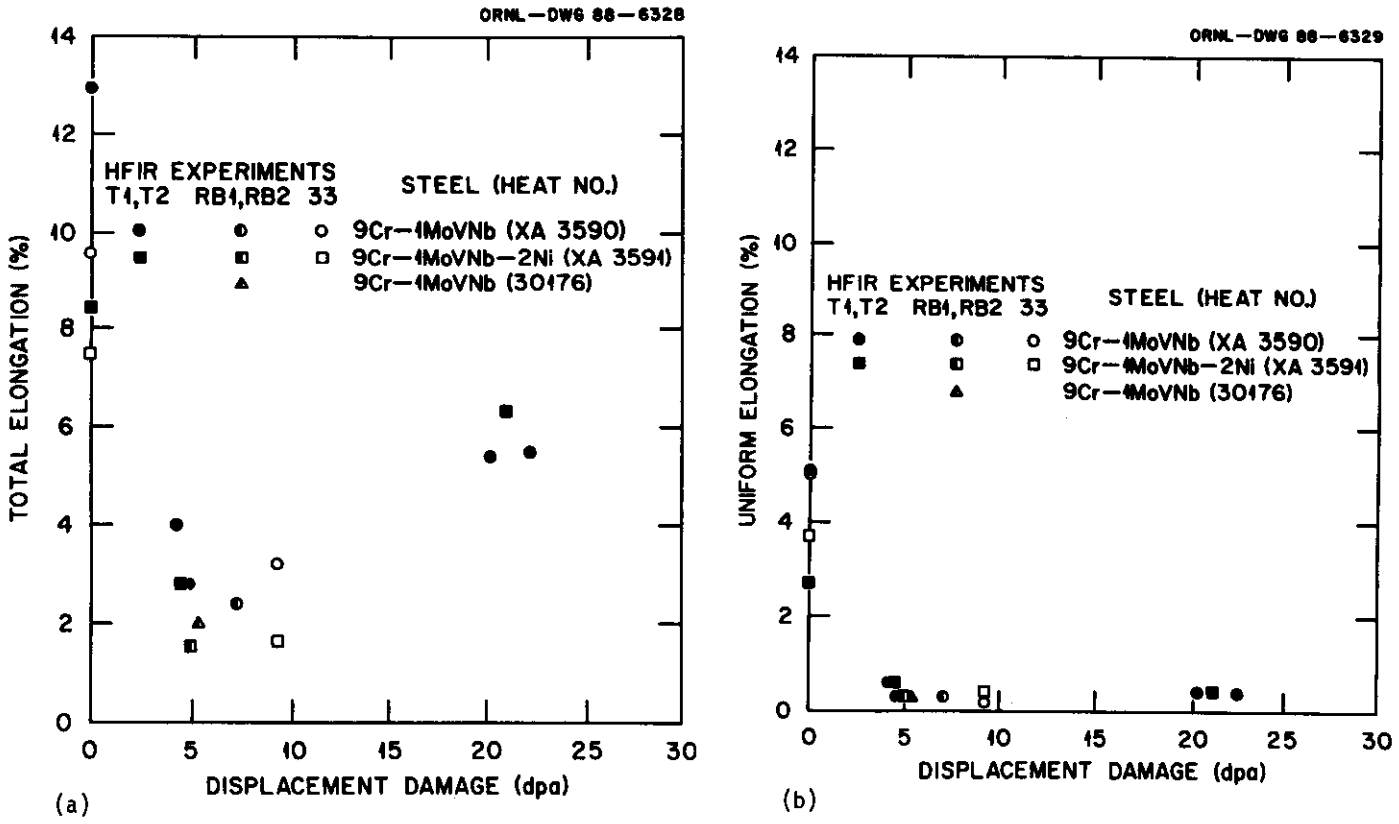

Fig. 2. The (a) total elongation and (b) uniform elongation of the 9Cr-1MoVNb and 9Cr-1MoVNb-2Ni steels as a function of fluence.

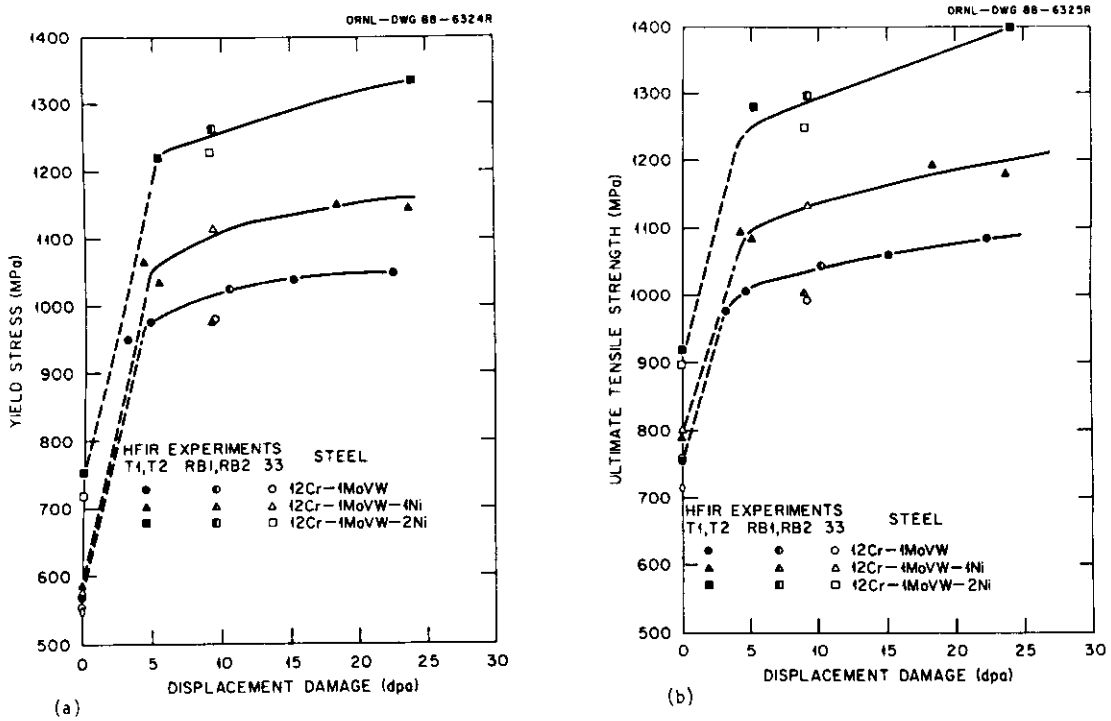

Fig. 3. The (a) yield stress and (b) ultimate tensile strength of the 12Cr-1MoVW, 12Cr-1MoVNb-1Ni, and 12Cr-1MoVW-2Ni steels as a function of fluence.

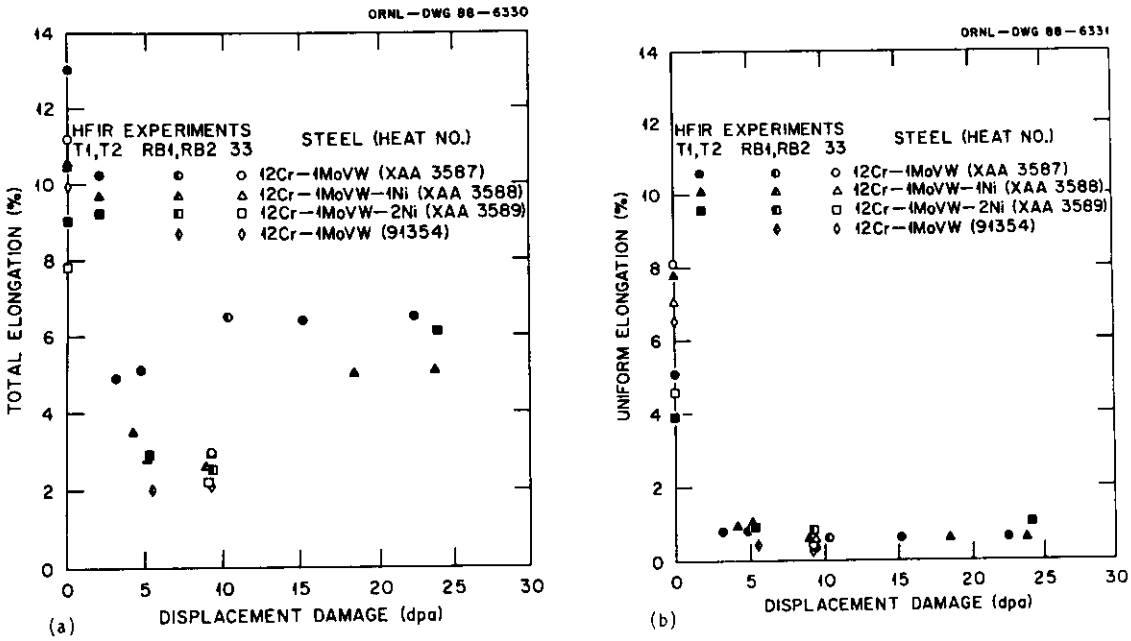

Fig. 4. The (a) total elongation and (b) uniform elongation of the 12Cr-1MoVW, 12Cr-1MoVNb-1Ni, and 12Cr-1MoVW-2Ni steels as a function of fluence.

The ductility behavior of the 12Cr steels (Fig. 4) was also similar to that for the 9Cr steels. The steel with no nickel added showed the largest decrease, followed by the steel with 1% Ni, because these steels had the highest ductilities before irradiation. The total elongation again showed indications of a minimum after displacement-damage levels of 5 to 10 dpa [Fig. 4(a)]. After 15 dpa or more, all three steels had elongations above those at 10 dpa. The uniform elongation decreased dramatically to less than 1% for damage levels of ~5 dpa, beyond which the uniform elongation leveled off at a value of ~0.6% [Fig. 4(b)].

The 2¼Cr-1Mo steel has received less attention as a candidate for fusion-reactor applications than 9Cr-1MoVNb and 12Cr-1MoVW. For that reason, fewer specimens of that steel were in the irradiation capsules being reported on in this report. Results for the 2¼Cr-1Mo steel specimens are given in Table 2. Io Fig. 5(a) the YS and UTS are shown as a function of displacement damage, and in Fig. 5(b), the uniform and total elongation are shown.

The trends in strength and ductility observed for the 9Cr-1MoVNb and 12Cr-1MoVW steels were also observed for the 2¼Cr-1Mo steel. There was a large increase in strength with fluence up to ~5 dpa. However, beyond 5 dpa the strength increased very little [Fig. 5(a)]. The trends for the uniform and total elongations [Fig. 5(b)] were also similar to those of the 9Cr-1MoVNb and 12Cr-1MoVW steels. Again, there was an indication of a minimum in the total elongation with increasing fluence, whereas the uniform elongation remained below 0.5% for damage levels greater than 4 dpa.

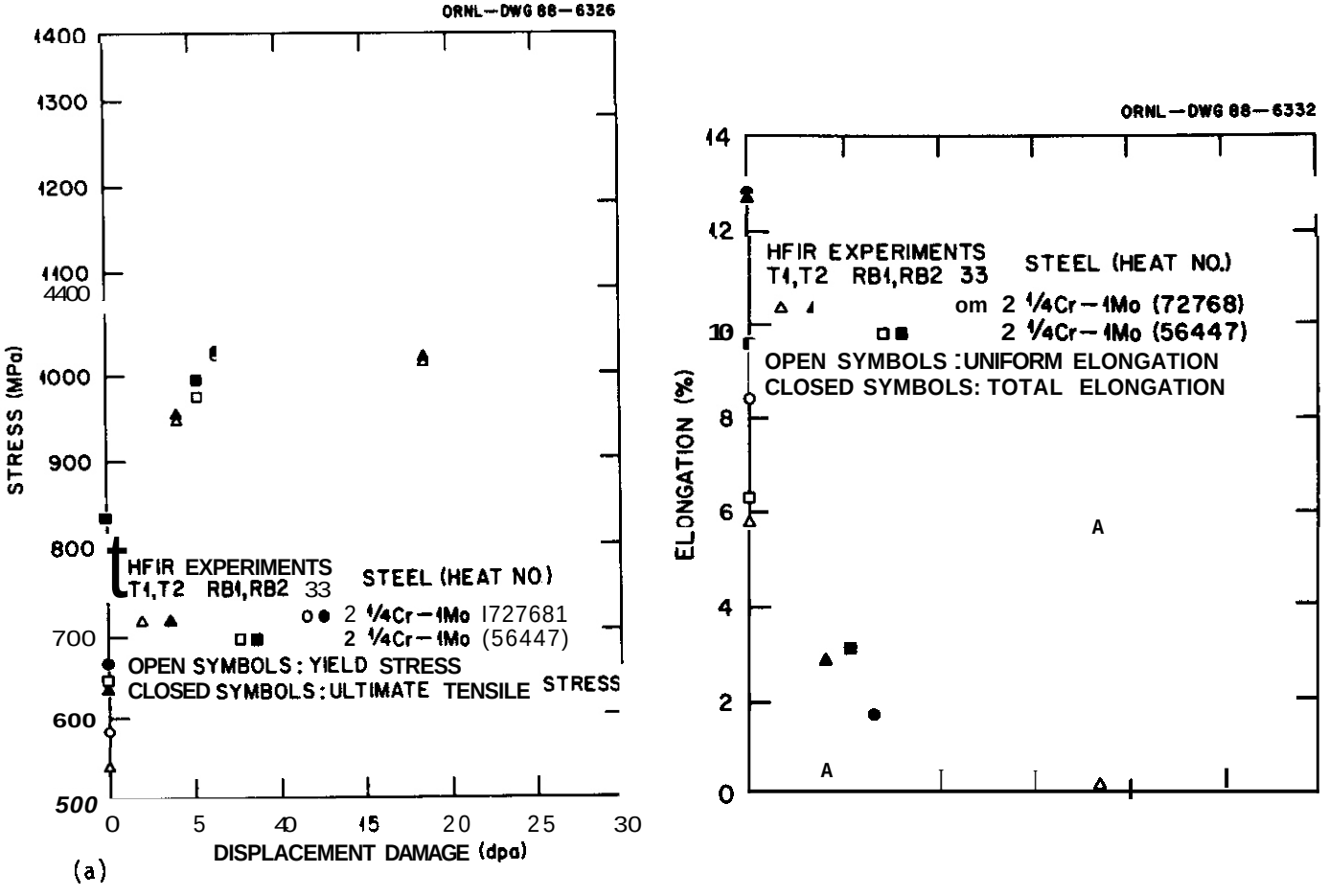

Fig. 5. The (a) yield stress and ultimate tensile strength and (b) uniform and total elongation of 2¼Cr-1Mo steel as a function of fluence.

Discussion

At low temperatures (<0.35 T_m, where T_m is the absolute melting point), the irradiation-induced defects (vacancies and interstitials) are expected to have limited mobility, and the primary mode of defect annihilation will be the recombination of vacancies and interstitials.[8,9] Interstitials remain mobile to much lower temperatures than vacancies. For temperatures of 0.35 T_m < T < 0.6 T_m, the mobility of the defects increases, resulting in a void and dislocation structure; the voids and dislocations become the primary sinks for the vacancies and interstitials, respectively.[8]

Interstitials are the mobile defects at the low temperature of the present tests. Those that are not annihilated by recombination with vacancies form dislocation loops, which cause an increase in flow stress and a decrease in ductility.[8] The excess vacancies are essentially frozen in the lattice and can also contribute to hardening. The number of loops -- and thus the strength -- saturates, although the loops will continue to grow.[9,10] Under a given set of irradiation and temperature conditions, a steady-state defect

concentration is expected, where the number of defects created by irradiation equals the number annihilated plus those incorporated in sinks.[8,9] There have been few studies on the effect of neutron fluence on tensile behavior at low temperatures to confirm this predicted behavior.

The Present results for the 9Cr and 12Cr steels indicated that irradiation in the low-temperature regime ($T < 0.35\ T_m$) caused the rate of increase in strength to decrease significantly with increasing fluence between about 5 and 10 dpa (Figs. 1 and 3). Although the data are limited, we interpreted the results for the steels with 2% Ni to indicate that after the rather rapid decrease in hardening rate beyond ~5 dpa, saturation had not yet occurred, and there was still an upward slope to the strength-displacement-damage curves. The limited data for the 2¼Cr-1Mo steel gives an indication that a saturation level may have been achieved (Fig. 5). Likewise, the slopes of the strength–fluence curves for the standard 9Cr and 12Cr steels are not as large as the slopes of the curves for the steels with 2% Ni (Figs. 1 and 3).

There was one important difference between the present experiment and previous work: the 9Cr and 12Cr steels both contained a larger range of helium than was present in previous experiments.** As pointed out in the Results section, the absolute increase in strength caused by the irradiation of the nickel-doped steels was substantially greater than that for the undoped steels. The main difference between the nickel-doped steels and the undoped steels was the transmutation helium produced by the presence of nickel. Previous studies[12] indicated that nickel does not affect the microstructure of the 9Cr and 12Cr steels in the unirradiated condition. The difference in unirradiated strengths in the steels with 2% Ni and those to which no nickel was added is caused by the difference in tempering and its relative effect on the microstructure, not new microstructural effects induced by the nickel addition.' Likewise, it was found that nickel additions did not in general have a significant effect on precipitation when irradiated in HFIR to 37 to 39 dpa at 300, 400, 500, and 600°C. except in the 9Cr-1MoVNb-2Ni steel at 400 and 500°C.[12] Because minimal diffusion of solutes is expected for the low-temperature irradiations in the present investigation, nickel would be expected to cause little change in precipitates.

To demonstrate a helium effect on the present results, it is necessary to examine the strength-dpa curves. For this discussion, we will concentrate on the YS behavior of the 12Cr-1MoVW and 12Cr-1MoVW-1Ni steels [Fig. 3(a)]. In the unirradiated condition, there was little difference in the YS of these two steels. Although the sparse amount of data at low fluences did not allow an accurate determination of the damage level at which the strength of the 12Cr-1MoVW-1Ni steel became greater than that of the 12Cr-1MoVW steel, it was higher at 5 dpa, which corresponds to about 35 and 15 appm He for the 12Cr-1MoVW-1Ni and 12Cr-1MoVW, respectively. Therefore, the data suggest that the difference between the 12Cr-1MoVW and 12Cr-1MoVW-1Ni steels after irradiation is caused by the larger amounts of transmutation helium in the 12Cr-1MoVW-1Ni steel. The differences in YS between the 12Cr-1MoVW-1Ni and the 12Cr-1MoVW-2Ni and between the 9Cr-1MoVNb and the 9Cr-1MoVNb-2Ni give similar indications when the preirradiation strength differences are taken into account. Based on the available data (few data are available below 5 dpa), the rate of increase in strength with dpa decreased abruptly somewhere around 5 dpa. The strength at which this decrease in slope occurred depended on the helium concentration: the higher the helium concentration, the higher the strength. By around 10 dpa, the slope of the strength-displacement-damage curves was much less than it was below 5 dpa. The UTS behavior was similar to that of the YS (Figs. 1 and 3).

The observation that the strength at which the rate of hardening increases depends on the helium (nickel) concentration of the alloy would seem to indicate that helium has a significant effect at the lowest helium concentrations. With the scatter inherent in the data along with the limited number of data points, it is not possible to estimate a slope for the strength-displacement-damage curve or for a strength-helium concentration curve in the region above ~5 dpa. As the strength-displacement-damage curves in Figs. 1 and 3 are now drawn, the slopes are quite flat, especially for the standard steels, indicating that the increase in strength with fluence is small compared with the hardening that has already occurred. Whether the slope remains constant or decreases beyond 20 dpa can only be determined by irradiations to higher dpa and helium concentrations.

For Irradiations up to about 5 dpa. the increase in strength is assumed to be caused by a combination of the effects of the displacement damage and helium. The exact proportion of the increase caused by helium depends on the helium concentration. One interpretation is that around 5 dpa, the strengthening due to the dislocation loops developed by the displacement damage begins to saturate. possibly corresponding to a transition from loop nucleation to growth. However, by this time significant amounts of helium are being generated, and although the rate of strength increase becomes lower, the strength continues to increase due to the continued helium buildup. An alternative interpretation is that hardening in the presence of significant amounts of helium occurs by the same processes that occur during displacement damage alone. However, the presence of helium extends the hardening to higher fluences.

The mechanism by which helium affects the strength can only be speculated upon, especially at low temperatures where there are few experimental data. When helium is in an interstitial position, it can readily diffuse through an alloy.** However, the interstitial helium can become imnobilized when trapped by a vacancy into a substitutional position. At temperatures below about 100°C, detrapping can occur primarily by irradiation (either directly by a neutron or by the knock-on process).[13] Alternatively, helium in vacancies could well interfere with natural helium-free bulk recombination of vacancies and interstitials. leading to more free self-interstitials in the presence of helium. At somewhat higher temperatures, detrapping

can involve replacement by self-interstitials. Larger helium-vacancy clusters can form when the helium and vacancies are mobile." In a detailed review of the literature, Maziasz cited references that indicated that helium refines the scale of loop nucleation and prolongs loop stability to high fluences.[15] These results, however, have generally been obtained at higher temperatures than those of the present experiments.

It is expected that helium in interstitial positions could cause an increase in strength, as would be the case if helium were trapped in vacancies, where the resulting increase in the self-interstitial concentration could lead to an increase in strength. Likewise, the refinement of the scale of loop nucleation would cause a strength increase. If the helium effect is primarily associated with the loop structure and the promotion of a higher loop saturation concentration, then a strength saturation should occur at higher displacement-damage levels. The effect of interstitial helium would perhaps continue with increasing fluence and be more persistent. However, saturation should again occur, because helium-vacancy clusters will form as more helium forms. At some point, no new clusters will form, and the newly generated helium will be incorporated in existing clusters and cause them to grow.

Verification by electron microscopy of the processes that occur during irradiation is hindered by the structures of the steel. Before irradiation, the tempered martensite and bainite contain a high dislocation density. Irradiation at low temperatures then superimposes a high density of dislocation loops on this structure, making it essentially impossible to delineate the irradiation-produced structure.

The observations on the loss of ductility due to the low-temperature irradiation [Figs. 2, 4, and 5(b)] are similar to previous results.[1-3] Such extremely low uniform elongation values are of concern to reactor designers. The low values in these steels were previously attributed to channel deformation.[3] On a microscopic scale, channel deformation occurs by dislocations sweeping out defect-free channels,[16] after which dislocation motion becomes easy and is then confined to these channels (i.e., the small loops are swept up in the present case). Deformation is then restricted to a very narrow region of the specimen. An instability occurs in this region, leading to a neck and a small uniform elongation. The uniform elongation decreased to a low value after about 5 dpa and remained low, while the total elongation went through a minimum. This minimum may be a reflection of the change that takes place in the dislocation structure with irradiation. As the loops grow in size, they should become more difficult to sweep up or annihilate to form a channel. If this occurs, the uniform elongation should then eventually begin to increase at some higher fluence.

Results from this study indicate that future studies of materials for the first wall and blanket structure of a fusion reactor must take into account the large amounts of helium to be generated in reactor components during operation. Previous results have indicated that the tensile behavior is affected by helium at 300 and 400°C,[17] and that the impact[5] and fatigue[6] behavior may also be affected. The details of these effects will be important to reactor designers.

SUMMARY AND CONCLUSIONS

Tensile specimens of 2¼Cr-1Mo steel, standard 9Cr-1MoVNb and 12Cr-1MoVW steels, and these latter two steels with up to 2% Ni were irradiated in HFIR at 55°C -- the HFIR coolant temperature. Irradiations were conducted over a range of fluences that gave displacement-damage levels of up to 25 dpa. Because of the nickel present in the steels, irradiation in the mixed neutron spectrum of HFIR produced up to 327 appm He. Specimens were tested at room temperature. The observations and conclusions can be sumnarized as follows:

1. Irradiation caused a large increase in the yield strength and ultimate tensile strength of all steels. The strength increased with increasing fluence, but the rate of increase with fluence decreased beyond damage levels of approximately 5 dpa.

2. The steels with nickel additions hardened more than the standard steels, and the steel with 2% Ni hardened more than the one with 1% Ni.

3. The results indicated that helium caused part of the observed strength increase; this was in addition to the strengthening caused by dislocation loops formed from the interstitials and vacancies created by the displacement damage in the helium-free material.

4. The increase in strength was accompanied by a decrease in uniform and total elongation. Unlike the strength, which continued to increase with fluence, the total elongation appeared to go through a minimum, with the ductility after 20 to 25 dpa greater than after irradiation to intermediate levels of ~10 dpa. Uniform elongation remained low at the highest damage levels.

5. The results indicate the importance of determining the effect of helium on mechanical properties of materials for fusion-reactor applications.

REFERENCES

1. R. L. Klueh, J. M. Vitek. and M. L. Grossbeck, Effects of Irradiation on Materials: Eleventh Conference, ASTM STP 782, H. R. Brager and J. S. Perrin, Eds., American Society for Testing Materials, Philadelphia. 1982, p. 648.

2. R. L. Klueh and J. M. Vitek, J. Nucl. Mater. 1036104' (1981) 887.

3. R. L. Klueh and J. M. Vitek. Ferritic Alloys for Use in Nuclear Energy Technologies. Eds., J. W. Davis and D. J. Michel, The Metallurgical Society of AIME, Warrendale, Pennsylvania, 1984, p. 615.

4. W. L. Hu and D. S. Gelles. Ferritic Alloys for Use in Nuclear Energy Technologies, Eds., J. W. Davis and D. J. Michel, The Metallurgical Society of AIME, Warrendale, Pennsylvania, 1984, p. 631.

5. J. M. Vitek, W. R. Corwin, R. L. Klueh, and J. R. Hawthorne, J. Nucl. Mater. 141-143 (1986) 948.

6. M. L. Grossbeck, J. M. Vitek, and K. C. Liu, J. Nucl. Mater. 141-143 (1986) 966.

7. R. L. Klueh, P. J. Maziasz, and J. M. Vitek, J. Nucl. Mater. 141-143 (1986) 960.

8. E. E. Bloom, Radiation Damage in Metals, Eds., N. L. Peterson and S. D. Harkness, American Society for Metals, Metals Park, Ohio, 1976, p. 295.

9. P. G. Shewmon, Fundamental Aspects of Structural Alloy Design, Eds., R. I. Jaffee and B. A. Wilcox, Plenum Press, New Vork, 1977, p. 173.

10. L. M. Brown. A. Kelly, and R. M. Mayer, Phil. Map. 19 (1969) 721.

11. R. L. Klueh and J. M Yitek, J. Nucl. Mater. 140 (1986) 140.

12. P. J. Maziasz. R. L. Klueh, and J. M. Vitek, J. Nucl. Mater. 141-143 (1986) 929.

13. L. K. Mansur, E. H. Lee, P. J. Maziasz, and A. F. Rowcliffe, J. Nucl. Mater. 141-143 (1986) 633.

14. N. M. Ghoniem, S. Sharafat, and L. K. Mansur, Point Defects and Defect Interactions in Metals, Eds., Jin-Ichi Takamura, M. Doyama, and M. Kiritani, University of Tokyo Press, Tokyo, 1982, p. 865.

15. P. J. Maziasz, Effects of Helium Content on Microstructural Development in Type 316 Stainless Steel Under Neutron Irradiation, ORNL-6121, Oak Ridge National Laboratory, 1985.

16. F. A. Smidt, Jr., Dislocation Channeling in Irradiated Metals, NRL Report 7078, Naval Research Laboratory, 1970.

17. R. L. Klueh and J. M. Vitek, J. Nucl. Mater. 150 (1987) 272.

6.2 Austenitic Stainless Steels

INFLUENCE OF THERMOMECHANICAL TREATMENT AND ENVIRONMENTAL HISTORY ON CREEP, SWELLING AND EMBRITTLEMENT OF AISI 316 AT 400°C AND 130 DPA - D. L. Porter, E. L. Wood (Argonne National Laboratory, EBR-II Project), and F. A. Garner (Pacific Northwest Laboratory)

OBJECTIVE

The object of this effort is to determine the mechanisms involved in radiation-induced deformation and embrittlement of structural materials and to apply these insights for extrapolation of available fast reactor data to fusion-relevant conditions.

SUMMARY

A comprehensive creep experiment on AISI 316 stainless steel involving irradiation at ~400°C to 130 dpa has been completed. The influence of material and environmental variables on creep and swelling of this steel at ~400°C is shown to have many similarities with the behavior exhibited in an earlier experiment conducted at ~550°C, but significant differences are also apparent. These arise because the 400°C experiment was clearly conducted in a regime dominated by the kinetics of point defect recombination whereas the 550°C experiment was conducted in the sink-dominated regime. At 400°C it is also shown that a severe embrittlement arises concurrent with ~10% swelling, requiring careful handling of test specimens and structural assemblies at room temperature.

PROGRESS AND STATUS

Introduction

In several earlier papers the neutron-induced irradiation creep in the EBR-II fast reactor of AISI 316 stainless steel at 550°C was discussed, concentrating on the tendency of irradiation creep to decline in rate and even disappear at exposures approaching 80 displacements per atom (dpa).[1-3] This phenomenon was shown to be related to the presence of significant levels (5 to 10%) of void swelling, which in turn is determined by the starting thermomechanical condition of the alloy and the accumulated neutron exposure. Swelling of this alloy is also known to be sensitive to the irradiation temperature,[4,5] another variable which can be used to study the phenomenon of creep disappearance.

The 550°C irradiation creep series was accompanied by another series at ~400°C, a temperature where void swelling in this alloy takes longer to develop.[5] The 400°C series was irradiated to much larger exposures (~130 dpa), however, so that swelling levels on the order of 5 to 10% were also achieved. While some subsets of the creep data at high exposures were published in earlier reports,[6,7] it became obvious as the examination proceeded further that the behavior of AISI 316 at ~400°C was quite different from that at ~550°C in two significant respects. First, the creep rate did not decline at comparable swelling levels. Second, the alloy becomes severely embrittled at swelling levels on the order of ≥10%. This embrittlement was not observed in the 550°C series.

This paper not only presents all of the creep data but also explores the development of severe embrittlement in 316 stainless steel.

Exoerimental details

The tubing employed in both the 400 and 550°C experiments was the N-lot heat V87210, previously used as a reference heat in the U. S. liquid metal reactor program. Its composition in weight percent was Fe-13.57Ni-16.36Cr-2.88Mo-1.42Mn-0.47Si-0.07C-0.02P-0.01S with less than 0.005 weight percent boron. Four cold work levels (0, 5, 10 and 20%) as well as two separate aging conditions were used. These latter were 20% cold worked followed by aging at 482°C for 24 hours (heat treatment C) and heat treatment C followed by another aging at 704°C for 216 hours (heat treatment D).

It is important to note that the starting material for all conditions in this series was the 20% cold worked condition. The 0% cold work condition was produced by annealing at 1020°C for 20 min. and water-quenching (heat treatment A) and the 5% cold work condition was produced from the annealed condition. Since the objectives of this current study were somewhat limited, not all of the conditions were examined in the same depth.

Hoop stress levels of 0, 206, 276 and 343 MPa (0, 30, 40, and 50 ksi) were attained with pressurized helium. Most creep capsules were irradiated at constant stress and temperature but some were deliberately subjected to abrupt changes in stress level and/or temperature. Other capsules lost pressure during irradiation and were continued at zero stress.

The pressurized section of the capsules was 0.98 m in length but the bottom 0.71 m contained a loosely fitting stainless steel rod designed to reduce the pressure pulse that could result from a sudden failure.

The outer diameter of the capsule was 0.584 cm with a wall thickness of 0.038 cm. Irradiation was conducted in row 7 of EBR-II in two 37-pin subassemblies designated X101 and X133. Approximately 5 dpa (±10%) are produced in this reactor for each 1.0 x 10^{22} n/cm^2 (E > 0.1 MeV) depending on the position in reactor. The dpa levels cited for each datum in this paper incorporate the position dependence of this parameter.

To minimize the effect of swelling-induced axial growth on the experiment, only the section at or below the capsule center was used in the analysis. At the end of each irradiation period, a contact profilometer was used to measure the capsule diameter on a spiral trace along the entire length of the capsule. The majority of capsules were measured as many as 22 times during the irradiation, averaging between examinations approximately 6 dpa at capsule center. As shown in Fig. 1, the temperature over the region of interest rose from 385 to 400°C at capsule center.

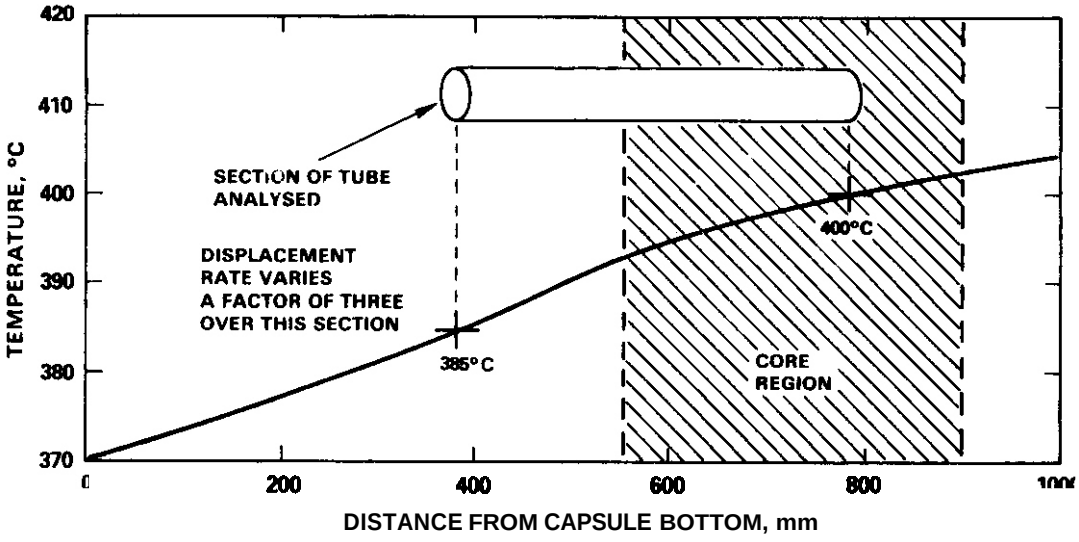

Fig. 1. Temperature profile along creep capsule.

When the experiment was terminated, selected capsules were sectioned into 2.5 cm increments and density changes were measured in order to separate the swelling and creep strains. The effects of displacement rate on creep and swelling were determined by comparing the strain at different positions along the capsule.

Not all metallurgical conditions received the same level of attention, both in the design of the experiment and its subsequent analysis. Most attention was directed toward the 10 and 20% cold worked conditions and the heat treatment D condition.

Results of creep and swelling studies

Figure 2 shows a comparison of the centerline diameter changes observed at 400°C and a hoop stress of 276 MPa (40 ksi) for five of the six thermomechanical starting conditions. The 5% cold work condition was not examined. Note that both short term aging and various levels of cold work had very little effect on the strain behavior while the double aging treatment of heat treatment D had a very pronounced effect on increasing the onset of swelling and creep deformation. The strain rate decreased somewhat as the cold work level increased, a behavior usually observed in this steel.'.'

The curves shown in Fig. 2 are composite trend curves representing the average behavior of a number of capsules. Fig. 3 through 5 show that there are not very large variations in deformation behavior between nominally identical capsules. The small differences probably reflect minor differences in irradiation conditions at various positions across the subassembly. Note that in none of these tubes did the strain rate approach the 0.33%/dpa upper limit observed in the 550°C series. (This limit signalled the complete disappearance of irradiation creep.) Each of Fig. 3 through 5 show one case where the gas pressure was lost at some point, probably resulting from a pinhole failure of a weld during one of the many rounds of removal, measurement and reinsertion into the reactor. From that point on, the diameter increases were only due to void swelling, assumed to be isotropic, where $\Delta D/D = \Delta V/3V$, an assumption verified many times previously.' Regardless of the displacement level at which the pressure was lost, the swelling rate remained relatively constant thereafter at values ranging from 0.04 to 0.09%/dpa, substantially below the 1%/dpa level characteristic of austenitic alloys in general at higher temperatures' and this steel at 550°C.[1-3]

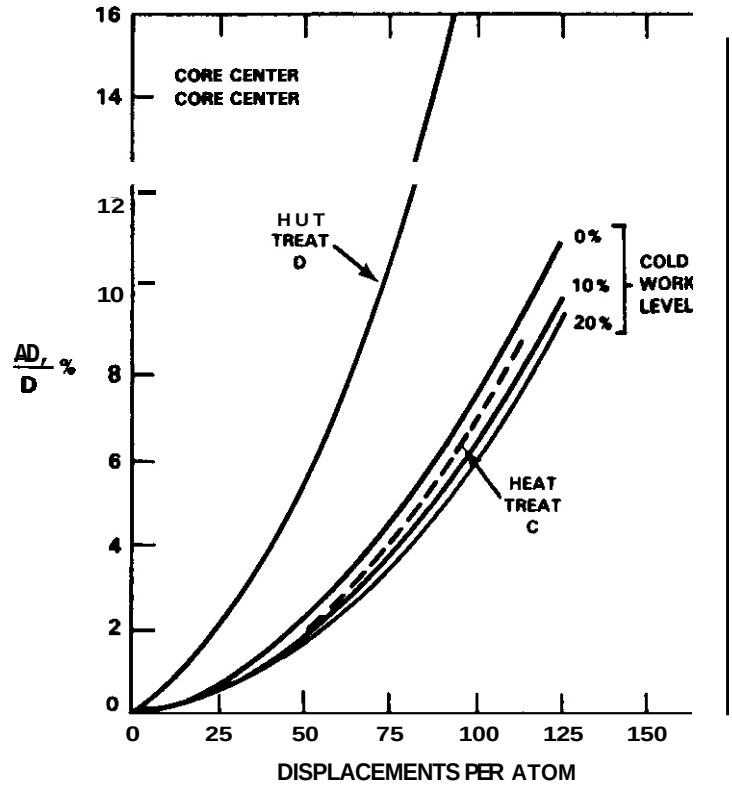

Fig. 2. Composite trend curves of total diametral deformation at ~400°C and core center for various starting thermomechanical conditions of AISI 316.

Also in contrast to the behavior of the highest swelling capsules at 550°C, the total diametral strain rate at 400°C increased continuously with increasing stress as shown in Fig. 6 for the 20% cold worked condition. Creep does not appear to be decreasing or disappearing at this temperature. Using a procedure described in detail elsewhere,[6] the instantaneous creep coefficient can be calculated from diameter measurements of both stressed and unstressed capsules, assuming that swelling at 400°C is not very sensitive to stress. Based on results of other studies, this assumption is known to be reasonable at 400°C although it does not apply at 550°C and higher temperatures.[8,9] Figure 7a shows that the instantaneous creep coefficient of 20% cold worked steel is independent of stress level with two of the three curves appearing to saturate in magnitude at higher exposure levels. Figure 7b shows that calculation of the creep coefficient for the 10% cold worked condition yields a remarkably similar set of curves with all three appearing to saturate. Thus, the creep coefficient is not sensitive to the cold work level in this range. The units of the creep coefficient are those typical of that used in the U. S. liquid metal reactor program and can be converted to SI units and displacements per atom using the conversion 1×10^{-6} MPa^{-1} dpa^{-1} = 4×10^{30}/(psi n cm^{-2}). This value of the coefficient also represents the y-axis intercept and therefore the creep rate in the absence of swelling.

The dependence of swelling on stress can be checked by comparing the density changes of each of these capsules. Figure 8 shows that in the three pressurized capsules, there was no observable effect of stress at any position along the capsule. Whereas the data in Fig. 7 were taken all at one position and displacement rate, the data in Fig. 8 were derived at different axial locations and incorporate relatively small differences in temperature. Figure 8 does not contain any density data for the unstressed capsule but does contain the last four measurements of swelling deduced from diameter change at capsule center. These data also confirm the insensitivity of swelling to stress at 400°C.

No density data were available for the stress-free capsule because the filler rod (which exists at a slightly higher temperature) had swelled into contact with the capsule wall at ~80 dpa, binding with and distorting it. Normally this does not occur at lower fluences or when gas-driven creep is operating on the capsule wall.

The swelling rate S implied by the data in Fig. 8 is on the order of 0.05 to 0.07%/dpa, and was derived over a considerable range of displacement rate. The effect of the flux and temperature variations on total deformation can be observed in Fig. 9. One can deduce from Fig. 9 that the swelling rate derived

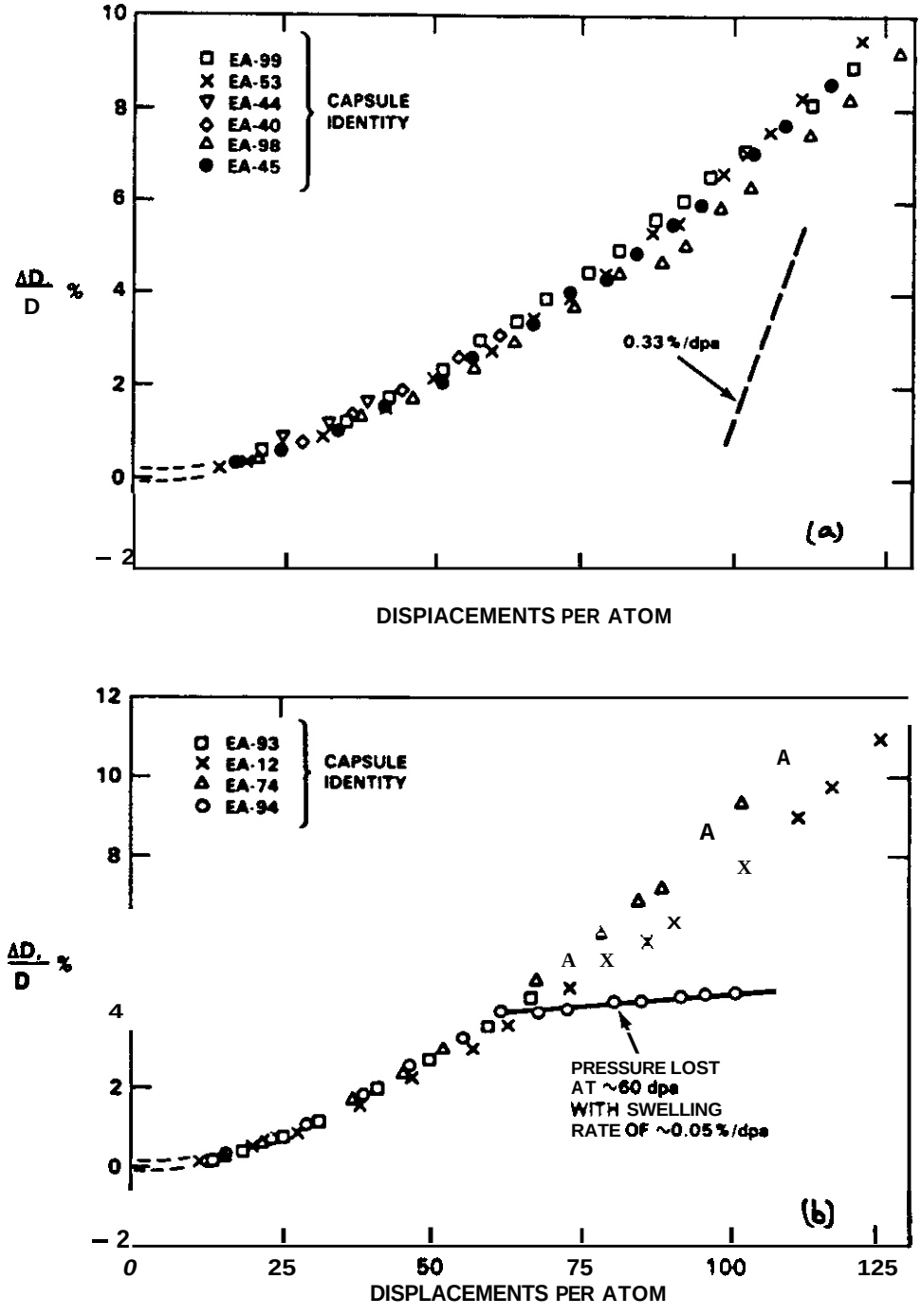

Fig. 3. Diameter changes observed in 10% cold worked steel for a) six nominally identical capsules at 276 MPa (40 ksi) and b) four nominally identical capsules at 343 MPa (50 ksi). Note that one capsule failed at ~60 dpa and swelled without stress thereafter.

from Fig. 8 might be an underestimate. The average stress-free swelling rate under isoflux conditions can be derived from Fig. 6 and is indeed somewhat larger at S = 0.11%/dpa over the range 70 to 130 dpa.

One would expect the strain rate to increase if the stress level and/or the temperature were to be increased. Figures 10a and 10b show that this indeed occurs in experiments where deliberate increases were made in these variables. Note in Fig. 10b that the combination of higher stress and an increase to 550°C

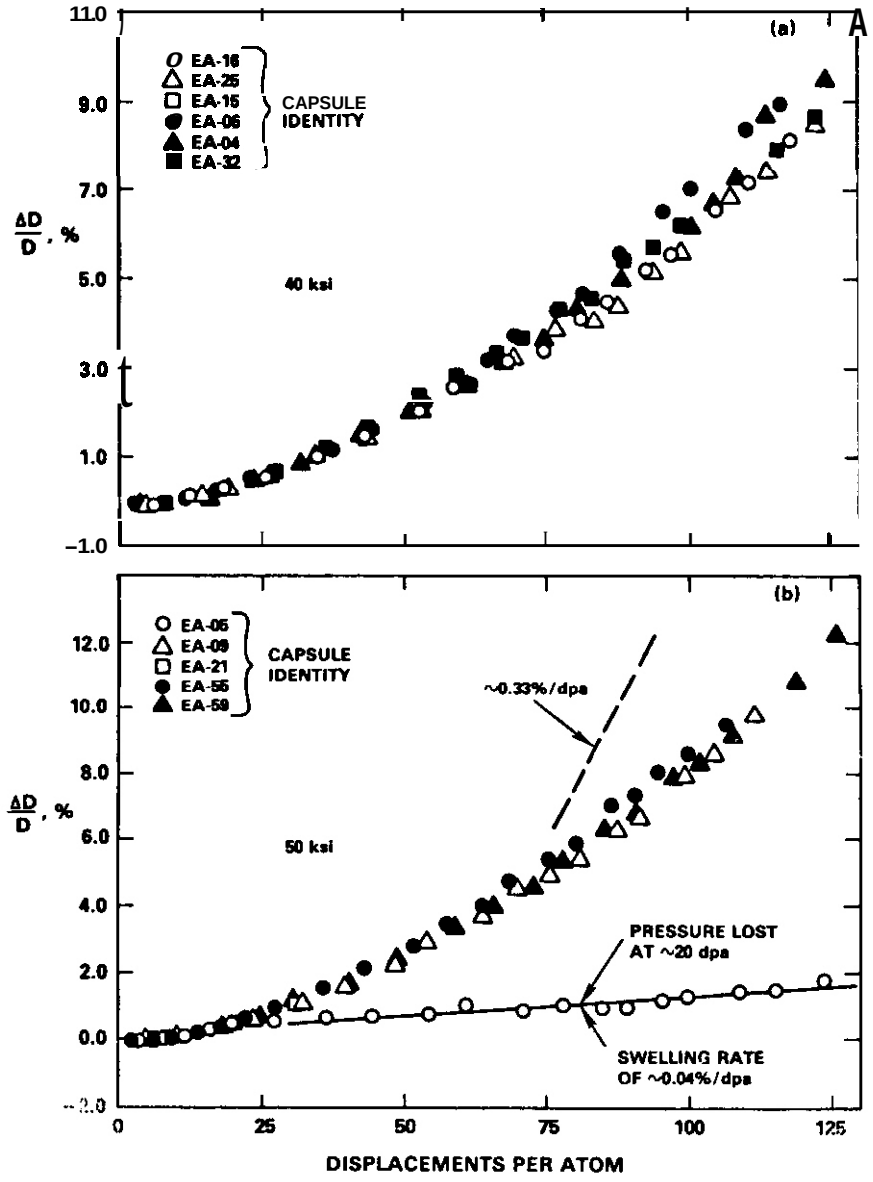

Fig. 4. Diameter changes observed in 20% cold worked steel for a) six nominally identical creep capsules at 276 MPa (40 ksi) and b) five nominally identical capsules at 343 MPa (50 ksi). Note that one capsule failed at 20 dpa and swelled without stress thereafter.

yielded a total deformation rate that approaches the $\Delta D/D = 0.33\%/dpa$ value observed as an upper limit of similar capsules irradiated isothermally at 550°C.[1,3] During isothermal irradiation at 400°C, the total strain rate of 20% cold worked 316 at 343 MPa (50 ksi) reached only $\Delta D/D = 0.14\%/dpa$ at 125 dpa.

The strain rates of AISI 316 are somewhat sensitive to material condition as well as environmental variables as demonstrated by looking at other conditions in this experiment. In the heat treatment D condition the total strain rate $\Delta D/D$ at 400°C reached 0.22%/dpa at 276 MPa (40 ksi), but when the temperature was changed from 400 to 550°C at 32 dpa, the total creep rate of heat treatment D at 276 MPa immediately went to the 0.33%/dpa limit.

Figure 11 shows the diameter changes of five nominally similar capsules initially irradiated at 550°C. (The experimental details of these two irradiations were described in refs. 1 and 3). At ~30 dpa two of these capsules were subjected to an abrupt decrease in temperature to 400°C. Prior to the changes these capsules were just beginning to exhibit accelerated swelling and creep rates but these quickly subsided from the increasing rates observed in the three capsules maintained at 550°C. The swelling rate of the unstressed capsule was found to be $S \approx 0.10\%/dpa$. This reduction in swelling rate tends to confirm that at 400°C the swelling rate is dominated by the kinetics of point defect recombination, a situation where the swelling rate is not influenced very strongly by the details of the microstructure.

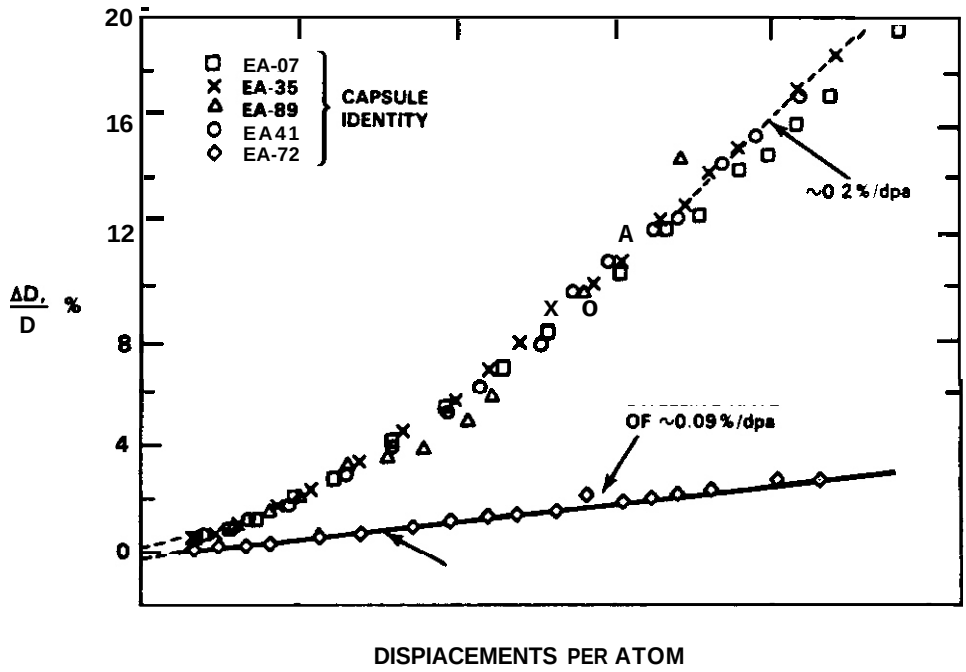

Fig. 5. Diameter change observed in heat treatment D for five nominally identical creep capsules at 276 MPa (40 ksi). Note that one tube lost its pressure very early in the experiment.

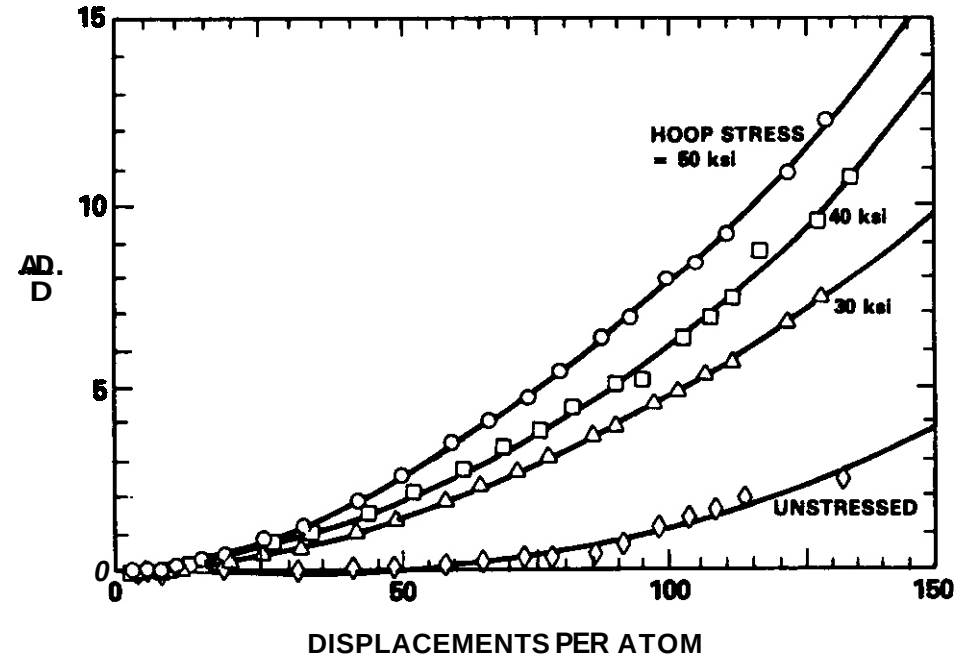

Fig. 6. Irradiation creep and swelling-induced strain at 400°C of the 20% cold worked condition in unstressed and stressed capsules. The stress levels were 206, 276, and 343 MPa (30, 40 and 50 ksi).

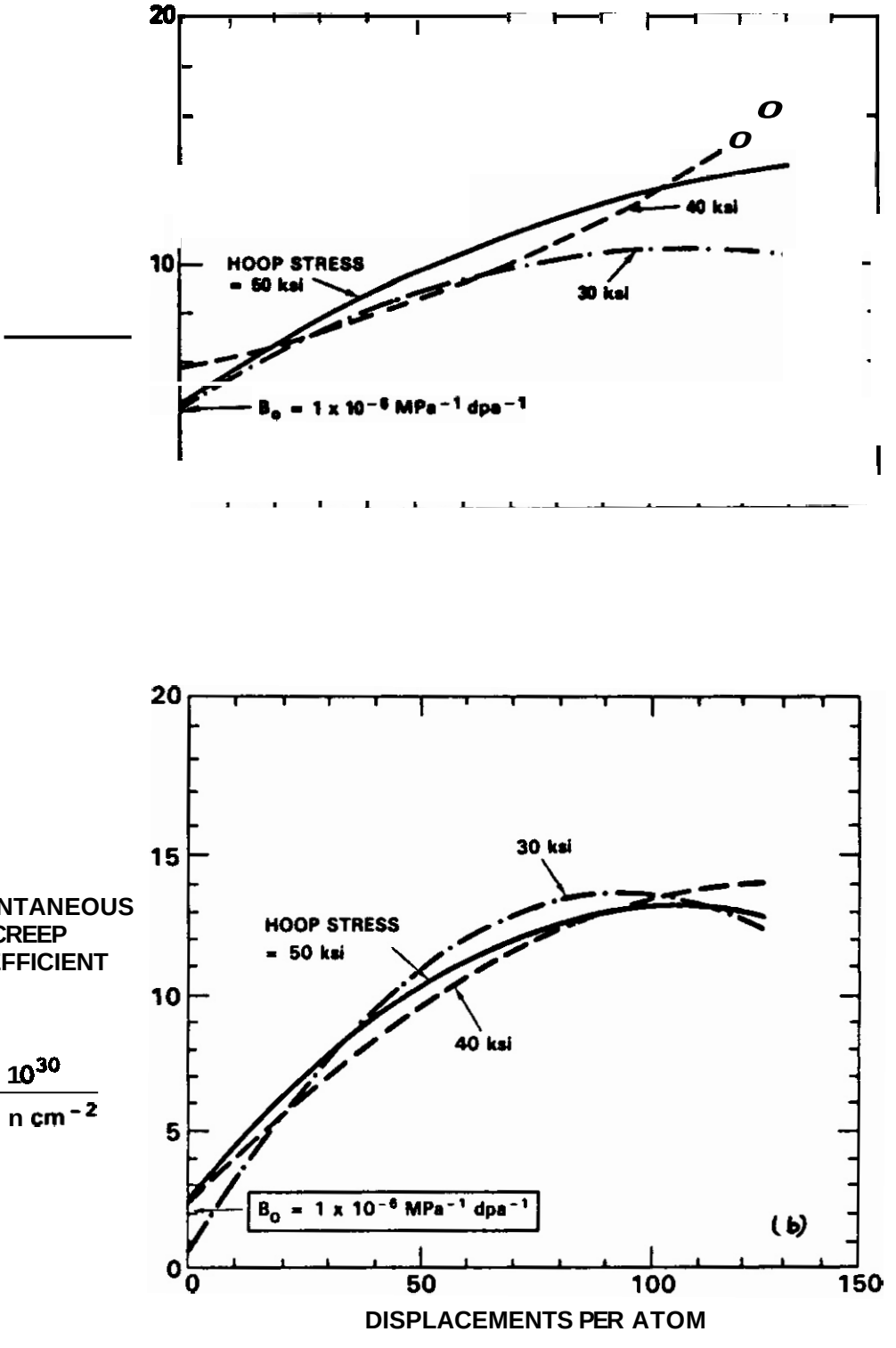

Fig. 7. (a) Instantaneous creep coefficients at 400°C of 20% cold worked AISI 316 derived from data in Figure 6 and (b) similar calculations for the 10% cold worked condition.

Figures 12 and 13 show the creep behavior of heat treatment D at 400°C. The instantaneous creep coefficient at 276 MPa is relatively large at first and increases steadily with exposure, possibly saturating somewhere between 20 and 30 x 10^{30} cm^2/n·psi. This is a higher level than observed in the cold worked steels, which saturated at ~15 x 10^{30} cm^{cm}/n·psi

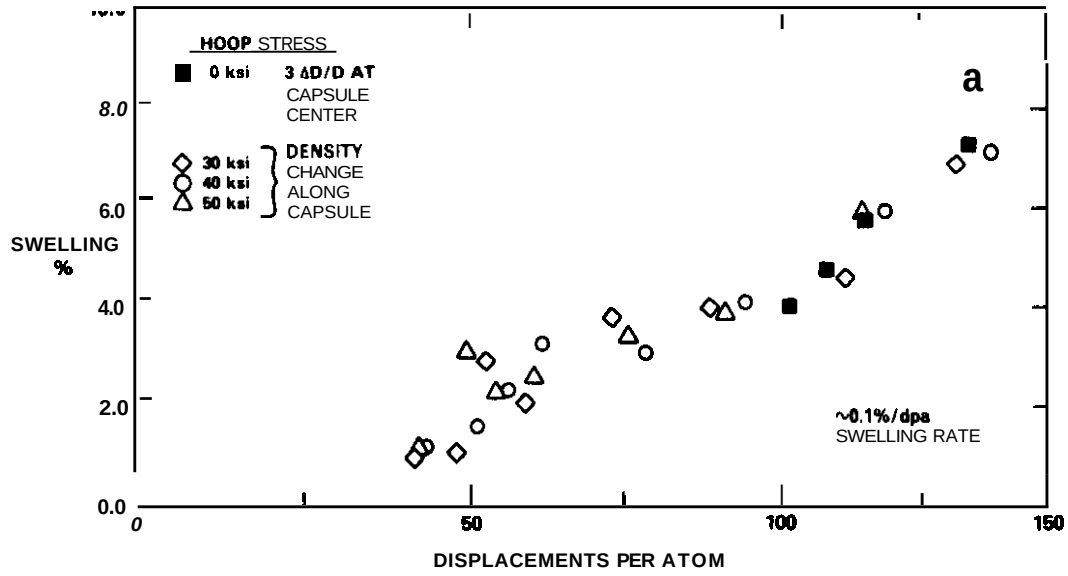

Fig. 8. Swelling measured along the length of the three pressurized creep capsules shown in Figure **6.** Also shown are the swelling values inferred from time-dependent diameter change measurements at the center of the unstressed capsule.

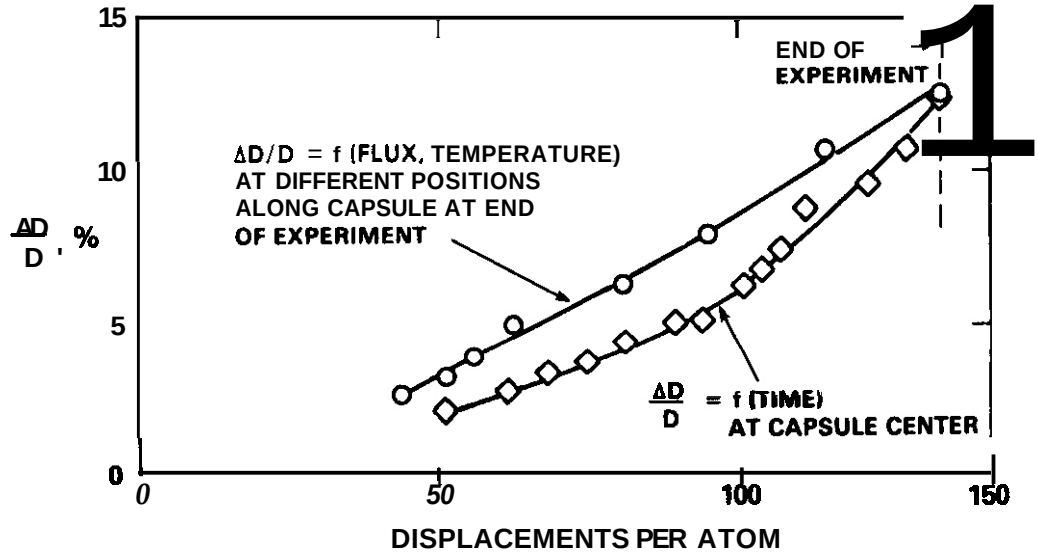

Fig. **9.** Influence of displacement rate and temperature variations on total strain observed in a 20% cold worked capsule with a hoop stress of **216** MPa (40 ksi).

Results of embrittlenent studv

When the 400°C capsules were removed for the last time from the hexagonal duct that encases them during irradiation, **it** became obvious that they would have to be handled with care. One capsule designated EA-35 was found to be fractured into a number of pieces, which apparently occurred during disassembly of the subassembly. The breakup was very severe in nature, resulting in a number of long shards, each of which exhibited a brittle appearance. Another capsule, designated EA-07, broke into three pieces while being clamped into a vise for cutting of density sections, as shown in Fig. 14.

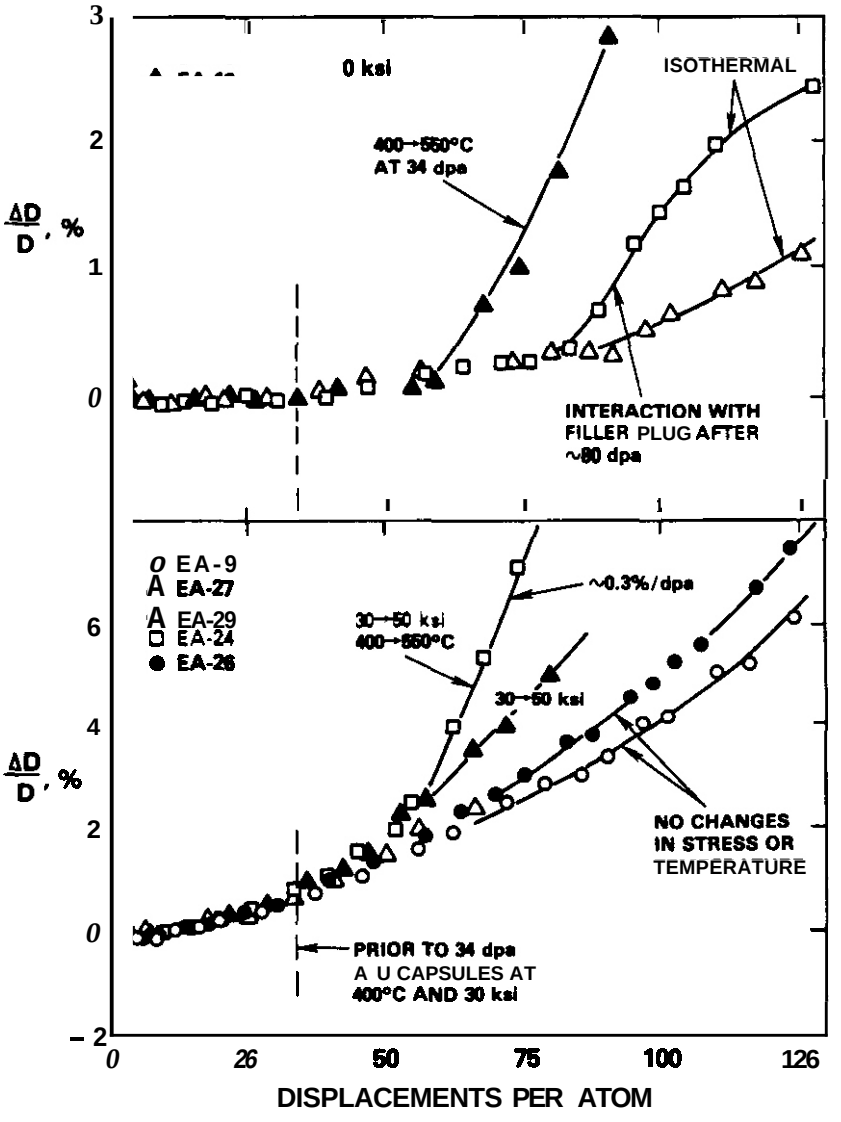

Fig. 10. Influence of radiation history on strain behavior of 20% cold worked steel at 400°C. Increasing the stress level accelerates the deformation rate but increasing both the stress and the temperature causes a more pronounced increase in deformation rate.

Both of these capsules were fabricated from the heat treatment D condition, reaching centerline deformation levels of 19 to 20% at exposures of 112 to 120 dpa at a hoop stress of 276 MPa (40 ksi). In each case it appeared that the fracture initiated near the region of peak swelling, which for EA-07 was measured at –14%. Thus both these capsules represented the highest level of swelling and creep attained in this experiment.

While the broken pieces of EA-07 were discarded, the broken sections of EA-35 were subjected to a variety of examinations. Several small pieces were taken from the broken end for metallographic analysis. The first was mounted to present a longitudinal and transverse view of the fracture, and showed that the fracture followed both grain boundaries and planar paths through the grains. A second specimen was saw-cut transversely from the same region and mechanically polished. It showed that the inside surface of the tube was covered with small cracks, some as deep as 0.0005 in (1.3 x 10^{-3} cm). The outer surface of the tube contained fewer and somewhat smaller cracks, consisting mostly of notches at grain boundaries.

Another piece measuring ~1 in (2.5 cm) in length was cut from the end of a six inch long fragment and then mounted on a stub of a scanning electron microscope (SEM) with silver paint. At this point it was apparent that the inside surface of the element had become discolored and was black in appearance. The brittle nature of the fracture is evident in the overall appearance of the broken piece as shown in Fig. 15a. A jagged fracture with a sawtooth outline forms one edge of the specimen with a somewhat smoother break along the other edge. Examination of the inside surface revealed numerous intergranular

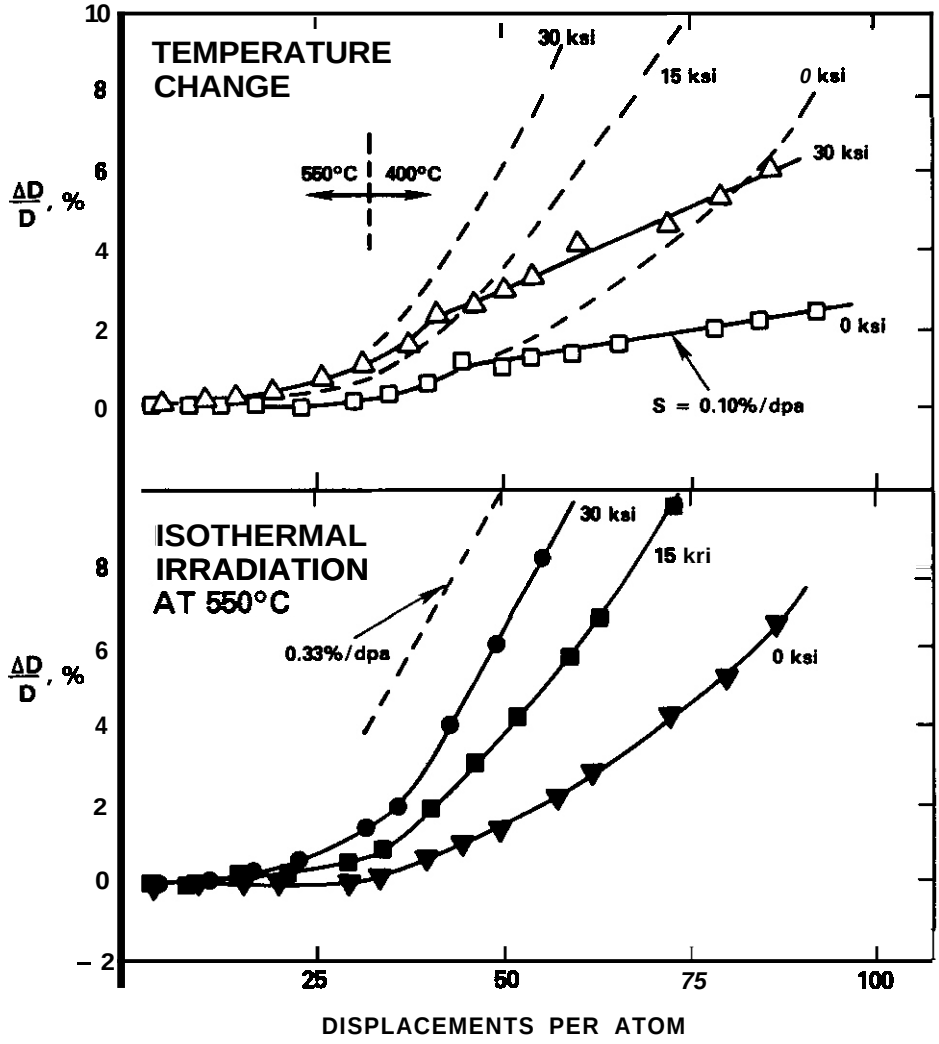

Fig. 11. Diameter changes of a) two 20% cold worked capsules at 0 and 206 MPa (30 ksi) subjected to an abrupt decrease in temperature and b) three others irradiated only at 550°C at 0, 103 and 306 MPa (0, 15, and 30 ksi).

cracks in the surface (Fig. 15c and 15d). The outside surface was cracked in this specimen to an even greater extent with almost every grain boundary showing some degree of cracking (Fig. 16). Many areas of the fracture surface exhibited extensive amounts of corrosion products (Figure 17) thought to have been formed in the subassembly after failure of the capsule but prior to final cleaning for examination. Some areas of the failure surface exhibited flat surfaces typical of cleavage.

Another piece was broken to produce a fresh fracture surface and was found to be free of corrosion products. It also displayed many areas of cleavage-type failure as shown in Figure 18. This piece was taken from a position approximately 4 in (10 cm) above the core centerline and was measured to have swelled *9.1%.*

Discussion

Although comparable levels of swelling were obtained at lower dpa levels in the 550°C creep capsule series in both heat treatment D and other conditions, embrittlement of the type observed at 400°C did not occur. A similar situation was observed by Hamilton and coworkers[10] in a series of tests conducted on various austenitic stainless steels. In each case, severe embrittlement occurred when the swelling reached levels on the order of ~10% and when fracture was initiated at room temperature or at relatively low temperatures with respect to the irradiation temperature, but only for irradiation temperatures of ≤450°C. At higher irradiation temperatures, no embrittlement was observed. The origin of this phenomenon was determined to arise from a compound mechanism involving large levels of voids. An increase in hardness arises not only from the voids themselves but also due to an indirect effect of the large surface area associated with the high density of voids at ~400°C, whereby nickel segregates to void surfaces and is

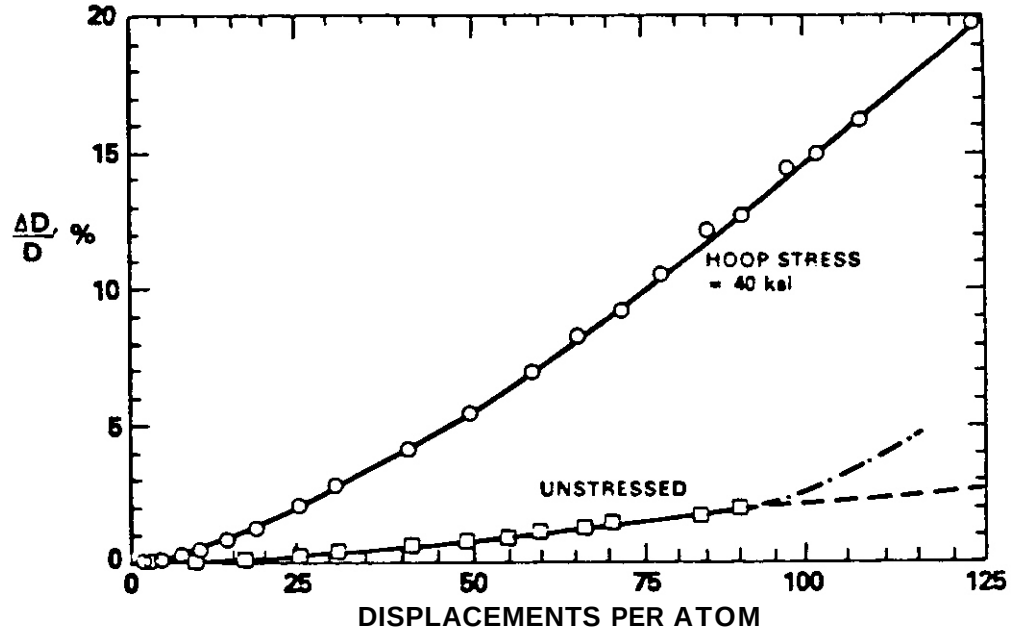

Fig. 12. Irradiation creep and swelling-induced strain at 400°C for the heat treatment D condition in the unstressed and stressed capsules.

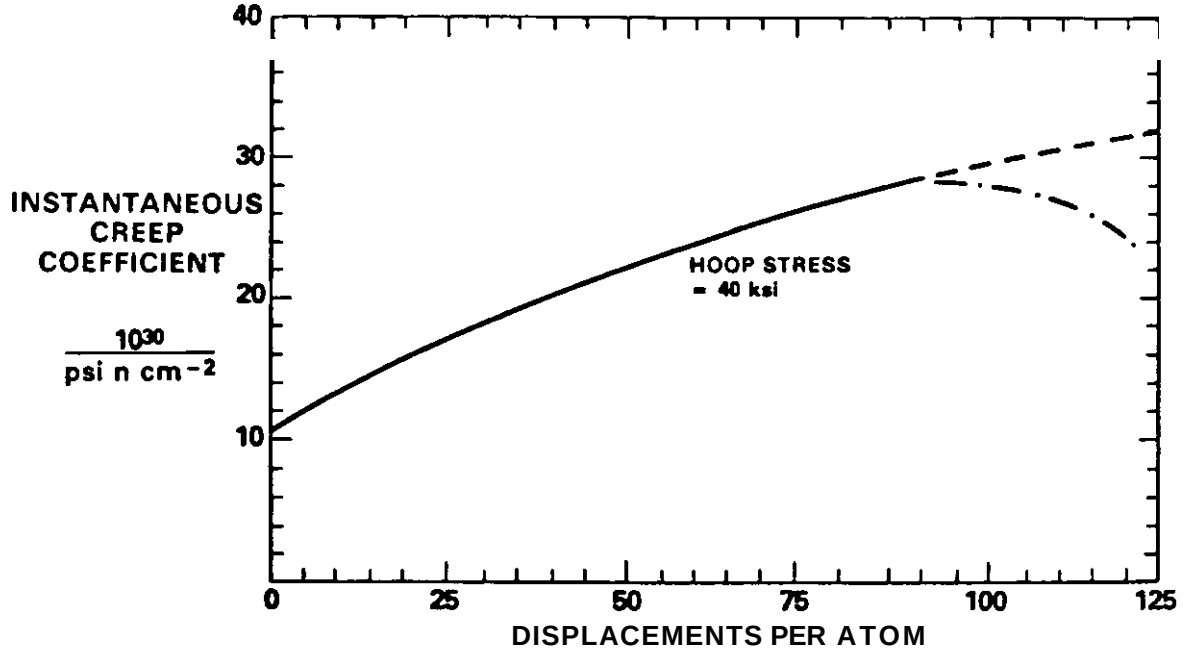

Fig. 13. Instantaneous creep coefficient of heat treatment D at 400°C derived from data in Figure 12.

depleted in the matrix of the alloy. Chromium is depleted at void surfaces. The strong dependence of stacking fault energy on nickel and chromium content, and particularly on deformation temperature combine to promote extensive stress-induced formation of epsilon martensite at room temperature. This leads to a very brittle failure more aptly characterized as quasi-cleavage. At higher deformation temperatures it leads to a less brittle failure mode designated channel fracture.

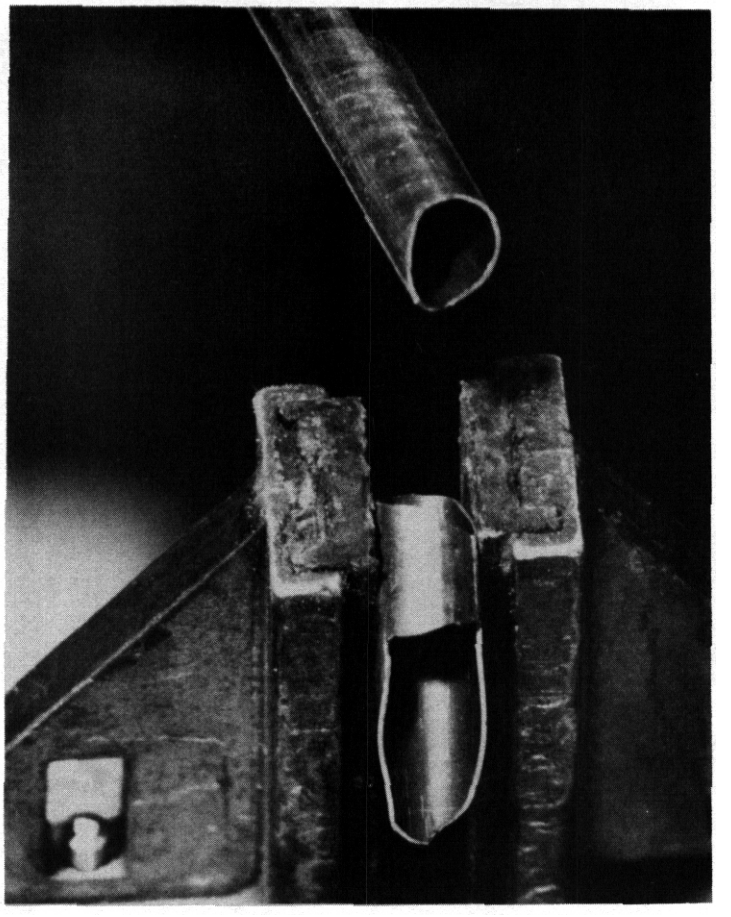

Fig. 14. Failure during mounting of severely embrittled AISI 316 capsule EA-07 in the heat treatment D condition after irradiation to 120 dpa at 400°C and a hoop stress of 276 MPa (40 ksi).

Hamilton and coworkers, however, did not observe the extensive surface cracking seen in this study. This is easily rationalized because in the various kinds of specimens employed in Hamilton's studies there were no applied stresses during irradiation and no creep deformation, which is known to induce such cracks at high strain levels. The outer surface of the capsule was also in contact with flowing sodium which can lead to etching of grain boundaries. On the inner surface, however, there is only helium gas. It is not clear from this study whether the cracks on the inner surface occurred before or during the fracture process.

It is clear, however, that failure in this experiment is associated with or at least coincident with swelling at levels on the order of 10%. The fact that only heat treatment D capsules failed is probably related to the higher creep and swelling of heat treatment D, but it may also reflect the greater care taken in removal of capsules once their brittleness was evident.

The reasons for the discoloration of the inside of the broken capsule have not been resolved, but may possibly reflect the injection of very large levels of recoiling helium following collisions with fast neutrons. The levels of injected helium can be exceptionally high and have been shown to contribute somewhat to the embrittlement phenomenon.[11] Sputtering of the surface by the injected helium gas may also be involved.

The creep portion of this study demonstrates that the creep disappearance phenomenon observed at 550°C cannot be attributed solely to the attainment of ~10% swelling but this does not rule out the possibility that it is somehow linked to the attainment of steady-state swelling at ~1%/dpa. This latter rate was never approached in the various types of capsules and conditions used in the 400°C study. This in turn suggests that at 400°C one will never develop the characteristic steady-state swelling rate (even at higher fluence) and that at this temperature the kinetics of void growth are dominated by point defect recombination rather than by sink-dominated considerations. Recombination will be dominant when the temperature is low enough such that the mean free path for point defects is smaller than the distances between sinks. It is considered particularly relevant that when the temperature was raised from 400 to 550°C the creep and swelling rates returned to values characteristic of isothermal irradiation at 550°C.

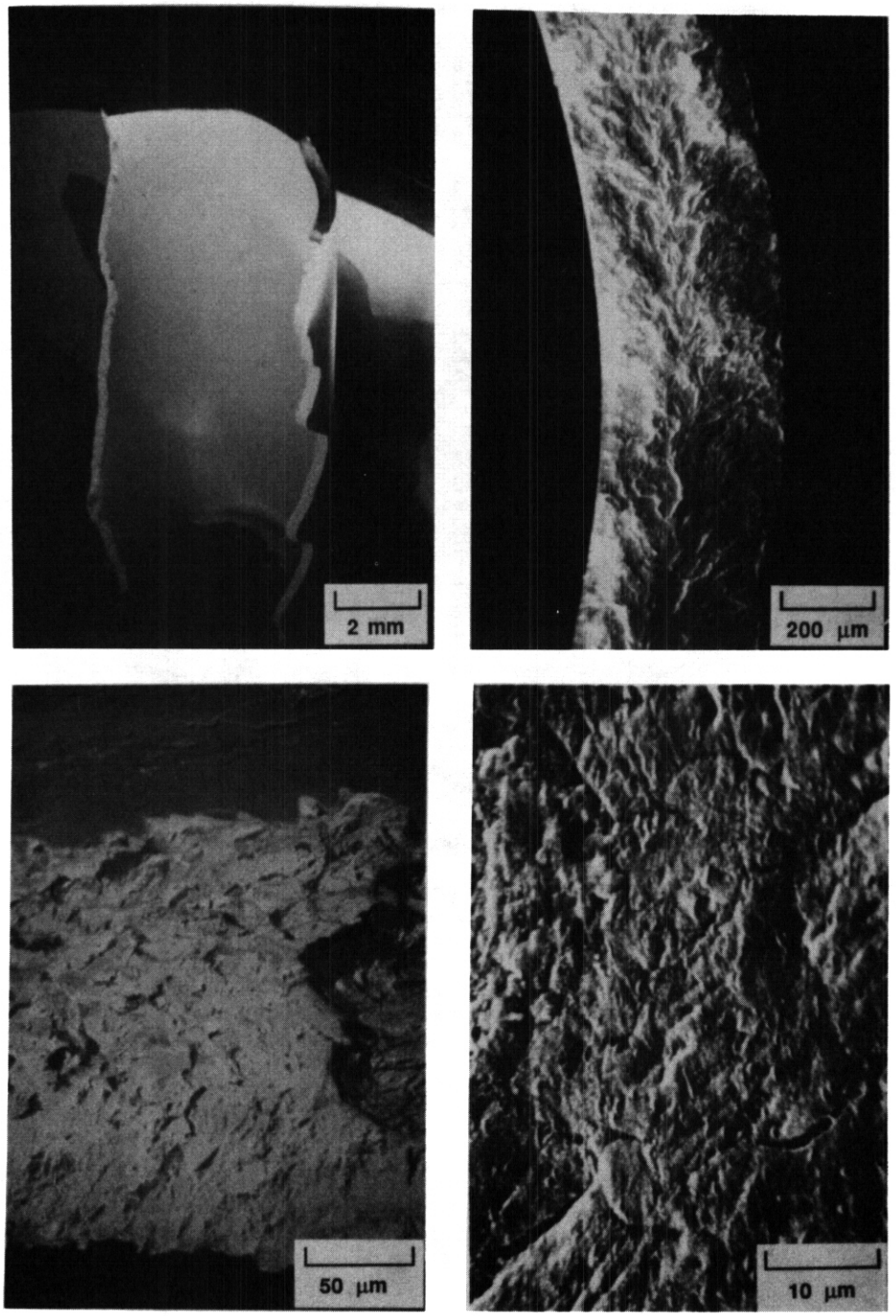

Fig. 15. SEM micrographs of a) broken piece of capsule EA-35, b) transverse section of fracture surface, c) combination of fracture surface and inside surface showing intergranular cracks, and d) higher magnification of inside surface.

It was shown in this study that the creep rate of 20% cold worked 316 stainless steel is linearly dependent on the stress level and increases with swelling. This is consistent with the proposal that the creep rate $\dot{\varepsilon}$ at any relevant temperature is linearly dependent on stress σ and related to the swelling rate $\dot{S}$ by the following relation:[4,12-14]

$$\frac{\dot{\varepsilon}}{\sigma} = B_o + D_o \dot{S}$$

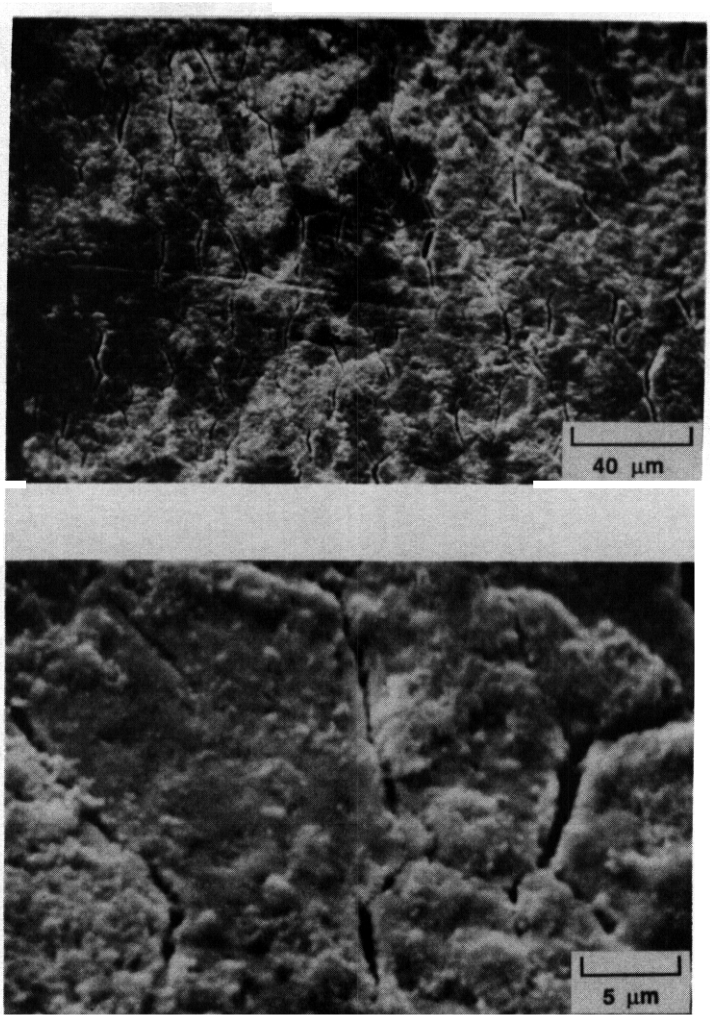

Fig. 16. Outside surface of capsule EA-35 showing intergranular cracks at almost every grain boundary.

The creep compliance B_o has been shown to be dependent on temperature and approximately equal to 1×10^{-6} MPa^{-1} dpa^{-1} for a wide range of austenitic steels.[12-14] The swelling-enhanced creep coefficient, D_o, is likewise thought to be relatively constant at ~10^{-2} MPa^{-1} over a wide range of steels and temperatures.[12]

Using the insight gained in an earlier study[6] of stress-independent swelling at 400°C to analyze the data in Fig. 6, the values of B_o and D_o can be calculated. Note in Fig. 7 that the instantaneous creep coefficient (B_o + $D_o S$) is independent of stress level as predicted and appears to saturate at higher exposures. At zero dpa and therefore zero swelling rate, B_o is indeed -1×10^{-6} MPa^{-1} dpa^{-1}. Assuming a swelling rate of ~0.04%/dpa and using the 276 MPa (40 ksi) curve at 130 dpa, D_o is calculated to be -0.6×10^{-2} MPa^{-1}. The estimates of both B_o and D_o thus appear to be in good agreement with the anticipated values.

CONCLUSIONS

Neutron irradiation of AISI 316 stainless steel at 400°C yields a very low swelling rate (≤0.1%/dpa) compared to that at 550°C, which persists to very high displacement levels and does not appear to be sensitive to stress or prior environmental history. The concurrent rate of irradiation creep is therefore also much lower than that at 550°C and retains a linear dependence on both stress and swelling rate. The aggregate deformation rate never approaches the upper limit of 0.33%/dpa observed at 550°C, primarily because of the lower swelling rate. Creep at 400°C also exhibits the expected behavior associated with either increases or decreases in both stress or irradiation temperature. When the swelling level approaches ~10%, however, the potential exists for severe embrittlement during handling at room temperature. This embrittlement has been observed in other irradiations of this steel.

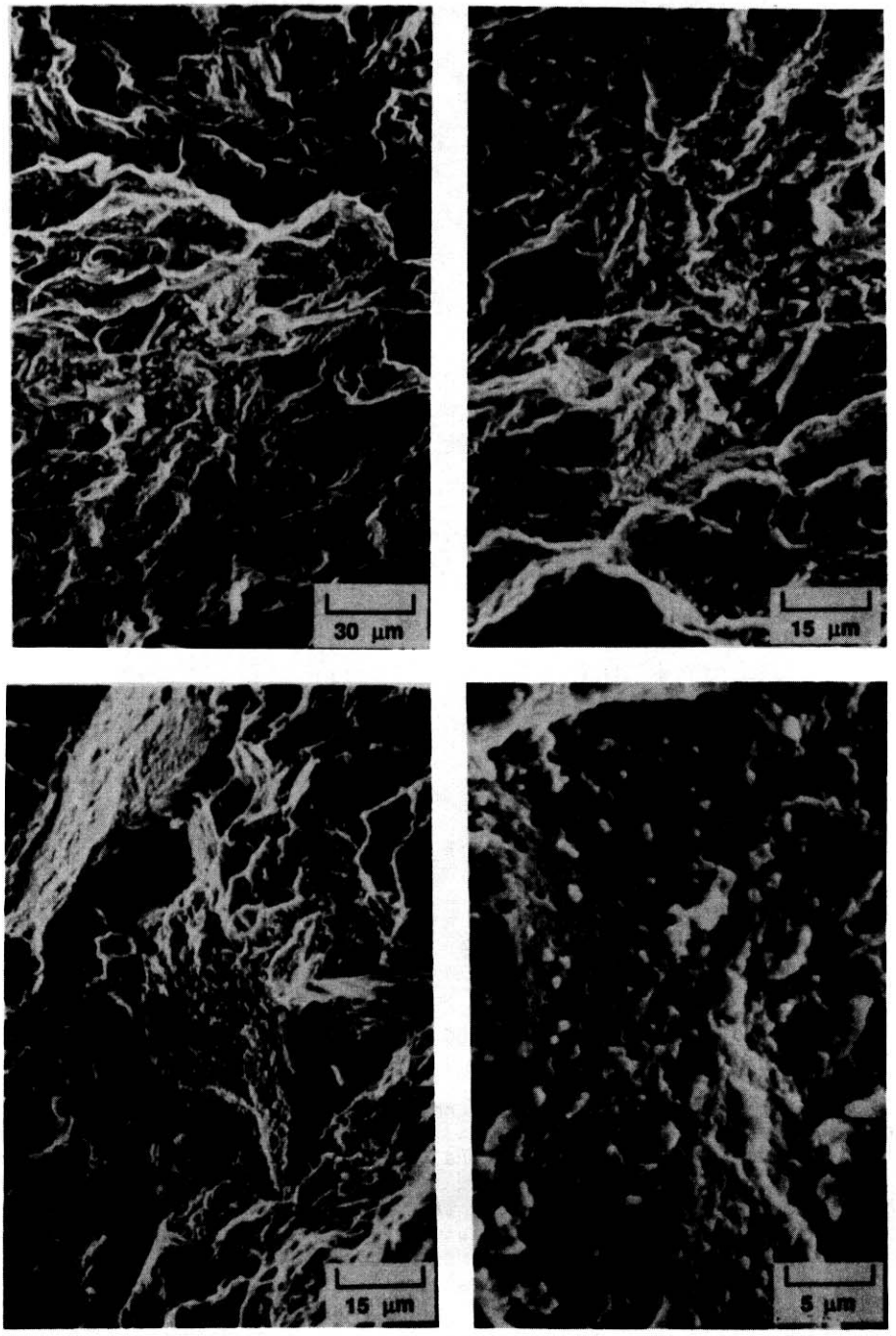

Fig. 17. Typical views of transverse fracture surface of EA-35, showing a,b) occasional grain boundary cracks and extensive corrosion products on surface, and c,d) areas with less corrosion product.

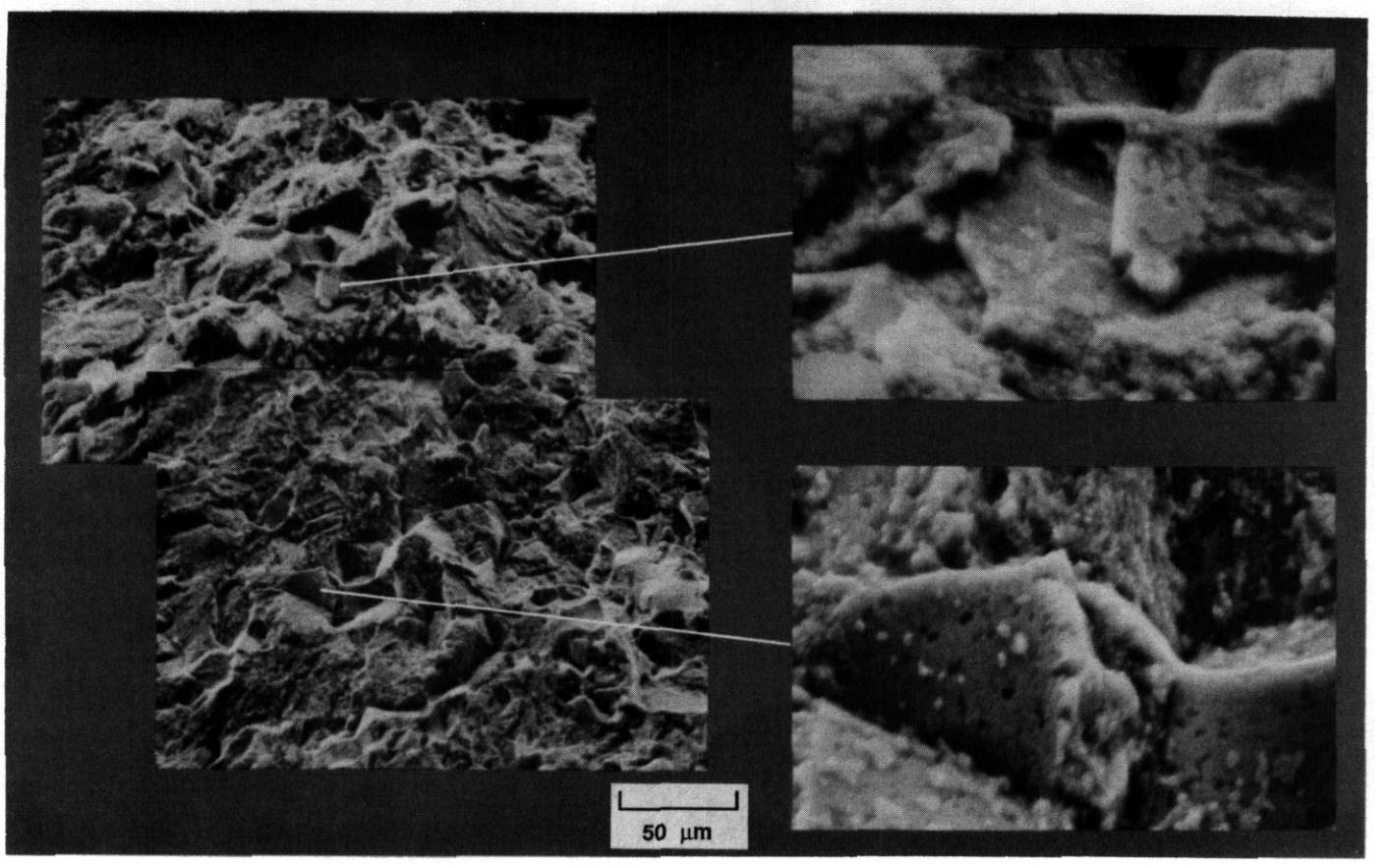

Fig. 18. Fresh fracture surface of EA-35, showing cleavage-like failure.

FUTURE WORK

This first stage effort is complete. Analysis of several other creep data fields will proceed in the next reporting period.

REFERENCES

1. F. A. Garner, D. L. Porter, and B. J. Makenas, Journal of Nuclear Materfals, 148, 279-287 (1987).

2. F. A. Garner, H. R. Brager, M. L. Hamilton, R. A. Dodd, and D. L. Porter, Radiation Effects, 101, 37-53 (1987).

3. D. L. Porter and F. A. Garner, pp. 11-21 in Influence of Radiation on Materfal Properties: 13th International Symposium (Part II), ASTM STP 956, F. A. Garner, C. H. Henager, Jr., and N. Igata, Eds., ASTM, Philadelphia, Penn., 1987.

4. F. A. Garner, Journal of Nuclear Materials, 122 & 123, 459-471 (1984).

5. F. A. Garner, pp. 113-139 in Optfmizfng Materials for Nuclear Applfcations, F. A. Garner, D. S. Gelles, and F. W. Wiffen, Eds., TMS-AIME, Warrendale, Penn., 1985.

6. F. A. Garner and D. L. Porter, Journal of Nuclear Materials, 154-156 (1988) in press.

7. D. L. Porter and F. A. Garner, Proceedings of International Workshop on Mechanisms of Irradfatfon Creep and Growth, Hecla Island, Manitoba, Canada, June 22-25, 1987, C. H. Woo and R. J. McElroy, Eds., in press.

8. D. L. Porter, M. L. Takata, and E. L. Wood, Journal of Nuclear Materials, 116, 272-276 (1983).

9. F. A. Garner, E. R. Gilbert, and D. L. Porter, pp. 680-697 in Effects of Radiation on Materials: 10th International Conference, ASTM STP 725, D. Kramer, H. R. Brager, and J. S. Perrin, Eds., ASTM, Philadelphia, Penn., 1981.

10. M. L. Hamilton, F. H. Huang, W. J. S. Yang, and F. A. Garner, pp. 245-270 in Influence of Radiation on Material Properties: 13th International Symposium (Part II), ASTM STP 956, F. A. Garner, C. H. Henager, Jr., and N. Igata, Eds., ASTM, Philadelphia, Penn., 1987.

11. F. A. Garner, C. W. Hunter, G. D. Johnson, E. P. Lippincott, and J. O. Schiffgens, Nuclear Technology, 58, 203-217 (1982).

12. K. Ehrlich, Journal of Nuclear Materials, 100, 149 (1981).

13. J. P. Foster, W. G. Wolfer, A. Biancheria, and A. Boltax, p. 273 in Proceeding BNES Conference on Irradiation Embrittlement and Creep in Fuel Cladding and Core Components, London, England, 1972.

14. J. L. Boutard, Y. Carteret, R. Cauvin, Y. Guerin, and A. Maillard, p. 109 in Proceedings BNES Conference on Dimensional Stability and Mechanical Behavior of Irradiated Metals and Alloys, Vol. 1, Brighton, England, 1983.

NEUTRON-INDUCED SWELLING OF COMMERCIAL ALLOYS AT VERY HIGH EXPOSURES - F. A. Garner and D. S. Gelles, Pacific Northwest Laboratory

OBJECTIVE

The objective of this effort is to determine the factors which influence the swelling resistance of irradiated alloys.

SUMMARY

Density change measurements have been completed on a wide variety of commercially available structural alloys irradiated to neutron fluence levels as large as 2.8 x 10^{23} n/cm^2 (E>0.1 MeV) or ~140 dpa in EBR-II at eight temperatures between 399 and 650°C. While there was essentially no swelling in some ferritic alloys and some austenitic superalloys, other austenitic alloys exhibited a wide range of swelling depending on composition, heat treatment and irradiation temperature.

The swelling behavior of the austenitic alloy system is shown to reflect primarily the influence of the overall composition and the irradiation temperature on the duration of the transient regime of void swelling, and secondarily to reflect the influence of precipitation and cold work.

PROGRESS AND STATUS

Introduction

Neutron-Induced void swelling was recognized early in the 1970s as a process which could limit the lifetime of structural components both in fast reactors and in fusion reactors. Since that time there have been many hundreds of scientific papers published which examined the separate and synergistic influence of the many variables now known to influence swelling. While charged particle simulation studies have been used to examine many facets of the swelling phenomenon, it was recognized that the most relevant data must be generated in a neutron environment.

In the U.S. liquid Metal Reactor program a number of extensive irradiation studies were conducted in EBR-II to identify candidate alloys for use in structural components. One of the earliest of these was the AA-1 experiment. It did not focus on a single alloy or narrow range of alloys but involved irradiation of a very wide range of commercially available alloys. AA-1 was designed to proceed in stages to very high exposure levels, using interim examinations at intermediate exposure levels to narrow the number of alloys selected for inclusion in subsequent experiments. These follow-on experiments were directed toward optimization of alloys and alloy classes observed in AA-1 to exhibit resistance to void swelling.

A limited amount of the early data from the first several discharges of the AA-1 experiment has been published in previous reports.[1,2] The experiment was terminated after reaching a peak fluence of ~2.4 x 10^{23} n cm^{-2} (E>0.1 MeV). Some of the data from the last discharge have also been published elsewhere.[3] This paper reports the entire collection of data derived from the last discharge of AA-1 and some of the lower fluence data where it is needed to demonstrate the major conclusions of the study.

Also presented in this paper are the results of a higher fluence experiment wherein two alloys, AISI 316 and HT-9, were removed from the last phase of the AA-I irradiation series and continued to higher fluence in the AA-7 experiment.

Experimental details

The specimens were solid rods approximately 1.3 cm long by 0.3 cm in diameter, machined from solid stock that had already been given the appropriate thermomechanical treatment. The compositions of the various alloys and the thermomechanical treatments employed are listed in Tables 1 and 2 respectively.

The alloys were irradiated in sodium-filled subcapsules in Row 2 of the EBR-II fast reactor located in Idaho Falls, Idaho. The irradiation vehicle was of the B-7 type in which both the outer capsule and the subcapsules were constructed of 20% cold worked AISI 316 stainless steel. The target temperatures were obtained by the use of gama heating and by providing a gas gap between the subcapsules and the B-7 outer capsule. All data at any one temperature were obtained from one position in the core, and were therefore developed at the same neutron flux and displacement rate.

The nominal subcapsule temperatures were designed to be 399, 427, 454, 482, 510, 538, 593 and 650°C with estimated uncertainties of ± 25°C or less, the uncertainty depending on the design temperature. A subsequent run-by-run reanalysis of the subcapsule temperatures showed that for the majority of the

Table 1. Compositions of the alloys as supplied by the vendors (weight percent)

Type	Alloy	Fe	Ni	Cr	C	NO	Mn	Nb	Al	Ti	Si	Other
Ferritic	H11	bal.	0.12	4.97	0.42	1.31	0.37	--	--	--	0.88	V=0.49
	EN-12	bal.	--	9.12	0.09	2.02	1.00	0.40	--	--	0.28	V=0.27
	AISI 416	bal.	0.27	13.34	0.11	0.26	0.42	--	--	--	0.48	--
	430 F	bal.	--	17.64	0.04	0.04	0.40	--	--	--	0.50	
	FeCrAlY	bal.	--	22.5	0.009	--	--	--	5.W	--	--	Y=0.68
	Carpenter Custom 455	bal.	8.4	11.7	0.008	--	0.10	0.24'	--	1.2	0.08	Cu=2.14
	HT-9	bal.	0.47	12.0	0.020	1.03	0.50	--	--	--	0.41	W=0.5, V=0.32
	HT-9 P.M.[b]	bal.	0.64	12.3	0.020	0.86	0.64	--	--	--	0.3	WO.44. V=0.29, B=0.008
Austenitic	AISI 310	bal.	19.7	24.7	0.06	0.30	1.52	--	--	--	0.56	ud1.33
	RA-330	bal.	36.05	19.1	0.05	--	1.58	--	--	--	1.27	Cu=0.25
	Incoloy 800[c]	bal.	33.7	20.5	0.07	--	0.91	--	0.38	0.44	0.45	wv.54
	AISI 316	bal.	13.7	17.3	0.05	2.26	1.64	--	--	--	0.56	
Precipitation Strengthened	A286	bal.	24.6	14.2	0.05	1.21	1.22	--	0.17	2.20	0.54	V=0.25
	M813	bal.	34.1	18.35	0.34	4.26	--	--	1.59	2.38	--	Co=0.020, Zr=0.12
	D979	bal.	44.8	14.9	0.04	4.15	0.10	--	1.16	3.07	1.10	W=4.03, Zr=0.04
	Incoloy 901[c]	bal.	42.2	13.7	0.04	5.50	0.10	--	0.26	2.85	0.10	B=0.16
	Nimonic PE16[c]	bal.	43.4	16.5	0.08	3.15	0.01	--	1.20	1.27	0.01	B=0.M32
	Inconel 718[c]	18.5	bal.	18.6	0.04	2.83	0.10	5.28[a]	0.50	0.92	0.23	
	Inconel 706[c]	bal.	41.5	16.1	0.03	--	0.10	2.95[a]	0.27	1.66	0.10	B=0.006 Max
	Inconel X-750[c]	7.81	bal.	15.4	0.045	--	0.09	1.06'	0.68	2.45	0.07	
	Nimonic 80A[c]	0.17	bal.	19.5	0.07	--	0.03	--	1.42	2.57	0.14	
	Nimonic 115[c]	0.48	bal.	14.5	0.16	3.23	0.03	--	4.94	3.78	0.20	Zr=0.04, Cu=0.04
	Inconel 625[c]	4.36	bal.	21.9	0.02	9.17	0.09	3.35	0.29	0.28	0.15	
Nickel Base	Hastelloy X[c]	18.8	bal.	21.2	0.11	8.84	0.46	--	--	--	0.45	W0.5, Co=1.96
	Hastelloy S[c]	0.73	bal.	16.6	0.006	15.3	0.21	--	0.21	--	0.05	W=0.07, Co=0.11
	Hastelloy C-4[c]	0.45	bal.	15.3	0.002	14.3	--	--	--	0.42	0.04	
	Inconel 600[c]	8.03	bal.	15.8	0.08	--	0.24	--	0.18	0.25	0.21	Cu=0.32
Refractory	Nb-1Zr	<0.W5	<0.002	--	0.003	0.002	<0.002	bal.	--	<0.004	<0.005	Zr=0.96, Ta=0.095
	TZM	0.003	0.001	--	0.13	bal.	--	--	--	0.45	0.002	Zr=0.09

[a] Includes Ta.
[b] P.M. Alloy fabricated by hot isostatic pressing of powder.
[c] Incoloy and Inconel are registered trademarks of the International Nickel Company, Nimonic is a registered trademark of Henry Wiggin & Co., U.K., and Hastelloy is a registered trademark of the Cabot Corporation.

subcapsules these temperatures were within 15-20°C of the design temperature, usually but not always on the low side.' The 650°C subcapsule showed the greatest deviation, falling slowly in steps at the highest fluence levels, but it never fell below 600°C.

Examination of the specimens was conducted at peak fluences of 5.7, 9.6, 14.0, 17.2 and 24.5 x 10^{22} n cm^{-2} (E>0.1 MeV). The neutron spectra across this irradiation vehicle produce 5.0 dpa (± 5%) for each 10^{22} n/cm^2 (E>0.1 MeV). The density of the specimens was determined by an immersion density technique accurate to ± 0.16%. The density of most of the alloys in the last discharge of this experiment were measured at all eight irradiation temperatures while others were irradiated only at 427 and 538°C. Measurements of density change include the separate but often synergistic contributions of both swelling and phase-related density changes. The latter can be either positive or negative in sign and can often be as large as several percent in magnitude. With density measurements alone, these two contributions cannot be separated.

After completion of the AA-1 experiment, two alloys which were of particular interest at the time were included for further irradiation in the B112e capsule of the AA-7 experiment, which was also located in Row 2 of EBR-II.[5]

Results and discussion

As shown in Tables 3 and 4 there were substantial variations in swelling levels attained by the various alloys irradiated in the last of the AA-1 irradiation series, reflecting the very wide and diverse collection of alloys. One can draw from these data some very general conclusions concerning the response of void swelling to material and environmental parameters.

First, swelling is obviously sensitive not only to alloy class, elemental composition and thermomechanical condition but also to irradiation temperature. The refractory alloys exhibited relatively low swelling, with only TZM exceeding 1% swelling. The ferritic alloys in general exhibited the least change in density, often increasing in density rather than decreasing in response to void swelling. With the exception of HT-9, the details of the swelling response of ferritic alloys in AA-1 were covered in Reference 3. Tables 5 and 6 contain the swelling data for HT-9 and AISI 316 after irradiation in AA-7. Fig. 1 shows a graphic example of the swelling resistance of HT-9 after irradiation in AA-1 compared to that of AISI 316 which swells relatively easily.

Table 2. Thermomechanical starting conditions of alloys

Alloy	Heat treatment[a]
H11	1010/1/W.Q.+570/2/W.Q.
EM12	1050/0.5/A.C.+750/1.5/A.C.
AISI 416	870/F.C. AT 13°C Per Hour to 590/A.C.
HT-9	Wrought Bar 1050/0.5/A.C.+780/2.5/A.C.
HT-9 (PM)	Hot Isostatic Pressing of Powder, Heat Treatment Same as Wrought Bar
430 F	1070/1/W.Q.
FeCrAlY	consolidated at 1150°C
C.C. 455	1070/1/W.Q. t 510/4/A.C.
AISI 310	1070/1/W.Q.
AISI 316	20% CW by Drawing
RA-330	1070/1/W.Q.
INC. 800	1070/1/W.Q.
A-286 (ST)	1070/1/W.Q.
A-286 (STA)	980/1/O.Q. t 720/16/A.C.
M813	1080/4/A.C. t 900/1/A.C. t 750/8/A.C.
0979	1020/2/W.Q. t 840/6/A.C. t 705/16/A.C.
PE16 (A)	1080/4/A.C. t 705/16/A.C.
PE16 (OA)	1080/4/A.C. t 840/24/A.C.
PE16 (ST)	1080/4/A.C.
PE16 (STA)	1080/4/A.C. t 890/1/A.C. t 750/8/A.C.
INC. 901	1100/3/W.Q. t 790/4/A.C. t 720/24/A.C.
INC. 706 (ST)	1070/1/W.Q.
INC. 706 (STA)	950/1/W.Q. t 840/3/A.C. t 720/8/F.C. to 620/18 total/A. C.
INC. 718	750/1/W.Q. t 720/8/F.C. to 620/18 total A. C.
INC. X-750 (ST)	1150/2/A.C.
INC. X-750 (STDA)	1150/2/A.C. t 840/24/A.C. t 700/20/A.C.
INC. X-750 (STA)	1150/2/A.C. t 840/0.5/A.C.
NIM. 80A	1080/8/A.C. t 705/16/A.C.
NIM115	1190/1.5/A.C. t 1100/6/A.C.
INC. 625	1150/1/W.Q.
HAST X	1190/1/W.Q.
HAST S	1070/1/A.C.
HAST C-4	1070/1.5/W.Q.
INC. 600 (ST)	1120/1.5/A.C.
INC. 600 (CW)	20% cold worked
Nb-1Zr	1200/1/V.C.
TZM	1300/2.5/V.C.

[a]Heat Treatment Code: temperature (°C)/time (hour)/W.Q. = water quench, A.C. = air cooled, F.C. = furnace cool, O.Q. = oil quench, V.C. = cool under vacuum.

Microstructural observations have been reported for the HT-9 specimen irradiated at 427°C to 1.2 x 10^{23} n/cm^2, indicating no contribution of void swelling even though a 0.1% density decrease was measured.[6] This conclusion is in disagreement with observations on similar specimens irradiated in both HFIR and FFTF. In both cases, irradiation induced void swelling was observed after fluences on the order of 6 x 10^{22} n/cm.[7,8] The swelling observed in specimens irradiated in HFIR might be explained as a consequence of the higher levels of helium generation, but swelling observed after irradiation in FFTF raises the possibility that the swelling behavior of HT-9 may be sensitive to heat to heat variations or differences in displacement rate.

The largest variations in swelling were observed in the austenitic alloy system. In general those alloys having nickel levels in the 40 to 60% range exhibited the lowest levels of swelling. This trend was also found in neutron-irradiated solute-free Fe-Cr-Ni alloys.[5] The strong dependence of swelling on nickel content appears to be relatively independent of the different precipitate microstructures known to evolve in the various alloys. Some high nickel alloys such as Inconel 706 appear to be particularly resistant to void swelling. Others in the Hastalloy series appear to be very resistant to swelling over the lower range of temperatures probed in this experiment but very prone to high rates of swelling at higher temperatures.

As discussed in an earlier paper it appears that austenitic alloys in general attempt to reach a steady-state swelling rate of ~1%/dpa over a very wide range of composition, displacement rate and

Table 3. Swelling of commercial alloys at eight irradiation temperatures in the AA-1 experiment

Alloy	Swelling ($\Delta V/V_o$, %)							
	399°C 1.60[a]	427°C 2.07	454°C 1.55	483°C 1.98	510°C 2.41	538°C 2.32	593°C 2.53	650°C 2.50
H11	0.16	0.14	0.18	-0.11	-0.05	0.04	--	--
EM12	0.57	0.56	-0.02	-0.28	-0.38	-0.29	--	0.08
AISI 416	0.35	0.25	0.08	0.08	0.20	0.05	--	0.21
430 F	0.23	0.20	0.09	0.17	0.24	0.05	--	0.11
HT-9	0.32	0.25	0.21	0.11	0.19	-0.01	0.23	--
HT-9 PM	0.14	0.03	0.05	0.08	0.07	-0.05	0.10	0.14
M813	1.87	1.75	1.67	2.36	4.26	1.84	0.65	-0.20
0979	-2.30	-1.91	-2.56	-0.06	-2.63	-2.45	-2.75	-2.77
INC. 901	0.03	0.15	0.13	0.13	0.04	-0.07	-0.08	-0.06
INC. 718	0.36	0.60	0.21	0.21	0.07	0.25	0.03	-0.05
INC. 625	0.36	1.01	-0.08	-0.01	0.90	-0.06	-0.24	-0.17
HAST X	-3.11	-2.30	-2.97	0.86	15.9	38.0	79.9	--
HAST S	-0.36	-0.30	-0.20	-0.10	0.19	0.06	--	2.46
HAST c-4	-0.23	-0.09	-0.03	0.35	2.48	4.79	11.6	18.4
INC. 600	4.34	12.7	2.00	3.14	4.58	1.60	1.72	1.04
INC. 600	2.90	7.92	2.90	0.99	1.06	0.07	0.05	0.15
RA-330	3.41	12.4	2.84	7.56	10.2	2.04	3.06	1.07
INC. 800	10.8	41.1	1.85	5.51	47.2	11.9	--	14.6
AISI 316	3.19	19.0	20.7	46.7	72.1	57.4	49.6	18.8
INC. 706 (STA)	0.17	0.23	0.14	-0.06	0.04	-0.04	0.09	--
PE16 (STA)	0.07	0.43	1.07	2.54	4.68	4.45	1.25	0.09
Nb-1Zr	0.43	0.53	0.25	0.16	0.43	0.31	0.39	0.56
TZM	0.35	0.03	0.03	0.02	0.36	0.05	3.77	2.86

[a]Neutron Fluence (E > 0.1 MeV) in units of 10^{23} n cm^{-2}.

temperature.[9] This was found to be particularly true for simple Fe-Cr-Ni ternary alloys.[5,9] It was also shown that the sensitivity of swelling to irradiation temperature and composition was found to reside primarily in the duration of the transient regime of swelling. The temperature dependence of the transient regime is most easily demonstrated in Fig. 2 where the full AA-1 data base for 20% cold worked AISI 316 is plotted, including that derived from subsequent reirradiation in the AA-7 experiment to a peak exposure of 2.8 x 10^{23} n/cm^2 (E>0.1 MeV). The swelling rate is indeed on the order of 1%/dpa over a wide range of irradiation temperature with only the data at ~400°C (and perhaps 650°C) suggesting a lower swelling rate. In another experiment where 130 dpa was reached, the swelling rate of AISI 316 at ~400°C was clearly shown to be much lower than 1%/dpa with a number of measurements in the range 0.04 to 0.1%/dpa.[10,11]

The largest level of irradiation-induced swelling ever reported was 212% and was found in AISI 316 stainless steel irradiated in the annealed condition with 140 KeV protons.[12] This alloy irradiated in the 20% cold worked condition also holds the record for the largest level of neutron-induced swelling ever reported. As shown in Fig. 2 a value of ~88% swelling was observed at 510°C and 26.8x10^{22} n cm^{-2} (E>0.1 MeV) after being irradiated in both the AA-1 and AA-7 experiments. When the AA-1 experiment is considered by itself, however, Hastalloy X exhibited the largest level of swelling, 79.9% vs. 49.6% measured for 20% cold worked 316 at 593°C and 25.3x10^{22} n cm^{-2}. If Hastalloy X had also been included in the AA-7 experiment, it is expected that it would have outswelled AISI 316 at this temperature. Note in Table 3 that Hastalloy X does not swell very much at lower temperatures and densifies considerably (2-3%). signalling a large microstructural alteration, probably involving precipitation due to the very large amount of molybdenum in this alloy. Such instabilities may alter the matrix composition sufficiently at high temperatures to account for the high swelling of this alloy.

In addition to temperature, the duration of the incubation period of swelling in relatively simple alloys is known to be sensitive to the nickel, chromium and solute content.[5] Fig. 3 shows that this trend is obeyed in more complex alloys. AISI 330 with 20% Ni and 25% Cr swells sooner than does A286 with 25% Ni and 14% Cr. Raising of the nickel and lowering of the chromium content are both known to extend the duration of the transient regime of swelling.[5] Inconel 800 and RA 330 have similar compositions but the latter has a much larger level of silicon, an element known to have a strong but temporary suppressant effect on void nucleation.[5,13] Inconel 600 and RA 330 exhibit comparable swelling even though the former

Table 4. Swelling of comrcial alloys at two irradiation temperatures in the A4-I experiment

	Swelling ($\Delta V/V_o$, %)	
	425°C 2.07×10^{23}	538°C 2.32×10^{23}
FeCrAlY	0.12	-0.18
C.C. 455	-0.36	1.78
AISI 310	49.8	17.9
A-286 (ST)	31.6	0.51
A-286 (STA)	--	0.81
INC. X-750 (STA)	1.06	-0.06
INC. X-750 (ST)	4.18	0.46
INC. X-750 (STA')	1.47	-0.05
INC. 706 (ST)	-0.29	-0.11
INC. 706 (STA)	023'	-0.04
PE16 A	0.15	3.86[a]
PE16 OA	0.81	5.20
PE16 ST	0.24	3.80
PE16 STA	0.43[a]	4.45[a]
NIM. 80A	1.16	0.33
NIM.115	2.05	7.17

[a]These values also included in Table 3.

Table 5. Swelling of HT-9 at high neutron exposure

AA-1 Data (B116c)			AA-7 Data B112e		
Nominal Temperature	Neutron Fluence	Swelling	Additional Neutron Fluence	Total Fluence	Swelling
°C	10^{22} n cm^{-2}(E>0.1)	%	10^{22} n cm^{-2}(E>0.1)	10^{22} n cm^{-2}(E>0.1)	%
399	16.0	0.32	2.2	18.2	0.10
427	20.7	0.25	2.8	23.5	0.18
454	15.5	0.21	2.1	17.6	0.14
482	19.8	0.11	2.6	22.4	0.09
510	24.1	0.19	3.3	27.4	0.08
538	23.2	-0.01	3.2	26.4	0.03
593	25.3	0.23	--	--	--

has more than twice the nickel content of the latter, reflecting the minimum in swelling that occurs at intermediate nickel levels in solute-free Fe-Cr-Ni alloys.5 Fig. 3 also shows that, in agreement with the behavior of solute-free Fe-Cr-Ni alloys,[5] the incubation period for commercial alloys with relatively high nickel levels is further extended at higher temperatures, although one exception (the apparently unstable Hastalloy X) has already been noted. For solute-bearing alloys with high nickel levels the full temperature dependence of swelling can be relatively complex compared to that of solute-free alloys. Examples are shown in figs. 4 and 5.

When the swelling resistance is eventually overcome, however, austenitic alloys tend to swell at ever increasing rates, approaching the 1%/dpa rate characteristic of solute-free austenitic alloys. At higher irradiation temperatures in AA-I the maximum swelling rates had not yet reached 1%/dpa, although higher rates have been observed in their solute-free counterparts at these temperatures. Note in Fig. 5b that cold work further, but temporarily, suppresses the swelling of Inconel 600. This trend has been observed in many austenitic alloys.

Table 6. Swelling of 20%, cold-worked AISI 316 after irradiation in both AA-1 and AA-7

Nominal Temperature	Total Fluence	Swelling
°C	10^{22}n cm^{-2}(E>0.1)MeV	%
399	17.8	5.1
427	23.0	26.7
454	17.2	30.7
482	21.9	55.9
510	26.8	87.9
538	25.9	73.6
593	28.3	64.9
650	27.9	26.8

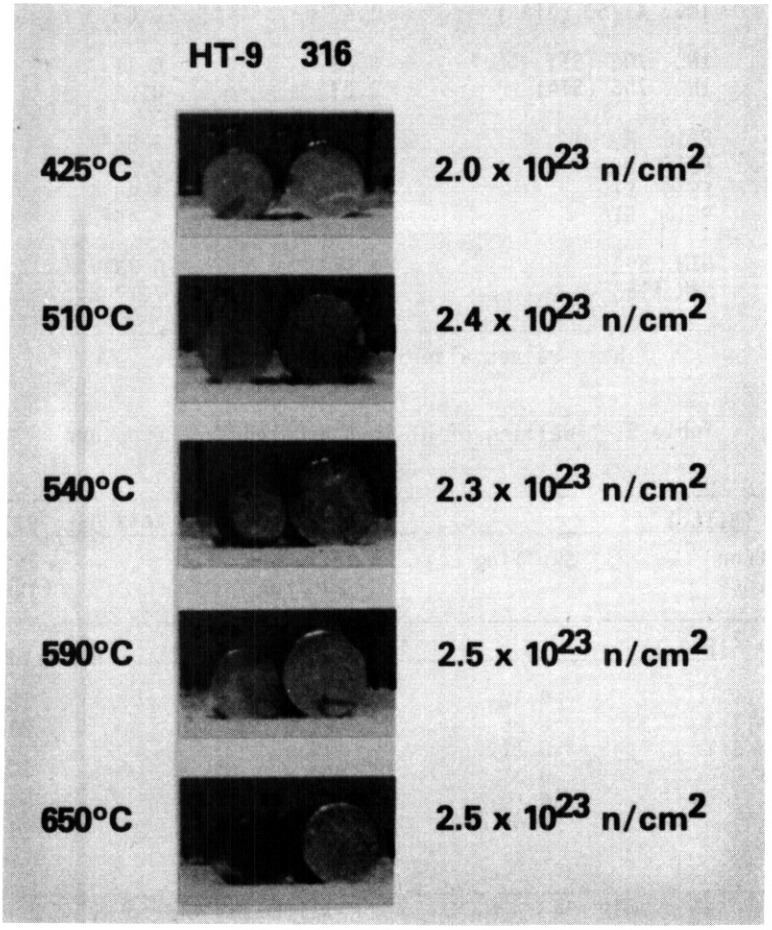

Fig. 1. Photographs of AA-1 specimens showing large increases in diameter of 20% cold worked rods compared to those of HT-9.

For those alloys with nickel contents in the 40-60% range the transient regimes are so long as to preclude the attainment of significant swelling rates in the AA-1 experiment. This may be a result not only of the nickel level but also the complex precipitate phases that develop upon addition of Nb, Al, Ti and Si. The full reasons for the swelling resistance of the Inconel and Incolloy alloys are not known and are unlikely to be discovered since the severe irradiation-induced brittleness found in alloys in this composition range precludes their use in neutron environments.[14-16]

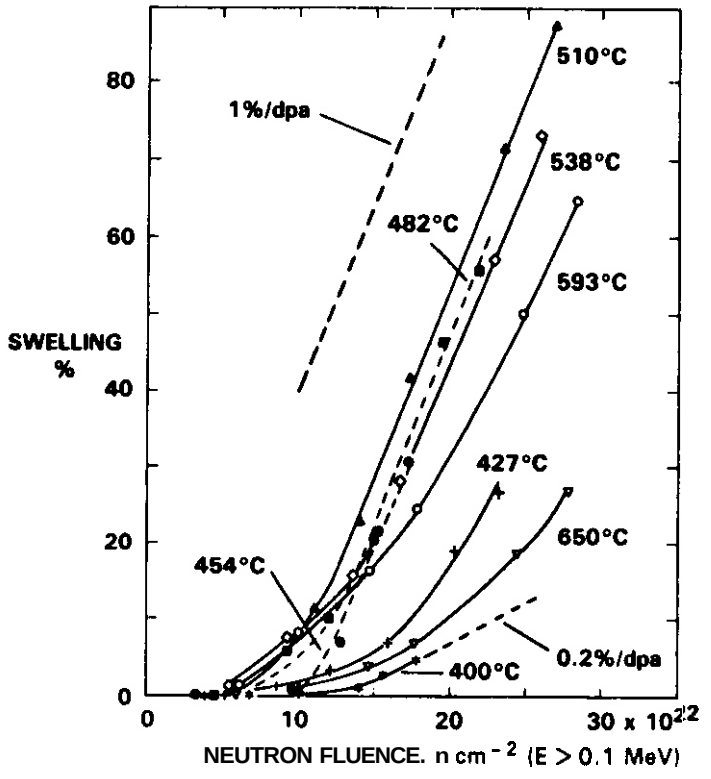

Fig. 2. Swelling observed in 20% cold worked AISI 316 stainless steel. The last data point on each curve was derived from irradiation in the AA-7 experiment after removal from the final discharge of the AA-1 experiment.

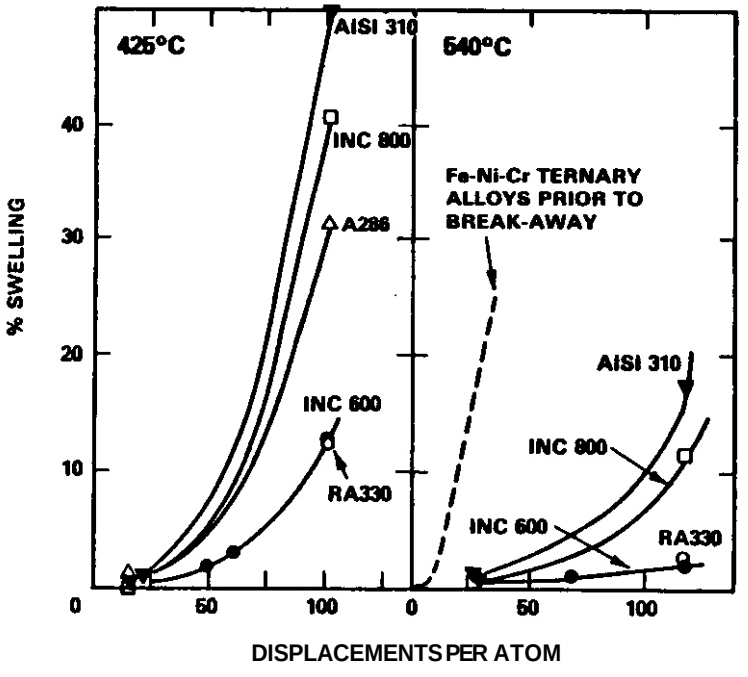

Fig. 3. Swelling observed in various annealed commercial alloys irradiated in the AA-1 experiment. The dotted line shows the swelling behavior of solute-free Fe-Cr-Ni alloys in the low nickel regime where neither composition or irradiation temperature affects swelling. Breakaway refers to the nickel and/or temperature levels above which the transient regime is extended.

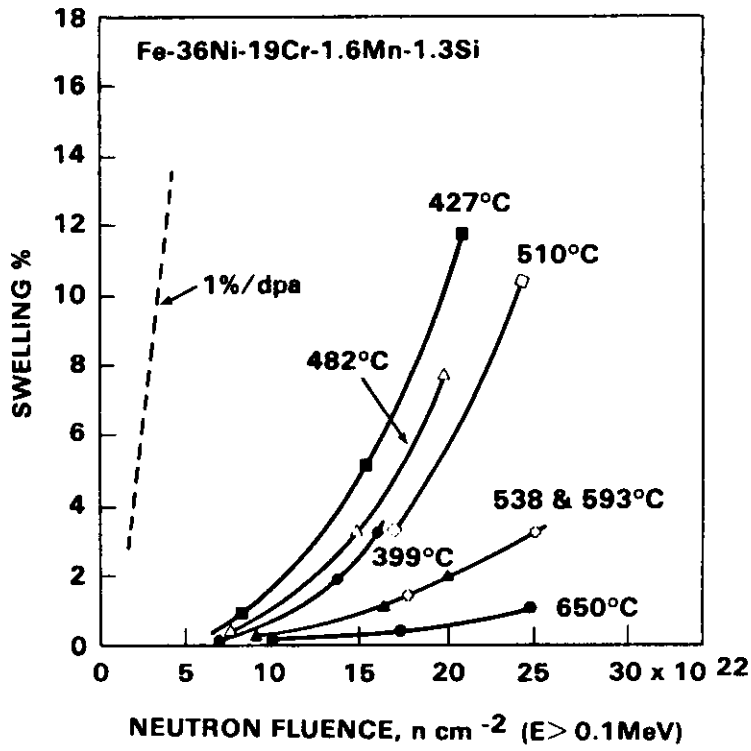

Fig. 4. Temperature-dependent swelling observed in annealed RA 330 in the AA-1 experiment.

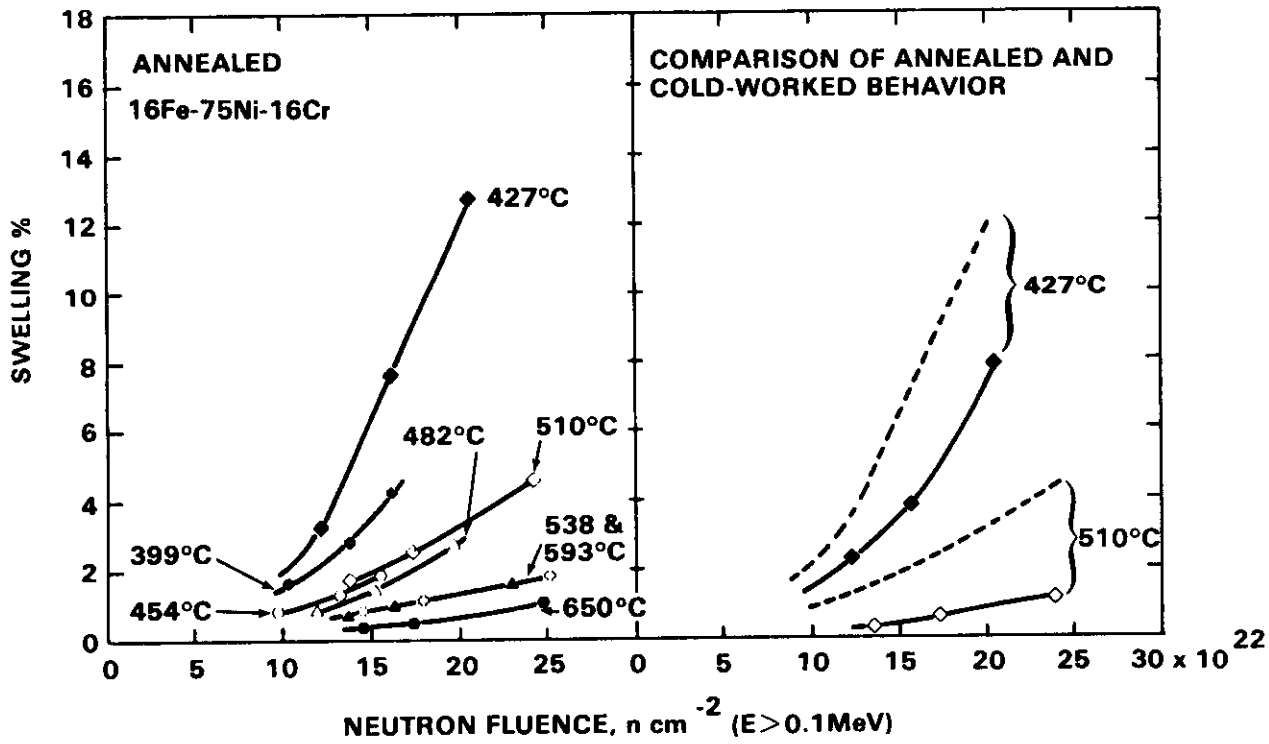

Fig. 5. Temperature and cold-work dependence of swelling of Inconel 600 irradiated in the AA-1 experiment.

CONCLUSIONS

The neutron-induced swelling behavior of austenitic alloys exhibits a much larger variation than that observed in the ferritic alloy class, members of which are uniformly low in swelling. The trends observed in simple Fe-Cr-Ni alloys with temperature, composition and cold-work are mirrored in the more complex commercial alloys. In some cases, however, it appears that precipitate formation can lead to a pronounced shortening or lengthening of the transient regime of swelling.

FUTURE WORK

This effort is complete.

REFERENCES

1. J. F. Bates and R. W. Powell, Journal of Nuclear Waterials 102, 200-213 (1981).

2. R. W. Powell, D. T. Peterson, M. K. Zimnerschied, and J. F. Bates, Journal of Nuclear Naterials 103 and 104, 969-974 (1981).

3. D. S. Gelles, Journal of Nuclear Waterials 122 and 123, 207-213 (1984)

4. R. W. Clark, "Dimensional Change Correlations for 20% Cold Worked AISI 316 Stainless Steel for Fusion Applications," Master's Thesis, University of Missouri-Rolla, 1986.

5. F. A. Garner and A. S. Kumar, pp. 289-314 in Radiation-Induced Changes in Microstructure: 13th International Symposium (Part I), ASTM STP 955, eds. F. A. Garner, N. H. Packan; and A. S. Kumar, ASTM, Philadelphia, Penn., 1987.

6. D. S. Gelles and L. E. Thomas, in Proceedings of Topical Conference on Ferritic Alloys for Use in Nuclear Energy Technologies, J. W. Davis and D. J. Michel, Eds., The Metallurgical Society, Warrendale, PA, 1984, pp. 559-568.

7. O. S. Gelles in Alloy Development for Irradiation Performance Semiannual Progress Report for the Period Ending *March* 31, 1985, DOE/ER-0045/14, pp. 129-136.

8. C. Y. Hsu, D. S. Gelles, and T. A. Lechtenberg, ibid. reference 5, pp. 545-559.

9. F. A. Garner, Journal of Nuclear Naterials 122 and 123, 459-471 (1984).

10. F. A. Garner and D. L. Porter, Journal of Nuclear Naterials 154-156, in press (1988).

11. D. L. Porter, E. L. Wood, and F. A. Garner, in these proceedings.

12. A. S. Kumar and F. A. Garner, Journal of Nuclear Naterials 117, 234-238 (1983).

13. F. A. Garner and W. G. Wolfer, Journal of Nuclear Naterials 102, 143-150 (1981).

14. S. Vaidyanathan, T. Lauritzen, and W. L. Bell, pp. 289-314 in Effects of Radiation on Naterials: Eleventh Conference, ASTM STP 782, eds. H. R. Brager and J. S. Perris, ASTM, Philadelphia, Penn., 1987.

15. W. J. S. Yang, Journal of Nuclear Naterials 108 and 109, 339-346 (1982).

16. W. J. S. Yang and M. L. Hamilton, Journal of Nuclear Naterials 122 and 123, 748-753 (1984).

THE PHASE STABILITY OF THE AUSTENITIC COMMERCIAL LOW ACTIVATION ALLOY AMCR IRRADIATED IN FFTF-MOTA

J. M. McCarthy, (Pacific Northwest Laboratory)

OBJECTIVE

The objective of this work is to assess the suitability of Fe-Cr-Mn alloys for fusion reactor service. This is the continuation of previous work on Fe-Cr-Mn alloys.[1-6]

SUMMARY

AMCR is one of five commercial Fe-Cr-Mn alloys with various thermal-mechanical treatments irradiated in the Fast Flux Test Facility Materials Open Test Assembly (FFTF-MOTA) to a dose of 75 dpa at 420°C and 520°C and to 60 dpa at 600°C (see Tables 1 and 2). AMCR, when compared to the other commercial alloys with higher chrome content, namely 18/18 Plus and Nitronic Alloy 32, shows no homogeneous precipitation of $M_{23}C_6$, less heterogeneous $M_{23}C_6$ and small grains of α ferrite in a largely austenite matrix.[1] However, the chrome level in the matrix is depleted considerably in the aged thermal-mechanical conditions. There were some transformations to α' and ε martensite prior to and during irradiation. However, the amount of material transformed was much less than that which was transformed in the irradiated simple ternary Fe-Cr-Mn alloys of similar composition[2]. AMCR achieves many of the goals set for the performance of a low activation alloy for low temperature fusion reactor service; that is, it remains primarily austenite with a small volume fraction subject to phase transformations to α ferrite, α' martensite, ε martensite and $M_{23}C_6$ carbide.

Table 1. Composition of Commercial Fe-Cr-Mn Austenitic Alloys

Designation	Vendor	Composition wt%
Nitronic Alloy 32	ARMCO	18Cr-12Mn-1.5Ni-0.6Si-0.2Cu-0.2Mo-0.4N-0.1C-0.02P
18/18 Plus	CARTECH	18Cr-18Mn-0.5Ni-0.6Si-1.0Cu-1.1Mo-0.4N-0.1C-0.02P
AMCR	CREUSOT-MARREL	10Cr-18Mn-0.7Ni-0.6Si-0.06N-0.2C
NMF3	CREUSOT-MARREL	4Cr-19Mn-0.2Ni-0.7Si-0.09N-0.02P-0.6C
NONMAG 30	KOBE	2Cr-14Mn-2.0Ni-0.3Si-0.02N-0.02P-0.6C

Table 2. Thermal-Mechanical Starting Conditions

Description	Conditions
Nitronic Alloy 32	CW
18/18 Plus	CW, CWA
AMCR 0033	CW, CWA, SAA
NMF3	CW
NONMAG 30	CW, CWA, SAA

Note: CW = 1030°C/0.5 h/air cool + 20% cold-work. CUA = cold-worked condition + 650°C/h/air cool. SAA = 1030°C/1 h/air cool + 760°C/2 h/air cool.

PROGRESS AND STATUS

Introduction

AMCR contains moderate amounts of chrome and manganese when compared to the other commercial alloys (see Table 1). The moderate chrome content inhibits diffusion-driven transformations to $M_{23}C_6$ and intermetallics, χ and σ phases as was shown in the earlier work on simple ternaries and the other commercial alloys.[1, 2, 3] The moderate manganese content prevents transformations to α' martensite and ε martensite that occurs in low manganese (13wt%) alloys and prevents the spinodal-like decomposition that occurs in high manganese (35wt%) alloys[1,2]. Therefore, the bulk of the alloy remains austenite with small volume fractions of α martensite, ε martensite, α ferrite and $M_{23}C_6$ carbide.

AMCR Phase Stability Results by Thermal-Mechanical Treatment

Cold Worked (CW)

The CW alloy, prior to irradiation, is primarily austenite with some α' martensite, ε martensite, heterogeneous $M_{23}C_6$ carbide, twins and dislocations (see Figures 1, 2, 3 and 4). The CW condition is the result of 0.5 hr at 1030°C, with an air quench, followed by 20% cold work.

Following irradiation at 420°C to a dose of 75 dpa some regions of austenite containing twins and ε martensite transformed to austenite regions containing α' martensite as is shown in Figure 5. A second morphology of α' martensite was also visible as shown in Figure 6. The α' martensite orientation relative to the austenite was $\langle 111 \rangle_{\alpha'} \parallel \langle 110 \rangle$ 7 for both morphologies.

The CW AHCR irradiated at 520°C to 75 dpa had large α' martensite plates, some as large as 30 μm in length (see Figure 7). Heavy $M_{23}C_6$ precipitation has occurred within these α' martensite plates and at the austenite/α' grain boundaries (see Figure 8). There was no evidence of ε martensite in the selected area diffraction patterns at this temperature.

When this same alloy was irradiated at 600°C there was no evidence of α' or ε martensite. The alloy was austenite with chrome-rich $M_{23}C_6$ carbide at grain boundaries (see Figure 9). Tetragonal σ did not occur in the AMCR as it did in 18/18 Plus and Nitronic Alloy 32 at 600°C, nor was the $M_{23}C_6$ precipitation as heavy at 600°C as in these other comnercial alloys with 18 wt% chrome.

Solution Annealed and Aged (SAA)

The SAA AMCR condition is the result of 1 hr. at 1030°C with an air quench, followed by 2 hr. at 760°C with an air quench. The SAA AMCR following irradiation at 420°C to a dose of 75 dpa exhibited chrome-rich $M_{23}C_6$ in an austenite matrix. The morphologies are rods, platelets or spheres (see Figure 10).

The SAA AMCR irradiated at 520°C to 75 dpa, in contrast, did not have the $M_{23}C_6$ but did have a high number density of roughly rectangular prisms or cubes of recrystallized material 50 to 200 nm in length that proved to be α ferrite (see Figure 11).

Following irradiation at 600°C to 60 dpa the SAA AMCR exhibited large 0.5 to 1 μm $M_{23}C_6$ in an austenite matrix with stacking faults and some large voids (see Figures 12 and 13). As a result of the precipitation and growth of the large $M_{23}C_6$, the matrix is depleted in Cr. The chrome content of the bulk alloy is 9.9 wt%. The chrome content of the $M_{23}C_6$, as measured in the matrix at the edge of the foil, is 40.6 wt%, the actual content being higher. The chrome content in the adjacent matrix is only 3.6 wt%. There were also recrystallized grains present with a composition in wt% of 94.7 Fe-3.3 Cr-0.7 Si which proved to be α ferrite when electron diffraction patterns were measured.

Cold Worked and Aged (CWA)

This condition consisted of 0.5 hr at 1030°C, an air quench, followed by 20% cold work, 1 hr at 650°C and finally a second air quench. CWA AMCR irradiated at 420°C is primarily austenite with voids 6 nm to 20 nm in diameter (see Figure 14). There is a general heterogeneous precipitation of $M_{23}C_6$ on grain boundaries and regions near the grain boundaries of decomposition of the austenite to $M_{23}C_6$ and α ferrite. The decorated grain boundaries and regions of decomposition polished preferentially due to the depletion of chrome from the adjacent matrix by the carbides as is shown by Figure 15.

CWA AMCR irradiated at 520°C to 75 dpa has a largely austenite matrix with heterogeneous $M_{23}C_6$ carbides within the grains and a high number density of voids 50 to 100 nm in diameter (see Figure 16).

The CWA AHCR irradiated at 600°C to 60 dpa was also primarily austenite with heterogeneous precipitation of $M_{23}C_6$ carbide on stacking faults ranging from 10 to 100 nm in length (see Figure 17). There were also larger $M_{23}C_6$ carbides within the austenite matrix. The austenite also contained some ε martensite (see Figure 18).

Discussion

A moderate manganese content in Fe-Cr-Mn alloys is 20 wt%, considering that heavy martensitic transformations occur in simple ternaries at bulk manganese contents of 13 to 15 wt% and spinodal-like decomposition occurs near 35 wt%. AMCR with 18 wt% manganese is in the range where martensitic transformations do not occur on arge scale, manganese being an austenite former and spinodal-like decomposition is also prevented. a21

Chrome content is another important variable in controlling transformations to brittle phases. These phases may embrittle the alloy on the whole if a large enough volume fraction is transformed or if grain boundaries are coated. A brittle phase that requires chrome is the face centered cubic $M_{23}C_6$ carbide. High chrome and carbon contents lead to the nucleation, growth and coarsening of this carbide as was shown by the irradiation of 18/18 Plus, a commercial alloy with 18 wt% chrome.[6] High chrome content also leads to the precipitation of χ and a phases. AMCR with a Cr content of 10 wt% seeks to provide corrosion resistance but not encourage excessive $M_{23}C_6$ carbide precipitation. Aging prior to irradiation leads to more precipitation of chrome-rich $M_{23}C_6$ carbide, depleting the matrix of chrome which reduces the corrosion resistance of the alloy. Chrome content in the matrix should not drop much below 10.5 wt% to maintain corrosion resistance in austenific stainless steels in general.[7] The solution annealed and aged AMCR irradiated at 600°C to 60 dpa had a matrix Cr content of 3.6% in some regions. Aging can also degrade mechanical properties by causing heavy intergranular and intragranular $M_{23}C_6$ precipitation which can prematurely embrittle the alloy.

Aging prior to irradiation also leads to the precipitation of α ferrite, another embrittling phase, as is demonstrated in the SAA AMCR irradiated at 520°C and in the CWA AMCR irradiated at 420°C. This indicates that aging may embrittle an alloy prematurely.

Conclusions

The composition of AMCR inhibits the transformation of the austenite matrix to brittle phases such as α' martensite, α ferrite, ε martensite, $M_{23}C_6$ carbide, χ and a.

The precipitation of a and χ phases does not appear to be a problem in AMCR when irradiated at 420, 520 and 600°C.

$M_{23}C_6$ precipitation can deplete the matrix of AMCR of chrome, thereby reducing its corrosion resistance. Therefore, aging prior to service is not recommended for AMCR.

Future Work

Bulk mechanical property measurements need to be performed to determine what volume fraction of the matrix can be transformed to α and/or ε martensite, inter and intra-granular $M_{23}C_6$ carbide and still preserve acceptable mechanical properties.

Corrosion studies also need to be done on the irradiated AMCR to determine the effect of the observed Cr depletion of the matrix near chrome-rich carbides within grains and at grain boundaries.

Glossary of Phases

γ - Austenite-face centered cubic a=0.358nm

α' - Alpha martensite-body centered cubic a=0.287nm with a composition that is the same as the parent austenite

ε - Epsilon martensite-hexagonal close packed composition same as parent austenite a-.2532 nm c/a=1.625

α - Alpha ferrite-body centered cubic a=0.287nm with a composition 95-100wt% iron

χ - Chi-phase-body centered cubic a=0.889 nm

$M_{23}C_6$ - Carbide face centered cubic-Cr, Mn, Fe and C; chrome-rich compared to the matrix a=1.06 nm

References

1. J. M. McCarthy and F. A. Garner, Fusion Reactor Materials (Semi-Annual Progress Report) DOE/ER-0313/4 (March 1988) p. 146.
2. J. M. McCarthy and F. A. Garner, Journal of Nuclear Materials, 155-157 (1988) pp. 877-882.
3. F. A. Garner, F. Abe and T. Noda, Journal of Nuclear Materials, 155-157 (1988) pp. 870-876.
4. F. A. Garner, H. R. Brager, D. S. Gelles and J. M. McCarthy, Journal of Nuclear Materials 148 (1987) p. 294.

5. F. A. Garner and H. R. Brager, in: Radiation-Induced Changes in Microstructure, A S M STP 955, Eds. F. A. Garner, N. H. Packan and A. S. Kunar (American Society for Testing and Materials, Philadelphia, PA, 1985) p. 195.

6. H. R. Brager, F. A. Garner, D. S. Gelles and M. L. Hamilton, Journal of Nuclear Materials 133 and 134 (1985) p. 907.

7. R. M. Davison, T. DeBold, M. J. Johnson, ASM Metals Handbook Vol. 13 p. 550.

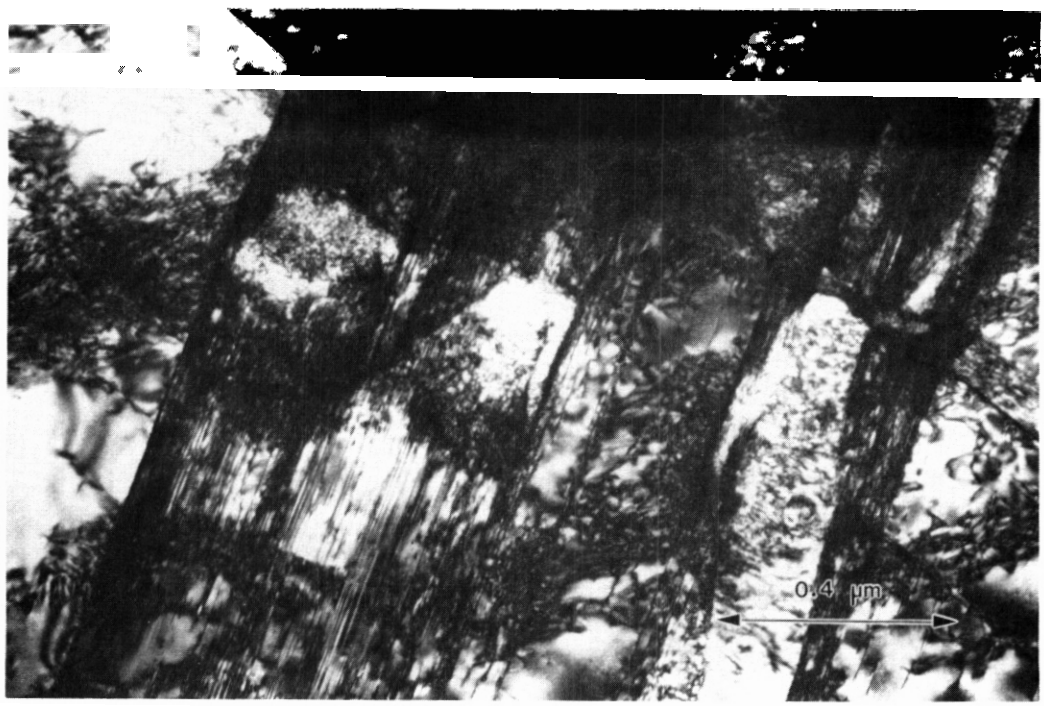

Fig. 1. Bright field transmission electron (TEM) image showing austenite matrix with twins and ε martensite plates in unirradiated CW AMCR

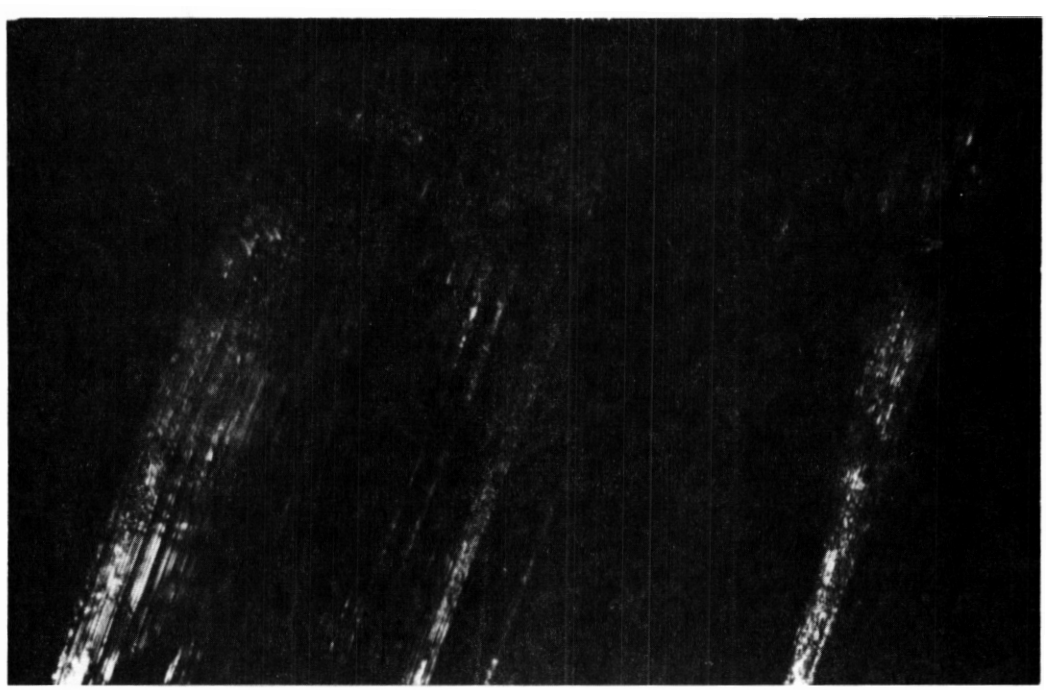

Fig. 2. Dark field TEM image of the same area showing ε martensite plates

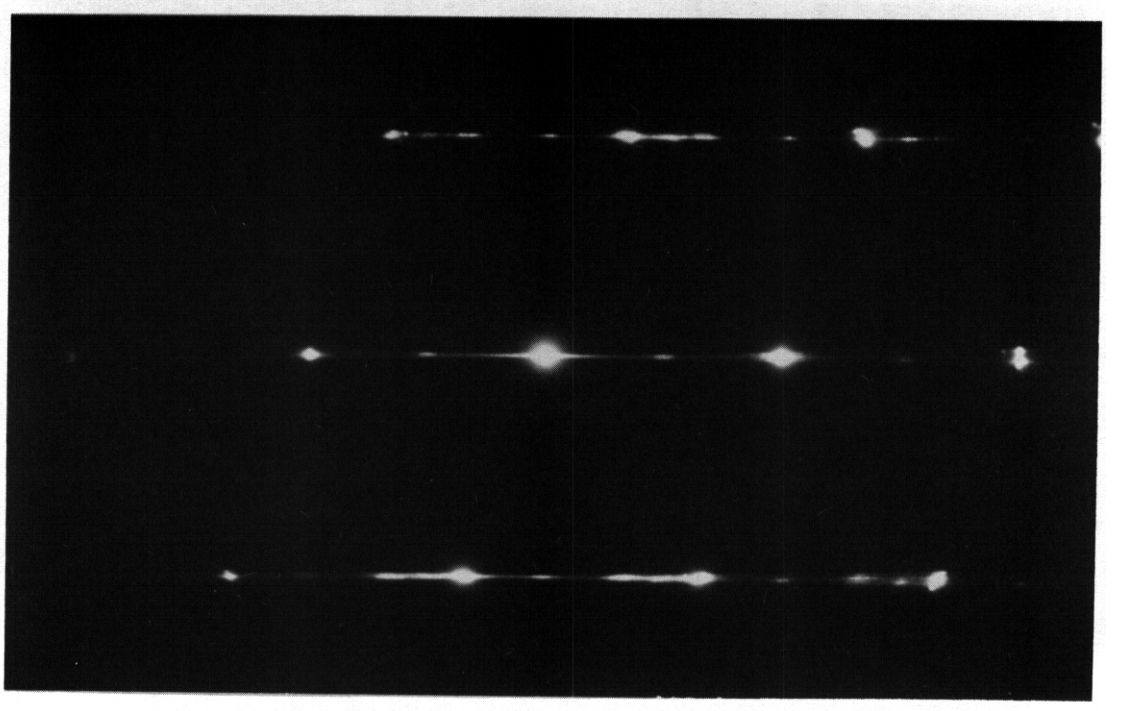

Fig. 3. Selected Area electron diffraction pattern from this area showing $\langle 1\bar{1}0 \rangle_{\gamma} \parallel \langle 12\bar{1}0 \rangle_{\epsilon}$

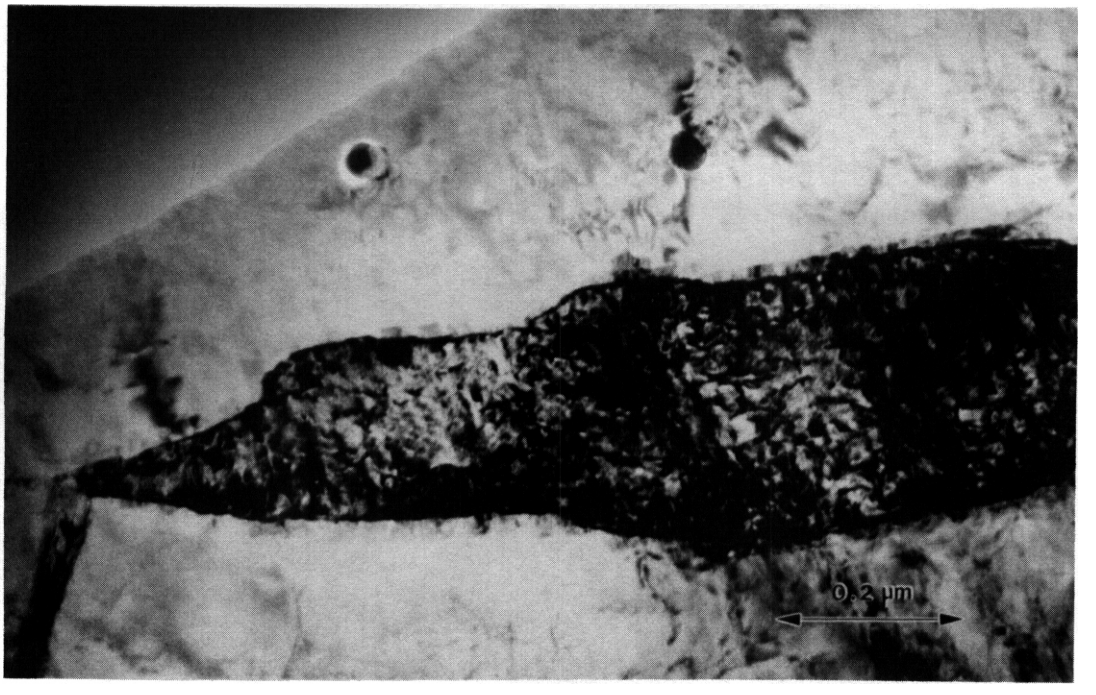

Fig. 4. Bright field image of a lenticular α' martensite plate in the austenite matrix of the unirradiated CW AMCR with some heterogeneous $M_{23}C_6$ carbides

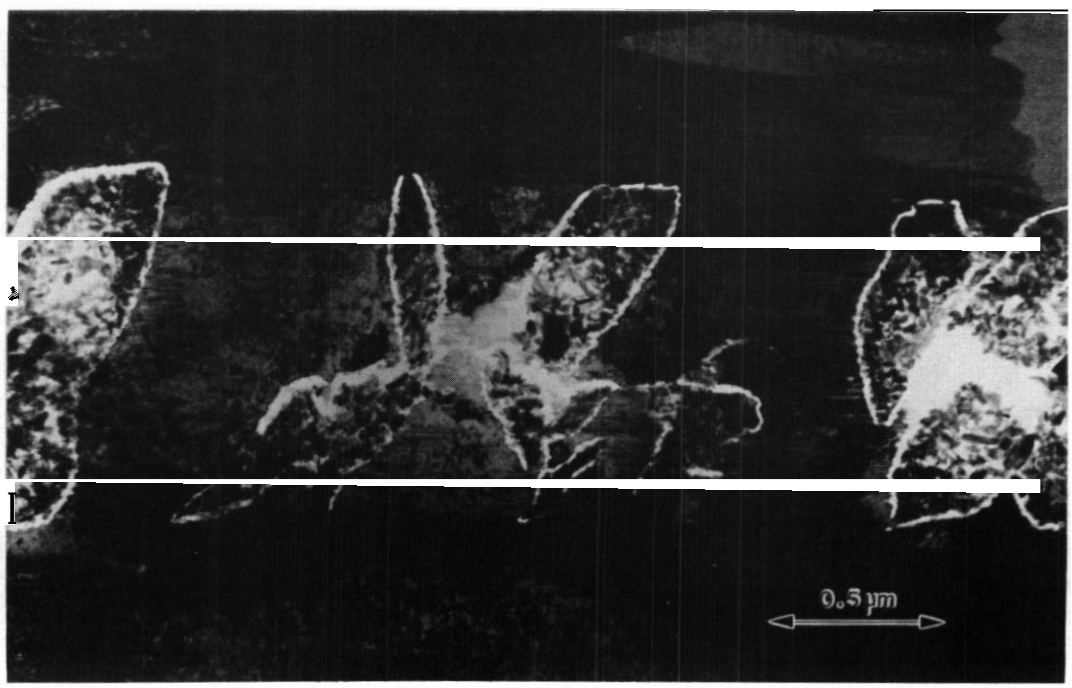

Fig. 5. TEM bright field image of region of austenite in CW AMCR with twins and lenticular α' martensite grains following irradiation at 420°C to 75 dpa $\langle 111 \rangle_{\alpha'} \parallel \langle 110 \rangle_{\gamma}$

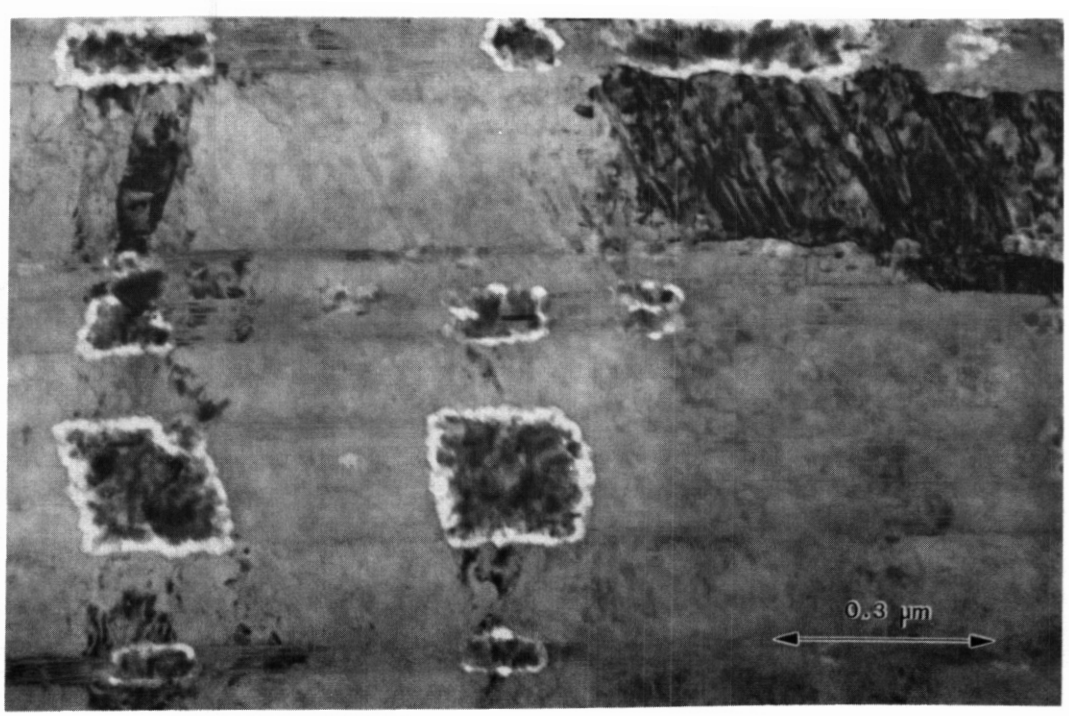

Fig. 6. TEM bright field image of a second morphology of α' martensite in the same specimen as in figure 5 with $\langle 111 \rangle_{\alpha'} \parallel \langle 110 \rangle_{\gamma}$ also

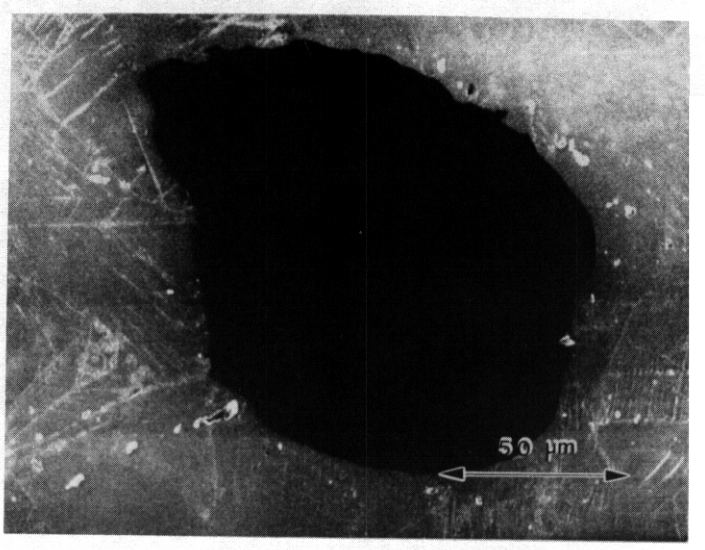

Fig. 7a. Scanning electron (SEM) image of the surface of the specimen showing α' martensite plates in CW AMCR irradiated at 520°C to 75 dpa

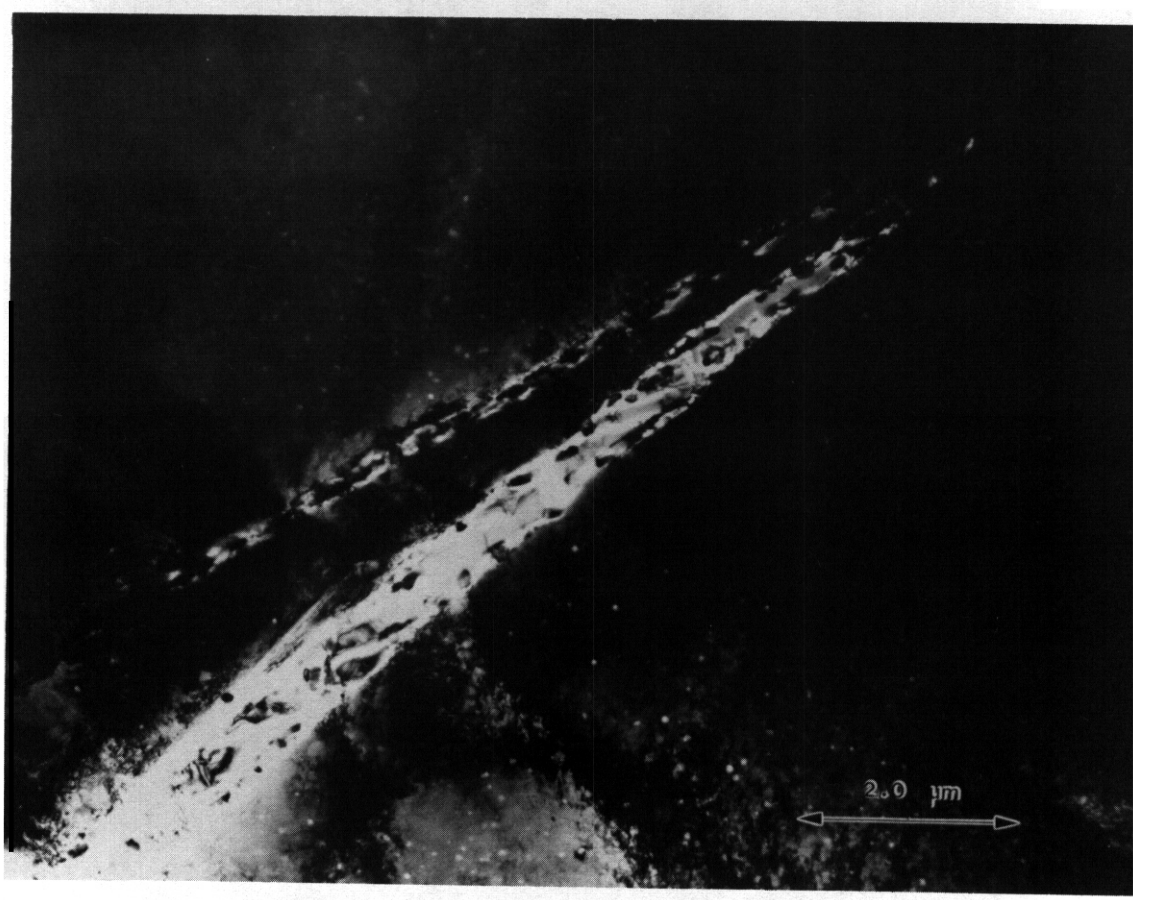

Fig. 7b. TEM bright field image of two of the *d* martensite plates in the austenite matrix with voids

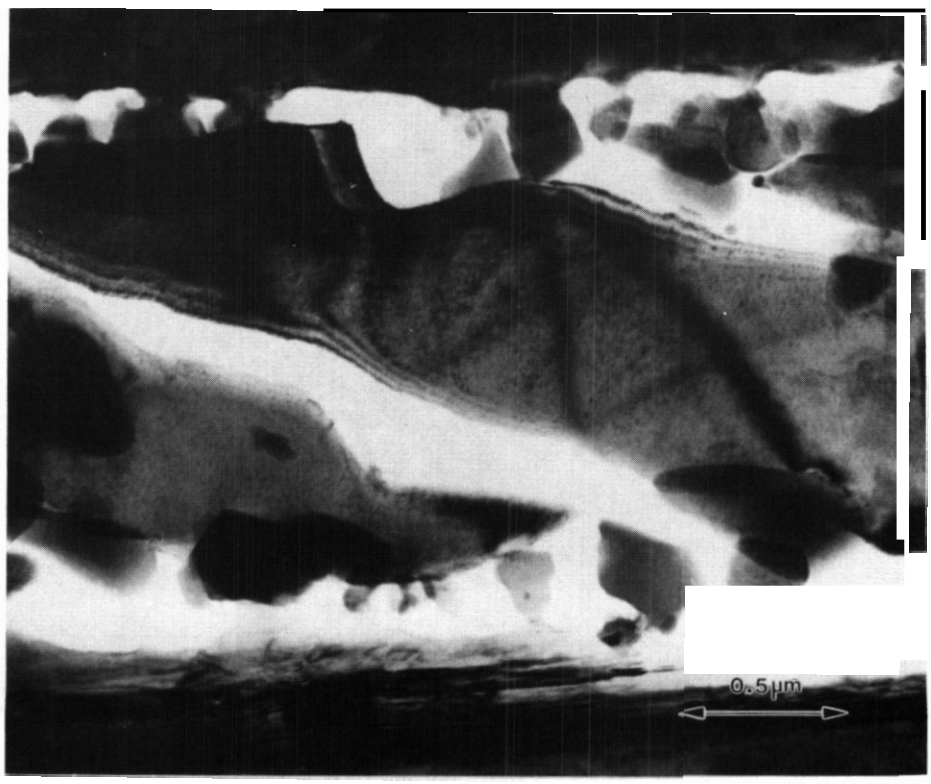

Fig. 8. Bright field TEM image at higher magnification of one of the a' martensite plates in figure 7b showing $M_{23}C_6$ carbides at the α'/austenite grain boundary and within the dislocation free a' martensite

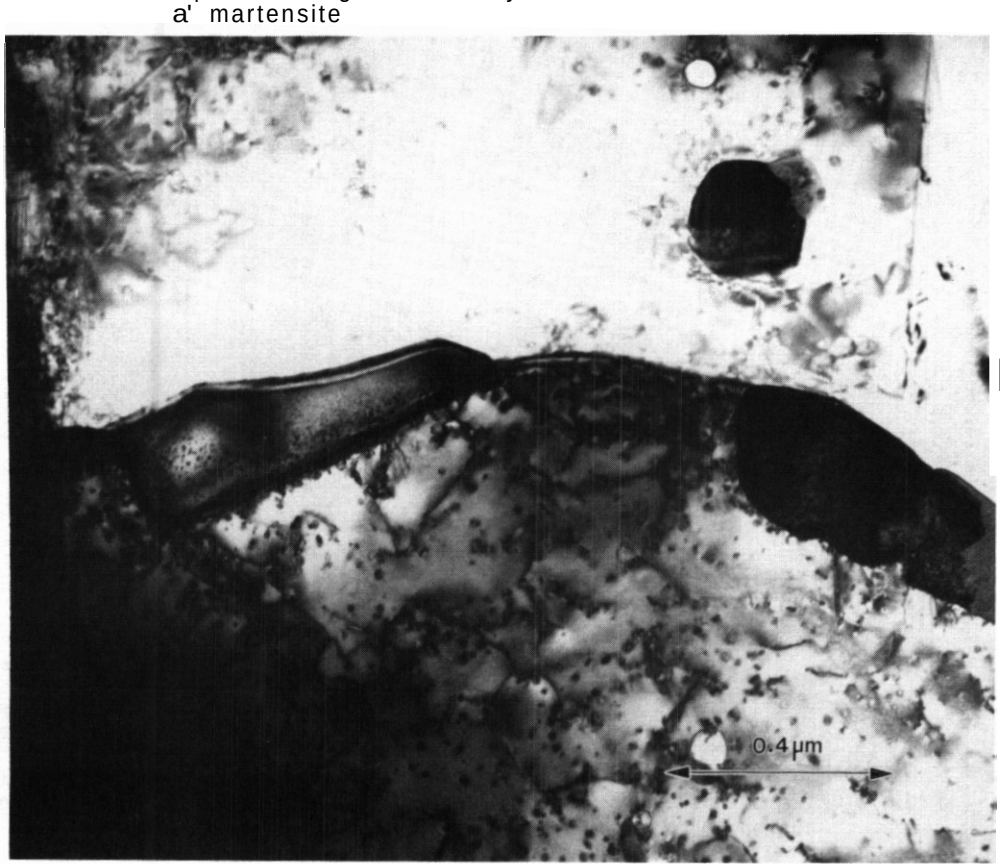

Fig. 9. Bright field TEM image of $M_{23}C_6$ carbides at a grain boundary and within the austenite of CW AMCR irradiated at 600°C

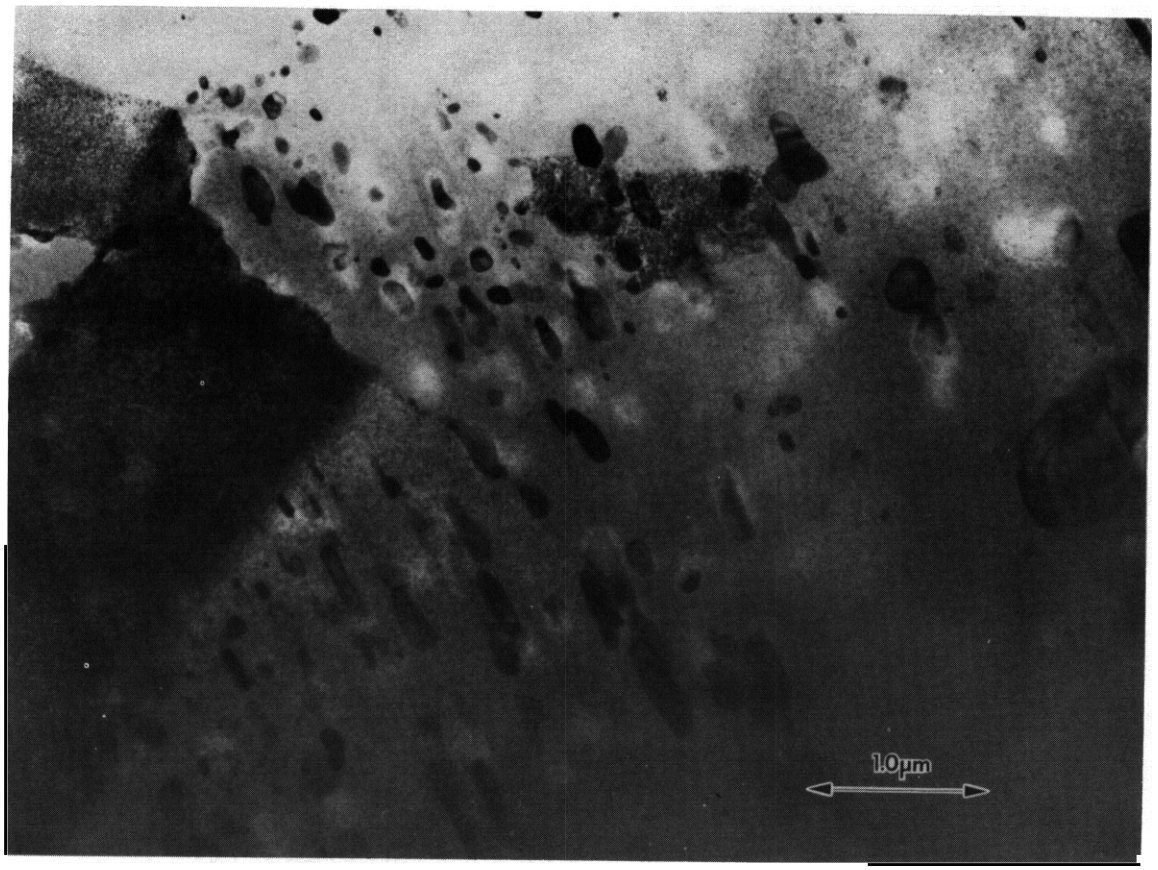

Fig. 10. Bright field TEM image of $M_{23}C_6$ carbides in the austenite of SAA AHCR irradiated at 420°C to a dose of 75 dpa

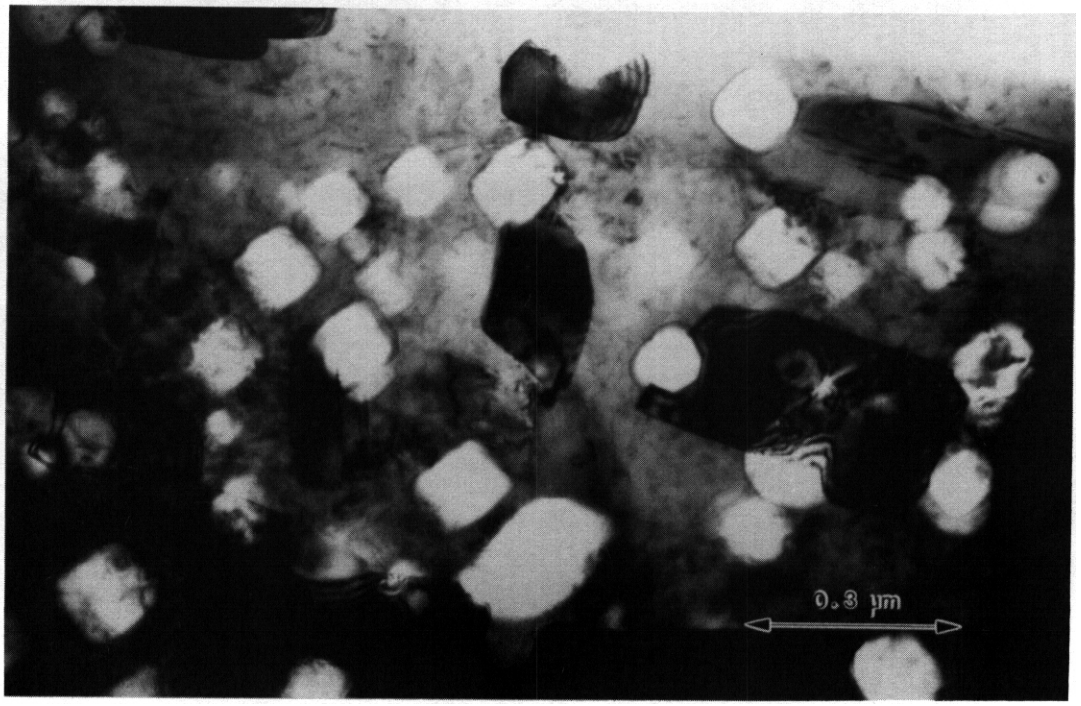

Fig. lla. Bright field TEM image of a-ferrite in austenite with voids in SAA AMCR irradiated at 520°C to 75 dpa

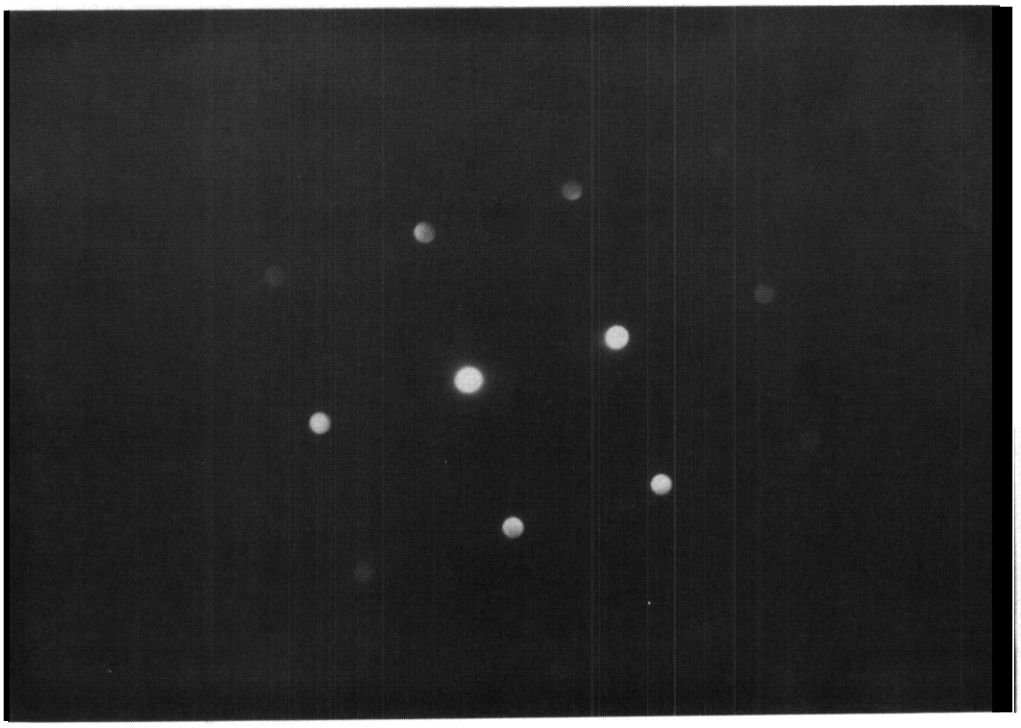

Fig. llb. Electron micro-diffraction pattern produced by *a* ferrite grain in lla at a <100> zone axis

Fig. 12. Bright field TEM image of SAA AMCR irradiated at 600°C to 60 dpa showing stacking faults, dislocations, voids and $M_{23}C_6$ carbides in an austenite matrix

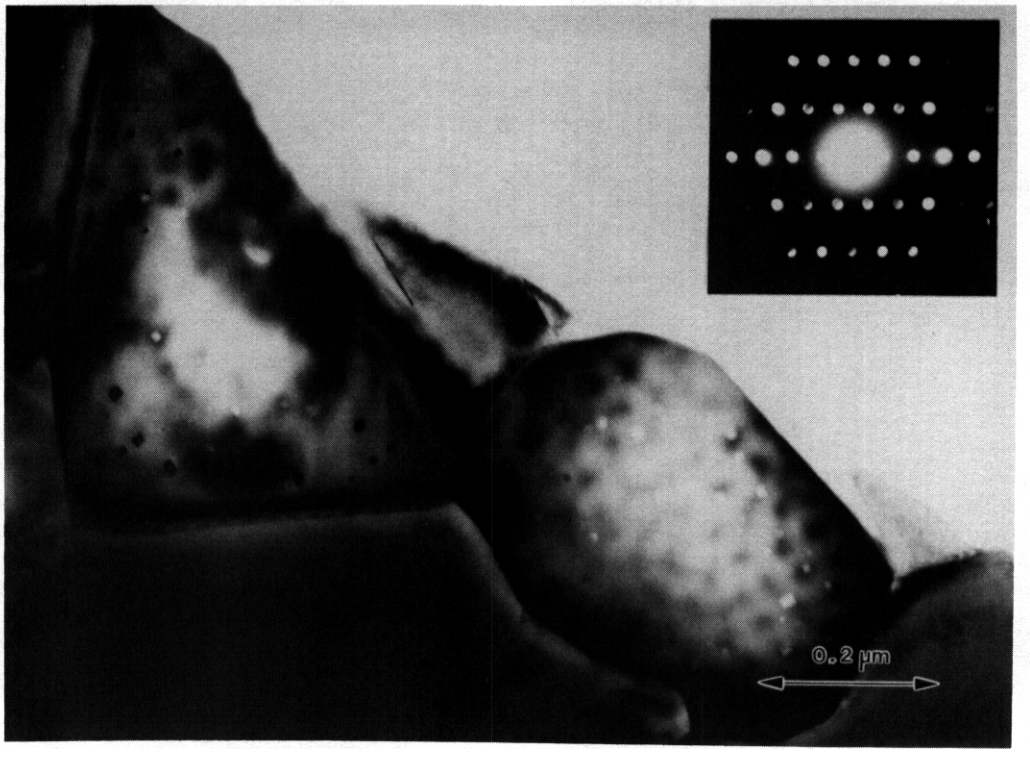

Fig. 13. Bright field TEM image of large M_2C_6 carbides in SAA AMCR irradiated at 600°C at foil edge stowing holes left by etched cuboidal precipitates and remaining small cuboidal precipitates within the carbides. Inset micro-diffraction pattern <013>$M_{23}C_6$ shows faint extra spots possibly from small precipitates within the carbide

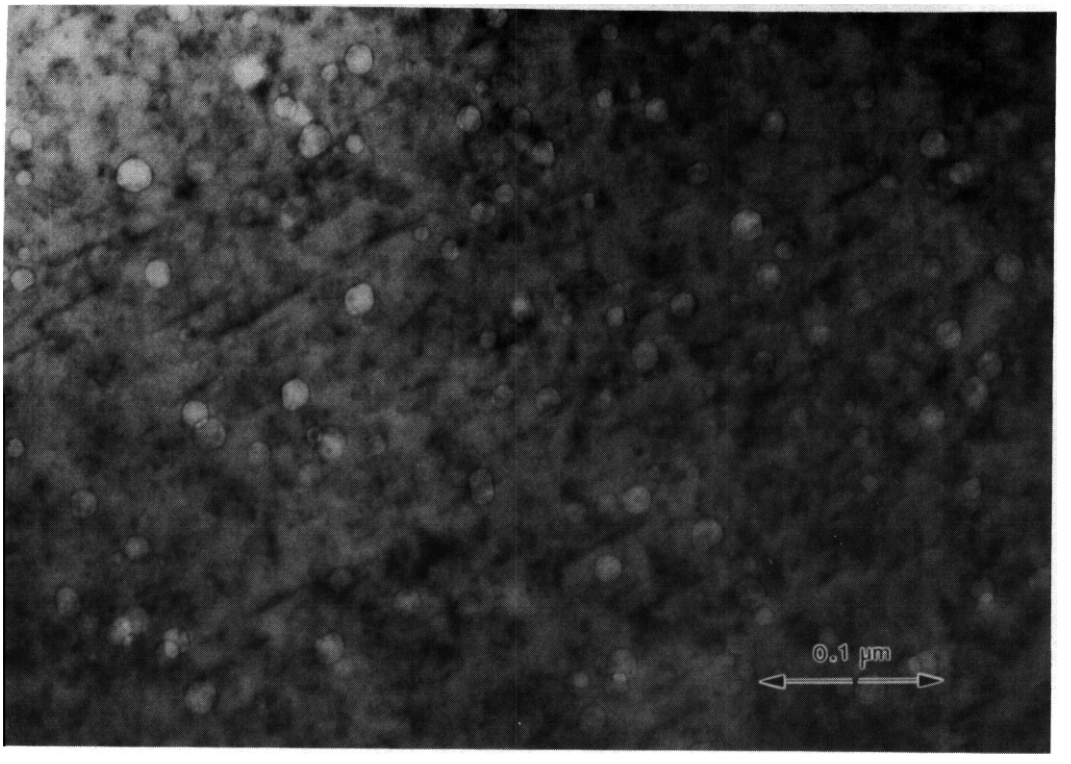

Fig. 14. Bright field TEM image of CWA AMCR irradiated at 420°C to 75 dpa shows voids in an austenite matrix

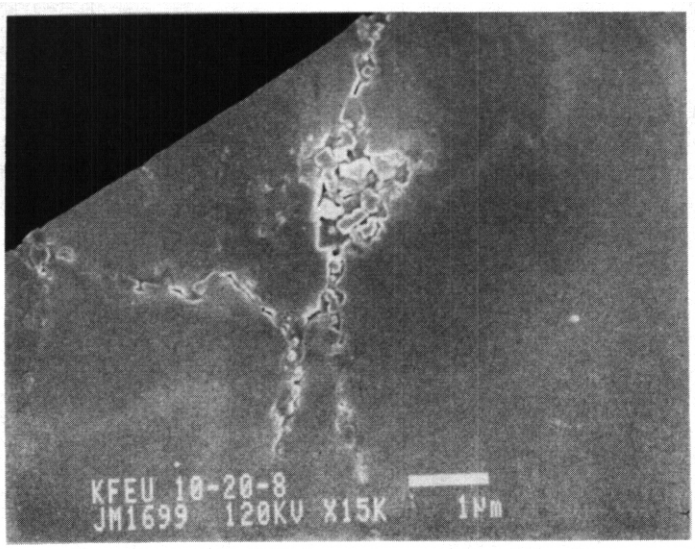

Fig. 15. SEM image of foil surface of CWA AMCR irradiated at 420°C showing preferential electropolishing at grain boundaries and regions of decomposition to a-ferrite and $M_{23}C_6$ due to Cr depletion of the matrix by $M_{23}C_6$ precipitation

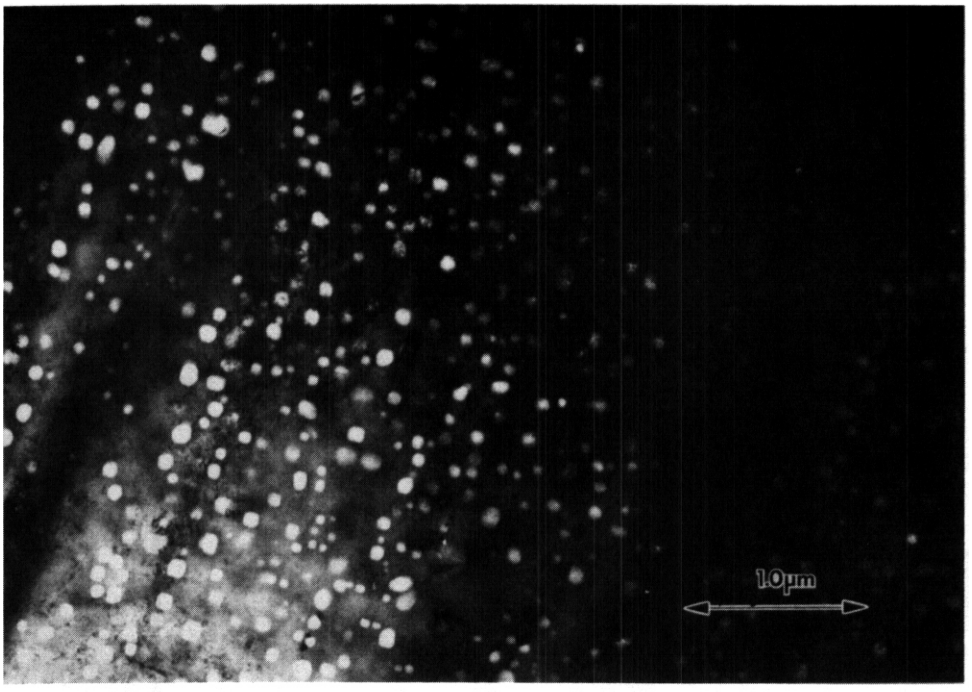

Fig. **16.** Bright field TEM image of CWA AMCR irradiated at 520°C to 75 dpa showing a high number density of voids and heterogeneous precipitation of $M_{23}C_6$

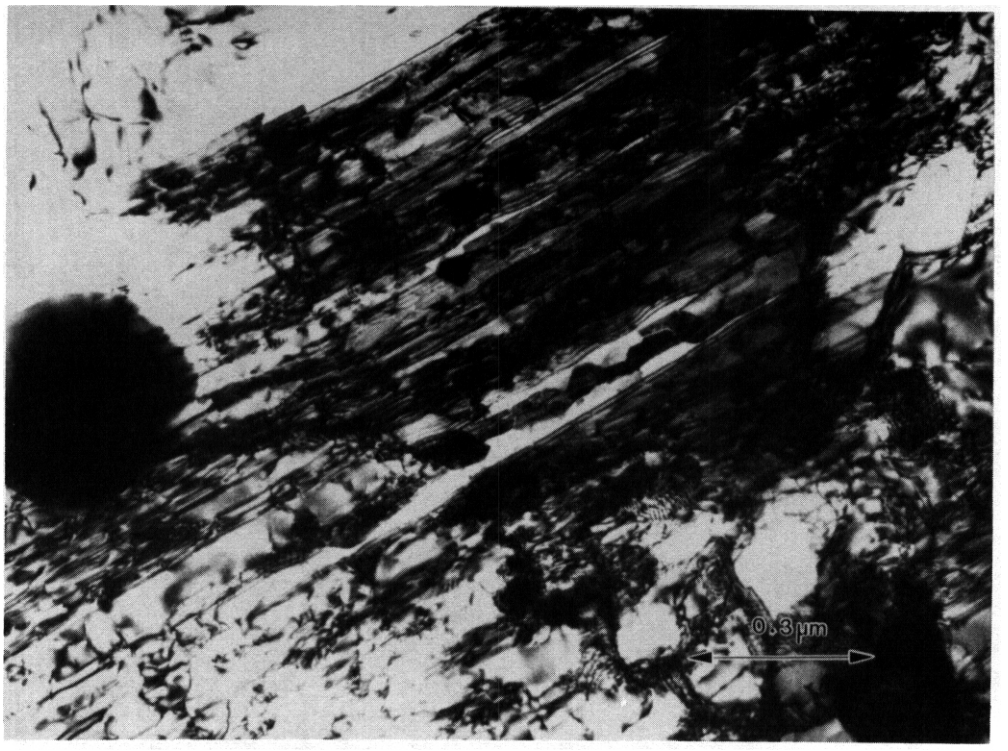

Fig. 17a. Bright field TEM image of CWA AMCR irradiated at 600°C to 60 dpa showing a region of austenite with stacking faults and $M_{23}C_6$ carbides

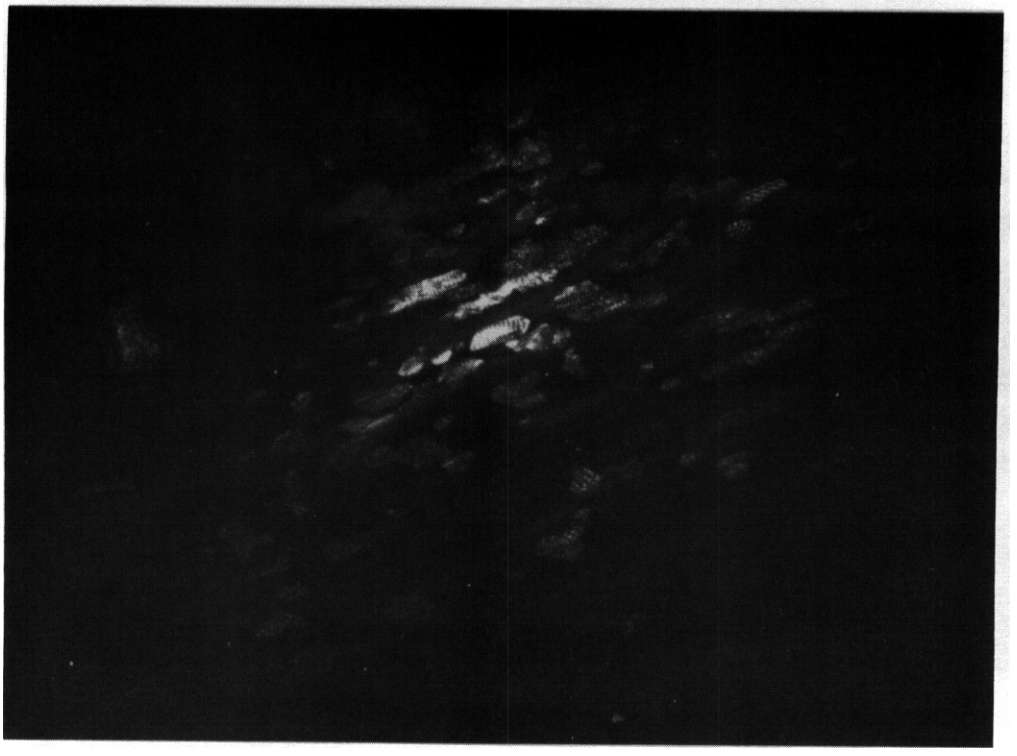

Fig. 17b. Dark field TEM micrograph of same area using a reflection from the $M_{23}C_6$ carbide

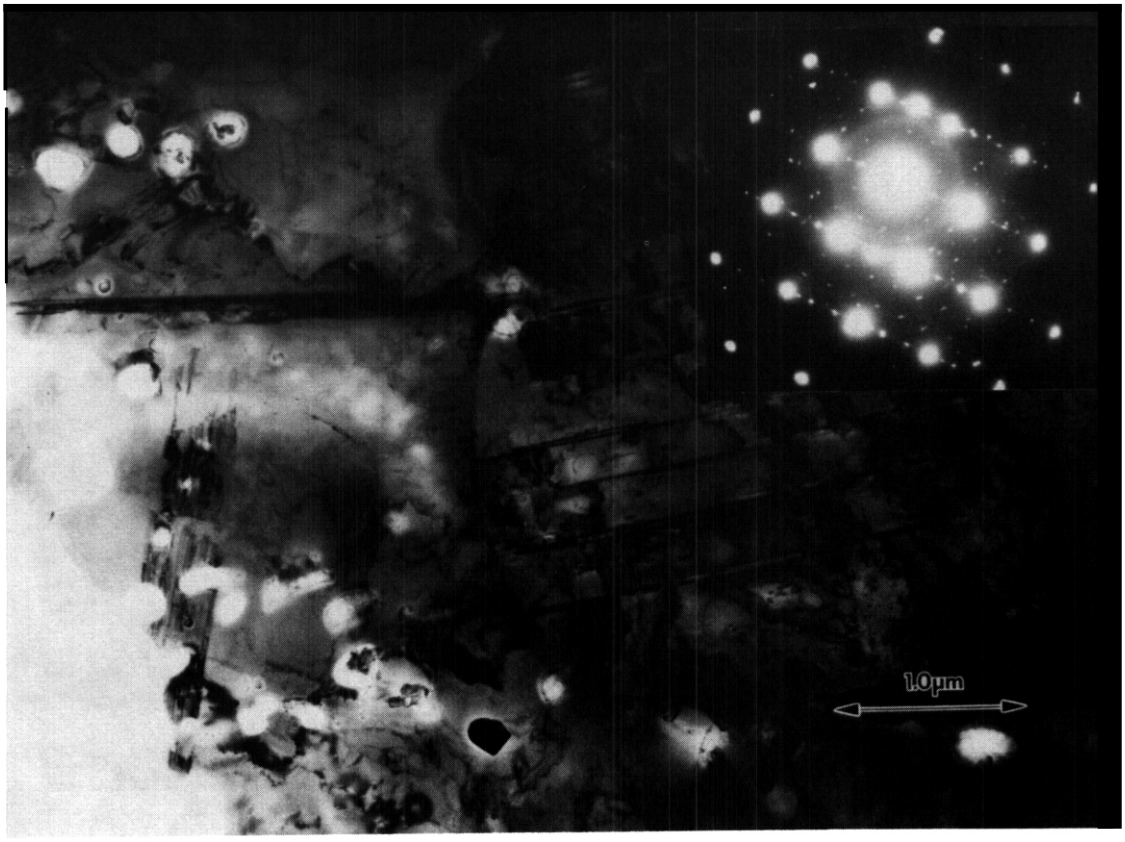

Fig. 18a. Bright field TEM image from the same specimen as in figure 17 second austenite region with ε martensite and $M_{23}C_6$ carbide as is shown by the selected area diffraction pattern $\langle 1\bar{1}0\rangle_{\gamma} \parallel \langle 1\bar{1}0\rangle_{M_{23}C_6} \parallel \langle 1\bar{2}10\rangle_{\varepsilon}$

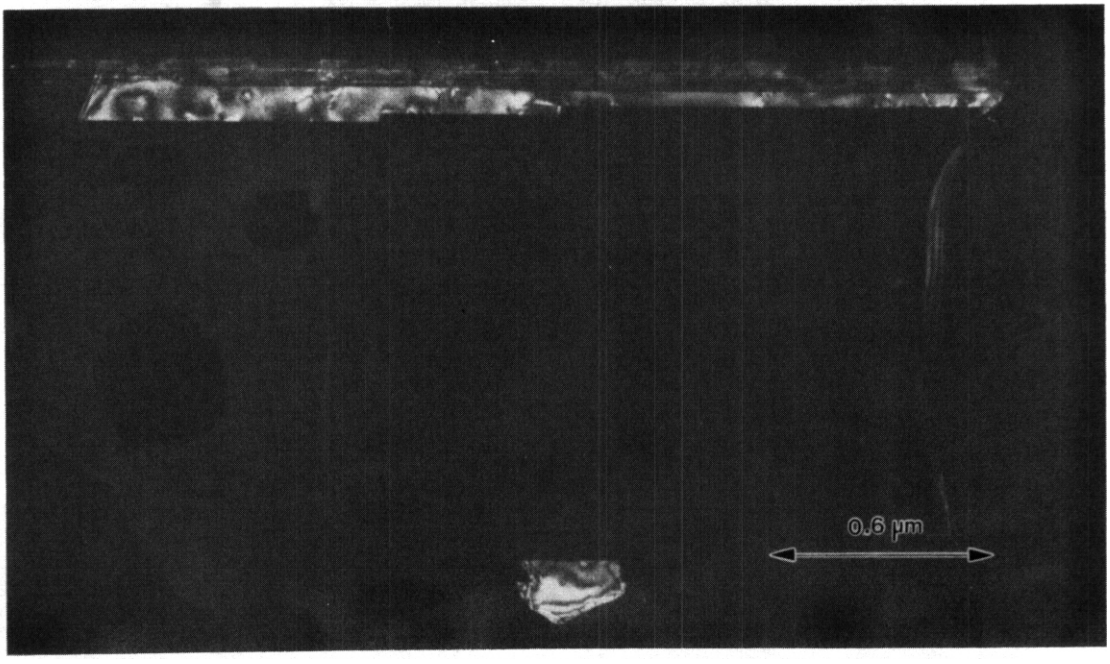

Fig. 18b. Dark field TEM image of ε martensite plate and a $M_{23}C_6$ carbide in area left of center of the austenite region in figure 18a (at higher magnification)

PRECIPITATION SENSITIVITY TO ALLOY COMPOSITION IN Fe-Cr-Mn AUSTENITIC STEELS DEVELOPED FOR REDUCED ACTIVATION FOR FUSION APPLICATION — P. J. Maziasz and R. L. Klueh (Oak Ridge National Laboratory)

OBJECTIVE

The objective of this work is to develop a reduced-activation Fe-Cr-Mn austenitic steel with similar or better properties relative to Fe-Cr-Ni-No austenitic stainless steels like AISI 316 or, PCA. Minor solute additions have been made to a base alloy composition of Fe-12Cr-20Mn-0.25C for improved strength and for swelling resistance. The purpose of this work is to report on the effects of these solute modifications on the precipitation behavior of these new Fe-Cr-Mn steels during high-temperature aging.

SUMMARY

Special austenitic steels are being designed in which alloying elements like Mo. Nb. and Ni are replaced with Mn. W. V. Ti. and/or Ta to reduce the long-term radioactivity induced by fusion reactor irradiation. However. the new steels still need to have properties otherwise similar to comnercial steels like type 316. Precipitation strongly affects strength and radiation-resistance in austenitic steels during irradiation at 400 to 600°C. and precipitation is also usually quite sensitive to alloy composition. The initial stage of development was to define a base Fe-Cr-Mn-C composition that formed stable austenite after annealing and cold-working, and resisted recovery or excessive formation of coarse carbide and intermetallic phases during elevated temperature annealing. These studies produced a Fe-12Cr-20Mn-0.25C base alloy. The next stage was to add the minor alloying elements W, Ti, V, P, and B for more strength and radiation-resistance. One of the goals was to produce fine MC precipitation behavior similar to the Ti-modified Fe-Cr-Ni prime candidate alloy (PCA). Additions of Ti+V+P+B produced fine MC precipitation along network dislocations and recoverylrecrystallization resistance in 20% cold worked material aged at 800°C for 166 h. whereas W, Ti, W+Ti, or Ti+P+B additions did not. Addition of W+Ti+V+P+B also produced fine MC. but caused some σ phase formation and more recrystallization as well. These new alloys. therefore, achieved several of the initial design goals. Their fine MC precipitation and recovery/recrystallization behavior during aging is similar to that of the PCA. Calculations show that the new steels have over 10^3 times less long-term radioactivity than type 316.

PROGRESS AND STATUS

Introduction

Austenitic Fe-Cr-Ni stainless steels are attractive as candidates for first-wall and structural materials for magnetic fusion reactor (MFR) applications, particularly near-term devices like the International Thermonuclear Experimental Reactor (ITER). Steels such as AISI 316 have good fabricability. strength, and ductility together with a large properties data base derived from commercial experience. Special Ti-modified austenitic stainless steels, like the prim candidate alloy (PCA) for the U.S. Fusion Materials Program, are the end product of years of alloy development efforts for radiation-resistance (resistance to void swelling and/or helium embrittlement).[1] However, since the U.S. Department of Energy sponsored the Panel on Low Activation Materials fn 1983,[2] awareness of the need to address the induced radioactivity issue for MFR structural components has increased.

Calculated radioactivity decay curves for various pure elements after exposure to a MFR neutron spectrum are shown in Fig. 1.[3] This radioactive decay behavior defines several categories for classifying potential MFR structural materials. The term low-activation ideally describes materials that would allow hands-on maintenance, and only materials like pure V or SiC can be classed as such. The term fast induced-radioactivity decay (FIRD) best describes engineering materials such as steels that would not allow hands-on maintenance, but could be disposed of by shallow land burial after reactor decommissioning.[4] A general strategy for the development of FIRD austenitic stainless steels was laid out by Klueh and Bloom in 1984.[4] Replacement of elements like Mo, Nb, and Ni in Fe-Cr-Ni-Mo steels such as type 316 or the Ti-modified PCA with elements like Mn, W, Ti, V, Ta, Si and C would produce an acceptable FIRD alloy. Efforts by others in this direction have included investigating the irradiation behavior of either comnercially available manganese stabilized steels (i.e., AISI 200 series steels or those produced by ARMCO or CREUSOT-MARREL),[5,6] or a wide range of pure or solute mdified Fe-Cr-Mn alloys.' By contrast, the approach of the Fusion Materials Program at the Oak Ridge National Laboratory (ORNL) has been to attempt to produce a new FIRD manganese stabilized steel with properties equivalent to the PCA.[4]

The ORNL program for developing manganese stabilized FIRD steels has been divided into several stages. The first stage involved selection of an appropriate Fe-Cr-Mn-C base alloy composition that would produce stable austenite in the range of 10 to 20 wt % Cr, 13 to 19 % Mn, and 0.07 to 0.4 % C.[8-10] From these alloys, a base composition of Fe-12Cr-20Mn-0.25C was selected for further alloying with minor element additions for

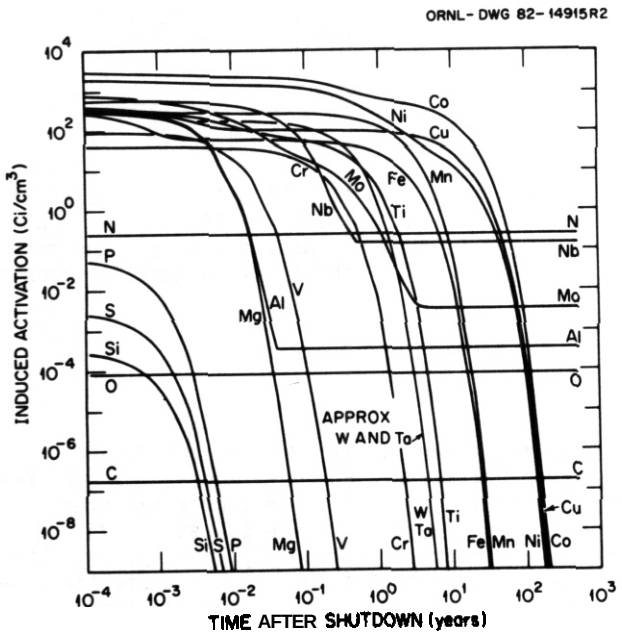

Fig. 1. A plot of the calculated radioactivity (in Curies/cm³) induced in various pure elements by frradiation in a MFR neutron spectrum and its decay as a function of time after reactor shutdown (taken from Wiffen and Santoro. Proc. of Topical Conference on Ferritic Alloys for Use in Nuclear Energy Technologies, TMS-AIME. 1984, p. 195).

more strength and radiation resistance.'" The new phase information also led to the development of a modified Schaeffler diagram (originally developed for Fe-Cr-Ni alloys) for predicting the constituent phases of Fe-Cr-Mn-C alloys after annealing.[11] The second stage involved additions of appropriate amounts and combinations of W, Ti, V, P, and B to produce fine, stable MC precipitation without upsetting the austenite stability of the base alloy or degrading its properties. Unirradiated mechanical properties and reactor irradiation response of the second stage alloys are currently being investigated. A third stage of alloy development will broaden the compositional range of the base alloy (i.e., more Cr if more corrosion resistance is needed). adjust the minor element additions, and extend the scope of properties investigations. particularly if there is interest in these alloys for ITER.

The purpose of this report is to examine the precipitation behavior and microstructural evolution of stage I and stage II alloys during high temperature aging in the cold worked condition. Data from stage I alloys was used in designing the stage 11 compositions. While thermal aging does not directly simulate irradiation exposure, the behavior of radiation-resistant steels during reactor irradiation, particularly in high He/dpa ratio irradiation environments, has some relationship to their behavior during thermal aging at higher temperatures.[2,12,13] In austenitic stainless steels, recrystallization resistance of a heavily (20-25%) cold worked dislocation structure during high-temperature aging is related to (1) the stability of the dislocations against recovery, (2) the formation and stability characteristics of fine precipitates like MC that nucleate along dislocations and (3) the resistance of the alloy to the formation of coarse carbide and intermetallic phases.[2] Radiation-resistant austenitic steels, like 25% CW PCA. experience enhanced-thermal microstructural evolution during reactor exposure because irradiation-induced processes (which cause unusual and often undesirable microstructural evolution that is usually very different from thermal aging) are suppressed.[2,12-14] MC precipitate formation and stability are crucial for causing the point defect mechanisms which produce void swelling resistance to operate, particularly at the higher He/dpa ratios expected in an MFR first-wall.[12,13,15] This approach of controlling precipitation behavior was first used to design new PCA (14Cr-16Ni) steels modified with minor solutes. These new Fe-Cr-Ni steels are nmre void swelling resistant during HFIR irradiation at 500°C than the original PCA. due to better MC formation and stability.[16] Improved MC behavior also gives these same steels outstanding thermal creep resistance at 700°C.[17] The focus, therefore, during stage II of the FIRD alloy development effort was what influence minor element additions have on MC formation and recrystallization of these new Fe-Cr-Mn alloys during aging at 800°C.

EXPERIMENTAL

In stage I. fifteen 500-g heats of Fe-Mn-Cr-C alloys (PCMA-0 through -14) were cast at ORNL to determine a stable austenitic base composition, and then seven more alloys (PCMA-15 through -21). with various combinations of minor alloying element additions made to a Fe-20Mn-12Cr-0.25C base composition, were cast in Stage II. The compositions of these various alloys are given in Tables 1 and 2. More details on production and fabrication of these alloys can be found elsewhere.[8,9,11]

The PCMA-0 through -9 alloys were annealed for 1 h at 1150°C after casting and then cold rolled to a 30% reduction in area. Samples were then either aged for 166 h at 800°C or homogenized for 24 h at 1275°C and reannealed for 1 h at 1150°C or 8 h at 1050°C. The PCMA-10 through -21 alloys were hot rolled at 1050°C to a 50% reduction in area and then homogenized for 5 h at 1200°C. Final 0.76-mm sheet was produced by several cold rolling steps of up to 50% with intermediate anneals of 1 h at 1150°C; the final sheet was in the 20% cold-worked (CW) condition. Samples of this material were then either aged for 168 h at 800°C or reannealed for 1 to 2 h at 1150°C or 8 h at 1050°C.

Most of the specimens were examined using metallography or analytical electron microscopy techniques and. for magnetic phase content, using a FERRITE-SCOPE to detect magnetic eddy currents. Transmission electron microscopy (TEM) was performed using JEW 100C, 100CX, and 2000FX and PHILIPS EM430 and CW-12

Table 1. Chemical Compositions of Phase I Alloys

Alloy Designation	Composition, wt %[a]			
	Mn	Cr	C	N
PCMA-0	13.4	15.0	0.07	0.001
PCMA-1	14.2	14.8	0.01	0.001
PCMA-2	17.1	15.2	0.056	0.001
PCMA-3	13.9	10.0	0.09	0.002
PCMA-4	18.9	9.9	0.093	0.002
PCMA-5	13.9	15.3	0.18	0.002
PCMA-6	14.3	16.0	0.18	0.003
PCMA-7	19.1	14.8	0.38	0.005
PCMA-8	17.7	20.1	0.13	0.003
PCMA-9	17.6	20.2	0.26	0.006
PCMA-10	19.9	10.0	0.081	0.005
PCMA-11	20.0	11.9	0.084	0.009
PCMA-12	20.0	11.95	0.18	0.008
PCMA-13	19.1	14.0	0.088	0.013
PCMA-14	19.9	15.9	0.17	0.0012

[a]Balance iron.

Table 2. Chemical Compositions of Phase II Alloys

Alloy Designation	Composition, wt %[a]					
	Mn	Cr	C	W	Ti	V
MnCrC (PCMA-15)	20.6	11.8	0.24	t0.01	t0.01	0.01
MnCrCTi (PCMA-16)	20.5	11.7	0.25	0.09	0.11	0.01
MnCrCW (PCMA-17)	20.5	11.8	0.23	0.83	<0.01	0.01
MnCrCTiW (PCMA-18	21.1	11.7	0.25	0.77	0.12	0.01
MnCrCTiBP (PCMA-19)	20.5	11.9	0.24	<0.01	0.10	0.01[b]
MnCrCTiVBP (PCMA-20)	20.8	11.8	0.22	<0.01	0.10	0.10[b]
MnCrCTiWVBP (PCMA-21)	20.4	11.7	0.25	1.08	0.10	0.10[b]

[a]Balance iron.
[b]With B and P.

RESULTS

Phase Formation in Annealed Stage 1 Alloys

After annealing for 1 to 2 h at 1150°C, most of the stage I alloys contained other phases in addition to the austenite matrix except for PCMA-7 and PCMA-12 alloys, which were completely austenitic. The phases identified in each alloy after annealing are listed in Table 3. Metallography of the microstructure of PCMA-7 is shown in Fig. 2(c) and TEM of PCMA-12 Is shown in Fig. 3. Alloys PMCA-0 through -2 contained large amunts of 6-ferrite due to their low C and high Cr contents (Table 1) and were highly magnetic.[8] A typical microstructure for this group of alloys is shown for PCMA-2 in Fig. 2(a). The PCMA-4 alloy with low Cr and high Mn contents had a significant amount of martenslte in the as-annealed microstructure. This phase appeared to be e-martensite (hexagonal close packed, hcp) because this sample was not highly magnetic.[8] After 30% cold working, however, PCMA-4 became very magnetic, presumably due to the formation of strain-induced a'-martensite (body centered tetragonal, bct).[18] The PCMA-10 through -14 alloys, all with about 20 wt % Mn, tend to confirm these effects of alloy composition on e-martensite and 6-ferrite formation. Alloys 10 and 11 with lower Cr contents form ε-martensite, while alloys 13 and 14 with more Cr form 6-ferrite. In general, the alloys with about 20 wt % Mn had more austenite and less of the other phases than alloys with less Mn.

The PCMA-5 through -9 alloys generally had higher C and Cr contents and formed primarily austenite with similar amunts of instruments; matrix and precipitate phases were identified by using selected-area and convergent-beam electron diffraction techniques (SAD and CBED, respectively) as well as X-ray energy dispersive spectroscopy (XEDS) for quantitative compositional analysis (JEM 2000FX with TN 5500 Series II Analyzer or PHILIPS EM400T/FEG with EDAX 9100 Analyzer).

Table 3. Oualitative microstructural phase identification in annealed or cold-worked and aged Fe-Mn-Cr-C alloys

Alloy	Phases Identified	
	SA (1 to 2 h at 1150°C)	20 to 30% Cold-Worked and Aged (166 h at 800°C)
	Stage I Alloys[a]	
PCMA-0	γ + δ	n.d.
PCNA-1	γ + δ	γ + σ
PCMA-2	γ + δ	γ + σ + $M_{23}C_6$
PCMA-3	γ + δ	n.d.
PCMA-4	γ + M	γ + $M_{23}C_6$ + σ
PCMA-5	γ + δ + M	n.d.
PCMA-6	y + 6 ε carbides	γ + σ + $M_{23}C_6$
PCMA-7	γ	γ + $M_{23}C_6$
PCMA-8	γ + 6 + carbides	n.d.
PCMA-9	Y + 6 + carbides	γ + $M_{23}C_6$ + σ
PCMA-10	γ + M	n.d.
PCMA-11	γ + M	n.d.
PCMA-12	Y	n.d.
PCMA-13	γ + δ	n.d.
PCMA-14	γ + δ	n.d.
	Stage 11 Alloys[b]	
MnCrC	$M_{23}C_6$	$M_{23}C_6$
MnCrCTi	MC	$M_{23}C_6$ + MC
MnCrCW	$M_{23}C_6$	$M_{23}C_6$ + some Fe- and Cr-rich phases
MnCrCTiW	$M_{23}C_6$ + MC	$M_{23}C_6$ + MC
MnCrCTiBP	MC	$M_{23}C_6$ + MC
MnCrCTiVBP	MC	$M_{23}C_6$ + MC
MnCrCTiWVBP	$M_{23}C_6$ + MC	$M_{23}C_6$ + MC + σ

[a]Identified with either metallography or TEM/AEM techniques. γ — austenite, 6 — ferrite, M — martensite, a — sigma phase.
[b]Identified with both metallography and TEM/AEM techniques.

ORNL PHOTO 10000-88

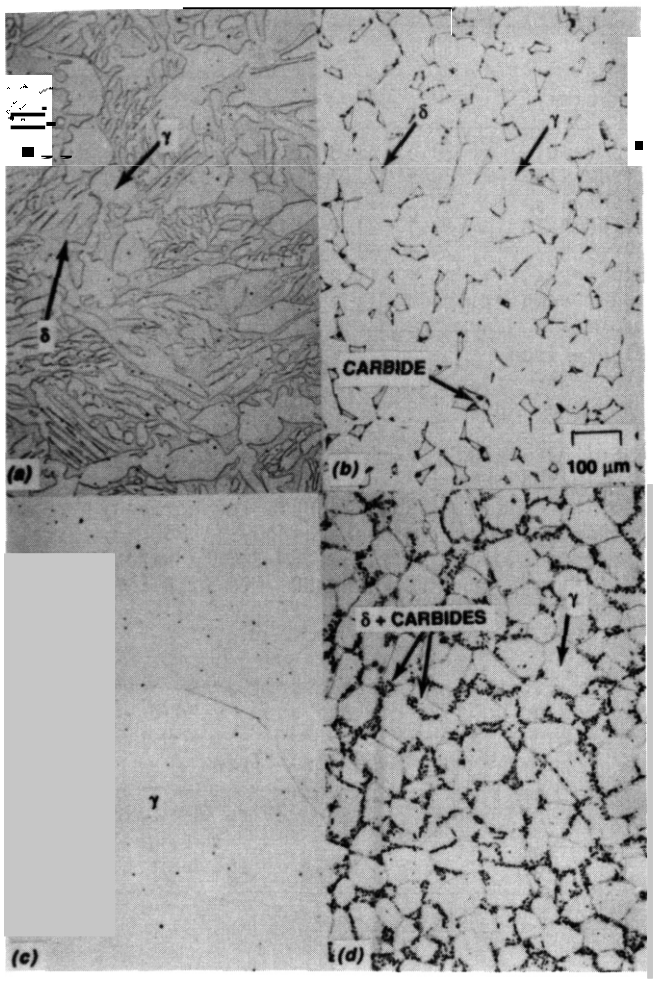

Fig. 2. Metallography showing the microstructure developed after annealing 30% cold worked material for 1 h at 1150°C in alloys (a) PCMA-2, (b) PCMA-6, (c) PCMA-7, and (d) PCMA-9.

ORNL PHOTO 10001-88

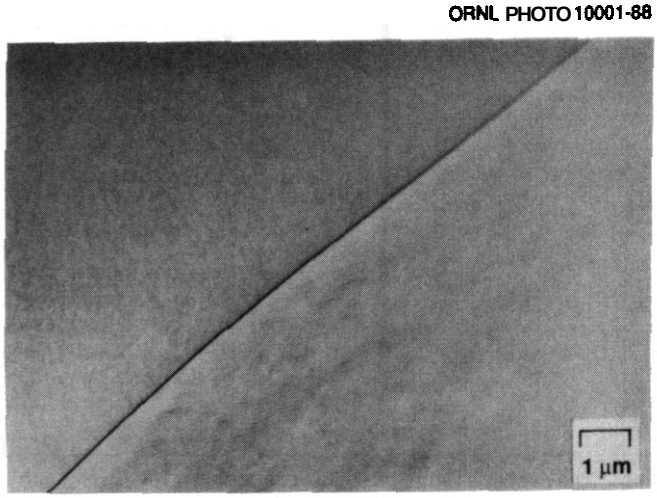

Fig. 3. TEM of the fully austenitic microstructure developed in PCMA-12 after annealing 20% cold-worked material for 1 h at 1150°C.

6-ferrfte at grain boundary triple point junctions and varying amounts of carbide phase (presumably $M_{23}C_6$) within the 6-ferrite particles. The microstructures of PCMA-6, -7 and -9 are shown in Fig. 2. PCMA-7 with the most C and Cr (0.36 and 19 wt %, respectively) was completely austenitic. PMCA-6 contained γ + 6 phases with only a few carbides, whereas PCMA-9 contained copious carbide precipitation within the 6-ferrite phase [see Figs. 2(b) and 2(d)]. These results, together with the behavior of the PCMA-10 through -14 alloys, show the need to balance Mn, Cr and C additions to produce a stable austenitic alloy. The Mn and C contents must both be raised to keep the austenite free of martensite, but above about 15 to 16 wt % Cr, it is difficult to keep the microstructure free of 6-ferrite and carbides. The TEM microstructure and AEM composition of a δ-ferrite particle analyzed in annealed PCMA-14 is shown in Fig. 4 (also see Table 4). The d-ferrite phase has more Cr than the γ-austenite matrix. Since Cr-rich carbides form within the 6-ferrite particles in PCMAs -6 and -9. C appears to be less soluble in the 6-ferrite than in the austenite.

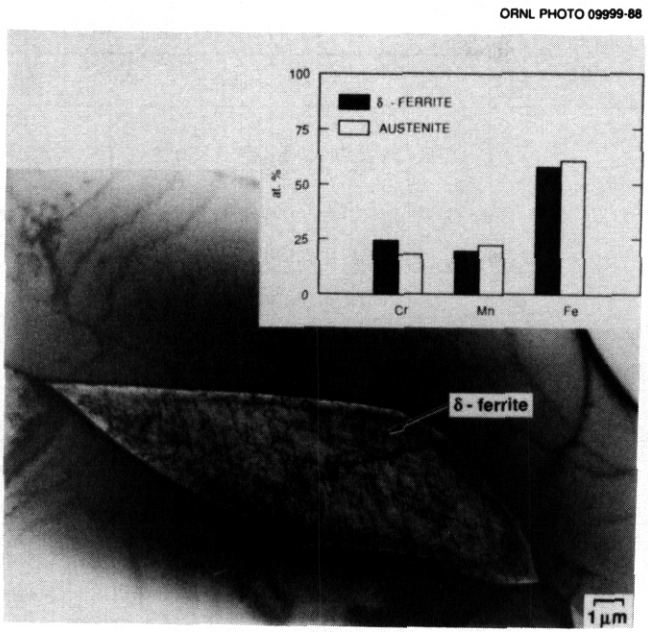

Fig. 4. TEM of a 6-ferrite particle formed in PCMA-14 during annealing for 1 h at 1150°C. The histogram shows the composition of the precipitate particle and the adjacent matrix as determined by quantitative XEDS analysis.

Phase Formation in Cold-Worked and Aged Stage I Alloys

Metallographic and TEM investigations of PCMA-0 through -9 alloys that had been 30% cold worked and those aged for 168 h at 800°C showed varying amounts of recovery and/or recrystallization together with the precipitation of carbide and/or intermetallic (σ) phases (see Table 3 for phases). There was no evidence of 6-ferrite or martensite in the aged materials and little or no detectable ferromagnetic behavior. Only the PCMA-1 alloy with the lowest C content (0.01 wt %) showed any detectable ferromagnetism. This could indicate a small amount of 6-ferrite present with the abundance of a-phase particles found in this sample. Metallography of PMCA-2, -6, -7, and -9 after aging is shown in Fig. 5 (compare with annealed alloys in Fig. 2). The PCMA-1, -2 and -4 alloys recrystallized completely into a new assembly of small grains [see PCMA-2 in Fig. 5(a)], whereas the PCMA-5 through -9 alloys retained the austenite grain structure established by annealing prior to cold working [Figs. 5(b) and 5(d)]. During aging, the entirely austenitic PCMA-7 was more recoverylrecrystallization resistant than the other alloys [Fig. 5(c)].

The TEM examination' showed that recrystallization of the PCMA-1 through -4 alloys produced dislocatlon-free grains with a high density of extended stacking faults. Examples of this type of microstructure are shown in Fig. 6(a) and 6(b) for alloys PCMA-2 and -4, respectively. The PCMA-5 through -9 alloys had either higher uniform dislocation contents or nonuniform mixtures of regions with higher dislocation network concentrations and dislocation-free regions. Both PMCA-7 and -9 had finer structures of stacking faults and a uniformly higher density of network dislocations. as shown in Figs. 6(c) and 6(d).

TEM observations also revealed considerable precipitation of coarse a and $M_{23}C_6$ (τ) phases after aging (see Table 3). The PCMA-1 alloy (lowest C) formed mainly σ phase, whereas the PCMA-7 alloy (highest C) contained mainly $M_{23}C_6$ phase. The other alloys had mixtures of coarse (0.5 to 5 mm in diam) a and $M_{23}C_6$ phases

Table 4. Quantitative XEDS compositional analyses of in-foil precipitate phase particles in Fe-Cr-Mn-C alloys

Phase	Composition,[a] at. %						
	Si	Ti	Q	Cr	Mn	Fe	W
PCMA-14, SA 1 h at 1150°C							
6-ferrite (3)[b]			0.2	23.1	19.6	56.7	
PCMA-9, 30% CW + Aged 168 h at 800°C							
τ-$M_{23}C_6$ (2)				73.0	12.0	14.9	
σ-phase (1)				28.8	18.7	51.2	
MnCrC, 20% CW + Aged 168 h at 800°C							
τ-$M_{23}C_6$ (6)	0.3	0.1	0.1	66.5	14.8	18.0	
MnCrCTi, 20% CW + Aged 168 h at 800°C							
τ-$M_{23}C_6$ (2)		0.1	0.1	67.4	14.6	17.5	0.3
MC (3)		77.6	0.2	3.6	4.9	9.5	4.2
MnCrCW, 20% CW + Aged 168 h at 800°C							
τ-$M_{23}C_6$ (3)		0.1	0.1	65.0	14.7	17.5	2.7
Fe-rich phase (2)		0.1	0.1	36.3	17.8	44.4	1.5
Cr-rich phase (2)		0.1	0.1	46.5	16.8	34.7	1.8
MnCrCTiW, 20% CW + Aged 168 h at 800°C							
τ-$M_{23}C_6$ (2)		0.1	0.3	67.5	13.4	16.2	2.1
MC (1)		67.4		3.3	5.1	13.1	11.0
MnCrCTiVBP, 20% CW + Aged 168 h at 800°C							
τ-$M_{23}C_6$ (2)		0.2	0.7	63.4	15.8	19.8	0
MnCrCTiBP, 20% CW + Aged 168 h at 800°C							
τ-$M_{23}C_6$ (2)		0.1		66.6	14.8	18.5	
MnCrCTiWVBP, 20% CW + Aged 168 h at 800°C							
τ-$M_{23}C_6$ (2)		0.2	0.8	63.9	14.0	17.9	3.0
o-phase (2)			0.2	22.0	21.0	54.3	2.5

[a]Composition of metal atoms heavier than aluminum. [b]Number of particles analyzed.

in the γ matrix, with PCMA-2 and -9 appearing to have the most abundant precipitation.[18] Figure 7 shows a typical o-phase particle with a low order CBED zone-axis pattern (ZAP) that clearly identifies the phase. Only the PCMA-7 alloy that resisted recovery/recrystallization contained a uniform dispersion of fine $M_{23}C_6$ particles, as shown in Fig. 8, along with a (001) CBED-ZAP.

The compositions of several coarse σ and $M_{23}C_6$ particles in PCMA-9 were determined via quantitative XEDS in-foil analyses, and data are given in Table 4. The $M_{23}C_6$ phase was mainly Cr-rich, whereas the σ-phase was rich in Fe and Cr. The phase compositions in this Fe-Cr-Mn-C steel were generally similar to those observed for the same phases formed in aged type 316 stainless steel (Fe-Cr-Ni-Mo),[14] but these phases found in the Mn-stabilized steels contain significant amounts of Mn (see Table 4), while both phases formed in aged type 316 are low in Mn and Ni.

The PCMA-10 through -14 alloys were also aged for 166 h at 800°C in the 20% cold worked condition. but were only examined by metallography and with regard to magnetic behavior. No ferromagnetic phases were detectable after aging, although small amounts of either a'-martensite or 6-ferrite were detected in the cold worked material prior to aging.[9]

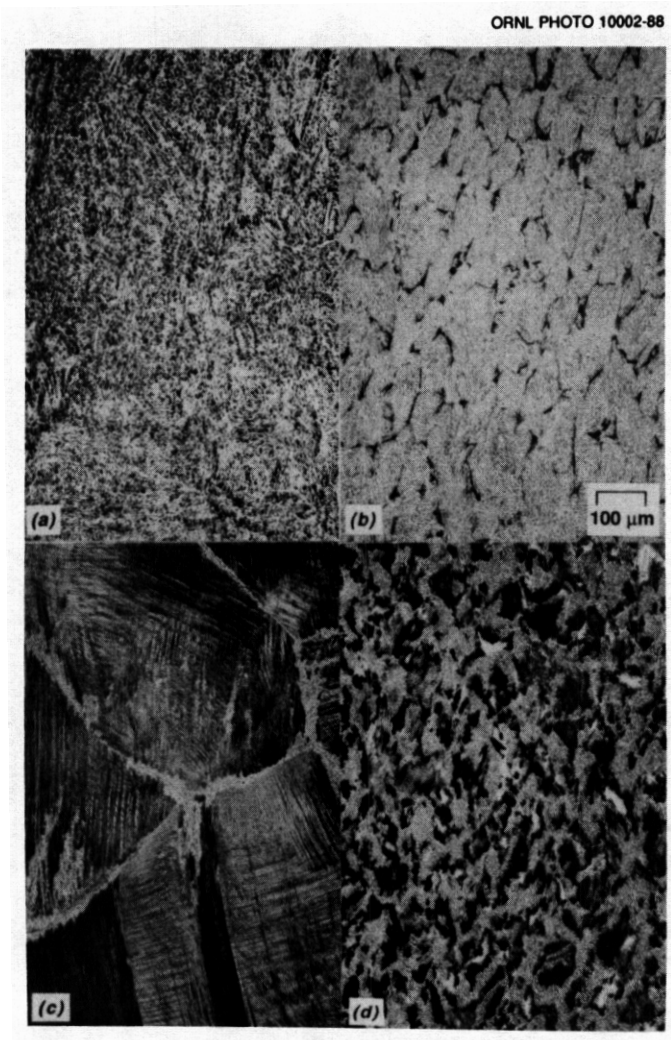

Fig. 5. Metallography of the microstructures developed after aging 30% cold-worked material for 166 h at 800°C in alloys (a) PCMA-2, (b) PCMA-6, (c) PCMA-7, and (d) PCMA-9.

ORNL PHOTO 10003-88

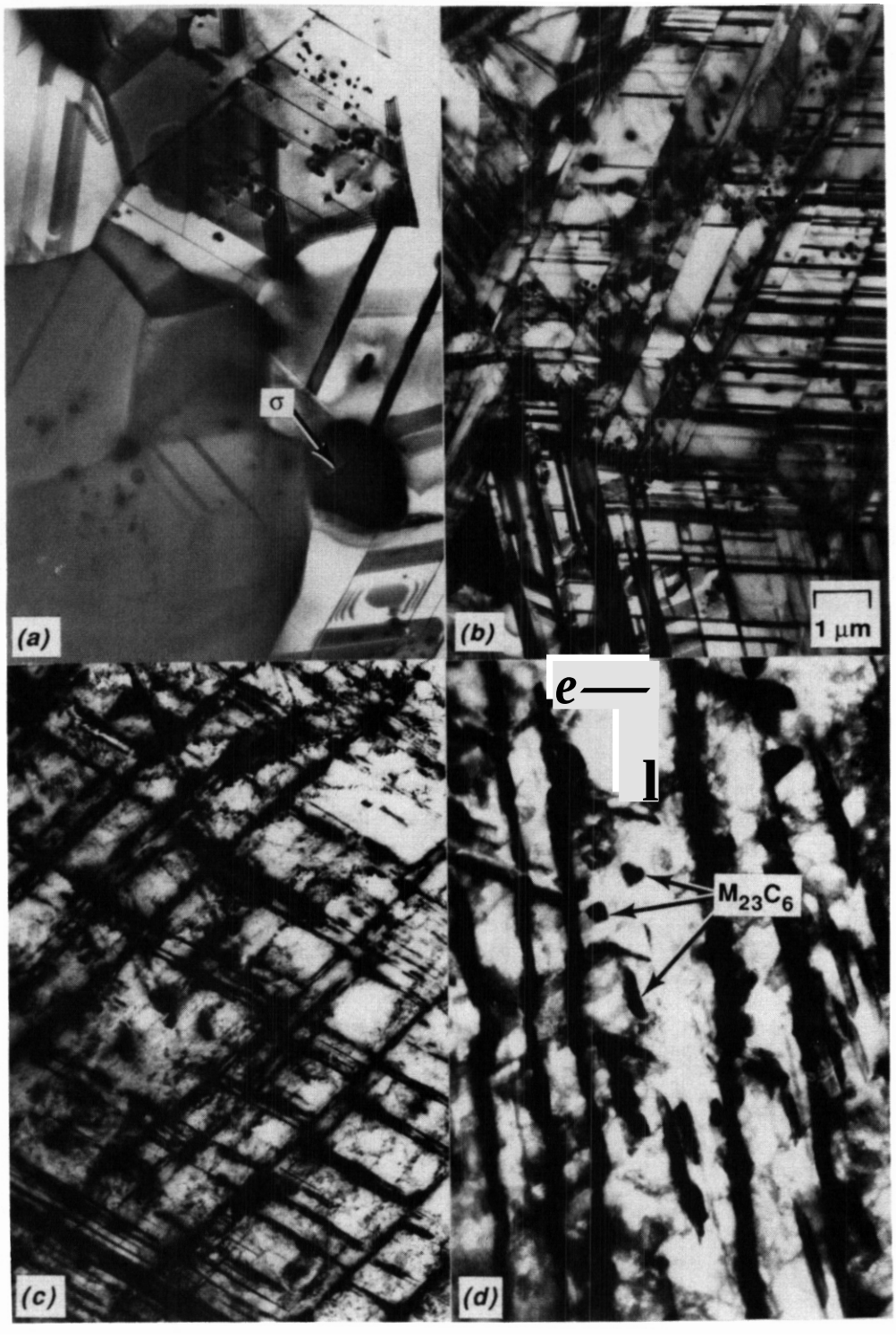

Fig. 6. TEM of the microstructures developed after aging 30% cold worked material for 166 h at 800°C in alloys (a) PCMS-2, (b) PCMA-D, (c) PCMA-7, and (d) PCMA-9.

ORNL PHOTO 10004-88

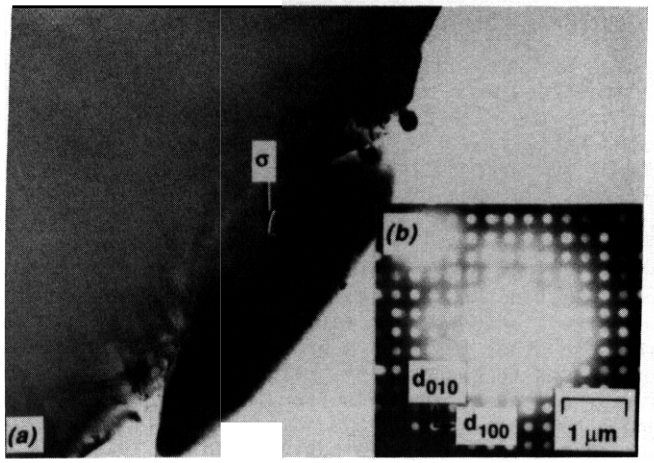

Fig. 7. (a) TEM of a u-phase particle formed In 30% cold worked PCMA-6 during aging for 166 h at 800°C and (b) CBED of the $(001)_\sigma$ ZAP for identification.

ORNL PHOTO 10005-88

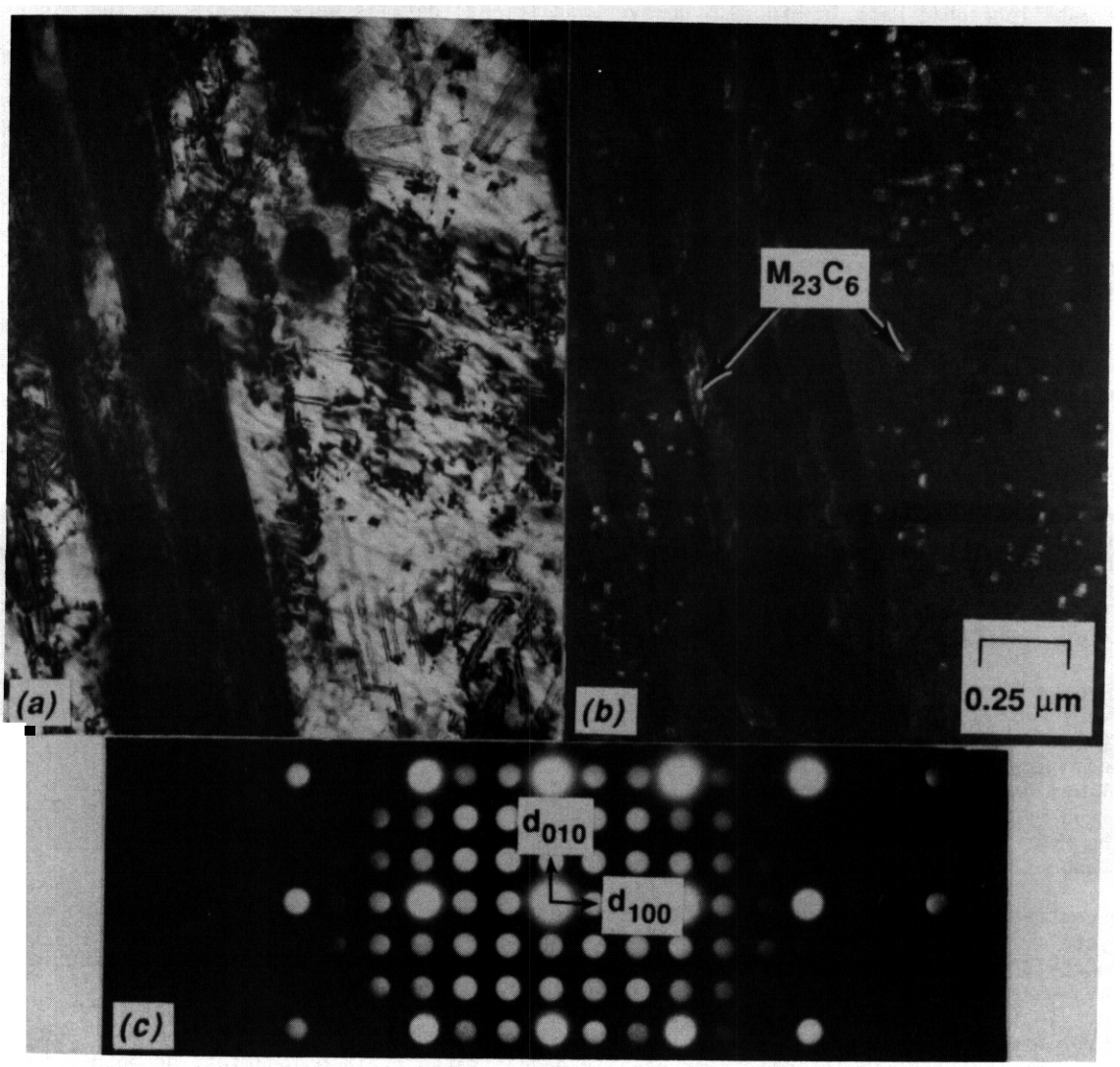

Fig. 8. TEM of fine $M_{23}C_6$ (τ) particles formed in 30% cold worked PCMA-7 during aging for 166 h at 800°C, imaged in (a) bright-field and (b) dark-field using a τ reflection, with (c) CBED of the $(001)_\tau$ ZAP for identification.

Phase Formation in Annealed Stage II Alloys

As a result of the Phase I studies, a base composition of Fe-12Cr-20Mn-0.25C (MnCrC or PCMA-15) was selected for the stage II alloys, and minor element solute additions were made to this base composition to improve its strength.[10,11] The nomenclature chosen to designate the alloys indicates the solute additions made to the base composition (i.e., Ti addition is designated MnCrCTi). The stage II alloys were cold worked 20% and then annealed for 2 h at 1150°C. All of the alloys were fully austenitic after annealing, but contained varying small amounts of $M_{23}C_6$ and/or MC carbides. The phases found in these alloys are listed in Table 3 and metallography of six of the seven alloys is shown in Fig. 9.

The base MnCrC alloy contained a sparse dispersion of inclusions after annealing and little or no precipitation was detected metallographically. The MnCrCTi, MnCrCW, and MnCrCTiW alloys had similar grain sizes and microstructures after annealing, but contained different amounts of precipitation. The MnCrCW alloy had little or no precipitation [see Fig. 9(b)], while the other two alloys had uniform dispersions of fine (on a lower magnification, metallographic scale) precipitates throughout the grains [Figs. 9(a) and (c)]; there was no obvious precipitation along grain boundaries. By contrast, the MnCrCTiBP, MnCrCTiVBP, and MnCrCTiV-WBP alloys showed distinct precipitation along grain boundaries, as shown in Fig. 9(d)–(f). The MnCrCTiVBP and MnCrCTiVWBP alloys also showed somewhat more intragranular precipitation than the MnCrCTiBP alloy.

TEM analysis showed that most of the alloys had some coarse or fine precipitates along the grain boundaries after annealing, (Fig. 10); diffraction analysis was used to identify the phases (Table 3). All of the alloys contained some MC and/or $M_{23}C_6$ carbides along grain boundaries or within the grains, consistent with the metallographic data in Fig. 9. However, additional details were revealed by the higher magnification TEM examination that were not obvious in Fig. 9. The MnCrC base alloy had very fine $M_{23}C_6$ particles distributed along the grain boundaries [Fig. 10(a)], but no precipitation was detected within the grains. The MnCrCTi alloy had fine intergranular MC together with some coarse particles in the matrix [Fig. 10(b)]. The MnCrCW alloy had coarse $M_{23}C_6$ along the grain boundaries [Fig. 10(c)], whereas MnCrCTiW steel had a mixture of coarse $M_{23}C_6$ and MC intragranularly, but virtually no precipitation along the boundaries [Fig. 10(d)]. The MnCrCTiBP, MnCrCTiVBP, and MnCrCTiWVBP alloys all contain similar distributions of coarse, blocky carbides along the grain boundaries [Fig. 10(e) and 10(f)] and some within the grains. The alloys with Ti+B+P and Ti+V+B+P had only MC phase particles, whereas the Ti+V+W+B+P alloy formed a mixture of MC and $M_{23}C_6$.

The morphological character of the high-angle, incoherent grain boundaries changed significantly with minor alloying element composition. After annealing, nearly all of the grain boundaries in the alloys without B and P (PCMA-15 through -18) were quite straight, similar to the boundary shown for PCMA-12 in Fig. 3. However, the grain boundaries in the alloys which contained trace additions of B and P (PCMA-19 through -21), had a zig-zag or kinked shape, with kink nodes occurring at the precipitate particles [Fig. 10(e) and 10(f)].

Phase Formation in Cold-Worked and Aged Stage II Alloys

The stage II alloys were cold worked 20% and then aged for 168 h at 800°C. Specimens were exanfned using TEM and AEM and diffraction and characteristic XEDS techniques were used for phase identification. Lower magnification TEM showed recoverylrecrystallization behavior in several alloys (Fig. 11). The base MnCrC alloy showed some recrystallization after aging, and recovery occurred in the regions that did not completely recrystallize [Fig. 11(a)]. Aging also produced coarse $M_{23}C_6$ particles (Tables 3 and 4).

In comparison to the base alloy, the alloys with solute additions of Ti, W, and Ti+W were more prone to recovery and/or recrystallization. The representative microstructure of the MnCrCTi alloy is shown in Fig. 11(b) to be almost fully recrystallized, with only small, isolated patches of deformed material remaining. The other two alloys showed more recovery but fewer large, dislocation-free grains. All of these alloys had significant amounts of coarse precipitation primarily in the recrystallized regions. The MnCrCTi and MnCrCTiW alloys, both of which contained Ti, had mixtures of coarse $M_{23}C_6$ and MC particles, while the MnCrCW alloy formed coarse $M_{23}C_6$ and particles of another phase that were rich in Cr and Fe, but did not appear to be either σ or χ phases (Tables 3 and 4).

By contrast, the alloys mdified with the solutes Ti+B+P, TitVtBtP. and Ti+W+V+B+P were quite resistant to recrystallization and recovery. The MnCrCTiVBP alloy showed the least recrystallization [Fig. 11(c)], while MnCrCTiBP had the least amount of coarse precipitation; most of the coarse phase particles in these two alloys were $M_{23}C_6$ (Table 4). The MnCrCTiWVBP alloy had somewhat more recrystallization than the other two alloys in this last group. but it also had the most coarse precipitation. These coarse particles in MnCrCTiWVBP were a mixture of $M_{23}C_6$ and σ phases, and the recrystallized regions were either associated with very coarse precipitates in the matrix or heavily precipitated grain boundaries, or both [Fig. 11(d)].

Higher magnification TEM provided a closer look at recovery of the dislocation structure and revealed fine precipitation in the unrecrystallized regions in these aged alloys, as shown in Fig. 12. Fine precipitation was not detected in the base MnCrC alloy or in the alloy with only W added [Fig. 12(b)]. Only sparse

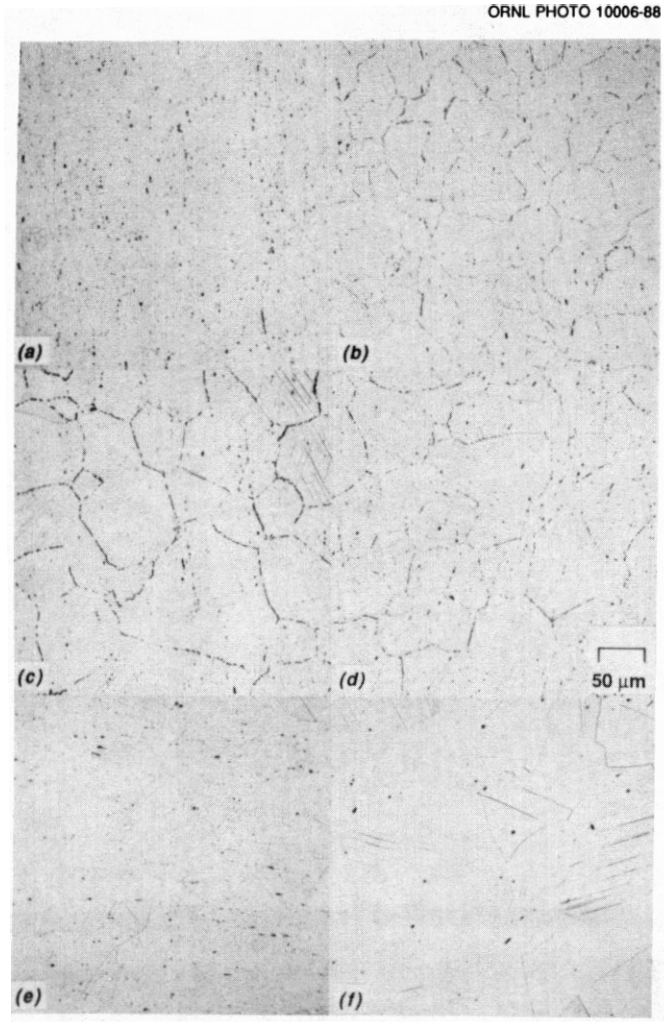

Fig. 9. Metallography of the microstructures developed after annealing 20% cold worked material for 2 h at 1150°C in alloys (a) MnCrCti, (b) MnCrCw, (c) MnCrCtiW, (e) MnCrCTiVBP, and (f) MnCrCTiWVBP.

ORNL PHOTO 10007-88

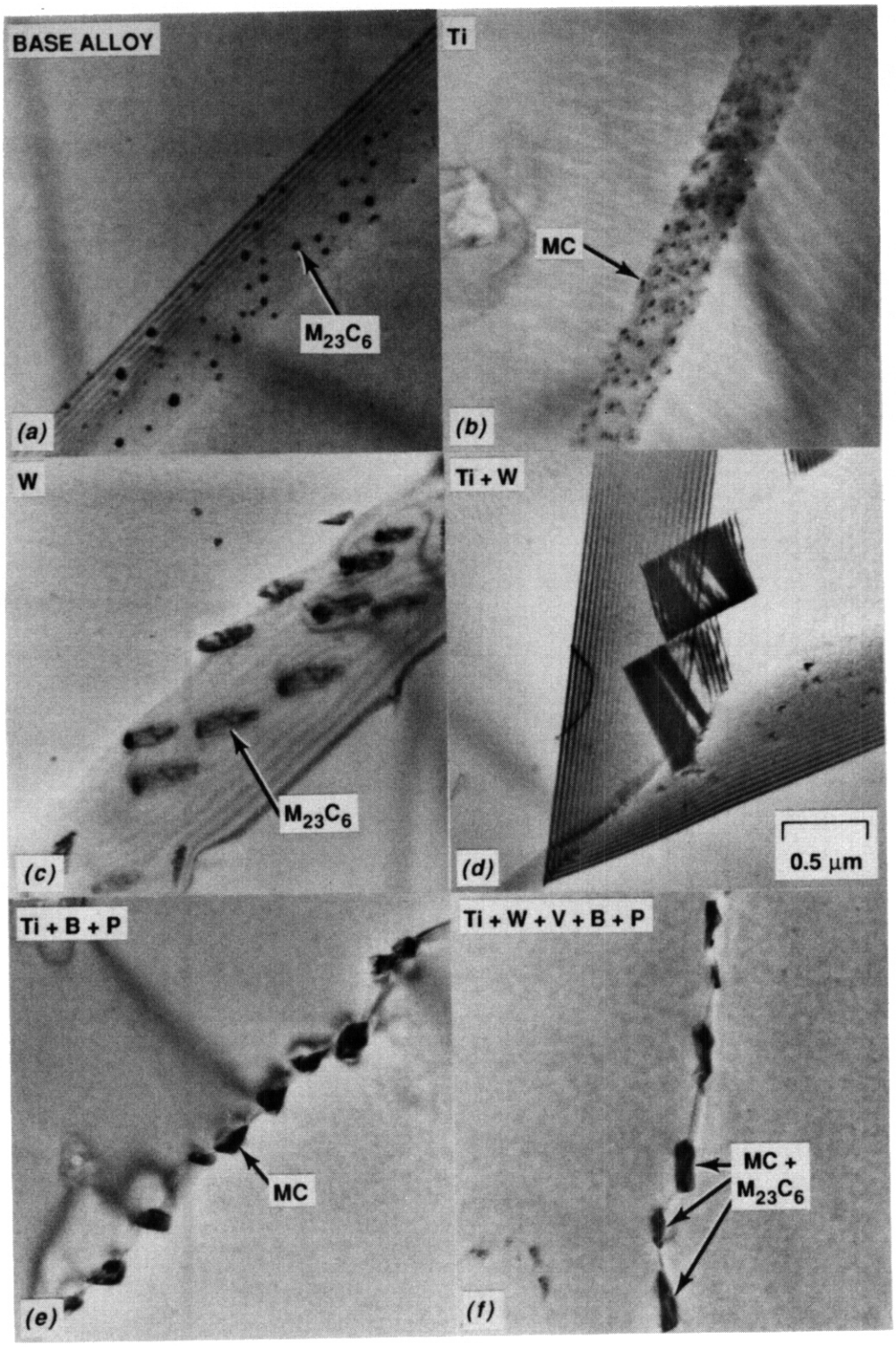

Fig. 10. TEM of the microstructures developed at the grain boundaries after annealing 20% cold-worked material for 2 h at 1150°C in alloys (a) MnCrC, (b) MnCrCTi, (c) MnCrCW, (d) MnCrCTiW, (e) MnCrCTiBP, and (F) MnCrCTiWVBP.

ORNL PHOTO 10008-88

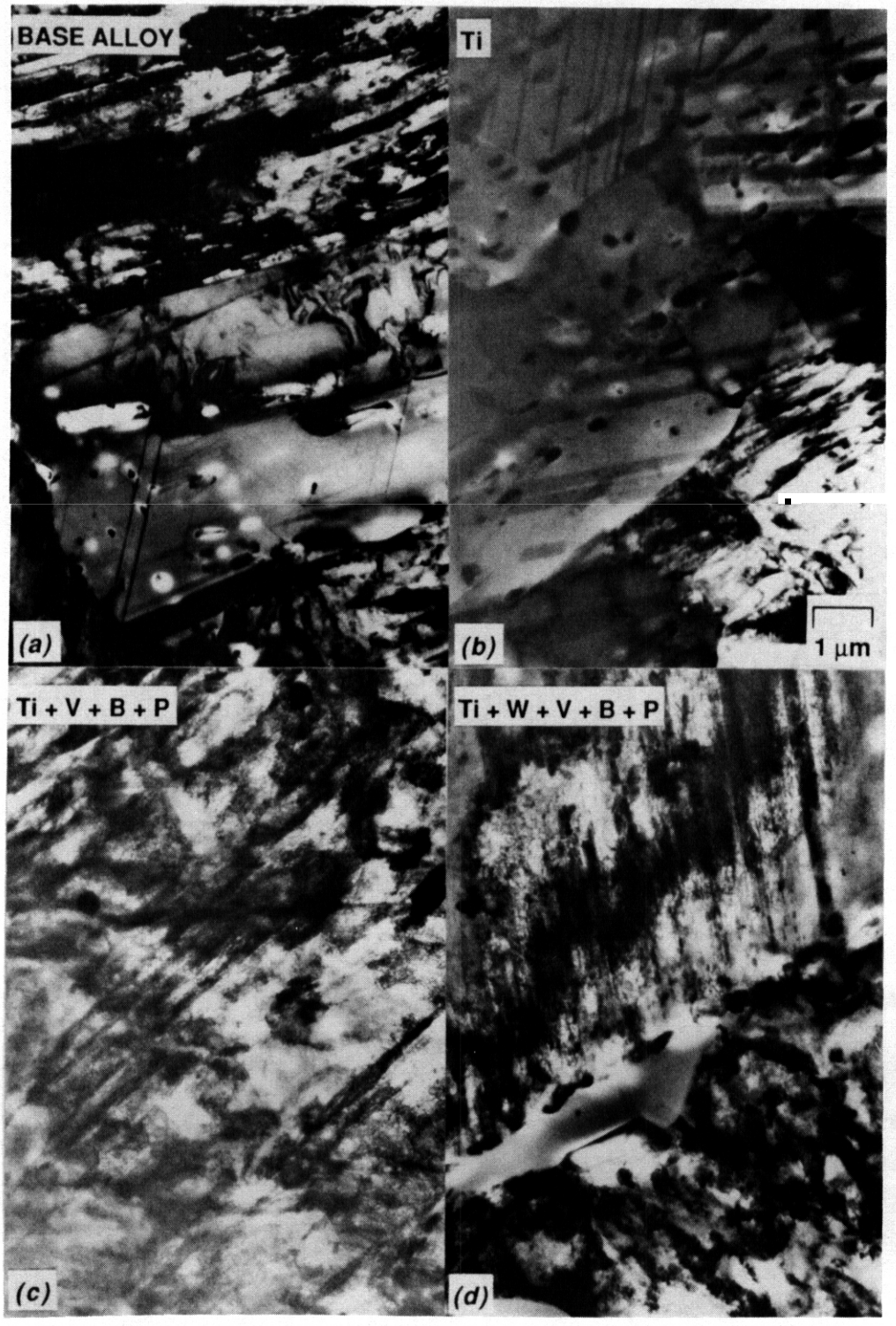

Fig. 11. Lower magnification TEM of the microstructures developed after aging 20% cold-worked material for 168 h at 800°C in alloys (a) MnCrC, (b) MnCrCTi, (c) MnCrCTi-VBP, and (d) MnCrCTiWVBP.

ORNL PHOTO 10009-88

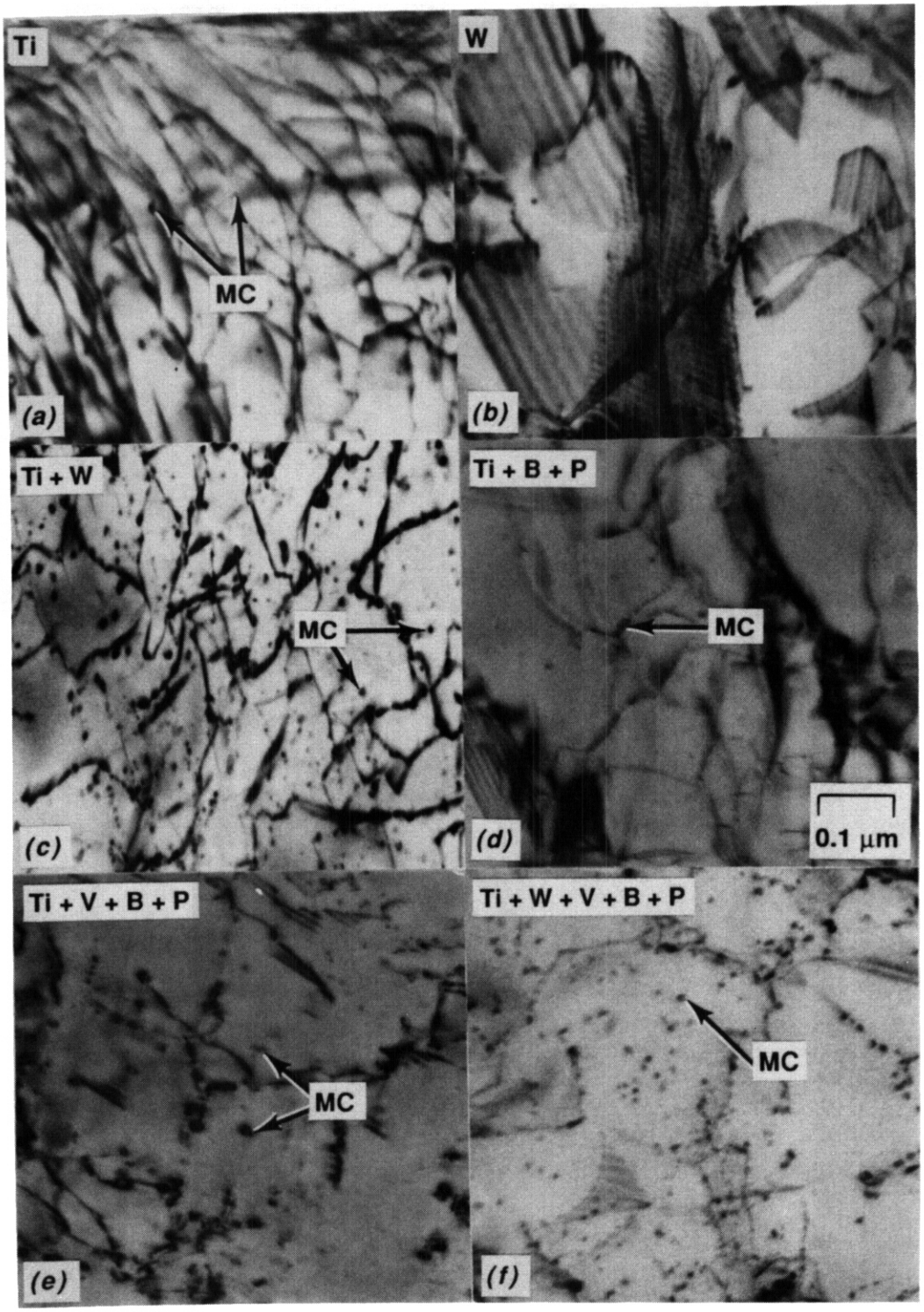

Fig. 12. TEM of the fine precipitate and dislocation microstructures developed in the matrix after aging 20% cold-worked material for 168 h at 800°C in alloys (a) MnCrCTi, (b) MnCrCW, (c) MnCrCTiW, (d) MnCrCTiBP, (e) MnCrCTiVBP, and (f) MnCrCTiWVBP.

amounts of very fine (2 to 6 nm in diam) precipitation were detected in the alloys mdified with only Ti or with TitBtP [Fig. 12(a) and 12(d)]. The particles were too small and too few for sufficient electron diffraction, but their presence in the alloys with Ti additions suggests that they could be MC phase. In the MnCrCTi alloy, there were only a few recovered regions, whereas in the MnCrCW and MnCrCTiBP alloys which were much more resistant to recoverylrecrystallization (particularly the latter), there were higher concentrations of large, intersecting faults. Roth of these latter alloys also appeared to have many dislocations which had dissociated into partials so that fault fringes were visible. Both features can be seen in Fig. 12(b) and 12(d), but they are especially prominent in Fig. 12(b) for PCMA-17. Although detailed Burgers vector analysis was not performed, these differences were quite noticeable when comparing one alloy with another. Widely separated partial dislocations would suggest that some of the alloying additions had lowered the stacking fault energy relative to the base alloy.

The PCMR-18, -20 and -21 alloys all had abundant dispersions of fine MC distributed throughout the unrecrystallized matrix regions, as shown in Fig. 12(c), 12(e) and 12(f), respectively. The MC phase was easily identified by diffraction analysis with its characteristic cube-on-cube crystallographic habit relative to the y-austenite matrix. The alloys mdified with Ti+V+B+P and Ti+W+V+B+P showed more resistance to recovery than the alloy with only Ti+P, which despite only a modest amount of recrystallization did show large recovered regions, with loose tangles of dislocation network and a coarser structure of the intragranular faulted-bands common to many of these steels [i.e., Fig. 11(c) and (d)]. Figure 12(c) shows that many of the fine MC particles in the MnCrCTiW steel are not directly associated with the visible network dislocations, whereas there is a high degree of association between dislocation segments and fine MC particles in the MnCrCTiVBP and MnCrCTiWVBP steels shown in Fig. 12(e) and (f), respectively. Many of the dislocations also showed fault contrast images in the alloys mdified with TitVtBtP and Ti+W+V+B+P, suggestive of dissociation and lower stacking fault energy, whereas the dislocations in the Ti+W alloy did not. These observations suggest that the MC-dislocation association and the splitting of dislocations into partials are in fact related. Dissociated dislocations would be less mobile and more easily pinned by fine precipitate particles. These detailed observations are indeed consistent with the good recoverylrecrystallization resistance exhibited by the MnCrCTiVBP and MnCrCTiWVBP alloys during aging at temperatures as high as 800°C.

Calculations of Radioactive Decay Behavior with Time for the Stage II Alloys

An important goal in the development of FIRD alloys is that they show less long-term residual radioactivity than conventional steels such as type 316 stainless steel, and that they meet the 10 CFR 61 Class C requirements for waste disposal by shallow land burial." The radioactive decay behavior as a function of time after exposure to MFR irradiation for a typical heat of type 316 and for the actual composition of one of the solute-modified Fe-12Cr-20Mn steels (PCMA-21, Table 2) was calculated by F. M Mann[19] of the Westinghouse Hanford Company (Fig. 13). While normal chemical analysis showed less than 0.01 wt % Nb in the MnCrCTiWVBP (PCMA-21) steel, the normal detectability limit for such techniques, residual element analysis using spark-source mass spectrometry, was not performed on these Mn-stabilized steels, and they were assumed to have 0.0001 wt % Nb. Normal chemistry methods show that some heats of type 316 have up to about 0.1 wt % Nb (ref.16), while trace element analysis methods show Nb levels in other heats as low as 0.0005 wt % (ref. 20). Niobium is not an intentional alloying addition to type 316. Figure 13 shows that long-term irradiation exposure (10 years or 36 MWy/m^2) in a comnercial conceptual MFR like STARFIRE produces roughly similar levels of radioactivity in type 316 and the new FIRD Fe-Cr-Mn steels immediately after shutdown. However after a period of about 50 to 100 years, the residual radioactivity of a FIRD alloy like PMCA-21 is over 10^3 times less than that found in conventional type 316. Comparison of several other classes of alloys together with type 316 and PCMA-21 steels is made in Fig. 14, by expressing the ratio of calculated radioactivity to that allowed by 10 CFR 61 Class C standard. Numbers greater than 1 indicate that the materials do not qualify as Class C waste, whereas numbers of 1 or less mean that they do qualify. None of the alloys qualify for class C disposal after irradiation to STARFIRE-type conditions, although "low-activation" alloys come much closer than conventional materials like type 316 or 9Cr-1MoVNb steels. Similar calculations and comparisons for much lower irradiation exposures (1.4 years or 5 MWy/m^2) in a STARFIRE-type machine indicate that FIRD steels like PCMA-21 can then qualify as Class C waste, whereas type 316 cannot.

DISCUSSION

The systematic alloy development approach pursued at ORNL for FIRD Fe-Cr-Mn steels has been successful in terms of the goals initially set.[4,8] The stage I alloys revealed Fe-Cr-Mn-C composition! in which austenite was stable, without 6-ferrite formation during high-tenerature annealing, or E- and a -martensite formation after cooling to room tenperature or cold working.[10,21] These same experimental data also produced enough new information to modify the normal Schaeffler that describes Fe-Cr-Ni alloys to adequately describe Fe-Cr-Mn-C alloys as well." The new diagram was used to define the base Fe-12Cr-20Mn-0.25C alloy composition for the stage II solute mdified alloys. The microstructural results of the stage I alloys made it clear that with more than 15 to 16 wt % Cr, it was difficult to keep the austenite free of 6-ferrite and carbides at most levels of Mn and C. At lower Cr contents, it was important to have at least enough C to prevent martensite from forming.

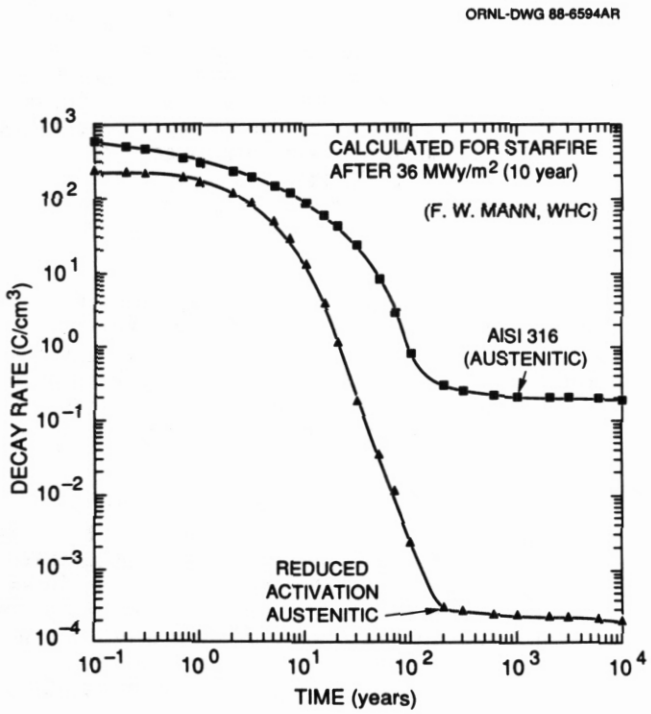

Fig. 13. A plot of the calculated radioactivity (In Curies/cm³) induced In type 316 stainless steel and In a new ORNL FIRD steel (PCMA-21) by irradiation In a MFR neutron spectrum and its decay as a functlon of time after reactor shutdown (courtesy of F. W. Mann, 1988 [19]).

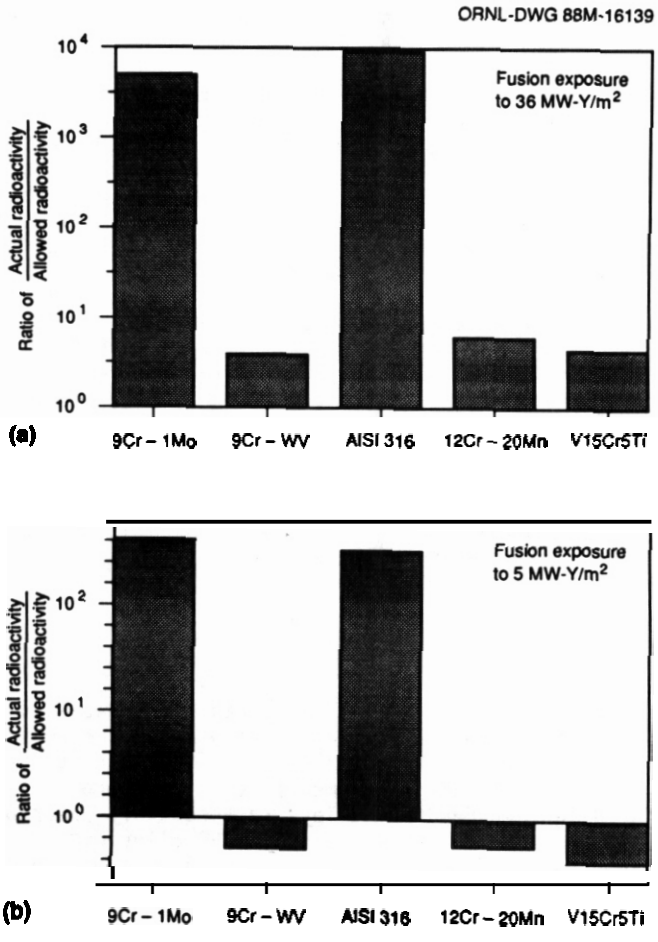

Fig. 14. Histograms of the ratio of calculated radiactivity decay behavior with time after shutdown to that allowed by the 10 CFR-61 Class C standard for various conventional and reduced activation first wall materials being considered by the U.S. Fusion Materials Program exposed to irradiation In a STARFIRE fusion reactor spectrum for (a) 10 y or 36 MWy/m² and (b) 1.4 y or 5 MWy/m² (courtesy of F. M. Mann, 1988 [19]).

The results for cold-worked stage I alloys aged at 800°C showed that the ε- and α′-martensite and δ-ferrite phases of concern in the annealed material are replaced by concerns about the formation of coarse a and $M_{23}C_6$ phases during aging. One very important aging result from the PCMA-0 through -9 alloys was that the most stable austenitic alloy (PCMA-7) was the most resistant to the formation of coarse $M_{23}C_6$ and σ phases during aging. Carbon has been found to be very important for resistance to intermetallic phase formation during the development of Fe-Cr-Ni steels optimized for irradiation resistance.[2] Consistently, the lack of C in pure Fe-Cr-Mn alloys studied by Garner and co-workers appears to be part of the reason for excessive formation of a phase in those alloys during FBR irradiation or during high tenperature aging.[21-23] The other important result from aging studies of the first alloy series was the formation of fine $M_{23}C_6$ precipitates in the alloy with the highest C content. These finely dispersed precipitates are obviously related to the recovery/recystallization resistance of that alloy (PCMA-7). which in turn may also relate to a phase resistance. The formation of a phase often occurs in conjunction with recrystallization in both the stage I and II alloys investigated in this work, and Garner et al.[22] recently presented more detailed data and mechanisms for a phase formation in the recrystallized grains of Fe-Cr-Mn ternary alloys. The formation of fine $M_{23}C_6$ precipitation in PCMA-7 probably reflects the fact that as the kinetics of carbide precipitation increase with increasing C supersaturation, precipitation becomes rapid enough to occur before recrystallization. Precipitate nucleation along the dislocations in the cold-worked structure would naturally be much easier and finer than nucleation in the recrystallized grains.

The annealing studies of the stage II solute mdified alloys produced several important results. Most of the minor alloying elements added to the base alloy were ferritizing elements, but all of the alloys were still fully austenitic after annealing. The base alloy did not contain excessive carbide precipitation after annealing. which would indicate the solubility limit for carbon had not been exceeded. The effect of the minor solutes varied, but the alloys that had precipitation of carbides along the grain boundaries did not contain excessive carbide precipitation within the grains. Commercial Fe-Cr-Mn steels considered in several other studies have C contents that range from 0.02 to 0.6 wt %, and our alloys fall within that range. Most of the commercial alloys also contain N contents that range from 0.02 to 0.6% as well, and current FIRD guidelines limit N to much lower levels.[24] Some commercial high-Mn steels, like the Russian EP-838 steel, contain Ni and Al additions, and most contain up to 0.02 wt % P, but none appear to contain the W, Ti, V, and B additions explored in the steels being developed at ORNL. The higher C content of the MnCrC and various solute mdified steels required annealing at about 1150°C or more, because annealing at 1050°C generally produced more precipitation than 1150°C. The effect of the minor alloying elements on grain boundary morphology and precipitation behavior are probably important to the processing behavior, because the MnCrCTiBP and MnCrCTiWVBP alloys with zig-zag grain boundary shape and coarser MC + $M_{23}C_6$ precipitates did not exhibit excessive grain growth at 1150°C [Fig. 10(e) and 10(f)]. These grain boundary precipitate effects could also be important for strength at temperatures of 600 to 800°C (ref. 2).

The recrystallization resistance of the PCMA-19 through -21 alloys and the fine, stable MC observed in the MnCrCTiVBP and MnCrCTiWVBP steels are important results from the studies of cold-worked and aged stage II alloys. While these initial solute-modified alloys are not yet optimized, their recrystallization resistance and fine MC microstructures are similar to the original PCR alloy and newer solute-modified versions of the PCA given the same cold-work plus aging test.[2,25] This similarity was one of the goals set to measure alloy development progress for these alloys, particularly with regard to achieving radiation-resistance. Several recent studies of swelling resistance in the Fe-14Cr-16Ni PCA or JPCA (a closely related Japanese heat of Ti-modified steel) irradiated in HFIR have shown that the swelling resistance of these steels depends on the formation and stability of fine MC precipitation during irradiation at high He generation rates.[2,26,27] Therefore, we believe that the MC-formation characteristics of the MnCrCTiVBP and MnCrCTiWV-BP alloys represent significant progress toward our goals for stage II of our alloy-development program. In recent work, a wide range of binary and ternary Fe-Cr-Mn alloys irradiated in FFTF at 400 to 600°C showed significant swelling. However, swelling was similar to or in some cases less than comparable Fe-Cr-Ni alloys.[7,22] Similar irradiation studies in FFTF show that cold work reduces swelling in the binary Fe-Mn and ternary Fe-Cr-Mn alloys. and that various commerial high-Mn steels can have better swelling resistance in the cold-worked condition after irradiation to about 80 dpa, particularly at 420°C (refs. 22.23). Although these irradition results do not include the He/dpa generation ratio expected for-an MFR first wall and include alloys that do not meet the FIRD compositional requirements, they nonetheless support our approach to alloy development. This approach includes producing alloys with stable dispersions of fine precipitates and stable cold-worked dislocation structures. The effects of minor solutes, either alone or synergistically with other elements, on subtle phenomena like stacking-fault energy, dislocation dissociation, and dislocation pinning by fine precipitates are preliminary results that will require careful study to confirm and understand. However, they are important to our expectations for the effectiveness of microstructural design and control for radiation-resistance.

All of the stage II alloys are currently being irradiated in experiments in the Fast Flux Test Facility - Materials Open Test Assembly (FFTF-MOTA) to determine swelling resistance in solution-annealed and 20% cold worked material at 400 to 600°C (irradiations began with reactor cycle 9).

The calculations shown in Figs. 13 and 14 indicate the progress made in reducing long-term radioactivity in these Fe-Cr-Mn FIRD alloys, and the results of Fig. 14(b) for lower dose irradiation provide encouragement for considering these steels in design studies of near-term fusion devices like ITER. New FIRD steels like the MnCrCTiWVBP steel can meet the 10 CFR-61 Class C requirements for shallow land burial

after fusion irradiation, whereas commercial steels like type 316 cannot. We are therefore beginning stage III of our alloy development to look at more alloys over a wider range of Cr-Mn levels while continuing to study the effects of combinations of minor element solute additions and to expand the properties investigations to include corrosion, welding, and other properties of interest.

Finally, it is worth mentioning that, based on the effect that solute modifications have on producing fine precipitate dispersions and recovery/recrystallization resistance during aging at 800°C, the FIRD steels may also be useful for non-fusion applications requiring high-temperature strength and/or creep resistance. The base alloy (PCMA-15) showed good work hardening characteristics relative to type 316 (ref. 10). Recent efforts to produce tailored structures of fine precipitates for strength with similar solute modifications in Fe-14Cr-16Ni austenitic stainless steels[2] have resulted in steels with excellent creep-rupture resistance at 700°C [up to 10^3 times better than type 316 (ref. 28)]. Since these new FIRD steels contain Mn instead of Ni and have lower contents of strategic materials like Cr and Mo, they are probably cheaper as well. Recently, Tamura et al. from Nippon-Kokan and the Japan Atomic Energy Research Institute (JAERI)[29] have also developed a FIRD Fe-14Cr-25Mn-0.25C steel modified with 0.2 wt % Ti. They find good weldability relative to JPCA and suggest that corrosion resistance in water should be better than Fe-Cr-Ni steels. Thus, these new FIRD steels, or similar steels with less rigid compositional restrictions, may also have non-fusion spin-off applications.

CONCLUSIONS

1. A series of Fe-Cr-Mn-C alloys, annealed for 1 to 2 h at 1150°C, demonstrated that a stable austenitic steel could be produced with a composition of Fe-12Cr-20Mn with 0.2-0.25 wt % C. Alloys with high Mn and low C contained ε-martensite after annealing and often formed α'-martensite during subsequent cold working. Alloys with >15% Cr and >0.2% C contained δ-ferrite.

2. The same series of Fe-Cr-Mn-C alloys cold worked and then aged for 168 h at 800°C showed that alloys that were not entirely austenitic after annealing were also prone to excessive formation of coarse $M_{23}C_6$ and σ-phase particles and/or recrystallization and recovery. The austenitic PCMA-7 (Fe-15Cr-19Mn) with 0.4 wt % was resistant to recrystallization and recovery, and contained finely dispersed $M_{23}C_6$ particles.

3. A series of alloys with minor additions of combinations of Ti, W, V, P, and B were made to a base composition of Fe-12Cr-20Mn-0.25C. These alloys were entirely austenitic after annealing for 2 h at 1150°C. Most contained either coarse or fine carbides ($M_{23}C_6$ and/or MC) along very straight grain boundaries or in the matrix. However, the alloys modified with additions of Ti+B+P, Ti+V+B+P, and Ti+W+V+B+P all had peculiar zig-zag shaped grain boundaries which contained carbides.

4. After cold working and then aging for 168 h at 800°C, the alloys modified with solute additions of Ti+B+P, Ti+V+B+P, and Ti+W+V+B+P were the most resistant to recrystallization and recovery, with the Ti+V+B+P alloy being the best of this group. Only the alloys modified with both Ti and W (PCMA-18, -20 and -21) had abundant disperions of fine MC precipitation along the dislocation network. The TitVtBtP alloy had the least amount of coarse $M_{23}C_6$, and only the alloy with all the solutes (PCMA-21) had some σ-phase.

5. The fine MC precipitate microstructures and recrystallization and recovery behavior at 800°C of PCMA-20 and -21 are similar to the behavior of the Ti-modified Fe-Cr-Ni PCA steel. These results represent signlficant progress toward one of the goals of the ORNL development program for Fe-Cr-Mn FIRD steels.

6. Calculations of the decay of fusion-induced radioactivity wlth time indicate about a 10^3 reduction of 50 to 100 years after shutdown for PCMA-21 relative to type 316, and the potential to meet Class C burial requirements.

REFERENCES

1. R. W. Conn et al., Panel Report on Low Activation Materials for Fusion Applications, UCLA Report PPG-728, University of California at Los Angeles, June 1983.

2. P. J. Maziasz, MiCon 86: Optimization of Processing, Properties, and Service Performance through Microstructural Control, ASTM STP 979, eds. B.L. Bramfitt, et al., Am. Soc. for Testing and Matls., Philadelphia. PA, 1988, p. 116.

3. Calculations by R.W. Mann, Westinghouse Hanford Company, Richland, WA, 1982.

4. R. L. Klueh and E. E Bloom, Alloy Development for Fast Induced Radioactivity Decay for Fusion Reactor Applications, ORNL/TM-8944, Oak Ridge National Laboratory Report, March 1984.

5. P. Fenici et al., Nucl. Engin. Des./Fusion 1 (1984) 167.

6. D. S. Gelles and F. A Garner, J. Nucl. Mater. 1336134 (1985) 521.

7. H. R. Brager et al.. J. Nucl. Mater. 1336134 (1985) 907.

8. R. L. Klueh and P. J. Maziasz. AOIP Semiannu. Prog. Rept.. Sept. 30, 1984, DOE/ER-0045/13, USOOE Office of Fusion Energy (March 1985), p. 69.

9. R. L. Klueh and P. J. Maziasz, AOIP Semiannu. Prog. Rept., Sept. 30. 1985. DOE/ER-0045/15, USOOE Office of Fusion Energy. (February 1986) p. 69.

10. R. L. Klueh and P. J. Maziasz, "Reduced-Activation Austenitic Stainless Steels: The Fe-Mn-Cr-C System," to be published.

11. R. L. Klueh, P. J. Maziasz, and E. H. Lee, Matls. Sci. and Engin., 102 (1988) 115.

12. P. J. Maziasz, J. Nucl. Mater. 1226123 (1984) 472.

13. P. J. Maziasz, J. Nucl. Mater. 1086109 (1982) 359.

14. P. J. Maziasz and C. J. McHargue. Internat. Matls. Rev. 32 (1987) 190.

15. R. E. Stoller et al., "Swelling Behavior of Austenitic Stainless Steels in a Spectrally Tailored Reactor Experiment: Implications for Near-Term Fusion Machines," to be published in Journal of Nuclear Materials, 1988.

16. P. J. Maziasz et al., Fusion Reactor Materials Semiannu. Prog. Rept.. March 31, 1987, DOE/ER-0313/2, USOOE Office of Fusion Energy (September 1987), p. 188.

17. P. J. Maziasz and R. W. Swindeman. Proc. Internat. Conf. Advances in Materials Technology for Fossil Power Plants, ASM-International, Metals Park, OH (1987), p. 283.

18. P. J. Maziasz and R. L. Klueh. AOIP Semiannu. Prog. Rept.. Sept. 30, 1985, DOE/ER-0045/15, USOOE Office of Fusion Energy (February 1986), p. 54.

19. F. M. Mann, Fusion Reactor Materials Semiannu. Prog. Rept., March 31, 1988, DOE/ER-0313/4, USOOE Office of Fusion Energy (August 1988), p. 12.

20. P. J. Maziasz, Conf. Proc. Phase Stability During Irradiation, eds. J. R. Holland, L. K. Mansur. and D. I. Potter, The Metallurgical Society of AIME, Warrendale, PA (1981), p. 477.

21. J. M. McCarthy and F. A. Garner, Fusion Reactor Materials Semiannu. Prog. Rept., September 30, 1987, DOE/ER-0313/3, USOOE Office of Fusion Energy (March 1988), p. 115.

22. F. A Garner, F. Abe, and T. Noda. Fusion Reactor Materlals Semiannu. Prog. Rept.. September 30, 1987, DOE/ER-0313/3, USOOE Office of Fusion Energy (March 1988). p. 123.

23. J. M McCarthy and F. A. Garner, Fusion Reactor Materials Semiannu. Prog. Rept.. March 31, 1988. DOE/ER-0313/4, USOOE Office of Fusion Energy [August 1988), p. 146.

24. O. G. Ooran, A F. Rwucliffe, and F. M. Mann, J. Nucl. Mater. 141-143 (1986) 1074.

25. P. J. Maziasz and S. Jitsukawa, AOIP Semiannu. Prog. Rept., March 31. 1985, DOE/ER-0045/14, USOOE Office of Fusion Energy (July 1985), p. 37.

26. M. P. Tanaka et al., J. Nucl. Mater. 141-143 (1986) 943.

27. M. P. Tanaka et al. "Microstructural Development of Austenitic Stainless Steels Irradiated in HFIR," to be published in Journal of Nuclear Materials in 1988.

28. P. J. Maziasz and R. W. Swindeman, Proc. Internat. Conf. Advances in Materials Technology for Fossil Power Plants, eds., R. Viswanathan and R. I. Jaffee, ASM-International, Metals Park. OH (1987) p. 83.

29. M. Tamura et al.. J. Nucl. Mater. 141-143 (1986) 1067.

HELIUM-INDUCED DEGRADATION IN THE WELDABILITY OF AN AUSTENITIC STAINLESS STEEL -- H. T. Lin and B. A. Chin (Auburn University), M. L. Grossbeck (Oak Ridge National Laboratory), and S. H. Goods (Sandia National Laboratories, Livermore)

OBJECTIVE

The object of this study is to investigate the effects of helium on the subsequent weldability of type 316 stainless steel and to simulate repair of irradiated structural components.

SUMMARY

Autogenous gas tungsten arc welding was performed on helium-doped type 316 stainless steel. Helium was uniformly implanted in the material using the "tritium trick" to levels of 21 and 105 appm. Severe intergranular cracking occurred in both fusion and heat-affected zones. Microstructural observations of the fusion zone indicated that the pore size, degree of porosity, and tendency to form cracks increased with increasing helium concentration. Scanning electron microscopy showed that cracking in helium-doped materials was due to the precipitation of helium bubbles on grain boundaries and dendrite interfaces. Results of the present study demonstrate that the use of conventional welding techniques to repair materials degraded by exposure to radiation may be difficult if the irradiation results in the generation of even small aniuunts of helium.

PROGRESS AND STATUS

Introduction

The exposure of metallic materials, such as structural components of the first wall and blanket of fusion reactors, to high-energy (14 MeV) neutron irradiation will induce changes in both the material composition as well as its microstructure. Along with these changes may come a corresponding deterioration in corrosion resistance and mechanical properties. It is not unreasonable, therefore, to expect that the repair and replacement of degraded reactor components will be necessary. Such repairs may require the joining of irradiated materials through the use of conventional welding techniques.

One of the most important considerations in determining the postirradiation weldability of a material is the fact that the exposure of a material to neutron irradiation will result in the production of entrapped helium. This helium is generated as the result of (n,α) reactions with the alloy constituents.[1,2] The very low solubility of helium in metals[3,4] results in its tendency to precipitate out as bubbles. Preferred nucleation sites for the helium bubbles are inhomogeneities such as precipitate interfaces, dislocations, and most importantly, grain boundaries. At elevated temperatures, these bubbles will grow rapidly under the influence of either internal or external (creep) stresses, weakening the grain boundaries. As these bubbles coalesce along the boundaries, intergranular fracture occurs. Since welding processes produce internal stresses (and elevated temperatures), the entrapped helium may severely affect the weldability and post-weld properties of the irradiated material. Furthermore, welding produces severe gradients in both stress and temperature which may enhance the growth rate of helium bubbles, further degrading the material properties.[5]

In fact, attempts to repair stress corrosion cracks in an irradiated reactor tank containing several atomic parts per million (appm) helium by gas tungsten arc (GTA) welding have proven to be difficult.[6] Recent examination of these welds has revealed the existence of grain boundary cracking in the heat-affected zone (HAZ) of the welds.[7] Because of the obviously hostile environment, detailed analysis of these welding-induced defects has proven to be extremely difficult. Developing a quantitative understanding of the relationship between helium and weld cracking is virtually impossible due to difficulty in performing in situ welding and subsequent analysis. The radiological hazards associated with the handling of these materials limit the scope of such studies and ensures that they will be extremely costly.

The present study was carried out to provide a quantitative background for understanding the effects of helium on the subsequent weldability of materials. To avoid hot cell investigations which are both lengthy and expensive, welding performed on helium-doped material was chosen to simulate the principal effects which occur during the joining of irradiated material. Helium was implanted into the test material via the "tritium trick." Type 316 stainless steel was chosen for the study because of the extensive data base, for both unirradiated and irradiated materials, detailing its microstructure and properties.

Experimental procedures

The material studied in this program was type 316 stainless steel (reference heat 8092297) of the U.S. Fast Breeder Reactor Program.[8] The chemical composition is listed in Table 1. The initial cold rolled 1.52-mn plate stock was annealed at 1050°C for 1 h in inert gas. It was then cold-rolled to 0.76 mm followed by a final anneal at 1050°C which resulted in a fully recrystallized microstucture with a grain size of 70 μm. To produce the desired concentrations of helium in a relatively short period and minimize radioactive hazards after inplantation. the "tritium trick" technique[9] was employed wherein helium is generated within a metal through the radioactive decay of tritium (tritium undergoes the decay reaction $^{3}He \rightarrow \beta^{-} + {}^{3}He$, and has a 12.3 year half-life). In order to dope the low-helium-content specimens, the stainless steel sheet stock was exposed to tritium gas at a pressure of 38 MPa for 30 days at 300°C. Since the diffusivity of tritium in stainless steel is rapid at 300°C,[10] this charging period ensured that a uniform concentration of tritium (and therefore a uniform distribution of helium) was established through the thickness of the starting material. At the end of this period, the exposed material was removed from the high-pressure charging vessel and outgassed at 400°C at 10^{-3} Pa in order to stop further generation of helium and to remove residual tritium. In order to achieve the higher helium content, the same procedure was followed except that a tritium charging pressure of 125 MPa was used. The concentrations of helium were then measured quantitatively. using a vacuum fusion mass spectrographic technique,[11] and were found to be 27 and 105 appm, respectively.

Autogenous bead-on-plate welds were made using GTA welding. Figure 1 shows the welding station that was located in a high-velocity air hood with an air velocity of 1.5 m/s. The semiautomatic motion of the welding torch was driven and controlled by a Unislide 8201M stepping motor controller. Welding was performed at 10 V-dc, 24 A at a travel speed of 3.6 mm/s under a protective argon atmosphere. Full, penetration welds were produced in the 0.76-mn-thick plate. The plates were laterally constrained during welding.

Table 1. Chemical composition for Reference Heat (8092297) of type 316 stainless steel

Element	Content, wt %
C	0.057
Mn	1.86
P	0.024
S	0.019
Si	0.58
Ni	13.48
Cr	17.25
Mo	2.34
Co	0.02
Cu	0.10
N	0.03
B	0.0005
Ti	0.02
Pb	0.034
Sn	0.004

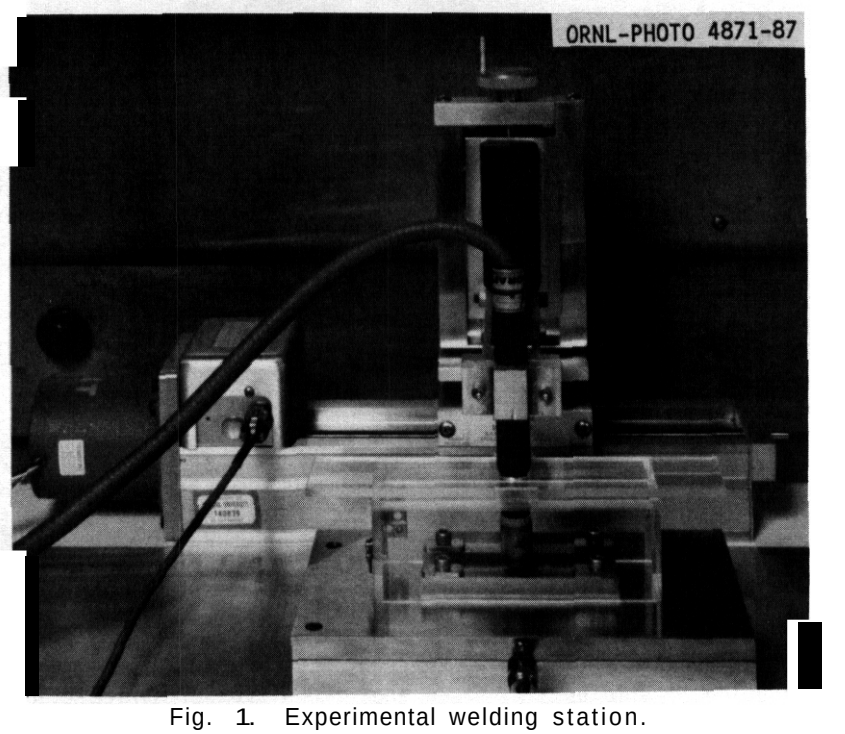

Fig. 1. Experimental welding station.

Metallographic sections transverse to the welding direction were prepared in order to study the weld microstructure. The specimen cross sections were electrolytically etched in a solution of 40% HNO_3–60% H_2O.

To study mechanical properties of the welds, tensile tests were performed on an Instron mechanical testing machine at an initial strain rate of 5×10^{-4} s^{-1}. Tests were conducted at temperatures between 25 and 700°C in a vacuum of 4×10^{-5} Pa. Fractographic analysis of fractured tensile specimens and weld cracks was conducted using a JEOL JSM-35CF scanning electron microscope.

Results

1. Weld Response

Figures 2 and 3 show the morphological features of the as-welded materials with helium levels of 27 and 105 appm, respectively. In the low-helium-content material, continuous through-thickness cracking in the

YP5167

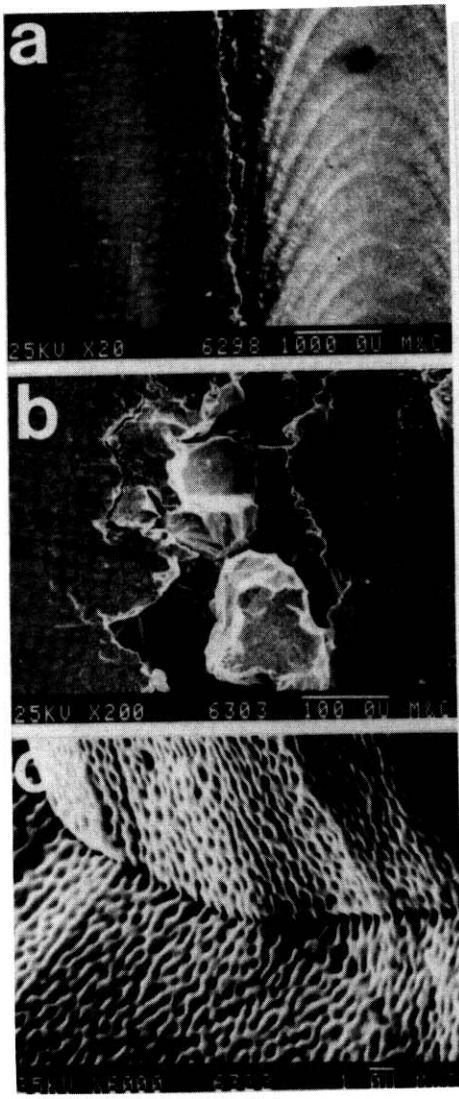

Fig. 2. Morphological features of as-welded material: helium level 27 appm. (a) Macrograph of HAZ showing intergranular fracture. (b) Scanning electron micrograph showing details of intergranular fracture. (c) Scanning electron micrograph of grain boundary facets decorated with a uniform distribution of dimples.

YP5169

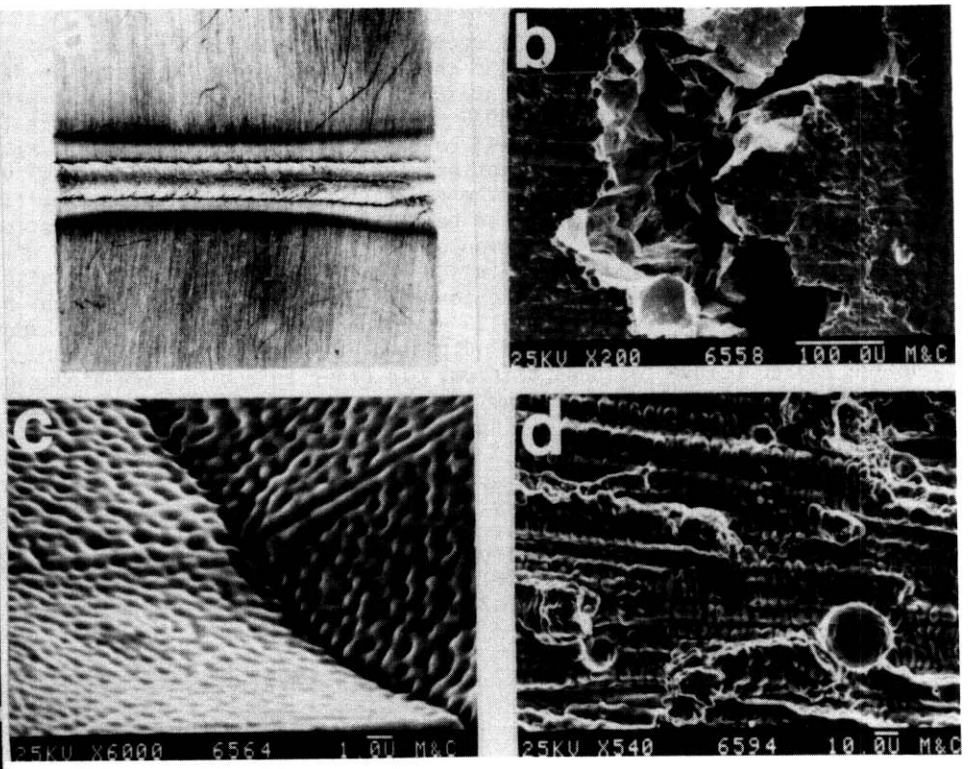

Fig. 3. Morphological features of as-welded material: helium level 105 appm. (a) Macrophotograph of brittle fracture in HAZ and fusion zones. (b) Scanning electron micrograph showing details of intergranular fracture. (c) Scanning electron micrograph of grain boundary facets decorated with a uniform distribution of dimples. (d) Scanning electron micrograph showing that brittle failure proceeded along an interdendritic path.

HAZ was observed in 75% of the welded plates (6 out of 8). In the remaining plates, the cracking was discontinuous. Typically, this cracking occurred in the HAZ immediately adjacent to the fusion zone and was intergranular in nature [Fig. 2(b)]. In the higher helium content material, all of the welded plates (9 out of 9) showed HAZ cracking; in addition, more than half of the welded plates (6 out of 9) exhibited evidence of centerline cracking in the fusion zone as well. As in the previous instance, the HAZ cracking was fully intergranular in nature [Fig. 3(b)] and occurred very near the weld interface. Since in all cases, no external loads were applied, the cracking resulted from shrinkage stresses as the laterally constrained plates cooled after welding.

Features of weld crack surfaces in the HAZ and fusion zone were studied in detail using scanning electron microscopy. Figures 2 and 3 show these typical surface features. As stated above, the weld cracking was entirely intergranular in nature, and at higher magnification the grain boundary facets were observed to be decorated with a uniform distribution of dimples [Figs. 2(c) and 3(c)]. The average dimple size was approximately 1 μm and was the same for both the high- and low-helium-content specimens. However, the dimple morphology (symmetry and spacing) observed on grain facets varied with the orientation of the grain boundaries with respect to thermal stresses in the HAZ. The dimples on the exposed facets exhibited symmetrical features which indicated that they were formed from cavities that grew under the action of stresses normal to the boundary. Incipient cracking, arising from coalescence of cavities, was also observed along the grain boundary intersections [Figs. 2(c) and 3(c)]. The shear ligaments separating the dimples have been rounded by surface diffusion, indicating that the cracking occurred at high temperatures. Examination of the fusion zone centerline cracking indicated that the brittle failure proceeded along an interdendritic path during material resolidification [Fig. 3(d)]. Isolated spherical pores resulting from the precipitation of the entrapped helium were also observed on the interdendritic fracture surface.

Figure 4 shows the optical metallography of the welds from a section taken transverse to the welding direction for the 27 and 105 appm He materials. A small amount of ferrite precipitation was observed near the fusion boundary. Generally, the microstructure of the fusion zone was primary austenite with visible

YP5165

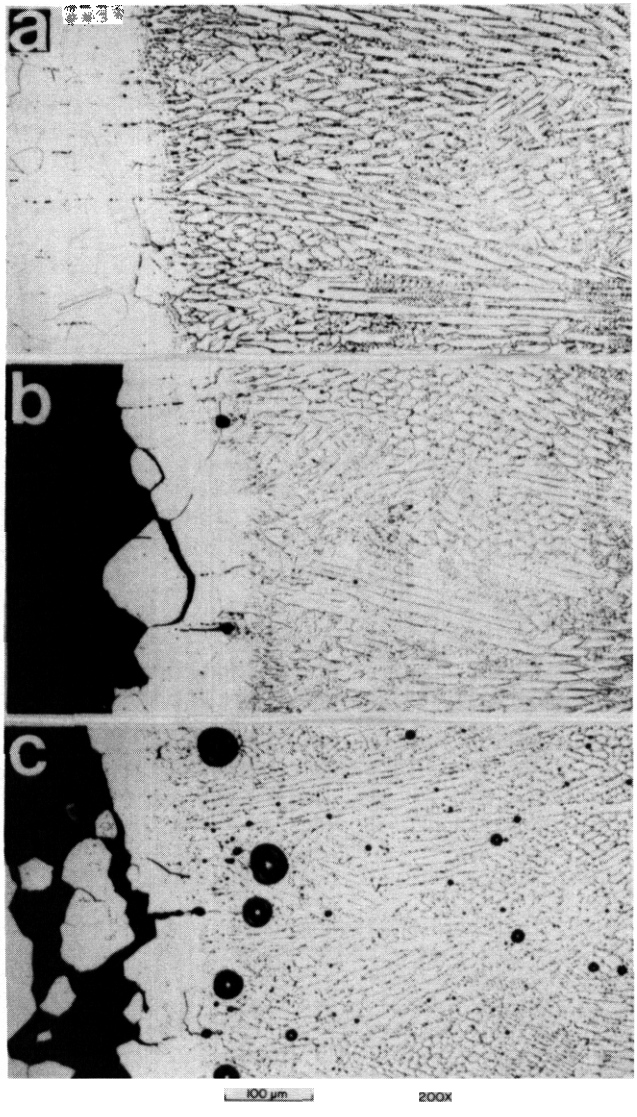

Fig. 4. Optical micrographs of welds taken transverse to the welding direction: (a) control material. (b) 27 appm; (c) 105 appm. Failure occurred in the HAZ. Larger pore size and greater density of helium bubbles occurred in the fusion zone near the fusion line.

spherical pores decorating the solidification dendrite boundaries. It is clear by comparing Fig. 4(b) and (c) that the degree and size of the porosity were greater in the material containing 105 appm He than in the lower helium concentration plates. The size of visible pores ranged from 0.5 to 70 μm. The larger pores were preferentially located in the fusion zone close to the fusion boundary. The tendency to form bigger bubbles adjacent to the weld interface suggests that convective flow patterns in the weld pool act to sweep the helium toward that region. and the stagnant flow in the weld interface enhances bubble coalescence.

The degree to which the pores decorated the dendritic interfaces is more clearly shown in Fig. 5 where once again it is seen that the size and extent of porosity increased with increasing helium content. As no such porosity occurred in helium-free stainless steel welded under identical conditions, it is reasonable to conclude that the spherical pores observed in the fusion zone are helium bubbles.

As shown in Fig. 4. the metallographic analysis revealed that the intergranular cracking occurred in the HAZ close to the weld interface. Within this narrow zone, secondary cracking away from the main fracture was observed along with porosity on the grain boundaries. Therefore, fracture appeared to occur due to the growth and coalescence of helium bubbles along grain boundaries. This is obviously the region of solid material which experiences the combination of the highest temperatures and the highest shrinkage stresses required to induce the cracking phenomenon.

2. Mechanical properties

Results of tensile tests on welded control and helium-doped specimens as a function of test temperature are shown in Figs. 6 through 8. For comparison purposes, tensile results of unwelded control (parent metal) and helium-doped specimens are also shown. Tensile specimens of welded materials were prepared using a punch and die in an orientation transverse to the welding direction, The portion in the center of the gage section contained both fusion and HAZ regions in approximately 50% of the gage length (12.7 mm).

The tensile results indicated that yield strength decreased linearly with increasing temperature for all cases (Fig. 6). The helium-doped materials have approximately the same yield strength as the undooed materials, indicating no significant strengthing effect was incurred by the presence of helium. There was a significant increase in the yield strength of the welded materials relative to unwelded parent specimens.

In all cases. the ultimate tensile strength (UTS) decreased with increasing test temperatures (Fig. 7). For unwelded materials, the results reveal that the UTS was insensitive to the presence of helium at these concentrations. The strength of the welded control (no helium) was the same as that of the unwelded control at room temperature. However, it was somewhat less at the elevated test temperatures. The UTS of the helium-bearing specimens subsequent to welding was severely degraded relative to welded control, unwelded control, and unwelded helium-doped materials. In fact, the UTS of the welded helium-doped specimens was virtually identical to their yield strengths (Table 2), indicating that the specimens failed imnediately upon yielding.

Prior to welding, the helium-doped specimens had the same ductility as the unwelded control specimens up to 600°C (Fig. 8). At 700°C the total elongation of unwelded, helium-doped specimens decreased with increasing helium content but never fell below 10%. The ductility of all welded specimens was found to be lower than that of unwelded specimens. This is due to the fact that the deformation and fracture are restricted to the fusion zone. The welded, helium-doped specimens showed the lowest ductilities, generally

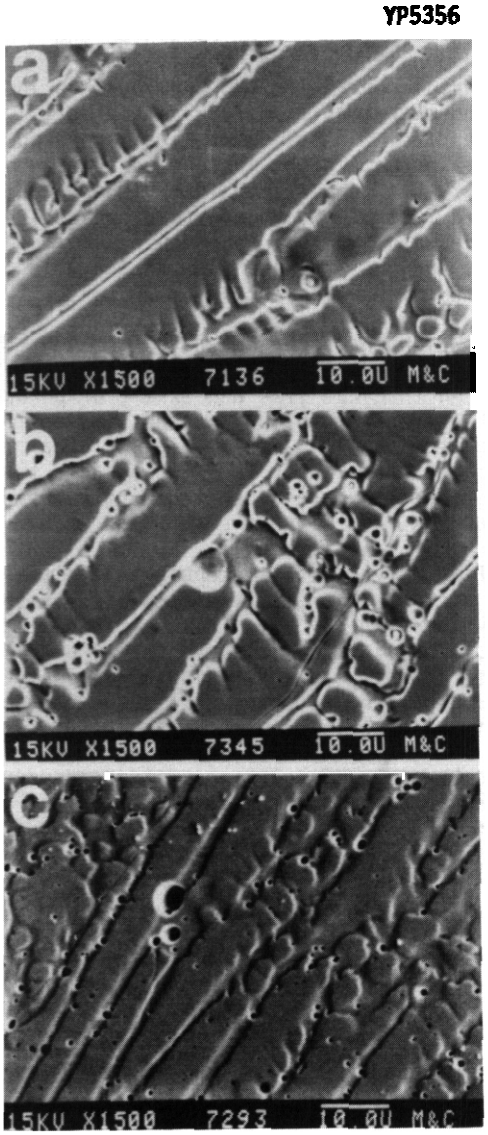

Fig. 5. SEM micrographs of the fusion zone. (a) Control material; (b) 27 appm; (c) 105 appm.

less than 2% and as low as 0.2%. All welded, helium-doped specimens failed at the fusion boundary. A typical fracture surface of a welded specimen containing 27 appm He tested at room temperature is shown in Fig. 9. The fracture surface was nearly 100% intergranular, and at high magnification the grain boundary facets exhibited a dimple structure that was quite similar to the weld crack surface in the HAZ. The main difference was that the dimple shear walls were much nmre sharply defined as the result of room temperature fracture.

DISCUSSION

1. Weld response, HAZ

The scanning electron micrographs of the welded material revealed that the brittle intergranular fracture observed in the HAZ was caused by the growth of helium bubbles at grain boundaries. The bubbles grew, reducing the load-bearing area of the grain boundaries until failure occurred. The growth kinetics of bubbles of insoluble gas are influenced by both temperature and stress. The bubble growth processes in the HAZ may be separated into three sequential regimes. Regime one is the heatup period before the fusion occurs. Regime two occurs when molten metal is present in the fusion zone resulting in a stress-free state. Regime three occurs after the nmlten metal has begun to re-solidify and internal shrinkage stresses are generated in the constrained plates. It should be recognized that the precipitation of mobile, interstitial helium is not a viable process for bubble formation or growth. This is because the helium introduced into the material during tritium exposure has clustered into small bubbles as a result of the 400°C off-gassing treatment (helium bubble formation has been shown to occur in austenitic stainless steels upon annealing at 350°C).[12] Helium trapped in even small clusters is very strongly bound (binding energies of 3.5 to 4.0 eV[13]) and is not free to migrate at any temperature appreciably below the melting point.

In the first regime, the bubble will grow as a result of the generation of thermal vacancies during the heatup period. However, the presence of compressive stresses will tend to delay bubble growth on grain boundaries normal to compressive stresses. Nevertheless, this heatup period will nucleate bubbles if the degassing treatment did not do so. In the second regime, bubble coarsening may occur by the migration of helium bubbles.[14-16] Since the solubility of helium in metals is negligible coarsening via Ostwald ripening[17,18] processes is not likely to be of importance. Bubble growth is also known to occur from grain boundary migration[19] or from recrystallization. However, the prior annealing treatments at 1050°C ensure that little driving force is available for such processes. Bubble growth may occur through the precipitation of vacancies into bubbles. Such a process is particularly favored at temperatures close to the melting point, since the vacancy concentration is quite high. The driving force for bubble growth is provided by the interior helium gas pressure, $2\gamma/r$, where γ is the surface energy and r is the bubble radius. Since the initial small bubbles are likely to be nonequilibrium. and highly overpressurized. this is a viable growth mechanism.

Once the material in the weld pool starts to solidify (regime 3), the kinetics of helium bubble growth will be controlled by the shrinkage stresses developed during cooling. Models of stress-driven bubble growth have been extensively reviewed by Reidel.[20] In general, cavity growth is attributed to stress-driven diffusion of vacancies along grain boundaries to the bubble-grain boundary junction. The vacancy flux along the grain boundary is coupled to the flux along the internal cavity (bubble) surface so that an equilibrium cavity profile is maintained.

Formulating a rigorous model of bubble growth during a welding procedure is beyond the scope of the current work. However. the critical stress necessary to achieve unstable bubble growth can be estimated. This critical stress is given by $\sigma = 0.76\ \gamma/r$ (ref. 21). For stresses greater than this, growth will continue indefinitely causing coalescence with resulting intergranular failure. Murr et al.[22] reported a surface energy for stainless steel of 2.74 J/m^2 at 700°C. Bubbles 40 nm in diameter have been observed in 316L stainless steel containing 33 appm He subsequent to an 850°C anneal.[23] From these values, a critical stress is calculated to be approximately 50 MPa. This is considerably below the measured yield strength of the welded, helium-doped material at the highest temperatures examined. Thus, it is not unreasonable to suggest that the tensile

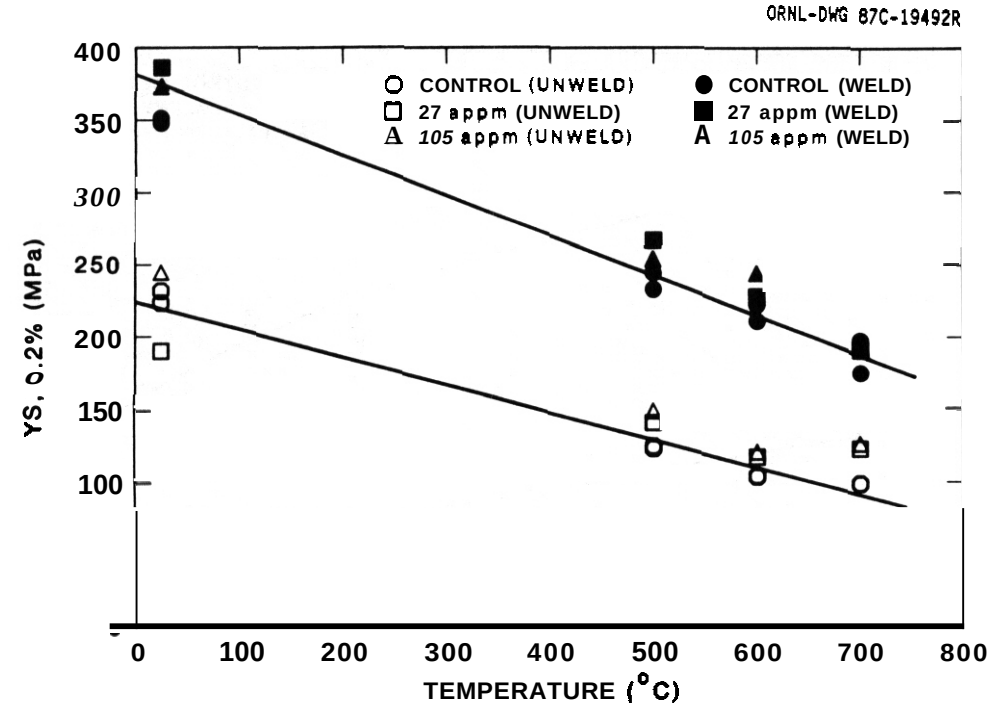

Fig. 6. Temperature and helium concentration dependence of yield strength.

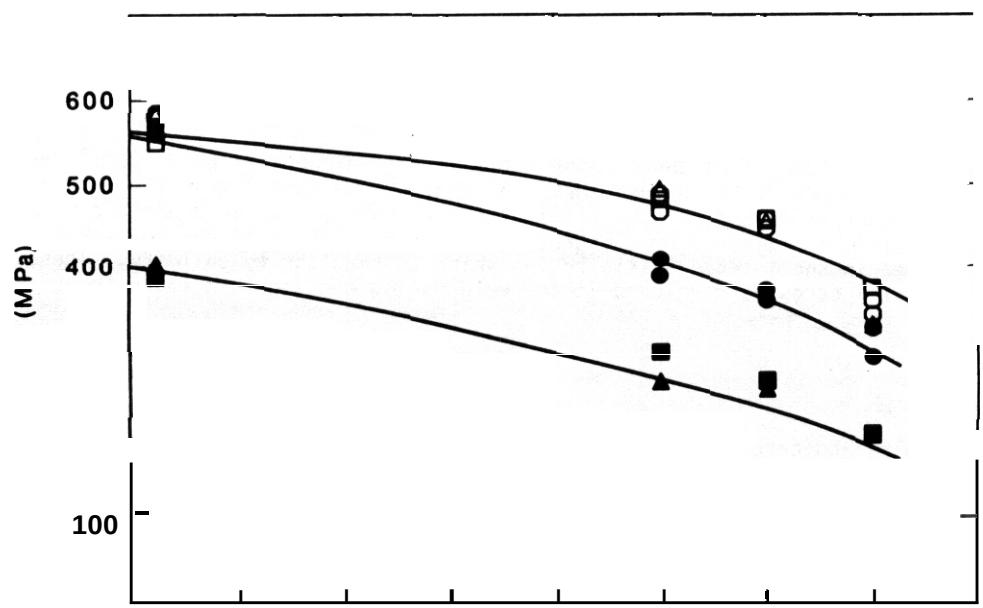

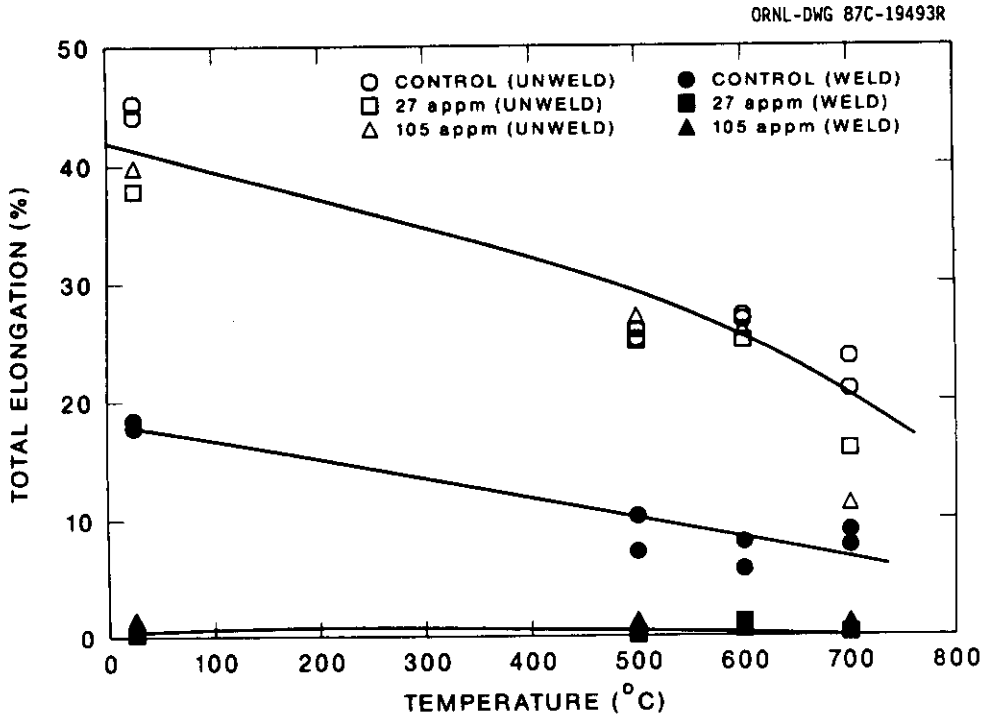

Fig. 8. Temperature and helium concentration dependence of total elongation.

shrinkage stresses generated during cooling are sufficient to promote bubble growth and that these bubbles will continue to grow until they coalesce and intergranular failure occurs or until temperature falls below the growth range.

2. Weld response, fusion zone

Weld crack features of the fusion zone of the 105 appm welded material [Fig. 3(d)] reveal that brittle fracture occurred along interdendritic paths. Metallography of the fusion zone (Fig. 5) suggests that the brittle failure had its origin in the precipitation of helium bubbles in the dendritic boundaries. As solidification proceeds, helium is rejected by the growing dendrites because of the low solubility of helium in the metal and is trapped in the interdendritic region which is the last to solidify. These bubbles coalesce into microcracks. Tensile stresses developed in the weld during cooling then cause these cracks to propagate.

3. Mechanical properties

Tensile test results indicate that the helium concentrations studied did not significantly degrade the mechanical properties of the materials for temperatures up through 600°C (Figs. 6 through 8). The increase in the yield strength of the welded materials relative to unwelded specimens, though not studied in detail, may be attributed to three possible mechanisms: an increase in the dislocation density from deformation induced by shrinkage stresses, the development of second phase precipitates, and grain refinement in the fusion zone. It was found that annealing at 1050°C for 1 h restored the yield strength to the value for parent material. The lower UTS observed in the welded helium-doped material compared with the undoped material is believed to have resulted from the onset of fracture prior to achieving any significant amount of work hardening by plastic deformation. Indeed, as shown in Fig. 8 and Table 2, the welded specimens containing helium were unable to sustain any appreciable amount of plastic deformation. This loss of ductility of the welded, doped material is attributed to deformation-induced growth and coalescence of helium bubbles along grain boundaries. Such a situation would be intolerable for a weld-repaired containment vessel or another load-bearing structure.

Table 2. Tensile test data of type 316 stainless steel

Material	Temperature (°C)	Strength, MPa		Elongation (%)
		Ultimate Tensile	Yield	
Unwelded material				
Control	20	584.5	231.5	44.1
	20	580.1	223.5	45.2
	500	466.4	123.2	26.0
	500	487.5	124.8	25.2
	600	458.3	103.7	26.8
	600	447.0	104.6	27.2
	700	357.0	98.5	23.7
	700	340.3	99.1	21.0
27 appm	20	549.7	190.1	37.8
	500	481.2	141.0	25.0
	600	458.3	117.4	25.1
	700	372.7	123.0	15.9
105 appm	20	583.0	244.5	39.8
	500	494.0	149.0	27.1
	600	456.1	121.0	26.1
	700	328.4	126.4	11.3
Welded material				
Control[a]	20	560.2	351.2	17.8
	20	569.1	347.8	18.5
	500	387.5	244.2	7.2
	500	408.9	232.5	10.3
	600	369.7	222.3	6.0
	600	357.3	211.0	8.1
	700	325.0	197.5	7.7
	700	291.0	175.0	9.1
27 appm[b]	20	386.0	386.0	0.2
	500	296.4	266.8	0.6
	600	262.8	227.6	1.2
	700	200.0	191.0	0.3
105 appm[b]	20	404.0	373.0	1.5
	500	261.9	253.9	1.4
	600	253.1	244.1	0.6
	700	199.6	191.5	1.2

[a]Specimens failed in the fusion zone.
[b]Specimens failed at the fusion boundary.

VP 5193

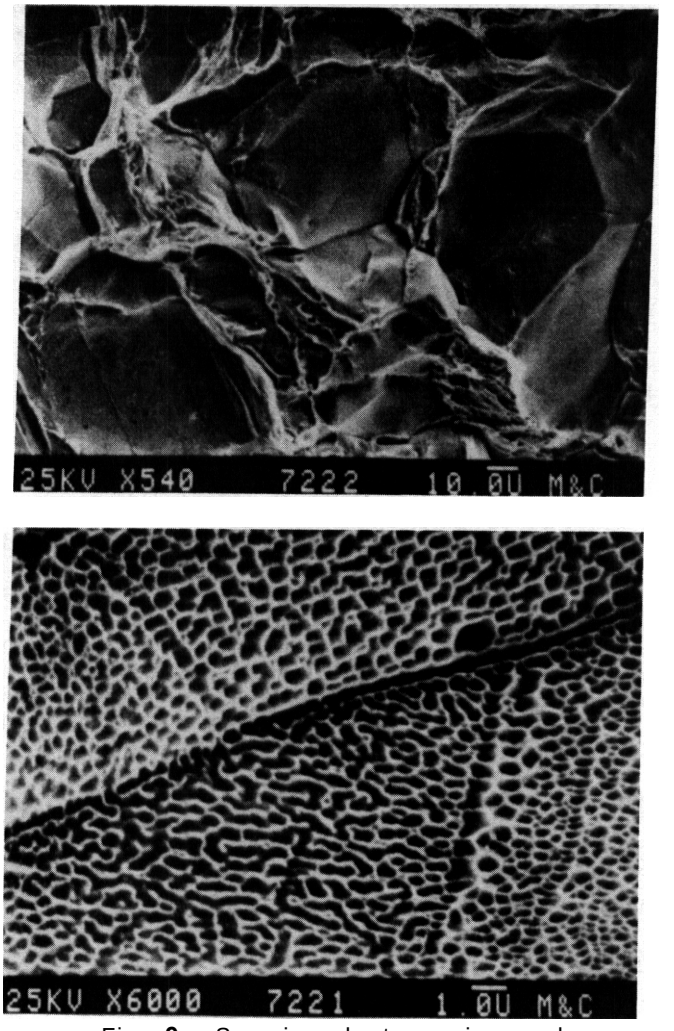

Fig. 9. Scanning electron micrographs of welded 27 appm material tested at 25°C. (a) Intergranular fracture; (b) feature showing uniform distribution of dimples.

CONCLUSIONS

The following conclusions were drawn from the present study:

- Severe intergranular cracking occurred during GTA welding of type 316 stainless steel plates containing helium concentrations of 27 and 105 appm.
- Brittle fracture in both fusion and heat-affected zones was induced by the precipitation of helium bubbles at dendrite interfaces and by the growth and coalescence of helium bubbles at grain boundaries.
- The size and density of pores in the fusion zone increased with increasing helium concentration. The largest pores and highest density of resolvable pores were found in the fusion zone near the fusion line.
- After welding, helium-doped materials exhibited poor tensile properties with ductilities close to zero. Fracture in these specimens was intergranular due to the plastic growth of grain boundary helium bubbles.

The results indicate that repair or replacement of irradiated structural components containing relatively small amounts of helium using conventional GTA welding techniques will be difficult in stainless steel. Furthermore, even if such repairs can be made, the very low ductility welds may still impose a severe risk for components which must serve at elevated temperatures under conditions of creep or fatigue loading.

FUTURE WORK

The helium bubble morphology in the HAZ of welds with 27 and 105 appm He will be examined. GTA welds of type 316 stainless steel containing 0.18, 2.5 and 256 appm He will be conducted.

REFERENCES

1. R. S. Barnes, "Embrittlement of Stainless Steels and Nickel-Based Alloys at High Temperature Induced by Neutron Radiation." Nature 206 (1965) 1307-1310.
2. D. R. Harries, "Neutron Irradiation-Induced Embrittlement in Type 316 and Other Austenitic Steels and Alloys." J. Nucl. Mater. 82 (1979) 2-21.
3. J.v.d. Driesch and P. Jung, "An Investigation on the Solubility of Helium in Nickel," High Temperature - High Pressure 12 (1980) 635-641.
4. J. Laakmann, P. Jung and W. Uelhoff, "Solubility of Helium in Gold," Acta Met. 35 (1987) 2063-2069.
5. S. L. Robinson, "Tensile Properties of Welded Helium Charged 304L Stainless Steel." J. Nucl. Mater. 152 (1988) 212-219.
6. J. P. Maloney et al.. Repair of a Nuclear Reactor Vessel, DP-1199. E. I. du Pont de Nemours & Co., Savannah River Laboratory, Aiken, SC, (June 1969).
7. "Safety Issues at the Defense Production Reactors," Committee to Assess Safety and Technical Issues at DOE Reactors. Commission on Physical Science, Mathematics and Resources and the Commission on Engineering and Technical Systems. National Research Council, National Academy Press, Washington, D.C., 1987.
8. B. A. Chin, R. J. Neuhold and J. L Straalsund, "Materials Developnent for Fast Breeder Reactor Cores," Nucl. Techno1. 57 (1982) 426-435.
9. Annual Rooks and ASTM Standards, "Standard Guide for Simulation of Helium Effects in Irradiated Metals." Vol. 12.02, E 942 - 83, pp. 808-811.
10. M. R. Louthan. Jr. and R. G. Derrick, "Hydrogen Transport in Austenitic Stainless Steel," Corrosion Sci. 15 (1975) 565-577.
11. B. M. Oliver, J. G. Bradley and H. Farrar IV. "Helium Concentration in the Earth's Lower Atmosphere." Geochim et Cosmochim. ACTA 48 (1984) 1759-1767.
12. S. L. Robinson, "Tritium and Helium Effects on Plastic Deformation in AISI 316 Stainless Steel." Mater. Sci. and Engr. 96 (1987) 7-16.
13. M I. Baskes and V. Vitek, "Trapping of Hydrogen and Helium at Grain Boundaries in Nickel: An Atomistic Study," Met. Trans. 16A (1985) 1625-1631.
14. R. S. Barnes, "A Theory of Swelling and Gas Release for Reactor Materials," J. Nucl. Mater. 11 (1964) 135-148.
15. E. E. Gruber. "Calculated Size Distribution for Gas Bubble Migration and Coalescence in Solids," J. Appl. Phys 38 (1967) 243-250.
16. E. M. Baroody, "Calculation on the Collisional Coalescence of Gas Bubbles in Solids," J. Appl. Phys. 38 (1967) 4893-4903.
17. G. W. Greenwood and A Boltax, "The Role of Fission Gas Re-Solution During Post-Irradiation Heat Treatment," J. Nucl. Mater. 5 (1962) 234-240.
18. A. J. Markworth, "On the Coarsening of Gas-Filled Pores in Solids," Met. Trans. 4A (1973) 2651-2656.
19. W. Beere, "The Growth of Sub-Critical Bubbles on Grain Boundaries," J. Nucl. Mater. 120 (1984) 88-93.
20. H Reidel, Fracture at High Temperature. Springer-Verlag, New York, 1987.
21. E D. Hyam and G Sumner, "Irradiation Damage to Beryllium," Proc. Conf. Radiation Damage in Solids. Vol. 1 (IAEA. Vienna, 1962), pp. 323-331.
22. L. E. Murr, G. I. Wong and R. J. Horylev, "Measurement of Interfacial Free Energies and Associated Temperature Coefficients in 304L Stainless Steel," Acta Met. 21 (1973) 595-604.
23. S. H. Goods, unpublished work.

INVESTIGATION OF LOU-TEMPERATURE IRRAOIATION CREEP OF AUSTENITIC STAINLESS STEELS IN AN ORR SPECTRAL TAILORING EXPERIMENT — M L. Grossbeck and L. K. Mansur (Oak Ridge National Laboratory) and M P. Tanaka (Japan Atomic Energy Research Institute)

OBJECTIVE

This research was directed at evaluating irradiation creep in fusion reactor candidate structural alloys at temperatures between 60 and 400°C in an environment that produces the same ratio of helium to displacement damage as a fusion reactor.

SUMMARY

Irradiation creep was investigated in the alloys PCA, JPCA. and AISI 316 stainless steel. Tubes pressurized to stress levels of 50 to 400 MPa were irradiated in the Oak Ridge Research Reactor (ORR) with the neutron spectrum tailored to achieve the fusion reactor He:dpa value of 12 appm/dpa in AISI 316 stainless steel. Irradiation temperatures of 60, 330, and 400°C were investigated, and the irradiation produced 8 dpa and a maximum of about 100 appm He.

Irradiation creep rates of 2.2 to 14×10^{-4} MPa^{-1} dpa^{-1} were observed at 60°C. At 330 and 400°C irradiation creep rates of 1.3 to 35×10^{-4} were observed, similar to those found previously in similar experiments in the ORR. The low temperature irradiation creep was interpreted in terms of a new model for irradiation creep based on transient climb-enabled glide.

The results are important in the design of experimental fusion reactors where temperatures below 100°C are being considered for the operation of high flux components.

PROGRESS AND STATUS

Introduction

Irradiation creep is an important deformation mechanism in materials exposed to a high neutron flux characteristic of fast breeder reactors and fusion reactors. Unlike thermal creep, irradiation creep has a weak temperature dependence throughout the range of comn reactor experience. 300 to 600°C.[1-3] In recent designs of fusion reactors, some components in a high neutron flux are expected to operate at rmch lower temperatures, perhaps 100°C. Some water-cooled components might operate as low as 50°C.[4] To address the temperature range of interest in such experimental fusion reactors, the present Irradiation experiment was designed to examine irradiation creep behavior in the range of 60 to 400°C.

In order to make the irradiation conditions relevant to the fusion environment, the neutron spectrum was tailored to achieve a helium to displacement ratio (He:dpa) in stainless steel of about 12 appm/dpa. This value is characteristic of a fusion reactor with a stainless steel. lithium-cooled blanket.[5] This was achieved by changing the core pieces surrounding the irradiation capsules as the irradiation progressed. Irradiation began with water surrounding the capsules, in order for the resulting soft spectrum to generate ^{59}Ni. As irradiation proceeded, the water was replaced with an aluminum core piece to harden the spectrum.

Experimental Procedure

Irradiation creep was studied using pressurized tubes 25.4 mm in length and 4.57 mm in diameter with a 0.254 mm wall thickness. Depending upon the alloy and temperature, the tubes were pressurized with helium with appropriate levels to achieve hoop stresses of 50 to 400 MPa. Three austenitic steels were investigated: the U.S. Magnetic Fusion Energy Program prime candidate alloy (PCA), a similar alloy in the Japanese Fusion Energy Program (JPCA), and AISI 316 stainless steel. Compositions are given in Table 1. The AISI type 316 stainless steel was studied in solution annealed and 20% cold-worked conditions; the PCA and JPCA were studied in 25% cold worked and solution annealed conditions, respectively. The specimens were prepared from drawn tubing with machined end caps electron beam-welded into place. The tubes were pressurized by laser welding the final orifice inside a pressure chamber with sapphire windows.

The specimens were irradiated in the Oak Ridge Research Reactor (ORR). Those irradiated at 60°C were exposed to the reactor coolant water. As expected, the austenitic alloys were not degraded by the water environment. At 330 and 400°C, the specimens were imnersed in NaK in order to achieve temperature uniformity. Temperature control was achieved by adjusting the composition of the gas in the gap surrounding the specimen chamber through a range of mixtures from pure helium to pure argon. Temperature was monitored with a series of thermocouples in the specimen chamber.[6-8]

Table 1. Chemical composition of alloys (in weight percent)

	PCA (K-280)	JPCA	316 (Japanese 316)
B	0.00003	0.003	
C	0.05	0.06	0.06
Co	0.003	0.002	<0.1
Cr	14.0	14.2	16.8
Fe	bal	bal	bal
Mn	1.8	1.8	1.8
Mo	2.3	2.3	2.5
Ni	16.3	15.6	13.5
P	0.01	0.027	0.028
Si	0.44	0.50	0.61
Ti	0.24	0.24	0.005

The ORR is a mixed spectrum reactor using 93% enriched uranium oxide fuel and water cooling and moderation. The thermal fluxes in the core positions that the experimental vehicles used were calculated to be 1.8×10^{18} n/m^2-s and 2.3×10^{18} n/m^2-s for MFE 6J (60°C) and MFE 7J (330, 400°C), respectively, based upon previously conducted dosimetry.[9] The neutron fluxes at energies above 0.1 MeV were 2.0×10^{18} n/m^2-s and 2.4×10^{18} n/m^2-s for MFE 6J and 7J, respectively.[10,11] Irradiation continued for 475 full-power days to achieve damage levels in stainless steel of 6.9 dpa for MFE 6J and 8.0 dpa for MFE 7J. Helium concentrations in type 316 stainless steel are calculated to be 62 and 97 appm for the specimens in MFE 6J and 7J, respectively. The evolution of the helium and damage levels are shown in Fig. 1.

The tubes were profiled with a non-contacting laser micrometer system with a precision of ±250 nm. Although the complete tube profiles were used to evaluate the shape and surface condition of the specimens, the average diameter of the central three-fifths of each tube was used to calculate strains. For 330 and 400°C, the arithmetic average of 300 measurements was used. The tubes irradiated at 60°C presented a less straightforward situation because deformations were so large that the tubes touched the holder in the irradiation capsule, causing them to be slightly elliptical. Since it is the increase in circumference that is really needed, the major and minor diameters (d_{max} and d_{min}, respectively) of the ellipses were used to calculate circumferences, and effective diameters, given by $d_{eff} = (\sqrt{2}/2)\,(d^2_{max} + d^2_{min})^{1/2}$, were computed from the circumference. This correction was very small in most cases.

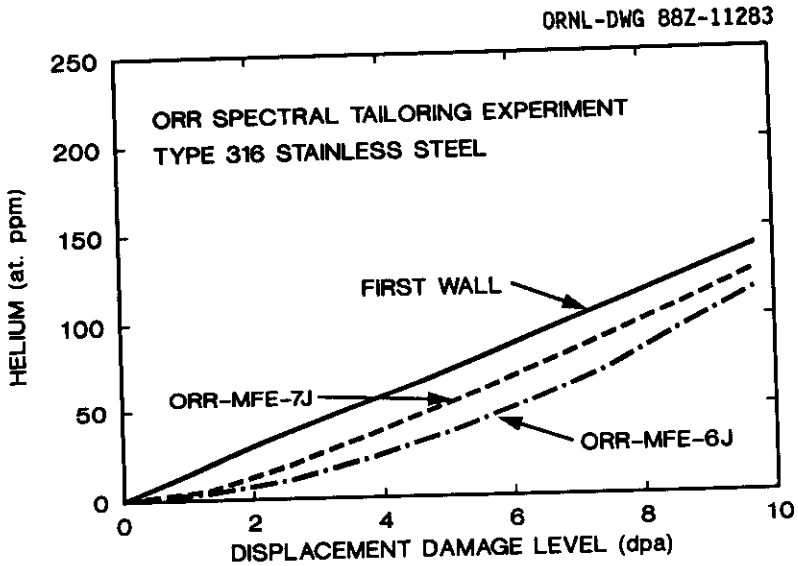

Fig. 1. Helium concentration as a function of displacement damage level for the spectrally tailored Oak Ridge Research Reactor Experiments, ORR-MFE-6J and ORR-MFE-7J. A similar curve for a fusion reactor with a stainless steel first wall and blanket and lithium coolant is also shown.

Results

The strains observed in the tubes are plotted as a function of stress in Fig. 2. For the alloys and conditions investigated, irradiation creep deformation appears to be linear in stress. Although non-linear behavior was observed previously in a similar ORR spectral tailoring experiment at stresses near 400 MPa (ref. 1), there are insufficient data in the present experiment to confirm this result. Effective values of stress and strain are given in order to relate them to uniaxial deformation; effective stress is 0.866 times the hoop stress and effective strain is 1.33 times the diametral strain.[12] The irradiation creep rates, defined as effective strain per unit effective stress per dpa, are given in Table 2.

After making allowance for displacement damage level, the creep rates at 330 and 400°C for both alloys are comparable to irradiation creep strains at the same temperatures observed previously in another ORR spectral tailoring experiment.[1] It is observed that the creep rates are slightly larger for both types of PCA than for 316 SS, also consistent with the previous experiment.[1] No correction has been made for swelling, since such data are not yet available. However, extrapolation of the creep strain curves to zero stress indicates either densification or swelling below or near the limit of detectability by immersion density measurement. At 60°C, deformations are slightly larger than those for the higher temperatures in the Japanese 316 and the U.S. heat of PCA. In the PCA, the creep deformation observed at 60°C was greater than that observed at 330 and 400°C by a factor of 4 to 7.

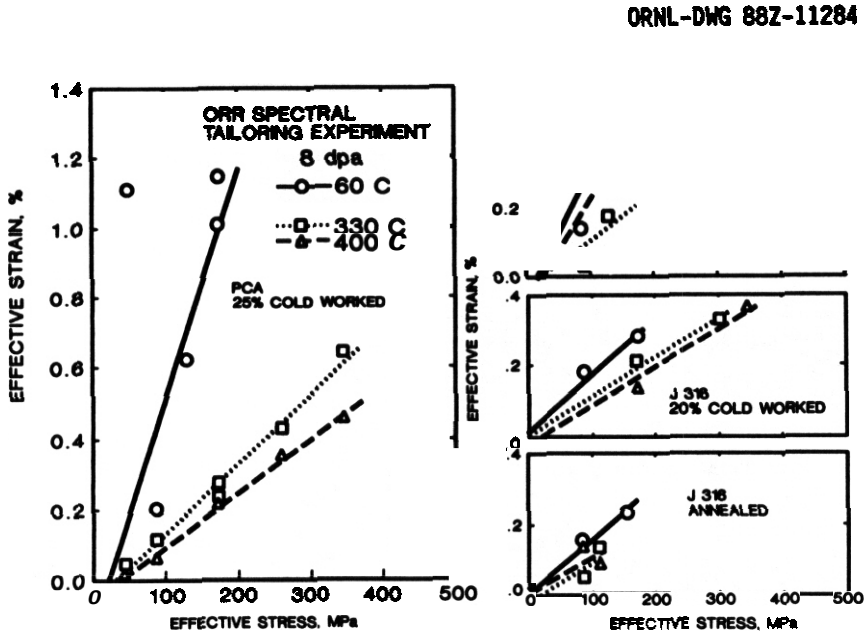

Fig. 2. Effectfve Strain as a function of effective stress for PCA, Japanese PCA, and a Japanese heat of AISI Type 316 Stainless Steel. The data are from pressurized tubes irradiated in the Oak Ridge Research Reactor.

Table 2. Creep rates for type 316 and PCA alloys (in terms of effective stress and strain — MPa^{-1} dpa^{-1} ×

Alloy	Temperature (°C) 60	330	400
USPCA	9.2–14	2.5	1.8
JPCA	5.1	1.7	3.5
J316SA	2.2	1.4	1.4
5316 20% CW	2.2	**1.3**	**1.3**

Discussion

Linear dependence of stress on strain is the commonly observed behavior. especially at low stresses.[13,14] It is consistent with the stress-induced preferential absorption (SIPA) mechanism of irradiation creep.[15-17] An increasing stress exponent has also been observed at higher stresses.[18-20] In particular it has been observed in type 316 SS and PCA in a previous spectral tailoring experiment in the ORR. Since deviation from linearity is seen only at the highest stress levels examined, the present data are not inconsistent with this result. There were simply not enough data at the highest stress levels. and the stress levels investigated were not sufficiently high to properly study this effect. Deviation from linear behavior at high stresses is expected on the basis of a transition from the SIPA mechanism to the climb-enabled-glide mechanism,[1,19,10] which predicts a quadratic stress dependence.[21]

What is interesting about the results observed is the magnitude of irradiation creep at 60°C. Low-temperature irradiation creep was observed previously in a low fluence neutron irradiation experiment by Hesketh.[22] He investigated irradtation creep in pure nickel and the austenitic stainless steel EN58B as well as other materials at 38°C and in some cases at —195°C using helical springs. He observed creep rates about an order of magnitude lower than those in the present experiment. However, his entire rod specimen did not experience the maximum flux. This might account for a lower creep rate but probably not an order of magnitude.

There are two results from Hesketh's experiment considered relevant to the present work: he observed irradiation creep at temperatures far below 300°C, and he found the creep rate to increase with decreasing temperature. Hesketh attributed the irradiation creep to collapse of displacement cascades into vacancy loops. Since an external stress can bias the direction of collapse so as to form more loops perpendicular to the axis of a compressive stress, a stress dependent deformation will occur. Hesketh predicted the deformation to be linear in stress and fluence and of the same order as he observed. Other investigators have proposed similar mechanisms for irradiation creep.[23]

Gilbert assembled low-temperature irradiation creep data from three reactors and demonstrated a decrease in creep rate with increasing temperature.[24] He pointed out the similarity with low temperature swelling in mlybdenum due to accumulation of single vacancies and vacancy clusters. Similar behavior has been observed in SiC where the phenomenon is exploited in the use of SiC as a temperature monitor.[25] Here again the deformation has an inverse temperature dependence but is not volume conserving.

In searching for an explanation for the high creep rate at low temperatures, a logical starting place might be the temperature dependence of the point defect concentrations, which drive irradiation-induced processes. We will start with the rate equations for defect populations.

$$dC_v/dt = G_v - RC_vC_i - K_vC_v \quad ;$$

$$dC_i/dt = G_i - RC_vC_i - K_iC_i \quad . \qquad (1)$$

The quantities C_v and C_i are the concentrations of vacancies and interstitials. G_v and G_i ($G_i = G_v = G$) are the production rates of vacancies and interstitials from atomic displacements. R is the recombination coefficient for vacancies and interstitials. K_v and K_i are reaction rate constants that describe the loss of defects to sinks. In steady state, Eqs. (1) can be solved for steady state values of C_v^{ss} and C_i^{ss}. It is found that

$$C_v^{ss} = \frac{1}{2K_vR} \{[(K_vK_i)^2 + 4RG\ K_vK_i]^{\frac{1}{2}} - K_vK_i\} \quad (2)$$

and

$$C_i^{ss} = \frac{1}{2K_iR} \{[(K_vK_i)^2 + 4RG\ K_vK_i]^{\frac{1}{2}} - K_vK_i\} \quad . \quad (3)$$

Usfng Mansur[26] as a guide,

$$R = 4\pi r_0(D_i\ t\ D_v) \quad , \quad (4)$$

and

$$K^j_{i,v} = S^j_{i.v}\ D_{i,v} \quad (5)$$

for vacancies and interstitials and the jth type of sink (e.g., dislocations, cavities, or precipitates). Then, using the same reference.

$$S_{v,i} = 4\pi r_\ell Z_{v,i} \quad . \quad (6)$$

for small loops and

$$S_{v,i} \approx Z_{v,i}L \quad (7)$$

for edge dislocations of density L, r_ℓ is the radius of the equivalent sphere when the stress field interaction is excluded, and the Z's are capture efficiencies. For large loops, Eq. (7) is a good approximation. where L is re-interpreted as the total loop circumference per unft volume.

At this point, microstructural data are required. For 60°C, data are avallable for austenitic stainless steels from Maziasz,[27] and for higher temperatures. data are available from Brager and Straalsund[28] and from a review by Stoller.[29] The loop diameter, D_ℓ in nm, and loop density, C_ℓ in cm^{-3}, are found to obey the equations:

$$D_\ell = (0.017\ T - 30.5)\ [1 - \exp(-T/350)] + 13 \quad . \quad (8)$$

and

$$C_\ell = 7 \times 10^{16} \exp\ (-T/2.6 \times 10^7)^{T^2}\ t\ 4.05 \times 10^{22} \exp\ (-0.037\ T - \frac{1500}{T}) \quad , \quad (9)$$

where T is the temperature in °C. The network dislocation density, L in cm^{-2}, is found to obey the following relation:

$$L = 5 \times 10^6 \exp\ (0.0126/T) \quad . \quad (10)$$

Using Wolfer,[30] values for Z_v and Z_i are calculated as a function of temperature, permitting the defect concentrations to be plotted as a function of temperature in Figs. 3 and 4. Values of parameters used are listed in Table 3.

The curves in Fig. 3 indicate a weak dependence of point defect concentration on temperature in the range of 330 to 600°C and suggest the source of the temperature Insensitivity of irradiation creep observed in this range in the present experiment and in the previous similar experiment,' although irradiation creep is also dependent on microstructural parameters, as will be discussed. However, the very rapid decrease in interstitial concentration at low temperatures gives a result quite the opposite of what was observed. If we use the stress-induced preferential absorption (SIPA) model as a guide in our thinking, the true temperature dependence of SIPA creep can be shown by substituting the above-derived quantities into the expression for the SIPA creep rate, $\beta_{i,j}$, derived by Wolfer and Ashkin[15]

ORNL-DWG 88Z-11280

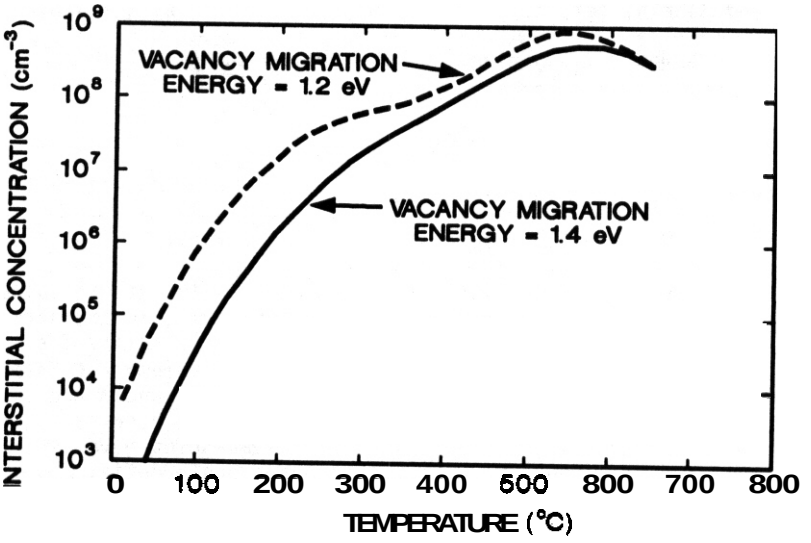

Flg. 3. Steady state interstltlal concentration as a functlon of temperature for condltions of the present irradiation experlaent.

ORNL-DWG 882-11281

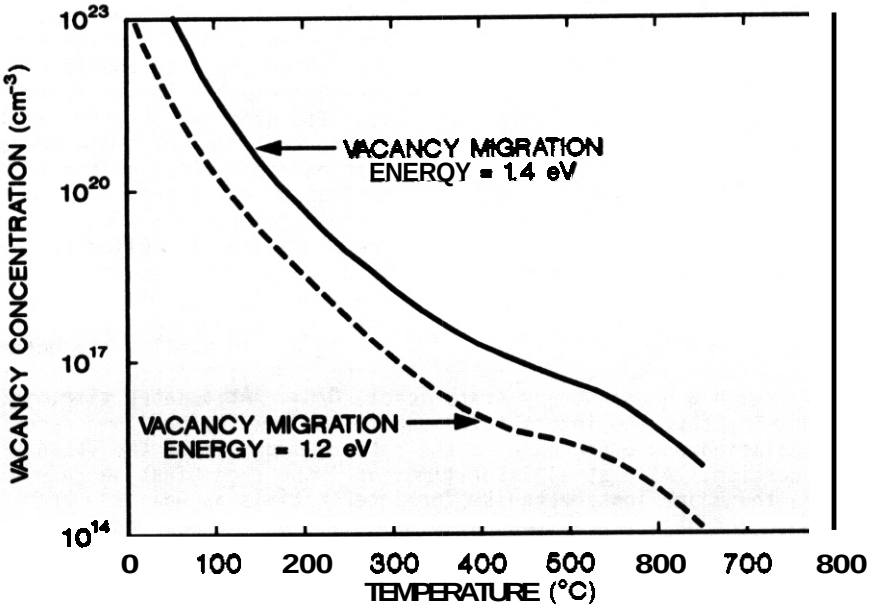

Fig. 4. Steady state vacancy concentration as a function of temperature for conditions of the present Irradiation experiment.

Table 3. Values of parameters used in calculations (largely after Uolfer and Ashkin. ref. 15)

Parameter	Symbol	Value
Vacancy migration energy	E_v^m	1.2, 1.4 eV
Interstitial migration energy	E_i^m	0.15 eV
Defect generation rate	G	1.3 x 10^{16} s^{-1}
Burgers vector	b	25 x 10^{-10} m
Atomic volume	n	1.6 x 10^{-29} m^3
Relaxation volume		
Interstitial	V_i	1.4 Ω
Vacancy	V_v	−0.2 n
Bulk Polarizability		
Interstitlal	α_i^k	100 eV
Vacancy	α_v^k	−150 eV
Shear Polarirability		
Interstitial	α_i^G	−150 eV
Vacancy	α_v^G	−15 eV
Inner Cutoff radius for dislocation:		
Interstitial	D_{ii}	10 b
Vacancy	D_{vv}	4 b

$$\dot{\beta}_{i,j} = \gamma L D_i C_i \sigma_{i,j} \quad , \tag{11}$$

where

$$\gamma = \frac{-\Omega \alpha_i^G V_i (1 + u)(5 - 4\nu)}{1440\,\pi\,[kT\ a\ (1-\nu)\ \ln (R'/a)]^2} \quad . \tag{12}$$

where Ω is the atomic volume, K is Boltzmann's constant, $\sigma_{i,j}$ is the stress tensor. α_i^G is the shear polarizability for interstitials. V_i is the relaxation volume for interstitials. ν is Poisson's ratio, and R' and a are the range of the stress field and the core radius of a dislocation. Since vacancies have essentially no stress-induced preferential absorption, the effect of vacancies has been neglected.[15]

Using Eq. (11), the creep rate was calculated as a function of temperature and shown in Fig. 5. Activation energies for the dlffusion of vacancies of 1.2 and 1.4 eV were used in the calculations. The temperature dependence suspected on the basis of interstitial concentration is confirmed.

The curves in Fig. 5 seem to negate an explanation of the low-temperature creep behavior by the SIPA or a similar mechanism, but the previous discussion considered only steady-state defect concentrations. It is proposed that the significant creep observed at low temperature may be explained by a new mechanism of irradiation creep based on the transient in the buildup of point defect concentration. In the present report, a semiquantitative evaluation of the mechanism is applied to the data. A more detailed description and evaluation of the model are given in ref. 31. The expected behavior of point defect populations is shown schematically in Fig 6. Initially, the defect population rises at the production rate G, the atomic displacement rate. At some time $\tau_i = 1/K_i$, the interstitials reach the sinks and thereafter rapidly reach a quasi-steady state level, G/K_i. At a later time, τ_{R_1}, the vacancies reach a sufficiently high density that the interstitial population now suffers some recombination with them, resulting in a declining population and a decrease in the rate of increase of the vacancy population, since they too now have a loss mechanism. At a still later time, τ_{R_2}, the recombination rate will have reached a point where recombination is the major loss mechanism for interstitials as well as vacancies. The vacancy concentration will continue to increase thereafter but at a still lower rate, and the interstitial concentration will decline more slowly since its loss rate is becoming constant and balancing the production rate. Finally, at a time $\tau_v = 1/K_v$, the vacancies diffuse to sinks and the populations adjust until the now-unchanging loss rate is equal to the production rate. This is the steady state discussed previously.

The values for the transition times may now be estlmated. At τ_i, one can write for the interstitials,

$$dC_i/dt = G - K_i C_i \quad . \tag{13}$$

Then solving this equatlon it is seen that C_i changes exponentially with a time constant $1/K_i$, which is the reason for using this value for τ_i. At τ_{R_1} we will arbitrarily say that the recombination rate is 1% of the production rate. the point where recombination is beginning to become significant. Then we have

$$RC_i C_v/G = \delta_1 = 0.01 \quad . \tag{14}$$

At T_{R_1} as well as between τ_i and τ_{R_1}, we have

$$dC_i/dt = G - K_i C_i = 0 \quad , \tag{15}$$

ORNL-DWG 88Z-11282

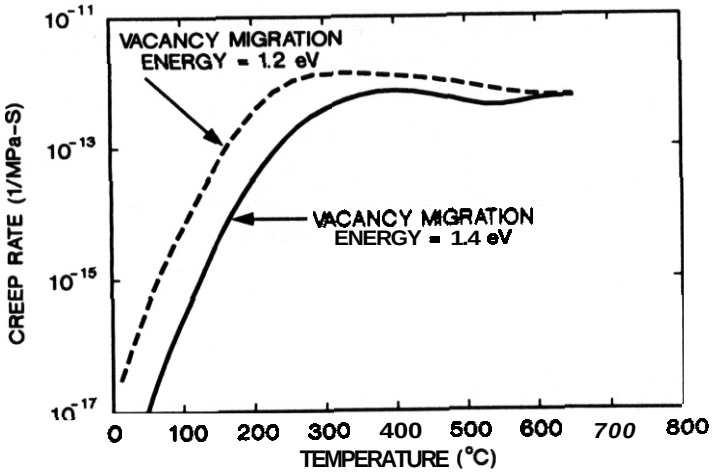

Fig. 5 Irradiation creep rate per unit stress predicted by the SIPA mechanism as a function of temperature.

ORNL-DWG 88Z-11562

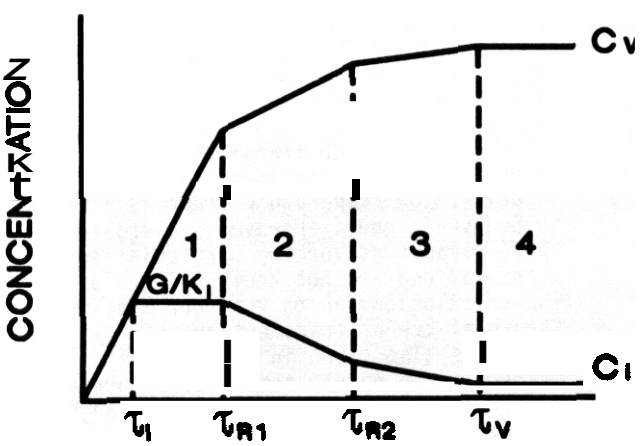

Fig. 6. A schematic representation of point defect concentration as a function of time for the case of a strong sink density; C_v and C_i are concentrations of vacancies and interstitials. respectively.

or

$$C_i = G/K_i \quad , \tag{16}$$

and

$$C_v = G\tau_{R_1} \quad . \tag{17}$$

Then substituting into Eq. (14), we have

$$\tau_{R_1} = \frac{\delta_1 K_i}{RG} = \frac{0.01\ K_i}{RG} \quad . \tag{18}$$

Similarly. τ_{R_2} can be defined as the time where recombination is the dominant loss rate, let us say 99% of the production rate. Then

$$\tau_{R_2} = \frac{\delta_2 K_i}{RG} = \frac{0.99\ K_i}{RG} \quad . \tag{19}$$

The time τ_v is arrived at in a similar manner to τ_i; thus

$$\tau_v = 1/K_v \quad . \tag{20}$$

These time intervals and estimates of point defect concentrations may now be used to make estimates of the total number of interstitials diffusing to dislocations and producing climb. For time, $t < \tau_{R_1}$ interstitials are lost only by capture by dislocations so that the number captured, N_1, is the number produced minus the concentration in the lattice or

$$N_1 = G\tau_{R_1} - G/K_i \quad . \tag{21}$$

where G/K_i is entirely negligible with respect to the first term for sink densities of interest here. For the interval $\tau_{R_1} < t < \tau_{R_2}$, the number captured by dislocations is the number produced in that Interval less the number recombined less the concentration remaining in the lattice at τ_{R_2}, $C_i(\tau_{R_2})$. Since at the beginning of the interval, recombination is nearly zero and it is essentially the entire production rate at the end of the interval. the fraction captured by dislocations, f, will be considered to be 50%. a rough average. Then we have

$$N_2 = fG(\tau_{R_2} - \tau_{R_1}) - C_i(\tau_{R_2}) = 0.5\ G(\tau_{R_2} - \tau_{R_1}) - C_i(\tau_{R_2}) \quad , \tag{22}$$

where $C_i(\tau_{R_2})$ may be neglected since recombination has caused the concentration of interstitials to drop significantly. In the interval $\tau_{R_2} < \tau < \tau_v$, the concentration of vacancies is decreasing frm $C_i(\tau_{R_2})$ to the steady state value of C_i at τ_v, C_{iss}, given by Eq. (3). Since the value of $C_i(\tau_{R_2})$ is not calculated exactly, C_{is} will be used for the interstitial concentration over this entire interval. This will certainly underestfmate the flux of interstitials to dislocations and give a lower limit to the creep predicted by this new model. A refinement to this estimate is given in ref. 31. Then the number of interstftials captured by dislocations, N_3, is given by

$$N_3 = C_i^{ss} D_i S_i (\tau_v - \tau_{R_2}) \quad , \tag{23}$$

where S_i is the sink strength for interstitials at dislocations. The transient ends at τ_v; beyond this point steady state creep applies.

The volume swept out by a climbing dislocation may be expressed as

$$V = bLv\Delta T \quad , \tag{24}$$

where b is the Burgers vector, L is the dislocation line length. and v is the average climb velocity over time interval AT. Then since the total volume of interstitials diffused to the dislocations is

$$\Omega(N_1 + N_2 + N_3) = bLv\Delta T \quad , \tag{25}$$

and

$$v = \frac{\Omega(N_1 + N_2 + N_3)}{bL\Delta T} \tag{26}$$

For the mechanism of climb-enabled glide irradiation creep, the expression for the creep rate is given in terms of the climb velocity as follows.[21]

$$\dot{\varepsilon}_{cg} = \frac{a}{E} (\pi L)^{\frac{1}{2}} v \quad . \tag{27}$$

where σ is the stress and E is the elastic modulus. Then substituting Eq. (26) into (27) and multiplying by AT, the total climb enabled-glide creep during the transient may be calculated. For this particular experiment, which had 35 transient periods during reactor startups, the creep strain is plotted as a function of tenperature in Fig. 7. A phenomenon which reduces the effect of the transients is that the vacancies do not have sufficient time to completely relax to their equilibrium concentration during the shutdown. Since a major part of the creep occurs in the interval $\tau_{R_2} < \tau < \tau_v$, this effect was not accounted for in this analysis.

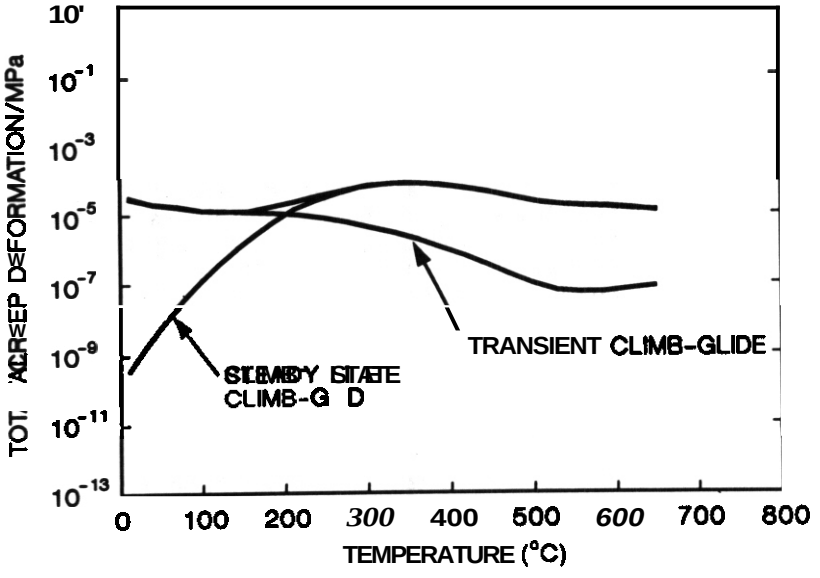

Fig. 7. Total creep deformation per unit stress as a function of temperature for the ORR-MFE-6J and ORR-MFE-7J experiments The steady state climb-glide curve was generated from Eq. (11) using ref. 21 to relate SIPA and climb-enabled glide creep. The sum of the transient and steady state curves is also shown.

glide mechanism using steady state values is also plotted for comparison.[21] Since the contribution to transient creep was underestimated in the last transient interval, low-temperature creep is likely to be even higher. However, microstructural parameters for the particular specimen over a very wide temperature range. The climb-enabled glide mechanism appears to overpredict the experimental data in the region above 300°C and the transient creep at 60°C underpredicts the data. but in light of the approximations used, some discrepancy is expected.

CONCLUSIONS

Higher levels of irradiation creep were observed at 60°C than at 330 and 400°C after neutron irradiation to a displacement damage level of 8 dpa. An analysis was made only to suggest a new mechanism for

irradiation creep at low temperatures. The description of the model presented here is not intended to be used to predict irradiation creep; the reader is referred to ref. 31 for a more careful analysis. Continued irradiation of the same specimens and short term irradiations are expected to confirm the transient creep hypothesis.

Since recent conceptual designs of fusion devices have high flux components operating below 100°C, the results of this study are of direct relevance to the design of such machines. Irradiation creep might relieve the stresses at crack tips causing the cracks to be self-arresting. However, irradiation creep might also produce undesirable deformations from primary loads. In either case, these findings of significant irradiation creep at low temperatures must be accounted for in the design.

FUTURE WORK

Two major tasks remain on this project. One is to examine the pressurized tubes irradiated at 200°C. This capsule has not yet been disassembled, but creep measurement and analysis will be done as soon as the specimens are available. The second task is to complete analysis of the ferritic steels in this series of Irradiation experiments. This is expected during the next reporting period.

REFERENCES

1. M. L. Grossbeck and J. A. Horak, "Irradiation Creep in Type 316 Stainless Steel and US PCA with Fusion Reactor He/dpa Levels," J. Nucl. Mater. 155-157 (1988) 1001–1005 (Third International Conference on Fusion Reactor Materials, October 4-8, 1987. Karlsruhe, F.R. Germany).

2. J. R. Hudson and R. S. Nelson, "The Irradiation Creep of Nickel and AISI 321 stainless Steel During 4 MeV Proton Bombardment," J. Nucl. Mater. 65 (1977) 279.

3. H. Hausen, Critical Survey of the Neutron-induced Creep Behaviour of Steel Alloys for the Fusion Reactor Materials Program. Report EUR 9924 EN, Commission of the European Communities, Joint Research Centre, Petten Establishment, 1985.

4. O. L. Smith et al.. "Blanket and First Wall." in INTOR Study, Argonne National Laboratory. October 1987.

5. T. A. Gabriel, B. L. Bishop. and F. W. Wiffen. Calculated Irradiation Response of Materials Using a Fusion-Reactor First-Wall Spectrum, ORNL/TM-5956, Oak Ridge National Laboratory, 1977.

6. J. A. Conlin and J. W. Woods, "Irradiation Experiments for the U.S./Japan Collaborative Testing Program in HFIR and ORR," AOIP Semiannual Progress Report for Period Ending March 31, 1984, DOE/ER-0045-12, Oak Ridge National Laboratory, 1984, P. 37.

7. T. A. Gabriel. K. R. Thoms. and J. W. Woods, "Design of Materials Irradiation Experiments Utilizing Spectral Tailoring." AOIP Quarterly Progress Report for Period Ending December 31. 1979, DOE/ER-0058/4, Oak Ridge National Laboratory, 1979, pp. 10-17.

8. T. A. Gabriel, K. R. Thoms, and M. L. Grossbeck, "Design of Materials Irradiation Experiments in the ORR Utilizing Spectral Tailoring and Reencapsulation," ADIP Quarterly Progress Report for Period Ending March 31, 1979, DOE/ER-0058/5, Oak Ridge National Laboratory, 1980, pp. 20-22.

9. L. R. Greenwood, "Neutron Source Characterization for Materials Experiments," AOIP Semiannual Progress Report for Period Ending September 30, 1982, DOE/ER-0045/9, Oak Ridge National Laboratory, 1983, pp. 6-16.

10. L. R. Greenwood, "Dosimetry Measurements for the ORR 6J Prototype Experiment," DAFS Quarterly Progress Report, July-September 1985. DOE/ER-0046/23, Hanford Engineering Development Laboratory, 1985, pp. 5-8.

11. R. A. Lillie, "Neutronics Analysis in Support of the U.S.-Japan Spectral Tailoring Capsules," Fusion Reactor Materials Semiannual Progress Report for Period Ending September 30, 1987, DOE/ER-0313/3, Oak Ridge National Laboratory, 1988. PP. 28-29.

12. E. R. Gilbert and L. O. Blackburn, Trans. ASME, J. Engr. Mater. & Technol. (April 1977) 168-180.

13. J. L. Straalsund. "Radiation Effects in Breeder Reactor Structural Materials." Eds.. M. L. Bleiberg and J. W. Bennett. The Metallurgical Society of AIME. New York, 1977, pp. 191-207.

14. L. C. Walters, G. L. McVay, and G. D. Hudman, "Irradiation-Induced Creep in 316 and 304L Stainless Steels," ibid., pp. 277-294.

15. W. G. Wolfer and H Ashkin. "Diffusion of Vacancies and Interstitials to Edge Dislocations," J. Appl. Phys. 47(3), 1976. 791-800.

16. P. T. Heald and H V. Speight. "Steady-State Irradiation Creep." Phil. Hag. 29. 1974, 1075-1080.

17. R. Bullough and J. R. Willis, "The Stress-Induced Point Defect-Dislocation Interaction and Its Relevance to Irradiation Creep," Phil. Mag. 31. 1975. 855-859.

18. R. J. Puigh. "The In-Reactor Deformation of the PCA Alloy," J. Nucl. Hater. 141-143, 1986, 954-59.

19. J. A Hudson and R. S. Nelson, "The Irradiation Creep of Nickel and AISI 321 Stainless Steel During 4 MeV Proton Bombardment." J. Nucl. Hater. 65, 1977. 279-294.

20. C. Wassilew. Analysis of the In-reactor Creep and Creep-Rupture Life Behaviour of Stabilized Stainless Steels and the Ni-Base Alloy Hastelloy X, Primarbericht, KFK, Darlsruhe (February 1987).

21. L. K. Hansur, "Irradiation Creep by Climb-Enabled Glide of Dislocations Resulting from Preferred Absorption of Point Defects." Phil. Hag. A 39, 1979. 497-506.

22. R. V. Hesketh. "Collapse of Vacancy Cascades to Dislocation Loops." in Proceedings of the International Conference on Solid State Physics Research with Accelerators, September 25-28. 1967. A. N Goland, Ed.. BNL 50083 (C-52), Brookhaven National Laboratory, pp. 389-401.

23. A. D. Brailsford and R. Bullough. "Irradiation Creep Due to the Growth of Interstitial Loops." Phil. Hag. 27, 1973. 49-64.

24. E. R. Gilbert, "In-Reactor Creep of Reactor Materials." Reactor Tech. 14(3), 1971. 258-285.

25. J. E. Palentine, "The Development of Silicon Carbide as a Routine Irrradiation Temperature Monitor, and Its Calibration in a Thermal Reactor," J. Nucl. Hater. 61, 1976, 243-253.

26. Mansur. L. K, "Void Swelling in Metals and Alloys Under Irradiation: an Assessment of the Theory.' Nucl. Tech. 40, 1978. 5-34.

27. P. J. Maziasz, "Microstructures Developed in Austenitic Stainless Steels Irradiated in HFIR at 55°C," Trans. ANS 39. 1981. 433-435.

28. H. R. Brager and J. L. Straalsund. "Defect Development in Neutron Irradiated Type 316 Stainless Steel." J. Nucl. Hater. 46. 1973. 134-158.

29. R. E. Stoller, Microstructural Evolution in Fast-Neutron-Irradiated Austenitic Stainless Steels, ORNL-6430, Oak Ridge National Laboratory, 1987.

30. W. G. Wolfer. 'Segregation of Point Defects by Internal Stress Fields." Fundamental Aspects of Radiation Damage in Metals, Proceedings of an International Conference held at Gatlinburg, TN. October 6-10. 1975, pp. 812-819.

31. L. K. Mansur, R. E. Stoller. and M. L. Grossbeck. "Irradiation Creep at Low Temperatures from Transient Climb-Enabled Glide." Oak Ridge National Laboratory, to be published.

6.3 Vanadium Alloys

TEMPERATURE DEPENDENCE OF THE FRACTURE BEHAVIOR AND THE DBTT FOR DEHYDROGENATED AND HYDROGENATED VANADIUM-BASE ALLOYS - B. A. Loomis, B. J. Kestel, B. D. Edwards. and O. L. Smith (Argonne National Laboratory)

OBJECTIVE

The objective of this research is to provide guidance on the applicability of vanadiun-base alloys for structural components in a fusion reactor.

SUMMARY

The temperature dependence of the fracture behavior and the DBTT were determined for the V-3Ti-0.5Si, V-9Cr-3Fe-1Zr, V-10Cr-5Ti, V-20Ti, V-15Cr-5Ti, V-10Cr-10Ti, and V-15Ti-7.5Cr alloys fran Charpy impact tests. The DBTT for these alloys was less than 30°C if the alloy was in the fully recrystallized, dehydrogenated condition. The presence of 400-1000 appm hydrogen in the V-9Cr-3Fe-1Zr, V-10Cr-5Ti, V-20Ti, V-15Cr-5Ti, V-10Cr-10Ti, and V-15Ti-7.5Cr alloys caused a significant increase (40-225°C) of the DBTT for these alloys. The DBTT for the V-3Ti-0.5Si alloy decreased with an increase of the hydrogen concentration up to at least 1000 appm. The DBTT for these vanadium-base alloys mas dependent on the canbined concentration of alloying elements. The V-3Ti-0.5Si, V-9Cr-3Fe-1Zr, V-20Ti, and V-15Ti-7.5Cr alloys have an intrinsic resistance to crack propagation whereas the V-15Cr-5Ti, V-10Cr-10Ti , and V-10Cr-5Ti alloys have a relatively low resistance to crack propagation.

PROGRESS AND STATUS

Introduction

The V-15Cr-5Ti alloy has been considered to be a reference alloy for the evaluation of vanadium-base alloys as structural materials for a fusion reactor, based on the generally attractive mechanical, corrosion, fabrication, and irradiation performance of the alloy However. recent data obtained fran Charpy impact tests and tensile tests on this alloy after neutron irradiation (10-90 dpa) suggest that the DBTT may be unacceptable for this alloy.[1,2] In this report we present the results of an investigation on the OBTT and fracture behavior during impact loading of the V-15Cr-5Ti alloy and several other vanadiumbase alloys for the purpose of providing guidelines in the selection of candidate vanadiun alloys for evaluation.

Materials and procedure

Vanadium-base alloys with the nominal compositions of V-15Cr-5Ti, V-20Ti, V-10Cr-10Ti , V-10Cr-5Ti, V-15Ti-7.5Cr, V-3Ti-0.5Si, and V-9Cr-3Fe-1Zr (Vanstar 7) were obtained in the form of sheet with 50% thickness reduction, i.e., cold work, having a nominal thickness of 3.8 mm. The alloy canpositions are listed in Table 1.

Table 1. Vanadium-base alloy canpositions

Nominal Composition	Heat No.	Concentration (wt %) Cr	Ti	Si	Fe	Zr	O	N	C
V-15Cr-5Ti	ANL 101	13.5	5.2	0.04	0.05	-	0.12	0.04	0.05
V-15Cr-5Ti	ANL 204	14.5	5.0	0.04	0.02	-	0.03	0.01	0.01
V-20Ti	CAM 832	-	17.7	0.05	0.04	-	0.08	0.02	0.04
V-10Cr-10Ti	TWC 2729	9.9	9.2	0.03	0.04	-	0.03	0.01	0.02
V-10Cr-5Ti	ANL 206	9.2	4.9	0.03	0.02	-	0.02	0.01	0.03
V-15Ti-7.5Cr	ANL 94	7.2	14.5	0.04	0.09	-	0.11	0.03	0.04
V-3Ti-0.5Si	WI 8505	-	3.1	0.54	0.02	-	0.06	0.02	0.01
V-9Cr-3Fe-1Zr (Vanstar-7)	CAM 837	9.0	-	-	3.2	1.2	0.04	0.06	0.07

Hiniature Charpy impact specimens were prepared for a determination of the tmperature dependence of the fracture behavior for the dehydrogenated and hydrogenated alloys. The Charpy specimens had overall dimensions of 3.30 mm x 3.30 mm x 25.4 mm and a notch depth of 0.61 mm. Specimens were prepared with the notch orientation either parallel or perpendicular to the rolling direction that mas maintained during thickness reduction. Dehydrogenated Charpy test specimens in the fully recrystallized condition were

prepared from the 50% cold-worked alloys by annealing for one hour in a vacuum of 2×10^{-5} Pa. The V-15Cr-5Ti, V-10Cr-10Ti, V-10Cr-5Ti, V-15Ti-7.5Cr, and V-9Cr-3Fe-1Zr alloys were annealed at 1125°C. The annealing temperatures for the V-20Ti and V-3Ti-0.5Si alloys were 1100°C and 1050°C, respectively. Hydrogen was introduced into Charpy specimens of the alloys by annealing the cold-worked specimens at the previously mentioned temperatures in argon-filled quartz tubes for 1 h and subsequently quenching the tubes and their contents without rupture in water. These annealing conditions for the cold-worked alloys resulted in average recrystallized grain diameters in the range of 0.02-0.04 mm. The V-15Cr-5Ti alloy specimens from Heat No. ANL 101 and the V-9Cr-3Fe-1Zr alloy specimens had the smaller grain diameters. Dehydrogenated Charpy test specimens with 50% cold work were also prepared by heating the Charpy specimens at 420°C for 2 h in vacuum.

The hydrogen concentration in the Charpy specimens was determined from the total partial pressure of hydrogen that was evolved on heating a specimen at the rate of 15°C/min from 25°C to 1000°C. The procedure for these hydrogen analyses is discussed in more detail in Ref. 3. In the case of the Charpy specimens that were annealed in vacuum (dehydrogenated), the hydrogen concentration was determined to be 30 ±2 appn. The hydrogen concentration in the specinens that were annealed in quartz tubes ranged from 400 to 1200 appn. The hydrogen concentration in the specimens was intentionally altered in some instances by surface finishing prior to the anneal in the quartz tubes.[3]

The Charpy impact tests were performed using an instrunented Dynatup Drop Weight Impact Test machine. The impact velocity and load for these tests were 2.56 m/sec and 14.995 kg. respectively. The energy absorption during an impact test was determined from applied load-time data that were acquired during the impact. These data were analyzed and plotted using the GRC Model 730-1 data acquisition and analysis system. The temperature of a specimen at the instant of impact was determined from a thermocouple that was spot welded in close proximity to the notch. The Charpy tests were limited to specimen temperatures in the range of -190°C to 250°C.

The energy absorbed (E) during the impact tests versus test temperature (TI curves were fitted with the equation

$$E = A + B \ \mathrm{Tanh}\left[(T - T_0) / C_0\right] \qquad (1)$$

where A, B, T_0, and C_0 were curve fitting paraneters. The inflection point for a curve, viz., T_0, was used to define the ductile-brittle transition temperature (DBTT).

The microstructures of the annealed Charpy specimens are shown in Fig. 1. These microstructures were obtained by electropolishing at 24 volts open circuit potential in a solution of 20 parts HF, 20 parts HNO_3, and 60 parts glycerine at 25°C together with immersion in a solution of 20 parts HF. 20 parts HNO_3, and 60 parts lactic acid at 25°C. The microstructures of the alloys showed the presence of precipitates with diameters ranging from 0.002 to 0.005 mm and a precipitate nunber density ranging from 0.4×10^{10} mm^{-3} to 2×10^{10} mm^{-3}. Bands of precipitates were prevalent in the V-15Cr-5Ti, V-10Cr-5Ti, V-10Cr-10Ti, V-15Ti-7.5Cr, and V-20Ti alloy microstructures.

The surfaces of fractured Charpy specimens were exanined for their fracture behavior, i.e., ductile tearing. transgranular fracture, and intergranular fracture, by observation with a JEOL JSM-50A scanning microscope (SEM). The fracture surfaces were also routinely exanined for signlficant segregation of the major alloying and impurity atans by use of electron microprobe x-ray analyses. However. the analyses showed that the concentrations of these alloying and impurity atoms *in* the fracture surface were in all instances not significantly different from the concentrations that were present in the bulk of the specimen.

Experimental results

Fracture energy and DBTT. The dependence on temperature of the energy absorbed by the dehydrogenated and hyarogenated V-15Cr-5Ti, V-10Cr-10Ti, V-10Cr-5Ti, V-15Ti-7.5Cr, V-3Ti-0.5Si, V-20Ti, and V-9Cr-3Fe-1Zr alloy specimens during the Charpy Impact tests is shown in figs. 2-8, respectively. The formulations of Eq. (1) for the data in Figs. 2-8 are also shown in these figures. The DBTT for the dehydrogenated and hydrogenated alloys that were derived from these formulations of Eq. (1) are listed in Table 2.

There were tu, regimes in Figs. 2-8 with significant departure of the energy absorption-temperature data from the formulations of Eq. (1), viz., (a) Charpy impact tests at increasing temperatures on the upper energy shelf (Figs. 2,3,4, 6,and 8) and (b) tests at temperatures in the range of 0-50°C above the OBTT listed in Table 2 (Figs. 6 and 8). In the case of the (a) regime, the decrease of the energy absorption with increase of test temperature is attributed to the substantial decrease in strength of the alloys in the temperature range of 25 to 250°C.[4] In the case of the (b) regime, it will be shown in a subsequent section that the departure of the data is attributable to significant resistance of the alloy to crack propagation. All Charpy impact tests that were conducted on the dehydrogenated and the hydrogenated specimens at temperatures corresponding to the upper shelf of energy absorption resulted in specimens that were bent to an angle of 85° with no visual evidence for crack initiation.

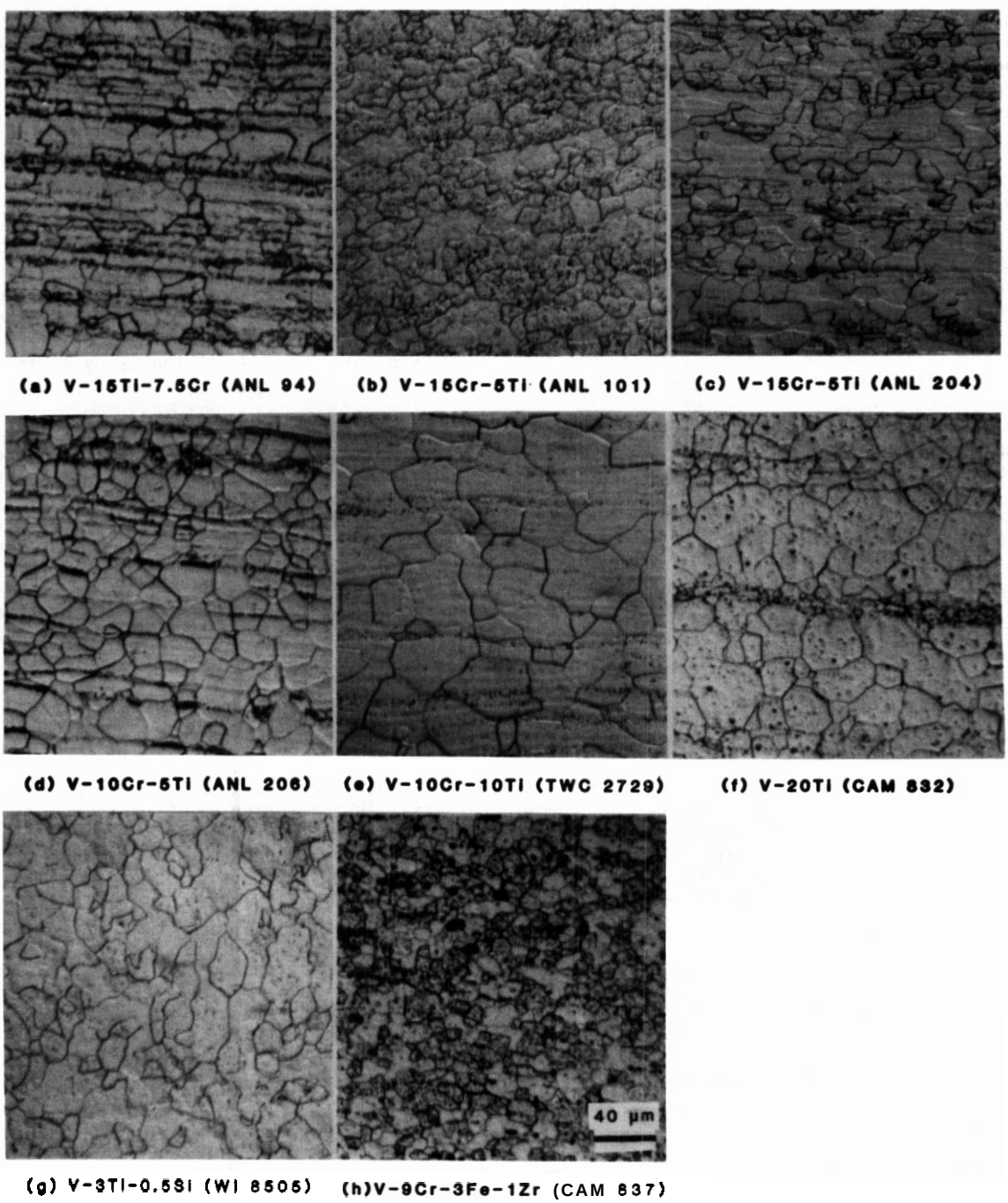

Fig. 1. Microstructures of annealed vanadim-base alloys.

The energy absorption-temperature curves in Figs. 2-8 suggest that the behavior of vanadium-base alloys on impact loading can, in general, be classified into three types, viz., (1) the transition from ductile to brittle behavior occurs abruptly over a relatively mall temperature range (25-50°C) with complete fracture of the specimens, which vas exemplified by the V-15Cr-5Ti (Fig. 2), V-10Cr-10Ti (Fig. 3), and V-10Cr-5Ti (Fig. 4) alloys; (2) the transition frm ductile to brittle behavior occurs over a relatively wide temperature range (100-150°C) with incomplete fracture of the specimens, which was exemplified by the V-15Ti-7.5Cr (Fig. 5), and V-20Ti (Fig. 7) alloys; and (3) the energy absorption-temperature curve for the alloy exhibits significant departure from the fonulim of Eq.(1) for test temperatures of 0-50°C above the DBTT, which was exemplified by the V-3Ti-0.5Si (Fig. 6) and V-9Cr-3Fe-1Zr (Fig. 8) alloys.

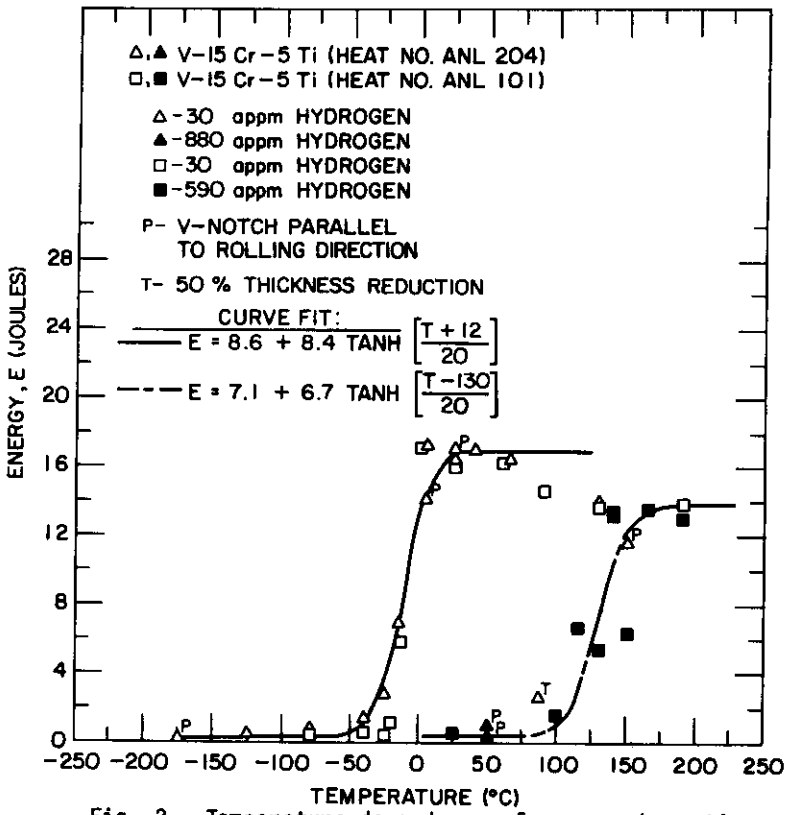

Fig. 2. Temperature dependence of energy absorption for the V-15Cr-5Ti alloy.

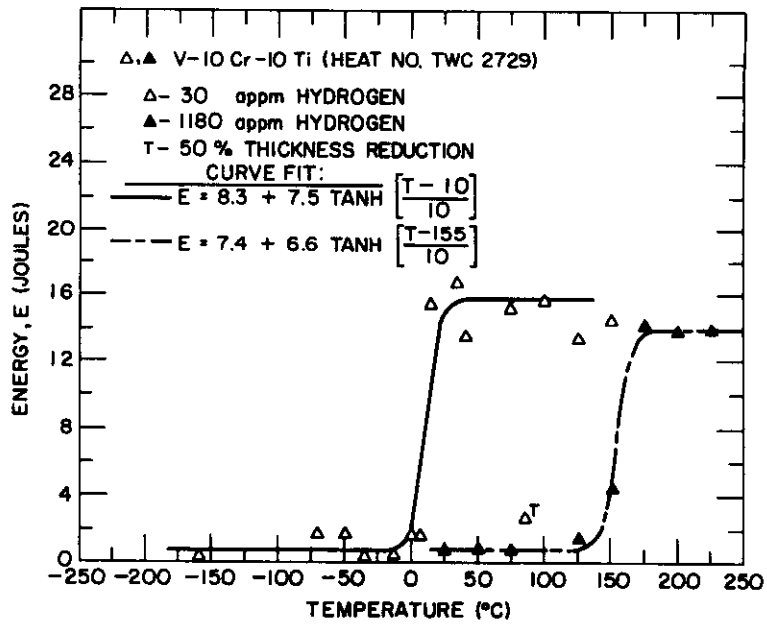

Fig. 3. Temperature dependence of energy absorption for the V-10Cr-10Ti alloy.

The DBTT for the hydrogenated and dehydrogenated vanadium-base alloys was dependent on the total concentration ($C_{Cr} + C_{Ti}^{0.95} + C_{Fe} + C_{Zr}$) of alloying elements (Fig. 9). Thus, the DBTT of a vanadium alloy increased in the order of the DBTT for the V-3Ti-0.5Si, V-9Cr-3Fe-1Zr, V-10Cr-5Ti, V-20Ti, V-15Cr-5Ti, V-10Cr-10Ti, and V-15Ti-7.5Cr alloys. A comparison of the DBTT for the V-15Cr-5Ti, V-10Cr-5Ti, and V-10Cr-10Ti alloys (Table 2) shows that the effect of the Ti solute in these alloys, in comparison with the effect

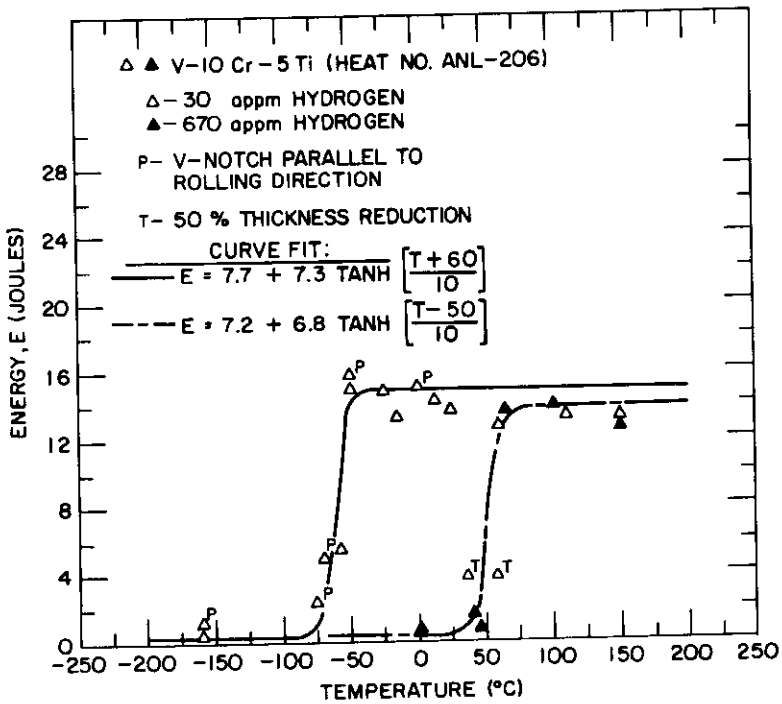

Fig. 4. Temperature dependence of energy absorption for the V-10Cr-5Ti alloy.

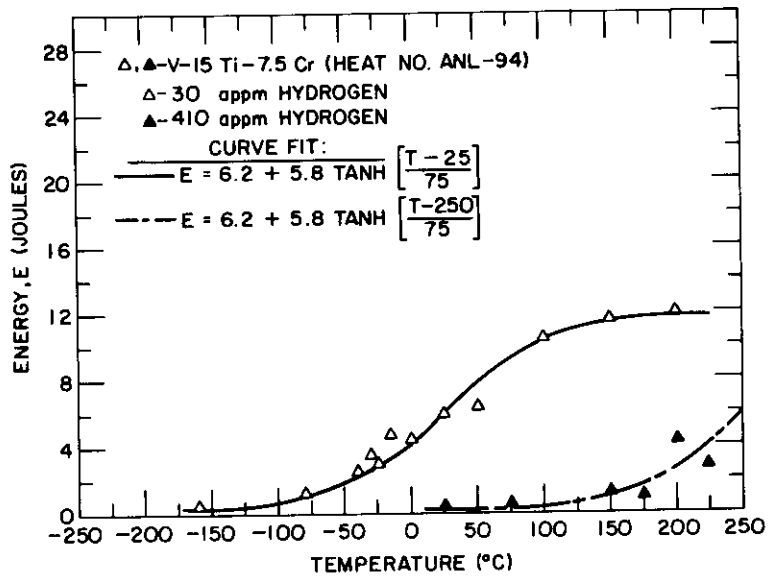

Fig. 5. Temperature dependence of energy absorption for the V-15Ti-7.5Cr alloy.

of the Cr solute, was to cause a larger increase of the DBTT. Even though a DBTT for the V-3Ti-0.5Si alloys was defined by the use of Eq.(1), the V-3Ti-0.5Si alloy fractured only by ductile tearing for Charpy test temperatures down to -190°C.

Effect of hydrogen. With the exception of the V-3Ti-0.5Si alloy, the effect on the temperature dependence of the energy absorption and on the DBTT by the introduction of hydrogen into the vanadium-base alloys was to shift the energy-temperature curves and, correspondingly, the DBTT to higher temperatures (Figs. 2-9 and Table 2). The effect of hydrogen introduction into the V-3Ti-0.5Si alloy was exceptional in that the energy-temperature curve derived from the Charpy impact tests was displaced to lower temperatures with an increase of the hydrogen concentration from 30 appm to 520 appm and to 970 appm (Fig. 6 and Table 2).

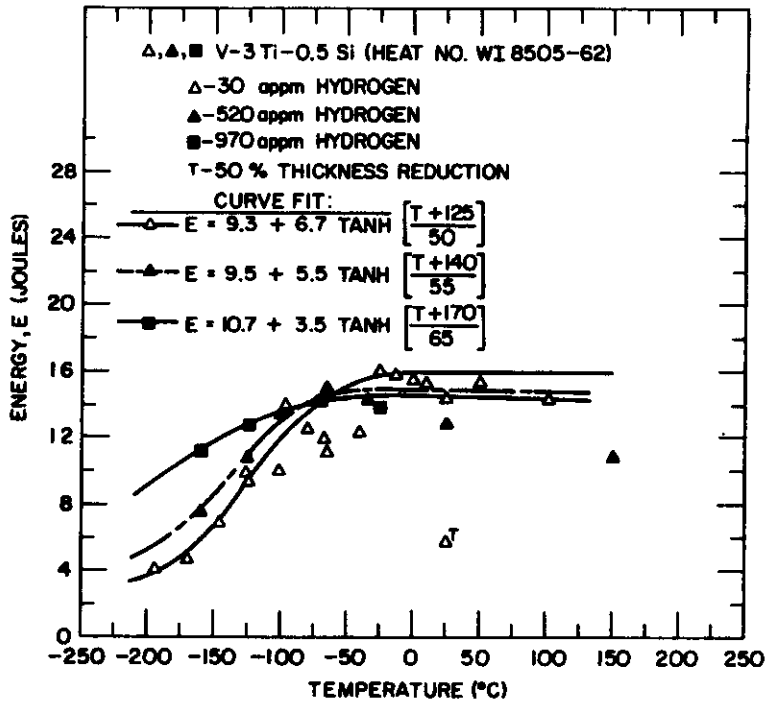

Fig. 6. Temperature dependence of energy absorption for the V-3Ti-0.5Si alloy.

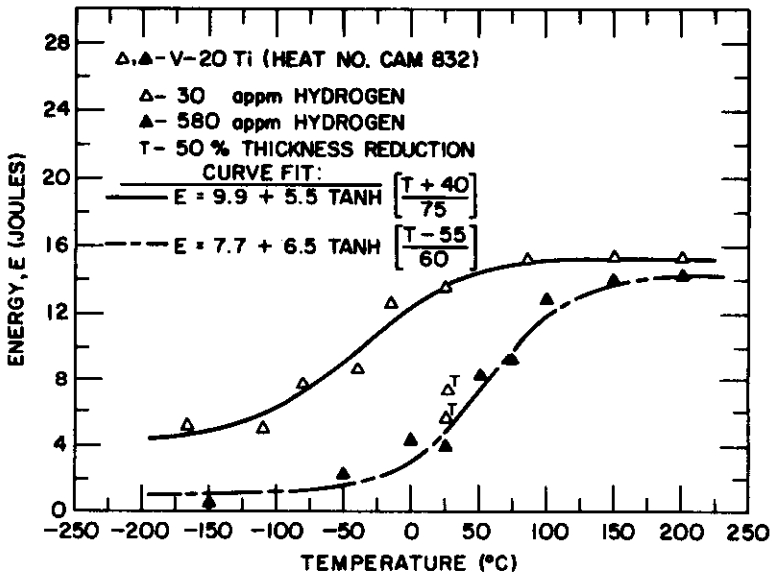

Fig. 7. Temperature dependence of energy absorption for the V-20Ti alloy.

Effect of oxygen, notch orientation, and cold work. Charpy tests were conducted on two different heats of the V-15Cr-5Ti alloy. The alloy from Heat No. ANL 101 contained 0.12 wt % oxygen whereas the alloy from Heat No. ANL 204 contained 0.03 wt % oxygen. The test results (Fig. 2) showed that specimens from both heats exhibited essentially the same response on Charpy impact testing, eventhough the microstructure of the alloy from Heat No. ANL 101 contained a much higher number density of precipitates (Fig. 1b and Fig. 1c).

In the case of the V-15Cr-5Ti and V-10Cr-5Ti alloys, specimens were tested with the V-notch oriented either perpendicular or parallel to the rolling direction. The test results (Figs. 2 and 4) showed that specimens with the different orientations had essentially the same response on Charpy impact testing, even though the microstructures of these alloys showed significant banding of precipitates in a direction that was parallel to the rolling direction (Fig. 1).

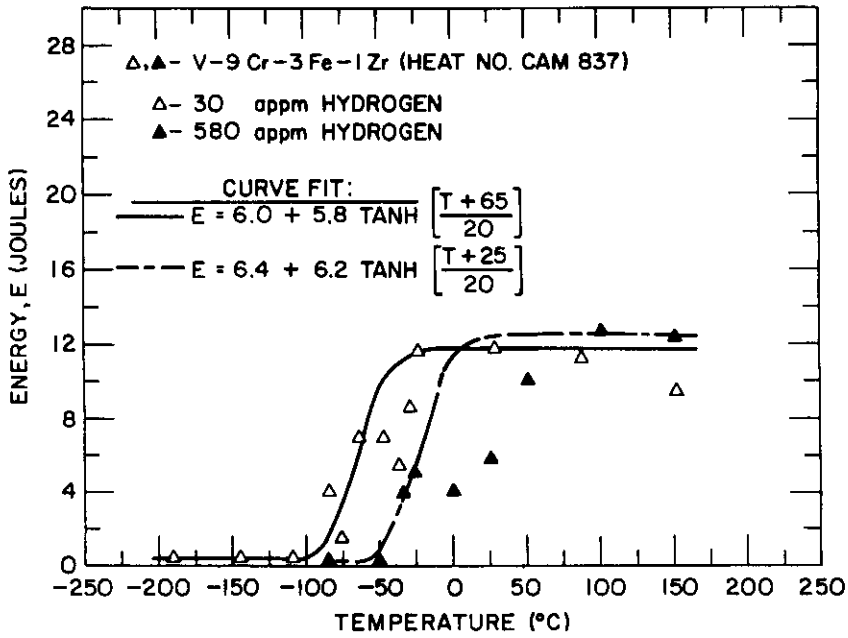

Fig. 8. Temperature dependence of energy absorption for the V-9Cr-3Fe-1Zr (Vanstar-7) alloy.

Table 2. DBTT for vanadium-base alloys

Nominal Alloy Composition	Hydrogen Conc. (appm)	DBTT (°C)	Δ DBTT (°C)
V-3Ti-0.5Si	30	-125	
"	520	-140	-15
"	970	-170	-45
V-9Cr-3Fe-1Zr	30	-65	
"	500	-25	40
V-10Cr-5Ti	30	-60	
"	670	50	110
V-20Ti	30	-40	
"	580	55	95
V-15Cr-5Ti	30	-12	
"	590	130	118
V-10Cr-10Ti	30	10	
"	1180	155	145
V-15Ti-7.5Cr	30	25	
"	410	250	225

Charpy specimens of the V-15Cr-5Ti, V-10Cr-10Ti, V-10Cr-5Ti, V-20Ti, and V-3Ti-0.5Si alloys were also tested in the 50% cold work condition. The hydrogen concentration in these specimens was approximately 32 appm. In the case of the V-15Cr-5Ti, V-10Cr-10Ti, V-20Ti, and V-10Cr-5Ti alloys, the effect of the deformation on the energy absorption during impact loading of these alloy specimens appeared, on the basis of very limited data, to be comparable to the effect of the introduction of hydrogen, i.e., a shift of the energy-temperature curve for the dehydrogenated, recrystallized alloys to higher temperatures (Figs. 2,3,4, and 7). The observed effect of deformation on the energy absorption for the V-3Ti-0.5Si alloy also suggested a significant displacement of the energy-temperature curve for the dehydrogenated, recrystallized alloy to higher temperatures, which was contrary to the observed effect of hydrogen on the energy-temperature curve (Fig. 6).

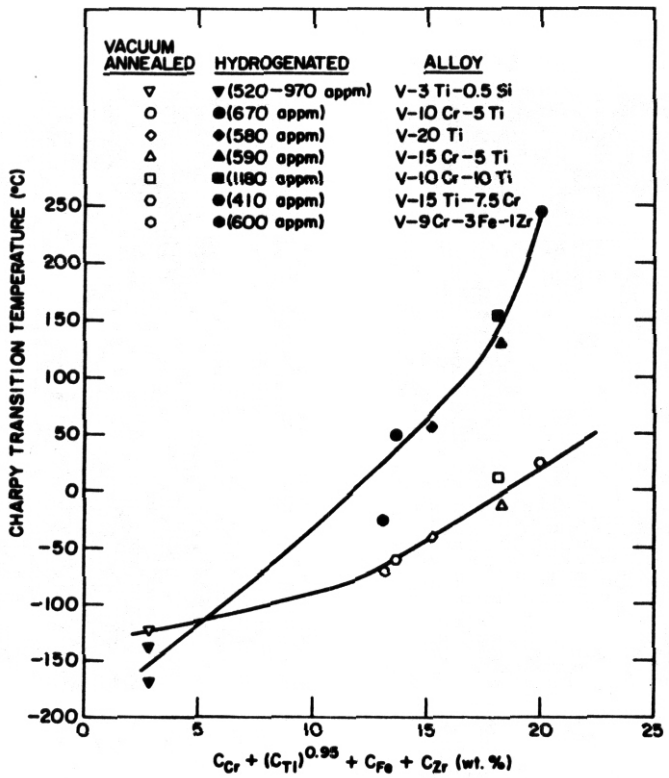

Fig. 9. Dependence of the DBTT on concentration of alloying elements.

SEM observations of fracture surfaces. The fracture surfaces from SEM observations of fractured Charpy spcimens of the V-15Cr-5Ti, V-10Cr-5Ti, V-10Cr-10Ti, V-15Ti-7.5Cr, V-20Ti, V-3Ti-0.5Si, and V-9Cr-3Fe-1Zr alloys are shown in Figs. 10-14, respectively. The SEM observations were limited to specimens that underwent impact tests at temperatures corresponding to the DBTT and the lower energy shelf; since specimens tested at temperatures on the upper energy shelf were bent to an angle of 85° without visible crack Initiation. With the exception of the V-3Ti-0.5Si alloy, fracture on the lower energy shelf for the V-15Cr-5Ti, V-10Cr-5Ti, V-10Cr-10Ti, V-15Ti-7.5Cr, V-20Ti , and V-9Cr-3Fe-1Zr alloys was dominated by transgranular cleavage. The contribution of Intergranular cleavage to the fracture of these alloys appeared to be relatively minor. The general appearance of the fracture surfaces for these alloys was not altered by the Introduction of hydrogen. i.e., fracture was daninated by transgranular cleavage.

Bands of precipitates were observed In the optical microstructures for the V-15Cr-5Ti, V-10Cr-10Ti, V-10Cr-5Ti, V-15Ti-7.5Cr, and V-20Ti alloy specimens (Fig. 1). The SEM observations of these fractured alloy specimens did not show unambiguous evidence for a correlation between bands of precipitates and crack initiation-propagation. However, the microstructures (optical) of these fractured alloy specimens showed occasional cracks that were sited in the precipitate bands and normal to the fracture surface.

Observations by SEM have not been perfonned, thus far. on the fracture surfaces for the V-15Ti-7.5Cr and V-20Ti alloy specimens that were tested at temperatures near to the DBTT to explain the broad transition temperature range for these alloys. me Charpy specimens of these alloys were only partially fractured in this tenperature range.

The fracture surfaces for the dehydrogenated and the hydrogenated V-3Ti-0.5Si alloy specimens were exceptional in that fracture was totally dominated by ductile tearing for test temperatures down to -190°C. Ductile tearing also dominated the fracture for the V-9Cr-3Fe-1Zr alloy specimens for test temperatures In the range between the DBTT and temperatures corresponding to the upper energy shelf (Fig. 14c).

The energy absorption-temperature data suggestea tnat the Ti solute in the V-Cr-Ti alloys contributed in greater measure to an increase of the DBTT for the alloys. However. the fracture behavior of these alloys suggested that the Cr solute contributed in greater measure to the susceptibility of the alloy to transgranular fracture.

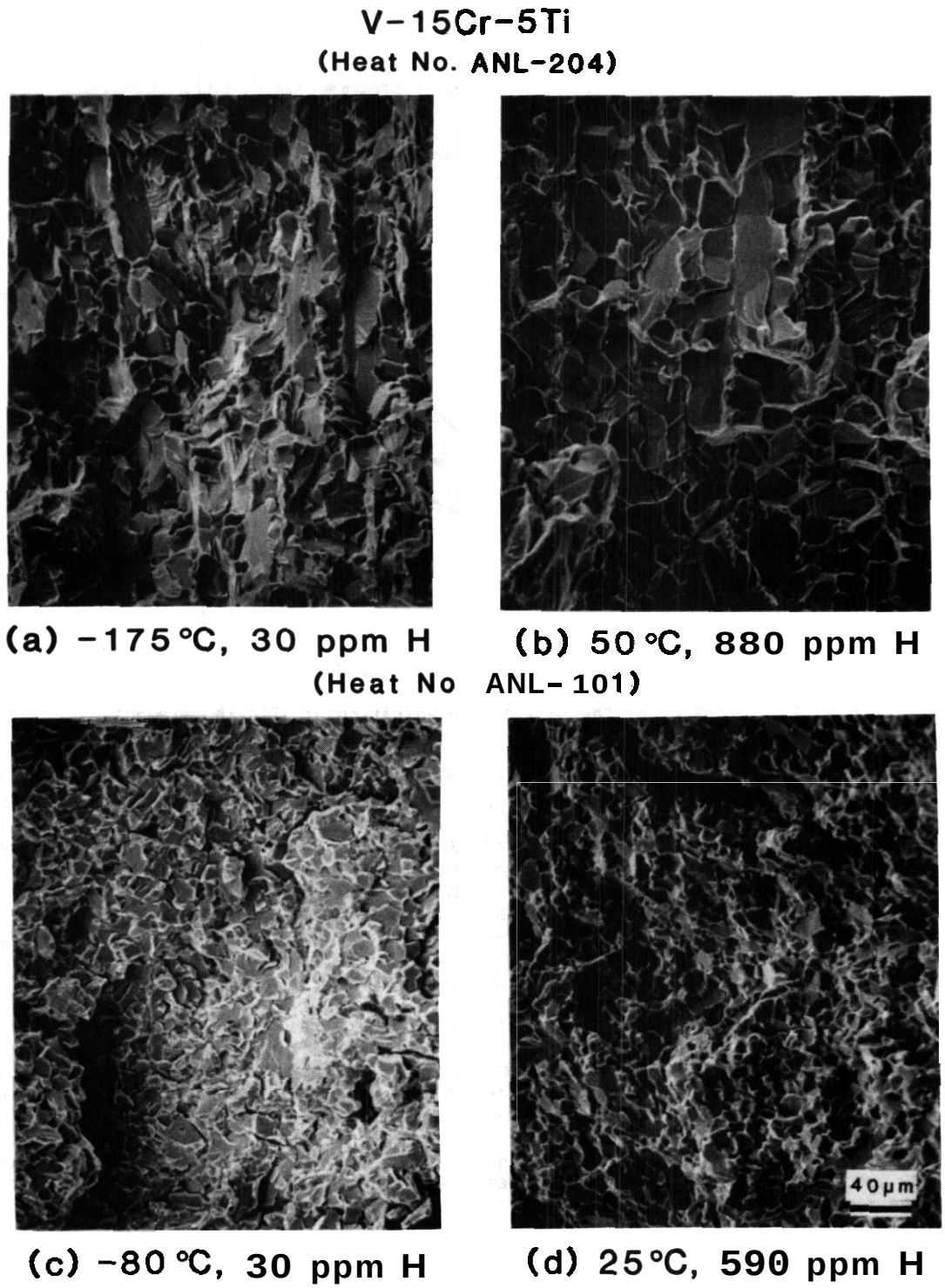

Fig. 10. Fracture surfaces for V-15Cr-5Ti Charpy specimens.

Discussion

The results of this experimental study on vanadim-base alloys utilizing impact loading (2.5 m/s) show that the DBTT for the V-3Ti-0.551, V-9Cr-3Fe-1Zr, V-10Cr-5Ti, V-20Ti, V-15Cr-5Ti, V-10Cr-10Ti, and V-15Ti-7.5Cr alloys is less than 30°C if the alloy is in the fully recrystallized. dehydrogenated (<30 appm) condition. The DBTT for the dehydrogenated alloys is dependent on the canbined concentration of alloying elements and increases from -125°C for the V-3Ti-0.5Si alloy to -12°C for the V-15Cr-5Ti alloy and to 25°C for the V-15Ti-7.5Cr alloy. With the exception of the V-3Ti-0.5Si alloy, the presence of 400-1000 appn hydrogen in these alloys causes a significant increase (40-225°C) of the DBTT for an alloy. The V-3Ti-0.5Si

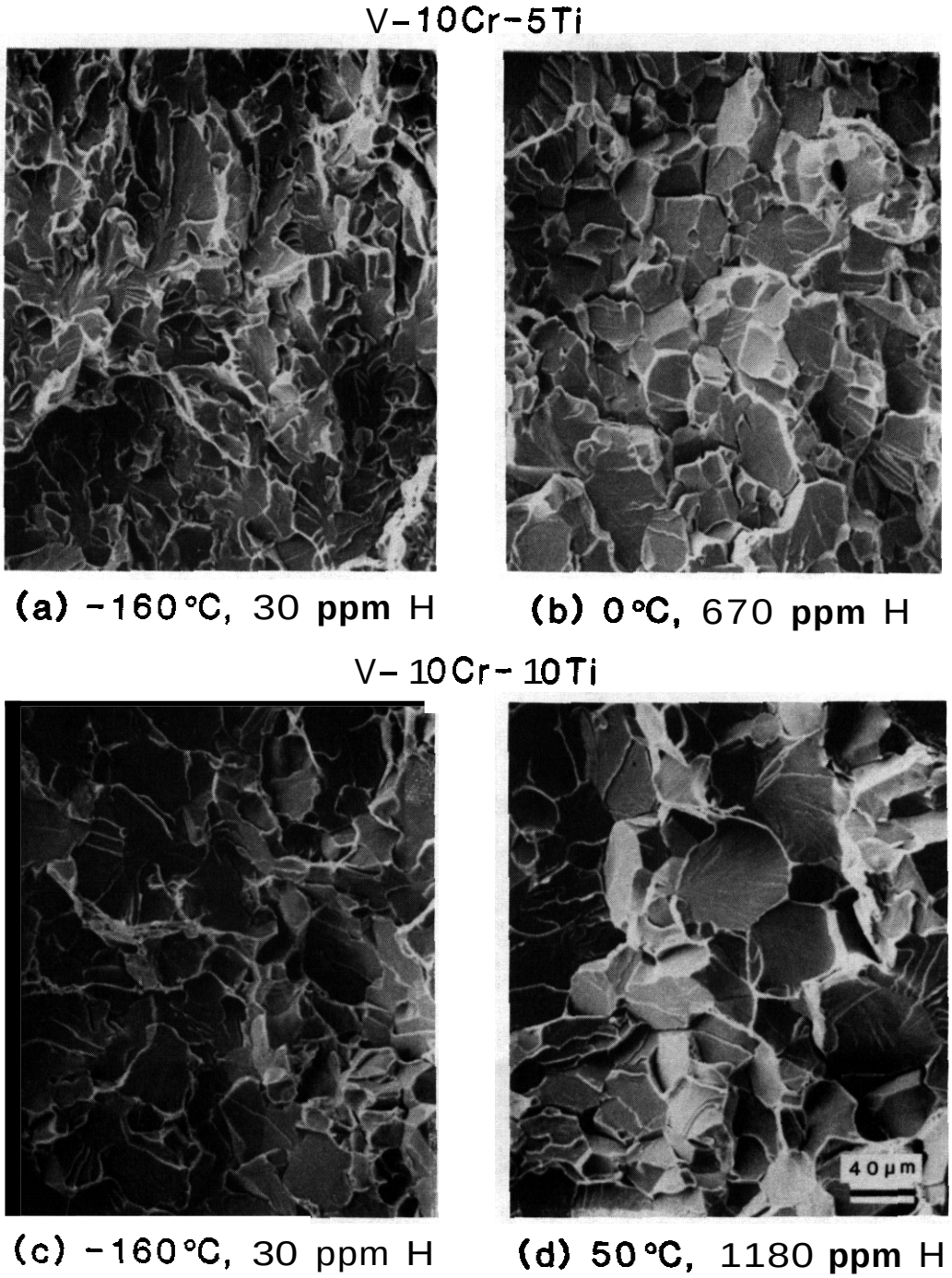

Fig. 11. Fracture surfaces for V-10Cr-5Ti and V-10Cr-10Ti Charpy specimens.

alloy is exceptional in that the DBTT for this alloy decreases for hydrogen concentrations up to at least 1000 appn. The OBTT for the hydrogenated alloys is also dependent on the combined concentration of alloying elements and increases from -170°C for the V-3Ti-0.5Si alloy to 130°C for the V-15Cr-5Ti alloy and to 225°C for the V-15Ti-7.5Cr alloy. Furthermore, there is a linear correlation (not shown) between the DBTT for the dehydrogenated and hydrogenated alloys and the tensile strength of the alloys at 25°C.[4]

The energy absorption data together with the SEM observations of fracture surfaces obtained for the V-15Cr-5Ti, V-10Cr-10Ti, and V-10Cr-5Ti alloys (with the thermomechanical treatment and impurity content for this study) are interpreted to show that these alloys have a low intrinsic resistance to crack propagation. A similar conclusion regarding the resistance to crack propagation on Charpy impact testing of the V-15Cr-5Ti alloy was previously reported by Cannon, et al.[1]

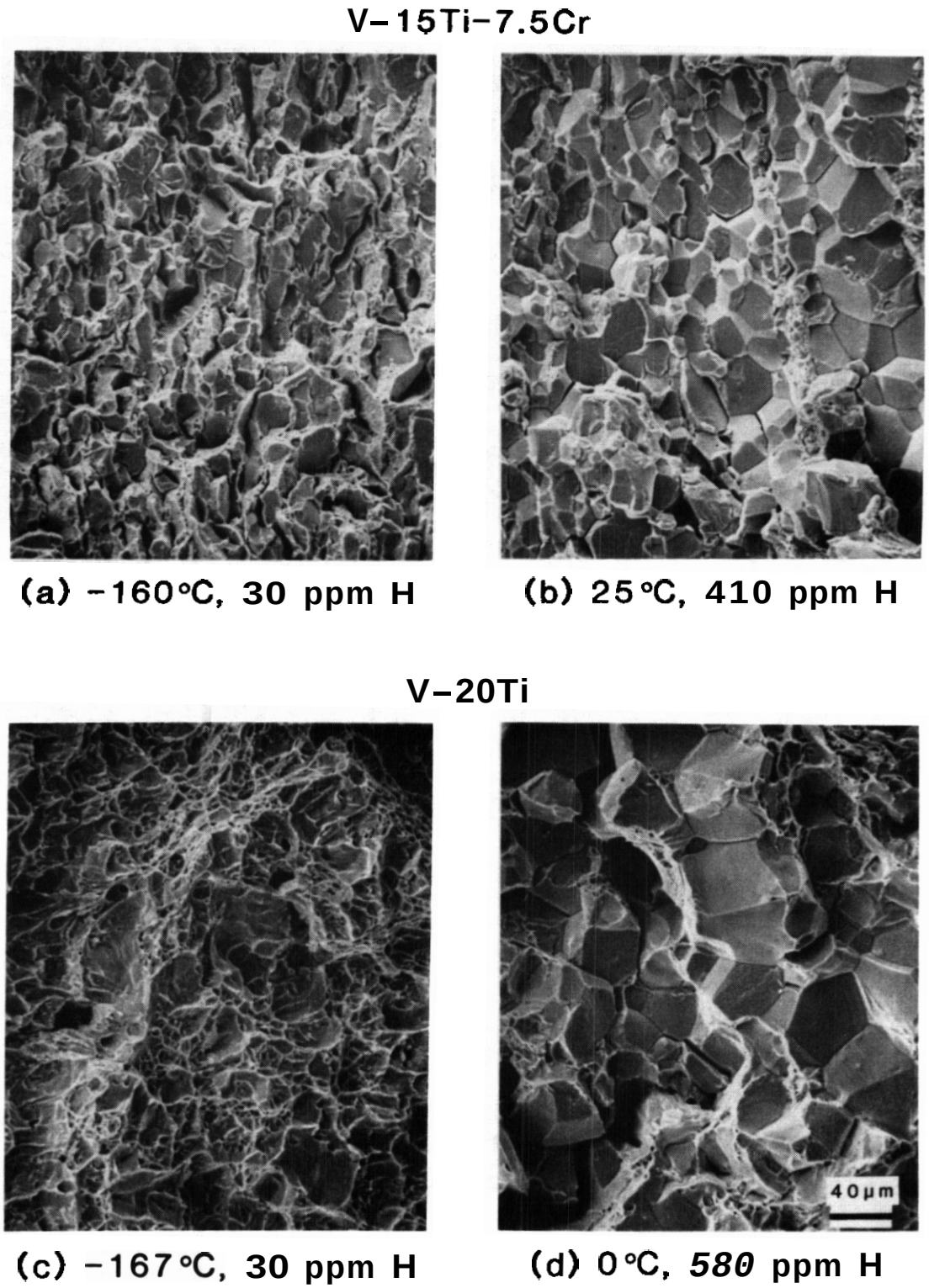

Fig. 12. Fracture surfaces for V-15Ti-7.5Cr and V-20Ti Charpy specimens.

The data and observations for the V-3Ti-0.5Si, V-9Cr-3Fe-1Zr, V-20Ti, and V-15Ti-7.5Cr alloys are interpreted to show that these alloys have an inherent resistance to crack propagation. Results have been reported on tensile tests for the V-3Ti-1Si, V-9Cr-3Fe-1Zr, and V-20Ti alloys after neutron irradiation at 400-600°C to damage levels of 10-90 dpa.[2,5] These results also show that the V-3Ti-1Si, V-9Cr-3Fe-1Zr, and V-20Ti alloys, in canparison to the V-15Cr-5Ti alloy, have significantly greater ductility, i.e., resistance to crack propagation.

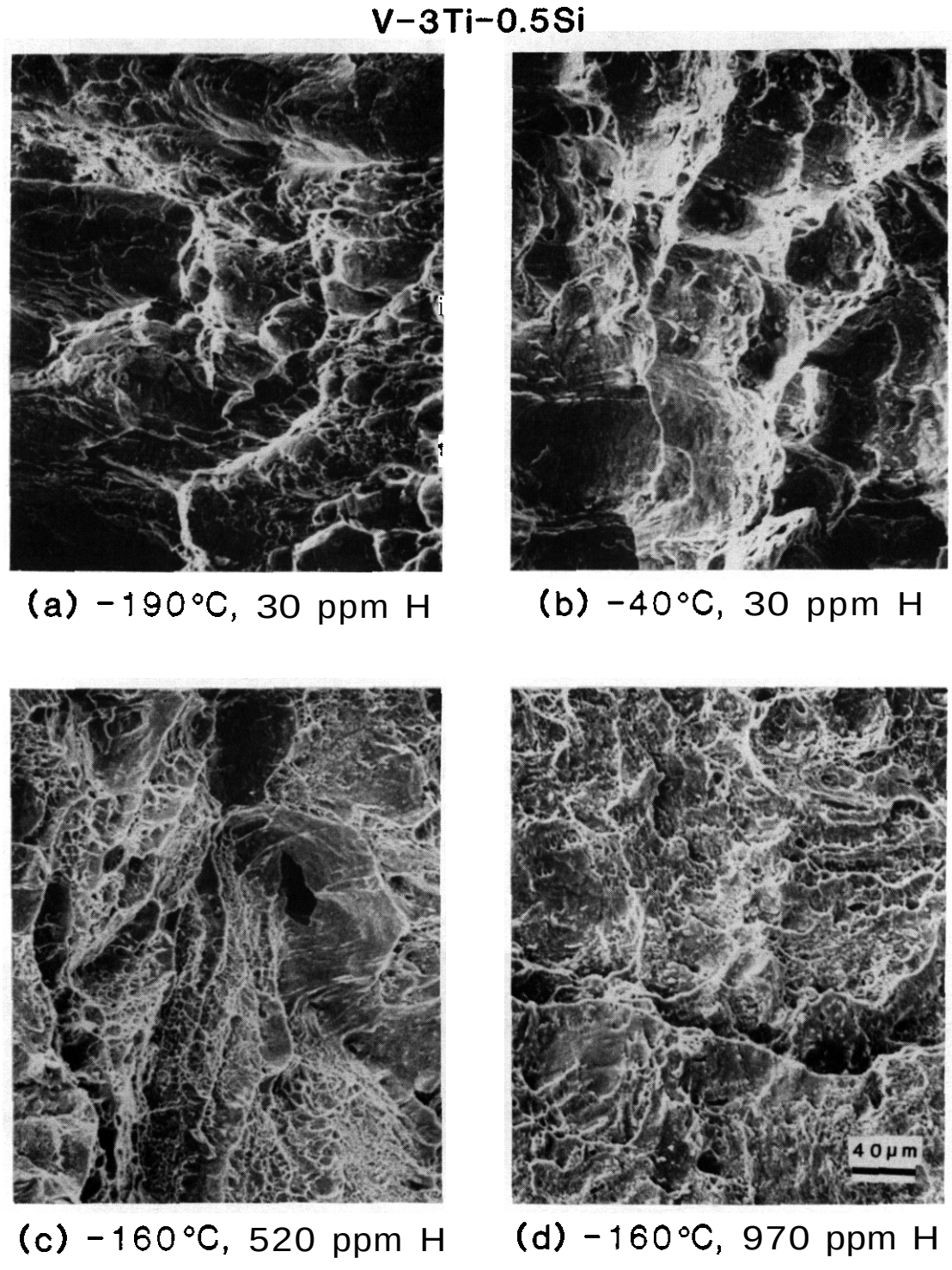

Fig. 13. Fracture surfaces for V-3Ti-0.5Si Charpy specimens.

The energy absorption-temperature data suggest that the Ti solute in the V-Cr-Ti alloys contributes in greater measure to an increase of the DBTT. However, the fracture behavior of these alloys on impact loading suggests that the Cr solute contributes in greater measure to the susceptibility of the alloy to transgranular fracture.

Resistance to crack propagation in a structural material is a mechanical property of paramount importance for a fusion reactor. The low resistance of the V-15Cr-5Ti, V-10Cr-10Ti, and the V-10Cr-5Ti alloys to crack propagation might be attributed to banding of precipitates, interstitial impurity concentration, or

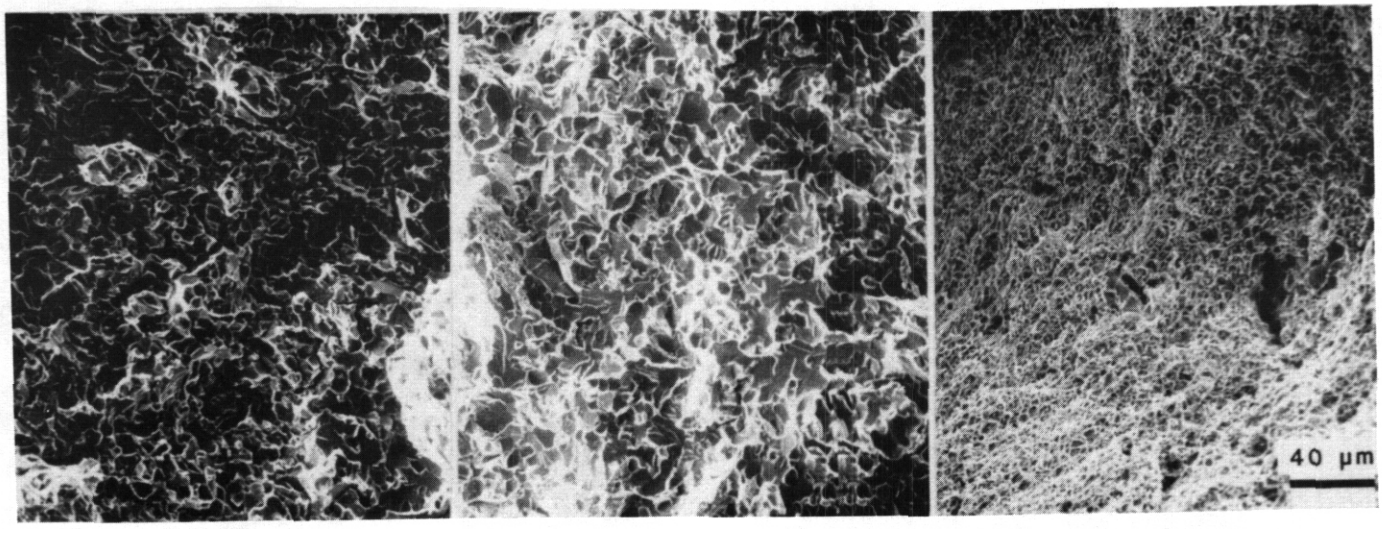

(a) −190°C. 30 ppm H (b) −50°C, 500 ppm H (c) 50°C, 500 ppm H

Fig. 14. Fracture surfaces for V-9Cr-3Fe-1Zr (Vanstar-7) charpy specimens.

segregation of impurities to grain boundaries. In the present study, different orientations of the notch in the Charpy specimens and substantially different oxygen impurity concentrations in the alloys did not significantly change the energy absorption-temperature curves. Moreover. there was an absence of significant intergranular fracture in these alloys. Therefore, we are not encouraged to believe that the resistance to crack propagation in the V-15Cr-5Ti, V-10Cr-10Ti, and V-10Cr-5Ti alloys can be substantially improved by minor canpositional and thermomechanical modifications.

CONCLUSIONS

1. The OBTT for the V-3Ti-0.5Si, V-9Cr-3Fe-1Zr, V-10Cr-5Ti, V-20Ti, V-15Cr-5Ti, V-10Cr-10Ti, and V-15Ti-7.5Cr alloys Is less than 30°C on impact loading if the alloy is in the fully recrystallized, dehydrogenated condition.

2. The presence of 400-1000 appn hydrogen in the V-9Cr-3Fe-1Zr, V-10Cr-5Ti, V-20Ti, V-15Cr-5Ti, V-10Cr-10Ti, and V-15Ti-7.5Cr alloys causes a significant increase (40-225°C) of the OBTT on impact loading of the alloy.

3. The OBTT for the V-3Ti-0.5Si alloy on impact loading decreases with an increase of the hydrogen concentratfon up to at least 1000 appn.

4. The OBTT for vanadiun-base alloys on impact loading is dependent on the combined concentration of alloying elenents.

5. The V-15Cr-5Ti, V-10Cr-10Ti, and V-10Cr-5Ti alloys on impact loading have a low Intrinsic resistance to crack propagation.

6. The V-3Ti-0.5Si, V-9Cr-3Fe-1Zr, V-20Ti, and V-15Ti-7.5Cr alloys have an inherent resistance to crack propagation.

FUTURE EFFORT

Charpy impact and tensile specimens of the vanadiun-base alloys considered in this report will be tested after retrieval from the FFTF-MOTA.

REFERENCES

1. N. S. Cannon, M. L. Hamilton, A M. Ermi, D. S. Gelles, and W. L. Hu, "Influence of Neutron Irradiation on the Charpy Impact Properties of V-15Cr-5Ti", Fusion Reactor Materials, Semiannual Progress Report for Period Ending September 30, 1937, DOE/ER-0313/3, U. S. Department of Energy, Office of Fusion Energy, pp. 239-245.

2. D. N. Braski, "The Tensile Properties of Several Vanadiun Alloys after Irradiation to 90 DPA in FFTF", Fusion Reactor Materials. Semiannual Progress Report for Period Ending September 30, 1987, DOE/ER-0313/3, U. S. Department of Energy, Office of Fusion Energy, pp. 235-238.

3. 8. A Loomis, A. B. Hull, O. K. Chopra, and D. L. Smith, "Hydrogen Concentration Distribution in Vanadiun-Ease Alloys after Surface Preparation and Exposure to Liquid Lithiun", Fusion Reactor Materials, Smiannual Progress Report for Period Ending March 31, 1988, DOE/ER-0313/4, U. S. Department of Energy, Office of Fusion Energy, pp. 160-167.

4. B. A. Loomis, R. H. Lee, and D. L. Smith, "Strength, Ductility, and Ductile-Brittle Transition Temperature for MFR Candidate Vanadiun Alloys", Fusion Reactor Materials, Smiannual Progress Report for Period Ending September 30,1937, DOE/ER-0313/3, U. S. Department of Energy, Office of Fusion Energy, pp. 246-253.

5. D. N Braski, "The Effect of Neutron Irradiation on Vanadiun Alloys", J. Nucl. Mater. 141-143, 1125 (1986).

THE SWELLING BEHAVIOR OF VANADIUM ALLOYS AT DAMAGE LEVELS UP TO 124 dpa — O. N. Braski (Oak Ridge National Laboratory)

OBJECTIVE

The goal of this research is to investigate the effects of neutron irradiation and helium generation on the microstructure of vanadium alloys.

SUMMARY

After irradiation at 420°C to 124 dpa, V-15Cr-5Ti and VANSTAR-7 exhibited negligible swelling, while V-3Ti-1Si and V-20Ti had swelling values of 0.64 and 1.12%, respectively. Helium, preimplanted to a level of 480 appm via the tritium trick, increased the swelling in V-3Ti-1Si to about 2.5%. V-3Ti-1Si disks irradiated at 520 and 600°C to 26 and 43 dpa, respectively, also exhibited relatively low swelling. Warm-working the alloy before irradiation reduced swelling at 520°C, but slightly increased swelling at 600°C where recovery occurred.

PROGRESS AND STATUS

Experimental

The source, chemical composition, and final heat treatment for each vanadium alloy are listed in Table 1. Note that two different heats of V-3Ti-1Si have been investigated. Disks (3 mm-diam) for transmission electron microscopy (TEM) were punched from 0.25-mm-thick sheets of each alloy. Some of the disks were doped with ^3He using a mdified version of the "tritium trick" technique where the specimens are held at 400°C during the decay of ^3H to ^3He.[1] One V-15Cr-5Ti disk was implanted with 100 appm ^4He at 420°C using the 102 MeV accelerator at the KFK Karlsruhe, West Germany.

Table 1. Vanadium allov data

Alloy	Heat	Composition, wt %								Final Heat Treatment
		Cr	Ti	Fe	Zr	Si	C	O	N	
V-15Cr-5Ti[a]	CAM-834-3	14.5	6.2				0.032	0.031	0.046	1 h at 1200°C
VANSTAR-7[a]	CAM-837-7	9.1		3.4	1.3		0.064	0.028	0.052	1 h at 1350°C
V-3Ti-1Si[b]	11153		3.4	0.04		1.28	0.045	0.091	0.026	1 h at 1050°C
V-20Ti	CAM-832		20.3				0.020	0.039	0.044	1 h at 1100°C
V-3Ti-1Si[c]	10837		3.2			1.0		0.015		1 h at 1050°C

[a]Source: Westinghouse Electric Corporation.
[b]Source: KFK, Karlsruhe, West Germany (Or. D. Kaletta).
[c]Source: ORNL.

The disks were encapsulated in TZM tubes containing ^7Li. Ouplicate disks were similarly encapsulated and thermally aged at the irradiation temperatures to provide control specimens for the experiment. However, the control specimens have not yet been examined and will, therefore, not be reported at this time. The capsules were irradiated in the FFTF, Materials Open Test Assembly (MOTA) at temperatures of 420, 520, and 600°C. and damage levels up to 124 dpa. Both the encapsulations and the irradiations were provided by the Westinghouse Hanford Corporation, Richland, Washington.

Following the irradiation, the capsules were cut open and the lithium dissolved away using liquid ammonia. The disks were further cleaned in successive baths of: (1) ethyl alcohol and water (1:1, by volume), (2) water, and (3) pure ethyl alcohol. The disks were polished for examination by TEM by employing a dual jet apparatus with a solution of conc. H_2SO_4 and methanol (1:7, by volume) at −30°C.

Cavity swelling was determined by measuring and counting cavities that were observed in the TEM micrographs, with a Zeiss particle-size analyzer. Foil thickness was measured using stereo techniques. A value for cavity swelling was calculated using the expression:

$$\Delta V/V_0 = \Delta V/(V_f - \Delta V),$$

where ΔV is the total cavity volume, V_0 is the original metal volume, and V_f is the final volume of the foil.

Results

Swelling results from two separate MOTA experiments are presented in Table 2. The first experiment, using capsule V403, is a continuation of the original screening study which includes the alloys: V-15Cr-5Ti, VANSTAR-7, and V-3Ti-1Si. A few TEM disks of V-20Ti were also included, but always without implanted helium. This capsule was irradiated at 420°C to a damage level of 124 dpa. The two capsules at 520 and 600°C were removed from the reactor before this damage level was reached because of over-temperature excursions. The second experiment concentrated on an ORNL heat of V-3Ti-1Si, with specimens (SS-3 tensile and TEM disks) in annealed and 50% warm-worked conditions. Some specimens of each condition were also preimplanted with ^3He (using the tritium trick) to levels that would give an approximate ratio of 5 appm He to 1 dpa at the time of removal from FFTF. Table 2 shows the swelling results for 520°C (V524) and 600°C (V631); all of the specimens from the 420°C capsule were, for some still undetermined reason, unable to be successfully polished.

Table 2. Swelling results

Capsule No.	Irradiation Temperature (°C)	Damage Level (dpa)	Alloy	Disk No.	Helium[a] Level (appm)	Swelling (%)
V403	420	124	V-15Cr-5Ti	RA41	0	<0.01
V403	420	124	V-15Cr-5Ti	RA73	14	<0.01
V403	420	124	V-15Cr-5Ti	RA37	80	<0.01
V403	420	124	V-15Cr-5Ti	RA13	300	0.01
V403	420	124	V-15Cr-5Ti	A16	100 (^4He)	<0.01
V403	420	124	VANSTAR-7	QA11	0	<0.01
V403	420	124	VANSTAR-7	QA38	8	0.02
V403	420	124	VANSTAR-7	QA39	42	<0.01
V403	420	124	VANSTAR-7	QA18	150	0.01
V403	420	124	V-3Ti-1Si[b]	85	0	0.64
V403	420	124	V-3Ti-1Si[b]	70	23	1.46
V403	420	124	V-3Ti-1Si[b]	78	135	2.39
V403	420	124	V-3Ti-1Si[b]	23	480	2.54
V403	420	124	V-20Ti	WA11	0	1.12
v524	520	26	V-3Ti-1Si[c]	R27	0	0.09
v524	520	26	V-3Ti-1Si[c]	R12	232	1.06
v524	520	26	V-3Ti-1Si[c]	R22	232	0.22
v524	520	26	V-20Ti	WB23	0	<0.01
V631	600	43	V-3Ti-1Si[b]	R39	n	0.06
V631	600	43	V-3Ti-1Si[b]	R44	232	0.02
V631	600	43		v43	232	0.25
V631	600	43	V-20Ti	WB55	0	t0.01

[a]Values not corrected for ^3He "burnup."
[b]Heat 11153.
[c]Heat 10837.

Capsule V403

Looking at the swelling results in Table 2, it is seen that the V-15Cr-5Ti and VANSTAR-7 alloys exhibited negligible swelling, even after 124 dpa. and with helium levels as high as 300 and 150 appm, respectively. However, the reader is reminded that less than one-third of the ^3He is actually left in the specimen at this damage level due to its conversion back to ^3H by the reaction, $^3He(n,p)^3H$ (ref. *2*). Nevertheless, the resistance to swelling demonstrated by these two alloys is quite impressive compared to nearly any other structural alloy. This outstanding performance at 420°C must be tempered with the knowledge that at least one of the alloys, namely VANSTAR-7, showed signlficant swelling at 520°C after only 40 dpa.[3] The good swelling resistance of V-15Cr-5Ti was seen earlier by Loomis[4] in ion bombardment experiments at 725°C.

The swelling results for V-3Ti-1Si (Table 2), after 124 dpa. show good continuity with those for the same alloy reported earlier for 82 dpa.[5] Swelling is plotted graphically as a function of helium level in Fig. 1, along with the number densities and sizes of the cavities. The broken curves from the earlier

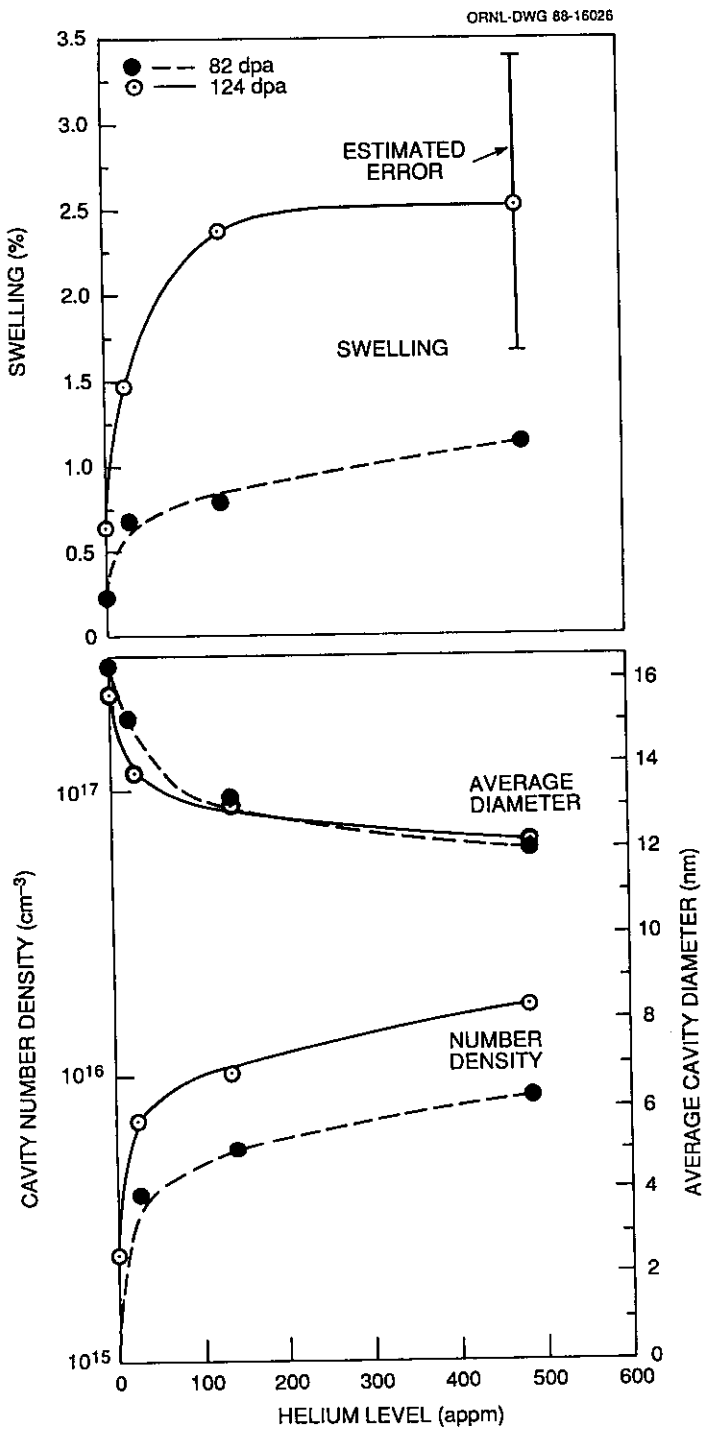

Fig. 1. Swelling, cavity number density, and average cavity diameter as a function of helium level in V–3Ti–1Si after irradiation in FFTF at 420°C to 124 dpa. Broken curves show the same parameters after 82 dpa under similar irradiation conditions.

82 dpa data are also shown for comparison. As in the lower damage level case, the swelling after 124 dpa increases rapidly with helium level at first, and then saturates. After 82 dpa, the maximum swelling reached about 1%, while a value of about 2.5% was measured after 124 dpa. Since the cavity sizes for specimens at both damage levels were nearly the same (see Fig. 1), the increase in swelling (for the 124 dpa specimens) was due to the increased number densities of cavities.

The swelling value of 1.12% for V-20Ti (Table 2) was only slightly greater than the 0.96% observed after 82 dpa.[5] However, since this value was measured in a specimen not containing helium, it puts the V-20Ti alloy in the position of being the highest swelling of the four alloys investigated. Even then, V-20Ti would be classed a low-swelling alloy when compared to other metallic alloy systems such as the austenitic and ferritic stainless steels, copper alloys, etc.[6] A comparison of the microstructures of the four vanadium alloys after irradiation at 420°C to 124 dpa is shown in Fig. 2. There were no obvious irradiation-induced precipitate phases in any of the four alloys.

Capsule V524

The V-3Ti-1Si disks in this capsule were irradiated at 520°C to a damage level of about 26 dpa. For this relatively low damage level, the swelling was quite high, especially in the presence of helium as evidenced by the 1.06% swelling value for disk R12 (see Table 2). Swelling was reduced markedly by warm working the microstructure before irradiation as shown by the result for V22. The micrographs showing the microstructures for both of these disks are presented in Fig. 3. A rod-like precipitate phase was observed in this heat of V-3Ti-1Si that was not observed in the heat supplied by KFK Karlsruhe, even after 124 dpa. More TEM analysis is needed to ascertain whether the phase was radiation-induced.

Capsule V631

After irrradiation at 600°C to 43 dpa, the amount of swelling in V-3Ti-1Si was generally lower than at 520°C, especially in the presence of helium (compare R44 with R12, Table 2). On the other hand, the warm-worked disk, V43 [Fig. 4(b)], exibited somewhat higher swelling than the annealed R44 [Fig. 4(a)]. This latter result seemed to conflict with that obtained at 520°C, until it was apparent that the warm-worked microstructure had undergone substantial recovery to form a cell structure as shown in Fig. 4(b). The recovery process, which may have taken place early in the irradiation, encouraged the growth of cavities along the subgrain boundaries.

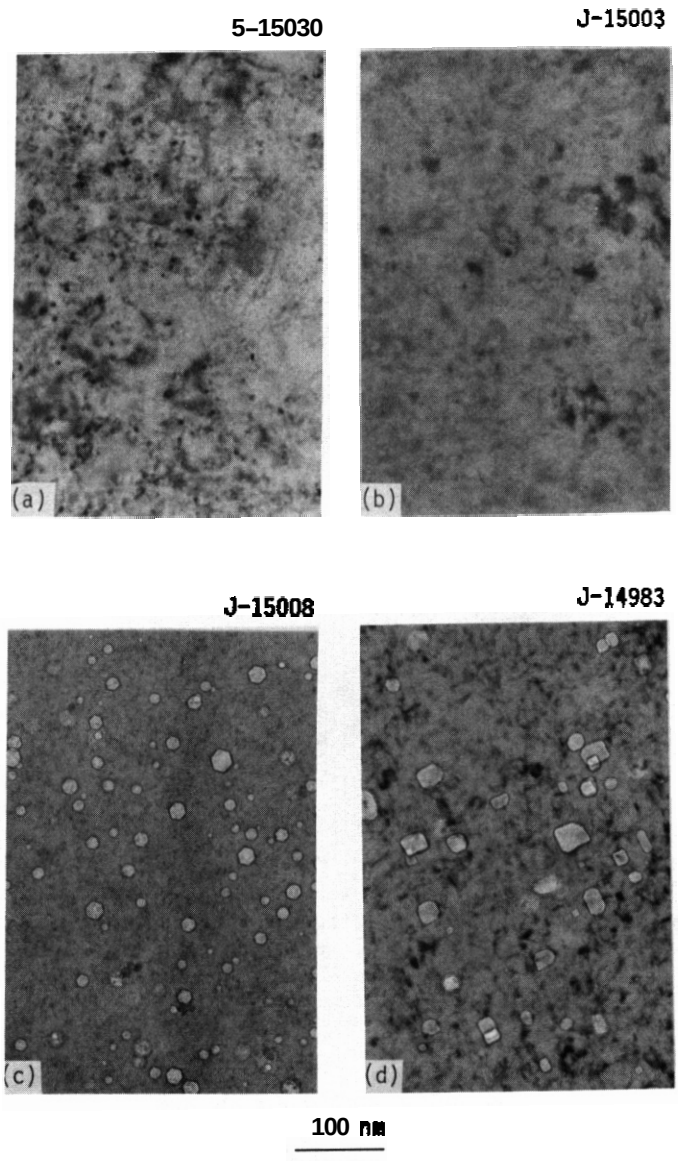

Fig. 2. Comparison of microstructure in (a) V-15Cr-5Ti, (b) VANSTAR-7, (c) V-3Ti-1Si, and (d) V-20Ti, after irradiation in FFTF at 420°C to 124 dpa. Specimens do not contain preimplanted helium.

REFERENCES

1. D. N. Braski and D. W. Ramey, pp. 1211-24 in Effects of Radiation on Materials: 12th Inter. Symp. (Part II), ASTM STP 870, F. A. Garner and J. S. Perrin, Eds., American Society for Testing and Materials, Philadelphia, 1985.

2. L. R. Greenwood, Argonne National Laboratory, private comnunication, July 19, 1983.

3. D. N. Braski, pp. 271-90 in Influence of Radiation on Material Properties: 13th Inter. Symp. part II), ASTM STP 956, F. A. Garner, C. H. Henager, Jr., and N. Igata, Eds., American Society for Testing and Materials, Philadelphia, 1987.

4. B. A. Loomis and D. L. Smith, pp. 66-71 in ADIP Semiannu. Prog. Rep. March 31, 1984, DOE/ER-0045/12, USDOE Office of Fusion Energy.

5. D. N. Braski, pp. 168-72 in Fusion Reactor Materials Semiannu. Prog. Rep. March 31, 1988, DOE/ER-0313/4, USDOE Office of Fusion Energy.

6. B. A. Loomis, pp. 62-67 in ADIP Semiannu. Prog. Rep. March 31, 1985, DOE/ER-0045/14, USDOE Dffice of Fusion Energy.

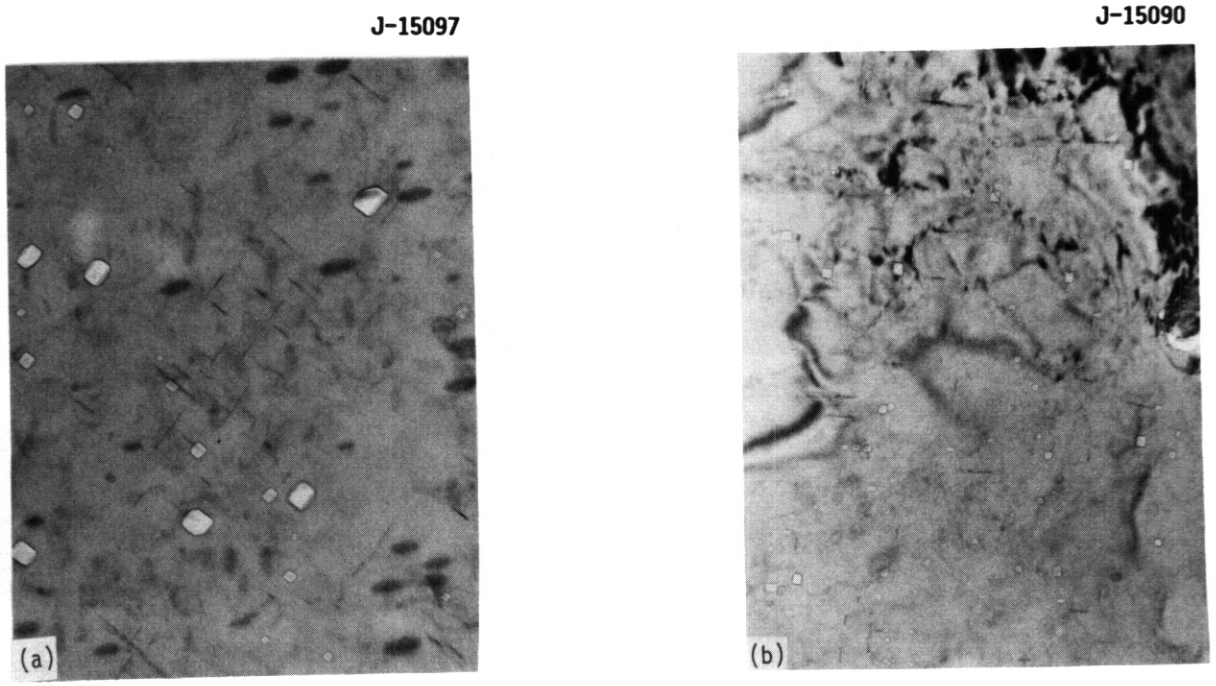

Fig. 3. Cavities in (a) annealed V-3Ti-1Si and (b) Warm-worked V-3Ti-1Si, after irradiation in FFTF at 520°C to 26 dpa. Both specimens were preimplanted with 232 appm ^{3}He. Note small rod-like precipitate particles.

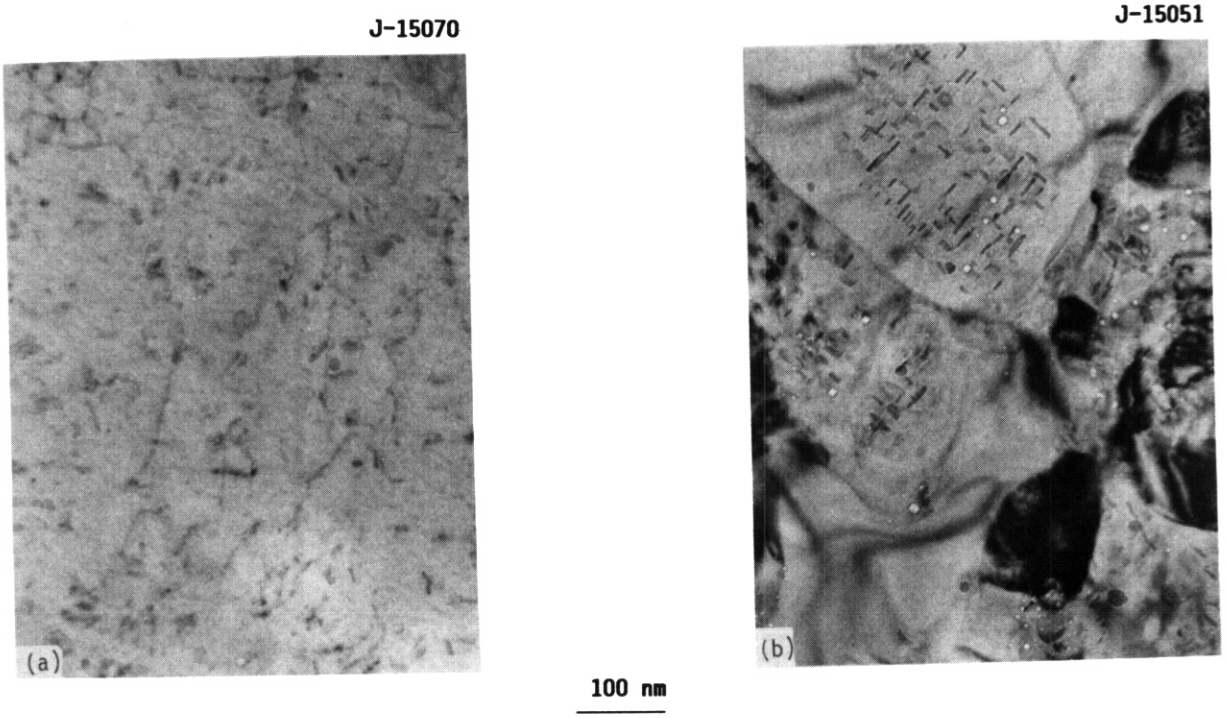

Fig. 4, Cavities in (a) annealed V-3Ti-1Si, and (b) Warm-worked V-3Ti-1Si, after irradiation in FFTF at 600°C to 43 dpa. Both specimens were preimplanted with 232 appm ^{3}He.

6.4 Copper Alloys

MECHANICAL PROPERTY CHANGES IN AN ION IRRADIATED HIGH STRENGTH COPPER ALLOY - D. H. Plantz, R. A. Oodd and G L. Kulcinski (University of Wisconsin-Madison)

OBJECTIVE

The objective of this study is to investigate the effect of heavy-ion irradiation and thermomechanical treatment on the mechanical properties of Cu-1.5% Ni-0.3% Be via microindentation techniques.

SUMMARY

Mechanical property changes in a high-strength copper alloy as a result of 14 MeV Cu ion irradiation have been investigated using a recently developed Mechanical Properties Microprobe (MPM). A Cu-1.5% Ni-0.3% Be alloy was irradiated in both the cold worked and aged, and the solution annealed and aged condition, to a peak damage dose of 40 dpa (10 dpa at 1 μm) over the temperature range of 100°C to 500°C. Ultra-low load microindentation hardness changes were measured parallel to the ion beam and perpendicular to the beam direction, the latter being made possible by cross-section techniques. Both thermally-induced and radiation-enhanced softening was observed in the cold-worked and aged material and the amount of softening increased as temperature increased. Irradiation had very little effect on the solution-annealed and aged material and only at 500°C was any thermally induced softening observed.

PROGRESS AND STATUS

Introduction

High damage rates associated with heavy ion irradiation have allowed scientists to study the effect of high damage levels in capper alloys.[1-4] However, until recently only neutron irradiation has been used in the investigation of radiation effects on mechanical properties in these alloys.[5-7] The limited damage region of heavy ion irradiation (typically ~ 1 μm deep) limits the usefulness of conventional mechanical property tests. A new technique has recently been developed which allows for direct measurements of mechanical properties in this narrow damage zone.[8] This technique has been used to investigate thermal and heavy ion irradiation effects on the hardness and elastic modulus of a Cu-Ni-Be alloy.

Experimental

High purity Cu-1.5% Ni-0.3% Be was received in the 20% cold-worked and aged condition.[9] Some of the alloy was solution annealed at 950°C and then aged for three hours at 482°C. Samples, of dimension 5 x 10 mm, were mechanically polished to an 0.05 μm finish and then electrapolished in a solution of 67% CH_3OH and 33% HNO_3 at 5 V and -40°C. Irradiation with 14 MeV Cu^{3+} was done using the tandem Van de Graaf accelerator facility at the University of Wisconsin-Madison.[3] The irradiations were done over the temperature range of 100-500°C to 10 dpa at 1 um (40 dpa at peak) to a maximum depth of about 3 μm.[3] The samples were masked such that only a 3 mm diameter area was irradiated. Irradiated samples for cross-sectional analysis were prepared using standard techniques.[10] These cross-section samples were subsequently mechanically polished to a 0.05 μm finish and then electropolished at -30 to -40°C for 2 to 3 seconds.

The mechanical properties microprobe (MPM) used for the hardness and modulus measurements consists of a fully automated, ultra-low load microindentation hardness tester.[11,12] Figure 1 is a schematic of the MPN. Loading is applied via a current source. and displacement is measured by the voltage across a capacitor. Load and displacement are monitored continuously with a resolution of 2.5 μN (250 μg) and 0.4 nm respectively. Indents are made using a Eerkovitch triangular pyramid which has an indent depth to projected area relation the same as a Vickers pyramid. A typical load versus displacement curve is shown in Fig. 2. Hardness under load (i.e. uncorrected for elastic effects) is defined as $H=AL/d^2$, where d is a depth on the loading curve, L is the load at that depth and A is a geometric factor relating depth to projected area of the indent. A hardness value corrected for elastic effects (plastic hardness) can be determined from the unloading curve and is defined as $H_p=AL_{max}/d_p^2$, where L_{max} is the maximum load applied and d_p is the depth corrected for elastic effects.[13] Elastic modulus values were obtained from the unloading curve using techniques detailed elsewhere.[13,14]

Indentations were made both normal to the irradiated surface (on as-irradiated specimens) and parallel to it (on cross-section specimens). The normal indents were made in both irradiated and unirradiated areas to depths of 500 and 1500 nm before unloading at a constant displacement rate of 5 nm/s. Ratios were calculated of these hardness values to those from the pre-irradiated states. Cross-section specimens were indented to a depth of 150 nm, which produced an indent of ~ 1 μm across, at a constant displacement rate of < 5 nm/s. A row of indents 5 μm apart were made at an angle of = 2.9° to the interface between the irradiated specimen and the copper plating, resulting in indents spaced about every 0.25 μm relative to the interface. Figure 3 shows two examples or indents made in cross-section. Ratios were calculated of hardness values to the average value obtained away from the irradiated zone as a function of distance from the interface.

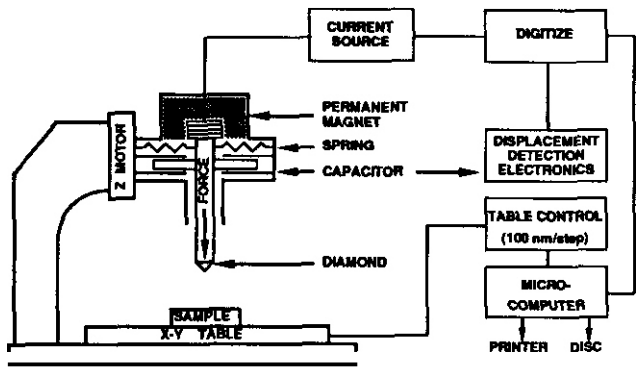

Fig. 1. Mechanical properties microprobe (MPM) schematic.

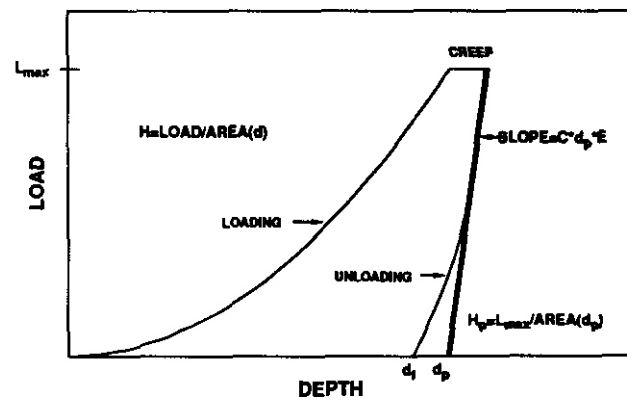

Fig. 2. Representative load-displacement curve from the mechanical properties microprobe.

Results

Table 1 shows the initial mechanical properties of the samples. The yield strength was measured prior to receiving the alloy.[9] The modulus measurements represent a comparison of values found in the literature using conventional tests[15] and those measured on the MPM, which have about a 10% standard deviation. The nanohardness measurements were made on the MPM and represent loads of about 10 g. The Vickers and MPM microindentation hardness values have comparable standard deviations of less than 5%.

Hardness ratios for indentations made normal to the irradiated surface are presented in Fig. 4. The Cu-Ni-Be alloy experiences softening in both conditions. The softening appears to begin at 300°C for the cold-worked and aged condition and is more pronounced in the irradiated region with hardness losses of up to 25%. For the solution-annealed and aged condition, only the 500°C sample experiences softening, with little difference between the irradiated and unirradiated regions. The hardness ratios, calculated from the loading data, for all irradiated samples were relatively constant from a depth of about 300 nm to 1.5 μm and were identical to those calculated at 500 nm and 15 μm from the unloading data. Both 500°C samples showed a dramatic drop in their ratios for depths less than 300 nm.

Ratios of irradiated to unirradiated bulk hardnesses made in cross-section are shown in Figs. 5 and 6 for the solution-annealed and aged and the cold-worked and aged conditions respectively. In the solution-annealed and aged condition the ratios show about a 5% decrease in hardness in the irradiated region with about a 5% standard deviation. The 400°C cold-worked and aged sample shows almost no softening in the irradiated region, but the scatter of data is large with standard deviations of about 10% for many points. At 500°C the cold-worked and aged sample shows about a 15% decrease in irradiated hardness and a fair amount of scatter in the data.

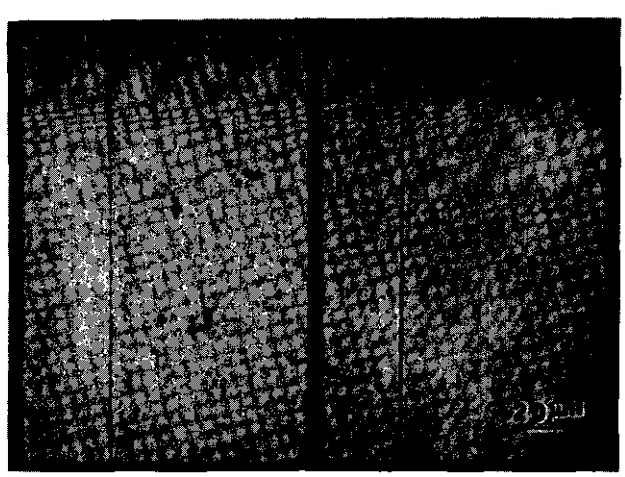

Fig. 3. Optical micrographs of indentations made in cross-sectioned samples of cold-worked and aged (left) and solution-annealed and aged (right) Cu-Ni-Be irradiated at 500°C. Copper plating is to the right and the Cu-Ni-Be to the left of the interface in each micrograph.

Modulus measurements made on cross-section samples did not show any change in irradiated modulus relative to unirradiated. However, the spread in the data prevented any changes less than 15-20% from being discernible. Small drops in modulus (5-10%) were seen in the 400°C cold-worked and aged sample and the 500°C solution-annealed and aged sample with indentations made normal to the surface. However, the 500°C cold-worked and aged sample showed a distinct 30% drop in modulus in the irradiated region.

Discussion

The hardnesses shown in Table 1 indicate that the solution-annealed and aged condition is stronger than the cold-worked and aged condition. Usually it is the other way around. However, different solutionizing treatments were employed for each condition. The cold-worked and aged samples were solution-annealed at 900°C prior to cold-working and aging.[9] The solution-annealed and aged samples were annealed at 950°C prior to aging in order to insure complete solution of the

Table 1. Initial Mechanical Properties of Cu-Ni-Be in GPa

Thermomechanical Treatment	Yield Strength	Voungs Modulus Standard[15]	MRM	VHN (200g)	Nanohardness (1500 nm)
Cold-worked & Aged	0.78[9]	140	160	2.20	3.10
Solution-annealed & Aged		140	160	2.35	3.45

solutes. Solution-annealing at temperatures near 950°C prior to cold-working and aging has been shown to significantly increase the strength of this alloy (σ_y = 900 MPa).[15] Therefore, it is not surprising that using a much higher solution-annealing temperature yields a solution-annealed and aged sample hardness higher than the cold-worked and aged sample hardness using a conventional solution-annealing temperature.

The fact that the alloy in both conditions exhibits softening at 500°C is reasonable considering that this temperature is above the aging temperature (482°C) for this alloy. The cold-worked and aged sample is obviously more sensitive to irradiation and/or temperature than the other thermomechanical treatment. It appears that the cold-worked and aged condition overages very easily at temperatures over 300°C. Micron size precipitates were observed on the electropolished surface of the cold-worked and aged specimens at 400 and 500°C and none were observed in any of the solution-annealed and aged samples (see Figure 3). Recovery and recrystallization is also expected to affect the cold-worked samples. Tensile tests on the two treatments of this alloy aged at 400°C for 1000 hours and neutron irradiated to 16 dpa at 450°C show a similar trend.[5] Microscopy of the neutron irradiated specimens[16] and of ion irradiated samples[4] shows that recovery and recrystallization as well as significant precipitate coarsening occurs in the cold-worked and aged treatment. Further optical and electron microscopy will have to be performed on the specimens in this study to confirm these processes.

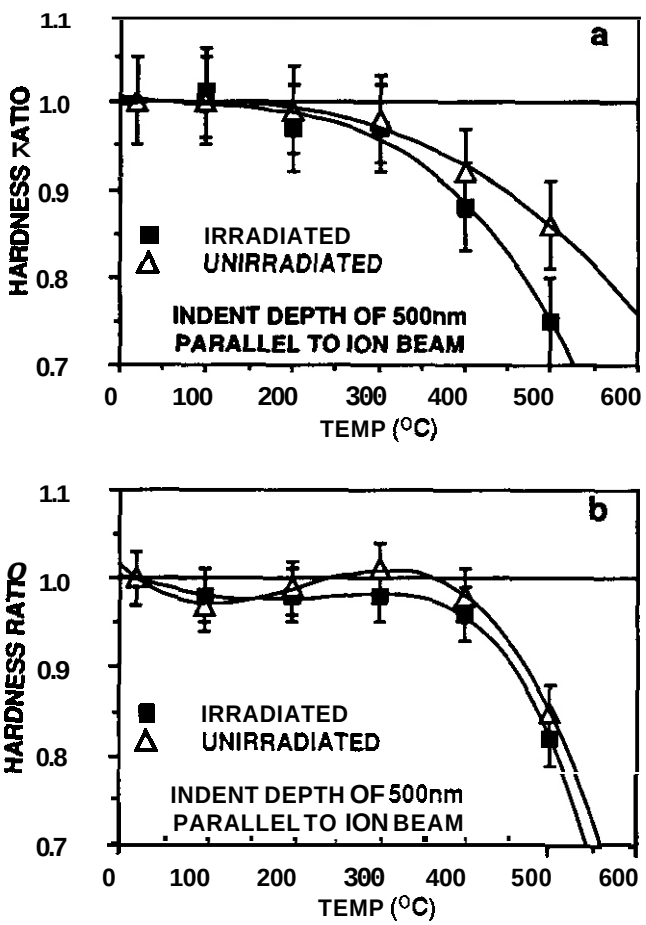

Fig. 4. Ratios of irradiated and unirradiated hardness to original hardness a a function of irradiation temperature for cold-worked and aged (a) and solution-annealed and aged (b) Cu-Ni-Be.

Hardness can be related to yield strength by $H \sim C\sigma_y$ (where C is usually taken to be 3 for Vickers indentations).[17-19] The change in yield strength can be related to the change in hardness by $\Delta\sigma_y/\sigma_y = \Delta H/H$ or $\Delta\sigma_y/\sigma_y = \sigma_y(H_f/H_i - 1)$, where H_f/H_i is the hardness ratio of irradiated and/or aged samples to samples with only the initial treatments. The hardness ratio is constant over varying depth or load so this relationship is valid for the nanohardness measurements. Using this relationship it was found that the solution-annealed and aged sample at 500°C had a drop in yield strength of 140 MPa in the aged and the irradiated zones. The 400°C cold-worked and aged sample hardness dropped 80 MPa in both areas, while the 500°C sample lost 120 MPa in the aged area and 200 MPa in the irradiated zone. The trends are similar to those found in the neutron study.[5] The yield strength dropped far more in the neutron study than in this study; however, the times spent at temperature are vastly different (~ 1000 hours versus < 10 hours respectively.)

Various factors probably affect the hardness values measured in this study. Hardness measurements include contributions from the sample at depths up to 10 times the indent depth.[20] However, the major fraction of the hardness comes from much shallower depths (3 to 4 times the indent depth). Thus normal indents to 500 nm should represent the hardness of the irradiated zone (~ 3000 nm deep).

Also the actual area that contributes to the hardness is larger than the indent area[20] (~ 1 μm^2 for a 150 nm deep indent). Therefore, indents made in cross-section are sampling a wide range of dpa values. The fact that the hardness ratio for normal indents is constant from 500 to 1500 nm and the cross-section ratios are constant in the irradiation zone is somewhat surprising considering the variation of dpa through the irradiation zone. Two other studies using this technique have found similar results.[8,21] With the hardness ratios of both methods being constant through the irradiation zone. it would indicate that the irradiation induced microstructural factors that contribute to hardness are independent of dpa level at the ion fluence of ~ 3 x 10^{20} ions/m^2.

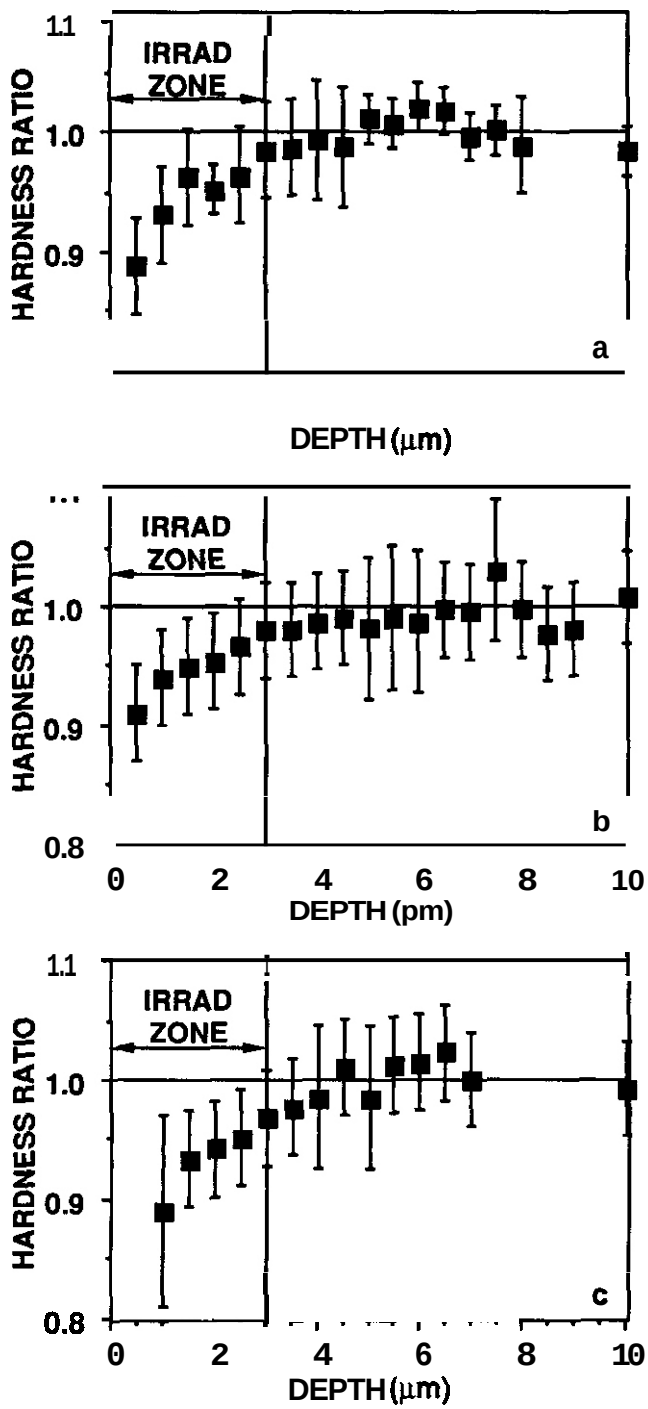

Fig. 5. Ratio of hardness to average unirradiated hardness versus deoth from the irradiated interface for solution-annealed and aged Cu-Ni-Be irradiated at 300°C (a), 400°C (b) and 500°C (c).

Indents were made normal to the irradiated surface and perpendicular to it in cross-section in order to compare the two methods. Table 2 shows hardness measurements for both treatments are in close agreement. The standard deviation for the cold-worked and aged condition is much larger than for the solution-annealed and aged condition, particularly in cross-section. Problems were encountered indenting the former because of the micron size precipitates which are about the same size as the cross-section indents. This can be seen in Fig. 3. The hardness values and their associated standard deviations do not include indents made directly on a precipitate, of which a number were made in the cold-worked and aged samples. If

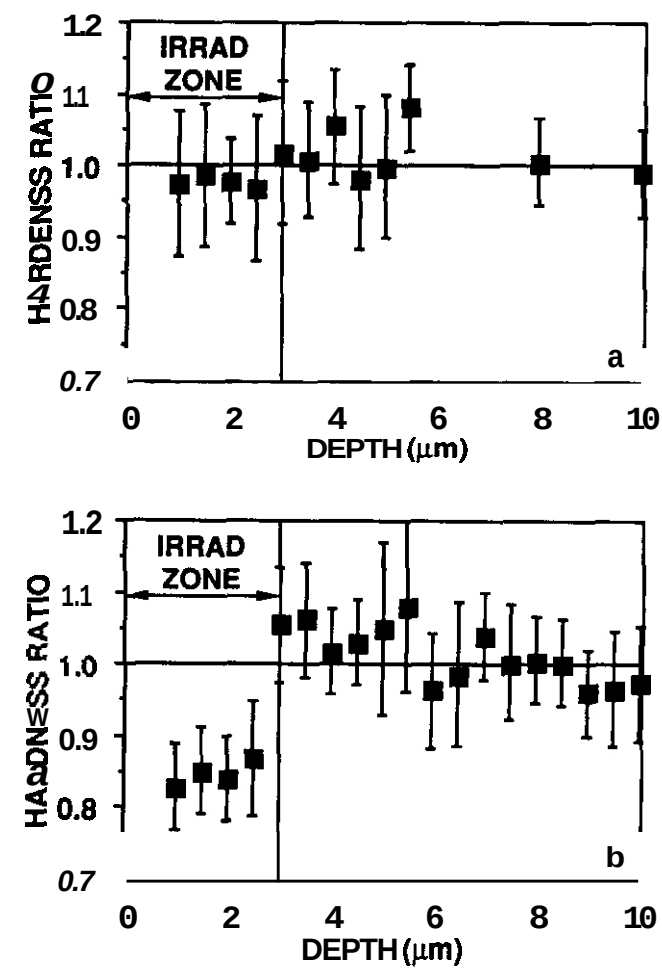

Fig. 6. Ratio of hardness to average unirradiated hardness versus depth from the irradiated interface for cold-worked' and aged Cu-Ni-Be irradiated at 400°C (a) and 500°C (b).

Table 2 Ratios of Hardnesses in the Irradiated Zone to Hardnesses in the Unirradiated Zone

Thermomechanical Treatment	Temperature (°C)	Normal	Cross-section
Cold-worked & Aged	300	0.97t0.03	0.95t0.04
	400	0.98	0.95
	500	0.97	0.94
Solution-annealed & Aged	400	0.95t0.05	0.98t0.10
	500	0.87	0.85±0.07

different and its standard deviation would be much larger. Normal indents of 500 nm or greater depth are not as severely affected by the coarsened precipitates.

For modulus measurements the scatter in data for the cross-section indentations made any conclusive trends impossible to detect. For the normal indents a significant change in modulus was observed only in the irradiated zone of the 500°C cold-worked and aged specimen where the modulus was observed to drop ~ 30%. This was seen in one other study using this technique where recovery and recrystallization occurred.[8] Modulus drops have been reported in stainless steels and attributed to swelling.[22,23] Without gas co-implantation this alloy is not expected to show any significant void formation under ion irradiatfon. The reason for such a large drop in modulus is not fully understood at this time.

CONCLUSIONS

A moderately high dislocation density (20% cold-work) appears to accelerate softening in a Cu-Ni-Be alloy when it is exposed to temperatures of 300°C or more. Overaging is further accelerated when irradiation is included for the cold-worked condition. When the alloy is only aged following solution-annealing, neither temperature nor irradiation affect the hardness, unless the alloy is exposed to temperatures higher than the aging temperature of 482°C and then only thermal effects are observed. In either case, even short term exposure to temperatures only slightly above the aging temperature results in rapid overaging and should be avoided. This study, coupled with the neutron results, indicates that the solution-annealed and aged condition has a far better resistance to irradiation at elevated temperatures than its cold-worked and aged counterpart.

Indentations made normal to the irradiated surface yield results similar to indentations made parallel to the surface in cross-section. This is possible as long as the hardness does not vary with dpa through the irradiated zone for a given ion fluence and the irradiated zone is deeper than 2 to 4 times the normal indent depth and 2 to 3 times the width of the cross section indent. Consistent results for indentations become difficult when features about the same size as the indent are present. Coarsening in the cold-worked and aged sample resulted in precipitates the same size as the indents made in cross-section which made data analysis more difficult due to the large scatter in data.

ACKNOWLEDGEMENT

The authors wish to thank Or. S. J. Zinkle of ORNL for his helpful advice. This work is supported by the U.S. Department of Energy, Office of Fusion Energy.

REFERENCES

1. S. J. Zinkle and R. W. Knoll: UWFDM-578, University of Wisconsin-Madison, June 1984.

2. S. J. Zinkle: Ph.D. Thesis, University of Wisconsin-Madison, May 1985.

3. S. J. Zinkle, G. L. Kulcinski and R. W. Knoll: J. Nucl. Mater., 1986, vol. 136, pp. 46-56.

4. J. A. Spitznagel, N. J. Doyle, W. J. Choyke, J. G. Greggi, J. N. Mcgruer, and J. W. Davis: Nucl. Instr. and Meth., 1986, vol. 816, nos. 2-3, pp. 279-287.

5. H. R. Brager, H. L. Heinisch and F. A. Garner: J. Nucl. Mater., 1985, vol. 133-134, pp. 676-679.

6. R. J. Livak, H. M. Frost, T. G. Zocco, J. G. Kennedy, and L. W. Hobbs: J. Nucl. Mater., 1986, vol. 141-143, pp. 174-178.

7. M. Ames, G. Kohse, T-S Lee, N. J. Grant and O. K. Harling: J. Nucl. Mater., 1986, vol. 141-143, pp. 174-178.

8. S. J. Zinkle and W. C. Oliver: J. Nucl. Mater., 1986, vol. 141-143, pp. 548-552.

9. S. Rosenwasser. Private comnunication, June 1984.

10. S. J. Zinkle and R. L. Sindelar: Nucl. Instr. and Meth., 1986, vol. B16, nos. 2-3, pp. 154-162.

11. J. B. Pethica, R. Hutchings and W. C. Oliver: Phil. Mag. A, 1983, vol. 48, pp. 593-606.

12. W. C. Oliver, R. Hutchings and J. 8. Pethica: Microindentation Techniques in Materials Science and Engineering, ASTM STP 889, P.J. Blau and B.R. Lawn, eds., pp. 90-108, ASTM, Philadelphia, 1986.

13. M. F. Doerner and W. 0. Nix: J. Mater. Res., 1986, vol. 1, no. 4, pp. 601-609.

14. J. L. Loubet, J. M Georges, 0. Marchesini. and G. Meille: J. Tribology, 1984, vol. 106, pp. 43-48.

15. A Guha: High Conductivity Copper and Aluminum Alloys, E. Ling and P. W. Taubenblat, eds., pp. 133-145, TMS-AIME, Warrendale, 1984.

16. H R. Brager: J. Nucl. Mater.. 1986, vol. 141-143, pp. 163-168.

17. D. Tabor: The Hardness of Metals, p. 95, Claredon Press, Oxford, 1951.

18. J. R. Cahoon, W. H Broughton and A. R. Kutrak: Metall. Trans., 1971, vol. 2, pp. 1979-1983.

19. J. J. Gilman: The Science of Hardness Testing and Its Research Applications, J. H. Westbrook and H. Conrad, eds., pp. 51-71, American Society for Metals, Metals Park, 1973.

20. L. E. Samuels and T. 0. Mulhern: J. Mech. Phys. Solids, 1957, vol. 5, pp. 125-134.

21. D. H Plantz, L. M. Wang, R. A. Dodd and G. L. Kulcinski: Metall. Trans. A., in press.

22. J. L. Straalsund and C. K. Day: Nucl. Tech., 1973, vol. 20, pp. 27-34.

23. M Marlowe and W. K. Appleby: Trans. Am. Nucl. Soc., 1973, vol. 16, pp. 95-96.

ITER MATERIALS DATA BASE FOR IRRADIATION EFFECTS ON M E DESIGN PROPERTIES OF Cu-Ni-Be AND $Cu-Al_2O_3$ ALLOYS - K. R. Anderson (University of Illinois) and D. S. Gelles (Pacific Northwest Laboratory)

OBJECTIVE

The objective of this effort is to provide the ITER design team with an irradiation effects data base for copper alloys to be used as divertor structural materials.

SUMMARY

This report provides an ITER materials data base on irradiation effects in copper alloys with regard to divertor structural material applications. The data base places emphasis on two copper alloys of particular promise: Cu-Ni-Be, a beryllium solid solution hardened alloy. and Cu-Al2O, an oxide dispersion strengthened alloy.

PROGRESS AND STATUS

Introduction

As input to the ITER (International Thermonuclear Experimental Reactor) Specialist's Meeting on Materials Data Base held August 22-26, 1988, in Garching, West Germany, an irradiation effects data base for copper alloys Cu-Ni-Be and Cu-Al2O was compiled. The purpose of this report is to make that information available to the US Fusion Reactor Materials Program.

Three U.S.A. laboratories have studied neutron irradiation effects on one or both alloys: Hanford Engineering Development Laboratory (HEDL) and Pacific Northwest Laboratory (PNL), Los Alamos National Laboratory (LANL), and the Nuclear Reactor Laboratory at Massachusetts Institute of Technology (HIT). The design property information was collected from these individual research efforts but is supplemented with additional European results.

Hanford

A Cu-1.8Ni-.3Be alloy. a Cu-2Be alloy and an alloy of Cu-.25Al (as Al_2O_3) were each given two separate thermal-mechanical treatments and irradiated in the FFTF/MOTA at ~ 450°C to damage levels of 16, 47, 63 and 98 dpa[1]. The swelling data for these alloys are given in Table 1 and shown graphically in Figures 1, 2 and 3.

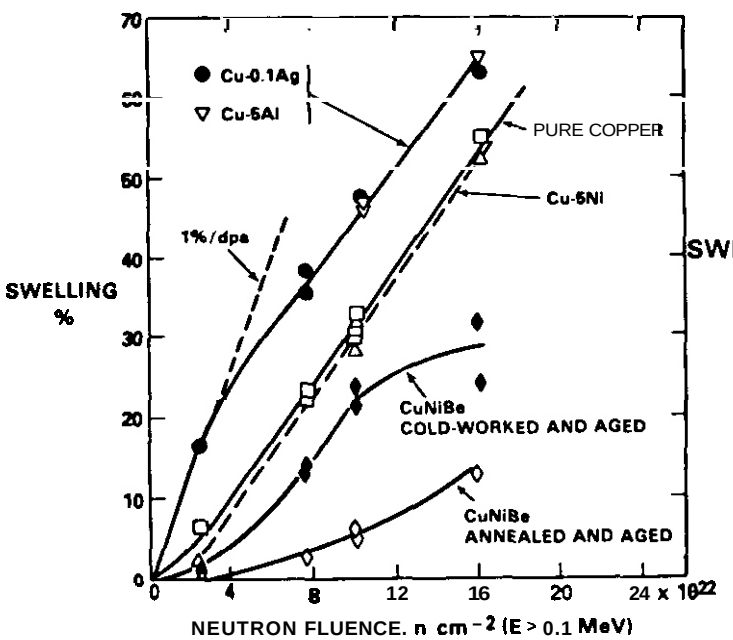

Fig. 1. Swelling observed in a variety of copper alloys at 450°C in FFTF-MOTA.

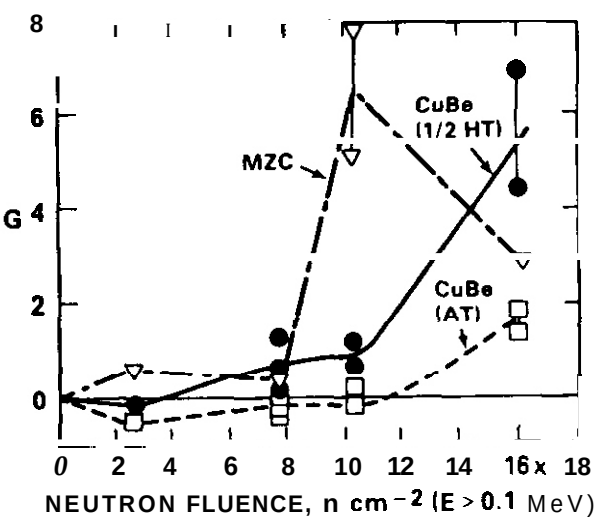

Fig. 2. Swelling of MZC and CuBe alloys observed in FFTF-MOTA at 450°C.

The electrical conductivity of both Cu-A125 and the Cu-Be alloy were determined up to damage levels of 63 dpa[2]. This data is shown graphically in Figures 4 and 5. The electrical conductivity of the Cu-Be-Ni alloy was determined for a damage level of 16 dpa. This is shown in Table 2.

Table 1. Swelling of various commercial copper alloys irradiated in FFTF/MOTA at approximately 450°C.

Alloy	Alloy Composition (wt%)	Condition	Swelling (%)			
		dpa:	16	47	63	98
		n/cm2(E>0.1MeV):	2.5x10^22	7.7x10^22	1.0x10^23	1.6x10^23
Cu (MARZ)	Cu(99.999)	annealed	6.5	22.2,23.3	30.1,31.3,33.2	55.8
Cu-5Ni	Cu-5Ni	annealed	215	—	27.7,31.8	52.9
Cu-5Al	Cu-5Al	annealed	—	—	46.8,45.8,39.4	66.0
CuAg	Cu-0.1 Ag	20% CW	16.6	35.4,38.2	47.4	63.9
CuAgP	Cu-0.3Ag-0.06P-0.08Mg	20% CW	7.9	16.0,16.2	17.1	24.0
CuNiBe (1/2 HT) a)	Cu-1.8Ni-0.3Be	20% CW and aged (3 h at 480°C)	1.70	13.9,14.6	22.3,24.6	23.4,31.1
CuNiBe (AT) a)	Cu-1.8Ni-0.3Be	20% CW and aged (3 h at 480°C)	0.29	3.05	5.73,6.59	132
CuBe (1/2 HT)	Cu-2.0Be	20% CW and aged (2 h at 320°C)	- 0.16	0.16,1.11,1.71	1.09,1.61	4.4,7.1
CuBe(AT)	Cu-2.0Be	annealed and aged (2 h at 320°C)	- 0.66	-0.45,-0.24,+0.12	-0.43,-0.25	1.4,2.0
MZC	Cu-0.9Cr-0.1Zr-0.05Mg	90% CW, aged (0.5 h at 470°C)	1.03	0.79	5.15,7.90	2.9
Cu-Al25 (CW)	Cu-0.25 Al(asAl_2O_3)	20% CW	0.13	0.23,0.36,0.66	0.28	1.3
Cu-Al25 (CWA)	Cu-0.25 Al(asAl_2O_3)	20% CW + aged (1 h at 550°C)	—	-0.18,0.05,0.52	0.04,1.45,1.85	1.5,3.3

a) 1/2 HT and AT are industry designations for half-hard and tempered, and annealed and tempered, respectively.

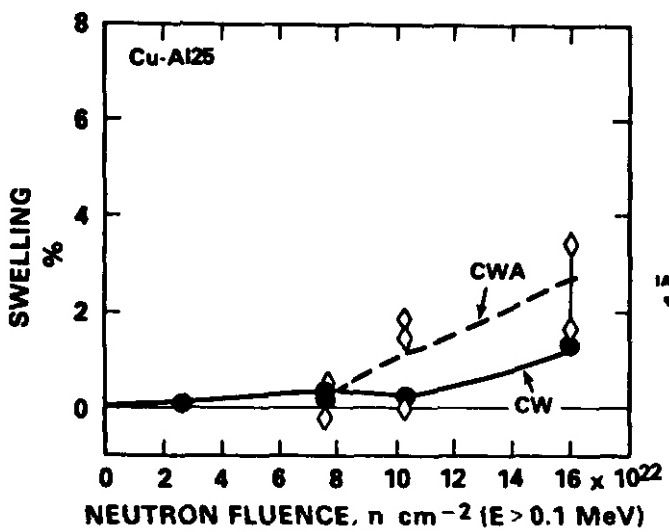

Fig. 3. Swelling of Cu-A125 in FFTF-MOTA at 450°C.

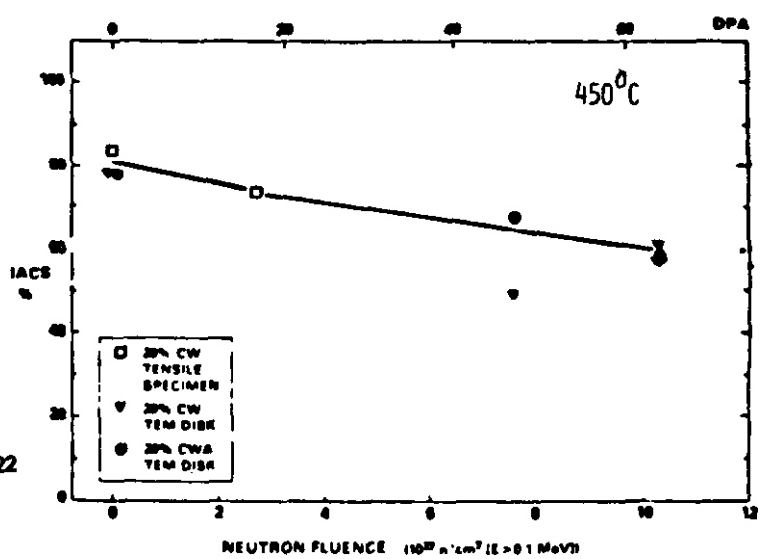

Fig. 4. The effect of neutron irradiation on the electrical conductivity of Cu-AL25 dispersion strengthened alloy.

The yield strengths and uniform elongations of miniature tensile specimens were determined for a damage level of 16 dpa for the CuBe, CuBeNi and Cu-A125 alloys[4]. These tensile properties are presented in Table 2 and are shown graphically in Figures 6, 7 and 8.

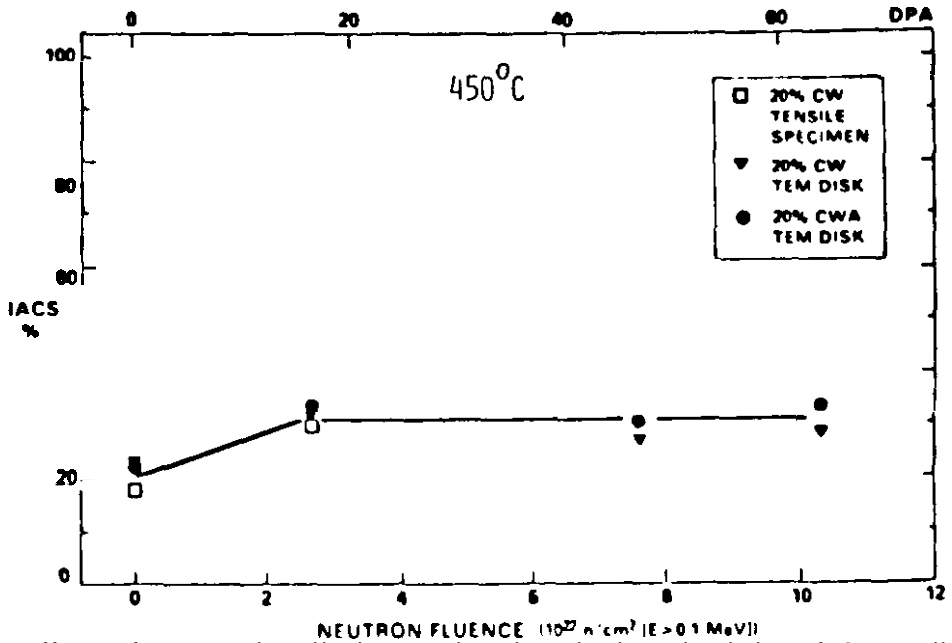

Fig. 5. The effect of neutron irradiation on the electrical conductivity of Cu-Be alloy. Conductivity appears to be unaffected by exposure above 2.7×10^{22} n/cm^2 (16 dpa) and by pre-irradiation thermal mechanical treatment.

Table 2. Electrical conductivity, yield strength and uniform elongation for unirradiated, aged or irradiated conditions of various copper alloys.

	Electrical conductivity (% IACS)		Yield strength (MPa)			Uniform elongation (%)		
	Unirradiated	Irradiated[b]	Unirradiated	Aged[a]	Irradiated[b]	Unirradiated	Aged[a]	Irradiated[b]
Zone-Reffned								
Copper (99.99%)	101	86	58	58	43	28	26	14
Solution Strengthened								
CuAg	97	77	254	78	57	2.2	34	11
CuAgP	96	80	408	115	109	2.1	24	9.8
Dispersion Strengthened								
CuA125	84	13	483	476	396	1.8	5.5	5.9
Precipitate Strengthened								
MZC(HT)	83	77	450	401	267	2.5	6.2	8.7
CuBeNi(½ HT)	74	84	563	308	211	3.2	8.9	12
CuBeNi(AT)	61	71	561	566	451	3.4	1.3	0.9
CuBe(½ HT)	18	29	647	403	351	2.7	15	11

a) Aged 1000 h at 400°C
b) Irradiated at ~ 450°C to ~ 16 dpa [2.5×10^{22} n/cm^2 (E>0.1 MeV)] in the MOTA of the FFTF

A separate. very low damage, neutron irradiation study utilizing miniature tensile specimens of Cu-A125 and Cu-1.8Ni-.3Be in two thermal-mechanical treatments was undertaken at RTNS-II (LLNL) and the Omega West Reactor (LANL)[4]. Both irradiations were performed at 90°C and 290°C. Cu-Be-Ni and Cu-A125 were exposed to fluences of up to 2.5×10^{22} n/m^2 in RTNS-II and from 5.2×10^{22} n/m^2 to 1.3×10^{24} n/m^2 in OWR. The changes in yield stress for these materials are shown graphically in Figures 9, 10, 11 and 12 for RTNS-II and Figures 13, 14 and 15 for OWR.

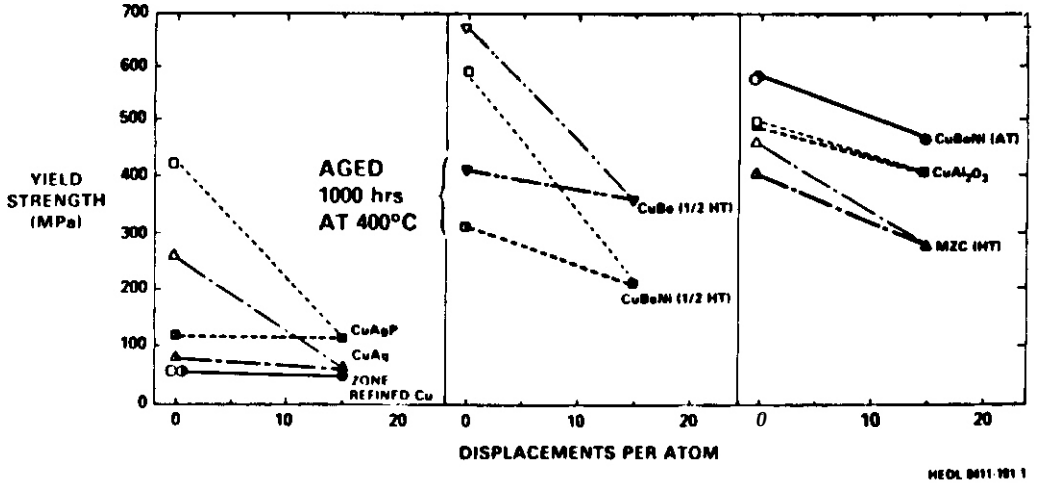

Fig. 6. Effects of aging or neutron irradiation on the yield strength of copper alloys. Open symbols denote as-prepared condition. half-filled symbols the aged condition (400°C for 1000 h) and solid symbols refer to the irradiated condition (16 dpa at ~450°C).

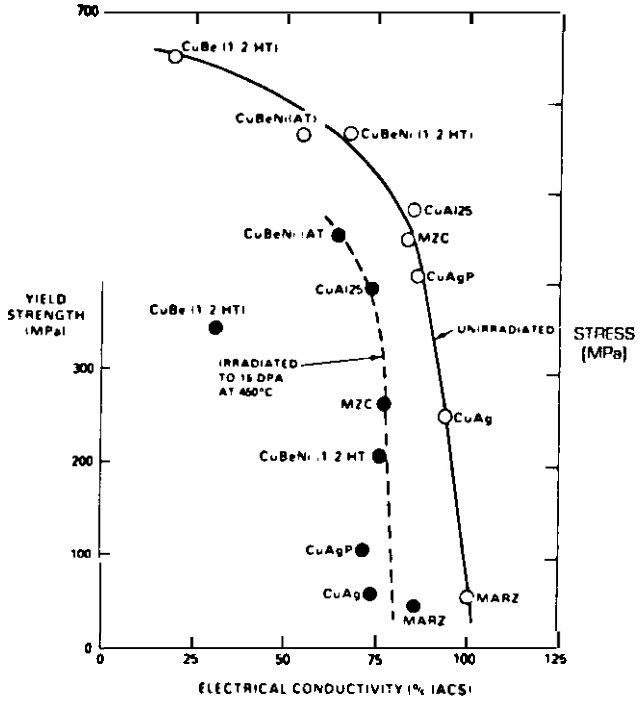

Fig. 7. Shift in strength and electrical conductivity of copper alloys due to irradiation to ~16 dpa at ~450°C. The trend lines shown in this figure do not imply an identical shift for each alloy.

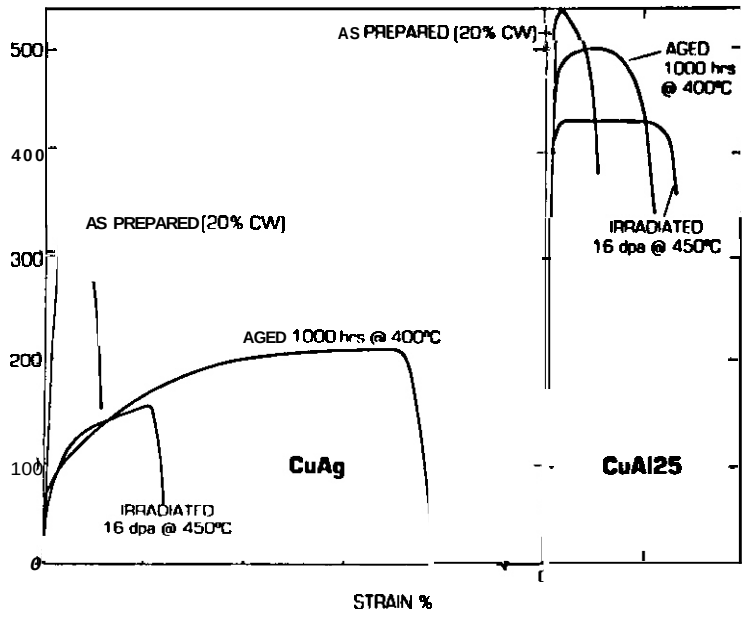

Fig. 8. Stress-strain curve for Cu-A125 after irradiation to 16 dpa at 450°C in FFTF.

A second generation copper alloy experiment has been designed. built and inserted into FFTF/MOTA for irradiation to 30, 60, 120 and 240 dpa at 450°C[5]. This test matrix, shown in Table 3, is heavily biased toward oxide dispersion strengthened (ODS) copper based alloys. There are 16 different Cu alloys under irradiation. all of which have been selected primarily for potential fusion divertor applications. Several weldable ODS alloys have been included in this test matrix. The first specimens, which have been irradiated to 30 dpa, have been removed from FFTF/MOTA and are awaiting evaluation.

LANL

Glidcop A1-20 was irradiated in the Experimental Breeder Reactor (EBR-II) at 385°C to damage levels of 3 and 15 dpa[6]. The swelling data is shown in Table 4. This work is in general agrement with the work performed at HEOL which used A1-25 instead of the A1-20 used in this experiment.

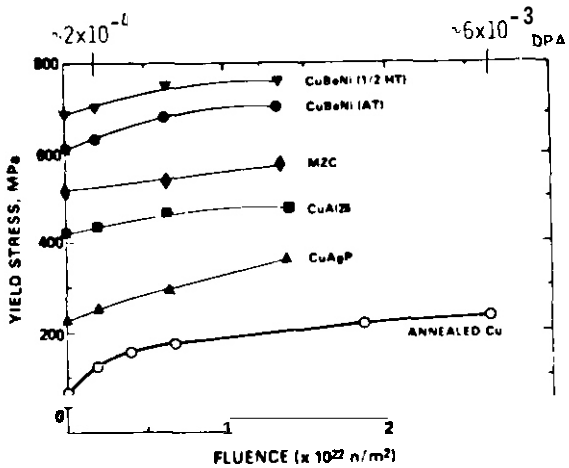

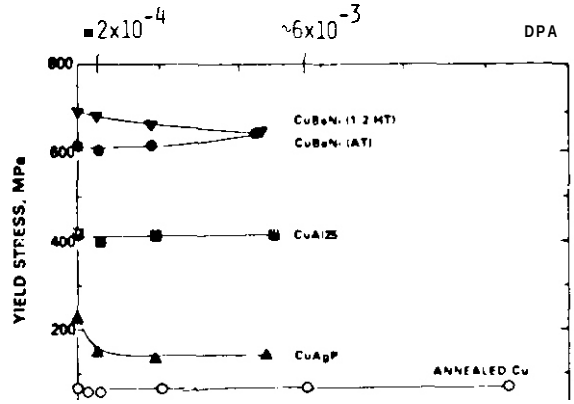

Fig. 9. The 0.2% offset yield stress as a function of 14 MeV neutron fluence for high purity copper and commercial copper irradiated at 90°C in RTNS-II.

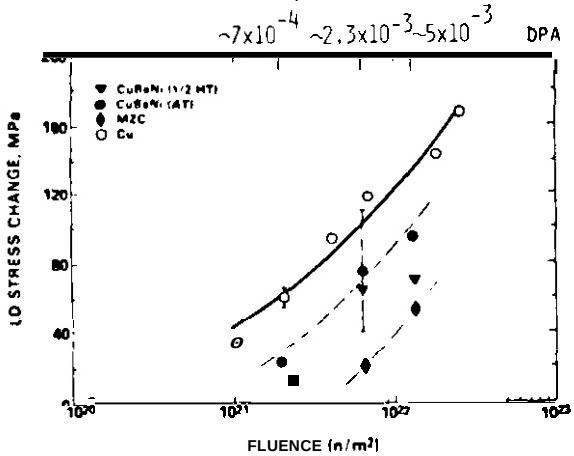

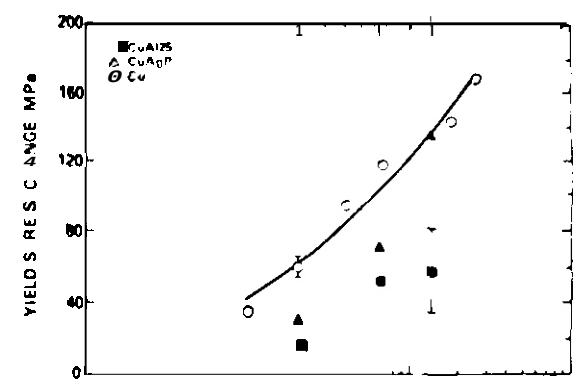

Fig. 11. The change in yield stress as a function of 14 MeV neutron fluence for pure copper, CuBeNi in two conditions. and MZC. The error bar represents an uncertainty of ± 5% in the value of the absolute yield stress of CuBeNi(AT).

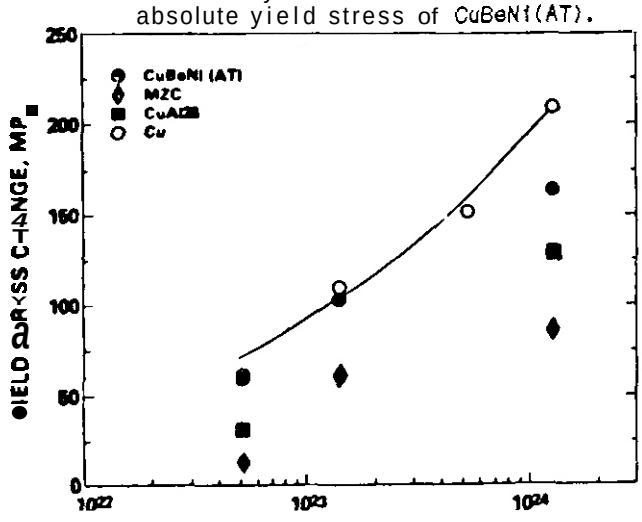

Fig. 13. The change in yield stress as a function of total-neutron fluence for pure copper and copper alloys irradiated in the Omega West Reactor at 90°C.

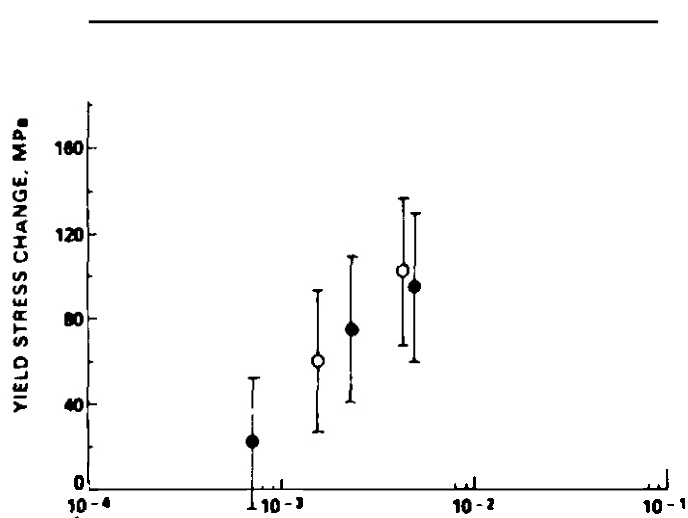

Fig. 14. The change in yield stress as a function of dpa for CuBeNi(AT) irradiated at 90°C in RTNS-II and OWR.

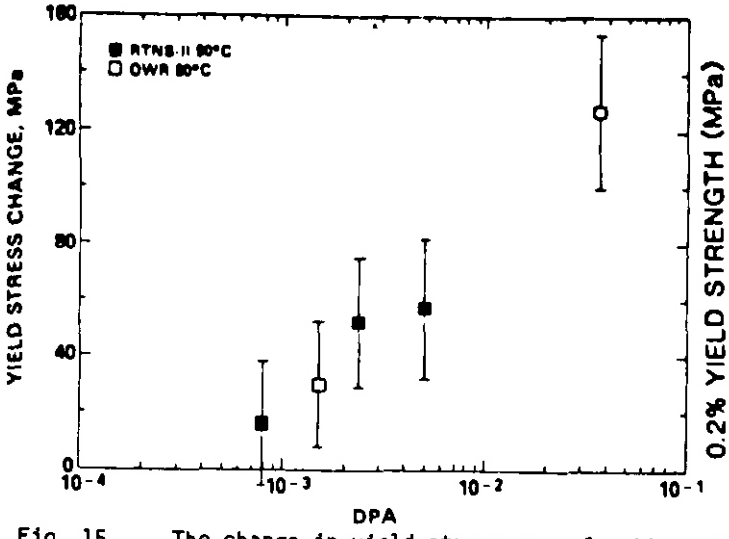

Fig. 15. The change in yield stress as a function of dpa for alumina dispersion-strengthened copper (CuAl25) irradiated at 90°C in RTNS-II and OWR.

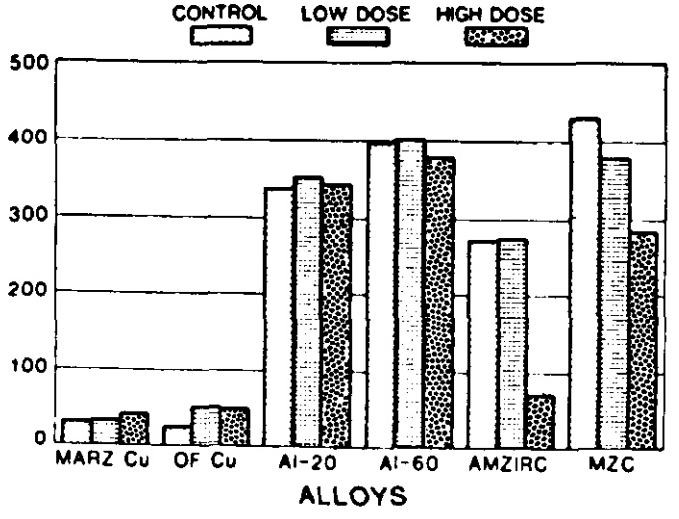

Fig. 16. Tensile yield strengths (0.2% offset), measured at room temperature, of control and irradiated copper-base materials.

Table 3. Copper alloys specimens irradiated in FFTF/MOTA.

Alloy	Condition		Specimen Engraving Code	Neutron Fluence 30 DPA (ET)*		60 DPA (IV)		120 DPA (E9)		240 DPA (17)	
				Tensile	TEM	Tensile	TEM	Tensile	TEM	Tensile	TEM
MARZ	--	SA	RO	1	4	1	4		4		4
AL25	--	CWl	R4	1	4	1	4	1	4	1	4
AL25	--	CWAW	RW	1	4	1	4	1	4	1	4
CuBe	--	HTA			4		4		4		4
CuBe	--	HTB	R3	1	4	1	4	I	4	I	4
A120	--	CUI	UX	1	4	1	4	1	4	1	4
MZC	--	HTA	U6		4		4		4		4
MZC	--	HTB	U7		4		4		4		4
MZC	MIT#2	STA	U9	1	4	1	4	I	4	1	4
MZC	MIT#3	HT	VB	1	4	1	4	1	4	1	4
Cu-SNi-2.5Ti	MIT#6	HT			4		4		4		4
Cu-SNi-2.5Ti	LANL	HT	VL		4		4		4		4
All5+B	LANL	HT	VO		4		4		4		4
CuCr	1111	HT	3A	1	4	1	4	1	4	1	4
CuHf	MIT	HT	38	1	4	1	4	1	4	1	4
CuCrZr	JPC	HT	3E		4		4		4		4
ODS-1	TRAA	CW	3F	I	4	1	4	1	4	1	4
ODS-1	TRAA	CWBW	3H	1	4	1	4	1	4	1	4
ODS-2	TRAB	CW	3K		4		4		4		4
ODS-3	TRAC	CY	3L		4		4	1	4	1	4
ODS-4	TRAD	CW	3M	I	4	1	4	1	4	I	4
				12	84	12	84	12	84	12	84

*Location codes engraved on Specimens are shan in parentheses.

Tensile tests were then performed on Irradiated miniature tensile specimens to determine yield strength. elongation and reduction of area which was measured fran the fractured specimens[7]. This data is presented in Table 5 and Figures 16 and 17.

The electrical resistivity of the specimens was also measured[7]. The electrical conductivity of the irradiated specimens is shown in Figure 18. A measure of the resistance to thermal stress can be calculated by multiplying the yield stress and the conductivity of the irradiated specimens. This is shown in Figure 19.

Table 4. Swelling of neutron irradiated copper alloys.

	Volume % increase after irradiation	
	Low dose[a]	High dose[b]
Copper		
MARZ-grade 199.999%)	1.8	6.8
Oxygen-free (99.95%)	2.1	6.6
Dispersion-strengthened[c]		
Al-20	0.8	0.9
Al-60	1.1	0.6
Precipitate-strengthened		
AMZIRC	Nil	3.6
MZC	Nil	Nil

a) Low dose exposure was 0.4×10^{26} n/m^2 (E_n>0.1 MeV) at 385°C giving ~ 3 dpa in copper.

b) High dose exposure was 2.0×10^{26} n/m^2 (E_n>0.1 MeV) at 385°C giving ~ 15 dpa in copper.

c) Densities measured after removal of oxygen-free copper clad. Typical standard deviation ~ 0.3% for each condition.

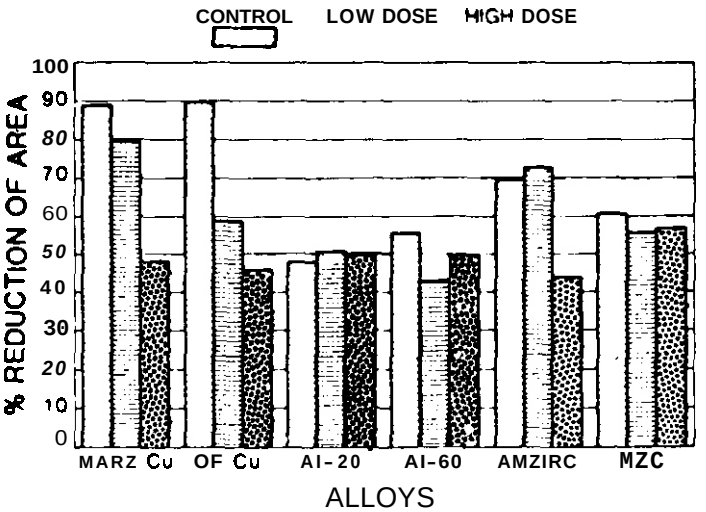

Fig. 17. Reduction of areas measured on broken tensile specimens of control and irradiated copper-base materials.

Table 5. Tensile properties of neutron irradiated comer allovs.

Alloy / Condition		0.2% Offset Yield Strength (MPa)	Ultimate Tensile Strength (MPa)	Elongation (%)
Marz Cu:	Control	31 ± 6	152 ± 7	23.6 ± 1.4
	Low dose	33 ± 9	155 ± 15	24.5 ± 3.1
	High dose	41 ± 1	149 ± 13	11.0 ± 1.0
OFHC Cu:	Control	26 ± 3	196 ± 1	21.4 ± 0.1
	Low dose	51 ± 9	200 ± 2	29.5 ± 0.5
	High dose	49 ± 1	185 ± 13	24.4 ± 0.5
Al-20:	Control	337 ± 8	395 ± 10	13.5 ± 1.0
	Low dose	353 ± 13	411 ± 10	13.7 ± 2.8
	High dose	343 ± 12	395 ± 18	20.4 ± 2.6
Al-60:	Control	391 ± 24	466 ± 3	12.1 ± 1.9
	Low dose	402 ± 20	468 ± 1	9.5 ± 1.1
	High dose	379 ± 18	449 ± 15	11.3 ± 0.9
Amzirc:	Control	271 ± 2	334 ± 9	9.3 ± 0.1
	Low dose	214 ± 6	311 ± 6	9.3 ± 2.6
	High dose	71 ± 5	226 ± 7	34.3 ± 1.1
MZC:	Control	431 ± 12	458 ± 7	10.1 ± 0.8
	Low dose	319 ± 10	437 ± 12	12.8 ± 0.8
	High dose	284 ± 10	354 ± 10	16.6 ± 0.4

MII

A Cu-.38Be-1.67Ni alloy supplied by INESCO in an optimally processed condition and four Cu-Al_2O_3 alloys were irradiated at 400°C to a damage level of 13.5 dpa in EBR-II[8]. The Cu-Al_2O_3 alloys contain substantially more Al_2O_3 than does Glidcop A1-20 as shown in Table 6. All the specimens irradiated in this study were in the form of 3 mm TEM discs. The amount of swelling for these alloys is given in Figure 20. The electrical conductivity of these alloys is given in Figure 21.

The tensile properties of yield stress and percent elongation were determined by the use of a miniaturized disc bend technique for specific specimens[8]. The yield strength and percent elongation of the Cu-Al_2O_3 alloys are given in Figures 22 and 23, respectively.

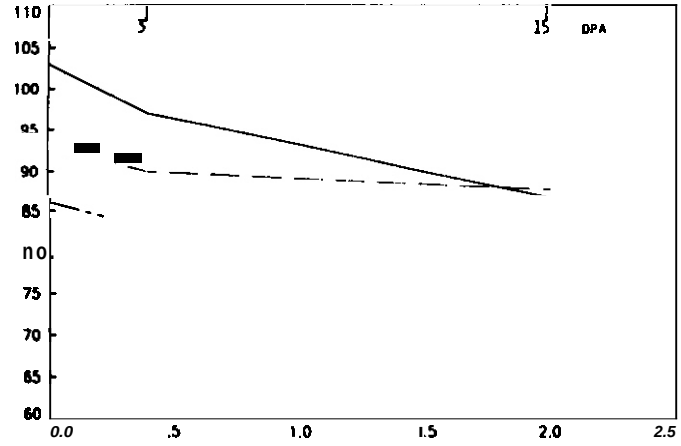

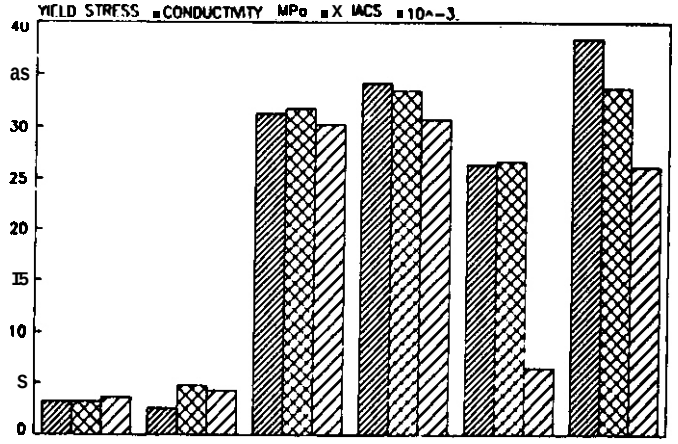

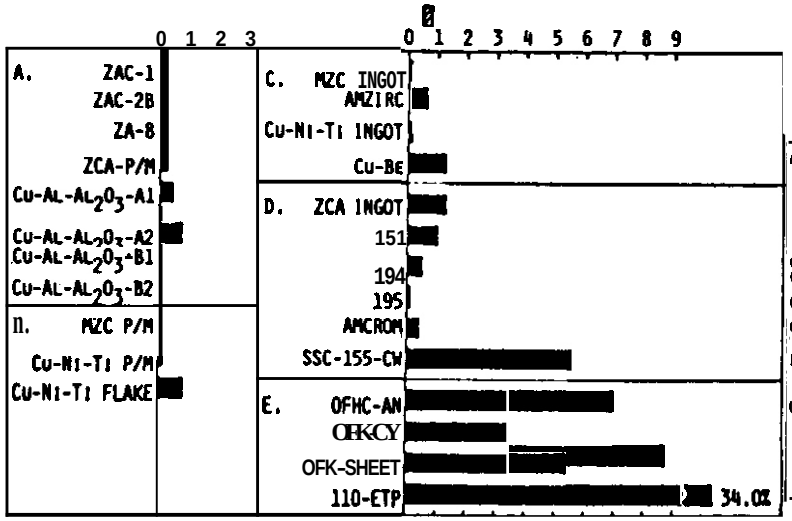

materials.

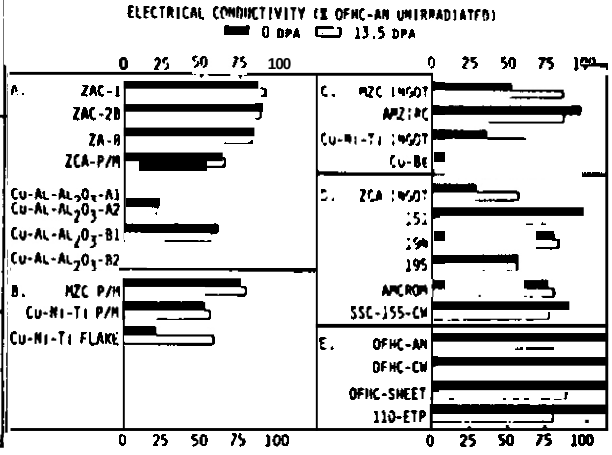

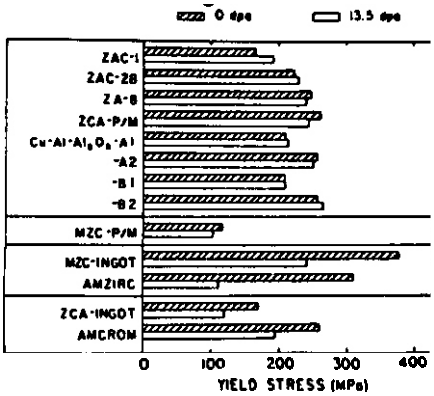

Fig. 22. Yield stress at 0 and 13.5 dpa for selected materials.

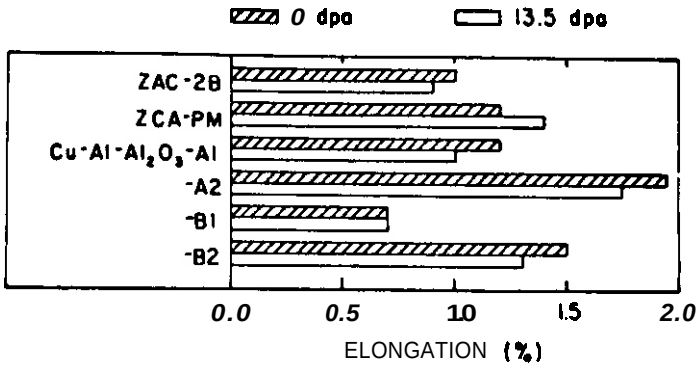

Fig. 23. Ductility estimated from miniature disk bend tests at 0 and 13.5 dpa for tested alloys with elongation < 5%.

Table 6. Chemical compositions of experimental alloys.

ALLOY		Elements wt% (a)						Oxides vol%	
		Al	Mg	Zr	Cr	Ni	Ti	Al_2O_3	ZrO_2
Cu-Al-Al_2O_3 (all P/M)	A1	0.65	--	--	--	--	--	2.3	--
	A2	2.8	--	--	--	--	--	2.9	--
	B1	0.58	--	--	--	--	--	2.9	--
	B2	2.65	--	--	--	--	--	4.2	--
MZC	Ingot	--	0.02	0.2	0.6	--	--	--	--
	P/M	--	0.02	0.2	0.6	--	--	--	--
Cu-Ni-Ti	Ingot	--	--	--	--	5	2.5	--	--
	P/M	--	--	--	--	5	2.5	--	--
	Flake	--	--	--	--	5	2.5	--	--
ZCA	Ingot	0.57	--	0.27	0.22	--	--	--	--
	P/M	0.39	--	0.20	0.22	--	--	0.74	0.15
ZAC (all P/M)	ZAC-1	--	--	0.1	0.32	--	--	--	0.22
	ZAC-2B	--	--	0.23	0.33	--	--	--	0.42
	ZA-8	--	--	0.8	--	--	--	--	0.48

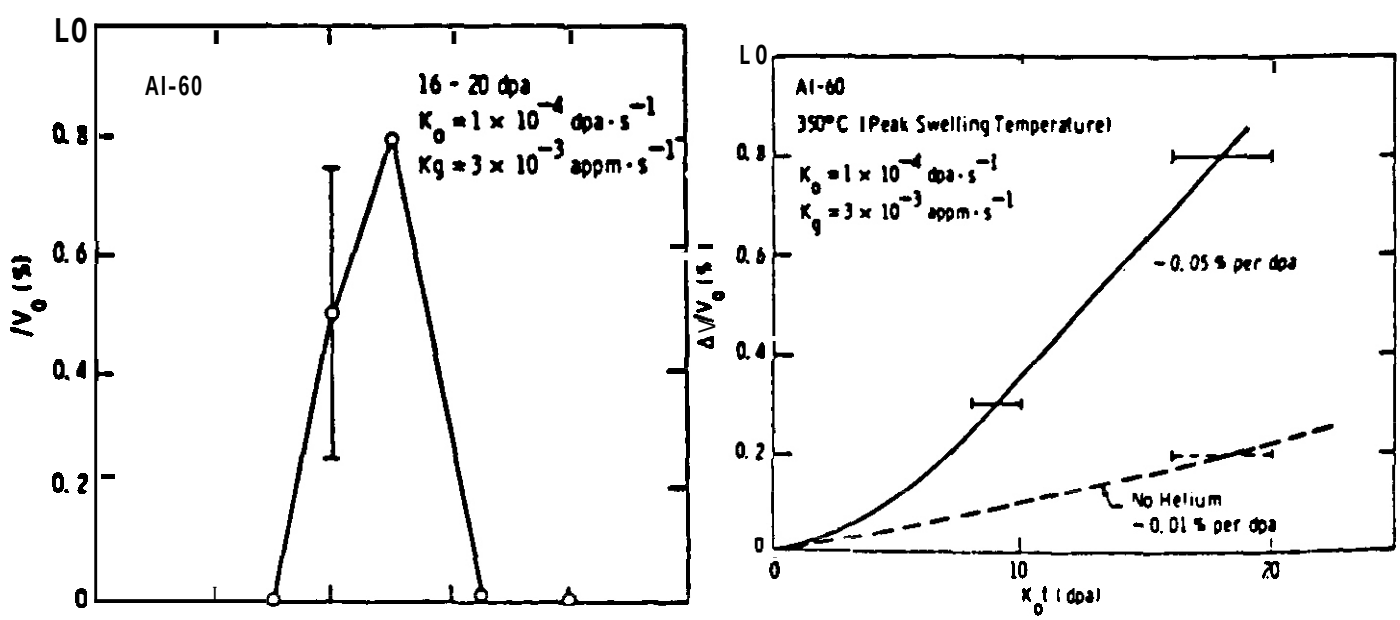

The degree of neutron irradiation-induced void formation is partially a function of temperature and dose rate. For Cu-Be-Ni and $Cu-Al_2O_3$, the relative importance of these dependencies has yet to be determined. There have been several French researchers who have studied the importance of temperature and dose rate on pure Cu as well as Cu alloys in which the stacking fault energy was varied[10-11]. This work was performed at low damage levels of ~0.7 dpa. A graph of swelling vs temperature is shown in Figure 26 with a maximum occurring at approximately 0.45 T_m (~337°C) for a flux of $3x10^{14}$ n/cm²·sec. A reduction in flux, at constant dose. displaces the maximum to lower temperatures. As the stacking fault energy of Cu was decreased by alloying. the amount of swelling was also found to decrease. This is shown in Table 7.

Table 7. Stacking fault energy (SFE) dependence on swelling in copper showing that as SFE decreases. swelling decreases.

Alloy	SFE (erg/cm²)	Swelling (%)	cavity density (#/cm3)	cavity diameter (nm)
cu	55	0.16	2.2 x 10^{14}	27.5
Cu - Ge 1%	50	0.10	2.5 x 10^{12}	48.0
Cu - Ge 3%	~45	~0	few cavities	60.0
Cu - Si 1%	~45	~0	few cavities	60.0
Cu - Al 1%	~45	~0	few cavities	-
Cu - Al 3%	~30	0	0	-
Cu - Al 5%	~5	0	0	-

ORNL researchers have irradiated pure copper to a damage level of approximately 1.3 dpa with neutrons as shown in Table 8[12]. The results indicate a broad swelling maximum in pure Cu at 0.42 T_m (~300°C). This determination of a swelling maximum may have been hindered somewhat due to the lack of swelling data above 350°C.

Table 8. Void swelling parameters for irradiated pure copper specimens.

Temperature (°C)	Void Density ($10^{18}/m^3$)	Mean Void Diameter (nm)	ΔV/V (%)	Damage Level (DPA)
182			0	1.3
220	146	19	0.06	1.3
250	155	28	0.23	1.5
275	66	46	0.38	1.4
300	65	45	0.37	1.3
350	38	49	0.35	1.3

Therefore. there is reasonable agrement in the tmperature of the swelling maximum for Cu. Several researchers have shown a broa maximum in swelling tmperature to occur at ~350% (.46T_m) as shan by Table 9 and Figures 27 and 28[10].

At the present time, neutron irradiation effects on the design properties of fracture toughness. creep and fatigue are undetermined for Cu-.5Be-2Ni and Glidcop Al-20.

CONCLUSIONS

A data base on irradiation effects for copper alloys Cu-Ni-Be and CuAL20 has been assembled and provlded to the ITER design team.

FUTURE WORK

This work will be continued when results became available.

REFERENCES

1.H. R. Brager and F. A. Garner. DOE/ER-0313/3, 254,

2.H. R. Brager, J. Nucl. Mater. 141-143 (1986) 79.

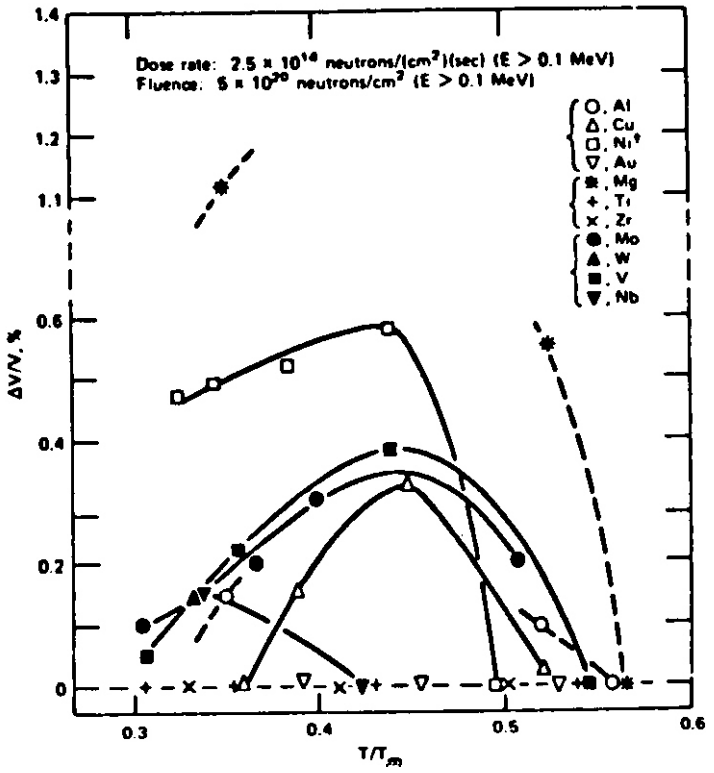

Fig. 26. Variation of the overall swelling verses temperature.

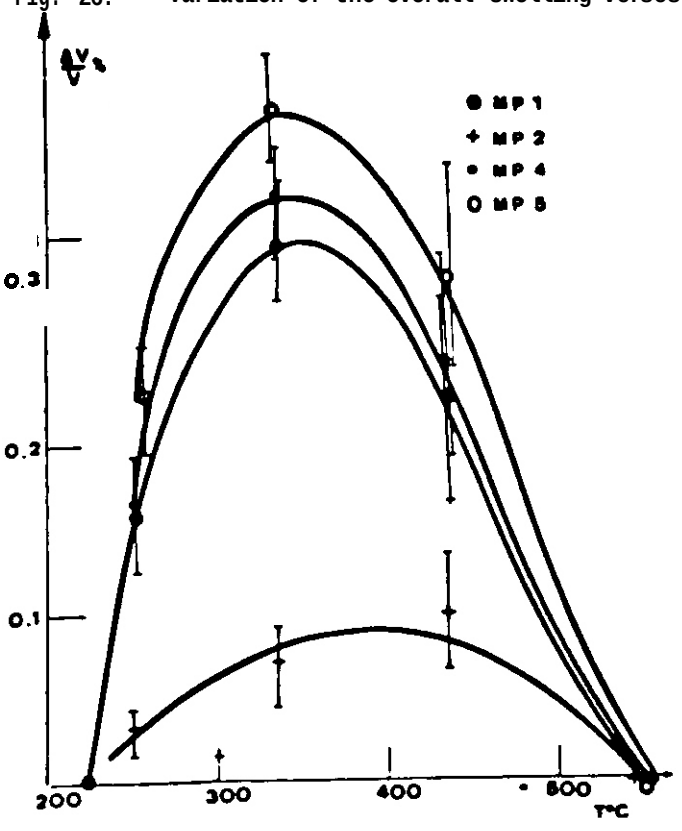

Fig. 27. Variation of swelling as a function of irradiation temperature for all experimental conditions.

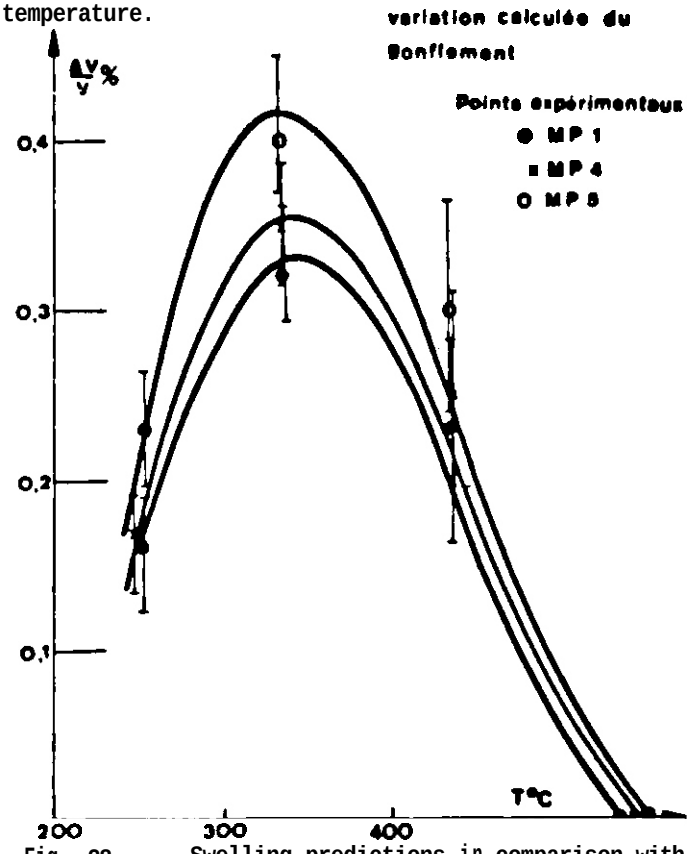

Fig. 28. Swelling predictions in comparison with experimental results shown in Fig. 27.

3.H. R. Brager, H. L. Heinisch and F. A. Garner. J. Nucl. Mater. 133-134 (1985) 676.

4.H. L. Heinisch and C. Martinez. J. Nucl. Mater. 141-143 (1986) 883.

5.H. R. Brager, DOE/ER-0313/1, 321.

6.R. J. Livak. H. M. Frost, T. G. Zocco, J. C. Kennedy and L. W. Hobbs. J. Nucl. Mater. 141-143 (1986) 160.

7.R. J. Livak, T. G. Zocco and J. C. Kennedy. "Swelling and Tensile Properties of Neutron Irradiated Capper Alloys for High Heat Flux Applications," LA-UR 85-1970.

8.O. K. Harling, N. J. Grant. G. Kohse, T-S. Lee and L. W. Hobbs. J. Mater Res. 2 (5) (1987) 568.

9.J. A. Spitznagel and J. W. Davis. DOE/ER-0045/13, 171.

10.M. Labbe and J. P. Poirier, J. Nucl. Mater. 46 (1973) 86.

11.M. Labbe, G. Brebec and J. P. Poirler, J. Hucl. Mater. 49 (1973/74) 232.

12. K. Farrell and S. J. Zinkle. DOE/ER-0313/3, 90.

6.5 Environmental Effects on Structural Alloys

INFLUENCE OF CARBON AND NITROGEN IMPURITIES ON THE CORROSION OF FERROUS ALLOYS IN A FLOWING-LITHIUM ENVIRONMENT - O. K. Chopra and A. B. Hull (Argonne National Laboratory)

OBJECTIVE

The objective of this research is to provide experimental data for the development of an analytical model that will predict the effect of nonmetallic elements on the corrosion behavior of ferrous alloys in lithium. Measurements of chemical and metallurgical changes are used to establish the mechanisms and kinetics of rate-controlling processes.

SUMMARY

The dissolution of major alloy elements, as well as chemical interactions between N and Cr or Mo, control the corrosion behavior of ferrous alloys. Carbon transfer does not appear to affect the dissolution behavior of ferrous alloys.

PROGRESS AND STATUS

This paper presents data on the surface morphology and canpositional changes of Li-exposed ferrous alloys. Data on the corrosion behavior of several ferritic and austenitic structural materials in flowing Li are reviewed and the effects of nonmetallic elements on corrosion are discussed.

Corrosion tests were conducted in a forced-circulation Li loop equipped with cold- and hot-trapping purification capabilities to control the concentration of nonmetallic elements. Detailed descriptions of the loop and the test procedure have been presented previously.? The exposure temperature and time, Li loop operating conditions, and the N content of the Li are given in Table 1. For all tests. Li was circulated at ~1 ℓ/min in the primary loop, and the concentrations of C and H in the Li were ~10 and 120 wppn, respectively.

Table 1. Lithiun loop operating conditions for various corrosion tests

Test Run	Loop Temperature (°C)				N Content of the Li (wppm)	Exposure Time (h)	
	Test Vessel	Exp.[a] Vessel	Supply Vessel	Cold Trap		Test Vessel	Exp. Vessel
1	482	482	432	212	<50	1295	5000
2	482[b]	482	407	230[c]	~250	--	1997
3	427	402	407	230	~100	1100	--
4	482	427	410	212	<100	5521	6501
5	427	372	372	206	~100	5023	4955
6	538	482	410	208	~50	3655	3330
8	402	427	426	213	~20	2158	2062

[a] Lithium flow was from the test vessel to the specimen exposure vessel.
[b] Test vessel temperature changed from 482 to 427°C after 1540 h.
[c] No flow occurred through the cold trap after 890 h due to plugging. Plugged sections were replaced and flow started after an additional 480 h.

After exposure to Li, the specimens were cleaned in alcohol and water. Several specimens were analyzed chemically to determine the changes in the concentration of nonetallic elements; the surface reaction products were analyzed by x-ray diffraction.

The data for weight losses and steady-state dissolution rates of HT-9, Fe-9Cr-1Mo, and Type 316 SS, reported elsewhere,[1-3] show that, for all alloys, an increase in the N content of the Li from 20 to 100 wppn increases the weight loss during the initial transient period.[1]

Nitrogen can react with alloy elements and Li to form stable ternary nitrides and thus accelerate the corrosion of ferrous alloys.[4,5] The equilibrium concentrations of N and C in Li for which metal nitrides and carbides are stable[6-8] are shown in Fig. 1. The ternary nitrides are soluble in alcohol or water and. therefore, are not observed on cleaned specimens. The presence of the ternary nitride Li_9CrN_5 on HT-9 and Type 316 SS specimens exposed during Run 6 was detected by chemical analysis of the methanol used for cleaning the specimens.[1] The concentrations of the major elements (expressed as wppm in Li) that were dissolved in the methanol are given in Table 2. The high concentration of Cr in the solutions indicates the

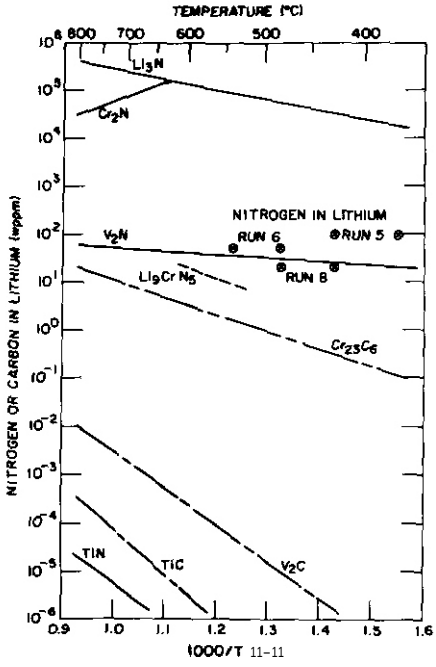

Fig. 1. Equilibriun values of nitrogen and carbon concentration in lithiun for which metal nitrides and carbides are stable.

Table 2. Concentrations (wppm) of alloy constituents in lithium[a] fran spectrochemical analysis of methanol used for cleaning corrosion specimens exposed to the lithiun at 538 and 482°C

Alloy	Major Elements (ppm)							
	538°C				482°C			
	Cr	Fe	Ni	Mo	Cr	Fe	Ni	Mo
T-9	19	67	<15	10	42	33	<15	12
Type 316 SS	46	68	13	135	207	31	14	60
Lithium[b]	<5	17	13	<10	<5	18	<15	<10

[a] Lithium film which adheres to the specimen when it is removed from the loop.
[b] Concentration of alloying element in the loop lithium.

formation of the ternary nitride of Cr on the alloy surfaces exposed to Li. The Cr content of the methanol solution after cleaning Type 316 SS specimens was significantly greater than the Cr content of the methanol after cleaning HT-9 specimens. This was particularly true for specimens exposed at 482°C. The relatively high concentrations of Mo in the solutions after cleaning Type 316 SS specimens also indicate the presence of ternary nitrides involving Mo. These results indicate that chemical interactions between alloy elements and N play a daninant role in the corrosion behavior of austenitic steels in Li. The effect of these interactions on the corrosion behavior will be larger at lower temperatures, e.g., at 482 or 427°C, because the driving force for nitride formation increases as temperature decreases.

An implication of such chemical interactions is that the corrosion behavior cannot be accurately obtained fran a single specimen exposed for various times, particularly for Type 316 SS. The formation of ternary nitrides during each exposure period and the subsequent loss during the cleaning procedure result in ight loss and corrosion rate. The relatively constant dissolution rates obtained for Type 316 SS (~2 mg/ h) at temperatures between 372 and 538°C may be attributed to chemical interactions involving N and the experimental procedure. Separate specimens should be exposed to Li for different times to accurately establish the dissolution rates of Type 316 SS. Figure 1 indicates that the N content of the Li should be below ~1 wppn to avoid formation of ternary nitrides and their effects on corrosion.

The corrosion data from the various test runs indicate large deposits on specimen surfaces[1,2] (for example see Fig. 2). A detailed examination of the Li-exposed specimens reveals surface deposits on all specimens exposed at 427 or 482°C. Specimens exposed at the downstream location contain very large particles whereas the specimens exposed at the maximun loop temperature contain fine surface deposits. Significantly fewer deposits are seen on HT-9 and Fe-9Cr-1Mo specimens than on Type 316 SS specimens. X-ray analyses indicate that these deposits are carbides and that the nature of the carbides changes with exposure time. For example, $M_{23}C_6$ carbides are observed after relatively short exposure times (~1000 h at 427 or 482°C) whereas both $M_{23}C_6$ and M_7C_3 are observed after longer exposure times (>2500 h). The total carbon content of the specimens, however, did not increase significantly with an increase in time from 1000 to 5000 h.

Surface deposits have also been observed on pure Cr specimens exposed to Li at 482 and 427°C.[3] The deposits were identified as $Cr_{23}C_6$ for the specimen exposed at 482°C (maximum loop temperature) and as $Cr_{23}C_6$ and Cr_7C_3 for the specimen exposed at 427°C (downstream location).

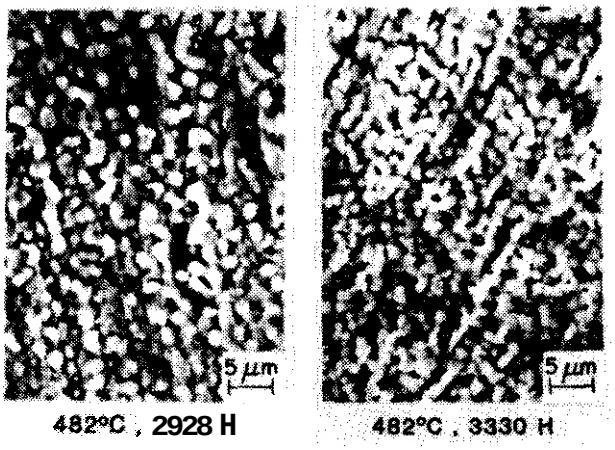

Fig. 2. Examples of surface deposits on HT-9 and Type 316 SS.

The ferritic and austenitic steels exposed to Li during Runs 4, 5, and 6 were analyzed chemically to detennine the changes in C content. The results are plotted in Fig. 3. Sane specimens were mechanically polished to remove the surface deposits or the ferrite layer on Type 316 SS before the bulk C concentration was measured. The results for Type 316 SS indicate that the material decarburizes at 538°C and carburizes at 482 and 427°C; little or no change was observed at 372°C. The influence of surface deposits is significant only for the specimens exposed at the downstrean location, viz., the bulk C content of these specimens is ~22% lower than that of the unpolished specimen. The presence of large surface deposits on the downstrean specimens is most likely due to the deposition of Cr fran Li. The decarburization/carburization behavior of Type 316 SS does not seem to be affected by the surface deposits. Specimens exposed at the maximun loop temperature of 482°C have little or no deposits but contain higher C concentrations (737 wppm) than the downstream specimens (652 wppm) exposed at the same temperature, which have surface deposits. The formation of ternary nitrides may, however, influence the C transfer. The lack of C transfer even after an ~5000-h exposure to Li at 372°C may be attributed to kinetic limitations and possibly to the presence of ternary nitrides on the specimen surface.

The results for HT-9 and Fe-9Cr-1Mo, Fig. 3b, indicate no C transfer after long exposure at tenperatures between 372 and 538°C. The slightly higher C content of specimens exposed at 482 and 427°C appears to be associated with the surface deposits.

These results indicate that chemical interactions involving C are not likely to influence the overall corrosion behavior of ferrous alloys significantly. The carbides that fonn on the alloy surfaces are adherent. The transfer of C to and from the alloys, and the carbide deposits on the surface, may, however, influence the weight change measurements. For example, a 300 wppn increase in bulk C content in the foil Specimens used in this investigation would correspond to an increase of ~0.35 g/m^2 in weight. Such weight changes will be insignificant for the austenitic Type 316 SS which shows 10- to 30-g/m^2 weight loss after the initial transient weight loss period. The ferritic steels show no change in the bulk C content.

CONCLUSIONS

(a) The dissolution of major alloy elements, as well as chemical interactions between N and Cr or Mo, control the corrosion behavior of ferrous alloys. The contribution of chemical interactions is significant for austenitic Type 316 SS. Thermodynamic data indicate that the N content in Li should be <1 wppn to avoid chenical interactions.

(b) The weight loss data for Type 316 SS obtained from a single specimen exposed for various times do not accurately represent the corrosion rates. The relatively constant dissolution rates reported for Type 316 SS at temperatures between 372 and 538°C are most likely due to the experimental procedure and contributions of chemical interactions.

(c) When exposed to Li containing ~10 wppn C, the austenitic Type 316 SS decarburizes at 538°C and carburizes slightly at 482 and 427°C. The ferritic HT-9 and Fe-9Cr-1Mo steels are resistant to decarburization/carburization and show little or no C transfer.

(d) Carbon deposits are observed on the ferritic and austenitic steel surfaces, particularly on specimens located at the downstrean position. Carbon transfer does not appear to affect the dissolution behavior of ferrous alloys.

FUTURE WORK

Over the next six months, the role of chemical activity in the decarburizationlcarburization reactions will be explicitly investigated.

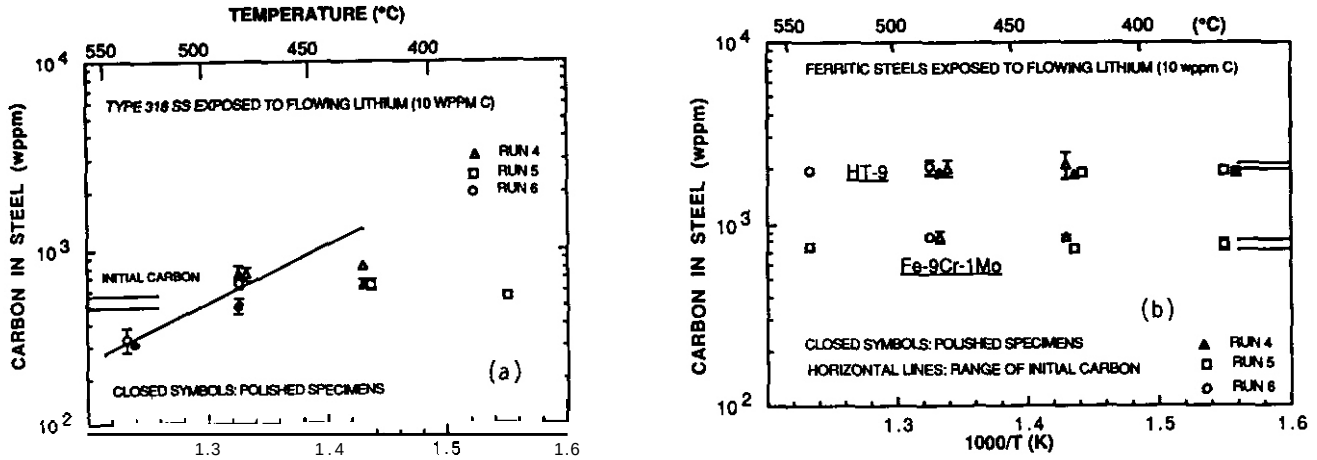

Fig. 3. Effect of lithium exposure on carbon concentration in (a) and (b) ferritic steels.

REFERENCES

1. O. K. Chopra and D. L. Smith, J. Nucl. Mater. 133&134, 861 (1985).

2. O. K. Chopra and D. L. Smith, J. Nucl. Mater. 141, 584 (1986).

3. O. K. Chopra and D. L. Smith, in Proc. 3rd Int. Conf. on Fusion Reactor Materials, Karlsruhe. FUG, October 4-8, 1987, to be published in J. Nucl. Mater. (1988).

4. M. G. Barker and S. A. Frankham, J. Nucl. Mater. 107, 218 (1982).

5. E. Ruedl and T. Sasaki, J. Nucl. Mater. 116. 112 (1983).

6. M. G Barker, J. A. Lees, and I. E. Schreinlechner, in Proc. 14th Symp. on Fusion Technology, Avignon. France, September, 1986.

7. D. L. Smith and K. Natesan. Nucl. Technol. 22, 392 (19741.

8. K. Natesan, J. Nucl. Mater. 115, 251 (1983).

INFLUENCE OF HYDROGEN, NITROGEN, AND CARBON IMPURITIES ON THE CORROSION OF VANADIUM ALLOYS IN A FLOWING-LITHIUM ENVIRONMENT - A. B. HULL, O. K. CHOPRA, B. LOOMIS, and D. L. SMITH (Argonne National Laboratory)

OBJECTIVE

The objective of this research is to provide experimental data for the dwelopnent of an analytical model that will predict the effect of normetallic elements on the stability of V alloys in Li.

SUMMARY

Vanadiun alloys pick up N and C from and release H to Li. Alloys with Ti or Cr develop a N-rich surface layer. Chemical interactions involving C play an important role in the dissolution behavior of V alloys. Results obtained in this study indicate that H embrittlement as a result of a higher concentration of H in Li is unlikely and tritium pickup by V alloys in the reactor structure will not be significant.

PROGRESS AND STATUS

The H distribution and corrosion tests were conducted in a forced-circulation Li loop that is constructed of Type 304 stainless steel and consists of a primary loop equipped with three test vessels and a secondary cold-trap purification system. Hydrogen partial pressure (P_{H_2}) was monitored daily with a H activity meter.[1] Filtered (5 μ metal frits) Li samples were analyzed for N and C. A detailed description of the loop and the procedure for Li sampling has been presented previously.[2,3]

Various V alloys were immersed in the flowing Li in two separate isothermal test vessels maintained at different temperatures. Following exposure, the specimens were cleaned in methanol to avoid the introduction of H. Specimens were chemically analyzed to determine the changes in the concentration of H,[4] N, and C.[5] The surface reaction products were analyzed by x-ray diffraction.

Hydrogen in lithiun

The temperature dependence of the terminal solubility, S_H, expressed in weight fraction (Fig. 1), is given by the following equation from Ref. 6:

$$\ln S_H = 1.578 - 5314/T, \quad (1)$$

where T is the absolute temperature. The relationship between the concentration of H in solution and P_{H_2} can be represented by Sieverts' constant, K_s, as follows:

$$C = K_s (P_{H_2}) \quad (2)$$

where P_{H_2} is expressed in torr and C is the weight fraction of H in the Li. The temperature dependence of the Sieverts' constant, K_s, is expressed as

$$\ln K_s = A + B/T, \quad (3)$$

where A and B are constants whose values for H in Li and various refractory metals have been determined.[4] To a first approximation, the H content in Li, i.e., the value of C in Eq. (2), is established by the cold-trap tenperature, and can be determined fran Eq. (1). Subsequently, P_{H_2-T}, the temperature-dependent pressure based on Sieverts' equation, can be calculated from Eq. (2) by substituting for C the value of S_H obtained fran Eq. (1) with the absolute temperature of the cold trap, and for K_s the value obtained from Eq. (3) with the absolute temperature of the supply vessel. Data from 232 pressure gauge readings, P_{gauge}, taken over a period of ~3 yr were plotted against the calculated partial pressure, P_{H_2-T}, corresponding to the same cold-trap and supply vessel temperatures. A linear least squares fit to these 232 data points was used to derive the following calibration equation for the normalized H partial pressure, P_{H_2-N}:

$$P_{H_2-N} = -0.16583 + 0.10566\ P_{gauge} \quad (4)$$

Subsequently, by substituting P_{H_2-N} into Eq. (2), and using Eq. (3) to determine K_s, we could derive the dissolved concentration of H in Li, C_N, from the normalized partial pressure and the temperatures of the cold trap and the Li supply vessel in which the pressure sensor was imnersed. In Fig. 2, such results (closed diamonds) are canpared with S_H determined by Eq. (1). Similarly, the theoretically derived values for the partial pressure, P_{H_2-T}, are canpared with the gauge-derived values, P_{H_2-N} (closed circles), as obtained in Eq. (4).

The temperature of the supply vessel and cold trap at the top of Fig. 2 can be seen to have an effect on both the measured and calculated values of H in Li. A case in point is that of $t = 5.07 \times 10^4$ h (the loop age of this batch of Li at the time of the gauge reading) where the cold-trap temperature drops 16°C and H concentrations plummet.

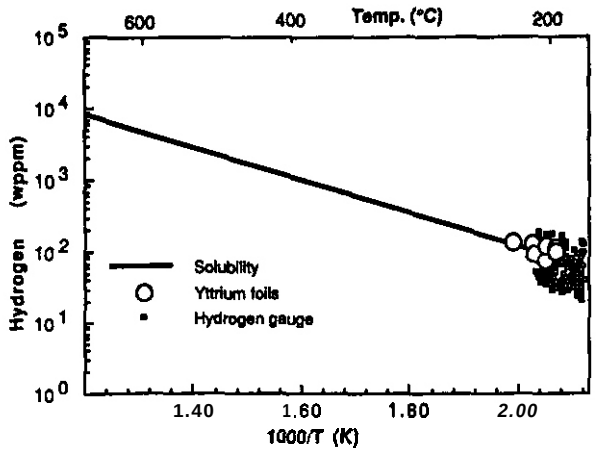

Fig. 1. Solubility of hydrogen in liquid lithium

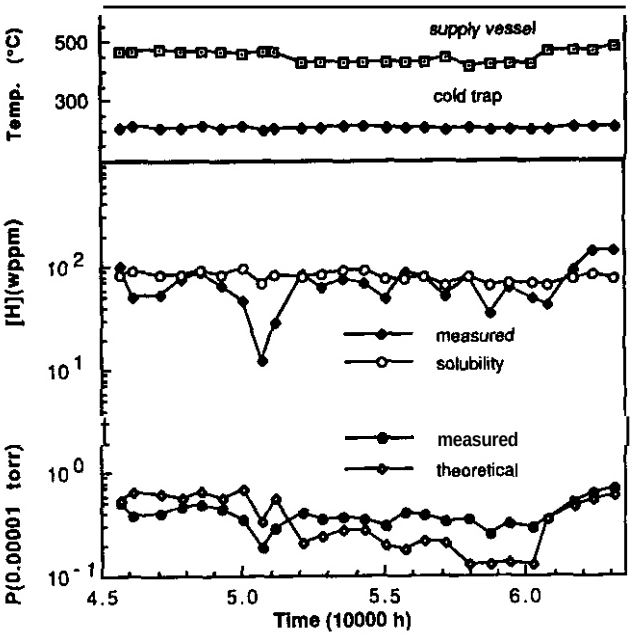

Fig. 2. Time-dependent concentration of hydrogen in lithium in the FFTL-3 forced-circulation loop.

Partitioning of hydrogen

Hydrogen will fractionate between Li and various refractory metals as a function of temperature. A distribution coefficient, K_w, can be defined as the ratio of the H concentration in the V alloy to that in the liquid Li:

$$K_w = C_V/C_{Li}, \qquad (5)$$

where C_V and C_{Li} are concentrations (wt %) of H in the V alloy and Li, respectively, at constant P_{H_2}. The temperature-dependent distribution of H between Li and several refractory metals takes the same form as Eq. (3). Using tabulated values[4] for A and B, the partitioning of H is shown graphically in Fig. 3.

Yttrium samples were immersed in the Li loop at temperatures ranging from 408 to 538°C. The concentration of H in the Y specimens, determined by vacuun fusion analysis (Table 1), was used in conjunction with calculated distribution coefficients to determine the H concentration in Li. These H concentrations, plotted as a function of cold-trap temperature (Fig. 1), show good agrement with the solubility curve. On the basis of canparison of the H concentrations obtained from equilibration of Y foils with those obtained fran P_{gauge} readings, it was concluded that the activity meter gave an acceptable correlation between the H content of the Li and the measured partial pressure.

Table 1. Calibration of hydrogen in loop via hydrogen content in yttrium specimens exposed to lithim

Spec. No.	Exposure Temp. (°C)	Cold-Trap Temp. (°C)	H (wt %) in Yttrium	K_w^a	H (wppm) in Lithium
Y8	408	221	1.00 ± 0.27	78.94	127
Y9	422	230	0.98 ± 0.24	69.03	142
Y15	482	210	0.48 ± 0.01	41.08	117
Y11	482	220	0.38 ± 0.06	41.08	92
Y16	482	210	0.41	41.08	100
Y60	538	215	0.21	27.13	17
Y61	538	215	0.32	27.13	118

[a]Calculated from distribution coefficient equations.[4]

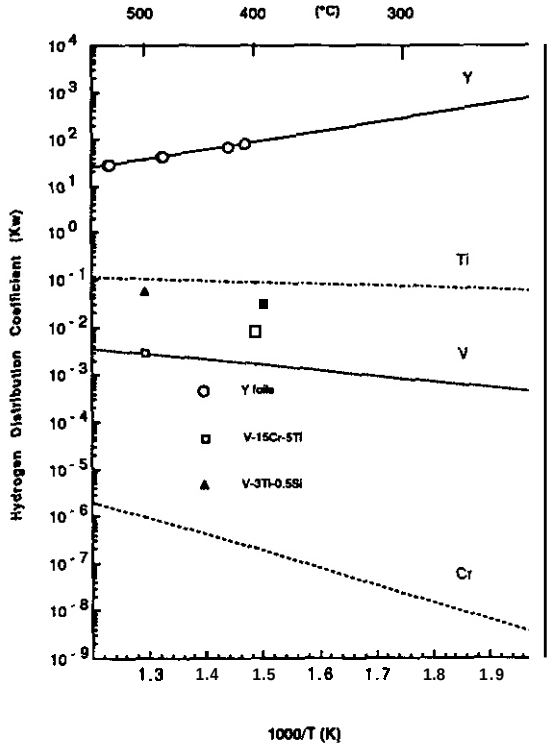

Fig. 3. Temperature dependence of equilibrium distribution coefficients for hydrogen between selected refractory metals and lithiun.

Carbon and nitrogen in vanadiun alloys

The concentrations of N and C in pure V and some alloys exposed to Li at temperatures between 427 and 538°C are given in Table 2. At 538, 482, and 427°C, the solubility of N in pure V is 4670, 3570, and 2640 wppm, respectively; that of C is 487, 366, and 265 wppm, respectively.[7] For pure V specimens, the measured N content is slightly below the solubility level and the C content represents the saturation level. V_2N is not stable at 482°C in Li containing 20 wppn N (conditions for Run 8).[5] The partitioning of N between pure V and Li can be obtained fran the equilibriun distribution coefficient, K_w,[7,8] given by Eq. (5) with a temperature dependence of

$$K_w = \exp (6.52 - 1394/T). \quad (6)$$

For 20 wppm N in Li, the equilibriun N content in V should be 2140 and 1840 wppn at 482 and 427°C, respectively. The measured N concentration in pure V exposed at 482°C is close to the equilibrium concentration. The equilibrium value is not achieved after ~1400 h at 427°C owing to kinetic limitations.

V_2C is stable under the present exposure conditions of 10 wppn C in Li. X-ray analyses of the pure V specimens, however, did not show any carbides or nitrides on the specimen surfaces. It is likely that the V_2C that forms on pure V specimens is not adherent and spalls during Li exposure. This may be the daninant contribution to the weight loss of V alloys.

The V alloys show an increase in N and C content. The gain in N increases with time and temperature. Analyses of the specimens with or without the surface scale indicate a significant increase in the N content of the bulk material, a finding that is confirmed by hardness measurements that showed an increase in microhardness of the surface region of the specimens.[9] It is highly probable that a N-rich scale forms that, being quite hard and brittle, can break off under thermal stresses, resulting in higher weight losses. Spalling of the surface scale was, however, rare.

CONCLUSIONS

To a first approximation, the cold-trap temperature had a significant effect on controlling the upper limit of H in the system, which is well under that necessary to affect the integrity of V alloys. The corrosion mechanisms for V alloys are most likely dissolution of alloy elements and chemical interactions involving C. Chemical interactions with N have a secondary effect, but may be more important for the effects on mechanical properties.

FUTURE WORK

Experiments are planned to better define temperature-dependent distribution coefficients between H and V alloys as a function of substitutional alloying elanents.

Table 2. Carbon and nitrogen contents in vanadiun alloys exposed to lithiun

Alloy	Test Run	Exposure Condition Temp. (°C)	Time (h)	Impurity Content[a] (wppm) Carbon	Nitrogen
Pure V	Unexposed			360	161 ± 41
	8	482	484	340 (330)	681 ± 65
	8	482	1508	270	3404 ± 187 (3410 ± 129)
	8	427	1405	320	656 ± 71
V-10Cr-3Fe-Zr	Unexposed			890	271 ± 66
	6	538	590	1190	12418 ± 621 (6258 ± 227)
	a	482	1080	1070	---
	6	482	687	990	4570 ± 250
V-15Cr-5Ti[b]	Unexposed			390	527 ± 109
	6	482	619	530	---
	8	482	1992	570	2361 ± 114 (1955 ± 78)
	8	427	1405	500	607 ± 84
V-15Cr-5Ti[c]	Unexposed			390	299 ± 68
	6	538	794	---	(4895 ± 179)
	6	538	1384	(670)	11935 ± 434 (10022 ± 505)
	6	482	1618	700	2808 ± 177
V-20Ti	Unexposed			---	566 ± 168
	6	538	1384	---	8862 ± 328 (5735 ± 295)
	6	482	619	---	604 ± 124
	6	482	1618	---	(2595 ± 110)

[a]Values within parentheses represent concentrations for specimens which were mechanically polished to remove the surface reaction products.
[b]ORNL heat.
[c]ANL heat.

REFERENCES

1. D. R. Vissers, J. T. Holmes, and P. A Nelson, Trans. An. Nucl. Soc. 14, 610 (1971).

2. O. K. Chopra and O. L. Smith, J. Nucl. Mater. 1336134, 861 (1985).

3. O. L. Smith, R. H Lee, and R. M Yonco, in Proc. Second Int. Conf. on Liquid Metal Technology in Energy Production, U.S. Department of Energy Report CONF-800401-P1 p. 272 (1980).

4. A 8. Hull, O. K. Chopra, B. Loomis, and D. L Smith, in Proc. Eighth Topical Mtg. Tech. Fusion Energy, October 9-13, 1988, Salt Lake City, UT; to be published in Fusion Technology (1988).

5. O. K. Chopra and A B. Hull, in Proc. Eighth Topical Mtg. Tech. Fusion Energy, October 9-13, 1988, Salt Lake City, UT; to be published in Fusion Technology (1988).

6. N. Rumbaut, F. Casteels, and M Brabers. Int. Conf. on Material Behaviour and Physical Chemistry in Liquid Metal Systems, March 24-26, 1981, Karlsruhe, FRG.

7. D. L. Smith and K. Natesan, Nucl. Technol. 22, 392 (1974).

8. K. Natesan, J. Nucl. Mater. 115 (2&3), 251 (1983).

9. O. K. Chopra and D. L. Smith, in Proc. Third Int. Conf. on Fusion Reactor Materials, October 4-8, 1987, Karlsruhe, FRG; to be published in J. Nucl. Mater. (1988).

MOLTEN EUTECTIC Pb-17Li ENVIRONMENT: EFFECT ON CORROSION AND TENSILE PROPERTIES OF FERRITIC STEELS AND WELDMENTS - O. K. Chopra, D. L. Smith, and A. B. Hull (Argonne National Laboratory)

OBJECTIVE

The objective of this research is to investigate the influence of a flowing Pb-17 at. % Li enviroment on the corrosion behavior and mechanical properties of structural alloys under conditions of interest for fusion reactors.

SUMMARY

The dissolution rates of the weldnent specimens are comparable to those of the base metal. The Pb-17Li enviroment has no deleterious effect on the tensile properties of postweld heat-treated HT-9 weldnents.

PROGRESS AND STATUS

Tests were conducted in a forced-circulation loop consisting of a high-temperature test vessel constructed fran plain carbon steel, and a cold leg constructed fran Type 304 stainless steel. Detailed descriptions of the loop and test procedure have been presented previously.[1,2] Constant-extension-rate tests were conducted on a postweld heat-treated KI-9 weldnent in flowing Pb-17Li to investigate environmental effects on the tensile properties.[2] Prior to testing, all specimens were exposed for ~18 h to flowing Pb-17Li at 425°C to achieve complete wetting of the specimen surface.

The corrosion behavior was evaluated by exposing HT-9 and standard Fe-9Cr-1Mo (T-9) weldment specimens which had received postweld heat treatment to flowing Pb-17Li at 425°C for ~900 h. An HT-9 specimen with a simulated heat-affected-zone (HAZ) structure (produced by blank GTA weld passes) was also included in the test. After exposure to flowing Pb-17Li, the HT-9 and T-9 weldnent specimens and the specimen with a simulated HAZ structure exhibited weight losses of 7.17. 3.19, and 3.73 $g \cdot m^{-2}$, respectively. The average dissolution rates for the weldnents are shown in Fig. 1 along with the results for the base metal. The dotted line represents a theoretical 316 SS curve; the solid line represents HT-9.

Metallographic examination of the exposed HT-9 and T-91 weldnents indicates that the corrosion behavior of the weldments is similar to that of the base metal. The surface of the exposed specimens showed nonuniform corrosion, i.e., preferential attack along grain boundaries and martensitic lathe boundaries. Micrographs of the surface of the HT-9 and T-9 weldments exposed to flowing lithiun are shown in Fig. 2

Similar corrosion behavior has been observed with normalized and tempered KI-9 alloy.[8] Micrographs of the surface of HT-9 specimens exposed to flowing Pb-17Li at 371, 427, and 482°C are shown in Fig. 3. The preferential attack increases with an increase in temperature. The specimen exposed at 371°C exhibits little or no corrosive attack, whereas the specimen exposed at 482°C shows preferential attack along grain boundaries and martensitic lathe boundaries.

The surface of the specimen with a simulated HAZ structure was quite different from the surfaces of the HT-9 and T-9 weldnents. The edge of the specimen, which represents the simulated HAZ, showed extensive corrosion, chromium depletion. and development of an ~20-urn-thick corrosion scale (Fig. 4).

The tensile properties of the HT-9 alloy and weldment determined in flowing Pb-17Li between 270 and 450°C are shown in Fig.5. Whereas the ultimate and yield strengths are higher than those of the HT-9 base metal, the reduction in area is lower. The Pb-17Li enviroment has no detrimental effect on the tensile properties. For all the weldment specimens, fracture occurred in the base metal, near the shoulder of the specimen (Fig. 6). The gauge length of the specimen, consisting of weld metal and HAZ, showed minimal elongation.

The gauge surfaces in contact with Pb-17Li did not show signs of corrosive attack or surface cracks. However, surface cracks oriented 45' to the tensile axis were observed in the necked region of the specimen. Micrographs of the fracture surface and gauge surface of the necked region are shown in Fig. 7. The gauge surface (Fig. 7b) very closely resembles the surface of a normalized and tempered specimen after exposure to canparable conditions.

CONCLUSIONS

Corrosion data obtained from HT-9 and T-9 weldments in flowing Pb-17Li at 425°C indicate that the corrosion behavior of weldnents that received postweld heat treatment is similar to that of the base metal. For both steels, the dissolution rates of the weldment specimens are canparable to those of the base metal. The exposed specimens show nonuniform corrosion, i.e., preferential attack along grain boundaries and martensitic lathe boundaries. However, the untempered HT-9 weld structure exhibited extensive corrosion.

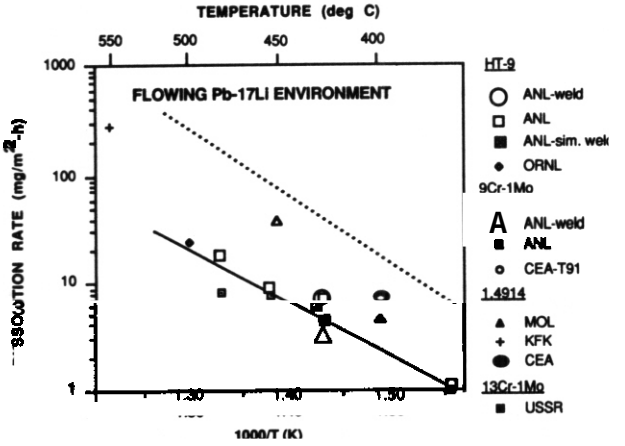

Fig. 1. Arrhenius plot of corrosion rate data for ferritic steels and weldnents in flowing Pb-17Li. Dashed line for austenitic 316 SS. References: ANL, USA; [1] ORNL, USA; [3] CEA. France; [4] MOL Belgium; [5] KfK, FRG; [6] USSR. [7]

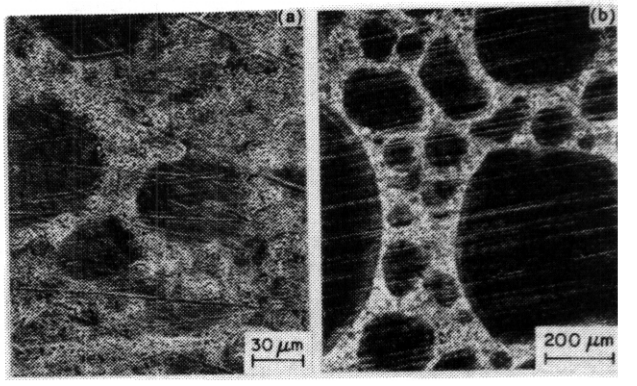

Fig. 2. Surface of (a) HT-9 and (b) 9Cr-1Mo weldnents exposed to flowing Pb-17Li at 425°C for 900 h.

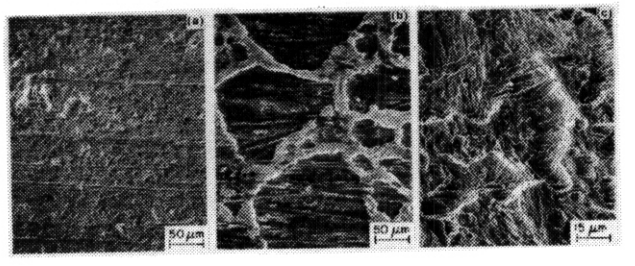

Fig. 3. Surface of HT-9 alloy exposed to flowing Pb-17Li at (a) 371. (b) 427. and (c) 482°C.

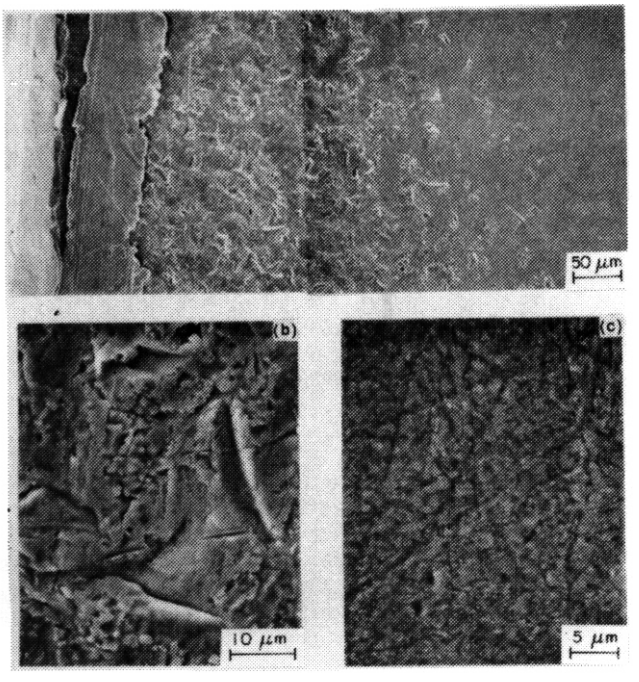

Fig. 4. Simulated HAZ structure exposed to Pb-17Li at 425°C for 900 h; (b) HAZ; and (c) base metal regions.

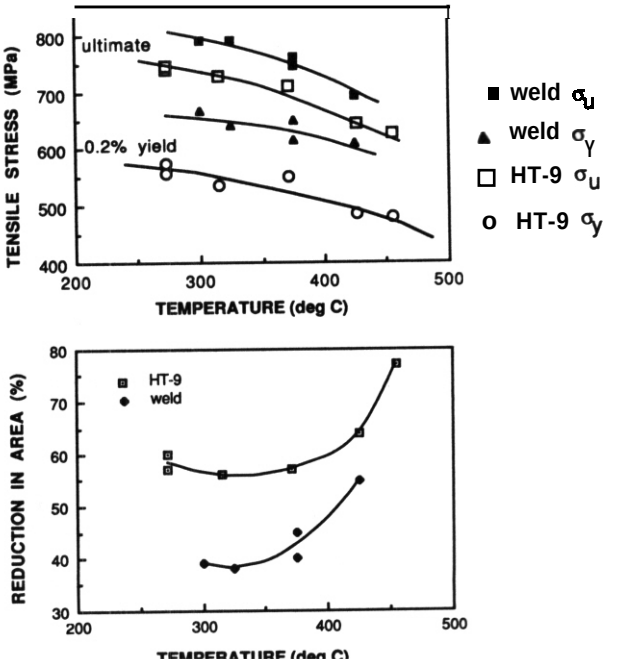

Fig. 5. (a) Tensile strength and (b) reduction in area for HT-9 base metal and weldment specimens tested in flowing Pb-17Li environment.

Fig. 6. Location of fracture in an HT-9 weldnent specimen.

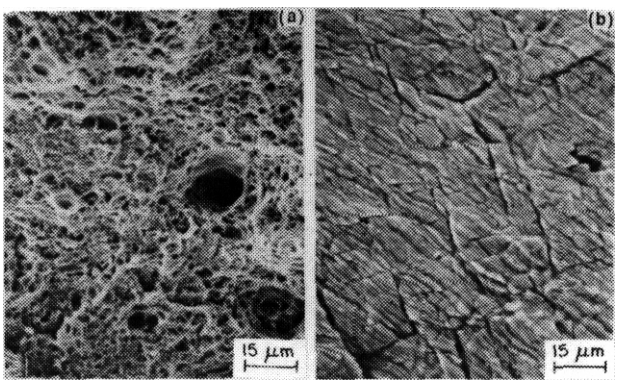

Fig. 7. (a) The fracture surface and (b) gauge surface of the necked region of a weldnent specimen tested in flowing Pb-17Li at 325°C.

Tensile data obtained in flowing Pb-17Li indicate that the properties of postweld heat-treated HT-9 weldnents are similar to those of the HT-9 base metal. The Pb-17Li environment has no deleterious effect on tensile properties of HT-9 weldnents.

FUTURE WORK

Comparative testing of U.S. and EC ferritic steels (1.4914) will be corrosion tested in Pb-17Li as part of a U.S./KFK collaboration.

REFERENCES

1. O. K. Chopra and D. L. Smith. J. Nucl. Mater. 122 & 123. 1219 (1984).

2. O. K. Chopra, D. L. Smith. and A. B. Hull, in Proc. Fourth Int. Conf. Liquid Metal Engineering and Technology, Palais des Papes, Avignon, France, Oct. 17-21, 1988.

3. P. F. Tortorelli and J. H. DeVan, J. Nucl. Mater. 141-143, 592 (1986).

4. M. Broc, T. Flanent. P. Fauvet, and J. Sannier, presented at the Third Int. Conf. Fusion Reactor Materials (ICFRM-3), Karlsruhe. Oct. 4-8, 1987.

5. H. Tas, Ja. Dekeyser, and F. de Schutter, presented at the Fourth Int. ENS/ANS Conference (ENC-4) Geneva, Switzerland. June 1-6, 1988.

6. H. U. Borgstedt, G. Drechsler, G. Frees, and Z. Peric, presented at the Third Int. Conf. on Fusion Reactor Materials (ICFRM-3), Karlsruhe. Oct. 4-8, 1987.

7. V. I. Nikitin et al., USSR Contribution to INTOR, Appendix VI (1983).

8. O. K. Chopra and D. L. Smith. J. Nucl. Mater. 141 & 143, 566 (1986).

CORROSION IN LIQUID METAL ENVIRONMENTS: EFFECT OF COLD WORK ON ATTACK *OF* STAINLESS **STEEL BY LITHIUM AND MASS TRANSFER OF STANDARD** *AND* **REDUCED ACTIVATION STEELS IN Pb-17 at. % Li** - P. F. Tortorelli (Oak Ridge National Laboratory)

OBJECTIVE

The purpose of this wrk is to characterize the corrosion of candidate or wdel fusion materials by slowly flowing lithium and Pb-17 at. % Li in the presence of a temperature gradient. Dissolution and deposition rates are measured as a function of alloy composition, expoaure time, temperature, and additions to the liquid mtals. These measurements are combined with microstructural analyses of the specimen surfaces to establish mechanisms and rate-controlling processes for the corrosion and mass transfer reactions, deterline the suitability of particular materials for service in specific liquid metal environments, and provide input into fusion materials development.

SUMMARY

A microstructural influence on the attack of PCA exposed to mlten lithiun was observed when comparing annealed and cold rolled specimens. Weight loss results for reduced activation austenitic and ferritic ateels in Pb-17 at. % Li were similar to those manured for their standard counterparts. Further examination of mass transfer depoaita in long-tam austenitic and ferritic steel thermal convection loops showed that depoait composition was a function of temperature only in the type 316 stainless ateel system and that. in contrast to the type 316 stainless ateel results, solubility-driven reactions appeared to be the most important depoaition process in the Fe-12Cr-1MoVW steel system.

PROGRESS AND STATUS

Effect of wld work on attack of *austenitic* ateel by molten lithium

It has previously been suggested that the effect of cold work vas to bias the penetration process of austenitic stainless steel in molten lead-lithium and that such an influence can be accommodated within a surface destabilization model.[1,2] Recent measurements of the depth of attack of annealed and wld worked PCA exposed to thermally convective lithium at 600 and 570°C revealed a similar effect. As shown in Fig. 1, the ratio of the corrosion depth on the long face of a specimen to that on the short face decreases significantly as the amount of cold work (grain elongation parallel to the long face) is increased. This behavior is consistent with Observations reported earlier for type 316 stainless steel exposed to lead-lithium[1,2] and can be ascribed to a biasing of the penetration process induced by the presence of slip lines and the elongation of grain boundaries in the rolling direction. Such an influence on microstructure is consistent with a surface destabilization mdel and the present observations suggest that this mechanism may trigger the irregular corrosion process of austenitic stainless steel undergoing preferential dissolution by lithium in a manner similar to what has been proposed for lead-lithium.[1,2] However, as concluded in the preceding progress report,[3] the aforementioned model cannot alone adequately describe the penetration kinetics for type 316 stainless steel exposed to mlten lithium because of complications caused by surface product reactions.

Reduced activation steels

During the current reporting period, the expoaure of representetive reduced activation austenitic and ferritic steela to thermally convective Pb-17 at. % Li (in separate loops) was completed. This work represented the final phase of the evaluation of the corrosion of such steels in both lithium and lead-lithium. The corrosion of austenitic steels by lithium was examined in the first stage of the planned experiments. which, by design. wes the most comprehensive. The results from that work. previously reported,[4,5] showed that these Mn steels were not particularly corrosion resistant to molten lithium. It was, therefore, not expected that such alloys would be resistent in lead-lithium, which is an even more aggressive environment. Consequently, only selected steels were exposed in order to check the predicted behavior. *An* with the austenitic steels, the lead-lithium work with ferritic steels was performed for confirmatory information relative to the lithium results with these materials (which showed little difference between standard and reduced activation ferritic steels).[4] The Pb-17 at. % Li results shoved that the 500°C corrosion losses Of the reduced activation eustenitic (PCMA-2, -6) and ferritic (V-64, steel 13) steels (see Table 1) were similar to those of standard steels exposed under similar conditions (see Fig. 2. There *was* certainly no indication that these reduced activation materials would perform better in lithium or lead-lithium than their standard counterparts. Indeed, there is some evidence from Fig. 2 and previous work with lithium[4,5] that the austenitic Mn steels may corrode at higher rates than Ni-based stainless steels.

Mass transfer in steel Pb-17 at. % Li systems

The net flux, J_i, of a given element out of a specimen exposed to the molten lead-lithium can be expressed as

$$J_i = k_i(C_i^o - C_i) \quad (1)$$

where k_i is the overall (net) rate constant for dissolution or deposition of element i, C_i^o is the solubility of that element in the liquid metal at a particular temperature, and C_i is the actual concentration of i in the liquid. For the present purposes, C_i can be considered constant around the loop so that the variation of the solubility with temperature determines whether dissolution ($C_i^o > C_i$, $J_i > 0$) or deposition ($C_i^o < C_i$, $J_i < 0$) occurs. The positioning of coupons around the loops therefore allows measurement of mass transfer profiles for a given exposure time (see Fig. 3). as well as examination of the types of deposits that form in the cold zone. As reported previously,[1] the exposed surfaces and polished cross sections of the cold leg coupons from the type 316 stainless steel loop experiment were analyzed by scanning electron microscopy and associated energy dispersive a-ray analysis (EDX). It was found that, on any one particular specimen, variations in deposit density were noted and, on some coupons, there were rather large areas free of deposits (possibly removed during handling and/or cleaning). The compositions of mass transfer deposits on each type 316 stainless steel cold leg specimen were determined by EDX and a marked dependence of deposit composition on loop temperature and position was noted.[1] At the higher temperature positions in the cold leg (460 and 445°C), the deposits were principally iron, while at lower temperatures. they were either iron-nickel or chromium-rich. At 430°C, most of the deposits were iron-nickel, while chromium-rich deposits dominated at 415°C. At the coldest loop coupon position (400°C), most deposits were chromium-rich, with a few being a mixture of these two compositions. Recent x-ray diffraction data for the surfaces containing these deposits showed only the presence of bcc and fcc structures consistent with metallic deposits and the underlying austenitic Stainless steel. In contrast to the results for the type 316 stainless steel TCL, the compositions of the deposits in the ferritic steel loop did not vary with position in the cold leg. EDX analysis showed almost all deposits to consist of Fe + 8-9 wt % Cr.

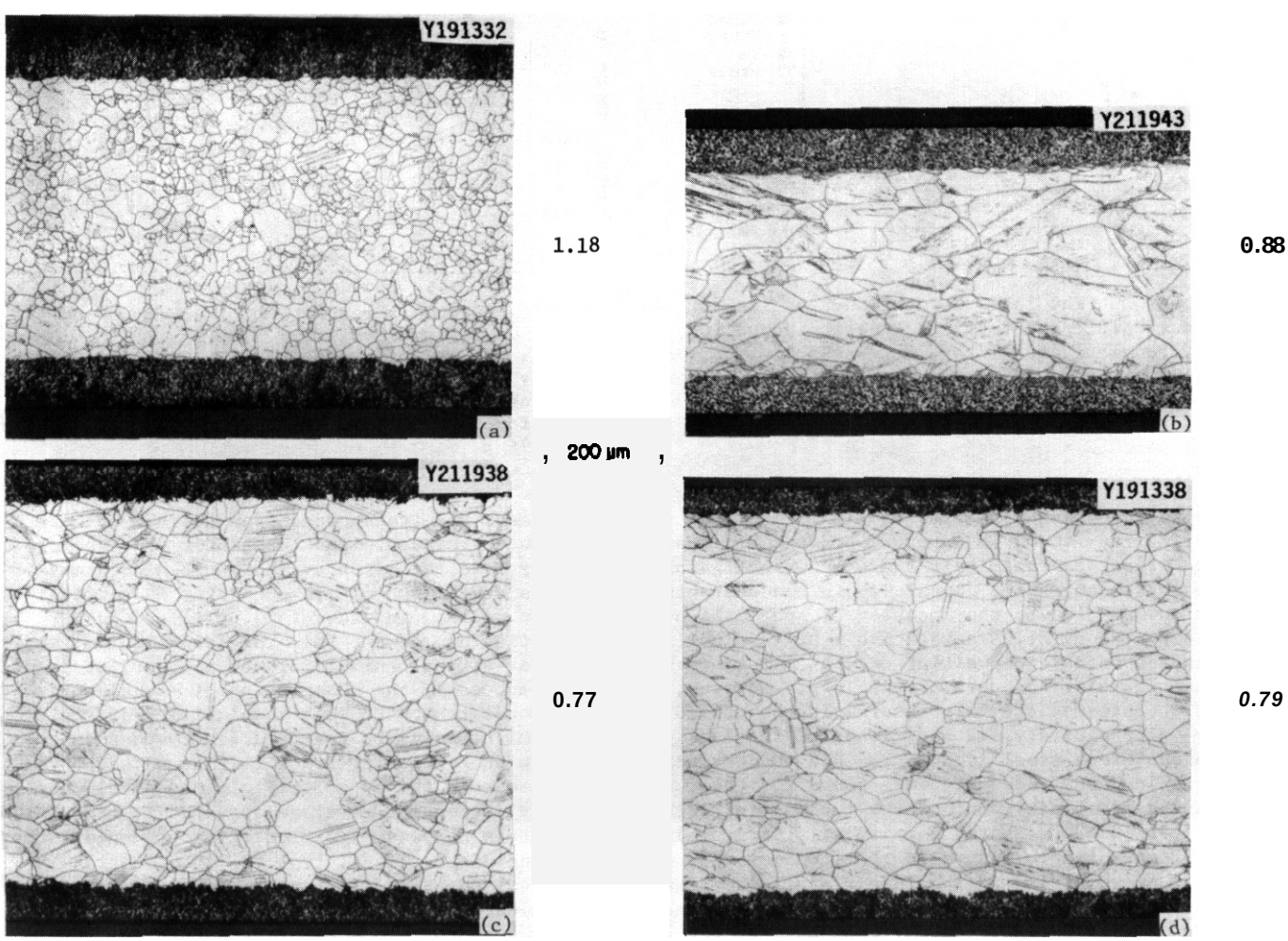

Fig. 1 Polished and etched cross sections of PCA exposed to thermally convective lithium. Numbers represent ratio of average depth of corrosion layer on long face (show) to that on short face. (a) Annealed, 600°C, 6696 h. (b) Cold rolled, 600°C, 6691 h. (c) Cold rolled, 600°C, 6691 h. (d) Cold rolled, 570°C, 6696 h.

Table 1. Starting compositions of reduced activation steels exposed to thermally convective Pb-17 at. % Li[a]

Steel	composition (wt %)[a]							
	Cr	Mn	V	W	Si	N	S	C
PCMA-2	15	17	-	-	0.04	0.001	-	0.06
PCMA-6	16	14	-	-	0.02	0.003	-	0.18
V-64[b]	91	0.02	0.52	0.01	0.09	0.003	0.003	0.001
Steel 13[c]	9.2	0.7	0.25	29	0.42	-	-	0.17

[a]Balance is Fe.
[b]Heat V02264, provided by D. S. Gelles of Pacific Northwest Laboratories.
[c]Heat 90E, provided by G. J. Butterworth of Culham Laboratory.

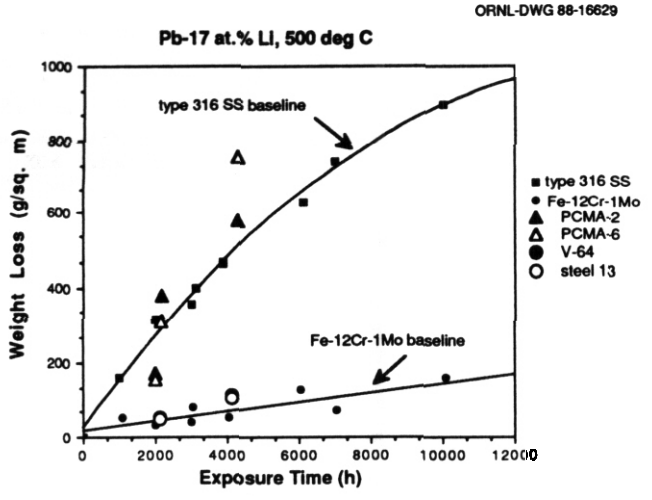

Fig. 2. Weight loss versus exposure time for various austenitic and ferritic steels exposed to thermally convective Pb-17 at. % Li at 500°C.

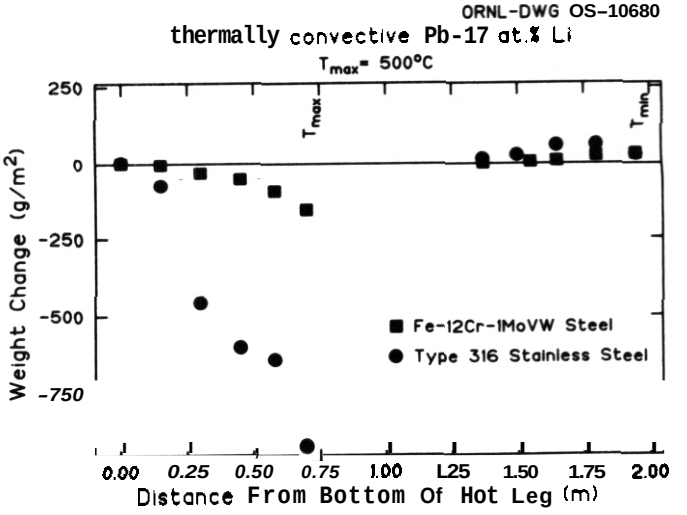

Fig. 3 Weight change versus loop position in thermally convective Pb-17 at. % Li at a maximum loop temperature of 500°C for type 316 stainless steel exposed for 10,008 h and Fe-12Cr-1MoVW steel exposed for 10.076 h

The weight change profiles of Fig. 3 indicate substantial mass was transported from the hot to cold zones during the >10,000 h exposure periods and that, despite much greater weight losses for the type 316 stainless steel, approximately the same weight gains were measured in both loop systems. Such data may indicate that arch of the deposition in the austenitic stainless steel TCL must be occurring in portions of the loop not sampled by the location of specimens or on the loop walls. In view of Eq. (1), and as discussed by Tas et al.,[6] a relatively high solubility of a particular element (Ni, for lead-lithium) may result in appreciable deposition only at a temperature below that of the minimum for the loop or. at least, in an inaccessible wld part of the loop. However, in the present case, the observation of nickel-enriched deposits at intermediate temperatures in the cooled zone is inconsistent with such a solubility-driven process. Alternatively, or additionally, the lack of greater weight gains on the wld leg coupons in the type 316 stainless steel loop may be due to poor adhesion or low nucleation of deposits. As noted above, variations in deposit density were found for the wld leg specimens in the type 316 stainless steel loop. As discussed previously, one of the reasons for such variability in deposit coverage appeared to be related to the adhesion of deposits, particularly for the lower temperature coupons.[1,2] Decohesion of deposits may have occurred during exposure to the liquid metal, during cooling after removal from the liquid stream, and/or during the standard specimen cleaning process with lithium. However, in some cases. deposits may never have formed on certain areas of a specimen because of nucleation constraints. The observations of small deposits in definite patterns on some of the surfaces may support such a hypothesis, particularly in view of the variability of deposit coverage from one specimen position to another and the accompanying change in deposit composition.[1,2] The growth of deposits requires registry with the underlying surface and, given that the starting wmpositions of all the wld leg specimens were the same (type 316 stainless steel), the accommodation and sticking of deposits of differing composition may vary considerably.

The variation in overall deposit composition as a function of temperature in the type 316 stainless steel system can be attributed to one or more factors: elemental solubilities, differing elemental deposition kinetics andlor sticking coefficients, various chemical reactions in the liquid or at the interface, and hydrodynamics. While the present data is not sufficient to definitively rank these factors in order of importance, it is apparent that, as discussed above, the variation of deposit composition cannot strictly be explained on the basis of solubilities [Eq. (1)]; the transition from iron to iron-nickel to chromium-rich deposits as the temperature decreases is not consistent with the elemental solubilities of these elements in lead-lithium. Furthermore, the lack of any evidence for nonmetallic deposits in the cold leg specimens would seem to indicate that chemical reactions with carbon are not playing an important role in this temperature regime. The relative consistency of the depoait composition throughout the cold leg of the Fe-12Cr-1MoVW steel loop is in sharp contrast to the results for the type 316 stainless steels TCL and, with increasing weight gains with decreasing temperature, would tend to indicate that solubility-driven depoaition is the most important factor for the ferritic steel system in the present case.

CONCLUSIONS

1. A microstructural influence on the attack of PCA exposed to molten lithium was observed when comparing annealed and cold rolled specimens. This effect was similar to what had previously been reported for type 316 stainless steel in Pb-17 at. % Li and may indicate a contribution of preferential dissolution-induced surface destabilization to the corrosion process.

2. Weight loss results for reduced activation austenitic and ferritic steels in Pb-17 at. % Li were similar to those measured for their standard counterparts.

3. Deposit composition was a function of temperature only in the type 316 stainless steel system. The density of deposits in the austenitic stainless steel loop varied from one specimen position to another and, in conjunction with net weight gains, appeared to be related to the effectiveness of nucleation andlor adhesion rather than to elemental solubilities. In the Fe-12Cr-1MoVW steel loop, solubility-driven reactions appeared to be the most important process in deposition.

FUTURE WORK

Small experimental heats of Pe-Mn-Cr steels have been made and will be used to qualitatively assess the effects of manganese and chromium on the sensitization and stress corrosion cracking susceptibility of this type of material. Liquid metal loop experiments will focus on effective methods of corrosion inhibition in lead-lithium.

REFERENCES

1 P. F. Tortorelli, "Thermal Gradient Mass Transfer in Ferrous Alloy Pb-17 at. % Li Systems," pp. 279-287 in *Fusion* Reactor *Materials Semiannual* Pmgresa Report March *31, 1987,* DOE/ER-0313/2, U.S. WE, Office of Fusion Energy, September 1987.

2. P. F. Tortorelli, "Corrosion and Mas Transfer of Ferrous Alloys in Pb-17 at. % Li," pp. 528-1 - 528-10 in *Proceedings Fourth International* Conference on *Liquid Metal* Engineering *and Technology,* Vol. 3, Societe Francais d'Energie Nucleaire, October 1988.

3. P. F. Tortorelli, "Corrosion in Liquid Metal Environments: Susceptibility of Fe_3Al Exposed in a Lithium Thermal Convection Loop and Mechanisms of Irregular Attack by Lithium and Lead-Lithium," pp. 176-179 in *Fusion Reactor Materials Semiannual* Progress Report March *31, 1988,* DOE/ER-0313/4, U.S. WE, Office of Fusion Energy, August 1988.

4. P. F. Tortorelli, "Corrosion Studies in Thermally Convective Lithium: 12Cr-1MoVW Steel and Low Activation Austenitic and Ferritic Alloys," pp. 331-336 in *Fusion* Reactor *Materials Semiannual Progress* Report September *30, 1986,* DOE/ER-0313/1, U.S. WE, Office of Fusion Energy, September 1987.

5 P. F. Tortorelli and J. H. DeVan, "Corrosion of Pe-Cr-Mn Alloys in Thermally Convective Lithium," *J. Nucl.* Mer. 141-143, 579-583 (1986).

6. H. Tas et al., "Mass Transfer in Pure Lithium and Lithium-Lead Dynamic Environments: Influence of System Parameters." *J. Nucl.* Mer. 141-143, 571-578 (1986).

7. SOLID BREEDING MATERIALS

ADSORPTION, DISSOLUTION. AND DESORPTION CHARACTERISTICS OF THE $LiAlO_2$-H_2O SYSTEM - A. K. Fischer and C. E. Johnson (Argonne National Laboratory)

OBJECTIVE

Adsorption of $H_2O(g)$, dissolution of OH^-, and rates of evolution of $H_2O(g)$ are being measured for the $LiAlO_2$-$H_2O(g)$ system. The thermodynamic and kinetic data for these processes relate to the issues of tritium retention and release and, hence, to concerns about tritium inventory in ceramic tritium breeder materials. The experimental data will enable (1) comparison of candidate breeder materials, (2) calculation of operating conditions, and (3) elucidation of the principles underlying the behavior of tritium in ceramic breeder materials.

SUMMARY

Measurements of adsorption and solubility isotherms for the $LiAlO_2$-$H_2O(g)$ system are continuing by techniques described in previous reports. In this report, the focus of experimental results is on the adsorption process up to the breakthrough point and on the immediate post-breakthrough rate of uptake as a means of determining corrections for a second uptake process that is concurrent with the main adsorption process. Isotherms are presented for adsorption of $H_2O(g)$ on $LiAlO_2$ at 573 and 623 K. From these data, together with earlier data for 673, 773, and 883 K, isobars and isosteres were derived. An overall analysis suggests that two adsorption processes are involved: physisorption at 573 K and below, and chemisorption at 873 K and above. Both processes function in the intervening tenperature range. Corrections were applied to the raw adsorption data from the breakthrough technique for postbreakthrough uptake of $H_2O(g)$. Adsorption on non-BET surfaces is believed to be involved in these corrections for the lower temperature isotherms.

PROGRESS AND STATUS

Experimental Results and Interpretation

New isotherms for $H_2O(g)$ adsorption on $LiAlO_2$ are reported for 573 and 623 K. Earlier reports of adsorption-solubility dealt with temperatures of 673, 773, and 873 K. Equilibration times for dissolution under the experimental conditions were estimated on the basis of the particle size and the range of reported diffusion coefficients for proton diffusion.2 For 673 K, there was borderline agreement (discussed below) between experimental equilibration tines (approximately 1200-1400 min) and calculated ones. Therefore, for neasurements at tenperatures lower than 673 K, it was regarded that dissolution was slowed sufficiently so that dissolution equilibrium was not likely to be reached. However, it was also observed that the curves recording $H_2O(g)$ uptake after the breakthrough point did not correspond to a step function condition. as they would be expected to if no uptake at all were occurring after breakthrough. Earlier, it had been recognized, for the higher temperatures, that though the dissolution rate is considerably lower than the adsorption rate, nevertheless, dissolution makes some contribution to the overall observed uptake before the breakthrough point. Consequently, the earlier quantities of 'adsorption' (for the higher temperatures) had to be corrected for some degree of simultaneous dissolution. For the current series at lower temperature, the remaining post-breakthrough uptake, presumably not significantly affected by dissolution, can be regarded as another adsorption process that involves surfaces that are not accessible to the relatively large krypton atoms in the Brunauer-Emmet-Teller (BET) surface area measurement. Such non-BET surfaces could be on grains forming a crevice that is too narrow to admit krypton but that allows the very small protons to diffuse in by surface diffusion (inter-oxide hopping) from OH^- at the mouth of the crevice. Pores with narrow openings could contribute additional surface that is inaccessible to krypton. Tanaka et a1.3 have recently reported a study on H_2O adsorption on $LiAlO_2$, also using the breakthrough technique and have labelled *phenomena in* the post-breakthrough region as 'Sorption-11," and the pre-breakthrough adsorption as "Sorption-I: They did not attempt corrections.

Figure 1 presents the five isotherms measured to this time. Figure 2 shows isobars for 10^{-3} to 10^{-5} atm (100 to 1 Pa) derived from the isotherm data. At high water vapor pressures, the isobar is essentially decreasing monotonically with rising temperature while at low water vapor pressures, a maximum appears in the isobar. Greater adsorption was found at 773 K than at 673 K. Such increasing adsorption at higher temperature is, however, a fairly common phenomenon involving two processes with different activation energies: the details were explained in the previous report.1

The slopes of the 573-773 K isotherms decrease monotonically from a value of 1.2 ± 0.2 at 573 K. A slope of 1 is expected for uninmlecular physisorption of H_2O; the low temperature process is taken to be physisorption. A decline in slope would be consistent with increasing contribution from the second process. At 873 K, the slope is 0.59 ± 0.16 and is consistent with dissociative chemisorption being the dominant process at this temperature (formation of two OH^- groups). A decline in slope from 0.5 would occur as temperature declines and the low temperature process becomes operative. Therefore, a minimum in slope in the intervening temperature range is expected and was observed. Adsorption of $H_2O(g)$ on $LiAlO_2$ is viewed as involving two kinds of adsorption in the temperature and range of the measurements: physisorption and chemisorption. The fact that the adsorption is described by Freundlich isotherms within each regime is consistent with surface heterogeneity.4

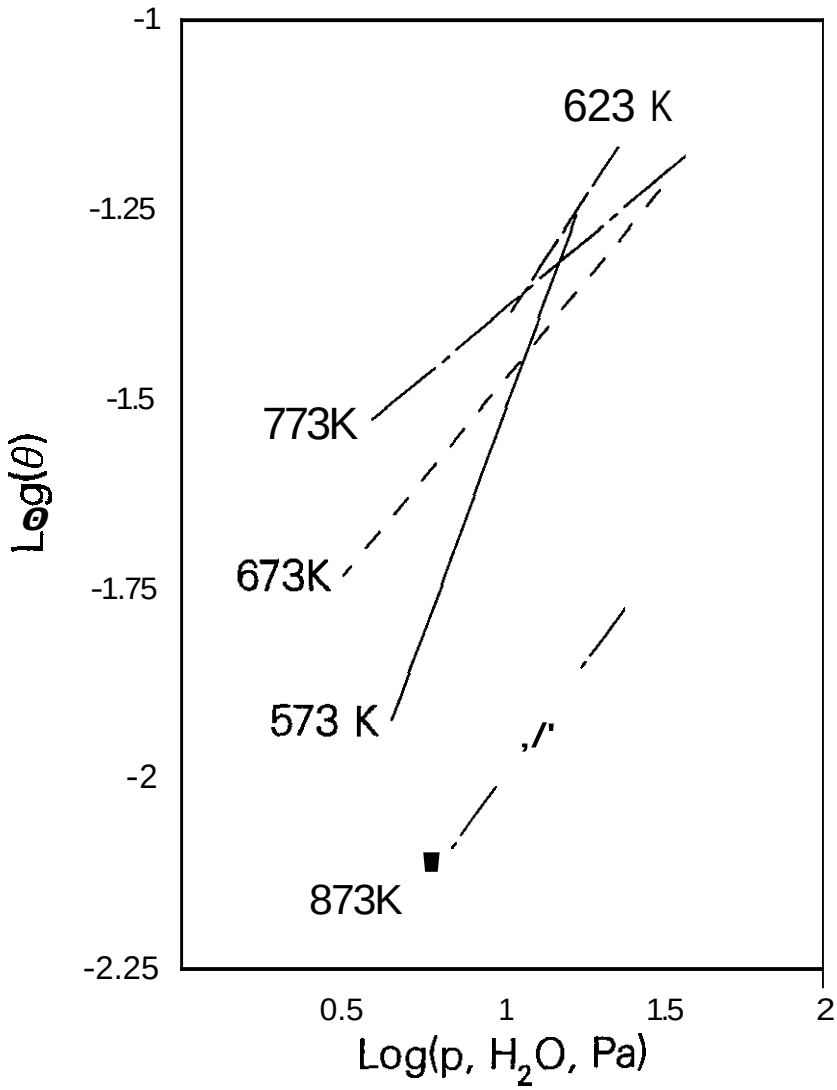

Fig. 1. Adsorption Isotherms for the $LiAlO_2$-$H_2O(g)$ System.

A system-wide atomic basis for heterogeneity of adsorption sites could be that one kind of adsorption site involves lithium ions and adjacent oxides, and another kind involves aluminum ions and adjacent oxides. Further evidence consistent with surface processes involving different kinds of sites was found for the reverse process relative to adsorotion, the evolution of water vapor from $LiAlO_2$, and was reported earlier.5 During heatup after a run, the water evolution curve showed a double peak that was interpreted as showing that different kinds of sites were involved.

For designers and planners needing estimates of degrees of adsorption for various combinations of temperature and pressure, the isosteres (curves for constant coverage) derived from the isotherms and plotted for θ = 0.1 to 0.001 in Fig. 3 are useful.

Oata on adsorption of $H_2O(g)$ on $LiAlO_2$ from Tanaka et al[3] cover a somewhat higher temperature regime (673-973 K) and a higher range of pressure ($1.7x10^{-4}$ to $1.7x10^{-3}$ atm, 17 to 170 Pa) than the present work. Only a few points in the present study fell in their pressure range. The Tanaka study did not get into the lower pressure and lower coverage regions that reveal the physisorption process that emerged in the present work. Post-breakthrough corrections for their data would be needed. For example, their 973 K curve is reported to have a slope of 0.36, which, if for a chemisorption process with an expected slope of 0.5, would suggest the presence of a systematic error leading to too high values of adsorption.

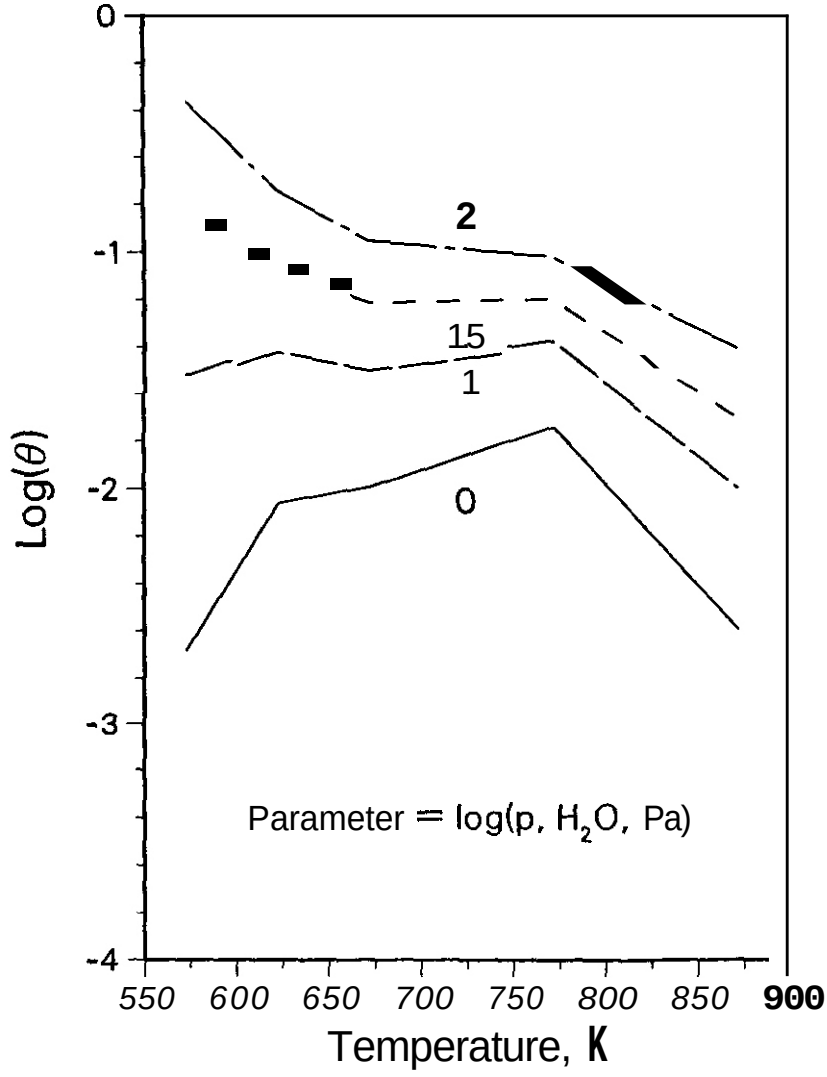

Fig. 2. Adsorption Isobars for the $LiAlO_2$-$H_2O(g)$ System.

The 673. 773, and 873 K isotherms in the present work were corrected for post breakthrough uptake by a slightly different technique than the 573 and 623 K isotherms, but are not expected to change substantially when they are treated by the same method. Post-breakthrough corrections were addressed as follows. First, raw values for the rate of uptake after the breakthrough point were corrected for the response curve of the water analyzer that measured the concentration of $H_2O(g)$ in the gas stream leaving the sanple. This correction, derived from separate calibration runs, takes into account the lag in response of the analyzer to a step change in the H_2O content of the gas stream. Next, the corrected rate of uptake of $H_2O(g)$ was calculated and plotted as the log of the rate vs. time after injection. Over a period lasting about 1 hour and starting soon after breakthrough, this curve was linear and was used to evaluate A and k In the equation, $r_u = Aexp(-kt_i)$, where r_u is the rate of uptake, A and k are constants, and t_i is the time after injection. Evaluation of $\int_0^{t_b} r_u dt$ where the limits are 0 for the time of injection and t_b for the breakthrough time gave the amount of uptake due to the second, slower process during the period up to the breakthrough time. This was subtracted from the gross amount of uptake up to the breakthrough point to give the corrected amount of adsorption on the BET surface of the sample.

Correlation of Measured Solubilities with TRIO Results

There is interest in comparing the solubility of OH- in $LiAlO_2$ as reported in the last report with the amount of OT^- found in $LiAlO_2$ at the end of the TRIO experiment[6]. In that experiment. the terminal concentration of tritium in the $LiAlO_2$ was 0.047 wppm, which is 1.03×10^{-6} mole fraction OT^-. In the run establishing these terminal conditions, there was a plateau in the release rate at 923 K of 3.4 μCi/min HTO into a 100 cc/min purge stream. If the pressure at the sample were 1 atm, this release rate corresponds to

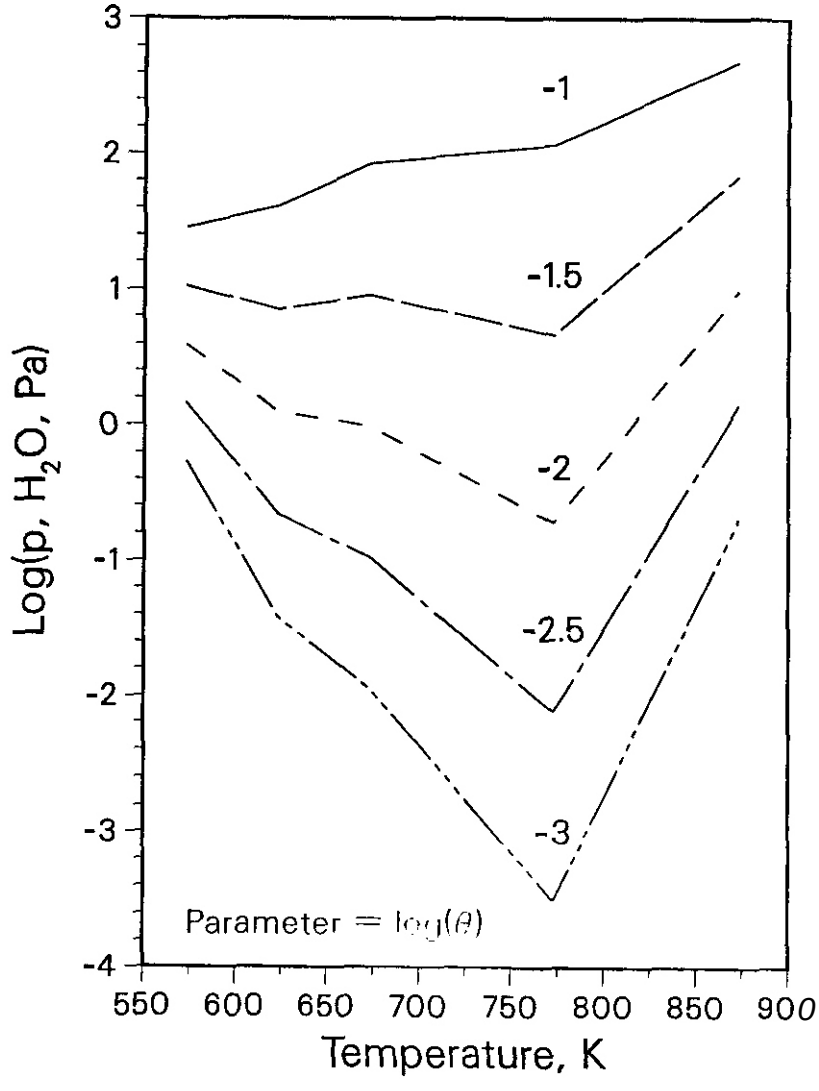

Fig. 3. Adsorption Isosteres for the $LiAlO_2$-$H_2O(g)$ System.

$8.8x10^{-8}$ atm HTO. For this partial pressure of H_2O, the 873 K isotherm in the last quarterly report for solubility of OH^- in $LiAlO_2$ (solubility was not measured at higher temperature) predicts a concentration of $2.1x10^{-6}$ mole fraction OH^-, or. if HTO is the gas, then $1.05x10^{-6}$ mole fraction OT^-; a somewhat lower value would be expected at the higher temperature of the TRIO case. Nevertheless, the close correspondence is interesting.

Diffusion Coefficients and Dissolution Equilibration Times

Because of the very small diffusion coefficients for "tritium" diffusion in $LiAlO_2$ that some investigators have reported, the question may arise whether adequate time was allowed for the achievement of solubility equilibrium at 673 K in the solubility measurements that were presented in previous reports. An assessment of the matter was made by using scanning electron micrographs of the $LiAlO_2$ particles, bulk density, and the BET surface area data to estimate average particle dimensions. If spherical geometry is assumed, a particle radius of 14.4 pm is obtained. However, flattening from a spherical shape will decrease the diffusional distance to the center of the particle. The SEM photographs show the grains to have a somewhat tabular nature. An edge view of such a grain suggests a thickness of 25 μm, or a diffusional distance of approximately 12.5 μm. The expression, $\tau = r^2/\pi D$, was used to estimate the diffusion time through a distance r with a diffusion coefficient, D.

The value of the diffusion coefficient is not well defined: data in the literature scatter over orders of magnitude. Claims for very small values calculated from tritium release data are in some cases compromised by misconceptions of the diffusing distance, and even by growing doubt that the data refer to a diffusion process. However, from a recent paper by Okuno and Kudo[2], the diffusion coefficient for tritium in $LiAlO_2$ at 673 K is taken to be 2×10^{-12} cm^2/sec. On the basis of thickness based on tubular geometry, a τ value of approximately 0.9 day emerges. The Okuno and Kudo diffusion coefficient curve is on the high end of the range covered by all the reported values. Coefficients from the low end of the range mould predict τ values that are orders of magnitude longer. Experimental equilibration times of about 1 day, sometimes extended over a weekend, were found to yield horizontal plateaus for $H_2O(g)$ uptake. This is the operational criterion for achievement of equilibrium in the present studies and appears to be in reasonable accord with expectations based on the Okuno and Kudo diffusion coefficients. Of course, if the reports of lower diffusion coefficients were correct, the implication would be that the plateaus do not correspond to solubility equilibrium because up to several years would be required to reach equilibrium. However, for the present time and until reliable diffusion coefficients allow a clear commentary on the question, at least the high temperature equilibrations will continue to be regarded as solubility neasurements. Additional insight will accumulate as the lower temperature isotherms are examined for their implications on this question.

FUTURE WORK

1. The correction for post-breakthrough uptake is one factor affecting data for adsorption on the BET surface of the sample. Since, in deriving the correction, rates of uptake corrected for the analyzer response were determined, these rates will be the basis of a kinetic analysis of the uptake process.

2. For higher temperature conditions where dissolution is important in the post-breakthrough period, it will become important for solubility measurements to derive a treatment for the post-breakthrough uptake data to separate the dissolution process from the non-BET adsorption process.

3. Data reduction for the kinetics of $H_2O(g)$ evolution for 573, 623, and 873 K still needs to be performed to identify the molecularity and activation energies of the processes.

4. Adsorption of $H_2O(g)$ on the BET surface for fusion reactor situations is complicated by the use of H_2 in the gas stream to enhance tritium release. Coadsorption of the two gases must be addressed with measurements of adsorption isotherms under conditions of representative levels of H_2 in the gas. In this connection, it is interesting that the adsorption of H_2 on alumina reported by Gruber[7] shows, like the present results for H_2O on $LiAlO_2$, a minimum in adsorption at about 573 K. However, the degree of adsorption on $LiAlO_2$ is likely to be lower for H_2 than for H_2O because even for the relatively high H_2 partial pressure of 0.25 atm (2.5×10^4 Pa) the adsorption on alumina amounted to only about $\theta = 0.001$.

REFERENCES

1. A. K. FISCHER and C. E. JOHNSON, 'Adsorption, Dissolution, and Desorption Characteristics of the $LiAlO_2$-H_2O System,' DOE/ER--0313/4, Fusion Reactor Materials Semiannual Progress Report for Period Ending March 31, 1988. p.198.

2. S. TANAKA, A. KAWAMOTO, M. YAMAWAKI, T. TERAI, Y. TAKAHASHI, H. KAWAMURA, and M. SAITO, 'In-situ Tritium Release Experiments from Solid Breeding Materials (TTTEx) - Tritium Diffusion Coefficients and Surface Reaction on Lithium Aluminate,' Proceeding of ISFNT, Tokyo, April 1988. This paper reviews data reporting the highest values of diffusion coefficients from K. OKUNO and H. KUDO, 'Diffusion Controlled Tritium Release from Neutron-Irradiated γ-$LiAlO_2$," J. Nucl. Mater., 138, 210 (1986).

3. S. TANAKA, A. KAWAMOTO, K. YAMAGUCHI, M. YAMAWAKI, H. MOHRI, T. TERAI. and Y. TAKAHASHI, 'Adsorption and Exchange Reaction of Hydrogen Isotopes on Solid Breeding Materials.' presented at the Third Topical Meeting on Tritium Technology in Fission, Fusion and Isotopic Applications, Toronto, Canada, May 1988.

4. D. O. HAYWARD and B. M. W. TRAPNELL. Chemisorption, Second edition, Butterworths, Washington, 1964. p. 174.

5. A. K. FISCHER and C. E. JOHNSON, 'Adsorption, Dissolution, and Desorption Characteristics of the $LiAlO_2$-H_2O System,' DOE/ER-0313/1, Fusion Reactor Materials Semiannual Progress Report for Period Ending September 30, 1986, p. 362.

6. R. G. Clemmer et al., 'The TRIO Experiment,: ANL-84-55, pp. VII-7 and VI-93.

7. H. L. GRUBER, 'Chemisorption Studies on Supported Platinum,' J. Phys. Chem., 66, 48 (1962).

MODELING OF TRITIUM TRANSPORT IN CERAMIC BREEDER MATERIALS - J. P. Kopasz, S. W. Tam, and C. E. Johnson (Argonne National Laboratory)

OBJECTIVE

The objective of this work is to develop a comprehensive model that will describe tritium behavior in ceramic breeder materials. The model should be able to. predict the transient tritium release behavior as well as the inventory at steady state.

SUMMARY

Tritium release experiments perfonned on Li_2O in the NRU reactor at Chalk River (the CRITIC experiment) showed some unusual results: when the temperature of the sample was increased tritium release initially decreased then rose to a maximum and decayed to steady state. Previous tritium release mdels cannot explain this type of behavior. A tritium release mdel based on diffusion and desorption as the rate controlling mechanisms and having a desorption activation energy which is dependent on surface coverage was developed. Calculations of tritium release from this model are in good agreement with the observed tritium release from the CRITIC experiment.

PROGRESS AND STATUS

Diffusion of tritium through the grain and desorption of tritium from the surface haS been considered the important processes controlling tritium release from neutron irradiated lithium ceramics. Modeling studies have focused on these two processes as the rate controlling steps in tritium release from lithium ceramics.[1-4] Experimental results from in-reactor on-1ine experiments[5-8] and out-reactor postirradiation anneal experiments[2,9,10] have been compared to theoretical predictions based on diffusion and/or desorption controlled release to determine the activation energy and preexponential in the rate constant of the form $K=K_0\exp(-Eact/RT)$. Eased on previous work performed on lithium oxide[2,10] tritium release from the CRITIC experiment was expected to be dominated by desorption due to the small grain size of the lithium oxide ceramic and the temperature range being investigated. However, measurements from the CRITIC experiment show some unusual behavior[11,12] which can not be explained by a desorption nmdel using a single activation energy, a diffusion model, or a combination of a desorption model and diffusion model using single activation energies for diffusion and desorption. In these CRITIC tests at ~500°C and for tenperature increases of 50°-100°C and a purge gas containing 0.1% hydrogen the tritium release initially decreased, then increased to a maximum followed by a decrease back to steady state. Similar temperature changes at higher temperatures with the same purge gas composition showed normal tritium release behavior.

We have developed a diffusion–desorption tritium release model which utilizes a surface coverage dependent activation energy of desorption to account for the unusual tritium release phenomena observed in the CRITIC experiment. Desorption and adsorption activation energies which are dependent on the anmunt of surface coverage have been reported. The current model is capable of reproducing both the unusual and the normal tritium release observed in CRITIC and predicts other regions where the surface coverage dependent release behavior may be observed. Results from the CRITIC experiment and our calculations imply that it is necessary to know the details of the surface phenomena in order to accurately predict the tritium inventory and changes in inventory which occur with changes in the sample environment.

Theory

The nmdel described in this paper considers diffusion and desorption as the rate controlling mechanisms for tritium release from a ceramic breeder. At the temperatures of interest, percolation in the gas phase and grain boundary diffusion should be orders of magnitude more rapid than diffusion in the grain. Desorption is included as a rate limiting mechanism based on 1) the observations of desorption controlled kinetics in some release experiments [2,15,16] and 2) the results of experiments in which the importance of surface reacttons was identified by changing the composition of the purge gas.[17,18,19] Diffusion is included based on the observation of diffusion-limited release in other cases.[10,20,21]

In the current model the desorption activation energy is not constant, but is dependent on the hydrogen surface coverage. Desorption activation energies which are dependent on the amount of surface coverage have been reported. Measurements of desorption of H_2O from ZnO identified desorption occurring with six different activation energies,[22] the particular activation energy of desorption under the conditions present at any one time depending on the anmunt of surface coverage at that time. Desorption of hydrogen from Al_2O_3 was determined to occur with two different activation energies.[23,24] Evidence also exists for multiple desorption activation energies in materials of interest in the ceramic breeder area. A recent investigation of the desorption of H_2O from $LiAlO_2$ suggest that there are two types of desorption sites (i.e., activation energies)[25] and tritium release from Li_4SiO_4 has been fit to a model using two desorption sites.[26]

To understand how the surface coverage would affect the desorption activation energy it is beneficial to look more closely at the desorption process. In tritium release experiments, what is regarded as the desorption step is really comprised of two processes; 1) a surface reaction between tritium, which has diffused to the surface as T^+, and chemisorbed hydrogen, to form surface bound HTO or HT, and 2) desorption of the surface bound HTO or HT.

1a) $T^+_s + OH^-_s \rightarrow HTO_s$ 1b) $T^+_s + H^-_s \rightarrow HT_s$

2a) $HTO_s \rightarrow HTO_g$ 2b) $HT_s \rightarrow HT_g$

The activation energy of either the surface reactions (1a or 1b) or the actual desorption of the surface bound molecule (2a or 2b) may be dependent on the surface coverage. If there are two or more adsorption sites for hydrogen on lithium oxide (ex. H^+ bound to an O on a normal oxygen site, H^+ bound to an O adjacent to a lithium vacancy) then at high surface coverage both the low energy and the high energy sites will be occupied. Reaction of T^+ at the surface will occur with the hydrogen least tightly bound to the surface, i.e., the hydrogen in the highest energy sites. At low surface coverage the hydrogen will occupy the lowest energy sites on the surface and the high energy sites will be unoccupied. The T^+ must now react with a hydrogen which is at a lower energy so the activation energy for the surface reaction will be larger than for the high surface coverage case. Alternatively, it is not necessary to have different sites of adsorption for there to be a dependence of the desorption activation energy on surface coverage. The surface coverage dependence of the activation energy may be due to interactions between the adsorbed molecules on the surface. Interactions between adsorbed hydrogen (as OH^- or H^-) will increase as the surface concentration of these species increases. The interactions between the adsorbed hydrogen will affect the binding energy of the hydrogen to the surface and therefore, have an affect on the activation energy for reaction of the hydrogen with T^+ at the surface. In addition, interactions of adsorbed hydrogen with surface bound HTO or HT will increase as the surface concentration of hydrogen increases. leading to a possible surface coverage dependence of the activation energy for reactions 2a and 2b above.

The dependence of the activation energy of desorption on surface coverage would be expected to be represented as shown in a plot of the natural log of the desorption rate constant vs. surface coverage (Fig 1). The slope of the plot is proportional to the desorption activation energy (surface coverage is proportional to inverse temperature for a constant pressure). This type of dependence would be expected for the case where the dependence is due to different adsorption sites and for the case where the dependence is due to interactions between adsorbed species. In region I. which corresponds to high surface coverage. reaction of T^+ occurs with hydrogen from the highest energy sites (those with the lowest actlvation energy). As the coverage decreases it approaches the point where reactions of T^+ begin to occur with hydrogen from the lower energy sites and the activation energy of reaction changes (region II). As the coverage decreases further, only the low energy sites are occupied so the T^+ reacts with the hydrogen In these sites and the activation energy observed is that for reaction of T^+ with hydrogen in the low energy sites. Alternatively, in the high coverage region, interactions between the surface species lower the activation energy for surface reaction or desorption of the surface species into the gas phase. As the coverage decreases these interactions decrease and the actlvation energy begins to change (region II). As coverage decreases still further the surface concentration gets to the point where the interactions between surface species are no longer important and the actlvation energy becomes constant (region III). One may expect that the activation energy would change smoothly in region II for the case where the dependence on surface coverage is due to interactions between the adsorbed species while it may change abruptly if the dependence was due to the existence of different adsorption sites. Since the exact nature of the change in desorption activation energy with coverage is not known over this region we have represented this portion of the curve as a dashed line showing a smooth change in the desorption rate constant.

To calculate the tritium release from a grain with a desorption activation energy which varies with temperature, the following partlal differential equation was solved with the boundary conditions indicated.

$$\frac{1}{D}\frac{\partial C}{\partial t} = \frac{1}{r^2}\frac{\partial}{\partial r}\left(r^2 \frac{\partial C}{\partial r}\right) + \frac{G}{D}$$

$$\frac{\partial C}{\partial r} = 0 \text{ at } r=0$$

$$J = K \cdot C_{surf} \text{ at } r=a$$

D = diffusivity
K = desorption rate constant
J = flux
C = concentration
r = radial distance
G = generation rate
t = time

The actlvatlon energy of desorptton was changed as a function of sample temperature. This should relate indirectly to the surface coverage, due to the dependence of surface coverage on temperature. For a constant hydrogen partial pressure the hydrogen surface coverage should decrease with increasing temperature. Desorption activation energies for the desorption of HTO from Li_2O of 24 kcal/mol,[27] 28.4 kcal/mol,[2] 28.7 kcal/mol,[28] and 35 kcal/mol[16] have been observed experimentally. In our calculations the

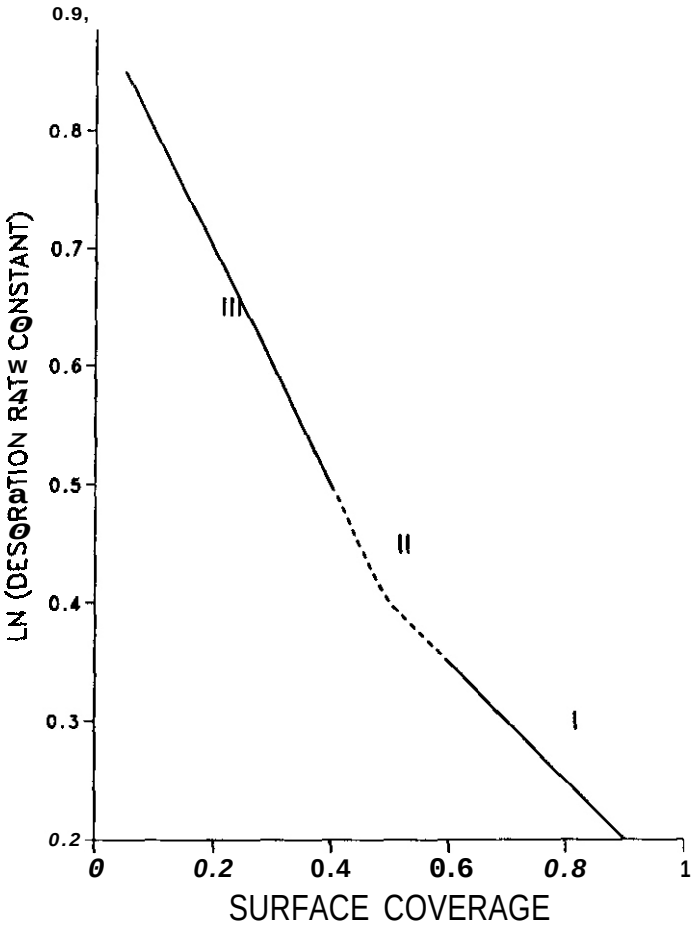

Fig. 1. Dependence of Desorption Rate Constant on Surface Coverage.

desorption activation energies used were between 24 and 35 kcal/mol, in agreement with those observed experimentally. The diffusion parameters used in the calculations were those obtained by Guggi et al.[10] The calculations were performed for changes in temperature of the form shown below. The value of alpha was obtained by fitting the measured temperature during the temperature increase to this equation.

$$T(t)=T_i+(T_f-T_i)x(1-\exp(-\alpha t^2))$$

T_i = initial temperature
T_f = final temperature
t = time since start of temperature change (sec)
α = time lag constant

Results and Discussion

Tritium release from samples in the CRITIC experiment for temperature increases of 50-100°C (at 450-550°C) with a 0.1% hydrogen concentration in the purge gas exhibited unusual behavior. The tritium release underwent a sharp decrease in release followed by an increase to a maximum then a decline to steady state release when the sample temperature was increased. An example of this type of release curve is illustrated in Fig. 2. Increases in sample temperature which began at temperatures of 550°C or greater with the same purge gas composition exhibited normal tritium release behavior (tritium release increases then decays to steady state after an increase in sample temperature). Normal tritium release was also observed for temperature increases in the 450°-550°C range when the purge gas contained 1.0% hydrogen instead of 0.1% hydrogen. The anomalous tritium release behavior can not be explained by a simple diffusion model, a one step desorption model (i.e., desorption with one energy of activation) or a combination of these two models. All these mdels predict an increase in tritium release followed by a decay to steady state for an increase in sample temperature.

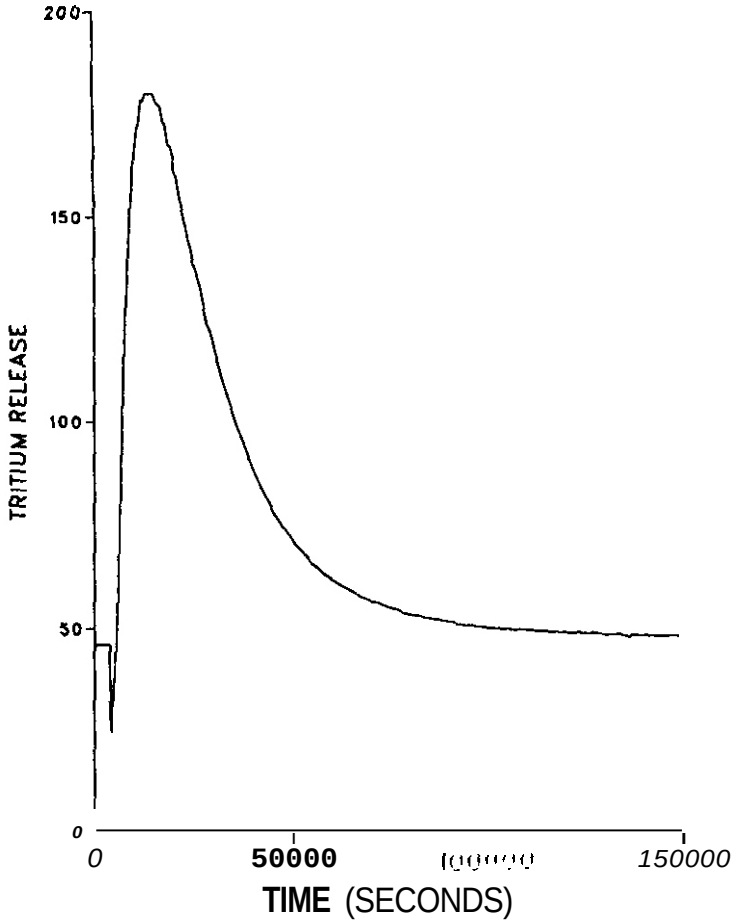

Fig. 2. Observed Tritium Release from Li_2O for a Temperature Increase.

The decrease in tritium release observed upon an increase in tenperature suggested to us that the activation energy of desorption had changed. This seemed reasonable since for many ceramic materials there are several modes of desorption.[22,23,24] To test this hypothesis we developed a computer program to calculate the tritium release from a spherical grain with diffusion and desorption as the rate limiting processes and with a desorption activation energy which varied with the temperature. Since the hydrogen surface coverage is dependent on temperature, this model relates to a surface coverage dependent desorption activation energy. Using this model tritium release curves were predicted for various temperature transients.

The model predicted three types of tritium release behavior associated with a tenperature change, the type of behavior being dependent on the magnitude of the change in the desorption activation energy. Uhen the change in the activation energy was relatively small an increase in sample tenperature resulted in a normal tritium release response, an increase in the tritium release followed by decay to steady state. Uhen the change in the desorption activation energy was relatively large an increase in sanple temperature resulted in a decrease in tritium release followed by a slow rise to steady state release. This type of behavior was observed in early tests in CRITIC.[11] The third type of behavior was observed for a small range of changes in the desorption activation energy. In this range the behavior was similar to the unusual behavior observed in the CRITIC experiment, i.e., an increase in sample temperature resulted in sudden decrease in tritium release followed by an increase to a maximum then decay to steady state release. However, for changes in temperature at the same rate as that observed experimentally the maximum in tritium release was reached in a short time relative to that observed. A model in which the temperature in the bulk changed at a slower rate than that observed at the surface resulted in a better fit to the observed data. This has a basis in the physics of the problem. The temperature in the bulk should change more slowly than the measured temperature at the surface due to the thermal diffusivity of the solid. With this model we were able to successfully reproduce the unusual tritium release curves observed in the CRITIC experiment. A characteristic example is illustrated in Fig. 3 which compares the tritium release calculated from our model with that observed in the CRITIC experiment for a temperature increase from 435° to 615°C.

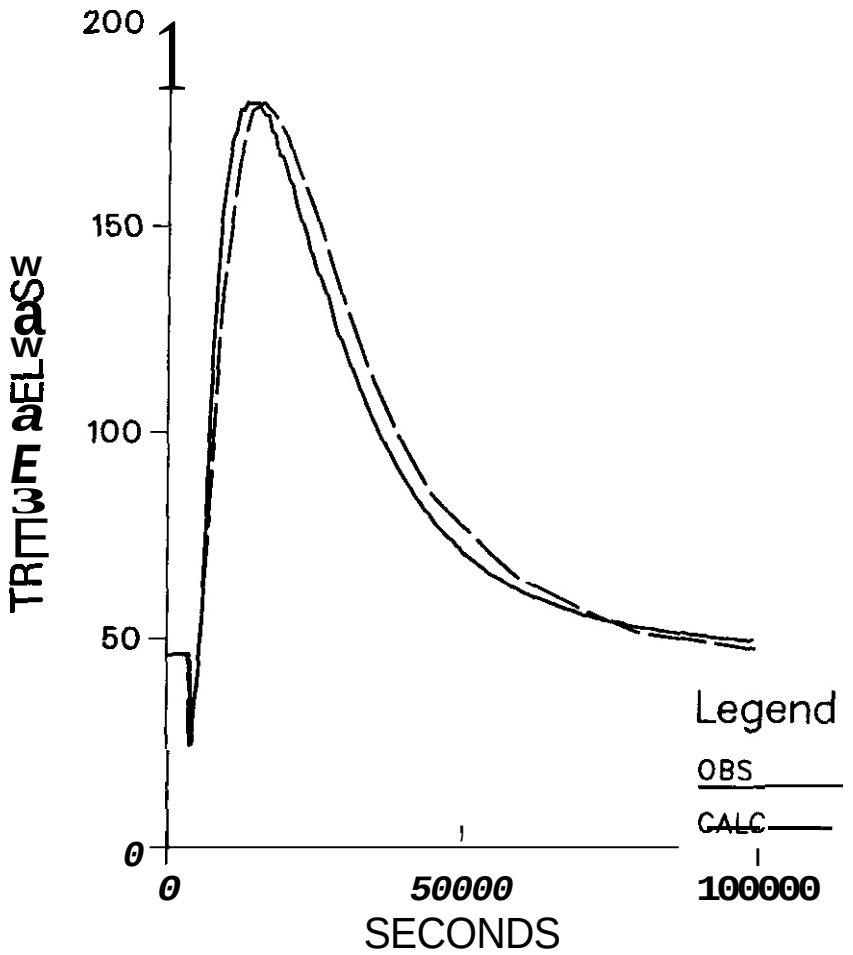

Fig. 3. Observed and Calculated Tritium Release for a Temperature Increase from 435 to 615°C.

The model attributes the anomalous tritium release behavior observed in the CRITIC experiment to a desorption activation energy which changes over a specific critical range of hydrogen surface coverage. The hydrogen surface coverage is also dependent on the hydrogen partial pressure in the purge gas. increasing with increasing pressure. To maintain a constant coverage when the pressure is increased the temperature must be increased. These effects are illustrated in Fig. 4 in which surface coverage is plotted against temperature for two different pressures. Region II, the critical region in surface coverage where the activation energy of desorption changes, is indicated in the figure. When the hydrogen pressure is increased the temperature range which corresponds to this region of coverage will be shifted to higher temperature. This explains why the tritium release curves obtained for tenperature changes in the 450-550°C range for purge gas compositions of 1.0% hydrogen did not show the unusual tritium release behavior that tests with 0.1% hydrogen showed. The dependence of the surface coverage on the hydrogen pressure also suggests that the unusual behavior may be seen for purge gas containing greater than 0.1% hydrogen at temperatures above 550°C and may be observed for purge gases with hydrogen concentrations less than 0.1% at temperatures below 450°C. A temperature decrease experiment with a purge gas containing 1.0% hydrogen supports this model. The tritium release for this test initially increased then decreased to a minimum and rose to steady state when the sample tenperature was decreased from approximately 740°C to 610°C. Temperature increase experiments over this temperature range with 1.0% hydrogen in the purge gas are scheduled to test our hypothesis further.

The results from the CRITIC experiment and calculations using the diffusion-desorption model with a surface coverage dependent desorption activation energy imply that In order to accurately calculate the tritium inventory the details of the surface phenomena must be known. Without knowledge of the details regarding the dependence of the desorption activation energy on surface coverage one would erroneously predict that the tritium inventory would decrease for any temperature increase. Results from the CRITIC experiment show that this is not the case. In some tests the inventory increased when the temperature was increased.[11] Our model attributes this to a change in the desorption mechanism (change in desorption activation energy) with changing surface coverage. This type of phenomenon should not be limited to Li_2O and it is likely that the other solid breeder candidates have desorption activation energies which are surface coverage dependent. Evidence of this has already been observed for $LiAlO_2$,[25] and for Li_4SiO_4.[26]

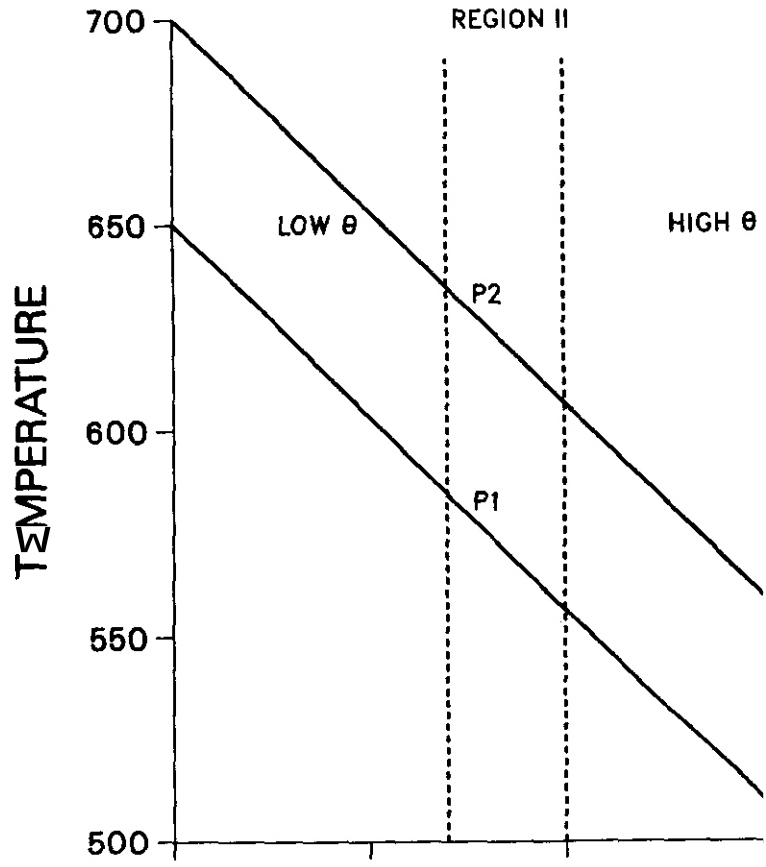

Fig. 4. Relationship Between Surface Coverage and Temperature for lwo Partial Pressures of H_2, Pressure $P_2 > P_1$.

FUTURE WORK

Additional CRITIC experiments are planned for a series *of* tests at temperatures and hydrogen concentrations where we expect the surface coverage dependence of the desorption activation energy to be evident to test our model. We will apply our model to this data to try to determine *how* the desorption activation energy behaves in this region and to try to more accurately locate the region of tenperature and pressure where the changes in desorption activation energy occur.

REFERENCES

1) J. P. Kopasz, S. W. Tam and C. E. Johnson, "Modeling of Tritium Behavior in Ceramic Breeder Materials,' presented at the Third International Conference on Fusion Reactor Materials (ICFRM-3), Karlsruhe, West Germany, 1987 Oct 4-8, to be published in J. of Nucl. Mater.

2) P. C. Bertone, 'The Kinetics that Govern the Release of Tritium from Neutron-Irradiated Lithium Oxide,' J. of Nucl. Mater. 151(1988)281.

3) K. Noda, T. Kurasawa and H. Watanabe, 'Status of Modeling Tritium Behavior In Fusion Blanket Ceramics at JAERI,' in Proc. IEA Int. Specialists' Workshop on Modeling Tritium Behavior in Fusion Blanket Ceramics, Chalk River, Canada (1987) Ed. I.J. Hastings (Atomic Energy of Canada Limited, Chalk River, 1987) p. 132.

4) R. Raffray, M. A. Abdou and G. Federici, A Conputer Program for Modeling Tritium Transport in Solid Breeders,' presented at the Int. Symp. on Fusion Technology, Tokyo, 1988 April 10-15.

5) M. Briec, J. J. Abassin, M. Masson, E. Roth, P. Sciers, and H. Werle, "In-Pile Tritium Extraction from Samples of lithium Aluminate,' presented at the Third International Conference on Fusion Reactor Materials (ICFRM-3), Karlsruhe, West Germany, 1987, Oct. 4-8, to be published in J. *of* Nucl. Mater.

6) T. Kurasawa, H. Watanabe, E. Roth, and D. Vollath, "In-Pile Tritium Release Behavior from Lithium Aluminate and Lithium Orthosilicate during VOM-23 Experiment," presented at the Third International Conference on Fusion Reactor Materials (ICFRM-3), Karlsruhe. West Germany, 1987, Oct. 4-8, to be published in J. of Nucl. Mater.

7) H. Yerle, M. Breitung, M. Briec, R. G. Clemmer, H. Elbel, H. E. Hafner, M. Mason, G. Schumacher, and H. Yedemeyer, 'The LISA-2 Experiment: In-Situ Tritium. Release from Lithium Orthosilicate," presented at the Third International Conference on Fusion Reactor Materials (ICFRM-3), Karlsruhe, West Germany, 1987, Oct. 4-8, to be published in J. of Nucl. Mater.

8) H. Kemst, R. Conrad, P. Kennedy, A. J. Flipot. and J. D. Elen, "Tritium Release from Various Solid Breeding Materials,' in Proc. Int. Symp. Fusion Reactor Blanket and Fuel Cycle Technology, Tokai-Mura, Japan (1986) Eds. Y. Takahaski and S. Tanaka (University of Tokyo, Tokyo 1986) p. 37.

9) J. M. Miller, R. A Verrall, S. R. Bokwa, and D. H. Rose, 'The Effect of Material Characteristics on Tritium Release from Lithium Oxide,' presented at the Symp. on Fabrication and Properties of Lithium Ceramics, Amer. Cer. Soc., Annual Meeting, Pittsburgh, PA., USA, 1987, April 16-30, to be published in Advances in Ceramics, Vol. 25, Eds. I_J. Hastings and G. Y. Hollenberg (Amer. Cer. Soc.).

10) D. Guggi, H R. Ihle, D. Bruning, U. Kurz, S. Nasu, K. Noda, T. Tanifuji, 'Diffusion of Tritium in Single Crystal Li_2O," J. of Nucl. Materl. 118(1983)100.

11) R. A. Verrall, J. M. Miller, S. R. Bokwa, and C. E. Johnson, 'CRITIC-1 Instrumental Irradiation of Lithium Oxide: Part 1 First Results,' presented at the Symp. on Fabrication and Properties of Lithium Ceramics, Amer. Cer. Soc., Annual Meeting, Pittsburgh, PA., USA, 1987, April 26-30. to be published in Advanced in Ceramics, Vol. 25. Eds. I. J. Hastings and G. W. Hollenbewrg (Amer. Cer. Soc.).

12) J. M. Miller, R. A. Verrrall, O. S. MacDonald, and S. R. Bokwa. "The CRITIC-I Irradiation of Li_2O-Tritium Release and Measurement." presented adt the Third Topical Meeting on Tritium Technology in Fission, Fusion, and Isotopic Applications, Toronto, Canada, 1988 May 1-6.

13) D. S. Applegate and R. B. Poeppel, 'The CRITIC-I Irradiation of Li_2O: Fabrication and Characterization," presented at the Symp. on Fabrication and Properties of Lithium Ceramics, Amer. Cer. Soc. Annual Mtg., Pittsburgh, PA., USA, 1987 April 26-30, to be published in Advanced in Ceramics, Vol. 25, Eds. I_J. Hastings and G. W. Hollenberg (Amer. Cer. Soc.).

14) I_J. Hastings et al., 'Canadian Fusion Breeder Blanket Program: Irradiation Facilities at Chalk river,' J. Nucl. Mater. 141-143, 1044 (1986).

15) M. Dalle donne, 'Tritium Release from a Lithium Ceramic: Interpretation of the TRIO Experiment,' Fusion Technology 9(1986)503.

16) T. Tanifuji, K. Noda, S. Nasu, and K. Nehida, "Tritium Release from Neutron-Irradiated Li_2O; Constant Rate Heating Measurements.' J. of Nucl. Mater. 95(1980)108.

17) H. Werle, J. J. Abassin, M. Briec, R. G. Clemmer, H. Elbel, H. F. Hafner, M. Mason, P. Sciers, and H. Yedemeyer, J. Nucl. Mater. 141-143 (1986)321, and unpublished results.

18) J. M. Miller, S. R. Bokwa, and R. A. Verrall, "Post Irradiation Tritium Recovery from Lithium Ceramic Breeder Materials,' J. Nucl. Mater. 141-143 (19861294.

19) R. G. Clemner et al., "The TRIO Experiment,' ANL-84-55. Argonne National Laboratory (1984).

20) H. Kudo and K. Okuno, "Kinetic Studies of the Tritium Release Process in Neutron-Irradiated Li_2O and LiOH," J. Nucl. Mater. 101(1981)38.

21) K. Okuno and H. Kudo, "Diffusion Controlled Tritium Release from Neutron-Irradiated γ-$LiAlO_2$," J. Nucl. Mater. 138(1986)210.

22) G. Zwicker and K. Jacobi, 'Site Specific Interaction of H_2O with ZnO Single-Crystal Surfaces by Thermal Desorption and UV Photoelectron Spectroscopy," Surface Science 131(1983)179.

23) D. B. Rosenblatt and G. J. Dienes, "The Effect of Reactor Irradiation upon Hydrogen Adsorption by an Alumina Catalyst,' J. of Catalysis 4(1965)271.

24) H. L. Gruber, "Chemisorption Studies on Supported Platinum,' J. Phys. Chem. 66(1962)48.

25) A. K. Fischer and C. E. Johnson, "Effect of H_2 on Adsorption, Solubility, and Kinetics in the $LiAlO_2$-$H_2O(g)$ System," to be Dresented at 8th Topical Meeting on Technology of Fusion Energy. Salt Lake City, Oct. 10-13 (1988).

26) W. Brietung, H. Elbel, J. Lebkucher, G. Schumacher, and H Uerle, 'Out-of-Pile Tritium Extraction from Lithium Silicate," presented at the Third International Conference on Fusion Reactor Materials (ICFRM-3), Karlsruhe, West Germany, 1987, Oct. 4-8, to be published in J. of Nucl. Mater.

27) J. Quanci, Princeton University, unpublished results (1988).

28) H. Kudo and K. Okuno, 'Kinetics and Mechanism of Tritium Release from Neutron-Irraidation Li_2O," J. of Nucl. Mater. 133(1985)192.

8. CERAMICS

DETUNING OF RESONANT RF WINDOWS BY NEUTRON IRRADIATION

H. M. Frost (Los Alamos National Laboratory)

OBJECTIVE

To develop and apply an analytical approach for assessing the impact of fast-neutron irradiation damage on reflectivity of rf windows made from ceramics intended for magnetic fusion energy (MFE) applications entailing electron cyclotron resonance heating (ECRH) of fusion plasmas.

SUMMARY

We present details here on calculations based on a model known for some time but not applied until very recently to radiation damage in the form of vindov detuning. It incorporates the fact that the transmissivity of a resonant rf vindov depends, as any resonant passive electromagnetic slab, on the dielectric constant as well as on the slab thickness -- both of which can be changed by irradiation. A major consequence of applying this model in the context of an alumina (α-Al_2O_3) or beryllia 'rf' vindov subject (during ECRH use) to swelling and dielectric changes induced by fast neutrons involves unwanted and potentially damaging reflection of millimeter wave (MMW) pover back toward the source (e.g., gyrotron).

PROGRESS AND STATUS

Introduction

The detuning model vas developed in response to observed changes in specimen dimensions and dielectric constants resulting from irradiation of alumina and beryllia ceramics in the fore of the EBR-II reactor at Idaho Falls for about a year, at a temperature of about 385°C and a fluence of about 10^{26} n/m^2.[1]

The model

It is well known that the power reflection coefficient. R_m, for a uniform slab of dielectric constant k and thickness L is given by:[2]

$$R = 2r^2(1-\cos A)/[1+r^2(r^2-2\cos A)], \text{ where} \qquad \text{Eq.(1)}$$

$$r^2 = [(1-n)/(1+n)]^2, \text{ with } n = \sqrt{k}, \qquad \text{Eq.(2)}$$

$$A = 4\pi nL/\lambda_o, \qquad \text{Eq.(3)}$$

and λ_o is the vavelength in free-space vacuum. Assumptions in Eq.(1) include normal incidence for the MMW's on a symmetric slab (same medium on both sides). An initial reflectivity of zero is obtained by choosing L to equal an integral number of half-wavelengths in the specimen material. i.e., $L_m = m\lambda_o/(2n)$. With this choice, the numerator in Eq.(1) vanishes,

To estimate the change in reflectivity of an rf vindov, it is convenient to start with the initial unirradiated condition of zero reflectivity. i.e., $R_o = R_m = 0$ obtained by the assumption $L = L_m$. Also. use is made of the 'irradiated' length and refractive index being given by $L = L_m + \Delta L$ and $n = n_o + \Delta n$, vith tha latter related to dielectric constant (to first order) via $\Delta n/n_o = (1/2)\Delta k/k_o$. Substituting these expressions into Eq.(3) gives to first order:

$$\cos A_m = \cos\{2\pi m[(\Delta L/L_o)+(1/2)(\Delta k/k_o)]\}, \qquad \text{Eq.(4)}$$

vith the 'zero' subscript denoting unirradiated values. For changes in L and k of the order of ten percent or less, retention as indicated of only the linear terms in the expansion yields reasonable accuracy.

Substitution of $\cos A_m$ into Eq.(1) permits calculation of the irradiated reflectivity in terms of measured fractional changes in length and in dielectric constant.

Results and discussion

It was recently reported that both a 99.5% Coors alumina and also a beryllia-based ceramic experienced a doubling (100% increase) in the dielectric loss factor at room temperature and 90-100 GHz as a result of the intense fast neutron exposure mentioned in the Introduction.[1] However, the changes in L and k were much smaller: For the alumina, they were +1.0% and -1.8%. respectively, and for the beryllia, +3.1% and -13%, respectively. From Eq.(4), it can be seen that the phase shift is nearly zero for the alumina but not so for the beryllia.

Substitution of the material property changes into Eq.(1) for windows that are initially 3/2 material wavelengths thick (m-3) gives the following results: R_s=0.081 (8.1%) for beryllia and R_s=0.00013 (0.013%) for alumina. For a double window configuration often chosen in designs far efficient cooling, these values are roughly doubled assuming that the channel spacing between slabs is (also) an integral number of half-wavelengths of the MMW's in the cooling fluid.

The m=3 condition corresponds to unirradiated slab thicknesses at 100 GHz of 1.43 mm for alumina and 1.80 mm for beryllia.

To realistically estimate the relative change in R_m between the unirradiated and irradiated cases, it is necessary to calculate what the unirradiated value of R_m actually is when low loss is present. That is, a tiny amount of power is reflected when low loss is present in an otherwise resonant-thickness window. The resulting small value of R_m then serves as the baseline needed for making comparisons on the logarithmic scale of 'reflection loss' RL, defined by $-10\log(R_m)>0$. This is done by transforming k in Eq.(2) to $k^*=k(1+j\tan\delta)$, the complex dielectric constant, with tan6 the lass tangent. (The dielectric loss factor is $k\tan\delta$.) The result from Eq.(1) after some manipulation is:

$$R_m \approx [\pi m \tan\delta/(\rho^{-1}-\rho)]^2, \qquad \text{Eq.(5)}$$

correct to second order in $\pi m\tan\delta$, with the definition of $\rho=r'^*r'$ where r' is now the complex version of r in Eq.(2) and the superscripted symbol * denotes the complex conjugate. For low loss, $\rho=r^2$. Calculated results are shown in Table 1, with 'VSWR' being the voltage standing wave ratio.

Table 1. Window detuning effects at 95 GHz

Material	Condition	R_3 (units of 10^{-3})	RL (dB)	VSWR
Alumina	Unirradiated	0.0067	52	1.0
(99.5%)	Irradiated	0.13	39	1.0
Beryllia	Unirradiated	0.010	50	1.0
	Irradiated	82.	11	1.8

The values in this table differ from those in the progress report cited in Ref.1, partly because of calculational errors. For example, the earlier values of k and tan6 were reported prior to development of the more accurate data-reduction algorithm for these properties used here and included in a prior progress report.[3]

By definition, the trends in R_m, RL, and VSWR go as follows: The larger the value of R_m (subject to $R_m \le 1$), the closer to zero the value of RL (subject to RL≥0) and the greater the departure of VSWR from unity (subject to VSWR≥1), and accordingly the greater the microwave power reflected from the window back to the source.

These results are interpreted as follows. If an irradiated alumina disk were used as a MMW window, about ten times more power would be reflected back to the source compared with the unirradiated case but with the consequence that the ideal VSWR value of 1.0 would still be retained. No source performance degradation would result. However, the case is different for the irradiated beryllia ceramic tested: The reflected power increases by about 10 fold over that from the unirradiated beryllia, causing the VSWR to change deleteriously from 1.0 to 1.8

for a single window -- and to an estimated 2.3 for a double window.

This is a matter of concern for performance of gyrotrons, and a fortiori, less robust microwave sources, as these VWSR values may exceed those allowed in manufacturers' specifications for their products. Other consequences include increased likelihood of electrical breakdown in the feed waveguides and decrease in the amount of rf heating of the fusion plasma.

A sense of perspective on the reflection-power significance of the R_m values tabulated in Table 1 is provided by realizing that a 1% linear swelling of a $3\lambda/2$ window of lossless alumina at 95 GHz, without any change in k, changes Rs from zero to a value of 0.02 that is about 10^2 times larger than the Rs for the irradiated alumina covered here.

The observed changes in k reported here are negative, thus at least partially compensating for the swelling effects. The detuning effect would be exacerbated, though, if Ak were positive such as observed by Pells, et al. at 1 MHz in 99.9% alumina for their much lower fluences of fast neutrons (10^{-3} to 10^{-5} of ours).[4]

CONCLUSIONS

Radiation-induced detuning of rf windows at millimeter-wave frequencies is a new known type of radiation damage. It can be avoided if the window's linear swelling from, say, neutrons, is one half of, and opposite in sign to, the change in dielectric constant, i.e., $\delta L/L = -(1/2)\delta k/k$. This condition was very nearly met by the Coors 99.5% alumina reported on here, but not for the beryllia-based ceramic. The possibility of $\delta k/k$ changing sign as the accumulated radiation fluence changes from weak to intense values, as suggested by the combination of our work and that of Pells, et al., indicates detuning may be a complex phenomenon, depending on material type.

FUTURE WORK

In future screening of candidate ceramics for fusion ECRH applications. we plan to include an examination of possible window detuning effects.

REFERENCES

[1] H.M. Frost and F.W. Clinard, Jr., "Dielectric changes in neutron-irradiated rf window materials." J. Nucl. Mater. (1988), in press; H.M. Frost and C.D. Kise, "In-waveguide measurements of MMW dielectric properties of candidate fusion ceramics," pp. 384-388 in Fusion Reactor Materials Semiannual Progress Report for Period Ending September 30, 1986, DOE/ER-0313/1, U.S. Department of Energy. Washington, D.C., June 1987.

[2] M. Born and E. Wolf, "Principles of Optics" (MacMillan, Nev York, 1964). pp. 61-66 and 627-632.

[3] H.M. Frost, "Improved computation of dielectric constants measured by in-waveguide techniques, pp. 297-298 in Fusion Reactor Materials Semiannual Progress Report for Period Ending September 30. 1987, DOE/ER-0313/3, U.S. Department of Energy, Washington. D.C., March 1988.

[4] G.P. Pells. S.N. Buckley, G.J. Hill, and M.J. Murphy, "Radiation effects in electrically insulating ceramics," Technical Report, *AERE* R 11715, United Kingdom Atomic Energy Authority, Harwell Laboratory, Oxfordshire, November, 1985.

PREPARATION AND CHARACTERIZATION OF ALUMINA CONTAINING ENRICHED OXYGEN ISOTOPES

— S. J. Zinkle, H. E. Kim, and W. R. Allen (Oak Ridge National Laboratory)

OBJECTIVE

The objective of this study is to determine the appropriate conditions for fabrication of high-quality fine-grained ^{17}O-enriched alumina specimens.

SUMMARY

Alumina specimens enriched in ^{17}O have been successfully fabricated from aluminum isopropoxide and water containing the ^{17}O isotope. The enrichment levels of specimens subjected to different preparation schedules were measured using a nuclear reaction analysis technique. Replacement of the ^{17}O isotope in the ceramic by atmospheric oxygen was observed to occur readily. Successful fabrication of suitably enriched alumina specimens required all processing steps to be performed in vacuum or inert environments. The optimized fabrication procedure produced enriched Al_2O_3 specimens of >99.5% theoretical density, ~10 μm grain size, and a flexural strength of 280 MPa.

INTRODUCTION

A number of studies have been performed using fission reactors to determine the relative resistance of various ceramics to radiation-induced degradation in a fusion environment.[1-3] However, this simulation suffers the disadvantage that the neutron energy spectrum is lower than that of the DT fusion reaction. In particular, calculations indicate that the helium generation rate in a typical ceramic such as Al_2O_3 in a fission spectrum is an order of magnitude less than the corresponding helium generation rate in a fusion reactor.[1] Radiation damage studies in metals have shown that material property changes such as void swelling can be dramatically altered when helium is present in sufficient quantities. One method that may be used to investigate helium effects in oxide ceramics is to take advantage of the thermal neutron reaction $^{17}O(n,\alpha)^{14}C$ as a means to produce controlled amounts of helium during irradiation in a mixed spectrum fission reactor. According to calculations presented elsewhere,[1] an isotopic enrichment of 17.9% ^{17}O in alumina will produce a helium generation rate per unit displacement damage in the High Flux Isotope Reactor (HFIR) that is identical to that expected for alumina of normal enrichment at the first wall of a fusion reactor.

This report describes a technique for producing ^{17}O-enriched alpha-alumina from water that contains the ^{17}O isotope. In the course of preparing suitably enriched Al_2O_3 specimens, a number of interesting observations were made on the diffusion and exchange of oxygen isotopes with atmospheric oxygen in alumina and its precursor hydroxide. The material was evaluated for isotopic enrichment using a nuclear reaction analysis technique and was further characterized by transmission electron microscopy and four-point bending flexural strength measurements.

EXPERIMENTAL PROCEDURES

The starting materials for the preparation of isotopically tailored alumina were aluminum isopropoxide, $Al(OC_3H_7)_3$, and water containing enriched concentrations of the ^{17}O isotope. These starting materials were chosen because of the availability of ^{17}O in aqueous form, and because of the high purity of commercial aluminum isopropoxide. The enriched water was obtained from the Monsanto Research Corporation (Mound Facility) in Miamisburg, Ohio. An isotopic analysis of the water found the oxygen isotope enrichment to contain the following atomic percentages: 11.5% ^{16}O, 64.0% ^{17}O, and 23.7% ^{18}O.

The basic procedure for preparing the isotopic tailored alumina consisted of mixing aluminum isopropoxide with a stoichiometric amount of the ^{17}O-enriched water to produce aluminum hydroxide (boehmite). The boehmite powder was then calcined, and the resultant alumina powder was mixed with 0.1 to 0.5 wt % MgO and sintered. A series of scoping experiments were performed to determine the effects of different processing temperatures and atmospheres on the final enrichment of the alumina. Specimens were prepared in air, argon, and vacuum environments. Two calcination temperatures were investigated along with several final sintering temperatures. The optimum calcination temperature was obtained from inspection of computerized DTA/TGA and high-temperature X-ray diffractometer measurements, which provided information on the thermal evolution and phase transformation, respectively. The efficiency of the oxygen isotope retention was found to be strongly dependent on the preparation atmosphere.

The microstructures and flexural strengths of alumina specimens prepared under two different calcination and sintering schedules were examined. In the first case, the calcination of the boehmite was performed

at 600°C for 1 h and the sintering conditions were 1600°C for 2 h. In the second case. the calcination conditions were 1300°C for 3 h and the sintering was performed at 1700°C for 3 h. Microscopy disks and bend bar specimens were cut from bulk samples, and the microscopy disks were mechanically dimpled. These disks were then thinned in an ion mill until perforation occurred so that suitable areas for transmission electron microscope observation were obtained. Strength measurements for the same two calcination/sintering schedules were obtained under four-point bending conditions. Specimens of cross-sectional dimensions of 1.25 mm by 2.5 mm were mechanically polished along the tensile surface using 1 μm diamond paste for an abrasive. The two edges along the tensile surface were beveled to avoid stress concentrators. The specimens were then fractured at room temperature under pure four-point bending conditions, using an inner span of 6.35 mm and an outer span of 19.05 mn.

The degree of isotopic enrichment in the alumina specimens was determined from nuclear reaction analysis and Rutherford backscattering energy measurements. Targets of the alumina specimens were bombarded with 450 or 750 keV protons to promote the $^{17}O(p,\alpha)^{14}N$ and $^{18}O(p,\alpha)^{15}N$ nuclear reactions. The scattered ions were collected by a surface barrier detector at a scattering angle of 145 deg and detected events were energy analyzed. The reaction energy for the ^{17}O reaction is Q = 1.2 MeV, whereas Q = 3.98 MeV for the ^{18}O reaction. The relatively low 9-value for the ^{17}O reaction produces alpha particles that have energies comparable to those of elastically scattered protons. This makes it difficult to distinguish the concentration of ^{17}O due to the overlap of its characteristic alpha particle energy with the background scattering energy spectrum of the elastic-scattered protons. On the other hand, the alpha particles emitted from the ^{18}O reaction are much more energetic than the elastic-scattered protons and appear free of background in the scattering energy spectrum. For this reason, the ^{18}O reaction was used to monitor the depletion of the enriched oxygen isotopes by ^{16}O replacement events. It was assumed that the replacement rate of the enriched isotopes by atmospheric oxygen was independent of isotope mass (i.e., it was assumed that the ratio of ^{17}O to ^{18}O remained at the ratio measured for the enriched water — 2.70). Each acquired scattering energy spectrum was interpreted to yield a depth profile of the ^{18}O concentration.[5] The use of 750 keV protons allowed the ^{18}O concentration to be directly determined from the alpha count rate, since the cross section for this reaction is known to be linear for proton beam energies between 650 and 750 keV (ref. 6). The ^{18}O depth distribution was normalized to the aluminum concentration deduced from the elastic proton scattering yield (with the assumption of proper aluminum to oxygen stoichiometry). This normalization accounted for slight inconsistencies in the accumulation interval for successive scattering energy spectra. These were attributed to the electrical insulating nature of the specimens and variations in secondary electron emission during ion bombardment.

RESULTS

After the hydrolysis reaction and the removal of isopropyl alcohol, boehmite (γ-AlOOH) enriched with ^{17}O was obtained. The X-ray diffraction patterns, as shown in Fig. 1(a), indicate that the boehmite is either amorphous or in a very fine crystalline state. The surface area of this powder measured by the BES technique was 800 m^2/g. Figure 2 shows the DTA and TGA curves of this powder. This figure shows that the dehydration of the boehmite to γ-Al_2O_3 occurs at 280°C, and that further phase transformation occurs at 500°C and 860°C to & - and θ-Al_2O_3, respectively, and finally to α-Al_2O_3 at 1200°C. The changes in the X-ray diffraction patterns of these phases with increasing temperature are shown in Fig. 1(b)—(d). These phase transformations are very detrimental to the densification during sintering because they can cause the development of microcracks. Some authors have employed an α-Al_2O_3 seeding technique to circumvent this problem.[7] In the present work, the calcination was done at 1300°C, which is higher than the θ to α-Al_2O_3 transformation temperature, to allow the transformation to occur first. The powder was subsequently milled in isopropyl alcohol to break down the partially sintered particles. The particle size distribution of the α-Al_2O_3 after milling is shown in Fig. 3. The sintered Al_2O_3 had consistently higher than 99.5% theoretical density, which is higher than the requirement for the irradiation experiments.

Based on the DTA/TGA and X-ray measurements, the optimum procedure for the preparation of isotopic-tailored alumina was determined to be the following: First, pure isopropyl alcohol, C_3H_7OH, was heated in a vacuum evaporator as shown in the schematic in Fig. 4. After the alcohol temperature reached 60°C, aluminum isopropoxide was added to the flask and the mixture was stirred until the $Al(OC_3H_7)_3$ had dissolved in the alcohol. A stoichiometric amount of ^{17}O-enriched water was then added to the solution while stirring vigorously. During the hydrolysis reaction, the temperature was kept at 60°C and flowing argon gas was used to keep environmental moisture out of the reaction flask. When the reaction was completed, the temperature was increased to 82°C and the vacuum evaporator was turned on to remove the isopropyl alcohol from the slurry. The calcination of the ^{17}O-enriched boehmite (γ-ALOOH) powder to produce alpha-alumina was performed at 1300°C for 3 h in an argon environment. After the heat treatment, 0.5 wt % MgO was added to the powder as a sintering aid. This powder was milled. in isopropyl alcohol for mixing and size reduction and then vacuum sintered at 1700°C for 3 h.

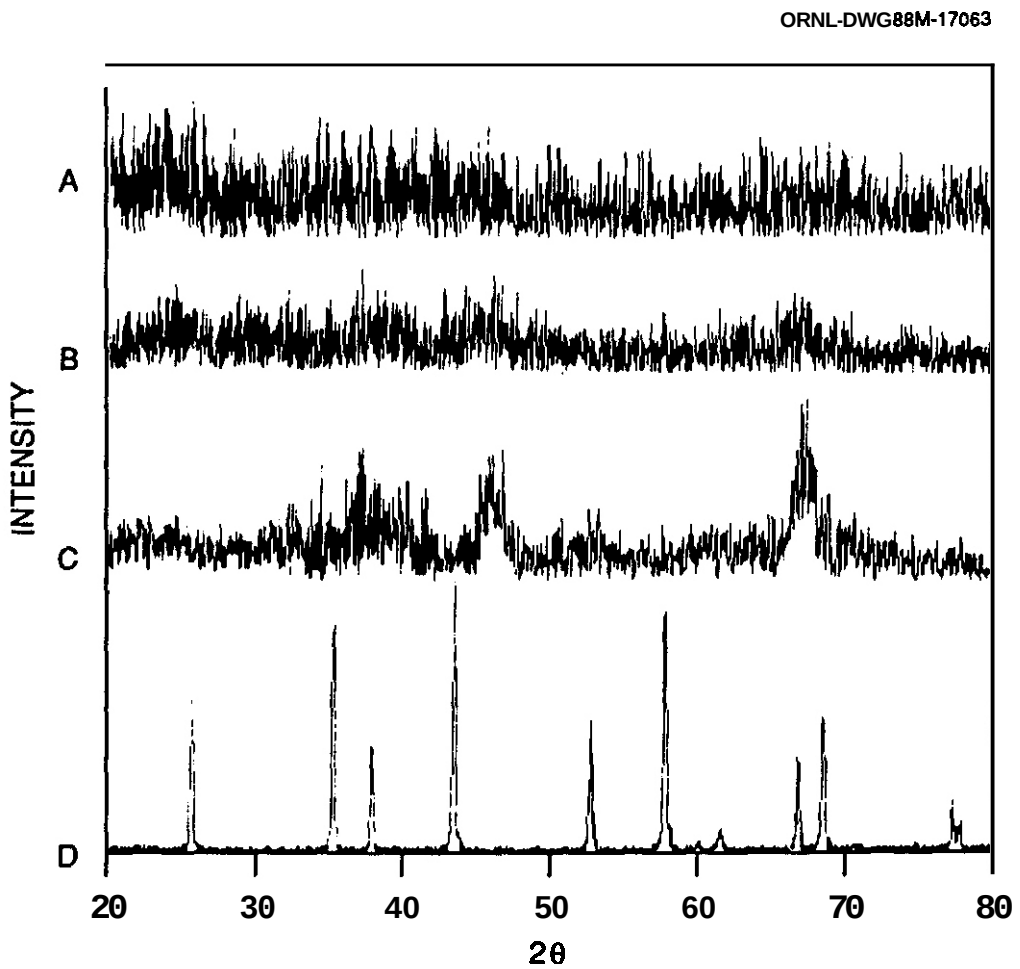

Fig. 1. X-ray diffraction patterns taken from boehmite powder: (a) before calcination, (b) calcined at 500°C, (c) calcined at 1000°C, and (d) calcined at 1300°C.

Isotope Enrichment Measurements

Oxygen isotope concentrations were measured in boehmite or alumina specimens for a total of 10 different processing conditions. As shown in Table 1, the residual concentrations of the enriched oxygen *isotopes* showed a sensitive dependence on processing environment. In all cases, the concentrations of the enriched oxygen isotopes were reduced as a result of the processing. In particular, the preparation of boehmite at 60°C in a flask exposed to air caused ~70% of the enriched oxygen isotopes in the water to be replaced by atmospheric oxygen (sample 1). Only ~25% of the enriched isotopes were replaced by ^{16}O when the hydrolysis was performed in an inert environment (sample 5). Calcination and sintering caused a further reduction in the enriched isotope concentration, particularly when these processes were carried out in air (samples 6-9). As expected, calcination at 1300°C caused a larger decrease in the enriched isotope concentration than calcination at 600°C (samples 2,7,9). Sintering at 1550 to 1700°C always produced a further decrease in the enrichment level, with the most pronounced effect occurring for the case of exposure to air. Rutherford backscattering energy measurements performed on sintered specimens indicated that the alumina contained stoichiometric amounts of aluminum and oxygen.

The nuclear reaction measurements also detected a sizeable impurity concentration that was tentatively identified as argon. An impurity concentration of 0.9 at. % was observed in specimen 9 (which was calcined and sintered *in* argon) and a concentration of 0.5% was observed in specimen 10 (which was calcined in argon and sintered in vacuum). It is possible that argon has been trapped in sintering pores present in the alumina.

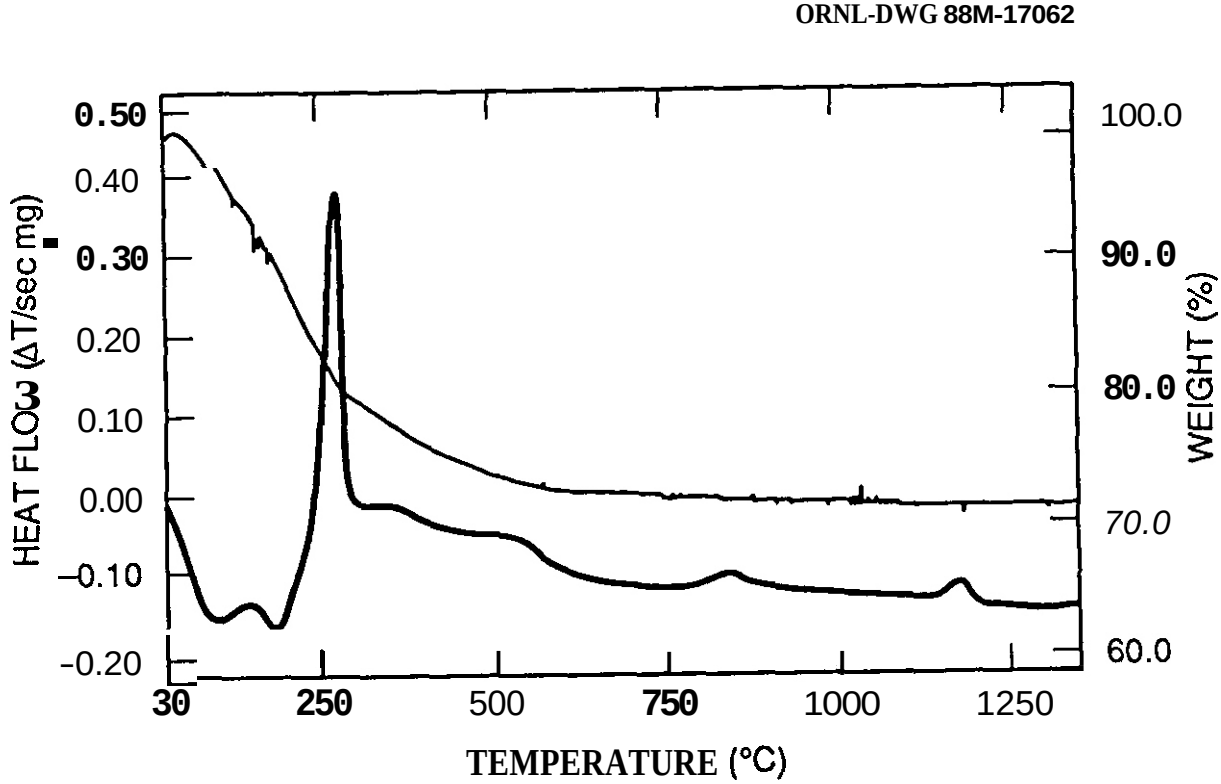

Fig. 2. Differential thermal analysis and TGA curves for boehmite powder.

Table 1. Efficiency of ^{17}O and ^{18}O Isotope Retention for a number of different processing schedules

Sample	Processing Environment			Retained Fraction of Enriched Isotopes (%)
	Hydrolysis	Calcination	Sintering	
1	Air, 60°C	--	--	30
2	Air, 60°C	Ar, 600°C, 1 h	--	27
3	Air, 60°C	Ar, 600°C, 1 h	Vac, 1600°C, 2 h	14
4	Air, 60°C	Air, 600°C, 1 h	Air, 1600°C, 2 h	0
5	Ar. 60°C	--	--	74
6	Ar, 60°C	Air, 600°C, 1 h	Air, 1550°C, 2 h	-8
7	Ar, 60°C	Ar, 600°C, 1 h	Vac, 1600°C, 2 h	52
8	Ar, 60°C	Air, 1300°C, 3 h	Vac, 1650°C, 3 h	<0.1
9	Ar, 60°C	Ar, 1300°C. 3 h	Ar, 1600°C, 2 h	43
10	Ar, 60°C	Ar, 1300°C, 3 h	Vac, 1700°C, 3 h	15

Mechanical Strength and Microstructure

It is apparent from the DTA/TGA and X-ray measurements that calcination of the boehmite should be performed at temperatures above 1200°C to avoid the deleterious effects of the transition alumina phases (γ,δ,θ). This expectation was confirmed in a study of the material properties of alumina specimens that were subjected to two different calcination temperatures, 600 and 1300°C. Table 2 summarizes the results of this study. It can be seen that the green density of boehmite that was calcined at 600°C is very low (27% theoretical density). This results in a final sintered density that is lower than desired. On the other hand, calcination at 1300°C produced a relatively high green density (49% theoretical density) which led to a sintered density of the alumina that was near the theoretical limit. The flexural strength of the samples calcined at 600°C was only about one-third the value of the 1300°C samples. This suggests that volume changes associated with transformations between the transition alumina phases may have introduced microcracks during sintering of the 600°C sample.

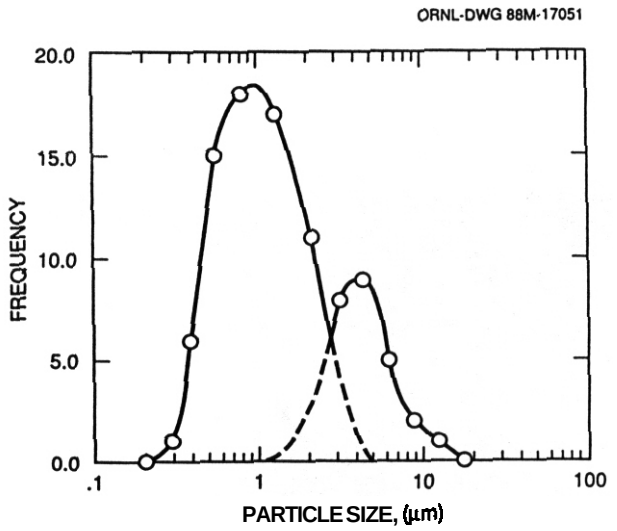

Fig. 3. Particle size distribution of alumina after ball milling.

Table 2. Materials Properties for Alumina Samples Prepared under Two Different Processing Schedules

	Sample 7	Sample 10
Calcination	600°C, 1 h	1300°C, 1 h
Sinter	1600°C, 2 h	1700°C, 3 h
Sintering aid	0.1 wt % MgO	0.5 wt % MgO
Density		
Green	27%	49%
Sintered	96.9%	99.8%
Grain size	6 μm	8 μm
Modulus of rupture	105 MPa	280 MPa

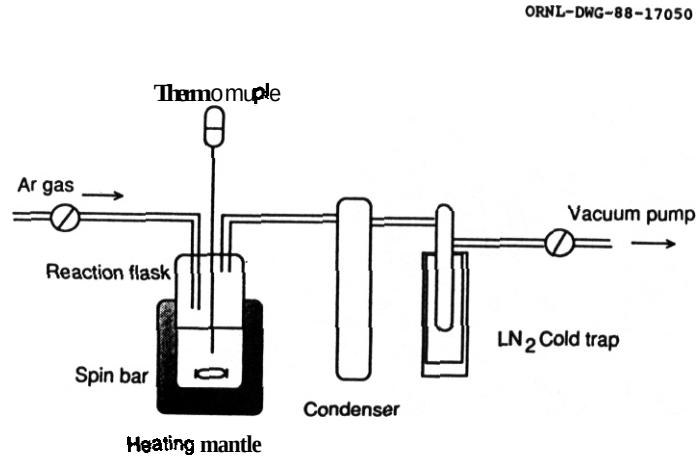

Fig. 4. Schematic view of the experimental setup.

Transmission electron microscopy was used to investigate the microstructures of specimens subjected to the two different calcination temperatures. The general microstructure consisted of defect-free grains with a grain size near 10 μm in both cases. Figure 5 shows the typical microstructure observed in the sample calcined at 1300°C (sample 10). A low density of sintering pores was observed in the interior of the grains. From nuclear reaction results presented earlier, it seems possible that the pores may contain argon, which was trapped between particles during the calcination and sintering process. Cracking along grain boundaries was observed in the specimen that was calcined at 600°C (Fig. 6). The existence of these cracks (which were not observed in the 1300°C specimen) explains the low flexural strength of the sample calcined at 600°C (Table 2). This observation supports the hypothesis that volume changes associated with phase transformations during sintering of alumina calcined at low temperatures can cause microcrack formation.

REFERENCES

1. J. L. Scott, F. W. Clinard, Jr., and F. W. Wiffen, J. Nucl. Mater. 1336134 (1985) 156.

2. G. P. Pells, J. Nucl. Mater. 1226123 (1984) 1338.

3. F. W. Clinard, Jr. and L. W. Hobbs p. 387 in Physics of Radiation Effects in Crystals, eds., R. A. Johnson and A. N. Orlov (Elsevier, Amsterdam, 1986).

4. R. J. LaBauve, R. J. Livak, and F. W. Clinard, Jr., Adv. Ceramic Mater. 3 (1988) 353–56.

5. M. B. Lewis, Nucl. Instr. Meth. 190 (1981) 605.

6. G. Amsel and D. Samuel, Anal. Chem. 39 (1967) 1689.

7. M. Kumagai and G. Messing, J. Amer. Ceram. Soc. 68 (1985) 500.

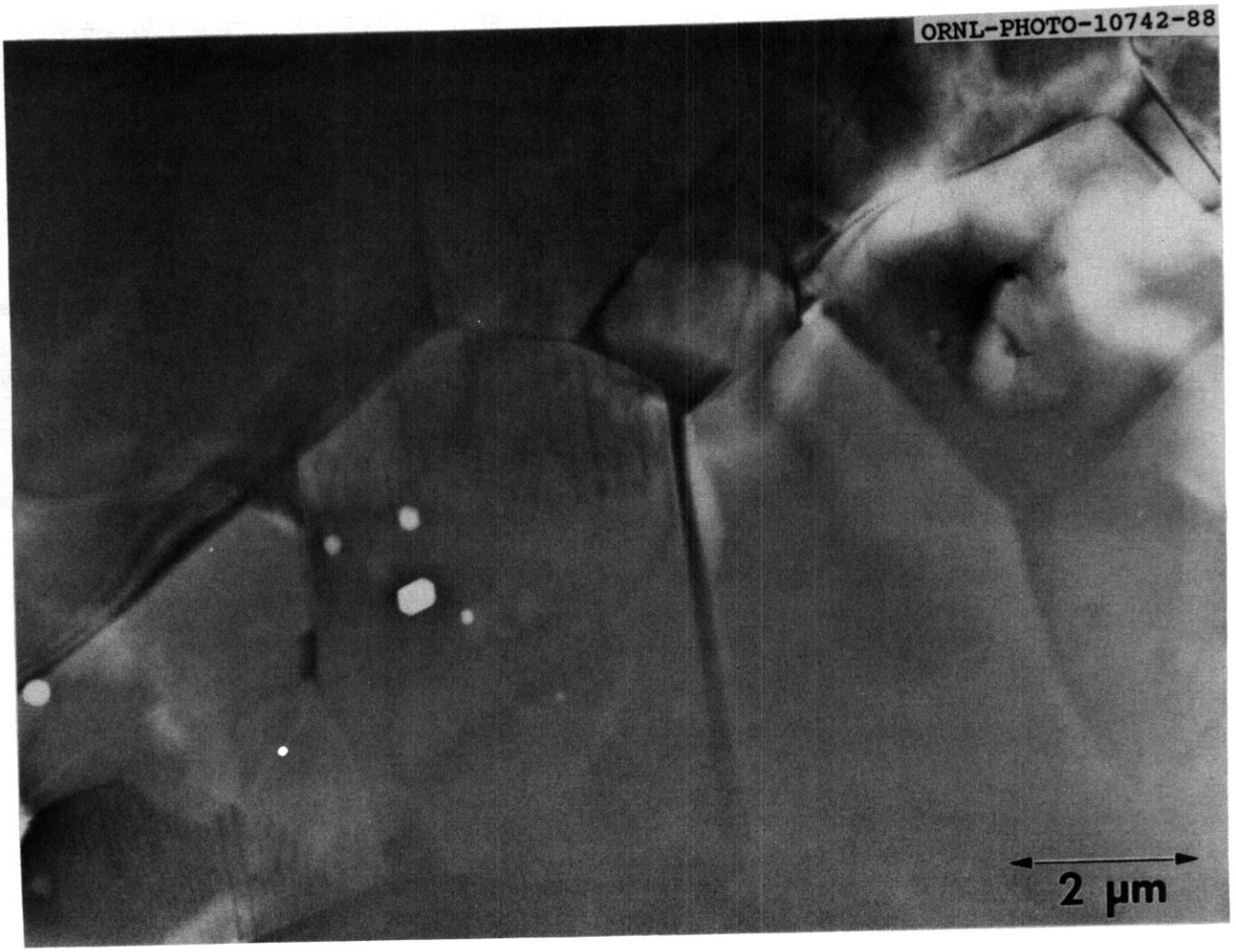

Fig. 5. General TEM microstructure of alumina calcined at 1300°C and sintered at 1700°C.

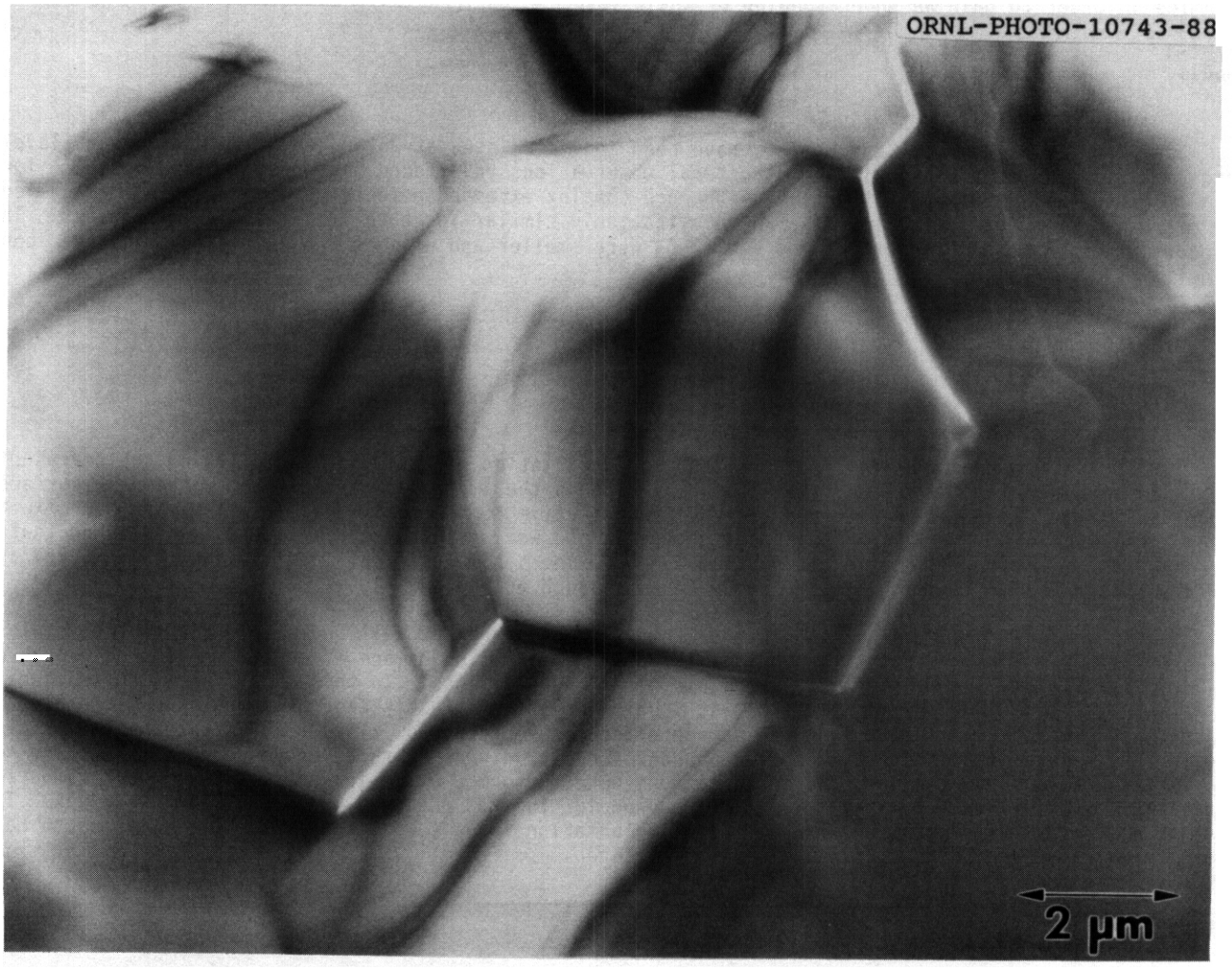

Fig. 6. Grain boundary cracking observed in an alumina specimen calcined at 600°C and sintered at 1600°C.

ION IRRADIATION STUDIES OF OXIDE CERAMICS — S J. ZINKLE (Oak Ridge National Laboratory)

OBJECTIVE

The objective of this study is to examine the irradiation microstructures of three different oxide ceramics in order to gain an understanding of their response to irradiation.

SUMMARY

Specimens of Al_2O_3, MgO, and $MgAl_2O_4$ have been ion irradiated at 25 and 650°C to peak damage levels between 0.5 and 35 dpa. Initial microstructural observations have found that dislocation loops are formed in all three ceramics at moderate doses, with more conplex extended defects observed at high damage levels. The microstructure for a given ceramic was qualitatively similar for both irradiation temperatures. The loops observed in the simple oxides MgO and Al_2O_3 were smaller and of much higher density than the loops in spinel.

PROGRESS AND STATUS

Introduction

Ion implantation is a useful tool for studying Irradiation effects and for modifying the near-surface mechanical properties of ceramic materials. Depending on the inplantation conditions, the mar-surface region may become hardened or softened (amorphized) relative to the substrate.[1] This may in turn exert a strong influence on the fracture toughness, strength, and wear resistance. It is now established that many ceramics can be made amorphous if the lattice damage exceeds some critical level,[1-3] which is ~5 keV/atom for a room temperature implantation of oxide ceramics such as MgO and Al_2O_3.

The fundamental processes responsible for amorphiration are not well understood due to the complex interaction between chemical (inplanted ion) effects and radiation damage effects. One approach that may be used to separate these effects involves the use of high-energy ions. In this case, the microstructure produced near the peak in the implanted ion distribution may be distinctly separated from the microstructure at shallower depths where only displacement damage effects have occurred. This report presents the initial results of an investigation of the depth-dependent microstructures of three oxide ceramics following ion implantation to moderate doses. The implantations were performed using ion species that occur as cations in the target material; for example, Mg^+ ions were used for the MgO and $MgAl_2O_4$ (spinel) irradiations. This minimized chemical effects associated with the Implantation and allowed a more direct evaluation to be made of the effects of imolanted ions on the microstructure.

2. EXPERIMENTAL PROCEDURE

The starting materials for the implantation study consisted of polycrystalline $MgAl_2O_4$ [grain size ≅30 μm), two types of polycrystalline α-Al_2O_3 (grain sizes of 0.8 and 30 μm), and single crystal MgO. The 5 by 10 by 2 mm mechanically polished MgO specimens were implanted at an orientation ~7° from (100) in order to minimize ion channeling effects. The $MgAl_2O_4$ and Al_2O_3 specimens were irradiated as mechanically polished transmission electron microscope specimens (3 mm diam by 0.5 mm thickness) in a 9-specimen array. The irradiations were performed at room temperature and 650°C using the Van de Graaff facility at Oak Ridge National Laboratory.' Table 1 summarizes the implantation conditions. The alumina implantations were performed with simultaneous beams of Al^+, O^+, and He^+ (the 0.2 to 0.4 MeV He^+ beam produced negligible displacement damage). The energies of the Al^+ and O^+ beams were chosen so that the calculated mean range of both ions in alumina was 1.2 m. The spinel and MgO irradiations were performed using 2.4 MeV Mg^+ ions. which have a calculated mean ion range of 1.6 em in both materials. In the following sections. the term 'damage peak" refers to the calculated peak in the displacement damage

Table 1. Ion implantation parameters

Material	Implanted Ion	Fluence	Peak Damage (keV/atom)	Irradiation Temperature (°C)
$MgAl_2O_4$	2.4 MeV Mg^+	1.4 × 10^{21}/m²	3.5	25. 650
Al_2O_3	2.0 MeV Al^+ 1.44 MeV O^+	6.9 × 10^{20}/m² **8.3** × 10^{20}/m²	3.1	25, **650**
MgO	2.4 MeV Mg^+	4.1 × 10^{19}/m²	0.10	25
MgO	2.4 MeV Mg^+	2.1 × 10^{19}/m²	0.05	650
MgO	2.4 MeV Mg^+	8.1 × 10^{20}/m²	**2.0**	**650**

profile. In the present experiment, this peak occurs at a depth that is ~0.1 μm closer to the surface than the mean ion ranges given above.

Transmission electron microscopy (TEM) was performed on cross-sectioned Specimens that were prepared by standard techniques.[5] The depth-dependent hardness and elastic modulus of the implanted $MgAl_2O_4$ and Al_2O_3 specimens were measured at Mom temperature with a specialized microindentation ("nano-indenter") hardness tester.[6] The indenter load and displacement were continuously measured during the Indentation process so that depth-dependent hardness measurements could be obtained on as-irradiated specimens.[6,7] Nine to fifteen indentation measurements were performed in the control and irradiated regions of each specimen. The maximum load for each indent was ~0.12 N (12 g).

3. RESULTS

3.1 Spinel

Ion irradiation of spinel at 25 and 650°C produced faulted interstitial dislocation loops at intermediate depths (~1 μm) along the ion range. The microstructure near the implanted ion region and damage peak consisted of a high density of dislocation tangles for both temperatures. All regions of the irradiated specimens remained crystalline following both room temperature and 650°C implantation. A detailed description of the irradiated microstructure observed in these specimens is given elsewhere.[7]

The cross-section microstructure of spinel following irradiation at 650°C is shown in Fig. 1. The near-surface region was devoid of any observable defects for depths up to ~0.9 μm. The damage microstructure at intermediate depths of the 650°C specimen is shown in more detail in Fig. 2. The loops exhibit fault contrast for g = <220> and no fault contrast for g = <440>. An analysis of the nature of the loops' revealed a mixture of interstitlal loops of the type a/4<110>{110} and a/4<110>{111} which, as explained by Clinard et al.[8] are faulted on the cation sublattice.

The depth-dependent microstructure of spinel following irradiation at 25°C was very similar to that observed for the 650°C case[7] except that interstitial loop formation was also observed in the near-surface region of the specimen implanted at 25°C. The microstructures at intermediate depths and near the peak damage region of the 25°C specimen are compared in Fig. 3. Isolated dislocation loops are visible at intermediate depths whereas the peak damage region is a complex mixture of dislocations with no observable loops. A further inspection of the peak damage region reveals the presence of dislocation tangles along with other unidentified defects that exhibit contrast similar to antiphase boundaries (APBs) in ordered crystals (Fig. 4).

Nanoindenter measurements made on specimens irradiated at the two temperatures showed no significant change (<5%) in the elastic modulus. The hardness at an indent depth of 0.5 μm increased from 8.2 GPa (unimplanted) to ~8.6 GPa (implanted) for both irradiation temperatures as a result of the irradiation.[7] The hardness change (implanted vs. unimplanted) of the 650°C specimen showed a gradual increase with increasing indentation depth that could be attributed to the loop-denuded region near the surface and the high defect density at deeper subsurface regions.' The hardness increase of the 25°C specimen was essentially independent of depth for indent depths between 100 and 600 nm (ref. 7).

3.2 Alumina

The microstructure of irradiated alumina consisted of dense arrays of dislocation loops and network dislocations, with no evidence of amorphization at either irradiation temperature. The loops were observed on (0001) and {10$\bar{1}$0} habit planes. There were no obvious microstructural differences between the fine-grained and coarse-grained alumina specimens. Some preliminary observations of the microstructure of irradiated alumina are described below.

As shown in Fig. 5. the dominant microstructural feature in the midrange region of alumina irradiated at 650°C is a network of dislocations. A low density of dislocation loops with habit planes near {01$\bar{1}$0} were also observed under different diffracting conditions. An example of the loop microstructure observed near the peak damage region of a 650°C specimen is shown in Fig. 6. Edge-on loops lying on the basal plane and on the (01$\bar{1}$0) plane are visible in Fig. 6. with a loop diameter of ~20 nm. The midrange microstructure of the 650°C specimen suggests that the loop density is significantly less than that found near the damage peak (implanted ion region). The network dislocations observed at intermediate depths have yet to be observed in the peak damage region, which suggests that either dose or implanted ion effects may be significant at this temperature.

The midrange microstructure of Al_2O_3 irradiated at 25°C was similar to the 650°C case. Figure 7 shows the typical midrange loop microstructure for alumina irradiated at 25°C. Loops with diameters ~10 nm were observed on (0001) and {10$\bar{1}$0} planes. An example of a loop on the basal plane is arrowed in Fig. 7. Dislocations were observed in both the midrange and peak damage regions along with the loops. An example of the dislocation microstructure observed near the peak displacement region of a 25°C specimen is shown in Fig. 8. A Burgers vector analysis of dislocations suggests that b = 1/3<01$\bar{1}$1>. A second set of aligned

ORNL-PHOTO-5715-88

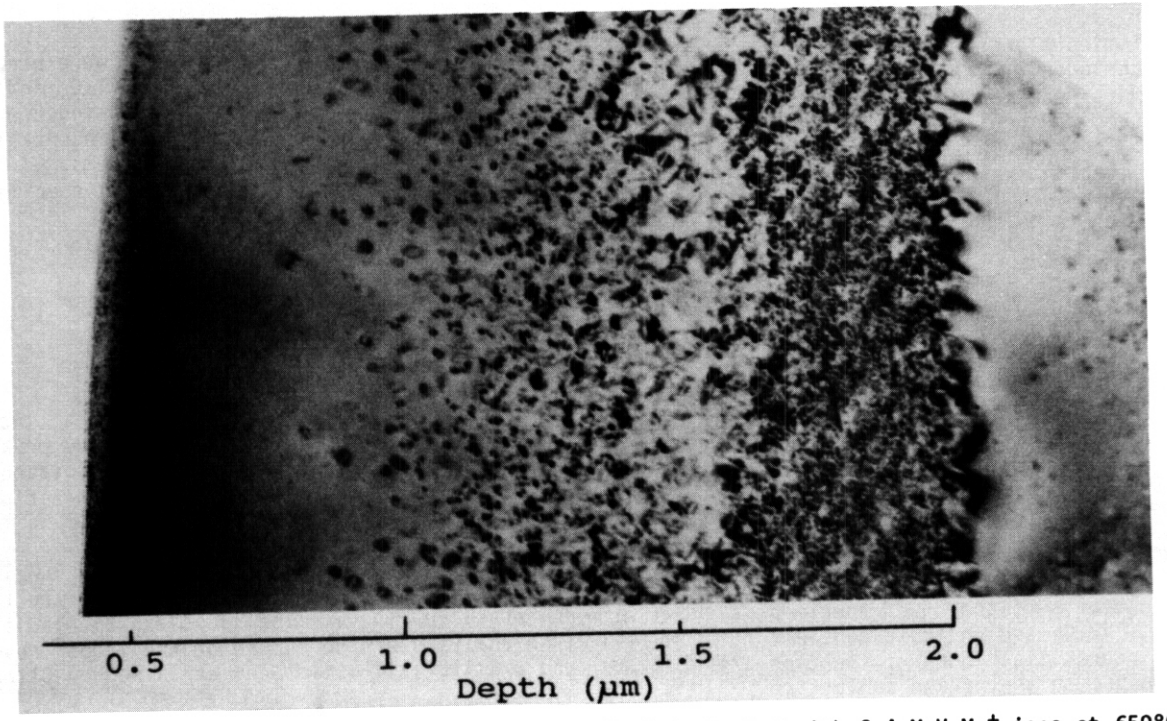

Fig. 1. Depth-dependent microstructure of spinel implanted with 2.4 MeV Mg^+ ions at 650°C.

ORNL-PHOTO-5716-88

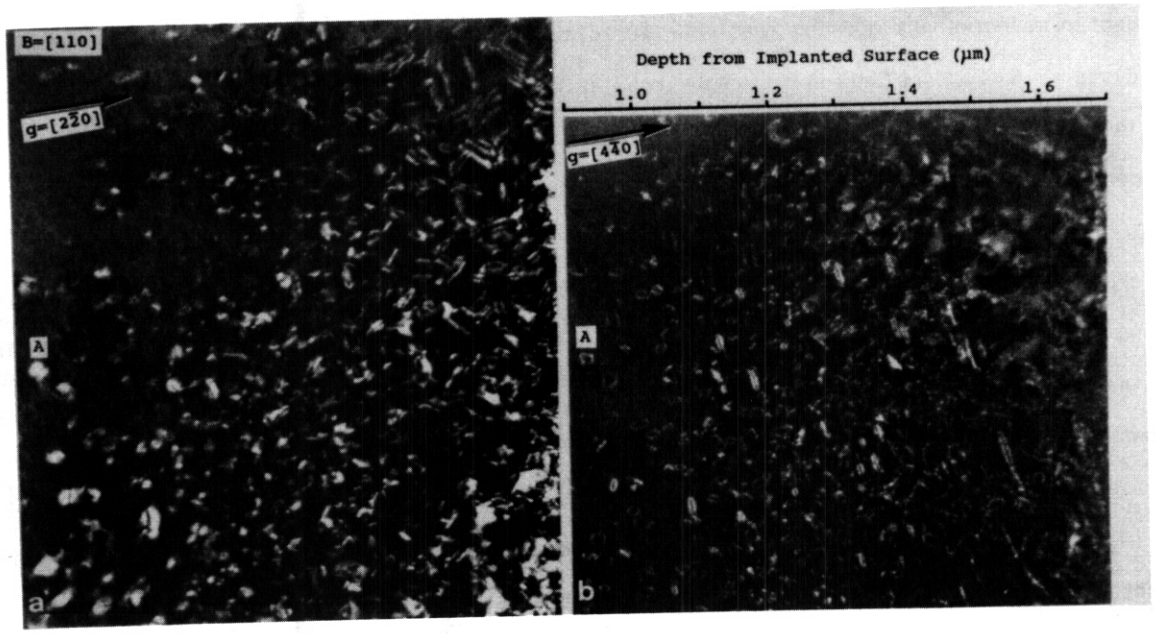

Fig. 2. Comparison of the midrange microstructure of spinel implanted at 650°C for two different diffraction vectors. (a) weak beam (g,4g), g = 2$\bar{2}$0. (b) weak beam (g,2g), g = 4$\bar{4}$0. Note the absence of stacking fault contrast in (b). The same area of the foil is shown for the two different diffracting conditions.

OWL-PHOTO-5717-88

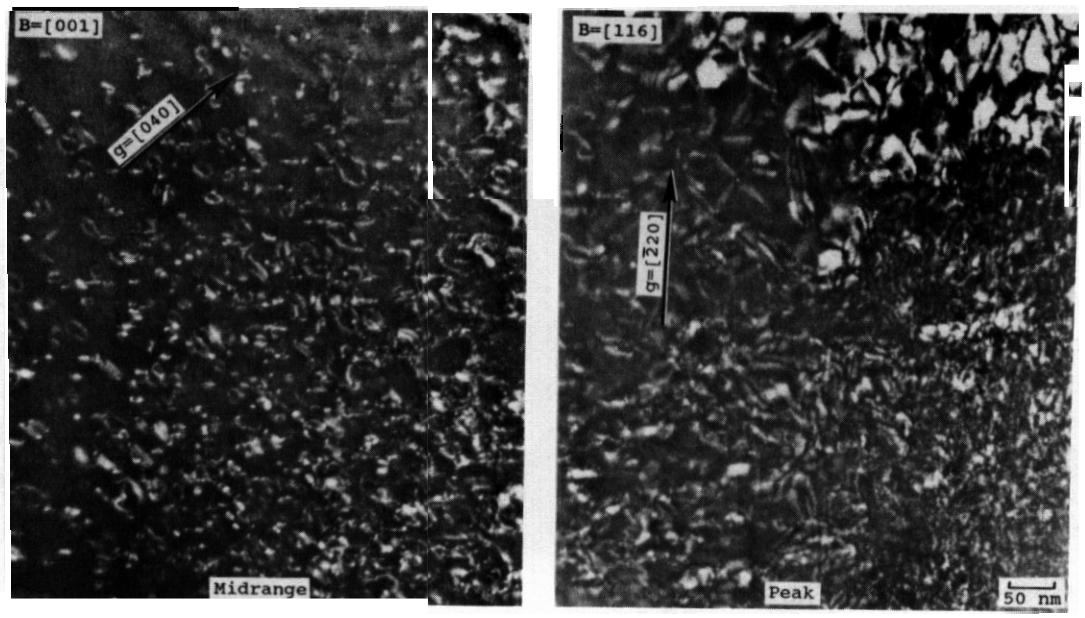

Fig. 3. Typical irradiated microstructures of spinel implanted at 25°C. The left photograph shows the weak beam (g,3g) microstructure for damage depths of 1.0 to 1.5 μm. The right photograph shows the weak beam (g,4g) microstructure for damage depths of 1.4 to 1.9 μm. The original irradiated surface lies to the left of both photographs.

ORNL-PHOTO-5718-88

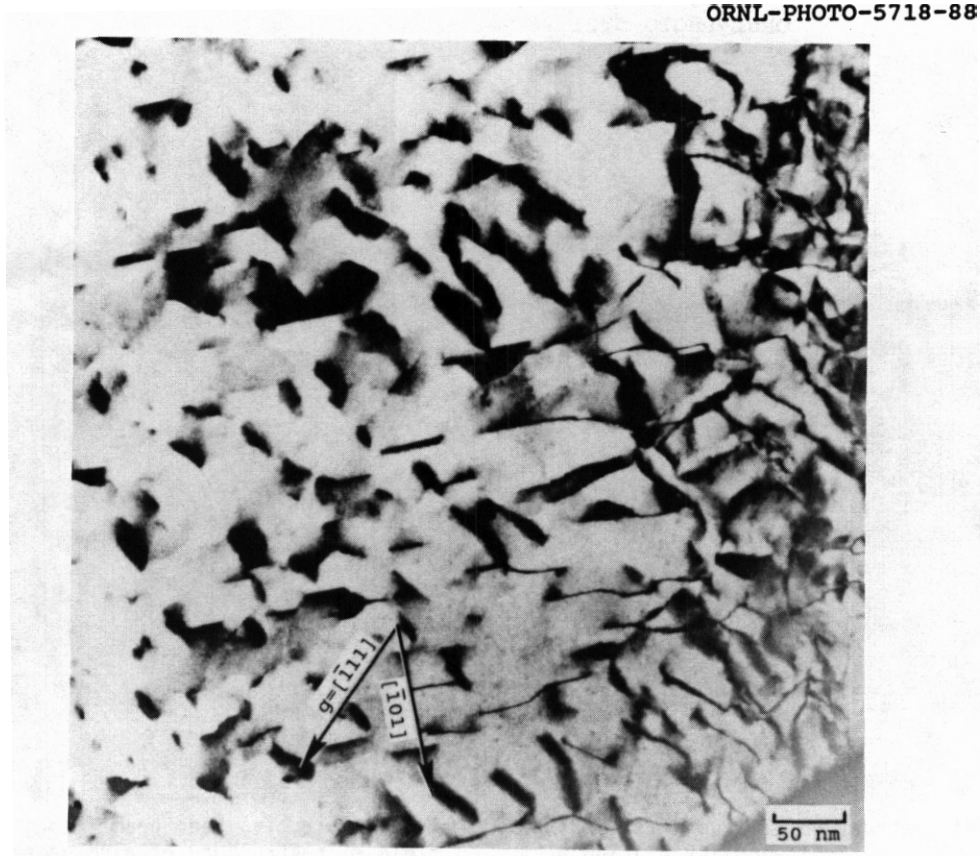

Fig. 4. Weak beam (g,4g) microstructure of spinel implanted at 25°C at damage depths of 1.3 to 1.8 μm. The irradiated interface lies to the left of the micrograph.

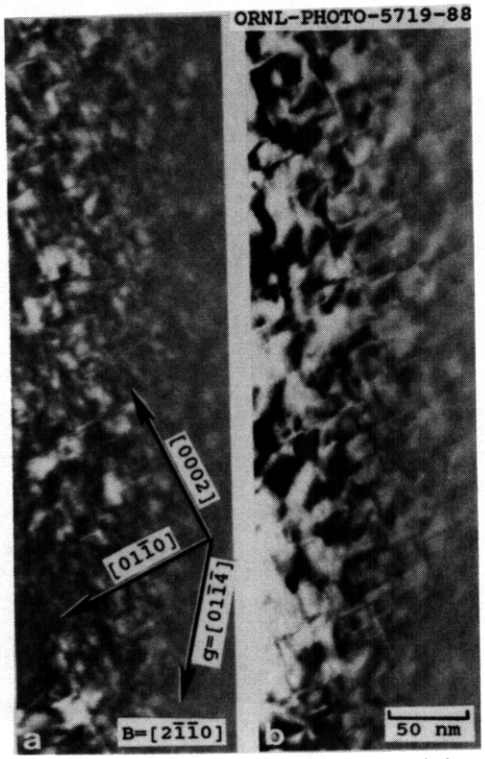

Fig. 5. (a) Weak beam (g,3g) and (b) bright field microstructure of alumina at an intermediate depth (~0.8 μm depth) following irradiation at 650°C.

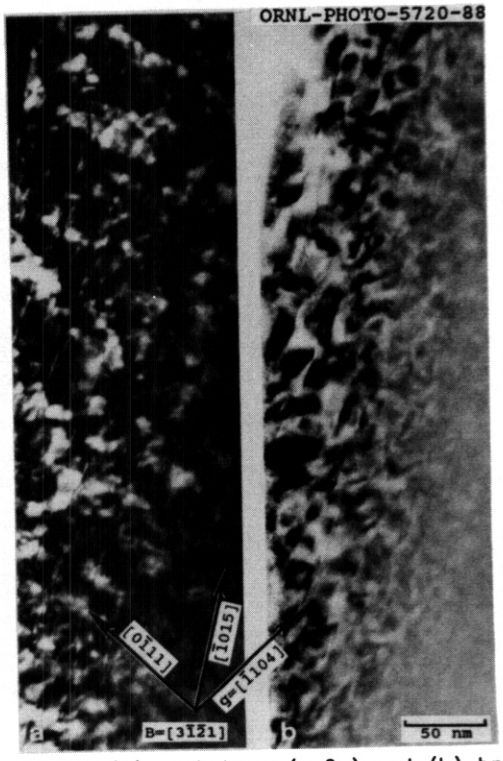

Fig. 6. (a) Weak beam (g,3g) and (b) bright field microstructure of alumina near the peak damage region (~1.3 μm depth) following irradiation at 650°C.

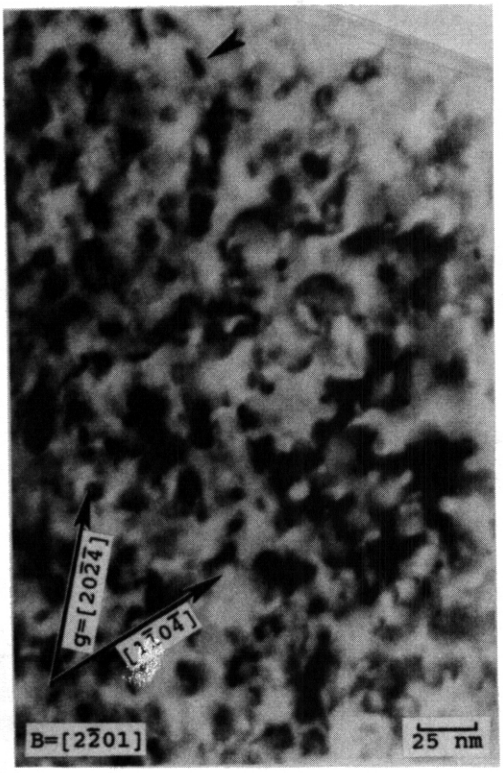

Fig. 7. Microstructure of alumina at an intermediate depth (~0.8 μm) following irradiation at 25°C. The arrow points to a loop on the basal plane.

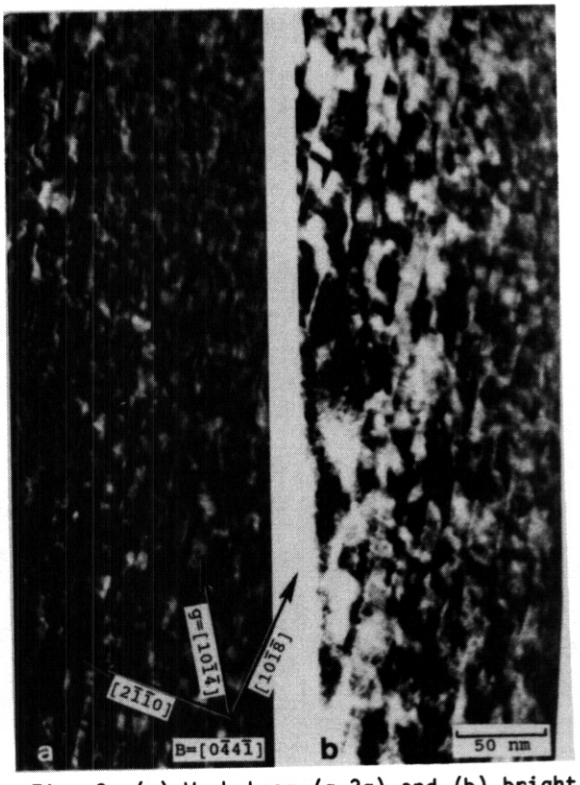

Fig. 8. (a) Weak beam (g,3g) and (b) bright field microstructure of alumina near the peak damage region following irradiation at 25°C.

dislocations were observed with their line vectors nearly perpendicular to [0001], but their Burgers vector has not yet been determined. Contrast similar to that associated with APBs was observed under suitable diffraction conditions (Fig. 9).

Nanoindenter and hardness measurements were performed at room temperature on the irradiated fine-grained ($d \approx 0.8$ μm) alumina specimens. As shown in Fig. 10, the elastic modulus of Al_2O_3 (determined from nanoindenter measurements) was unaffected by ion irradiation for indent depths up to 250 nm. The nanoindenter measurements also indicated that there was no significant (<5%) change in the depth-dependent hardness of Al_2O_3 following ion irradiation at 25°C (Fig. 11). The measurements suggested that the near-surface hardness of alumina following irradiation at 650°C (relative to the nonirradiated value) was increased by 10 to 20%. For the 650°C specimen, the unimplanted hardness was about 10% less than the 25°C unimplanted hardness; the irradiated hardness for the 25 and 650°C specimens was essentially equal. For comparative purposes, Knoop indentation measurements were made at a load of 0.25 N and the hardness was calculated from the long diagonal of the residual indentation. The indentation depth was ~0.5 μm. The Knoop hardness measurements were in reasonable agreement with the nanoindenter results.

3.3 Magnesia

High densities of small dislocation loops were formed in MgO during irradiation at a variety of experimental conditions. Irradiation at 650°C to a fluence of 2.1×10^{19} Mg^+/m^2 produced small (~10 nm diam) loops near the peak damage region. The loop density was lower and the mean loop size was larger in the near-surface region compared to the peak damage region. The damage microstructure following irradiation at 650°C to a higher fluence of 8.1×10^{20} Mg^+/m^4 was qualitatively similar to that observed following the low dose irradiation. The loop density was lower in the near-surface region and the mean loop diameter changed from ~40 nm at a depth of 0.5 μm to ~10 nm at the peak damage region (1.6 μm depth). Figure 12 shows some loops that were present at a depth of ~1 μm from the irradiated surface.

There was not a large depth-dependence to the irradiated microstructure for the 25°C implantation. Figure 13 shows a cross-section view of MgO following irradiation at 25°C to a fluence of 4.1×10^{19} Mg^+/m^2 (~0.7 dpa peak damage). An interesting feature observed for this moderate irradiation condition was the appearance of heterogeneous "patches" of small voids (Fig. 14). Small loops with diameters ~10 nm were also resolvable in the microstructure. Knoop hardness measurements showed a large increase in hardness for the 25°C case, and slight hardness increases for the two 650°C cases. Complete details of the irradiation microstructure and hardness measurements (including hardness anisotropy measurements) are given elsewhere.[9]

ORNL-PHOTO-5723-88

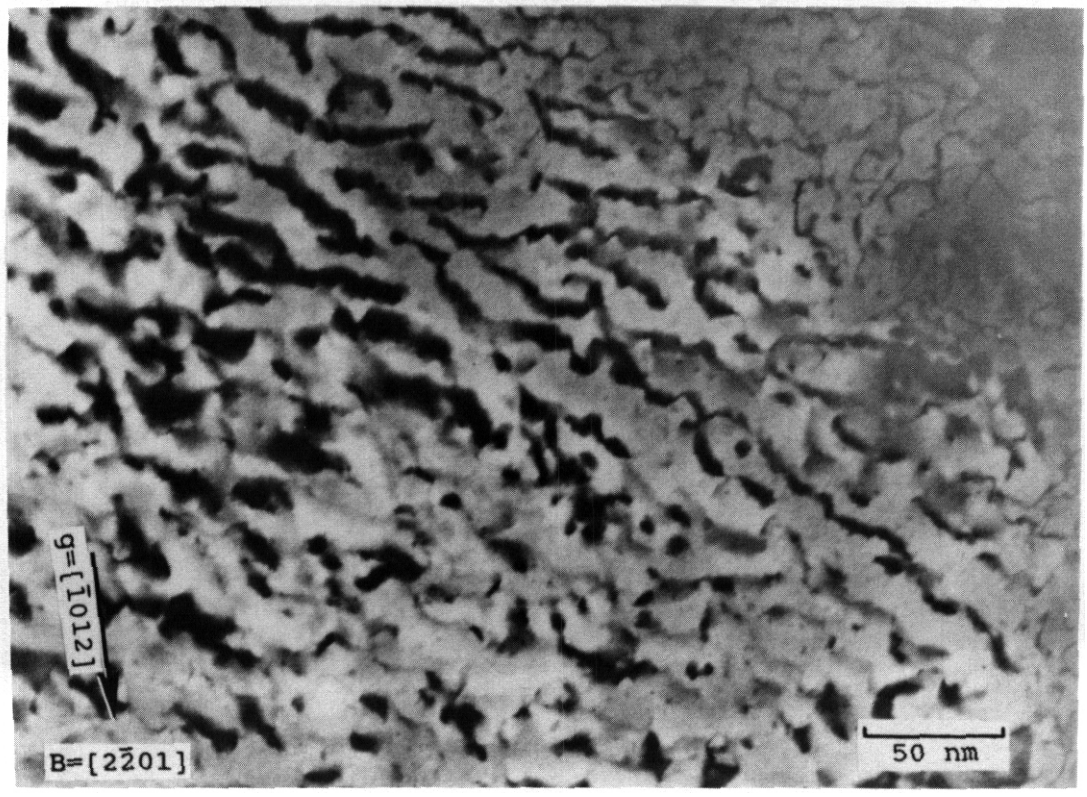

Fig. 9. Weak beam (g,2g) microstructure of alumina irradiated at 25°C.

ORNL-DWG 88-12754

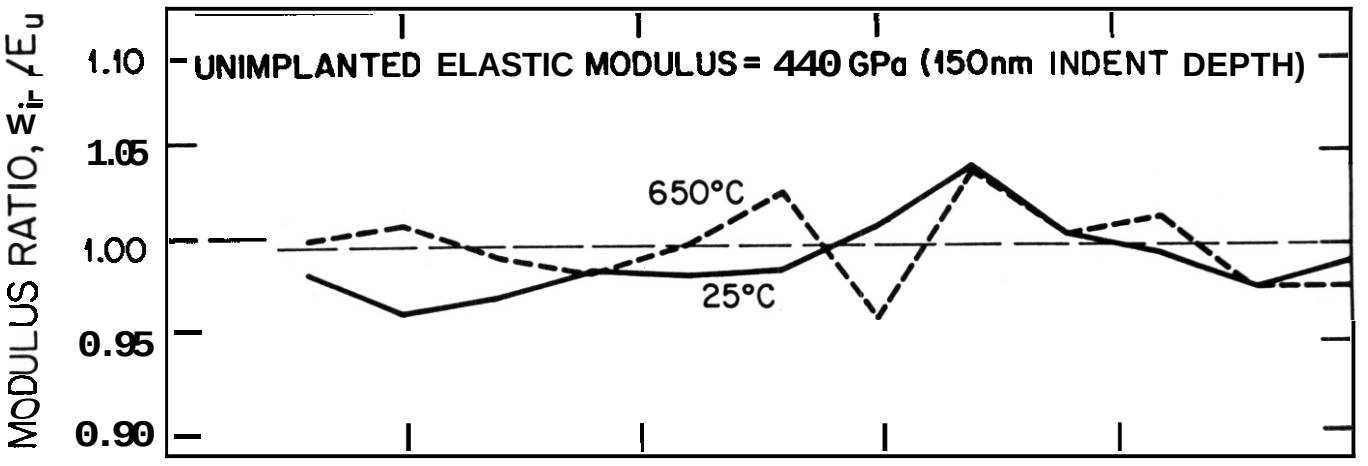

ORNL-DWG 88-12637

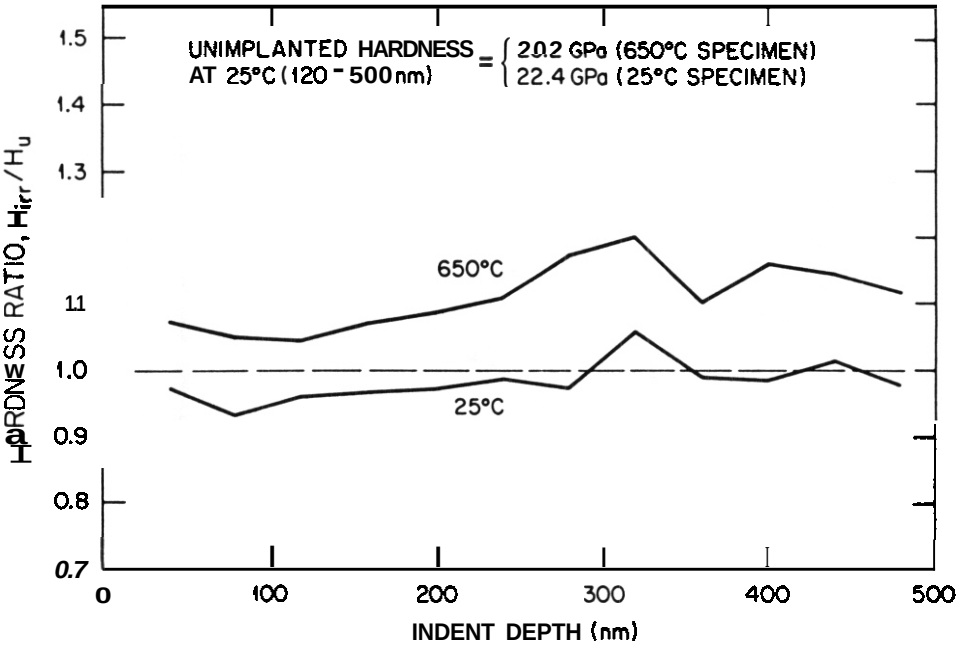

Fig. 11. Depth-dependent hardness ratio for ion-implanted Al_2O_3.

ORNL-PHOTO-5726-88

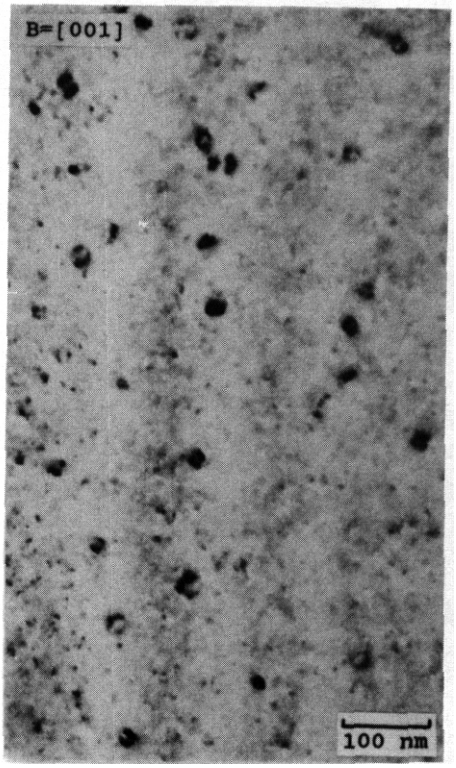

Fig. 12. Dislocation loops observed in MgO at a damage depth of ~1 μm following irradiation at 650°C.

ORNL-PHOTO-5724-88

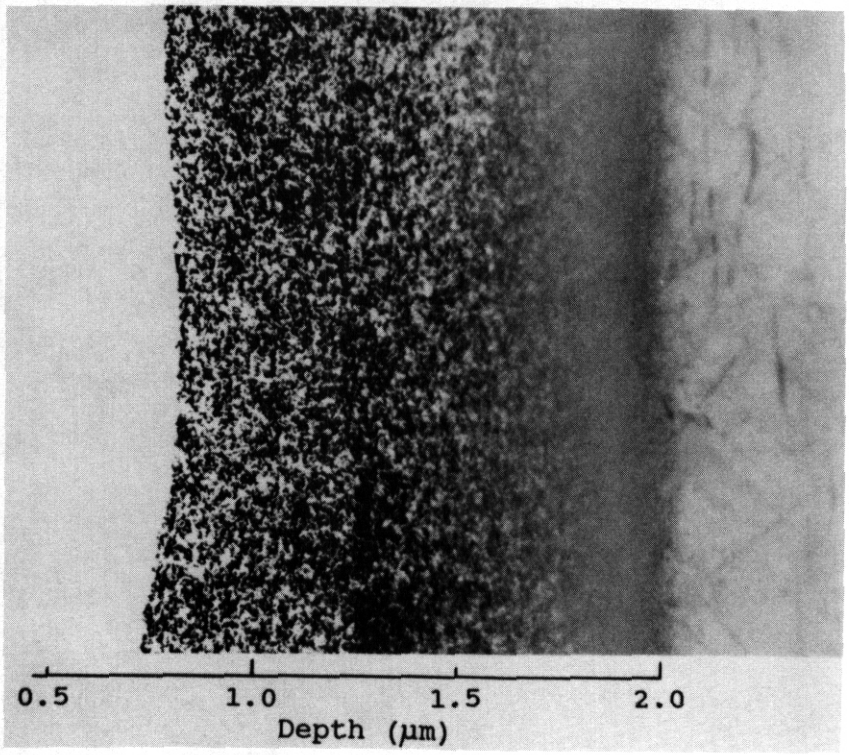

Fig. 13. General cross-section microstructure of MgO following implantation at 25°C.

4. DISCUSSION

4.1 General Microstructural Features

Amorphization was not detected in any of the implanted specimens. This indicates that the critical damage level required to amorphize spinel or alumina at room temperature by implantation with ions that minimize chemical effects is greater than 3.1 to 3.5 keV/atom. Implantation at damage levels below 3 keV/atom with certain ion species such as zirconium has been found to induce amorphization in alumina,[2] which shows that chemical effects can be important.

The fraction of defects retained from displacement processes in the form of visible clusters is much lower in spinel compared to MgO and Al_2O_3. In particular, only ~0.05% of the calculated displacements in spinel at an irradiation depth of 1 μm result in visible defect clusters.[7] Other researchers have made similar observations[8,10] and have attributed the resistance to damage accumulation in spinel to the structural complexity of forming stoichiometric clusters (a minimum of seven point defects are required). This implies that higher implantation doses may be needed to amorphize spinel compared to simpler oxide ceramics such as MgO or Al_2O_3.

4.2 Depth Dependence

The peak in the displacement damage profile occurs at a depth that is close to the location of the implanted ions. It is therefore difficult to attribute any depth-dependent microstructural changes solely to implanted ion effects unless additional tests have been made at lower or higher doses. On the other hand, if the observed microstructural features do not show a strong depth dependence then it may be argued that implanted ion and displacement dose effects are of secondary importance.

The microstructure of implanted spinel exhibited a strong depth dependence at both irradiation temperatures (Figs. 1–4). Some of the depth dependence may be attributed to differences in the damage level — with increasing dose, the density of loops increases until the close proximity of loops induces interactions that could lead to the formation of a dislocation network. However, the mechanism for this process is uncertain since the loops in spinel contain a cation fault and are therefore not glissile. The microstructure

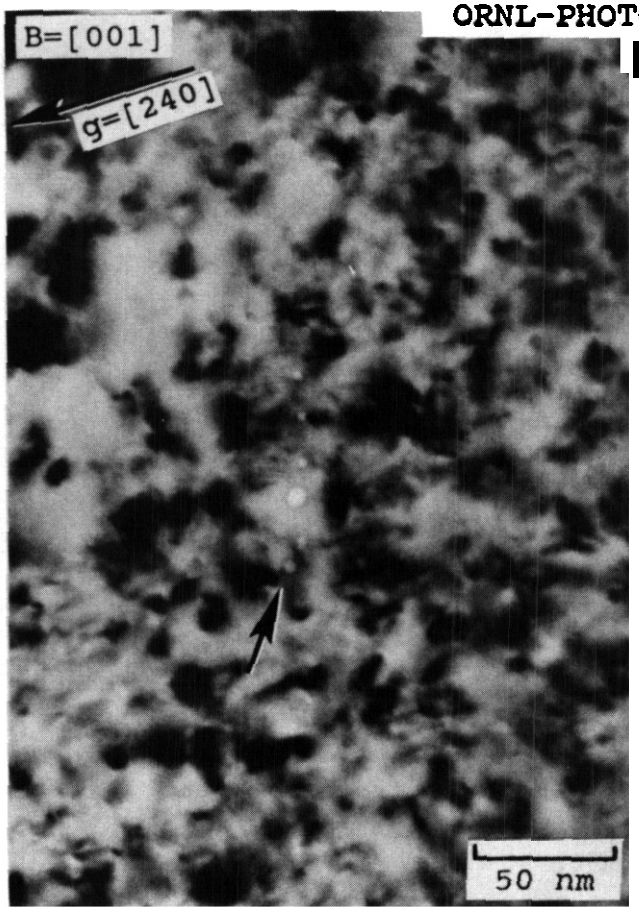

Fig. 14. Heterogeneous formation of small voids (arrowed) at a depth of ~1 μm in MgO irradiated at 25°C.

of alumina did not show a strong depth dependence for specimens implanted at room temperature (Figs. 7, 8). Alumina specimens irradiated at 650°C showed a slight microstructural depth dependence, changing from primarily aligned dislocations in the midrange region to aligned dislocations and an array of dislocation loops on (0001) and {10$\bar{1}$0} planes in the peak damage region (Figs. 5, 6). The MgO specimens showed a weak dependence on irradiation depth. The main observation was a decrease in loop size with increasing depth for specimens implanted at 650°C. A similar depth dependence of loop size has been reported for ion-implanted Al_2O_3 (ref. 11).

4.3 Temperature Effects

Irradiation at 650°C produced microstructures that were qualitatively similar to the room temperature irradiations. A general observation is that high implantation temperatures appeared to enhance the depth depehdence of microstructural features. For example, spinel showed a loop-denuded zone within ~0.9 μm of the implanted surface following irradiation at 650°C whereas the 25°C specimen contained loops in the near-surface and midrange regions. Most of the loops (~70%) in spinel had {110} habit planes for the 650°C case, whereas the loops were nearly evenly divided between {110} and {111} for the 25°C implantation.[7] Aligned dislocations were observed in the midrange region of Al_2O_3 following implantation at both 25 and 650°C. However. at 650°C there was a greater density of arrays of loops on (0001) and {10$\bar{1}$0} in the peak damage region compared to the 25°C case. The loop density in MgO was lower for the high-temperature irradiations compared to the 25°C irradiation.

5. SUMMARY AND CONCLUSIONS

Initial microstructural observations have been made on three ion-implanted oxide ceramics. The main microstructural features associated with the implantations are dislocation loops and network dislocations. The effect on the resultant microstructure of implantation with ions that minimize chemical effects is

uncertain, but the effect does not appear to be large for room temperature irradiations. Implantations at 650°C produced microstructural changes that were in general qualitatively similar to the 25°C implantation case. The high-temperature implantations appeared to enhance the depth dependence of the microstructure, although the effect was often slight.

ACKNOWLEDGMENTS

The author would like to thank C. P. Haltom, M. Williams, J. W. Jones, and A. T. Fisher for preparation of the TEM specimens, S. W. Cook and M. B. Lewis for performing the ion implantations, F. Scarboro for manuscript preparation, and P. Angelini and P. S. Sklad for manuscript review.

REFERENCES

1. P. J. Burnett and T. F. Page, Radiation Effects, 97 (1986) 123.

2. C. J. McHargue et al., Materials Science and Engineering, 69 (1985) 123.

3. W. C. Oliver et al., in Defect Properties and Processing of High-Technology Nonmetallic Materials, Y. Chen et al. (Eds.), Materials Research Society Symposium Proceedings, Vol. 60, Pittsburgh: Materials Research Society (1986), p. 515.

4. M. B. Lewis, et al., Nuclear Instruments and Methods, 167 (1979) 233.

5. L. L. Horton, J. Bentley, and M. B. Lewis, Nuclear Instruments and Methods, B 16 *(1986)* 221.

6. U. C. Oliver, C. J. McHargue, and S. J. Zinkle. Thin Solid Films, 153 (1987) 185.

7. S. J. Zinkle, submitted to Journal of the American Ceramic Society (July 1988).

8. F. W. Clinard. Jr., G. F. Hurley, and L. W. Hobbs, J. Nucl. Mater. 1086109 (1982) 655.

9. H. Laramie. S. J. Zinkle, and R. C. Bradt, manuscript in preparation.

10. T. E. Mitchell, M. R. Pascucci, and R. A Youngman, Proc. 40th Annual EMSA Meeting, (1982), p. 600.

11. S. Kobayashi, T. Hioki, and O. Kiamigalto, Proc. XI Int. Cong. on Electron Microscopy, Kyoto (1986), p. 1303.

DOE/ER-0313/5
Distribution
Categories
uc-423. -424

DISTRIBUTION

1–16. Argonne National Laboratory, 9700 South Cass Avenue, Argonne, IL 60439

M. C. Billone
O. K. Chopra
R. G. Clemner
D. R. Diercks
P. A. Finn
A. K. Fischer
L. R. Greenwood
C. E. Johnson
Y. Y. Liu
B. A. Loomis
R. F. Mattas
L. A. Niemark
O. L. Smith
S. W. Tam
E. R. Van Deventer
H. Wiedersich

17. Argonne National Laboratory, EBR-II Division, Reactor Materials Section, P.O. Box 2528, Idaho Falls, ID 83403-2528

D. L. Porter

18. Arizona State University, Department of Mechanical and Aerospace Engineering, Tempe, AZ 85281

W. A. Coghlan

19. Auburn University, Department of Mechanical Engineering, Auburn, AL 36849

B. A. Chin

20–35. Battelle–Pacific Northwest Laboratory, P.D. Box 999, Richland, WA 99352

J. L. Brimhall
D. G. Doran (5)
M. D. Freshley
F. A. Garner
D. G. Gelles
M. L. Hamilton
H. L. Heinisch
G. W. Hollenberg
R. H. Jones
B. D. Shipp
O. D. Slagle
J. L. Straaslund

36. EG&G Idaho, Inc., Fusion Safety Program, P.O. Box 1625, Idaho Falls, ID 83415-3523

D. F. Holland

37-38. Carnegie Institute of Technology, Carnegie–Mellon University. Schenley Park, Pittsburgh, PA 15213

W. M. Garrison, Jr.
J. C. Williams

39-42. GA Technologies, Inc., P.O. Box 85608, San Diego, CA 92138

J. Baur
G. R. Hopkinr
T. A. Lechtenberg
D. I. Roberts

43-44. General Dynamics Corporation, 5001 Kearny Villa Road, San Diego, CA 92138

T. L. Cookson
V. Stegar

45. General Electric, Advanced Nuclear Technology Operation, 310 Deguine Drive, Sunnyvale, CA 94088

S. Vaidyanathan

46. Georgia Institute of Technology, School of Textile Engineering, Atlanta, GA 30332

D. S. Tucker

47. Grumman Aerospace Corporation, c/o TFTR Project, Princeton Plasma Physics Laboratory, Princeton University, A. Site, Building I-E, Princeton, NJ 08540

R. G. Micich

48-50. Lawrence Livermore National Laboratory, P.O. Box 808, Livermore, CA 94550

E.N.C. Oalder
M. Guinan
J. Perkins

51–59. Los Alamos National Laboratory, P.O. Box 1663, Los Alamos, NM 87545

J. L. Andersen
L. D. Caudill
D. J. Dudziak
H. M. Frost
F. W. Clinard
G. Hurley
C. D. Kise
R. Liepens
T. Zocco

60. Manlabs, Inc., 231 Erie Street, Cambridge, MA 02139

D. Tognarelli

61. Massachusetts Institute of Technology, Department of Metallurgy and Materials Science, Cambridge, MA 02139

L. W. Hobbs

62. Massachusetts Institute of Technology, 138 Albany Street, Cambridge, MA 02139

O. K. Harling

63–64. Massachusetts Institute of Technology, 77 Massachusetts Avenue, Cambridge, MA 02139

I-Wei Chen
N. J. Grant

65–66. Massachusetts Institute of Technology, Plasma Fusion Center Headquarters, Cambridge, MA 02139

H. D. Becker
D. B. Montgomery

67. McDonnell-Douglas Astronautics Company, East, P.O. Box 516, Bldg. 92, St. Louis, MO 63166

J. W. Davis

68–69. National Institute of Standards and Technology, Boulder, CO 80302

F. R. Fickett
M. B. Kasen

70. National Materials Advisory Board, 2101 Constitution Avenue, Washington, DC 20418

K. M. Zwilsky

71. Naval Research Laboratory, Washington, DC 20375

J. A. Sprague

72–136. Oak Ridge National Laboratory, P.O. Box 2008, Oak Ridge, TN 37831

Central Research Library
Document Reference Section
Laboratory Records Department (2)
Laboratory Records - RC
Patent Section
D. J. Alexander
J. Bentley
E. E. Bloom
D. N. Braski
T. D. Burchell
M. L. Grossbeck
I. Inazumi
S. Hamada
R. L. Klueh
Eal Lee
A. W. Longest
L. K. Mansur
P. J. Mariasz
T. K. Roche
A. F. Rowcliffe (35)
J. Sheffield
S. Sawai
R. L. Senn
R. E. Stoller
K. R. Thorns
P. T. Thornton (2)
P. F. Tortorelli
F. W. Wiffen
S. J. Zinkle

137–139. Princeton Plasma Physics Laboratory, Princeton University, P.O. Box 451, Princeton, NJ 08540

J.P.F. Conrads
H. Furth
Long-Poe Ku

140. Rensselaer Polytechnic Institute, Troy, NY 12181

D. Steiner

141. Rockwell International Corporation, NA02, Rocketdyne Division, 6633 Canoga Avenue, Canoga Park, CA 91304

D. W. Kneff

142-143. Sandia National Laboratories, P.O. Box 5800, Albuquerque, NM 87185

M. J. Davis
W. B. Gauster

144-145. Sandia National Laboratories, Livermore Division 8316, Livermore, CA 94550

W. Bauer
W. G. Wolfer

146. San Diego State Univ., Mechanical Engineering Dept., San Diego, CA 92182-0191

L. O. Thompson

147-148. University of California, Department of Chemical and Nuclear Engineering, Santa Barbara, CA 93106

G. E. Lucas
G. R. Odette

149-151. University of California, Department of Chemical, Nuclear and Thermal Engineering, Los Angeles, CA 90024

M. A. Abdou
R. W. Conn
N. M. Ghoniem

152. University of California, Los Alamos National Laboratory, P.O. Box 1663, Los Alamos, NM 87545

T. Zocco

153. University of Michigan, Department of Nuclear Engineering, Ann Arbor, MI 48109

T. Kammash

154. University of Missouri, Department of Nuclear Engineering, Rolla, MO 65401

A. Kumar

155. University of Wisconsim, Nuclear Engineering Dept., 1600 Johnson Drive, Madison, WI 53706

G. L. Kulcinski

156-161. Westinghouse Hanford Company, P.O. Box 1970, Richland, WA 99352

H. D. Brager
A. M. Ermi
G. D. Johnson
F. M. Mann
R. J. Puigh
R. L. Simons

162. Department of Energy, Oak Ridge Operations Office, P.D. Box 2001, Oak Ridge, TN 37831

Assistant Manager for Energy Research and Oevelopment

163-166. Department of Energy, Office of Fusion Energy, Washington, DC 20545

S. E. Berk
J. F. Clarke
M. M. Cohen
T. C. Reuther

167-216. Department of Energy, Office of Scientific and Technical Information, Office of Information Services, P.O. Box 62, Oak Ridge, TN 37831

For distribution as shown in DOE/TIC-4500, Distribution Categories UC-423 (Magnetic Fusion Reactor Materials) and UC-424 (Magnetic Fusion Energy Systems)